The University of Adelaide
Department of Geology and Geophysics

Automatic Interpretation of Potential Field Data Applied to the Study of Overburden Thickness and Deep Crustal Structures, South Australia

Zhiqun Shi

November 1993

A thesis submitted to the University of Adelaide
in fulfillment of the requirements for the degree of
Doctor of Philosophy

Awarded 1994

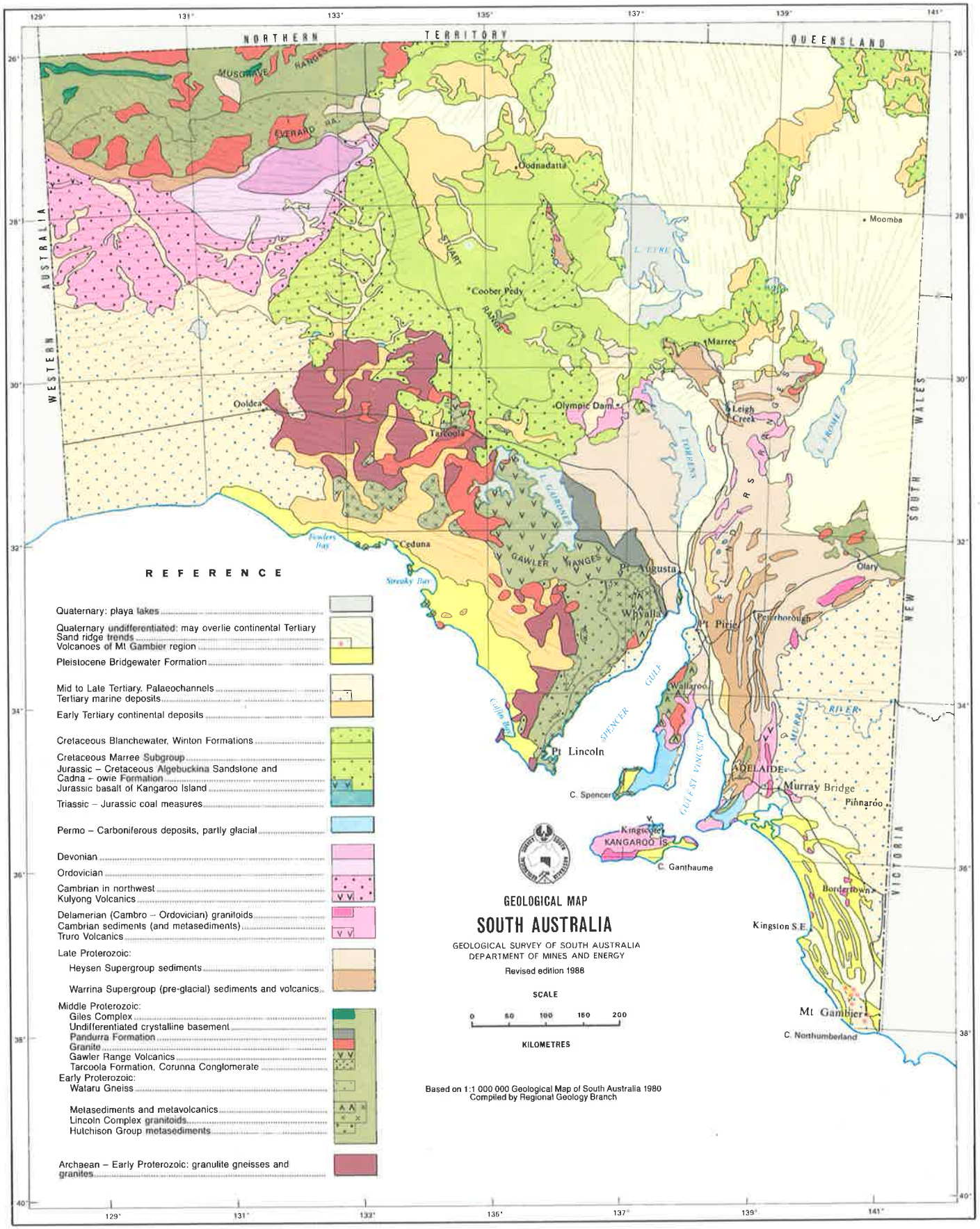

Plate 1: Geological Map of South Australia.

Contents

List of Figures

List of Tables

Abstract

Determination of overburden thickness is important in geology and mineral exploration.

AUTOMAG, a computer program system which was developed by the author from the original Naudy technique and applied to high resolution magnetic data, provides an effective way of determining the thickness of overburden and the weathered zone in areas of metamorphic and igneous basement rocks. The method also can be applied to much greater depths, e.g. magnetic basement underlying sedimentary basin.

AUTOMAG which uses a SUN SPARC 2 workstation and VAX-780 computer is at least five to ten times as fast as several standard methods of depth estimation used by the exploration industry and it also yields width, dip and susceptibility of magnetic causative bodies. The results are presented as a series of sections showing magnetic profile, similarity coefficients and estimated depths.

AUTOMAG has been tested on simple and complex synthetic data, using a set of basic models (dyke and edge with finite depth extents, and an extended thin plate model) designed to be suitable for most geological situations. The results from airborne magnetic data have been compared with the information obtained from a ground magnetic survey and drill holes in the Eyre Peninsula, South Australia; this shows that AUTOMAG provides reliable information about the thickness of overburden.

Spectral analysis was used with gravity data provided by the South Australian Department of Mines and Energy in the Eyre Peninsula area ($30°S$ to $35°S$ and $133°E$ to $139°E$) to determine the density structure of the crust. Applying an anomaly separation filtering in the frequency domain and combining with the information from the energy spectra of the Bouguer gravity data, several depth slice maps in the study area have been constructed. Depth estimations determined from spectral analysis in the Eyre Peninsula area indicate a density boundary which is between 32 to 38 kilometres deep. This is consistent with previous seismic estimations of the depth of the Mohorovičić discontinuity in this area. Felsic Gawler Range Volcanics are underlain by dense rocks, which may be a large, zoned, mafic magma chamber of underplated mantle material.

Suggestion for further work to develop AUTOMAG and spectral analysis technique are made in Chapter 8.

Statement

To the best of the author's knowledge and belief, and except where reference is made herein, this thesis contains no material previously published or written by another person, nor any material that has been accepted for the award of any other degree or diploma in any University.

If this thesis is accepted for the award of the degree, the author consents to the thesis being made available for photocopying and loan.

Zhiqun Shi
June 1993

Acknowledgements

This work was carried out with the assistance of a postgraduate scholarship from the South Australian Department of Mines and Energy from June 1989 to June 1993 (in the last 6 months the project was supported by Professor Boyd from his consulting fund). I wish to gratefully acknowledge SADME, for both the scholarship and supplying the aeromagnetic data on which the thesis is based, and I especially thank Mr. Reg Nelson, for providing me with the opportunity to undertake this project.

I am extremely grateful to my supervisor, Professor David Boyd, who provided constant support in all aspects of my research and greatly encouraged as well as astutely guided me throughout the entire period of my PhD study. He spent a lot of time in carefully reading and correcting the manuscript as well as giving me many fruitful and inspiring suggestions. Without his help and support I would not have been able to complete my thesis.

I am indebted to Dr. Shanti Rajagopalan, who now is my internal supervisor after Professor Boyd's official retirement. She also gave me support in many different ways and her warmth and enthusiasm gave me much encouragement. I am grateful for many stimulating discussions and critical review of the manuscript.

I wish to gratefully acknowledge Dr. David Tucker, who first suggested to me this interesting project (automatic depth estimation). During the first two years of my study we worked together on a SADME project. He taught me a lot of practical geophysics and field geology and also gave me many useful suggestions. I wish to express my grateful acknowledgement for his and his wife Marilyn's constant encouragement, help and friendship. I also wish to thank Dr. John Parker for his helpful discussions about the geology in the study area.

I thank Professor Colin Reeves for his careful and critical review of my thesis. I have amended my thesis to take account of the matters which he raised.

I wish to extend my special acknowledgement to Ursula McGowan of the ACUE, at the University of Adelaide, who helped me to learn about the organisation and principles of a thesis and guided me in the development of the academic English required for this thesis. She was very patient and always encouraged me. With her consistent help I have greatly improved in fluency in the English language. I also would like to thank Timothy Gent and Vivian Hope for helping me in a difficult moments.

I am indebted to Dr Peter Brooker, who helped me in many ways during my doctorate

research. I would also like to thank him very much for his careful review of part of my thesis and for his critical and helpful suggestions.

I wish to thank John Pitt, Dr. Chris Tarlowski, Dr. Tom Whiting, Brian Minty, David Clark, Dr. Atchuta Rao, Lee Rankin, Wayne Cowley and Alan Appleton for their helpful information and useful discussions concerning my project.

I wish to acknowledge Dr Shaohua Zhou for advice on the use of LaTeX and other aspects and to thank Nick Spencer who carefully reviewed part of my thesis. I also would like to acknowledge John Willoughby, Andy Mitchell, Dr. John Foden, Dr. Gabor Korvin, Chris Farmer, Don Creighton and Phil McDuie, who gave me help in geophysics or geology or computing. I also wish to thank Richard Barrett for photographic work for department seminars and Sherry Proferes for advice on drafting.

I am grateful to this Department, the Computing Centre of the University and also the National Centre for Petroleum Geology and Geophysics for providing computing facilities. I wish to thank Professor Larry Frakes, Dr. Pat James and Dr. Vic Gostin, who during their respective tenure as the Chairman of this Department extended all possible support. I would also like to thank Mary Odlum, Bronwyn Elliott, Sophie Craddock for their friendly assistance and cooperation.

I would like to express my thanks to the Beijing Computer Center of the Ministry of Geology and Mineral Resources in China, for giving me an opportunity and initial support in undertaking study in Australia. Professor Hou Chongchu of the Beijing Computer Centre passed away in May, 1992. She trained me in potential field theory and was my mentor for twelve years. Professor Hou was interested in the progress of my research and gave me useful suggestions. I shall always remember Professor Hou with great respect. I consider myself very fortunate that I had the opportunity to work alongside this illustrious geophysicist. Professor Shen Ninghua, of the University of Changchun Geology in China, has been my guide for many years. We have had interesting discussions concerning spectral analysis method and I would like to thank her for the benefit of her guidance and general advice on geophysics.

I wish to extend my appreciation to fellow postgraduate students during the past few years: Shanti Rajagopalan, Andrew Lewis, Robert O'Dowd, Shaohua Zhou, Kathy Stewart, Irena Kivior and Mohammad Haidarian. I specially thank Irena; we have similar projects and our work overlapped. A close friendship and many helpful discussions have benefited both of us.

Finally I would like to acknowledge the wonderful support and encouragement from my husband Yukang Chen and my beloved daughter Lin. I also want to express my thanks to my parents, brothers and sisters, especially my brother Zhicheng Shi who helped me check my mathematical derivations. Without their patience, understanding, encouragement and help, I would not have been able to complete this thesis.

Plate 2:

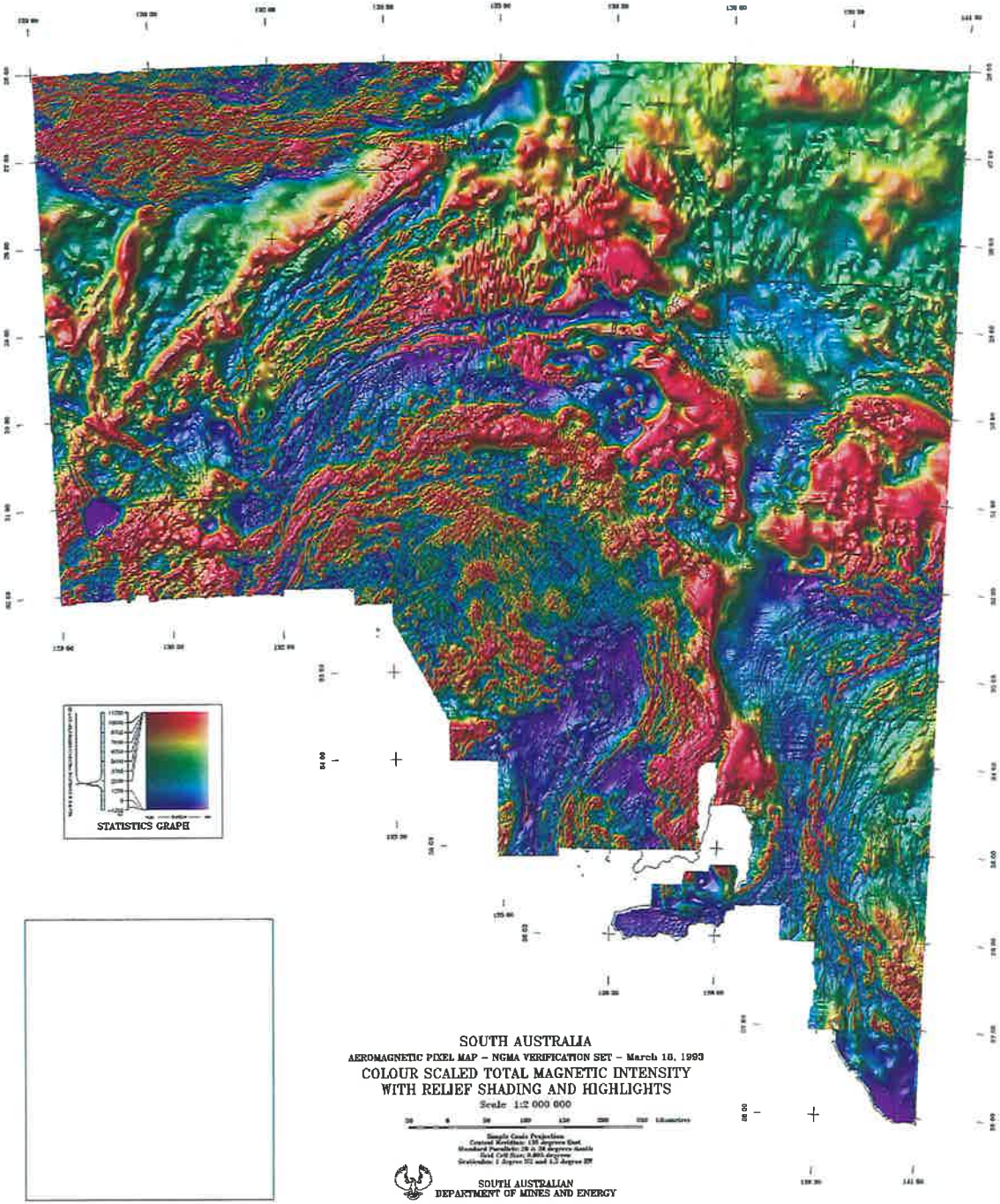
STATISTICS GRAPH
SOUTH AUSTRALIA
AEROMAGNETIC PIXEL MAP – NGMA VERIFICATION SET – March 16, 1993
COLOUR SCALED TOTAL MAGNETIC INTENSITY
WITH RELIEF SHADING AND HIGHLIGHTS
Scale 1:2 000 000
SOUTH AUSTRALIAN
DEPARTMENT OF MINES AND ENERGY
Flight path plot of map source data

Part I

Background

Chapter 1

Introduction

1.1 Aim and scope of the thesis

1.1.1 Aim of the research

This research project is concerned with two problems: the geological problem of superficial deposits which can totally obscure the underlying solid rocks and a geophysical problem of how to estimate the thickness of the superficial deposits and find out information about the geology underneath.

The aim of this research has been to find a fast and economical way to estimate the thickness of the material which lies above the metamorphic and igneous rocks which are such an important part of the geology of the Australian continent and so provide a tool to solve the geological problem.

The need for this research is evident in the western part of the state of South Australia where there are many large areas in which less than 0.1% of the solid rock can be seen at the surface (see Plate 1). Geologists must be able to see the rocks in order to make their predictions about the scientific or economic significance of the area. If the cover is thin it may be easy to obtain geological information from the surface; if the cover is thick then other more expensive methods of investigation must be employed. It is important to know which problem faces the geologist when plans to investigate the area are made. The same problem occurs in every state in Australia and in every country in Asia, Europe, Africa and America. If an effective solution to the problem can be found it will be useful in 20% to 30% of the continental areas of the world.

The development of a fast and cheap solution to the problem will be of direct benefit in many forms of geological exploration; it will be of benefit to mineral exploration companies to know where the soil cover is thin and hence easiest area to explore, to hydro-geologists looking for depressions in the zone of weathering and to engineers concerned with establishing sound foundations for their structures.

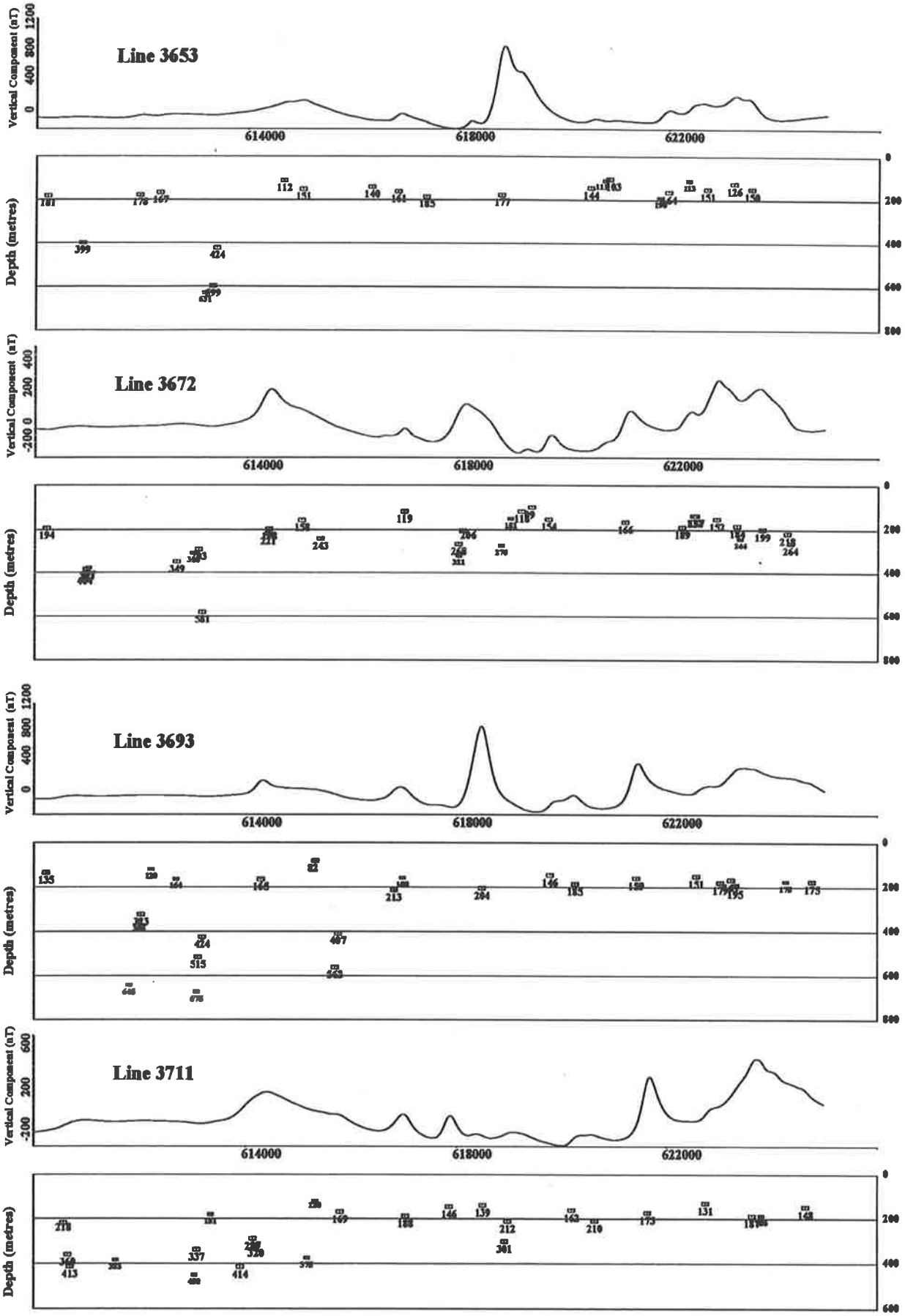

Figure 1.1: Magnetic anomalies and depth estimates using AUTOMAG in Bunora, Kimba, results from component data.

The starting point of the research was the recognition of the geological problem associated with superficial deposits; in some cases it is enough to know where the cover is thin and where it is too thick to find out easily what is underneath but in many cases it is necessary to be able to estimate the thickness of the cover and to identify changes in the thickness.

Figures 1.1 and 1.2 (from Chapter 7) present the results obtained from the use of AUTOMAG, the system developed to solve this problem. The figures show quite clearly that the primary aim of the research has been achieved.

1.1.2 Scope of research

To be effective research must be carried out within a wider context. To achieve the specific aim of the research the more general problem of estimation of depths using potential field data has been investigated and some of the results obtained can be applied to different types of geological problems. Spectral analysis of the data was carried out as a preliminary step in order to establish the initial parameters for automatic depth determination and a development of the same approach can be and has been applied to gravity data to outline anomalous bodies within the upper and lower crust. The principle of the method is the same, only the scale is different. Some of this work has been presented in Chapter 6; it has also led to a separate study of the structure of the upper and lower crust in South Australia using regional aeromagnetic data. The results of this work has been presented at a conference in Moscow in August 1993 (Boyd, Shi and Kivior, in press). This work is also related to the design of frequency filters for the aim of separating anomalies from different depth levels and providing depth slice maps.

In order to use the method developed in this research effectively it is essential to prepare contour maps and images of the whole data set in order to subdivide the region into parts with different character, each area requiring its own special treatment. This was done by producing conventional contour maps and images of reduction to the pole, pseudo gravity, vertical gradient, upward continuations and shaded relief of the magnetic field. As these maps can be used for a more geological oriented form of interpretation they are included in this thesis (see Section 7.2), so that they are at the disposal of other researchers who wish to study this area. A number of computer routines were written especially to produce these maps and images (see Appendix C) and are now in common use within the Department of Geology and Geophysics, the University of Adelaide.

1.2 The geological problem

The essence of the geological problem has already been stated in Section 1.1.1 above. Very large areas of metamorphic and igneous rocks, which could be the host to mineral deposits, are covered by a few tens or hundreds of metres of soil or sediments. Much of the geological work requires that geologists can obtain and examine specimens of rock, preferably of fresh rock, and this and further investigation and exploitation is usually done most easily and economically

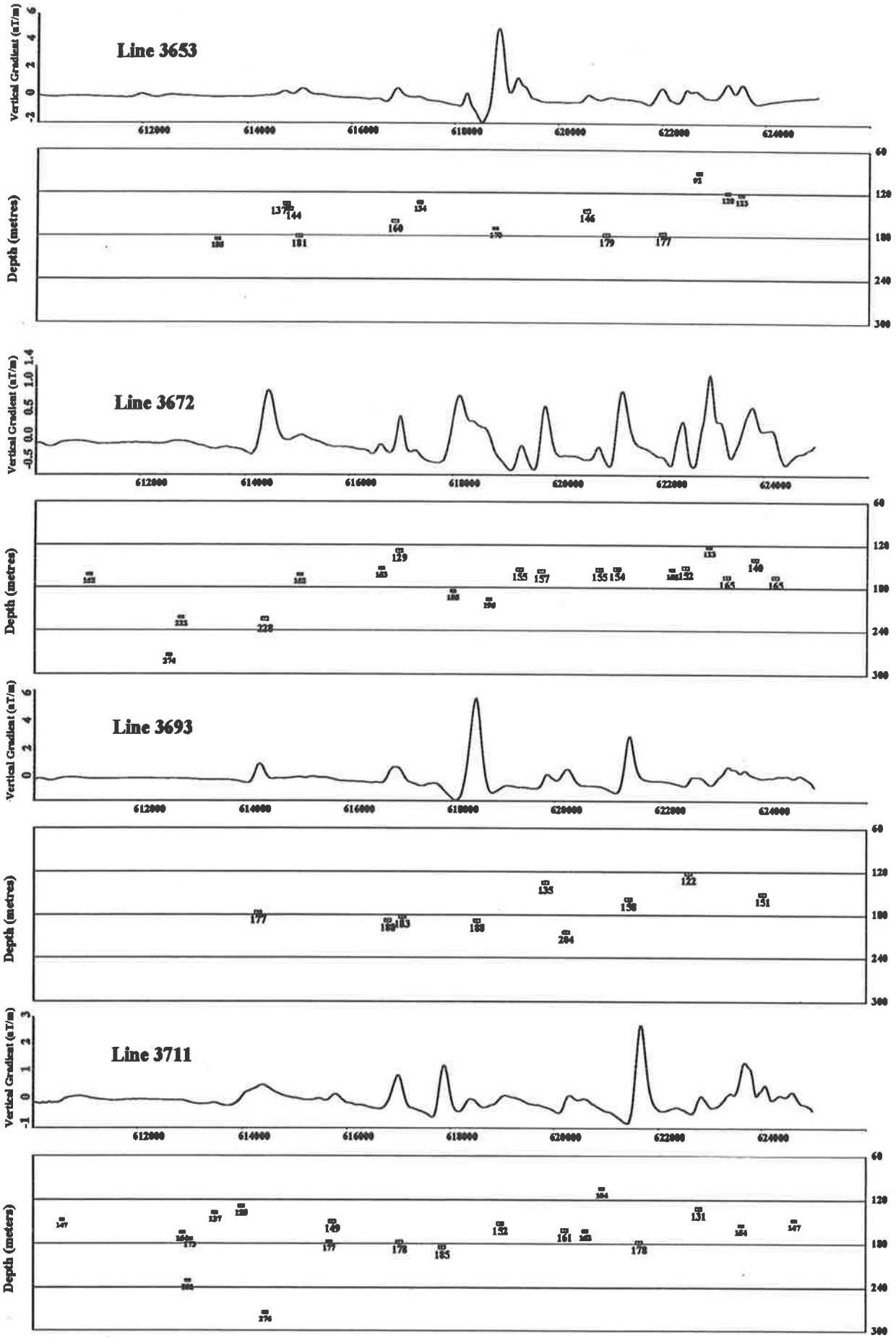

Figure 1.2: Magnetic anomalies and depth estimates using AUTOMAG in Bunora, Kimba, results from vertical gradient.

where the overlying cover is thin, preferably a few tens of metres thick. It is important to be able to find out in areas such as the Gawler Craton which lies in the western part of South Australia and where the solid rocks are almost totally obscured by a thin layer of soil and sediments, those areas where the cover is less than 100 metres thick and where it is thicker.

Magnetic surveys have been widely used, especially in petroleum exploration, for well over fifty years to provide this kind of information in many parts of the world. The method works because the sediments are usually not magnetic and the underlying basement rocks frequently are strongly magnetic.

The particular problem to be solved in South Australia is slightly more complicated. The upper part of the metamorphic and igneous basement rocks lying below the cover of sediments is usually weathered to a depth of at least thirty or forty metres so that depth estimates using magnetic methods may provide information not about the depth to the top of the basement rocks but rather the depth to the top of less weathered basement rocks. The magnetic method is only a partial answer to the problem.

In addition the sedimentary cover may contain magnetic material. Maghaemite is found in lateritic soils and in the stream channels and this produces anomalies which can interfere very seriously with the anomalies which contain the information about the depth to weathered or unweathered basement.

The complexity of the distribution of magnetic minerals means that this is not a trivial geophysical problem.

1.3 The geophysical problem

The starting point to devising a solution is the knowledge that magnetic methods have been used for fifty years or more to provide an estimate of the thickness of sediments for petroleum exploration. The same principle can be applied to making estimates of the depth of fresh magnetic basement rocks lying below the cover, provided high quality magnetic survey data are available on magnetic tape. Many millions of kilometres of such data have been collected by aircraft in Australia for the last two decades (see Plate 2). The biggest problem is the time required to interpret so much aeromagnetic data using the old fashioned manual methods, and the need was evident to do this either automatically or semiautomatically.

This is not an easy problem because the depths must be estimated with considerable accuracy to be useful and various errors are introduced because of assumptions which have to be made about the shapes of the magnetic bodies and the effect when the strike of the bodies is not at right angles to the direction of the flight of the aircraft. The shallow depths make this a more difficult problem than faced in petroleum exploration when basement depth may be two or more kilometres.

It is important too that the process of interpretation should not be over elaborate and the

results of the interpretation must be presented in a form that is readily assimilated by the non-specialists who will use the results.

Progress of the research was complicated by having to change from one computer system to another during the project or in having to use one system, the SUN SPARC 2 workstation for the computation and a second one, the VAX-780 for the presentation and printing of the results.

1.4 The geophysical program

The choice of research project was determined by the world-wide importance of the problem.

The section of the region where the work was carried out was influenced by the availability of 85,000 km^2 of high quality low level aeromagnetic data which were obtained for the South Australian Department of Mines and Energy (SADME) working in conjunction with the Bureau of Mineral Resources (now the Australian Geological Survey Organisation) in 1988 by Geoterrex Pty. Ltd. of Sydney.

This data set provided the standards of high resolution data and examples of the real problems which must be understood if the method was to be of practical value. The whole data set was processed and much work done which does not appear in the thesis because, although the experience influenced the final outcome of the work, the total bulk would overwhelm readers and obscure the important results.

Ground surveys were carried out with the support from SADME in 1989 and 1990. These surveys provided ground magnetic traverses which could be compared with airborne profiles and the opportunity to collect rock samples whose magnetic properties were measured.

The results of some of the work have been presented at the ASEG conferences in Sydney 1991 (Shi, 1991a) and put into a report for SADME (Shi, 1991b).

1.5 Organisation of the thesis

The results of the research carried out are presented in the conventional manner.

A review of methods used for manual and automatic interpretation of magnetic data already in use is presented in Chapter 2. The theory and developments of the Improved Naudy Technique as AUTOMAG, an automatic interpretation system which was selected as the most appropriate way to solve the problem is set out in Chapter 3. The examination of the reliability and error of the method carried out using synthetic data over simple and complex models is described in Chapter 4.

In Chapter 5 two techniques (spectral analysis and separation filtering) are applied to a set of synthetic data from theoretical models, simulated to real gravity data.

In Chapter 6 an account is given of the applications of the techniques to the regional gravity data in Gawler Craton. The mathematical basis of this work was initially a by-product of the work done to determine the best initial parameters to use for AUTOMAG, but information about hidden bodies at depth within crust is also part of the wider need to provide context to all geophysical interpretation.

Chapter 7 provides an account of AUTOMAG developed to provide a rapid and economic estimate of the overburden thickness and examples of the actual results obtained.

Although AUTOMAG may still be regarded as a prototype, the most difficult part of the problem has been solved. What is now required is

1. wide scale testing of the method in areas where conditions are different and where there is sufficient additional information from drilling or seismic surveys to test the reliability of the method and
2. some refinement of the program to make it easier to use.

1.6 The appendices

A considerable part of the time spent on this project was concerned with studies including field work which are essential for providing the wider background in which the work is done or in improving or adapting already developed techniques to the particular requirement of this research.

As this work is complementary to the central project the account of them is given in a series of appendices and not in the main text. The brief summaries of the appendices are given.

- Appendix A presents the formulae for magnetic field, including total field, vertical & horizontal components and gradients arising from various simple models e.g. edge, step, dyke, thin sheet, horizontal thin sheet, thin plate and horizontal cylinder. The derivations were based on Reford's work (Reford, 1978). In the formulae, symmetrical and anti-symmetrical components for each field (where applicable) are analysed, which can be applied for Naudy technique (Naudy, 1971).
- Appendix B shows the detailed derivation of the effective magnetic field which is useful for processing profile data. The original work is from Gay (Gay, 1963).
- Appendix C summarises all the programs used in this thesis. Most of these programs are written by the author. Other programs were written by J. Pain, S. Rajagopalan, A. Mitchell, R. Almond and A. Lewis.
- Appendix D reveals a relationship of magnetic fields from a thin plate and a slab model, which was used to establish a new basic model of thin plate in AUTOMAG. Magnetic

fields from this specific slab model which has a thickness equal to the depth to the top of the body are highly close to the magnetic fields from a thin plate, in which the ratio of two depths (from thin plate to slab) is $\sqrt{2}$; width and dip are the same; and products of the thickness and susceptibility are the same.

- In Appendix E, two methods were developed for correcting effects of estimated parameters (depth, width, dip and susceptibility) obtained from interpretation methods of 2-D bodies from which an oblique strike to the profile direction exists. The corrections significantly improve the results of estimates which are obtained from an interpretation method under the assumption that the strike of the body is perpendicular to the profile direction.

  This development in particular calls for mention. As no full account has been found in the literature, the correction has been developed from first principles.

- Appendix F presents the measured densities and susceptibilities of rock samples in the study area, the Eyre Peninsula. The rocks were collected by SADME, K. Stewart and the author and most measurements were made by the author.

- In the last appendix G, a study of shaded relief technique is presented. The author analyses all functions of factors in this technique and provides some suggestions for effective use of this powerful and popular technique.

Chapter 2

Review of interpretation methods

A typical aeromagnetic survey includes thousands of anomalies caused by a variety of magnetic sources. The ultimate aim of the geophysicist is to interpret as many anomalies as possible and thus determine the geometrical and geophysical properties of the different sources. The problem of selecting the right geometry and then solving for the parameters is compounded by interference from nearby magnetic sources and superposition from magnetic sources at different depths. Note however that even when an exact match between observed and modelled data is obtained, the problem of non-uniqueness or ambiguity is inherent in every method applied to the interpretation of geophysical surveys (Skeels, 1947; Roy, 1962).

This chapter reviews commonly used interpretation methods, eliminates unsuitable ones, and finally selects the most suitable methods for this research. Developments of interpretation methods have kept pace with the improvements in instruments used for surveys and collection of data, and with developments in computer software and hardware. The examples given below demonstrate the evolution of interpretation methods in relation to developments in computer science.

2.1 Computer technology and interpretation methods

From the first airborne magnetic survey in 1944 up to the present day, techniques of data interpretation have changed significantly. In the early days, geophysicists analysed individual anomalies by using simple techniques such as graphical and characteristic point methods which are only suitable for well resolved anomalies arising from single sources. The advent of computers has dramatically changed the whole geophysical field. Since 1960, when digital computers started to be used in geophysical exploration, geophysicists turned to computers to process and interpret geophysical information. As computing speed increased, a number of new techniques began to be used instead of the traditional data processing and interpretation methods (Clement, 1973). High speed computers have also stimulated much interest in computer graphics and person-machine interaction systems and forward and inversion modelling techniques began to be developed (Wuenschel, Treitel, Flinn, Keller and Pickett, 1969). In 1971 several automatic

depth estimation methods were applied to aeromagnetic profile data (Hartman *et al.*, 1971; Naudy, 1971; O'Brien, 1971). In recent years, as the availability of high speed, large memory personal computers improved and the application of software packages increased there were advances in forward modelling and inversion techniques. One of the best examples to show the link between new techniques and computer sophistication is the fast Fourier transform (FFT) technique.

Before computers became common in the workplace, the interpretation of potential field data was carried out primarily in the space domain although a few authors (Tsuboi, 1939; Nagata, 1938a; Nagata, 1938b; Dean, 1958) considered working in the frequency domain. The revolution of the computer shook the foundations of traditional interpretation methods, especially when Cooley and Tukey (1965) rediscovered the fast Fourier transform technique (Naidu, 1969). This technique influenced many scientific fields as well as the area of geophysics. At that time the speed of computation and the memory capacity of the computer were greatly restricted and it was very difficult to compile and process a great amount of data. However by using FFT technique these difficulties were reduced, and methods of processing and the interpretation of potential field data were greatly developed during the decade from 1965 to 1975.

The advantages of working in the frequency domain by using FFT technique are summarized below.

1. Expressions of potential fields in the frequency domain are much simpler than those in the space domain. It is well known that expressions in the **space domain** are formed as **convolutions** of factors depending on the type of observed field, the geometry of the causative body and the physical property of the body. In the **frequency domain** these expressions are given as **products** of the factors. Therefore by working in the frequency domain, transformations between different types of fields and operating filters are made easy. When multiple conversions and computations are necessary, then the speed of processing in the frequency domain is faster than processing in the space domain.

2. It is not just expressions of fields in the frequency domain that have simple representations, but expressions of model fields can be also simplified. Each model can be expressed as a product of different type of factors, such as physical property, depth, thickness, horizontal size and so on. Therefore some parameters of models can be determined easily in the frequency domain.

2.2 Overview of interpretation methods

Many interpretation methods have been developed for estimating depths of geological bodies. While certain methods are used to solve simple shaped anomalies, others may be required for complex anomalies. Most complicated geological structures can be represented by a combination of some simple geometrical models such as edge, dyke, plate, thin sheet, pipe, cylinder, sphere or dipole (examples of the geometries are given in Appendix A). However, some magnetic or gravity

Table 2.1: Interpretation methods in potential field

No.	Method	Application		Comments
		Profile	Grid	
1	Graphical including curve matching	•		
2	Characteristic point	•		uses information points, maxima, minima, etc.
3	Forward modelling	•	•	Model single anomaly each time to build a cross section or a grid
4	Inversion method	•	•	Use matrix inversion, special techniques to solve equation
5	Spectral analysis	•	•	Regional depth estimates for an area or a profile
6	Automatic depth determination including			
a	Euler deconvolution	•	•	Automatically identify location of an anomaly, then estimate depth or other parameters
b	Werner deconvolution	•		
c	Naudy technique	•		

anomalies are caused by geological bodies which may not be represented as simple models but should be dealt with as an ensemble statistical model.

A variety of methods are available as follows (see Table 2.1). All the methods shown in the Table 2.1 deal with interpretation of an anomaly arising from a simple body. For the analysis of complex magnetic anomalies, only two of these, viz. modelling (forward and inversion method) and spectral analysis, are appropriate. In this chapter four methods are specially emphasised. These are forward modelling, spectral analysis, Werner deconvolution and the Naudy technique.

2.3 Graphical and characteristic point methods

In the decade from 1950 to 1960, the favoured interpretation methods for dealing with potential field anomalies were graphical and characteristic point (e.g. Nettleton, 1942; Peters, 1949; Cook, 1950; Sokolov, 1956; Vacquier *et al.*, 1951; and others). In general, these methods use a number of special points and a section of the anomaly curve to obtain horizontal distances or amplitude from the maximum slope, half maximum slope or straight slope, and the maximum, minimum, inflection or other characteristic points of profile data. These distances are then converted into the depth to top, width, or other parameters. These methods are simple and

convenient and often only a pencil and a ruler are needed to work directly on profile data in order to obtain estimates of the parameters. The main problem with these methods is that the methods only use limited information from an anomaly. Thus, serious errors may result from either noise influence or interference from adjacent anomalies. As the methods are based on simple source geometries (e.g. dyke, plate, etc.), the method will not yield appropriate answers in cases where the model is not a good match for the geology.

In order to overcome the problem of the methods being suitable only for simple models, Smellie (1956), Paterson and Faessler (1957), and Hall (1959) prepared more complex interpretation curves of various models which included the point pole and dipole, the line of poles and dipole, and other models. However the problems of limited data being used, and effects from noises and neighboring anomalies were not addressed at that time.

The curve matching technique was developed to tackle these problems. The technique was to use the entire profile of the anomaly to match a set of theoretical master curves from various models with variable parameters. When the observed data had a good match with a theoretical curve, the parameters of the body were determined. The method provided a good prospect for interpreting the measured field data (Hutchison, 1958; Gay, 1963; Ackerman and Reford, 1962; Grant and Martin, 1966). This method is very slow to apply. Another problem was that the method was only suitable for anomalies caused by simple model sources, but not for more complex model curves caused by complicated geological cases. These problems were difficult to solve until high speed computers were widely available for use.

By the middle of the 1960s, when high speed computers had been developed and were being used in large geophysical companies and universities in the western countries, new processing techniques and interpretation methods quickly developed. The forward modelling method is an extension of the curve matching method. It overcame most of the drawbacks mentioned above. Computers provide accurate and fast facilities to establish various model curves. The forward modelling method has replaced the old 'cut and try' technique (graphical and characteristic point method) and is widely used in geophysical areas (Wuenschel *et al.*, 1969).

2.4 Forward modelling

The development of the forward modelling method has been flourishing since the late 1960s. In 1976 Levin *et al.* described the development of the forward modelling method in detail. At the time of the introduction of inexpensive interactive terminals, the efficiency of potential field modelling functions improved, because curves of models and observed anomalies could be displayed on the screen simultaneously. The interpreter could easily change the parameters of the model thought to be appropriate for the measured anomaly. Complicated models could be matched to complex anomalies.

Forward modelling is a very effective and convenient interpretation method. The first step is to look at the field data and then choose a model type which seems appropriate. Generally computer programs provide a choice of models which may be used. The second is to input a set

of parameters of the starting model. The computer then constructs a theoretical profile curve or a contour map. Comparing the profile or the gridded data of the theoretical model with the observed profile or areal data follows. If the match is satisfactory to the interpreter, the parameters of the model are presumed as the solution for the geological body of the measured data. If the match is unsatisfactory, the parameters of the model are changed and another set of model data is constructed and then compared with the observed data. This 'trial and error' procedure is repeated until a satisfactory answer is obtained. The method is suitable for very simple anomalies and also for anomalies caused by very complex geological bodies.

In summary, the forward modelling method can provide very satisfactory results for the interpretation of gravity and magnetic anomalies. The method can be made more powerful by adding an inversion algorithm (see Section 2.5) to refine model parameters. However the method is time consuming and it cannot provide fast solutions when dealing with data from a large area. Another problem is the non-uniqueness of the solution though this problem can be minimized by adding appropriate geological constraints.

2.5 Inversion method

Inversion and forward solution methods represent the opposite extremes of approaches to geophysical interpretation. The solution of the forward problem is to find an anomaly from a given geological structure, but the inversion problem is to obtain the geometry and physical properties giving rise to the anomalies, under certain constraints (Pedersen, 1977). While any interpretation method which provides geometric parameters and physical properties of causative bodies from its anomaly may be considered an inversion method, the term "inversion" reviewed here is specifically reserved for techniques using generalised matrix inversion or linear or non-linear programming or optimisation algorithms.

Essentially in an inversion method, the problem is stated as a system of equations relating the source parameters X to the field observations F. For a given model, the coefficients C of the equations are known. Then $CX = F$ and the problem is to 'invert' the system of equations and derive the source parameters from the field observations as $X = C^{-1}F$. In many inversion methods, the user provides an initial model and the error (e.g. least-squares) between the model data and observed data is then used to refine the starting model (Green, 1975). Note that the coefficient matrix is usually sparse and ill-conditioned.

Either a generalised matrix inversion method is chosen (since the matrices involved are not square), or modified using the Marquardt technique for instance (Marquardt, 1963 and 1970). Other optimization procedures include the Gauss-Seidel relaxation technique, method of steepest descent and linear and non-linear programming (Corbato, 1965; Johnson, 1969; McGrath and Hood, 1970 and 1973; Al-Chalabi, 1970, 1971 and 1972, Cribb, 1976; Fisher and Howard; 1980 and Enmark, 1982).

Inversion methods allow for many different kinds of model geometries: the traditional dyke, prism, plate, sphere, etc. but also complicated shapes which are more representative of the

true earth situation. The model can be a 2-D polygon or any other $2\frac{1}{2}$-D and 3-D shaped body (Talwani, 1960, 1965 and 1973; Talwani and Heirtzler, 1964; Shuey and Pasquale, 1973; Barnett, 1976; Rasmussen and Pedersen, 1979; Enmark, 1982 and Dedi, 1990). In some approaches the earth is considered to be composed of many simple elements, e.g. rectangular prisms. Each rectangular prism has only one unknown characteristic: its physical property contrast. Compact ore bodies, layered earth models, and the depth to magnetic basement can all be modelled using this approach (Tanner, 1967; Negi and Garde, 1969; Parker, 1973; Oldenbuga, 1974; Gerard and Debeglia, 1975; Hahn, Kind and Mishra, 1976; Gunn, 1976; Pedersen, 1977; Pilkington and Crossley, 1986; Hammer, Hildebrand and Parker, 1991; Xia and Sprow, 1992 and Guspi, 1992).

Inversion methods can be used in the space or frequency domain. Backus and Gilbert (1967, 1968, 1970), and Wiggins (1972) used inversion to model the structure of the whole earth. The methods are widely applied in geophysics: seismology, potential fields, electrical methods, electromagnetic methods, etc.

Inversion methods are very powerful but in general are designed to produce more detail interpretation for mineral exploration or produce simplified regional relief of magnetic or gravitational sources. Because the main target of the current research was to search for a fast tool to process vast amounts of data, inversion method were deemed unsuitable.

2.6 Spectral analysis

Spectral analysis is the technique to analyse characteristics of the field data in the frequency domain by using the Fourier transform. As mentioned in Section 2.1, expressions for the potential field in the frequency domain have simple and direct forms with separated factors. The parameters of a body can be estimated by analysing the energy or amplitude spectrum of the anomaly. This technique is widely used in interpreting potential field data. Applications are summarized in four parts as follows:

1. Simple model analysis
2. Statistical model analysis
3. Downward continuation and
4. Depth relief modelling.

2.6.1 Simple model spectral analysis

Research work has shown that most simple models in the potential field, for example the pole, dipole, dyke, prism, sphere, cylinder, fault, step and triangular prism, can be expressed in the frequency domain as the product of several factors which represent characteristics of the field and parameters of the causative body (Solovyev, 1962; Spector and Bhattacharyya, 1966;

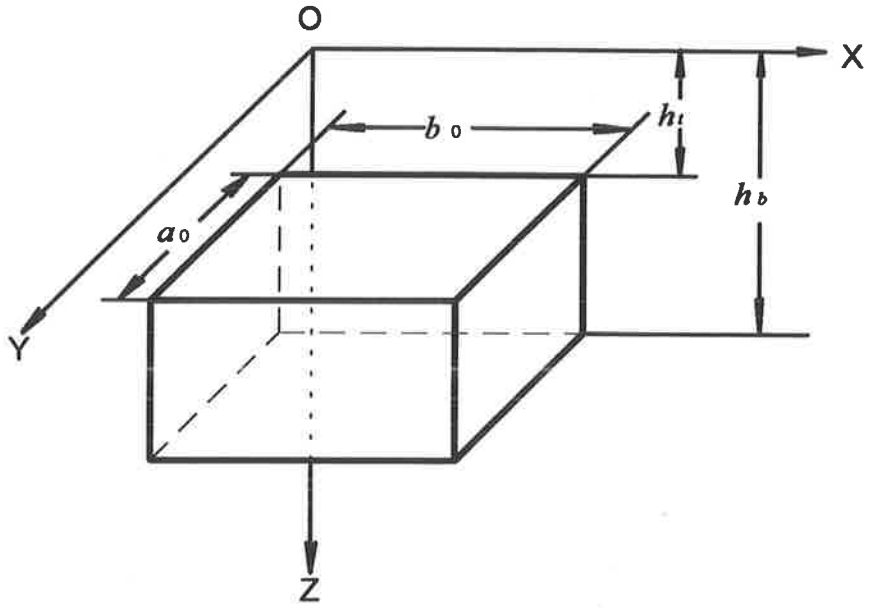

Figure 2.1 An elementary volume of the prism and the coordinate system. After Bhattacharyya, 1966b.

Table 2.2: Factors in expression (2.1)

Factor	Explanation
I_p	Magnitude of the polarization vector
$D(u,v)$	Dimensionless factor depends on inclination of earth magnetic field and also depends on the orientation of the polarization vector. When reducing the total field into magnetic north pole, the factor $D(u,v)$ simplifies to unity.
$B(u,v)$	geometrical factor dependent on the horizontal dimensions of the body.
$H(u,v)$	depth factor (including top and bottom depths) which can be separated into two parts as the depth to the top and the thickness of the body.
l,m and n	directional cosines of the earth's field vector
L,M and N	directional cosines of polarization vector
a_{12}	$Lm + Ml$
a_{13}	$Ln + Nl$
a_{23}	$Mn + Nm$
a	a half horizontal dimension of the body along the x axis
b	a half horizontal dimension of the body along the y axis
h_t	the depth to the top of the body
h_b	the depth to the bottom of the body

Bhattacharyya, 1965, 1966a, 1966b; Bhattacharyya and Navolio, 1976; Bhattacharyya and Leu, 1977; Odegard and Berg, 1965; Gudmundsson, 1966; Rao and Avasthi, 1973; Bhimasankaram, Nagendra and Seshagiri Rao, 1977). Such expressions make it possible to isolate each factor and to determine the parameters of causative body more easily than in the space domain.

An example from Bhattacharyya (1966b) demonstrates the principle of the analysis. The Fourier spectrum $F(\Delta T)$ of the total magnetic intensity (TMI) anomaly caused by a rectangular prism with a finite depth extent (see Figure 2.1) can be expressed as follows.

$$F(\Delta T) = T(u,v) = 2\pi I_p D(u,v) B(u,v) H(u,v). \tag{2.1}$$

The meaning of each factor in 2.1 is given in Table 2.2 and the expressions of the factors are given below.

$$
\begin{aligned}
D(u,v) &= \frac{(-lLu^2 - mMv^2 + nNr^2) - a_{12}uv + ja_{13}ur + ja_{23}vr}{r^2} \\
B(u,v) &= \frac{4}{uv}\sin ub \sin va \\
H(u,v) &= e^{-h_t r} - e^{-h_b r} \\
&= e^{-h_t r}(1 - e^{-(h_b - h_t)r}) \\
r &= \sqrt{u^2 + v^2}.
\end{aligned}
$$

The expression for the energy spectrum $E(u,v)$ (the square of the amplitude of Fourier spectrum) of the TMI anomaly can be written in terms of the polar wave-number coordinates (r,θ) in the u,v frequency plane (Spector and Grant, 1970), using the following transforms.

$r = (u^2 + v^2)^{\frac{1}{2}}$ and $\theta = tan^{-1}\frac{u}{v}$.

The energy spectrum $E(r,\theta)$ is then given as

$$
\begin{aligned}
E(r,\theta) &= |F(\Delta T)|^2 \\
&= 4\pi^2 k^2 e^{-2hr}(1 - e^{-tr})^2 S^2(r,\theta) R_t^2(\theta) R_k^2(\theta) \qquad (2.2)
\end{aligned}
$$

where

k is a magnetic moment/unit depth, $\frac{k}{4ab}$ is equal to I_p;

e^{-2hr} is the depth factor, in which h is the depth to the top of the body;

$1 - e^{-tr}$ is the thickness factor, in which $t = h_b - h_t$.

When the depth extent of the body tends to be infinity the factor is close to unity. It is clear that the combination of the depth and thickness factors relates to the factor $H(u,v)$ in (2.1).

$S(r,\theta)$, the horizontal dimensional (or geometrical) factor, which corresponds to $B(u,v)$ in (2.1), is expressed as

$$
S(r,\theta) = \frac{\sin(ar\cos\theta)}{ar\cos\theta}\frac{\sin(br\sin\theta)}{br\sin\theta}.
$$

$R_t^2(\theta)$ and $R_k^2(\theta)$, the factors of the geomagnetic field and magnetised vector corresponding to the factor $D(u,v)$, are given as

$$
\begin{aligned}
R_t^2(\theta) &= n^2 + (l\cos\theta + m\sin\theta)^2, \\
R_k^2(\theta) &= N^2 + (L\cos\theta + M\sin\theta)^2.
\end{aligned}
$$

In order to illustrate the method developed by Bhattacharyya some simplifications are introduced. Consider that the field has been reduced to the magnetic north pole and that the depth extent (t) is infinite. The energy spectrum can then simply be expressed as

$$
E(r,\theta) = 4\pi^2 k^2 e^{-2hr} S^2(r,\theta)
$$

Two important factors in the spectrum are now discussed.

1. Effect of horizontal dimension factor

   From analysis of the horizontal dimension factor $B(u,v)$ or $S(r,\theta)$, Bhattacharyya has shown that the factor of the spectrum either on the frequency plane (u,v) or along the radial frequency axis (r) is composed of two functions: sinusoid terms and reciprocal of frequency (or wave-number) ($\frac{1}{u}$, $\frac{1}{v}$ or $\frac{1}{r}$). The sine functions have periods which depend on the horizontal dimensions of the body. The wider the body, the smaller the period of the spectrum and conversely, the narrower the body size, the wider the period. Based on the wavelength in a period, the horizontal lengths ($2a_0$ along the x axis and $2b_0$ along the y axis) of the body can be estimated as $2b_0 = \frac{2\pi}{u_2-u_1}$ and $2a_0 = \frac{2\pi}{v_2-v_1}$, where $u_2 - u_1$ and $v_2 - v_1$ are the wavelengths of the periods on the u and v axes respectively.

   The period shown in the energy spectrum is the combined effect of the horizontal dimension factors in the two directions. If the horizontal sizes of the body along two directions have great difference, the estimated horizontal size of the body will be in great error. Under the effect of the reciprocal of frequency, the horizontal factor decreases in amplitude with increases in frequency. Combining these two functions, the horizontal factor displays the characteristics of a damped oscillation. Bhattacharyya also points out that by decreasing the size of the horizontal dimension, the higher frequency contents in the factor are increased. Thus it is clear that the dimension factor plays a complicated role.

2. Effect of depth factor

   When considering a rectangular body with infinite depth extent, the depth factor of the energy spectrum is represented by a simple function e^{-2hr}. Plotting the logarithm of the factor against the radial frequency r, a straight line is obtained and the slope of the line is related to twice the depth to the top of the body.

The above example demonstrates the application of spectral analysis to a prism model and shows how the parameters of the prism may be obtained. As the Fourier transform of the data requires that the length of the profile or the area of gridded data extends beyond an area of interest, it is important that there are sufficient data available (Regan and Hinze, 1976). In reality, a single anomaly rarely satisfies this condition in relation to the length of the profile or the size of the area. Moreover, because the use of a simple model for the analysis and interpretation of the potential field caused by complex geological structures cannot provide an accurate and reliable solution, many geophysicists consider statistical models (or ensemble of bodies) to be approximate and merely a first step in obtaining a better solution.

2.6.2 Spectral analysis of a statistical model

The first people to apply classical statistical theory to analyse the Fourier transform of potential field data were Tsuboi and Fuchida (1937), Tsuboi (1937, 1938a, 1938b and 1939) and Nagata (1938a and 1938b). Their work established the fundamentals for the analysis of potential field data in the frequency domain. Horton, Hempkins and Hoffman (1964) first used statistical analysis on the aeromagnetic two dimensional map based on the autocovariance function and

power spectrum. This method was used to analyse the trend directions of geological structures in the Northwestern Canadian Shield.

The most impressive work was carried out by Spector (1968) and Spector and Grant (1970). They considered an ensemble of bodies with varied depth, width, thickness and magnetisation as a statistical model and made the assumption that the observed total magnetic field anomalies were caused by several ensemble blocks. The basic model used in their method is the rectangular prism model which was first proposed by Bhattacharyya (1966b). They then carried out spectral analysis on total magnetic field data, and demonstrated how the average depths of deep-seated anomalies and near-surface anomalies and the thickness of shallow bodies could be determined.

Following Spector and Grant's work, many geophysicists have further developed this method of estimating depth. Treital, Clement, and Kaul (1971) extended the method to profile data by using a one dimensional statistical model of the line source. Green (1972) investigated the method and used a similar model (2-D prism) as Spector and Grant (1970) on magnetic profile data. Cassano and Rocca (1975) also examined the one dimensional transform of magnetic anomalies of multiple models. They assessed the practical possibility of the spectral method and indicated that the method was not suitable for automatic use, but might be useful as a semi-automatic procedure. Clanciara and Marcak (1976) adapted the method to the gravity field, including the cases of both 2-D and 3-D bodies. Mishra and Pedersen (1982) applied the technique to the one dimensional transform of potential field data of subsurface reliefs. More recently, Ruotoistenmäki (1983 and 1987) developed the method, and tried to overcome a problem in relation to the effect of the 'size factor' which arose in the approach of Spector and Grant (1975).

The method has been widely used for estimating the average depths to magnetic basement (Pal, Khurana and Unnikrishnan 1979, Seguin and Séńchal 1979). It was extended to calculate the depth to very deep seated sources of large parts of Japan and China respectively by Okubo *et al.* (1985) and Hou Chongchu *et al.* (1985 and 1989), who created depth contour maps of the Curie Point isotherm. Good correlations were found between these depths and the known underground thermal sources and regional geology.

The principle of the method is described as follows. Based on spectral analysis of the single rectangular prism by Bhattacharyya, Spector and Grant proposed an ensemble statistical model composed of rectangular bodies of varying depth, width, thickness and magnetisation. According to the concept of statistics, they used an ensemble average of the energy spectrum ($< E >$) to represent the effect of the energy spectrum from the statistical model. $< E >$ is given as

$$< E >= \int ... \int E \cdot \Phi(a, b, t, h, I, D, k) dV \tag{2.3}$$

where

Φ is the ensemble joint frequency distribution for parameters of bodies $a, b, ..., k$.

E has been shown in (2.2).

Assuming the parameters vary independently of one another, then Φ can be expressed as $\Phi(a,b,..,k) = \Phi(a)\Phi(b)...\Phi(k)$. Assume also that each $\Phi(...)$ is a rectangular distribution, and each variable has an uniform distribution. The limits of the variables are given as follows:

$a : (0, 2\overline{a}),\ b : (0, 2\overline{b}),\ t : (0, 2\overline{t}),\ h : (\overline{h} \pm \Delta h),\ I : (\overline{I} \pm \Delta I),\ D : (\overline{D} \pm \Delta D).$

Then it follows that

$$< E >= \frac{1}{V} \int ... \int E(r,\theta) da...dk, \tag{2.4}$$

where V is the 7-dimensional parallelopiped volume which is defined by the limits of the frequency distribution function. Putting 2.2 into 2.4, $< E >$ can be rewritten as

$$< E(r,\theta) >= 4\pi^2 \overline{k}^2 < e^{-2hr} >< (1 - e^{-tr})^2 >< S^2(r,\theta) >< R_i^2(\theta) >< R_k^2(\theta) > .$$

Under the hypothesis that the average values of the magnetic inclination (I) and declination (D) vary by less than 20° and reducing the anomalies to the north pole, the energy spectrum can be simplified as given below.

$$< E(r,\theta) >= 4\pi^2 \overline{k}^2 < e^{-2hr} >< (1 - e^{-tr})^2 >< S^2(r,\theta) > \tag{2.5}$$

When the horizontal dimension a (or b) is great enough, and because of the periodicity variation of the sine function, the quantity $< S^2(r,\theta) >$ varies (oscillatory function) unstably with angle θ. In order to decrease the effect from θ or to reduce the anisotropic effects, the values of averaged radial energy spectrum are calculated by averaging the radial component of the spectrum with respect to θ. Therefore the expression (2.5) is further modified as

$$< E(r,\theta) >= 4\pi^2 \overline{k}^2 < e^{-2hr} >< (1 - e^{-tr})^2 >< S^2(r) >$$

where

$$< S^2(r) >= \frac{1}{\pi} \int_0^{\pi} < S^2(r,\theta) > d\theta.$$

The properties of the energy spectrum are discussed below.

1. Effect of the depth factor

   The ensemble average depth factor $< e^{-2hr} >$ is similar to the depth factor of a single body when the variation of the depths is less than half of the average depth $|\Delta h| < \frac{1}{2}\overline{h}$. The logarithm of the factor is approximated by a straight line and the mean depth of the set of the statistical model can be determined from it.

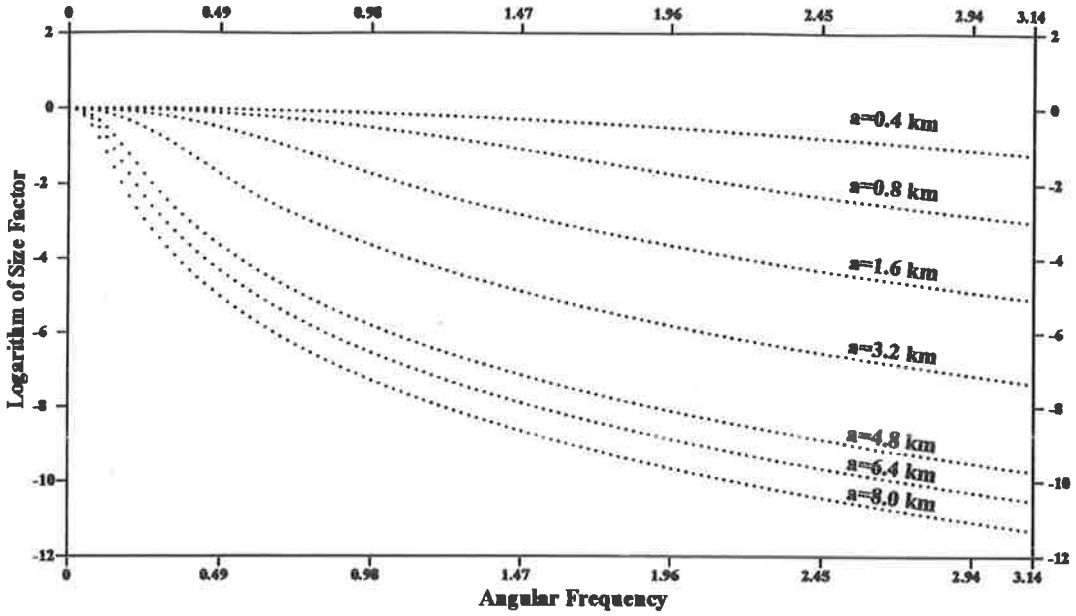

Figure 2.3: **Finite horizontal size effect. After Spector and Grant (1970).**
a: the average of horizontal size

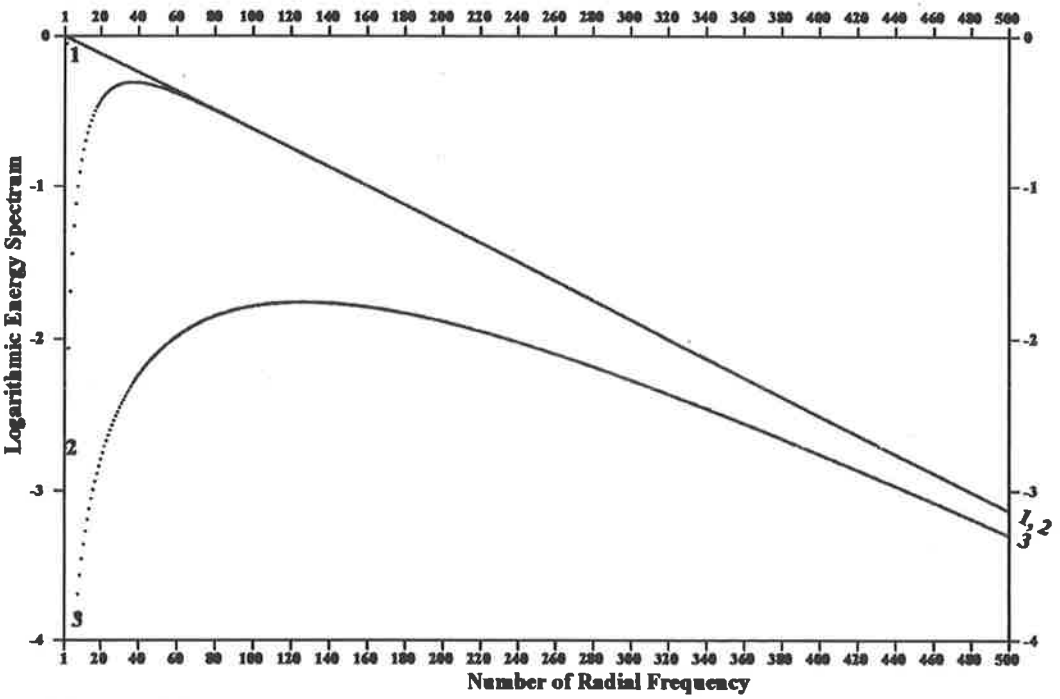

Figure 2.2: **Effect of finite thickness on the shape of the spectra,**
After Spector and Grant (1970.)

1: Bottomless source

2: Limited depth extent source

3: Thin plate source

2. Effect of thickness factor

   The thickness factor is a complex function but plays an important role in shaping the energy spectrum. This factor produces a peak in the spectrum, the position of which shifts toward low frequencies with increasing values of the average thickness. Figure 2.2 shows the effect achieved by analysing the combination of the depth and thickness factors. When $\overline{t}$ is great for bottomless body; i.e. the value of $\overline{t}$ tends to be infinity, the spectrum has a maximum at frequency $r = 0$ (see curve 1 in Figure 2.2); when $\overline{t}$ is small for thin plate body, the peak moves toward high frequency (see curve 3 in Figure 2.2). Curve 2 illustrates the shape of the spectrum when the values of the average thickness $\overline{t}$ are in the intermediate range for limited depth extent bodies. Based on the characteristics for the peak position of the radial energy spectrum, the shape of the ensemble of bodies (or blocks) can be inferred. The spectrum of a bottomless body has its maximum at $r = 0$ and a limited depth extent body has the peak of the spectrum away from the end of the low frequency. It is worth noting that, since the size of the calculated area also effects estimates of the depth and depth extent of the sources, it cannot be expected that information from very deep sources (such as the Curie Point isotherm) can be obtained from a small map area of the order of $100km^2$.

   An examination of the positions of different peaks in the spectra is very useful in distinguishing and hence identifying the energy spectra from different shaped bodies. The assumption is made that, if deep bodies have very large depth extent and shallow sources have limited depth extent, the majority of the energy spectra from the deep bodies will be in the low frequency range while the contents of spectra at the high frequency end indicate a major effect from shallow bodies. Under this assumption, by using spectral analysis, anomalies due to the deep-seated and near-surface sources can be easily separated. Consequently the average depths of the two groups of bodies can also be determined.

3. Effect of size factor

   The size factor $< S^2(r) >$ produces a strong influence in accurately determining values of the average depths. Figure 2.3 shows the effect of this factor: a set of curves of the logarithm of $< S^2(r) >$ with varying average horizontal size $\overline{a}$ indicates that the size factor decays when increasing the frequency for each $\overline{a}$. The curves also show that the larger the horizontal size $\overline{a}$ is, the quicker the decay occurs at the low frequency end. The effect of decreasing spectral energy especially at the low frequency end will bring some error to the determination of the average depth. In general, the values of the estimates will be greater than the actual values. Moreover the effect of the size factor is difficult to remove, because a complex earth model is difficult to represent by a mathematical quantity ($\overline{a}$). Therefore Spector and Grant (1975) made the conclusion that no simple rule can be found to relate spectral decay rates with depths of burial, even in a statistical sense.

In conclusion, effects from these factors indicate that the method cannot easily provide reliable estimates of the depths but the outline of the geological body distributions can be obtained by analysing energy spectra of areal or profile data. Another use for this method is in the separation of anomalies of near-surface noise and deep-seated sources by using the matched filtering technique developed by Spector (1975).

2.6.3 Downward continuation approach

As mentioned above, logarithmic radial energy spectrum can provide at least two segments which indicate different average depths from causative bodies of magnetic or gravity anomalies. Based on spectral analysis, Hahn, Kind and Mishra (1976) developed a depth estimation method by analysing the downward continuation spectrum. They noticed that when applying a proper downward continuation operator, in which the preliminary estimated depth is obtained from the slope of the averaged energy spectrum, the energy spectrum becomes oscillatory and the slope of the logarithmic radial spectrum is near horizontal. The fact is that when the depth of the continuation is close to the source, the field becomes seriously oscillatory. In other words, the function of downward continuation enhances the high frequency contents, and the resultant spectrum displays characteristics of white noise. Based on this feature, an initial estimate of the depth is obtained. This method is useful for determining a mean depth obtained either from gridded data or from profile data. This method is similar to the other Fourier transform methods which cannot provide more accurate and detailed information. Another problem as the authors (Hahn *et*, 1976) point out is that straight segments which occurred on the radial spectrum did not always represent different depths caused by magnetic sources, because much artificial noise, which may effect distribution of spectrum, can be produced from procedures of measuring, digitizing and smoothing.

2.6.4 Depth relief modelling

The spectral analysis technique can be a useful tool to help transform gravity or magnetic anomaly maps into isodepth maps of a contact surface between two homogenous media or into a map which shows the relief of a specific 'density surface' or 'magnetic surface'. The principle for constructing a depth relief map is based on the relationship between the potential field and its simplified sources (assuming the density or magnetisation in the area is homogenous). For example the anomaly is produced by many elements of rectangular prism bodies. By using spectral analysis, initial depth estimates can be obtained, and an automatic system for interpreting magnetic or density relief can be established. Gerard and Debeglia (1975) applied this technique and developed an automated method for interpreting 3-D gravity and magnetic anomalies. Hahn *et al.* (1976) also have used a similar approach to create magnetic relief maps and demonstrated their approach with an example from the north-western area of Germany.

2.6.5 Advantages and disadvantages of spectral analysis

The spectral analysis technique is a rapid, convenient and simple tool for interpreting potential field anomalies. The method can provide several average depth levels of anomalies from areal or profile data by using simple or statistical models. The method also efficiently deals with complex and superimposed anomalies, for which other methods may be inefficient or fail to provide solutions. The spectral analysis method is widely used for determining average

depths of basement and the method has been extended to estimate the depth to the Curie Point isotherm.

However, the application of the method is affected by several factors including unacceptable assumption about the geometries of the causative bodies and limitations of the Fourier transform. In summary the problems in using this technique are listed below.

1. The effect of the size factor distorts the depth estimates, especially when the size of the horizontal dimension is great. This effect is difficult to remove.
2. The averaged radial spectrum could produce some error for sources with significant linear extent.
3. Because of the calculation by means of FFT, some restrictions of this technique may influence the result. The interpreted anomalies should be completely covered by the profile or areal data set. The field values should taper to zero towards the edge of the surveyed area. If these conditions cannot be satisfied, errors will occur. In order to overcome this problem, corrections need to be applied before to spectral analysis.
4. When dealing with gridded data, detailed information cannot always be provided, because sample intervals are often great.
5. The method may not be suitable for automatic determination, but good for use in semi-automatic calculations.

Although spectral analysis cannot give accurate and detailed results, it can be applied to provide an outline of average depths from complex geological terrains. However, in order to overcome this drawback of spectral analysis, automatic depth estimation methods are recommended and they are discussed in the following sections.

2.7 Automatic depth estimation methods

2.7.1 Introduction

Automatic depth estimation techniques for aeromagnetic profile data were developed in order to rapidly obtain preliminary information regarding underground magnetic causative bodies. In the typical automatic method, the interpreter provides an entire aeromagnetic flight path (after modifications) or grid as input to a computer program together with a model type, e.g. dyke. The program then identifies all the anomalies it can based on some criteria, locates them along the flight path or on the grid, then solves for the depth to the top of the dyke model which would fit each anomaly. At the end of the execution, the interpreter is given the locations of every anomaly, along with solutions for the depth to each anomaly and some measure of the goodness of fit. The interpreter may repeat the previous step with a different model. Finally appropriate solutions are obtained. The significant difference between this class of methods and

other methods is that it is not the interpreter who selects which anomalies are to be interpreted but the program which identifies and locates anomalies. This first step is critical to the success of these methods.

Either profile or gridded data may be used but profile data are superior to gridded data in the following respects. Valuable information may be lost in the gridding process and possibly manufactured by interpolation between flight paths. Profile data represents the original flight line data with minor modifications. The spacing interval of profile data is much smaller than that of gridded data; thus more detailed information is provided by profile data.

Analysing profile data also has some flaws. Some conditions must be assumed before interpretation, namely that the strike of the causative sources are perpendicular to the direction of the profile, and that these sources are two-dimensional.

The simple and fast approach of automatic depth estimation methods makes them useful and practical. In 1970s several such methods were developed and provided a wide range of applications in varied magnetic field situations.

The Werner-based deconvolution was the first automatic depth estimation method. In 1971, Hartman, Teskey and Friedberg extended the idea from Werner (1953) of using the thin dyke body as an approximation for solving other kinds of magnetic anomalies (Ku and Sharp, 1983). In the same year, Naudy (1971) and O'Brien (1971) also published their automated depth estimation methods. In early 1980 another automatic depth estimation method, Euler deconvolution (Thompson, 1982; Barongo, 1984; Reid, Allsop, Granser, Millett and Somerton, 1990) was developed. The Werner method was the most widely used and developed. Jain (1976) carried out model experiments and showed the application and limitations of the Werner method. Ku and Sharp (1983) analysed the influence from interference and proposed an improved Werner approach. They expanded the application of the method to the inverse technique with the estimates from the Werner method taken as the initial parameters in the inversion problem. Kilty (1983) further discussed the advantages and limitations of the Werner method. Keating and Pilkington (1990) applied the technique to vertical gradient anomalies.

Compared to Werner deconvolution, little has been published on the Naudy method (1971) or on the O'Brien (1971) method. A brief description of Euler deconvolution, Werner deconvolution and the Naudy technique, are given in the following sections.

2.7.2 Euler deconvolution

The Euler depth estimation method (Thompson, 1982 and Reid, 1990) is an automatic interpretation method which is based on Euler's homogeneity relationship. The advantage of the technique is that, as no basic geological model is assumed, the method can be applied in a wide range of geological situations which can locate or outline confined sources, vertical pipes, dykes and contacts with remarkable accuracy. The method can employ both magnetic field and gradients without reducing them to the pole. Another advantage is that the method can be

applied to gridded data to process three dimensional geological cases. However, the quality of the interpretation greatly depends on the experience of the user. The sensitivity of technique to interference from adjoining anomalies and noise is another restriction of the method.

2.7.3 Werner deconvolution

Description of the method

Based on theoretical analysis of potential fields, both the potentials of gravity and magnetics can be expressed as the convolution integral of a source distribution and a spatial distribution from the observed point (Werner, 1953; Hartman, *et al.*, 1971; Gunn, 1975; Kilty, 1983). In the forward problem the parameters of the source distribution and field properties are assumed and by calculating the convolution integral of the functions of the parameters, theoretical field data are constructed. On the other hand, the inverse problem involves the resolution of the source distribution from its potential field expression and thus this procedure is called deconvolution.

Werner proposed an expression for a thin dyke body as a rational function as follows.

$$F(x) = \frac{A(x - x_0) + Bz}{(x - x_0)^2 + z^2} \tag{2.6}$$

Here x is the distance along a profile,

F is the intensity of the total magnetic field,

A and B are the functions of the field strength, susceptibility and the geometry of the dyke,

z is the depth to the top of the dyke from the observed point, and

x_0 is the distance between the observed point and the projection of the top of dyke.

(2.6) can be rewritten as

$$a_0 + a_1 x + b_0 F + b_1 x F = x^2 F \tag{2.7}$$

where the coefficients a_0, a_1, b_0, b_1 are given as

$$\begin{aligned} a_0 &= -Ax_0 + Bz \\ a_1 &= A \\ b_0 &= -{x_0}^2 - z^2 \\ b_1 &= 2x_0 \end{aligned} \tag{2.8}$$

A system of simultaneous linear equations is established based on four appropriate consecutive coordinates (x) and their corresponding total magnetic fields (F) of (2.7). After solving this system the four unknowns: a_0, a_1, b_0 and b_1 can be determined. From the set of equation (2.8), the depth z and horizontal distance to the top of the body x_0 can be estimated. When further resolving A and B into functions of dip and susceptibility, these parameters of the dyke can also be determined.

Werner considered that the interference caused by adjoining anomalies could be represented by a polynomial. If n is the order of the interference polynomial and C_0, ..., C_n are the coefficients, then adding this polynomial to (2.6) gives the following equation.

$$F(x) = \frac{A(x - x_0) + Bz}{(x - x_0)^2 + z^2} + C_0 + C_1 x + ... + C_n x^n. \tag{2.9}$$

Using $(n + 5)$ points and their corresponding fields, $(n + 5)$ unknowns can be solved from equation (2.6). In general, as first and second order polynomial are usually sufficient, only 6 or 7 points are required for the solution. By subtracting the influence of interference ($C_0 + C_1 x + ... + C_n x$) and iterating onwards based on the improved solution, the parameters of the body may be obtained (Ku and Sharp, 1983).

The Werner method is also suitable for determining the magnetic contact model (or edge model) by using the horizontal gradient of the total field data, and can also be applied to the horizontal cylinder of gravity by using the vertical component of the gravity (Kilty, 1983).

The limitations of the method

Werner deconvolution is very easy to program and simple to use. It has been a popular method, but it has some limitations. As the theory of the method is based on the rational function form of the field, only a few model fields are suitable, such as a thin dyke, contact and horizontal cylinder. These models include some extreme geometrical shapes for anomalous bodies while the case of the commonly found shape, a wide dyke, is not considered.

The method is very sensitive to noise, because the matrix of coefficients involved in the solution of the system of equations is generally ill-conditioned (Kilty, 1983). Kilty tested the method by adding random error and concluded that when the noise had a standard deviation of 1% of the peak amplitude of the anomaly, the estimation would bring 20% error in the true values. Further increase in the value of the random error led to rapid increase in the error of the estimated parameters. When the standard deviation exceeded 3% of the peak amplitude of the anomaly, the method became incapable of finding any acceptable estimates.

Kilty (1983) also pointed out the problem arising from the interference correction. The coefficients of interference are correlated with the parameters a_0, a_1, b_0 and b_1, which are used to determine the depth, location, dip and susceptibility of the model. As the shape and amplitude of the original anomaly are easily altered when correcting for interference, the subsequent estimates

of the parameters are also affected. Many users realised the problem of interpreting the results from the calculation. Too many solutions are provided and it is hard to determine their reliability.

For these reasons Werner deconvolution was considered unsuitable for the current study which requires the application of a method to the high resolution aeromagnetic data collected over Eyre Peninsula to reveal the depth to the magnetic basement. The last technique to the discussed, the Naudy technique, is presented in the following sections.

2.7.4 The Naudy technique

Introduction

Automatic methods of depth determination have the advantage of helping an interpreter with a quick analysis of large amounts of magnetic data. Naudy (1971) presented one such technique which analyses the total magnetic intensity (TMI) profile and the magnetic field reduced to the pole (RTP). The two fields are split into symmetrical and antisymmetrical parts and a coefficient of similarity is derived by comparing the two symmetrical parts with the anomaly from a vertically magnetised model. The locations of the minima of the similarity coefficient give the positions of the centres of anomalies corresponding to the magnetic sources. At each centre, a set of model curves is produced to compare with the two symmetrical components of TMI and RTP and their similarity coefficients are derived. Perfect correlations between the theoretical curve and the observed data yield the estimated depths. The Naudy technique uses a dyke and a thin plate model to approximate geological structures and mainly determines the depth of the causative magnetic bodies.

The method is divided into two stages; in the first stage the centres of all the anomalies on the profile are located; in the second stage each anomaly is analysed to obtain an estimation of its depth. The method is based on the curve matching approach. Several techniques are applied: curve splitting, reduction to the pole and application of the correlation coefficient. Detailed explanations of the techniques and the whole procedure of the calculation are given below.

Splitting a curve into symmetrical and antisymmetrical components

The approach of curve splitting (Hutchison, 1958; Powell, 1967; Koulomzine *et al.*, 1970; and Naudy, 1971;) utilises the fact that any curve can always be split into symmetrical and antisymmetrical components at any point on the abscissa. Supposing the original curve is $y(x)$, then its symmetrical component is $S_1(x)$ and the antisymmetrical component is $S_2(x)$.

$$y(x) = S_1(x) + S_2(x). \tag{2.10}$$

If x' is a conjugate point of x about central point s, ie. $(x + x')/2 = s$, then

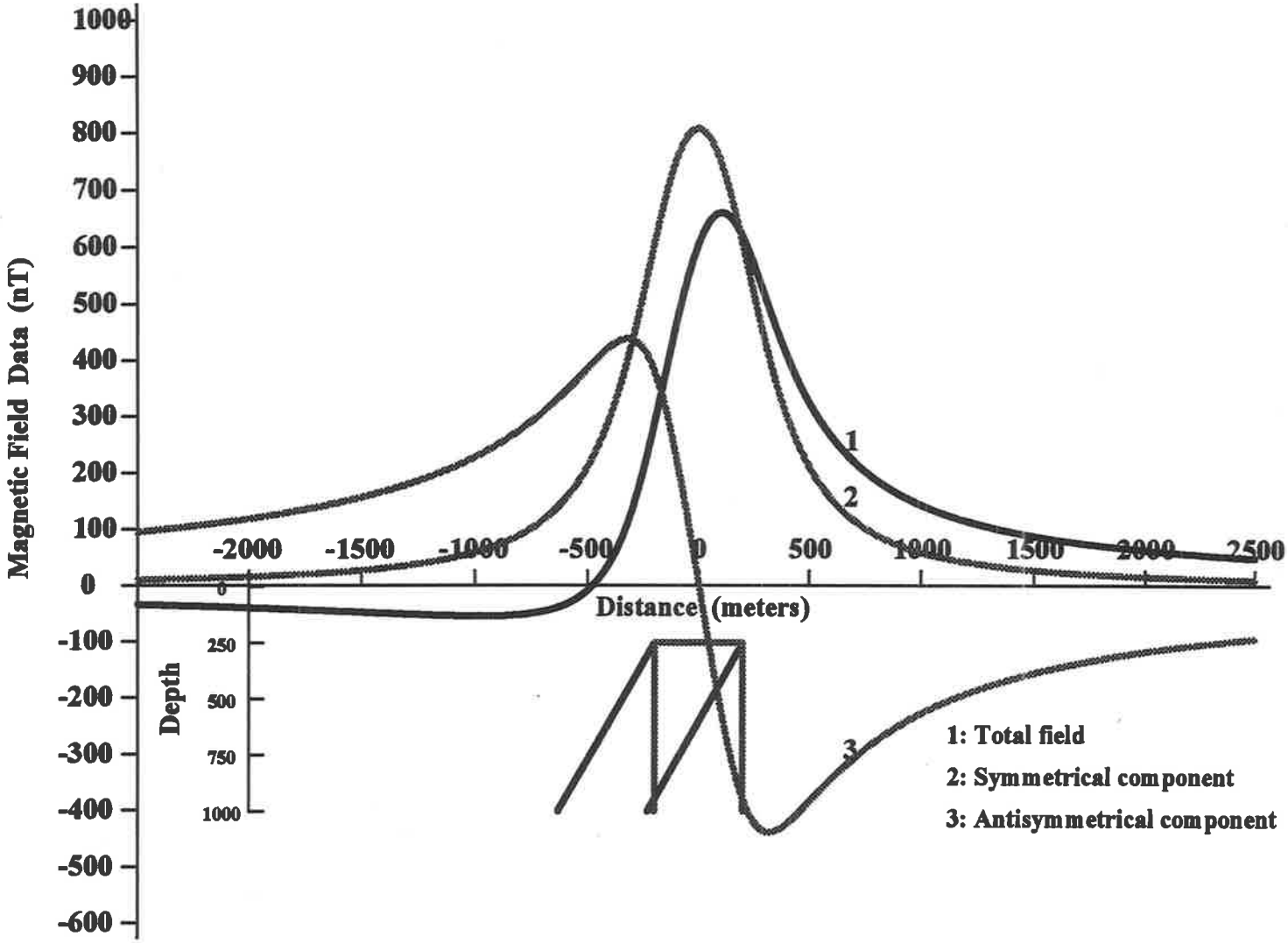

Figure 2.4: **Total magnetic field and its symmetrical & antisymmetrical components and their correspoding causative dykes**

$$y(x') = S_1(x') + S_2(x'). \tag{2.11}$$

According to the definitions of symmetrical and antisymmetrical components

$$S_1(x') = S_1(x),$$

and

$$S_2(x') = -S_2(x).$$

then $y(x')$ is rewritten as

$$y(x') = S_1(x) - S_2(x). \tag{2.12}$$

Thus, based on expressions (2.12) and (2.14), the symmetrical component ($S_1(x)$) and antisymmetrical component ($S_2(x)$) can be obtained from the original curve (y) as:

$$S_1(x) = \frac{y(x) + y(x')}{2}, \tag{2.13}$$

and

$$S_2(x) = \frac{y(x) - y(x')}{2}. \tag{2.14}$$

For the application of the Naudy method, only the symmetrical component is used. If $y(x)$ has been sampled at equal spacings p, at each point s the symmetrical curve S_1, in which the number of samples is $2m + 1$, is created.

The technique for splitting any curve into symmetrical and antisymmetrical components is a useful tool which simplifies curve matching between field data and magnetic anomalies caused by some simple shaped bodies, such as edge, dyke, thin sheet, thin plate, horizontal cylinder and others. The total magnetic field caused by these bodies can split into a symmetrical and an antisymmetrical component (see Appendix A). These two components are proportional to the vertical and horizontal components respectively, in which the causative body has the same depth and width as that of the total field, but both the angles of magnetisation and dip of the body are 90 degrees. Figure 2.4 gives a typical example where curve 1 is the total field anomaly caused by a dipping bottomless dyke. The splitting is carried out at the centre 0 above the body. Curve 2 is the symmetrical component which is also the vertical component in the vertical magnetisation direction of a vertical dyke. Curve 3 is the antisymmetrical component produced by the same body as curve 1. This represents either the horizontal component of the TMI where the dyke is

vertically magnetised or the total field anomaly where both the direction of magnetisation and the inclination of the measured field are parallel and equal to 45 degrees (see Appendix A).

Therefore the technique of curve splitting provides a simplification by comparing a symmetrical or an antisymmetrical component of observed TMI data with a theoretical curve caused by a simple model. Additionally, after splitting curves and using the symmetrical component, any linear regional field will be removed.

Reduction to the pole

Naudy (1971) has pointed out that the curve splitting technique is not suitable for those asymmetrical anomalies similar to curve 3 (see Figure 2.4). After splitting curves, the anomalies similar to curve 3 will disappear or have greatly reduced amplitudes and can therefore not be interpreted properly. For this reason a technique is needed to transform curves of the shape of curve 2 into curve 1 type. Reduction to the pole (RTP) fulfills this function.

The function of reduction to the pole (Baranov and Naudy, 1964) is to convert total magnetic fields measured where the magnetic inclination is not vertical into the field which would be observed if the body were at the magnetic pole. The advantage in analysing the RTP anomaly is that this anomaly has a pattern directly related to the the geometry of the causative body and interpretation is simplified.

Similarity coefficient of correlation

Correlation coefficients can be used to identify the similarity of two curves which are a theoretical model curve T_1 and a symmetrical curve S_1.

Let $\overline{S}_1$ be the mean value of $(2m+1)$ samples along $S_1(x)$ and $\overline{T}_1$ be the mean value of $(2m+1)$ samples along $T_1(x)$. The correlation coefficient for $(2m+1)$ samples then becomes r_1 where each sum covers $(2m+1)$ points.

$$r_1 = \frac{\sum (S_1 - \overline{S}_1)(T_1 - \overline{T}_1)}{\sqrt{\sum (S_1 - \overline{S}_1)^2 \sum (T_1 - \overline{T}_1)^2}}. \tag{2.15}$$

r_1 varies from -1 to 1. If $r_1 = -1$ this indicates a perfect similarity between S_1 and T_1 but with opposite curve signs; $r_1 = 1$ indicates a perfect similarity with same curve signs; and 0 indicates a dissimilarity between S_1 and T_1. As is known, the coefficient r_1 only indicates the similarity of two curves in shape, but the curve may not necessarily have the same range of amplitudes. The curves T_1 and S_1 may have the same shapes, while the difference in their amplitudes can be even up to 10 times, but the correlation coefficient is still 1. Therefore when comparing the theoretical anomaly with the observed anomalies, it is only necessary to provide one typical theoretical curve to match anomalies of differing amplitudes.

To simplify the calculation, Naudy defined a new correlation coefficient, R_1, which varies from 0 to 10^5; the perfect similarity being zero.

$$R_1 = (1 - |r_1|) \cdot 10^5. \tag{2.16}$$

The coefficient of similarity (R) was defined by Naudy as a weighted mean value of the correlation coefficients of the original and transformed profiles, where R_u is obtained at each point for R_1 of a theoretical curve and a symmetrical curve from an original profile (TMI), and R_v comes from the transformed profile (RTP).

$$R = \frac{B_u R_u + B_v R_v}{B_u + B_v}. \tag{2.17}$$

The weights B_u and B_v are calculated by the formula given below.

$$B = \sum (S_1 - \overline{S}_1)^2.$$

In the next sections, the two stages in the application of the Naudy method, finding the centres of the anomalies and then the depth estimates, will be discussed.

Finding the centres of anomalies

A theoretical anomaly curve T_1 is chosen as typical of the most frequently measured anomalies. It is calculated only once and comprises $(2m + 1)$ values. The depth h of the theoretical model creating T_1 is given as the product of the sampling interval p and a constant e; i.e. $h = ep$. The observed data are sampled with successive intervals, $p_1, p_2, ..., p_n$, and for each sampling interval the following procedure is repeated.

1. The transformed profile (RTP) is computed by reduction to the pole from the observed profile (TMI).

2. At each point the symmetrical components are calculated from both the RTP and TMI profiles. The similarity coefficient R with the theoretical anomaly T_1 is then calculated for the whole profile.

3. The points are accepted as centres of anomalies, if they satisfy the two conditions that R is a local minimum and $R < R_m$. R_m is a user-specified limit beyond which the similarity is assumed to be too poor for the result to be trustworthy.

Final determinations of depths

From the procedure of locating the centres of anomalies, the preliminary depth estimates are provided. However the estimates are rough and must be improved. In order to arrive at final determinations, two approaches may be adopted.

1. By changing to an interval q, slightly different from p, a better similarity result may be obtained.
2. By using another theoretical model curve instead of T_1 a higher degree of similarity coefficient may be obtained.

In the first approach, a set of fractional intervals is introduced to change the shape of the model curves, providing additional opportunities for matching the observed data.

The same applies to the second approach in which a set of model curves is established by changing ratios of the half width and the depth of the initial model. The computed models are consistent with the structural hypothesis of a vertically magnetised, vertical dyke with infinite downwards depth extent.

In the calculation, both approaches are combined to construct model curves of a number of sets. A table of the similarity between the variable model curves and the fixed observed data (i.e. the symmetrical components of TMI and RTP of the measured profile) is then established. A minimum value of R is obtained from the table, the final depth estimate being that of the best matched model.

Summary of the Naudy technique

Naudy proposed a very good technique for the rapid analysis of aeromagnetic profile data. Other advantages of using this method are listed below.

1. As the method uses a curve matching technique, it does not use just a few points on an anomaly. Therefore it provides reliable results.
2. By using a curve splitting technique, a wide range of models (dyke, edge, thin sheet, thin plate, horizontal cylinder and others) can be applied (see Appendix A). Based on these models, varied geological structures can be constructed, making the method powerful and flexible.
3. The method extends the classical statistical technique (correlation coefficient) to magnetic data processing. The fit between the theoretical curve and observed curve can be objectively used by the interpreter to select the most suitable solutions.

For these reasons, the method appears an appropriate one to solve the geological problems in the present research. However there are still limitations in using the method and these are listed below.

1. The method provides a good way to interpret individual anomalies, but it is not suitable for complicated anomalies especially those corrupted by interference from adjoining bodies.
2. The method is also not suitable for processing data with a high noise level.
3. The method provides a depth estimate and the determination of the other parameters of causative bodies is not discussed in the original paper.
4. Published information about the method was limited to the original paper by Naudy (1971). An MSc thesis by Minty (1981) contained a little more information about the method.
5. Based on all the published information available at the start of this thesis, the Naudy method looked promising despite its limitations. It was obvious that more work needed to be carried out to refine the method in order to make it suitable to use on the problem of automatic interpretation of aeromagnetic data collected over basement with a thin cover.

2.8 Summary of interpretation methods

This section summarises all the methods mentioned above, and provides the reasons for the selection of spectral analysis and the Naudy methods as the appropriate starting points for the development of the interpretation methods for this research.

1. Graphical and characteristic points method can provide rough results only for well-resolved anomalies from sources of simple geometry and are unsuitable for complicated anomalies. Inversion methods and forward modelling are particularly attractive because the geologically realistic models can be chosen but all three groups of methods are time consuming when applied to a large survey and rapid results cannot be obtained.
2. Spectral analysis, in which an ensemble statistical model is assumed (Spector and Grant, 1970) is a good approach for providing regional geological information. It has been widely applied to magnetic data. The applications of this technique still raises some problems. The author presents some refinements of this technique and application to real data in later chapters (see Chapter 5).

   The depth estimates obtained from spectral analysis are valid as a regional approximation. The significance of the solution is restricted by the assumptions made (model conditions, average depth of statistical model) and some application conditions of Fourier transform technique (e.g. edge effect, end correction). The method is not well suited for detailed interpretation. In order to overcome this drawback automatic interpretation methods need to be used.

3. Euler deconvolution is a powerful automatic depth estimation method which has no restriction of the model type. The method can provide the information of depth and location in a wide range of geological bodies, e.g. vertical pipes, dykes and contacts. The method can be applied to both the profile and gridded data of magnetic field and gradients. However, because the solution of the method is obtained by solving Euler's equation, it is sensitive to noise. Other restrictions are that it is difficult to interpret the results and other parameters of causative body, e.g. dip and susceptibility are not provided.

4. Werner deconvolution can rapidly produce determinations of various parameters of the causative bodies, but the hypothesis of the model limits the application of the method. The method is very sensitive to the noise level.

5. The original Naudy technique quickly provides an estimate of the depth to the individual anomaly, and the technique can be easily applied to various simple geological structures. One limitation of this method, which it shares with the other automatic depth estimation methods, is that it is unsuitable for the analyses of complicated anomalies. In addition, only the depth could be determined from the original technique.

Normally these methods are not used on their own, but as part of an interpretation system in which the most appropriate method is applied at a certain stage of the interpretation. In order to rapidly estimate depth and obtain other information from an aeromagnetic or regional gravity data, a combination of interpretation methods is recommended. The suggested sequence of methods is given below.

- First step: Spectral analysis may be used to outline regional geology and in particular provide information about very deep structures.
- Second step: Automatic depth estimation method, e.g. the Naudy technique, may be employed to rapidly obtain the depth to magnetic basement.
- Final step: The forward modelling method is used in specific areas to give more detailed and exact information about geological structures using an intial model developed from spectral analysis and/or the Naudy technique. By carrying through this sequence the amount of time consuming forward modelling is reduced.

However there is still a lot of work for refinement and improvement. The focus of this thesis has been to refine individual methods, to combine them into a practical and fast interpretation system, and then to show that it can be applied effectively to real data. The following chapters describe the research into the improvements to the Naudy technique and spectral analysis method to make them more powerful and practical.

Part II

Techniques for data interpretation

Chapter 3

Improved Naudy Technique for profile data

The original Naudy technique, because it suggested a way to automate the interpretation process looked very promising. However the method has a major deficiency and in this chapter I explain the problem and present a solution. I also present improvements to the original technique. The solution together with the modifications are referred to from now onwards as the **"Improved Naudy Technique"**.

3.1 Problems in the original technique

The Naudy automatic depth estimation method (Naudy, 1971) to interpret magnetic profile data uses a forward modelling approach. The method requires the input of some simple parameters (**initial parameters**), for example the depth and width of an initial theoretical model. Then by using the curve splitting technique, a simplified procedure of curve matching between theoretical and observed data is carried out and depth estimates are obtained. The use of this technique on a wide range of anomaly types makes the Naudy depth estimation method very powerful. Additionally, as this method does not depend on a few characteristic points alone, the depth estimates are relatively reliable.

For the purpose of this research, the original Naudy method was thought to be suitable for the interpretation of profile data from a large aeromagnetic survey. Accordingly some tests were carried out on model profiles calculated according to survey specifications and for the appropriate latitudes. The computer program, DEPTH, based on the original Naudy paper, supplied by Brian Minty (1981) was used to interpret the simulated survey data.

The program produced multiple solutions when the model dyke was oriented north-south and the profile direction was east-west. As mentioned in Section 2.7.4, an important stage of this method is to locate the centres of anomalies by using the minimum values of the similarity coefficients which are obtained from the comparison between a theoretical model curve with

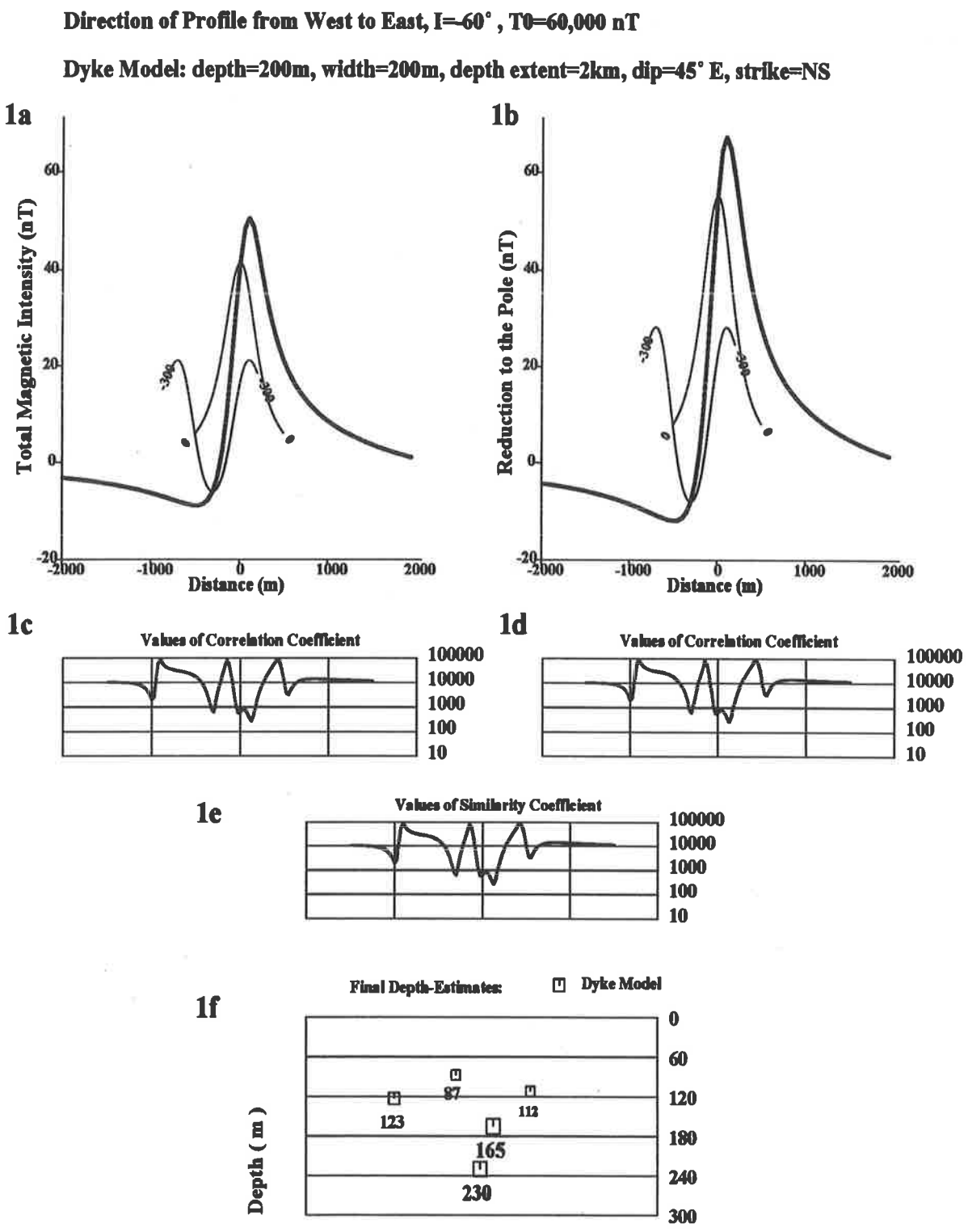

Figure 3.1: Application of original Naudy technique to a magnetic profile in E-W direction.

Table 3.1: Parameters of the 2-D dyke model

Parameter	Value	Parameter	Value
Depth	200 metres	Depth extent	2000 metres
Width	200 metres	Dip of body	45°
Strike of body	NS	Sampling interval	25 metres
Susceptibility	0.0010 CGS 0.01257 SI	Profile Direction	EW

observed total magnetic intensity (TMI) data and the field reduced to the pole (RTP). Applying this approach to analyse profiles whose directions are EW, it can be shown that multiple centres occur over a single source. Consequently spurious values arise from this depth estimation method in this particular instance (Shi, 1991).

Figure 3.1 shows the problem in a test using a theoretical model. The TMI and RTP anomalies along the EW profile are caused by a dyke, the parameters of which are given in Table 3.1. The five different depths of the dyke, ranging from 87 to 230 meters (see Part 1f of Figure 3.1), were derived by using the computer program DEPTH. From the figure it can be readily seen that the technique creates a number of minima of the similarity coefficient (see Part 1e), each corresponding to an estimate of the depth, giving rise to uncertainty. Application of the Naudy technique to surveys at high magnetic latitudes results in the same phenomenon.

Figure 3.1 is discussed in detail in Section 3.2. Note that parts 1c and 1d of Figure 3.1 show the correlation coefficient curves of TMI and RTP respectively. The thin lines in parts 1a and 1b of Figure 3.1 are the symmetrical curves converted from the observed data and the numbers marked on the profile correspond to the coordinates of the curve centres.

In addition, mainly depth estimates could be determined and vertical gradient anomalies could not be analysed using the original method. Having recognised these problems, further developments of the technique were deemed necessary. The problems tackled in this chapter are listed below.

- **[Major deficiency - The accurate location of the centre of the anomaly:]**

  The deficiency therefore relates to the inability of the algorithm in some instances (EW profiles and at high magnetic latitudes) to locate the anomaly centre uniquely for a model anomaly. Since this preliminary stage is critical to the subsequent success of the method, I present an alternative approach in Section 3.2 which overcomes this problem.

- **[Extension to vertical magnetic gradient anomalies:]**

  As some modern magnetic surveys employ systems for measuring vertical gradient, the extension of the method to vertical gradient anomalies is necessary. Even where the gra-

dient is not measured, it may be computed from the TMI data: the extension is presented in Section 3.3.

- **[Determination of source parameters other than depth:]**

  Mainly the depth is determined from the original technique. Solutions for the other parameters (width, dip, susceptibility contrast, etc.) were not given from the original paper (Naudy, 1971) and were not directly given from the unpublished CGG Naudy program. These solutions for the dyke, edge and plate models are explained in Section 3.4.

3.2 The accurate location of the centre of the anomaly

This section focuses on finding the reason for producing spurious centers on EW profile data or on profiles from high magnetic latitude areas and then provides a solution. Before the discussion, it is necessary to review the concept of the effective magnetic field along the profile.

3.2.1 Effective magnetic field

In general, when processing magnetic profile data, in order to simplify the calculation, it is assumed that: the magnetic source is two dimensional, that its strike is perpendicular to the profile direction, that the direction of any remanent magnetisation is parallel to the direction of the induced magnetic field, and that the effect of demagnetisation of the body is negligible.

With these assumptions, the effective magnetic field is used to simplify calculations involving profile data (Koulomzine and Massé, 1947; Gay, 1963). Briefly speaking, the effective magnetic field is the combined effect of the vertical magnetic field and the horizontal field in which the plane crosses the profile. It allows for the azimuth angle D' which is the angle between the magnetic north and profile direction. The effective inclination i and the effective magnetic intensity T_0' can be obtained from the following formulae for the inclination I, the azimuth angle D', and the total magnetic field T_0 (Gay, 1963) (see Appendix B).

$$\tan i = \frac{\tan I}{\cos D'},$$

or

$$i = \tan^{-1}(\tan I \cdot \sec D'), \tag{3.1}$$

and

$$T_0' = T_0 \cdot \frac{\sin I}{\sin i}. \tag{3.2}$$

When the strike of a source is NS, then the observed profile is perpendicular to the direction of the strike, i.e. the profile is along the EW direction. Assuming that the direction of the remanent magnetisation is parallel to the induced field direction, then the effective inclination can be obtained from expression (3.1) as follows.

$$i = \tan^{-1}(\tan I \cdot \sec 90°) = 90°.$$

Then the effective magnetic field is given by expression (3.2) as

$$T_0' = T_0 \sin I.$$

Therefore the effective inclination i on the EW profile is 90°. This is true for all magnetic inclinations as long as the profile direction is EW. When carrying out reduction to the pole on the profile TMI data, only the effective inclination i and the intensity T_0' are important. Since i is equal to 90° for EW profiles, the RTP data is identical to the TMI data except for a constant factor $1/\sin I$.

For NS profiles, the effective inclination angle obtained from expression (3.1) is given below.

$$i = \tan^{-1}(\tan I \cdot \sec 0°) = \tan^{-1}(\tan I) = I.$$

When the survey area is a high latitude region (inclination i is greater than 60°), RTP and TMI anomalies are similar in shape.

Summarising, for EW profiles or high magnetic latitude areas, RTP anomalies are similar in shape to TMI anomalies and therefore provide no additional information. The next step is to investigate the character of the similarity coefficient curve for these data.

3.2.2 Characteristics of the similarity coefficients

According to the definition of the similarity coefficient R (see expression 2.17), if the total magnetic intensity (TMI) anomaly and its reduction to the pole (RTP) have similar shapes (see parts 1a and 1b of Figure 3.1), their correlation coefficients R_u and R_v are also similar (1c and 1d in Figure 3.1). As a result, the similarity coefficient R (1e in Figure 3.1) has similar values to the correlation coefficients R_u (TMI) and R_v (RTP). In this case, if the correlation coefficient curves have a number of minima, the similarity coefficient curve will also display this characteristic (Figure 3.1).

Why should there be a number of minima in the correlation coefficient curve for a simple shaped anomaly? Figure 3.1 shows some examples of symmetrical curves converted from the original data. As mentioned in Section 2.7.4, the correlation coefficients are calculated by comparing a theoretical curve with the symmetrical curves from observed data by moving a window along the profile. In fact, for a single anomaly several symmetrical curves with good correspondence to the theoretical curve can always be produced. This is still a problem even in the case

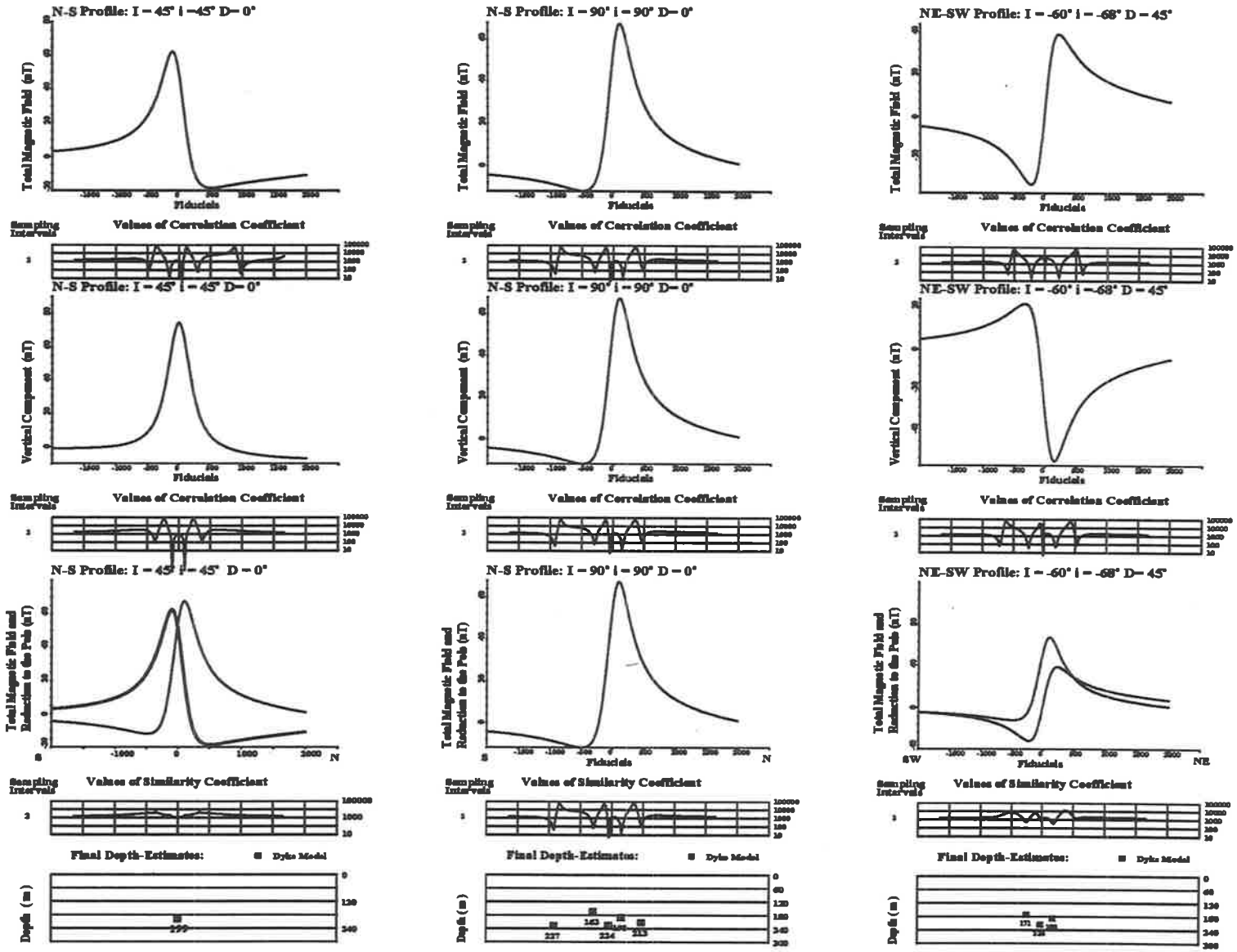

Figure 3.2: Depth estimates in varied situations using original Naudy technique.

of a profile with a symmetrical anomaly which has the exact shape as the theoretical curve. The method cannot be used on a short profile.

A further discussion about the characteristics of the similarity coefficient curves from different situations of the TMI and RTP pairs is given as follows.

Figure 3.2 shows three sets of correlation coefficient curves, their combined similarity coefficient curves and the final depth estimate produced by TMI and RTP anomalies in which all geometries and susceptibilities of models are the same as given in Table 3.1, but the geomagnetic inclination (I) and azimuth (D') are varied and the directions of the profiles are also changed. The effective inclination angle (i) is calculated based on expression (3.1).

- In the case of the EW profile (Figure 3.1), the pairs of correlation coefficient curves from TMI and RTP anomalies have exactly the same shapes and they all have several minima. The combined similarity coefficient curve also has the same shape as the two correlation coefficients. This leads to the location of several centres by these minima. Therefore no good solution is obtained by using TMI and RTP anomalies in this case to construct the similarity coefficients.

- In the case of the NS profile (Figure 3.2), if the effective inclination angle (i) is close to $+45°$ or $-45°$, although there are still several minima in the correlation coefficient curves, the shapes of the correlation coefficient curves from TMI and RTP anomalies are totally different. After combining them, the similarity coefficient curve has only one global minimum which indicates the correct centre of the anomaly. If the absolute value of the effective inclination angle is greater than $60°$ or in the extreme case $i = 90°$, the shapes of the curves (R_u and R_v) become more and more similar. Therefore the curve of the similarity coefficient becomes similar to R_u and R_v, and this leads to an increase in the number of spurious anomaly centres located.

- In the case where the profile direction is neither NS nor EW (Figure 3.2), the correct centre is located by the similarity coefficients of TMI and RTP only when the effective inclination angle (i) is close to $45°$. If the effective inclination angle is close to $90°$, the same problem of having many spurious centres will occur.

From these examples, it is clear that using a pair of fields such as the TMI and RTP, the correct located centre occurs in the case when the effective inclination $i = 45°$, but that poor centre location occurs in the case of i close to $90°$. Why should it provides a perfect result in the case of $i = 45°$, but not for the other cases? The answer will be given later (Section 3.2.3).

3.2.3 A solution: using horizontal and vertical components

The above examples indicates that there exist a right way to locate the centre of the anomaly, which is to find a pair of magnetic fields whose shapes are always different for all geomagnetic field directions and profile orientation. One solution is to use the vertical and

Direction of Profile from West to East, I=-60° , T0=60,000 nT

Dyke Model: depth=200m, width=200m, depth extent=2km, dip=45° E, strike=NS

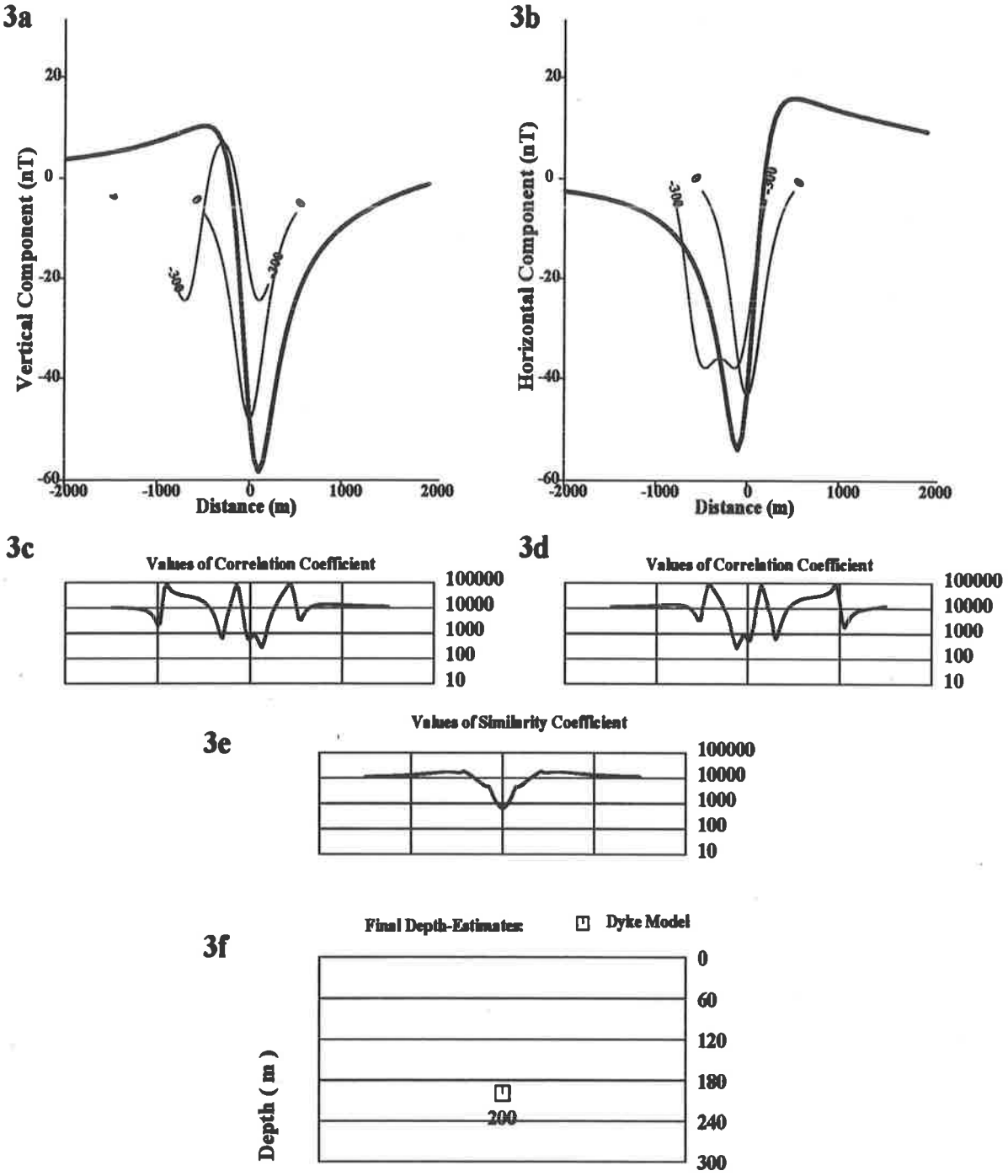

Figure 3.3: **Application of improved Naudy technique to the profile shown in Fig. 3.1.**

horizontal components of the magnetic field. These two components are a Hilbert transform pair (Shuey, 1972 and Nabighian, 1984), which are always of different shapes. As a consequence, the correlation coefficients from these two components are totally different, and therefore the combined similarity coefficients leads to a good solution.

The reason why the correct centre is located by using the TMI and RTP in the instance where the inclination $i = 45°$ is that this pair of fields is equivalent to the horizontal component (HC) and vertical component (VC) pair when the source is vertically magnetised (see Appendix A).

Figure 3.3 illustrates the significant improvement in locating the centre and determining the depth by using HC and VC components for the same model as shown in Figure 3.1.

Now in the new approach, the horizontal and vertical components are used instead of the total magnetic field and its reduction to the pole. In this case the direction of magnetisation in HC. or VC can be arbitrary. The horizontal and vertical components are obtained from a computer program (ONED2 which is a linear transform program for profile data using the FFT algorithm) developed by the author. Using this improved approach (HC and VC), the centers of the anomalies may be located accurately. Additionally, it will be shown later that by using the vertical and horizontal components it is easy to estimate the other parameters of the magnetic source.

3.3 Extension to vertical magnetic gradient anomalies

Since the vertical or horizontal magnetic gradient is sometimes measured in addition to the total magnetic intensity during an aeromagnetic survey, and because of the resolving powers of the gradient, extending the Improved Naudy Technique to process gradient and transformed data could be very useful and may provide a significant improvement to geological interpretation.

Hood (1975) and Hood *et al.* (1976 and 1979) discuss the merits of interpreting gradient data and a summary of the discussion is presented below.

1. Gradient data enhance magnetic effects from shallow sources. The data can be directly used to delineate geological contacts and can provide valuable controls on geological mapping.
2. The regional gradient of the earth's magnetic field and most long-wavelength anomalies caused by deep-seated sources in the crust are removed by the gradiometer measurements.
3. The data are free from the diurnal effect.
4. Anomalies produced by sources close to each other are well resolved.
5. Levelling of the data, required during compilation, is minimised.

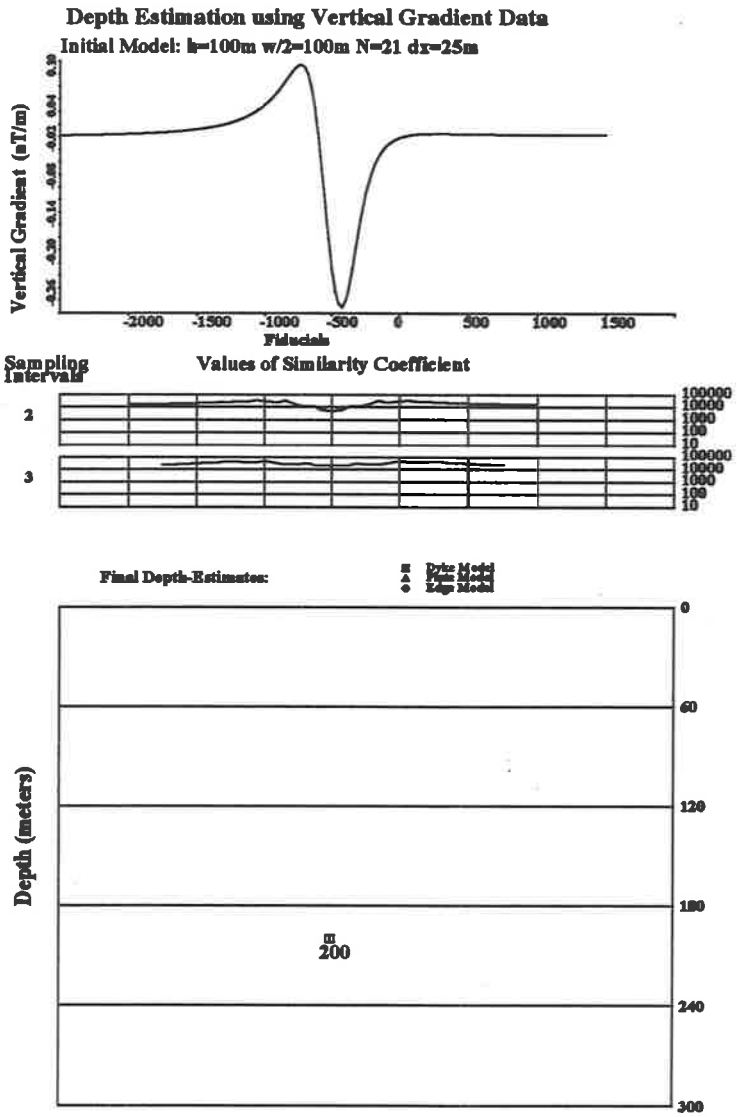

Figure 3.4: Depth estimate of a vertical gradient profile using improved Naudy technique.

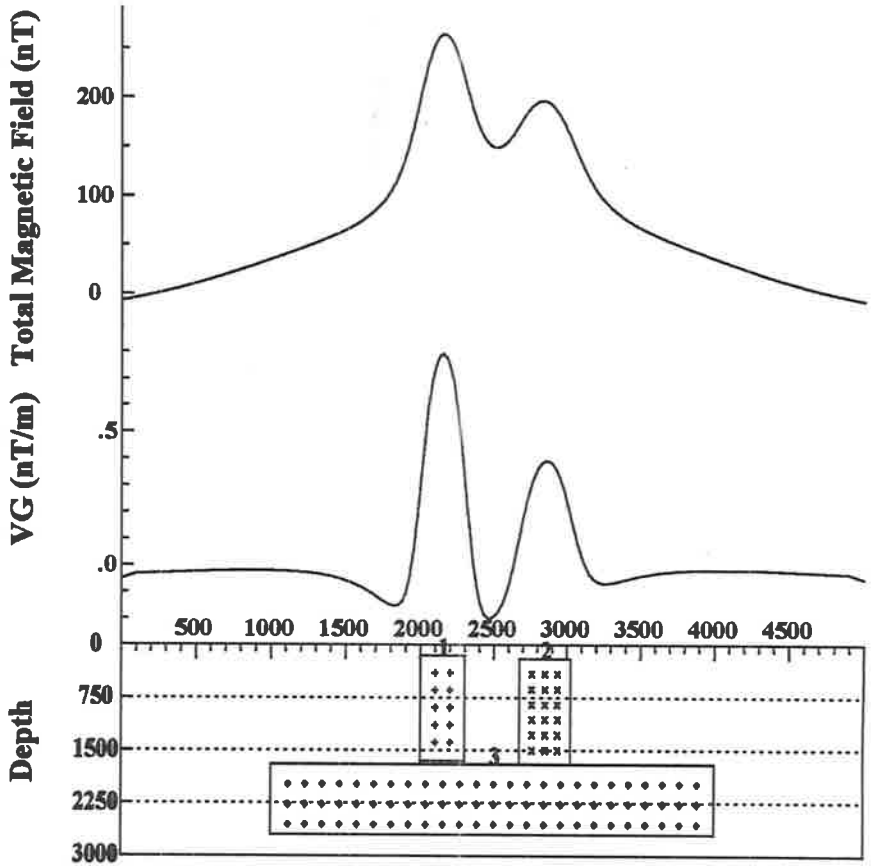

Figure 3.5: Three bodies and their magnetic fields.

The advantages of magnetic gradient data in anomaly resolution and image processing for the purpose of geological mapping have been known for some time (Nelson, 1988). A small amount of research into quantitative interpretation in the traditional style (characteristic point, graphical methods and others) has been developed by some workers (Rao and Prakasa Rao, 1970; Rao *et al.*, 1972; Green and Stanley, 1975; Stanley, 1977; Atchuta Rao et al., 1980 and 1981; Barongo, 1985; Nelson, 1988; Rajagopalan, 1989). To judge from publications, only a limited amount of work has been carried out on the application of automated computer interpretation techniques to magnetic gradient data. Nabighian (1972, 1974 and 1984) proposed a theoretical method to deal with magnetic fields (ΔT, or ΔZ or ΔH) caused by a polygonal cross-sectional body by analysing the square of the amplitude of the transformed vertical and horizontal derivatives (a Hilbert transform pair) to obtain the parameters of the body (which include depth, susceptibility or dip of the body). From the practical point of view, this method seems to be difficult to use. Keating and Pilkington (1990) recently developed a Werner-based deconvolution technique to process vertical gradient magnetic anomalies. The technique uses thin sheet and edge models. It successfully deals with real data with low noise content, but some limitations, which have been mentioned in the previous chapter for the Werner-based method, still have not been solved. Therefore, extending the Improved Naudy Technique to process gradient data appears to be advantageous.

Because of the similar characteristics of the basic model being used in the Naudy technique in the vertical gradient (Z'_z and H'_z) and the component data (ΔZ and ΔH), it is not difficult to extend the method to process gradient data. The modifications mainly consist of two stages described as follows.

1. The first stage is to obtain the vertical gradient of vertical and horizontal components (Z'_z and H'_z) which can be transformed from total field (ΔT) or vertical gradient (T'_z) or horizontal gradient (H'_z) data by using ONED2 program in the frequency domain.

2. The second stage is to generate a theoretical model curve of the vertical gradient in the vertical magnetisation direction. The chosen model is a vertical dyke with a finite depth extent. The reason for choosing this type of model is that it represents a wide ranges of models. For example, when the depth extent tends to infinity, the model becomes a dyke; on the other hand, when the depth extent becomes extremely limited, the model becomes a thin plate; and when the width of the body is very narrow and the depth extent is at least ten times the depth to the top, then the model reduces to a thin sheet. Therefore three different types of models can be applied in the calculation.

Except for these two modifications described above, the whole procedure of processing gradient data is identical to the case of processing component data. Figure 3.4 shows an example using gradient data in which the calculated model is the same as in Figure 3.1. As can be seen readily, the estimated depth of the body is exactly the same as the true depth of the model and the result is of the same precision as obtained from the component data.

Another example of processing vertical gradient data is shown in figures 3.5 and 3.6. The anomalies are composed of three parts, two of them are caused by shallow-seated dyke bodies,

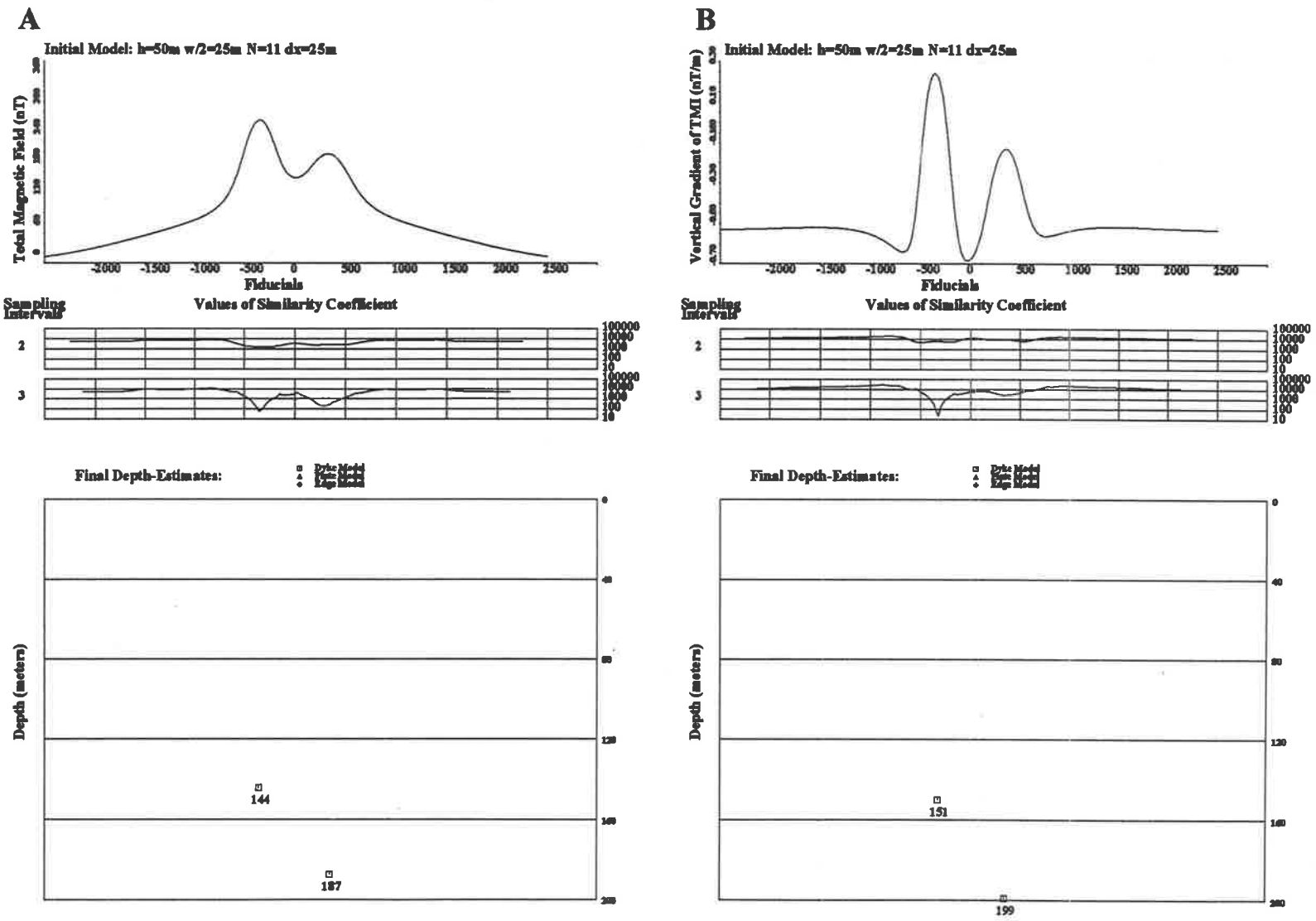

Figure 3.6: Comparison of depth estimates from component and gradient data using improved Naudy technique

A: Depth from component data. **B: Depth from vertical gradient data.**

Table 3.2: Parameters of three combined models

Parameters	Dyke A	Dyke B	Plate C
Centre Position	−350 meters	350 meters	0 meter
Depth	150 meters	200 meters	1700 meters
Width	300 meters	350 meters	3000 meters
Depth Extent	1500 meters	1500 meters	1000 meters
Dip	90°	90°	90°
Susceptibility	0.0010 CGS 0.01255 SI	0.0007 CGS 0.0088 SI	0.002 CGS 0.0251 SI
Strike	NS	NS	NS

Note:
$I = -60°$, $T = 60,000\ nT$,
Profile is along EW direction,
Sample spacing of data is 25 m.

another represents the regional field in the background which is caused by a thick plate body (see Figure 3.5). The parameters of the three models are listed in Table 3.2. The depth estimates and their relative errors of the two shallow bodies from analysing component data and from analysing vertical gradient data are given in Table 3.3. Due to the effect of the regional magnetic field and the interference from nearby sources, the magnetic anomalies of these two shallow sources are difficult to separate. In consequence, the depth estimates from analysing component data are in error. However the vertical gradient enhances the effects of individual sources and these anomalies are well separated. As a result the gradient data provide a much better solution.

3.4 Determination of source parameters other than depth

In this section, the determination of source parameters from the Improved Naudy Technique is discussed. Appendix A provides a set of formulae, including total field (ΔT), vertical and horizontal components (ΔZ and ΔH), vertical gradient of total field (T'_z), vertical gradients of vertical component and horizontal component (Z'_z and H'_z), for some simple two dimensional bodies including edge, step, dyke (with infinite and finite depth extent), thin sheet, horizontal thin sheet, thin plate and horizontal cylinder. The total fields (or the vertical gradient of total fields) caused by the infinite dyke, edge, thin sheet, thin plate and horizontal cylinder can be resolved into their symmetrical and antisymmetrical parts. These two components are proportional to ΔZ and ΔH (or Z'_z and H'_z) respectively, in which the causative body has the same depth and width as that of the total field (or T'_z), but both the oblique angles of magnetisation and the causative body are 90°. Figure 3.7 illustrates the relationships between

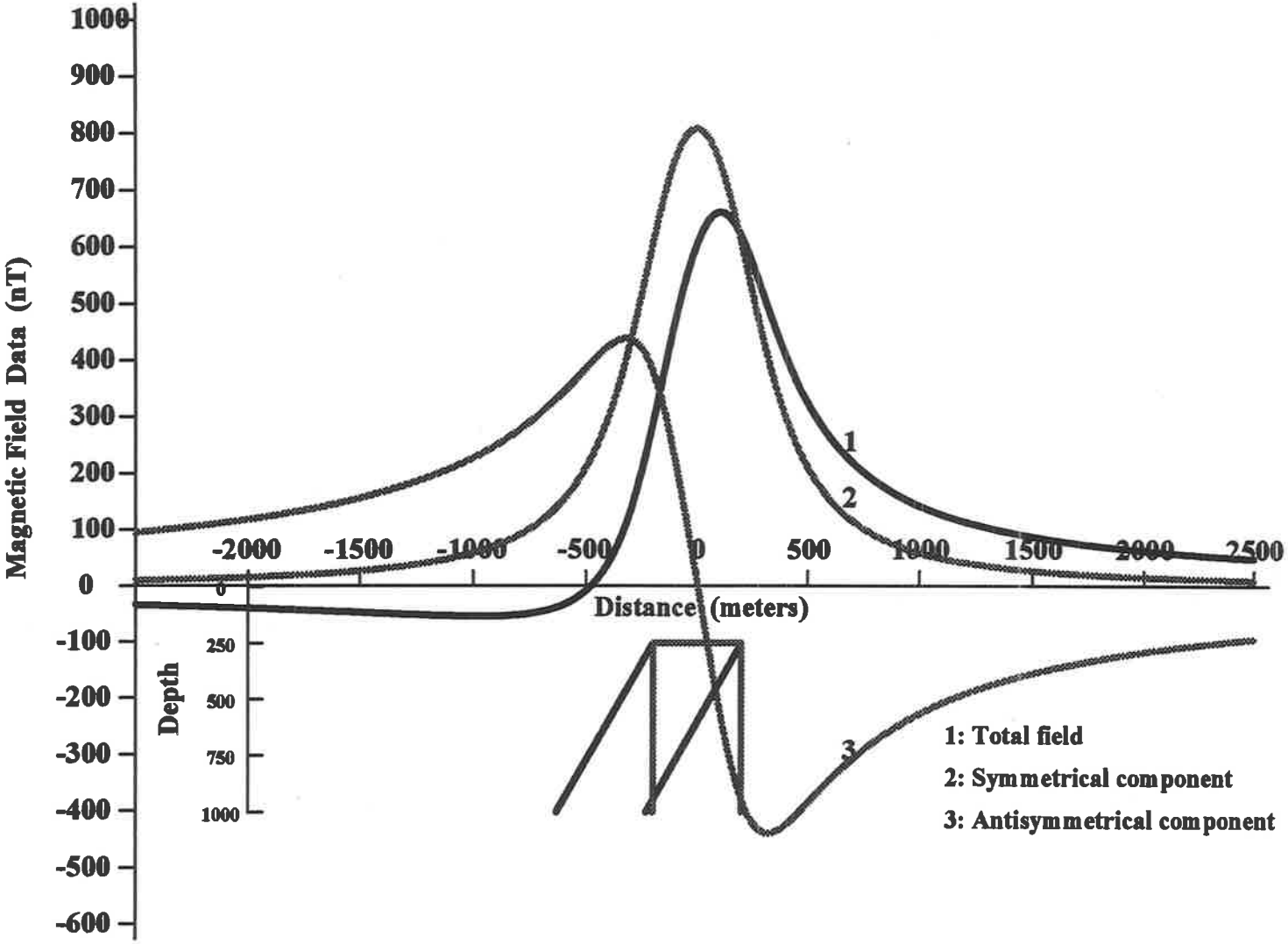

Figure 3.7: **Total magnetic field and its symmetrical & antisymmetrical components and their correspoding causative dykes**

Table 3.3: The comparison of depth estimates from component and gradient data having a regional background field

Model		Component Data		Gradient Data	
Body	Depth	Depth Estimate	Relative Error	Depth Estimate	Relative Error
Dyke A	150 m	144 m	4%	151 m	0.7%
Dyke B	200 m	187 m	6.5%	199 m	0.5%

Notation:
Parameters of initial model:
Depth= 50 m, Width=100 m,
Number of window points is 11,
Sampling interval number are 2, 3.

the total field and its symmetrical and antisymmetrical components as well as the causative body which produces them. The total field (or T'_z) caused by the horizontal thin sheet and the vertical step, the symmetrical and the antisymmetrical parts of the total field (or T'_z) correspond to the horizontal component (or H'_z) and the vertical component (or Z'_z) in the vertical magnetisation.

Based on those expressions of the vertical and horizontal components (or Z'_z and H'_z) shown on Appendix A, in which the total field (or T'_z) can be resolved into symmetrical and antisymmetrical components, the angle between the direction of magnetisation and the dip of the magnetic body can be determined from the ratios of the symmetrical or antisymmetrical components of the vertical and the horizontal components (or Z'_z and H'_z) at any position along the profile. If there is only induced magnetisation, the magnetisation angle is equal to the effective inclination of the induced magnetisation on the profile. From this the dip of the magnetic body can be obtained directly. After obtaining the effective inclination (i), effective magnetic intensity (T'_0) and the dip of the body (d), the susceptibility contrast (k) can be obtained from either the vertical component (or Z'_z) or the horizontal component (or H'_z) with their basic even and odd functions which are indicated in Appendix A. Each type of model produces different even and odd functions.

The dyke, edge and thin plate models can adequately represent many geological situations. The determination of the dip and susceptibility for these typical models is derived in the following sections. Note that the depth to the top of these models is estimated as described in the original Naudy method (Naudy, 1971).

3.4.1 Determinations of dip and susceptibility for a dyke model

In order to derive parameters for a dyke model with infinite depth extent (see Figure A.3 in Appendix A), the vertical and horizontal components can be expressed as

$$\begin{aligned}\Delta Z &= 2kTb\sin d[-\sin(i-d)\cdot\ln\frac{R_2}{R_1}+\cos(i-d)\cdot\theta],\\ \Delta H &= 2kTb\sin d[\cos(i-d)\cdot\ln\frac{R_2}{R_1}+\sin(i-d)\cdot\theta],\end{aligned}$$

where

k: susceptibility contrast,

T: the intensity of the earth's magnetic field,

I: the inclination of the earth's magnetic field from the horizontal (negative in southern hemisphere),

i: the effective inclination of the earth's magnetic field from the horizontal (see Appendix B),

b: the ratio between $\sin I$ and $\sin i$ (see Appendix B),

d: dip of the body, measured clockwise from the positive profile direction.

And

$$\begin{aligned}R_1 &= [(x+\frac{w}{2})^2+h^2]^{\frac{1}{2}},\\ R_2 &= [(x-\frac{w}{2})^2+h^2]^{\frac{1}{2}},\\ \theta &= \cos^{-1}(\frac{x^2+h^2-(\frac{w}{2})^2}{R_1\cdot R_2}),\end{aligned}$$

or

$$\begin{aligned}\theta &= \tan^{-1}(\frac{x_1}{h})-\tan^{-1}(\frac{x_2}{h}),\\ x_1 &= x+\frac{w}{2},\\ x_2 &= x-\frac{w}{2}.\end{aligned}$$

The angular function θ is an even function which is composed of the basic symmetrical curve for the dyke model. The logarithm function $\ln\frac{R_2}{R_1}$ is an odd function which forms the basic antisymmetrical curve for the dyke. The vertical and horizontal components can be split into symmetrical and antisymmetrical parts.

From the symmetrical parts, the index angle $(i-d)$ can be obtained as follows.

$$\frac{\Delta Z}{\Delta H} = \frac{2kTb\sin d\cdot\cos(i-d)\cdot\theta}{2kTb\sin d\cdot\sin(i-d)\cdot\theta} = \cot(i-d),$$

Therefore

$$i-d = \cot^{-1}(\frac{\Delta Z}{\Delta H}).$$

From the antisymmetrical parts, the index angle $(i-d)$ can be obtained as shown below.

$$\frac{\Delta Z}{\Delta H} = \frac{2kTb\sin d\cdot[-\sin(i-d)]\cdot\ln\frac{R_2}{R_1}}{2kTb\sin d\cdot\cos(i-d)\cdot\ln\frac{R_2}{R_1}} = -\tan(i-d),$$

Therefore

$$i-d = \tan^{-1}(-\frac{\Delta Z}{\Delta H}).$$

In the case where magnetisation may be assumed to be induced only, i can be obtained from the expression $i = \tan^{-1}(\tan I \sec D')$, where D' is the angle between magnetic north and the profile direction (see appendix B), and the dip d of the magnetic body can be obtained either from the symmetrical part as

$$d = i - \cot^{-1}(\frac{\Delta Z}{\Delta H}),$$

or from the antisymmetrical part as

$$d = i - \tan^{-1}(-\frac{\Delta Z}{\Delta H}).$$

After establishing the parameters T, b, i, d, as well as the vertical and horizontal components (ΔZ and ΔH), which can be computed using the ONED2 program (see Appendix C) by using the fast Fourier transform algorithm, it is possible to determine the value of the susceptibility. The procedure is as follows.

- Using the Naudy technique (see Section 2.7.4), the centre of the anomaly is located and the depth and width based on the best fitting curve from the theoretical models are estimated.
- The estimated depth and width are used to compute the basic even and odd functions, for example θ and $\ln(\frac{R_2}{R_1})$.
- Finally the susceptibility can be estimated by

$$k = \frac{\Delta Z}{2Tb\sin d\cdot[-\sin(i-d)\cdot\ln\frac{R_2}{R_1}+\cos(i-d)\cdot\theta]},$$

or

$$k = \frac{\Delta H}{2Tb\sin d\cdot[\cos(i-d)\cdot\ln\frac{R_2}{R_1}+\sin(i-d)\cdot\theta]}.$$

In order to avoid excess calculation and to obtain a more reliable result, the calculation of dip and susceptibility should be done only at the centre of the anomaly. The formulae can be simplified to

$$d = i - \cot^{-1}\left(\frac{\Delta Z_{x=0}}{\Delta H_{x=0}}\right),$$

$$K = \frac{\Delta Z_{x=0}}{2Tb\sin d \cdot \cos(i-d)\cdot\theta},$$

or

$$K = \frac{\Delta H_{x=0}}{2Tb\sin d \cdot \sin(i-d)\cdot\theta},$$

where $\theta = 2\tan^{-1}(\frac{w}{2h})$.

The vertical and horizontal components are used to calculate the dip and susceptibility. Because they are not obtained through observation, so the accurate determination of the vertical and horizontal components is very important. In general, the component transform program is adequate, but occasionally a datum levelling problem can occur where the horizontal and vertical components might not be at the same background level. This datum levelling problem may affect the precision of the estimated parameters. As is well known, the first derivatives of the magnetic fields significantly reduce the effect of the regional gradient. It follows that using the vertical and horizontal gradients to calculate the dip and susceptibility may provide a reliable answer.

The vertical and horizontal gradients for a dyke with infinite depth extent can be expressed as

$$Z'_z = 2kTb\sin d[-\sin(i-d)\cdot\left(\frac{h}{{R_1}^2} - \frac{h}{{R_2}^2}\right) + \cos(i-d)\cdot\left(\frac{x_1}{{R_1}^2} - \frac{x_2}{{R_2}^2}\right)],$$

and

$$H'_z = 2kTb\sin d[\cos(i-d)\cdot\left(\frac{h}{{R_1}^2} - \frac{h}{{R_2}^2}\right) + \sin(i-d)\cdot\left(\frac{x_1}{{R_1}^2} - \frac{x_2}{{R_2}^2}\right)].$$

where $x_1 = x + \frac{w}{2}$, and $x_2 = x - \frac{w}{2}$.

It is clear that the common function $(\frac{x_1}{{R_1}^2} - \frac{x_2}{{R_2}^2})$ is an even function, and the function $(\frac{h}{{R_1}^2} - \frac{h}{{R_2}^2})$ is an odd function. The vertical and horizontal gradients can be resolved into symmetrical and antisymmetrical components. For the symmetrical part, the angle $(i-d)$ can be obtained from

$$\frac{Z'_z}{H'_z} = \frac{2kTb\sin d\cdot\cos(i-d)\cdot\left(\frac{x_1}{{R_1}^2} - \frac{x_2}{{R_2}^2}\right)}{2kTb\sin d\cdot\sin(i-d)\cdot\left(\frac{x_1}{{R_1}^2} - \frac{x_2}{{R_2}^2}\right)} = \cot(i-d),$$

from which it follows that

$$i - d = \cot^{-1}\left(\frac{Z'_z}{H'_z}\right).$$

For the antisymmetrical part, the angle $(i-d)$ can be obtained as follows.

$$\frac{Z'_z}{H'_z} = -\frac{2kTb\sin d\cdot\sin(i-d)\cdot(\frac{h}{R_1{}^2}-\frac{h}{R_2{}^2})}{2kTb\sin d\cdot\cos(i-d)\cdot(\frac{h}{R_1{}^2}-\frac{h}{R_2{}^2})} = -\tan(i-d),$$

from which it follows that

$$i-d = \tan^{-1}(-\frac{Z'_z}{H'_z}).$$

Using the same procedure as used for the component data, the dip and susceptibility can be obtained from the following expressions. For the symmetrical component:

$$d = i - \cot^{-1}(\frac{Z'_z}{H'_z}),$$

For the antisymmetrical component:

$$d = i - \tan^{-1}(-\frac{Z'_z}{H'_z});$$

For the whole anomaly:

$$k = \frac{Z'_z}{2Tb\sin d\cdot[-\sin(i-d)\cdot(\frac{h}{R_1{}^2}-\frac{h}{R_2{}^2})+\cos(i-d)\cdot(\frac{x_1}{R_1{}^2}-\frac{x_2}{R_2{}^2})]},$$

or

$$k = \frac{H'_z}{2Tb\sin d\cdot[\cos(i-d)\cdot(\frac{h}{R_1{}^2}-\frac{h}{R_2{}^2})+\sin(i-d)\cdot(\frac{x_1}{R_1{}^2}-\frac{x_2}{R_2{}^2})]}.$$

Z'_z and H'_z can be obtained from ONED2 program, the even and odd functions can be obtained following the same procedures as used to derive the component data. In practise, the dip and susceptibility are calculated from the centre of the anomaly, for which the formulae are as follows.

At the centre of the anomaly, Z'_x and H'_z can be simply expressed as

$$Z'_z|_{x=0} = 2kTb\sin d\cdot\cos(i-d)\cdot\frac{w}{(\frac{w}{2})^2+h^2},$$

and

$$H'_z|_{x=0} = 2kTb\sin d\cdot\sin(i-d)\cdot\frac{w}{(\frac{w}{2})^2+h^2};$$

then the dip is given by

$$d = i - \cot^{-1}(\frac{Z'_z|_{x=0}}{H'_z|_{x=0}}).$$

The susceptibility is obtained by

$$k = \frac{Z'_z|_{x=0}}{2Tb\sin d\cdot\cos(i-d)\cdot\frac{w}{(\frac{w}{2})^2+h^2}},$$

or

$$k = \frac{H'_z|_{x=0}}{2Tb \sin d \cdot \sin(i-d) \cdot \frac{w}{(\frac{w}{2})^2+h^2}}.$$

A method has been established to estimate the dip and susceptibility of a dyke model. Dyke-type bodies exist widely in real geological situations, e.g. dolerite dykes, banded iron formations, geological contacts, and dipping magnetised layers. All these bodies may produce dyke-type anomalies. Therefore the method could be widely used to deal with magnetic anomalies caused by these geological sources.

In most real cases, the depth extent of the dyke-type geological bodies do not tend to infinity but are limited, and their influence may require to be taken into account. The next section will provide a more detailed analysis of errors caused by limited depth extent when infinite depth extent has been assumed.

3.4.2 Analysis of estimated dip and susceptibility from a finite extent dyke

When the depth extent of the body is finite or the width is relatively great or the dip of the body is not vertical, the estimates of the dip and susceptibility, using the formulae derived from a dyke with infinite depth extent, can introduce some errors. The size of the error depends on the ratios of the depth extent and width relative to the depth to the top of the body and the dip of the body. In practice, if the absolute error of the dip estimate is less than 15° and the relative error of the susceptibility estimate is less than 20%, this size of error is deemed acceptable and the estimates are appropriate for determining the parameters of the magnetic body.

After a great deal of model testing, using ideal shaped models, the relationship between errors in parameter estimates and the resolution of the parameters of the body are revealed as follows.

If the depth extent is more than five times the depth to the top of the body, the width is less than five times the depth and the dip of the body is between 60° and 120°, the error of the estimated dip and susceptibility will be less than 20% if using total field data, and be less than 15% if using gradient data. These conditions are satisfied by many geological terrains. This study is based on an analysis of purely theoretical models where the centre of the body is known exactly. Therefore there are no errors due to the incorrect location of the centre of the body.

Effect of width on error

The error in the estimates comes from the three sources: the width of the body, the depth extent and the dip. Firstly the study checks the influence of the width. The width is a very important parameter in defining a dyke, in geophysical terms. For a thin dyke, in general, the width is equal to or less than the depth to the top of the dyke, and the depth extent is greater than five times the top depth. A thick dyke is defined as having a width greater than the depth

Error Analysis of Theoretical Model for Varying Width

(Dip of Body is 90 Degrees)

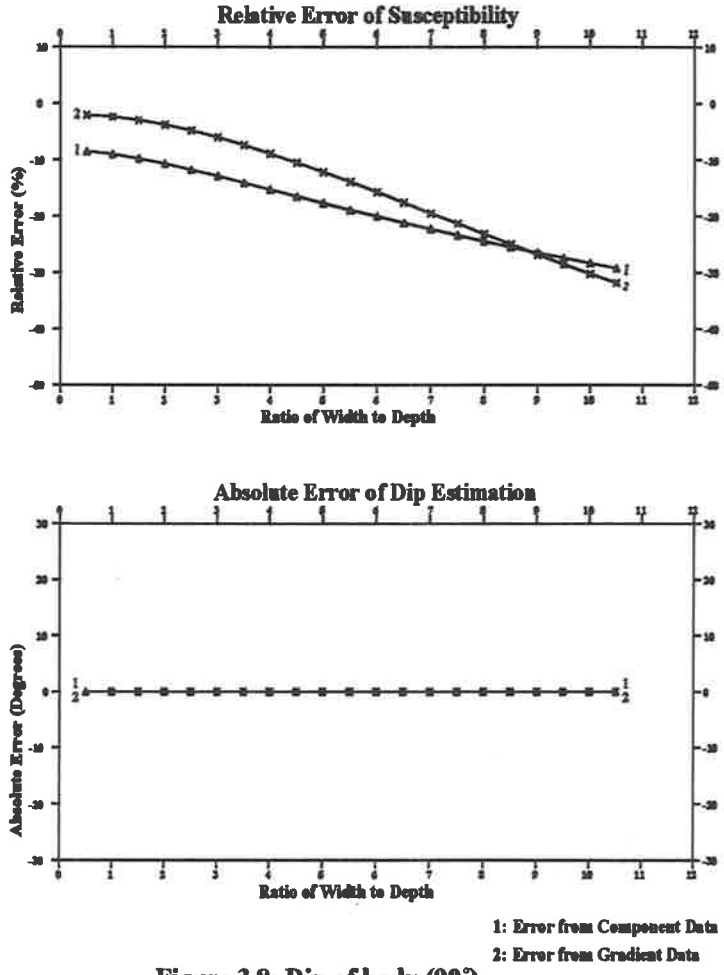

Figure 3.8: Dip of body (90°)

Error Analysis of Theoretical Model for Varying Width

(Dip of Body is 45 Degrees)

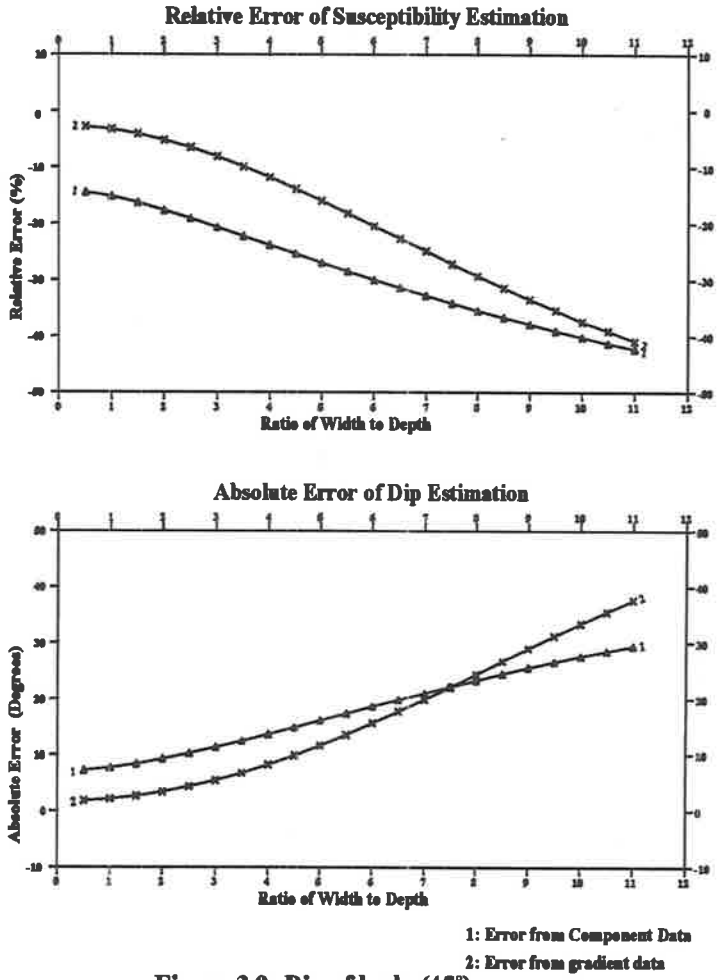

Figure 3.9: Dip of body (45°)

Table 3.4: Parameters of a set of dyke models to check the influence of varied width

Parameter	Value		Parameter	Value
Depth	100 metres		Depth Extent	1000 metres
Dip	90°		Susceptibility	0.005 CGS or 0.0628 SI

Notation:
$I = i = -60°$,
Intensity of total field= 60,000 nT,
Strike direction is NS,
Sampling interval is 25 metres,
Total number of data points is 101.

to the top of the dyke. If the depth extent is not more than five times the width, it is considered to be a thick plate. Here, the dyke is not only discussed as defined by geological or geophysical terms, but as calculated by the formulae shown in Appendix A (A.5), which may include both the thin or thick dykes with finite depth extent and the thick plate as well. In order to check the effect of changing width, the dip of a set of dykes is defined as vertical, and the depth, depth extent and susceptibility are fixed as constants.

Figure 3.8 provides an example for an error analysis for varying widths of a set of dyke models. The parameters of the calculated models are in Table 3.4. The top graph illustrates the relative error of estimating susceptibility and the bottom graph shows the absolute error of the dip estimation. From the diagram, when the ratio of the width to the depth is less than five the error curve of the susceptibility calculated from the component data is close to a linear curve and the error is less than 20%. The error curve from the gradient data is composed of two sections: in the first part where the ratios are less than four, the curve is not linear and the values of the errors are less than 10%. When the ratios of the width to the depth are greater than four, the slope from the gradient is greater than the slope from the component data. This means that when the ratio of the width to the depth is high, the estimation of the susceptibility from gradient data becomes worse than the estimate determined from component data. When the dip angles are chosen to be 90°, the absolute errors of the dip estimates are zero. If the dip angle is not vertical, the errors from the estimations of the susceptibility and dip are larger than the errors from the model with vertical dip angle. When the dip angles are further from the vertical even larger errors occur. Figure 3.9 provides the error analysis curves for a set of models with a 45° dip angle. The length of the body is equal to the depth extent of the first model set shown in Figure 3.8, and the other parameters are also the same as the parameters of the first model set.

In conclusion, if the ratios of the width to the depth are increased, the relative errors will also increase and vice versa. A further point is that when the ratios of the width to the depth is less

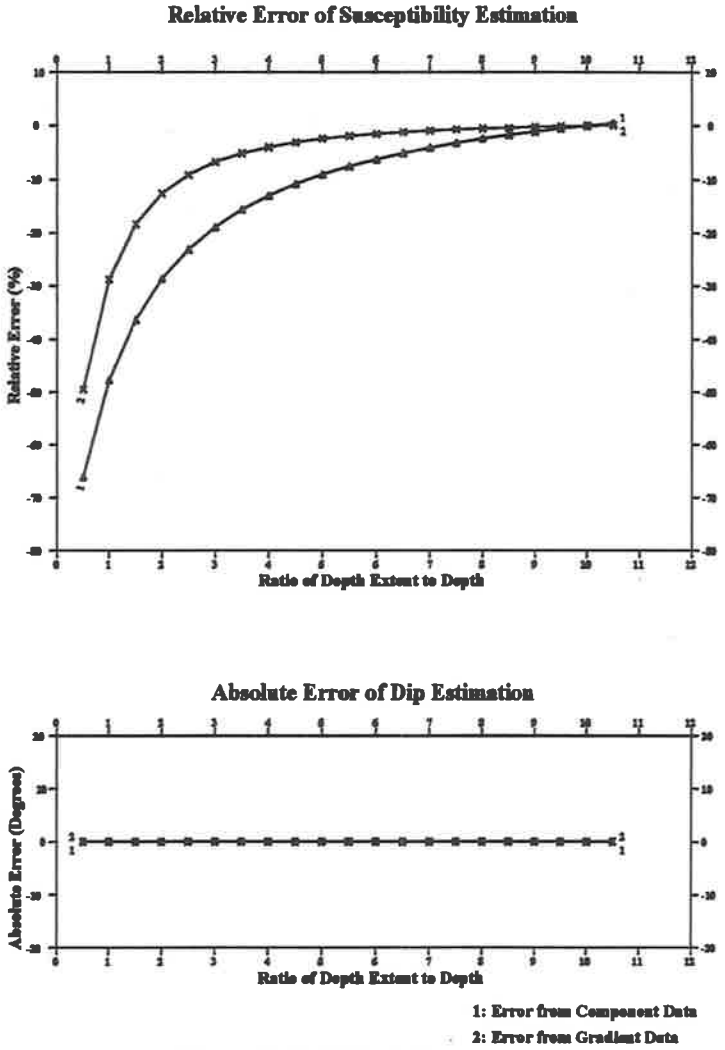

Figure 3.10: Thin Dyke

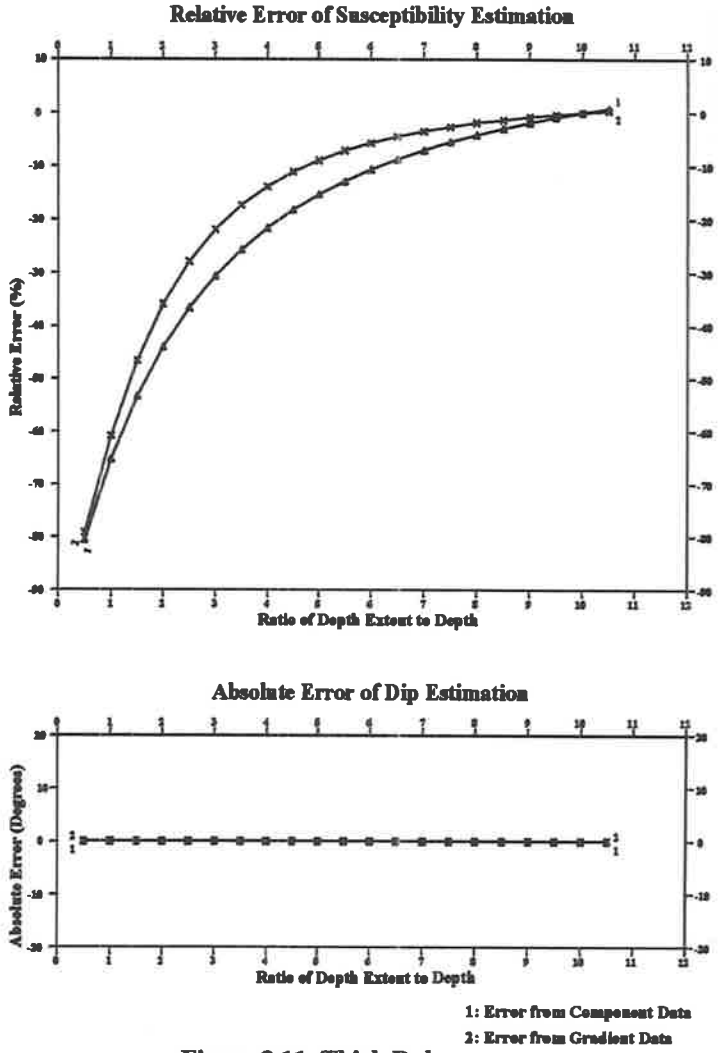

Figure 3.11: Thick Dyke

Table 3.5: Parameters of two sets of dyke models to check the influence of varied depth extent

Parameter	Value		Parameter	Value
Depth	100 metres		Strike	NS
Dip	90°		Susceptibility	0.005 CGS
Thin Dyke			**Thick Dyke**	
Width	100 metres		Width	400 metres

Notation:
$I = i = -60°$,
Intensity of total field= 60,000 nT,
Sampling interval is 25 metres,
Total number of data points is 101.

than five, the errors from the gradient data are much less than the errors from the components of total field data. For the situation when the ratio of the width to the depth is greater than five, the edge model is used to deal with such anomalies, and a more detailed discussion is presented in the following sections.

Error effect from depth extent

Under the assumption that the width of the dyke is less than five times the depth of the body, Figures 3.10 and 3.11 show the errors of the parameter estimates with varying depth extent of the body for thin and thick dyke models. In order to check the influence of changing depth extent, the models are designed as a set of vertical dykes. The parameters of the dyke models are listed in Table 3.5. The top graph shows the relative errors from the susceptibility estimates and the bottom graph gives a zero error from the dip estimates for the dip angle of the calculated bodies at 90°. From the top graph, it is evident that when the ratios of the depth extents to the depths are small the estimates contain significant errors. As soon as the ratios increase the errors rapidly drop off. If the ratios are greater than five, the errors become stable and small. Compared with errors from the thin and the thick dyke models, it verifies the conclusion from varying widths that the thin dyke model gives a much better result than the thick dyke model. For example, if the ratio is five, the error of the thin dyke model for field data is about 9%, but in contrast the error of the thick dyke model is around 15%.

Figures 3.12 and 3.13 show that the error analysis of varying depth extent to thin and thick models respectively, in which the dips of the body are not vertical and the other parameters are the same as in Table 3.5. Note that if the dip is not vertical, some error will be introduced. The smaller the ratios of depth extent to the depth the bigger the errors. When the ratios are greater than four, the errors tend to be stable and small. If the dip angle is 45°, errors of the

Error Analysis of Theoretical Model for Varying Depth Extent

(Dip of Thin Dyke Body is 45 Degrees)

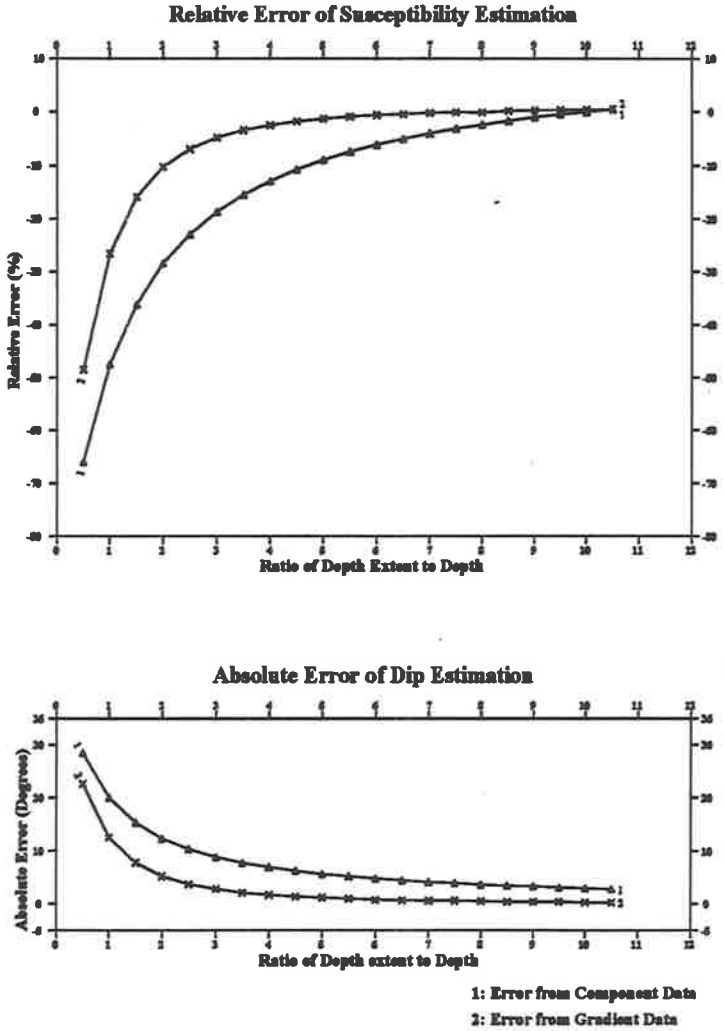

Figure 3.12: Thin Dyke

Error Analysis of Theoretical Model for Varying Depth Extent

(Dip of Thick Dyke Body is 60 Degrees)

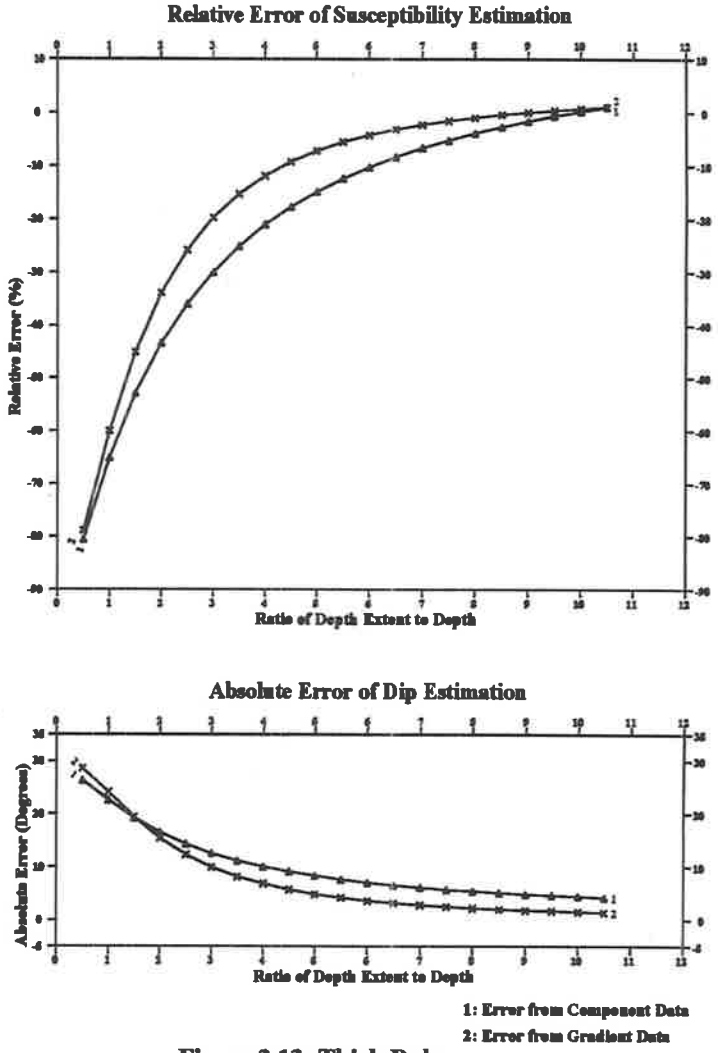

Figure 3.13: Thick Dyke

Table 3.6: Parameters of two sets of dyke models to check] the influence of varied dip

Parameter	Value	Parameter	Value
Depth	100 m	Strike	NS
Length of Body	500 m	Susceptibility	0.005 CGS/0.0628 SI
Thin Dyke		Thick Dyke	
Width	100 metres	Width	400 metres

Notation:
$I = i = -60°$,
Intensity of total field= 60,000 nT,
Sampling interval is 25 metres,
Total number of data points is 101.

susceptibility are similar to the results from that for the vertical dykes.

The size of the error for changing depth extent depends on the values of the depth extents and also on the influence from the dip angles. The greater the depth extent the smaller the errors, and the closer the dip angle to the vertical the more stable and the smaller the errors. Once again the errors of the estimates provided by using gradient data are much smaller than those made by using field data.

Effect from varying dip

In the last part, the influence of changing dip angles is discussed. Figures 3.14 and 3.15 illustrate the error effect for the differing dips of thin and thick bodies respectively. In order to clearly define the problem, the dyke models are allocated the same body length (the parameters of two sets of models are given in Table 3.6). However, the depth extent of the body may be different. Under this assumption, when the dip of the body is further away from the vertical the distance from the observed plane to the depth to the bottom of body is decreased. In this case, when the dip angles are close to the horizontal plane, the magnetic effect from the bottom part of the body will be significant.

The formulae which are derived from the infinite depth extent dyke are not suitable for estimating the susceptibility and dip of the body, because they will lead to significant errors. According to the results from model tests in figures 3.14 and 3.15, when the angles are beyond 45° and 135°, the errors grow even larger. For the results from varying dip angles, the thin dyke case provides a more accurate set of estimates than for the thick dyke case and the errors from the gradient data are also smaller than the errors from analysing the components of the total field data.

Error Analysis of Theoretical Model for Varying Dip of Body

(Thin Dyke Model)

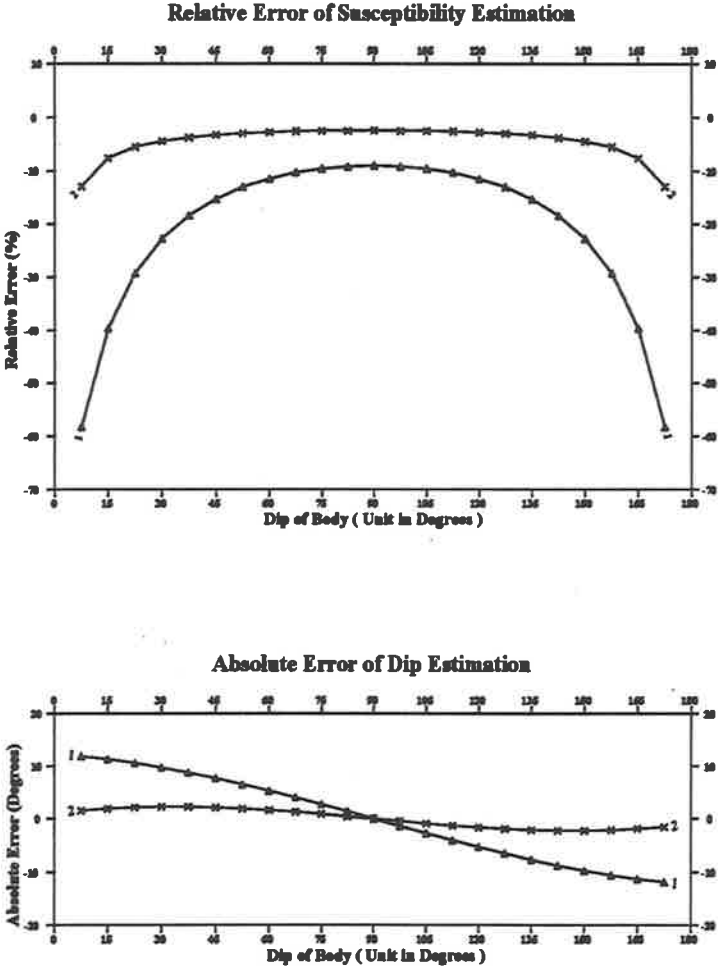

Figure 3.14: Thin Dyke

Error Analysis of Theoretical Model for Varying Dip of Body

(Thick Dyke Body)

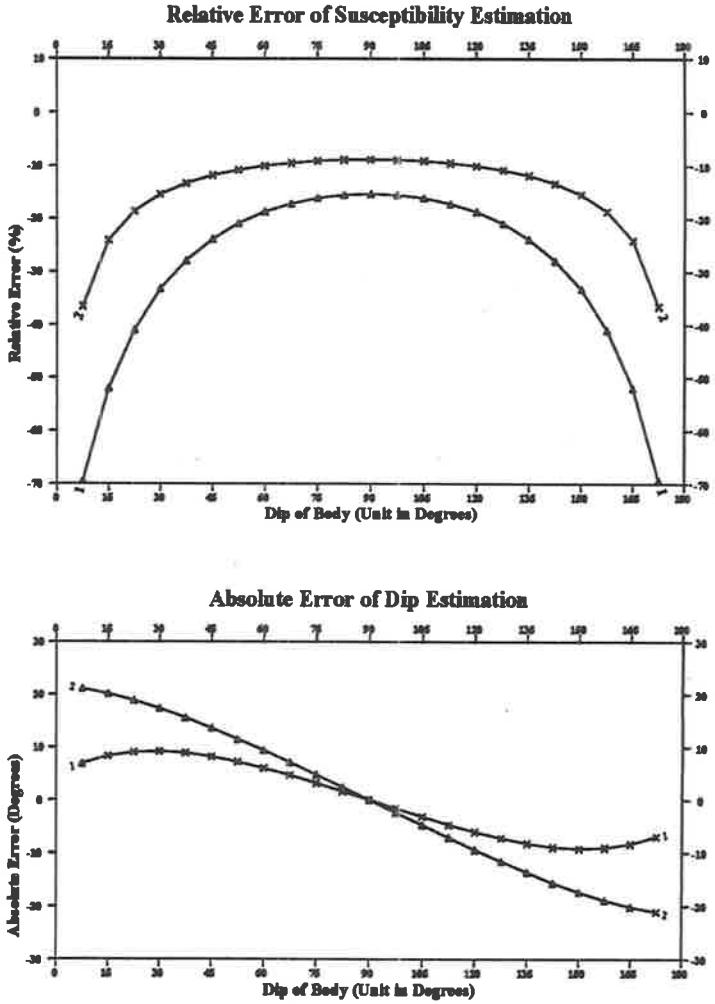

Figure 3.15: Thick Dyke

Summary of error effects

In conclusion, a combination of all the effects from varying width, depth extent and the dip angle of the dyke, produces a few points worth noting.

1. The depth extent is the most important factor controlling parameter estimates. As the ratio of the depth extent to the depth of the body is increased, the errors will decrease rapidly. When the ratios are greater than four or five, the errors tend to be stable and small.

2. The width of the body also affects the size of the error. When the ratio of the width to the depth to the top of the body is less than two, the errors are very small, but as the ratio increases, the error grows (see figures 3.8 and 3.9).

3. When the dip angle is close to the horizontal plane, the estimates are inaccurate, especially susceptibility estimates. When the dip of the body is close to the vertical, the errors tend toward zero and become more stable.

4. A fact is that when observed data are not disturbed by noise, gradient data can produce more accurate results than the component data. In the general case, the errors from analysing gradient data are only equal to half the value of the errors produced by analysing field data. This point demonstrates the advantages of using gradient data.

Finally mention should be made of the conditions for determining a theoretical standard model which is used for creating theoretical curves to match measured anomalies. In most geological situations, the depth extents of the bodies are not infinite but limited. The assumption that the depth extent of the standard model is ten times the depth to the top of the body would probably be more suitable for the real geological situation. Furthermore, under this assumption, when the width of the body is less than five times the depth to the top of the body, the magnitude of the error from the component data is 9%, and from the gradient data is only 1%. When the width is narrow, the error will be smaller, so it is reasonable to establish as the basic standard model that the depth extent be ten times the depth to the top of the body.

3.4.3 Determinations of dip and susceptibility for the edge model

In the last section, it was mentioned that errors occur if the dyke width is many times the depth to the top. This problem can be solved by using the edge model. When the width of the body is greater than four or five times the depth to the top of the body, the anomaly is easily separated into two opposite signed anomalies by using the horizontal gradient (in addition, the sampling interval of the profile is required to be small). These two anomalies correspond to the thin sheets located at the two edges of the original wide body. The formulae of the fields caused by thin sheet are the same as the horizontal gradients of the fields caused by the edge model, except for a width factor w (Reford, M.S., 1978).

It is worth noting that when people consider using the edge model to deal with data, the horizontal gradient of the original data is often used in the interpretation (Hartman *et al.*, 1971; Naudy, 1971; Nabighian, 1972; Green and Stanley, 1975). Instead of using the total field anomaly produced by the edge, interpreters often refer to the horizontal gradient of the edge anomaly which is equivalent to the total field anomaly of a thin sheet.

Now the same analysis as shown in the dyke model is used to treat the thin sheet model. The formulae for the components and gradients caused by the thin sheet are given in (A.6) (see Appendix A). The formulae used here are little different from the expressions from (A.60) to (A.65), which are without the constant factor w (width), because horizontal gradients of anomalies caused by the edge model (Z'_x and H'_x) are directly applied in the calculations.

The horizontal gradients of the vertical and horizontal components of the edge model, i.e. the vertical and horizontal fields of the thin sheet, are given as

$$\Delta Z = 2kTb \sin d[\sin(i-d) \cdot \frac{x}{R^2} + \cos(i-d) \cdot \frac{h}{R^2}],$$

and

$$\Delta X = 2kTb \sin d[-\cos(i-d) \cdot \frac{x}{R^2} + \sin(i-d) \cdot \frac{h}{R^2}],$$

where $R^2 = x^2 + h^2$.

The common function $\frac{h}{R^2}$ is an even function, and $\frac{x}{R^2}$ is an odd function. From the central anomaly alone, an estimate of the dip can be obtained by

$$\frac{\Delta Z_{x=0}}{\Delta H_{x=0}} = \frac{2kTb \sin d \cdot \cos(i-d) \cdot \frac{1}{h}}{2kTb \sin d \cdot \sin(i-d) \cdot \frac{1}{h}} = \cot(i-d), \tag{3.3}$$

from which it follows that,

$$i - d = \cot^{-1}(\frac{\Delta Z_{x=0}}{\Delta H_{x=0}}),$$

or

$$d = i - \cot^{-1}(\frac{\Delta Z_{x=0}}{\Delta H_{x=0}}).$$

The susceptibility can be determined by

$$k = \frac{\Delta Z_{x=0}}{2Tb \sin d \cdot \cos(i-d) \cdot \frac{1}{h}},$$

or

$$k = \frac{\Delta H_{x=0}}{2Tb \sin d \cdot \sin(i-d) \cdot \frac{1}{h}}.$$

For the case of vertical gradients of the measured data, the formulae can be expressed as

$$Z'_z = 2kTb \sin d[\sin(i-d) \cdot (\frac{2hx}{R^4}) + \cos(i-d) \cdot (\frac{h^2-x^2}{R^4})],$$

and

$$H'_z = 2kTb \sin d[-\cos(i-d) \cdot (\frac{2hx}{R^4}) + \sin(i-d) \cdot (\frac{h^2-x^2}{R^4})].$$

The dip can be obtained from gradient data at the centre of the anomaly by

$$\frac{Z'_z|_{x=0}}{H'_z|_{x=0}} = \frac{2kTb\sin d\cdot\cos(i-d)\cdot\frac{1}{h^2}}{2kTb\sin d\cdot\sin(i-d)\cdot\frac{1}{h^2}} = \cot(i-d),$$

and this leads to

$$d = i - \cot^{-1}\left(\frac{Z'_z|_{x=0}}{H'_z|_{x=0}}\right).$$

The susceptibility can be obtained from the central gradient data by

$$k = \frac{Z'_z|_{x=0}}{2Tb\sin d\cdot\cos(i-d)\cdot\frac{1}{h^2}},$$

or

$$k = \frac{H'_z|_{x=0}}{2Tb\sin d\cdot\sin(i-d)\cdot\frac{1}{h^2}}.$$

As mentioned before, when the edge model is proposed to deal with measured anomalies, the theoretical curve from the thin sheet model is used to match the horizontal gradient data of the measured profile.

There are three cases when processing horizontal gradient data, in which the original data may be composed of a wide, or a narrow or an intermediate width anomaly. In the first case, the width of the causative body is probably more than four or five times the depth to the top of the body. This type of anomaly will give a reliable estimate for location, depth, dip and susceptibility of the causative body, but the estimated width has no meaning. However, if the magnetisation of the body is uniform and consistent, the distance between the two centres of the thin sheet anomalies will indicate the width of this wide body. For the second case, the causative body may be a thin body. The theoretical curve is not suitable to match the horizontal gradient of this narrow anomaly. As a consequence the estimations will be in error. However an interesting point is that this estimated dip is related to the true dip angle, in which the angle between the true dip and the estimated dip is 90°. This solution can be used as an auxiliary parameter for determining the dip of the body. The proof is given in the later paragraphs. In the third case, the width of the body is probably between one to four times the depth to the top of the body. In general, using the edge model approach it is difficult either to accurately locate the centre of the anomaly or to estimate the other parameters of the causative body.

The proof of using the horizontal gradient for the thin sheet anomaly to estimate the dip of edge anomaly is presented here. In Appendix A.6 (thin sheet case), the vertical gradient of the horizontal component H'_z and the vertical gradient of the vertical component Z'_z are presented but there are no horizontal gradients of vertical and horizontal components (Z'_x and H'_x). Based on Laplace's equation of the two dimensional potential field (2-D field), it is easy to derive the relationships between Z'_x and H'_z, and H'_x and Z'_z. The derivation is given as follows.

Laplace's equation of the 2-D magnetic field, where $U(x,z)$ is the magnetic potential, can be expressed as follows.

$$\frac{\partial^2 U(x,z)}{\partial x^2} + \frac{\partial^2 U(x,z)}{\partial z^2} = 0. \tag{3.4}$$

Based on potential field theory, $\frac{\partial U(x,z)}{\partial x}$ is the horizontal component of total field (ΔH), and $\frac{\partial^2 U(x,z)}{\partial x^2}$ is the horizontal gradient of the horizontal component (H'_x). That is

$$\Delta H = \frac{\partial U(x,z)}{\partial x},$$

and

$$H'_x = \frac{\partial^2 U(x,z)}{\partial x^2}.$$

In the same way, it is given ΔZ and Z'_z as

$$\Delta Z = \frac{\partial U(x,z)}{\partial z},$$

and

$$Z'_z = \frac{\partial^2 U(x,z)}{\partial z^2}.$$

Therefore expression (3.4) can be rewritten as

$$H'_x + Z'_z = 0,$$

and this leads to $H'_x = -Z'_z$.

The vertical gradient of horizontal component (H'_z) and the horizontal gradient of vertical component (Z'_x) can be expressed as

$$Z'_x = \frac{\partial}{\partial x}[\frac{\partial U(x,z)}{\partial z}], \tag{3.5}$$

and

$$H'_z = \frac{\partial}{\partial z}[\frac{\partial U(x,z)}{\partial x}]. \tag{3.6}$$

With (3.5) and (3.6) it is easy to see that by changing the order of partial differentials (∂z and ∂x), that Z'_x is equivalent to H'_z. So the horizontal gradients of the horizontal and vertical components of the thin sheet model can be derived and given as follows:

$$H'_x = -2kTbw \sin d[\sin(i-d) \cdot (\frac{2hx}{R^4}) + \cos(i-d) \cdot (\frac{h^2 - x^2}{R^4})],$$

and

$$Z'_x = 2kTbw \sin d[-\cos(i-d) \cdot (\frac{2hx}{R^4}) + \sin(i-d) \cdot (\frac{h^2 - x^2}{R^4})].$$

The dip of the body is determined by using the central anomaly as

$$\frac{Z'_x|_{x=0}}{H'_x|_{x=0}} = \frac{2kTbw \sin d \cdot \sin(i-d) \cdot \frac{1}{h^2}}{-2kTbw \sin d \cdot \cos(i-d) \cdot \frac{1}{h^2}} = -\tan(i-d),$$

i.e.

$$\frac{Z'_x|_{x=0}}{H'_x|_{x=0}} = -\tan(i-d). \tag{3.7}$$

The expression (3.7) can be rewritten as a cotangent function as

$$\frac{Z'_x|_{x=0}}{H'_x|_{x=0}} = -\cot[90° - (i-d)] = \cot[(i-d) - 90°]. \tag{3.8}$$

Comparing expression (3.8) with the expression (3.3) which gives the relationship between the components and dip angle for dealing with the anomaly of the edge-type model, it is clear that the two sets of the angles, which are inside the cotangent functions, are orthogonal. As a result, for the case of the narrow anomaly, the estimated dip is equal to the true dip minus 90°. In practice, if the estimated dip angle obtained from the narrow anomaly is used to determine the susceptibility, the susceptibility estimate may be highly inaccurate.

It has been shown that the edge model approach is suitable for wide anomalies but not for narrow anomalies where the errors in parameter estimates may be unacceptable.

3.4.4 Determinations of dip and susceptibility for a plate model

In this section the estimates of dip and the susceptibility for a thin plate model are discussed. In geophysical terms, the thin plate indicates a causative body composed of a very thin magnetised layer in which the thickness may be less than one tenth of the depth to the top. According to the definition, the dip of the thin plate may be determined as 90°. The basic formulae for the components and gradients can be obtained from (A.8) (see Appendix A) and the geometry of the thin plate is shown in Figure A.7.

From the central anomaly, the resultant inclination i of the magnetisation can be obtained by

$$\frac{\Delta Z_{x=0}}{\Delta H_{x=0}} = \frac{2kTb \sin i \cdot \frac{w}{\frac{w}{2}^2+h^2}}{-2kTb \cos i \cdot \frac{w}{\frac{w}{2}^2+h^2}} = -\tan i,$$

and this leads to

$$i = -\tan^{-1}\left(\frac{\Delta Z_{x=0}}{\Delta H_{x=0}}\right).$$

The susceptibility can be obtained from

$$k = \frac{\Delta Z_{x=0}}{2Tb \sin i \cdot \frac{w}{\frac{w}{2}^2+h^2}},$$

or from

$$k = \frac{\Delta H_{x=0}}{-2Tb \cos i \cdot \frac{w}{\frac{w}{2}^2+h^2}}.$$

Based on the vertical gradient and horizontal gradient at central anomaly, the inclination (i) and susceptibility (k) can be given by

$$\frac{Z'_z|_{x=0}}{H'_z|_{x=0}} = \frac{2kTb \sin i \cdot \frac{2hw}{(\frac{w}{2}^2+h^2)^2}}{-2kTb \cos i \cdot \frac{2hw}{(\frac{w}{2}^2+h^2)^2}} = -\tan i.$$

from which it follows that

$$i = -\tan\left(\frac{Z'_z|_{x=0}}{H'_z|_{x=0}}\right),$$

and

$$k = \frac{Z'_z|_{x=0}}{2Tb \sin i \cdot \frac{2hw}{(\frac{w}{2}^2+h^2)^2}},$$

or

$$k = \frac{H'_z|_{x=0}}{-2Tb \cos i \cdot \frac{2hw}{(\frac{w}{2}^2+h^2)^2}}.$$

3.5 Summary of the Improved Naudy Technique (AUTOMAG)

The original Naudy technique formed the basis for the development of the Improved Naudy Technique presented in this chapter. By analysing the vertical and horizontal components of the total magnetic field or its vertical gradient, it is possible to determine the parameters (depth, depth extent, dip, and susceptibility) of a number of different sources (dyke with infinite and finite depth extent, edge and thin plate). The study area is characterized by regions of dominantly linear magnetic anomalies. To apply the Improved Naudy Technique to the analysis of the study area, a computer program, AUTOMAG, was written by the author. Henceforth in this thesis, the program AUTOMAG will be referred to rather than the technique described here as the Improved Naudy Technique.

Chapter 4

Testing of AUTOMAG, using synthetic data

4.1 Introduction

This chapter shows a number of synthetic data tests on different types of models and their combinations using AUTOMAG, and provides some error analyses for the estimated parameters. After a series of error tests for simple models, a set of new basic models to be used in AUTOMAG is established. This set includes limited depth extent dyke and edge models, and an extended thin plate model. As these models represent most common geometries of geological bodies, the method provides an application which can be used for a variety of magnetic anomalies. The study of complex model and error analysis of random noise data provides useful information and suggestions for the effective application of AUTOMAG to real data.

For the purpose of this research, the DEPTH program (using TMI and RTP), which was written by Minty (Minty, 1981) based on the original Naudy technique (Naudy, 1971), was revised by the author. The new computer program AUTOMAG incorporates the Improved Naudy Technique and analyses magnetic components or vertical gradient data along profiles to automatically provide the position, depth, width, dip and susceptibility of the magnetic source. AUTOMAG, the software package, is combined with several programs including the modified DEPTH (using ΔZ and ΔH) or DEPTHVG (using Z'_z and H'_x), EQUAL, ONED2, ALTITUDE_COR and PLOT_H or PLOT_VG which are used to plot the depth estimate (the original PLOT program was written by Minty), process the original magnetic profile data and provide preliminary interpretations of magnetic profiles. The descriptions and functions of AUTOMAG and other programs which are used in this research are presented in Appendix C. All the model test work was carried out by using this package on a Vax-780 computer and a SUN SPARC 2 workstation in the Department of Geology and Geophysics, the University of Adelaide.

The following sections present results from a number of simple model tests including infinite dyke, dyke with limited depth extent, wide dyke, thin plate and slab models. The estimated

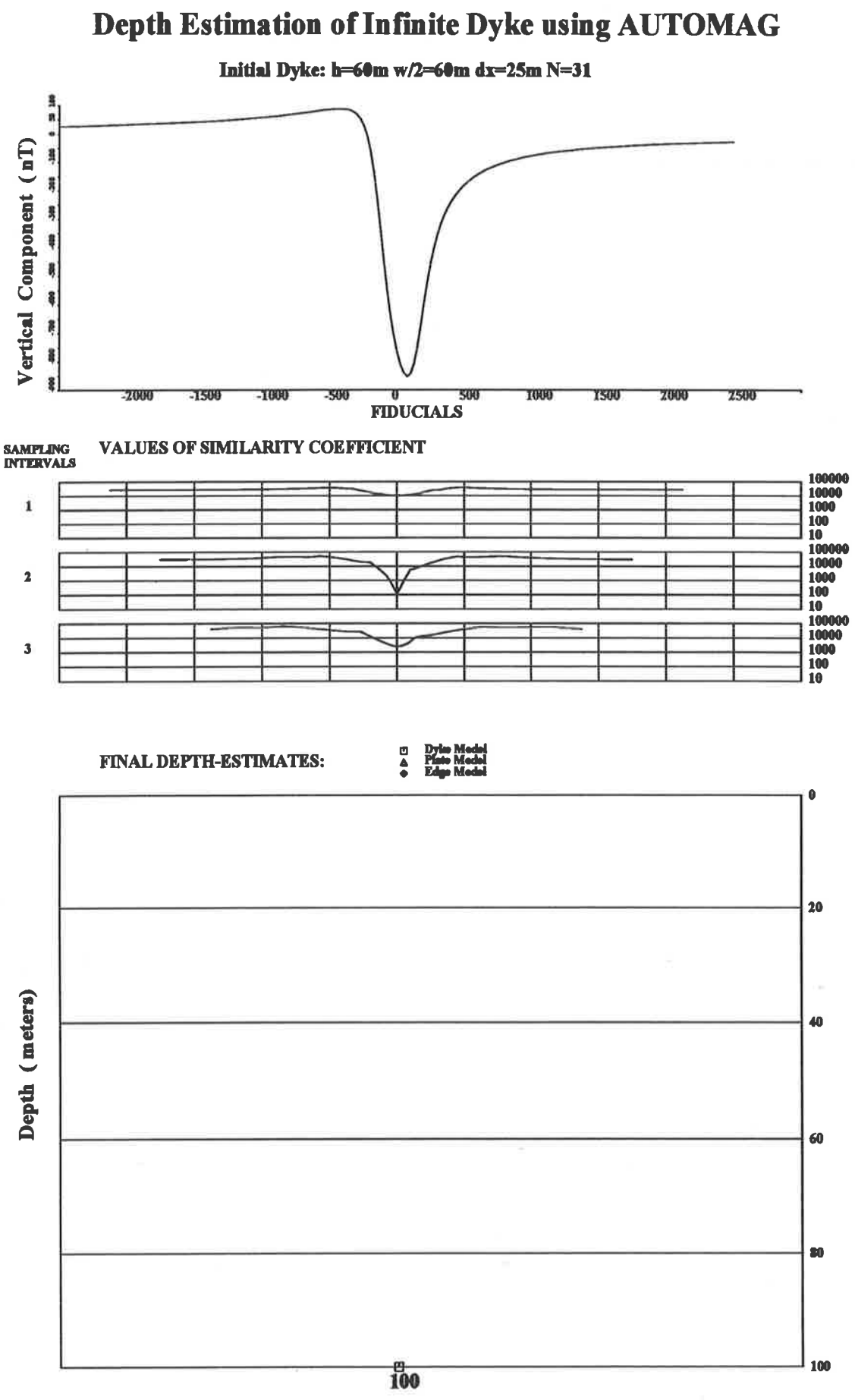

Figure 4.1: Depth estimation of infinite dyke using AUTOMAG

parameters of each type of model have been examined by varying the depth extent, width and dip. In order to compare results due only to different shaped models using the AUTOMAG program, it is assumed that the location of the centre of the model is known.

4.2 Dyke with infinite depth extent

Figure 4.1 gives an example of the depth estimation procedure using the vertical and horizontal components applied to a dyke model with infinite depth extent, in which the parameters of the dyke and its estimates are shown in Table 4.2. The initial parameters (explanation see 3.1) for applying the program are as follows:

- both the depth and half width of the initial model are 60 metres;
- the number of the sampled points for locating anomaly center is 41;
- the number for refining the depth estimate is 31;
- the spacing interval of the profile is 25 metres.

Note that in order to reduce the effect from adjacent anomalies, the window length or the number of calculated points for estimating the parameters is usually smaller than the length or point number for locating the centres of anomalies (Naudy, 1971; Minty, 1981).

The anomaly of the vertical component of the dyke is shown at the top of the graph (Figure 4.1), coordinates or fiducial are along the x-axis, and the amplitude of the field is marked on the z-axis. The middle part illustrates similarity coefficients for each value of the sampling interval. When a suitable interval number is chosen, the curve of the similarity coefficient indicates a global minimum corresponding to the center of the anomaly. On the left hand of the graph, the values 1, 2, 3 represent the index of the sampling interval. For example, number 2 indicates the sampling interval was twice the initial 25 metres, i.e. 50 metres. The numbers 10, 100, ..., 10000 on the right hand of the graph represent amplitudes of the similarity coefficients. The bottom part shows the depth estimate, and the numbers on the right hand of the graph indicate the interval of the depth, unit in metres. Each model type is given by a different symbol, the sizes of the symbol and the value of the depth estimate are varied according to the goodness of fit between the theoretical curve and the measured curve. The better the fitness, the bigger the size of the symbol. In the graph, the unique depth estimate is given as 100 metres which is equal to the true depth of the model. According to Table 4.1, all the determinations in the different sample intervals are coincident with the true values of the model.

Table 4.2 shows results from the vertical and horizontal gradient data when the same dyke model as shown in Figure 4.1 is processed, and the same input parameters are applied to the DEPTHVG program. The table gives accurate estimates for the depth, width, dip as well as susceptibility of the model. As a result, AUTOMAG provides a reliable determination of parameters for a simple dyke model.

Table 4.1: Parameters of test dyke model and estimates using AUTOMAG from the component data

Parameters of Dyke Model					
Depth	$\frac{Width}{2}$	**Dip**	**Susceptibility**	**Center of Body**	**Sample Interval**
100 m	150 m	60°	0.005 CGS	0 m	25 m
Estimates from AUTOMAG					
No. of Sample Intervals	**Depth**	$\frac{Width}{2}$	**Dip**	**Susceptibility**	**Center of Body**	**Sample Interval**
1	100 m	150 m	60°	0.00500 CGS	0 m	25 m
2	100 m	150 m	60°	0.00501 CGS	0 m	50 m
3	100 m	150 m	60°	0.00501 CGS	0 m	75 m

Table 4.2: Estimates from gradient data using AUTOMAG

No. of Sample Intervals	**Depth**	$\frac{Width}{2}$	**Dip**	**Susceptibility**	**Center of Body**	**Sample Interval**
1	100 m	150 m	60°	0.00500 CGS	0 m	25 m
2	100 m	150 m	60°	0.00499 CGS	0 m	50 m
3	100 m	150 m	60°	0.00501 CGS	0 m	75 m

Error Analysis of Thin Dyke Model for Varying Depth Extent

(Using Dyke Model Approach)

Relative Error of Depth Estimation

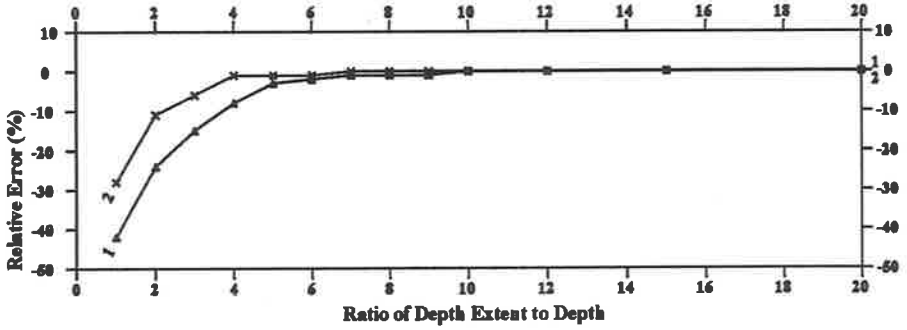

Relative Error of Width Estimation

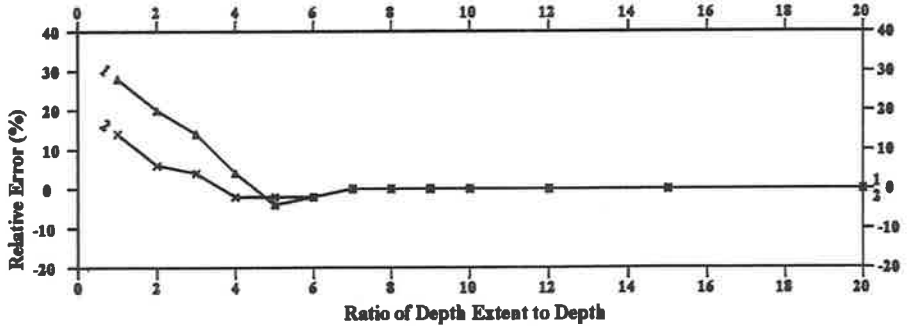

1: Error from Component Data

2: Error from Gradient Data

Figure 4.2a

Error Analysis of Thin Dyke Model for Varying Depth Extent

(Using Dyke Model Approach)

Relative Error of Susceptibility Estimation

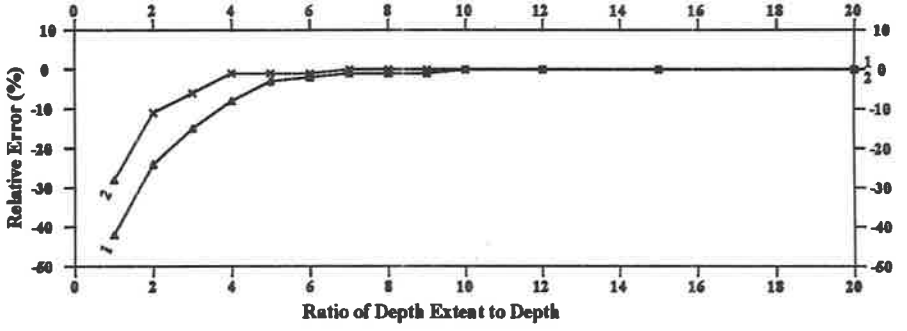

Absolute Error of Dip Estimation

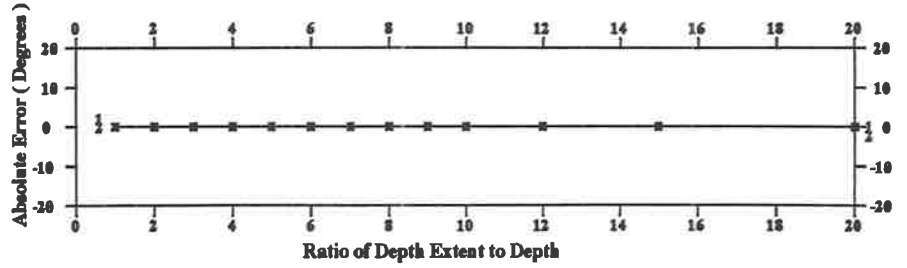

1: Error from Component Data

2: Error from Gradient Data

Figure 4.2b

4.3 Dyke with finite depth extent

Chapter 3 demonstrated detailed error analyses of susceptibility and dip estimates for a dyke with limited depth extent. Here the emphasis is on error analyses for estimating depth and width using AUTOMAG. In the test (Chapter 3), the standard theoretical dyke model was used in AUTOMAG with a depth extent of ten times the depth to the top of the body. A proof is given here to show that this assumption is correct and also satisfied with the case of depth and width. With this assumption, the errors are analysed for a body with varying depth extent, width and dip angle. Same conclusion is made as for estimating the susceptibility and dip:

1. The depth extent, width and dip of body are important factors which affect the accuracy of the parameter estimates.
2. the smaller the depth extent, or the greater the width, or the closer the dip to the horizontal, the greater the error of the estimate.

A detailed analysis follows.

4.3.1 New standard dyke model

Error distributions for estimating parameters of a body with varied depth extent are checked. In the program, the standard model for producing a theoretical curve was designed as a dyke with an infinite depth extent. Figures 4.2 and 4.3 illustrate errors introduced into the estimates of depth, width, susceptibility and dip estimates by changing the depth extent in two sets of model cases; i.e. a thin dyke and a thick dyke; they are the same models as shown in Chapter 3 (see Table 3.5).

According to the error curves for both the thin and thick dyke cases (Figure 4.2 and 4.3),

1. the smaller the depth extent, the bigger the errors;
2. if the ratio of depth to depth extent is greater than ten, all the errors of the estimated depth, width and dip are less than 1%;
3. if the ratio is greater than ten, error of estimated susceptibility are less than 15% for component data and less than 5% for gradient data.

As a result, if the depth extent of dyke model is designed as ten times the depth to the top of the body, a reliable solution can be provided. In reality the depth extent is more likely to be limited than infinity, and therefore the basic dyke with limited depth extent is more suitable to match the natural geological bodies. From now on the depth extent of the theoretical dyke model in AUTOMAG is designed as ten times the depth to the top of the body.

Error Analysis of Thick Dyke Model for Varying Depth Extent

(Using Dyke Model Approach)

Relative Error of Depth Estimation

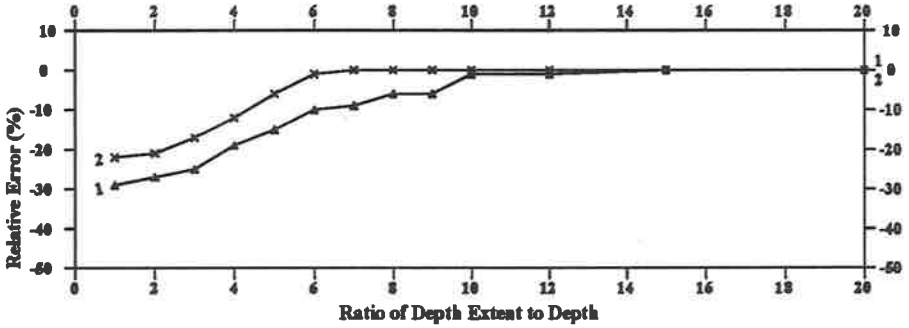

Absolute Error of Width Estimation

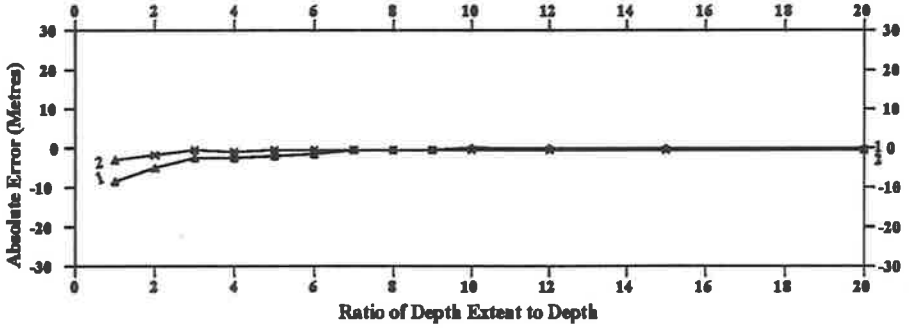

1: Error from Component Data

2: Error from Gradient Data

Figure 4.3a

Error Analysis of Thick Dyke Model for Varying Depth Extent

(Using Dyke Model Approach)

Relative Error of Susceptibility Estimation

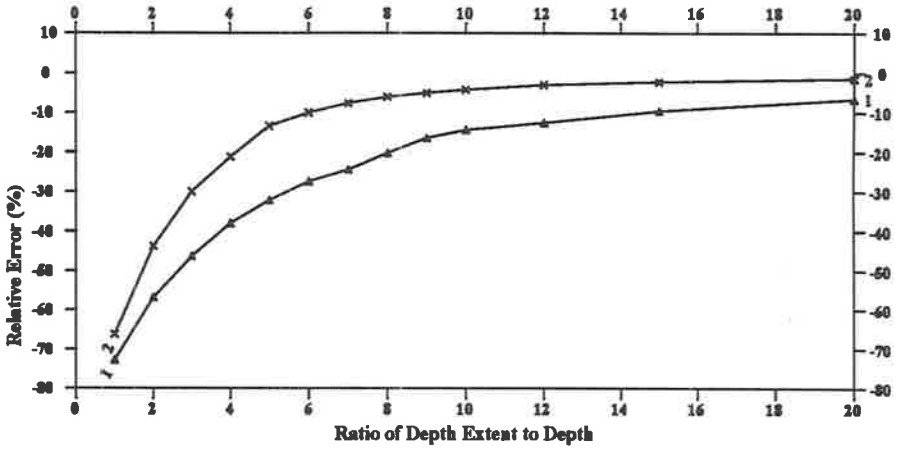

Absolute Error of Dip Estimation

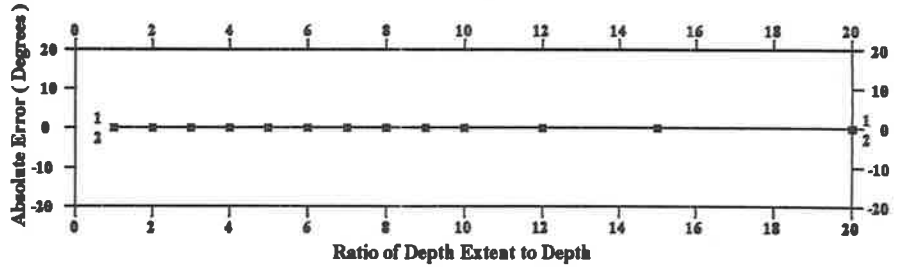

1: Error from Component Data

2: Error from Gradient data

Figure 4.3b

Table 4.3: Estimates from component and gradient data using AUTOMAG with the new designed dyke model

From Component Data						
No. of Sample Intervals	**Depth**	$\frac{Width}{2}$	**Dip**	**Susceptibility**	**Center of Body**	**Sample Interval**
1	101 m	150 m	60°	0.0057 CGS	0 m	25 m
2	103 m	154 m	60°	0.0058 CGS	0 m	50 m
3	119 m	143 m	60°	0.00641 CGS	0 m	75 m

From Gradient Data						
No. of Sample Intervals	**Depth**	$\frac{Width}{2}$	**Dip**	**Susceptibility**	**Center of Body**	**Sample Interval**
1	100 m	149 m	60°	0.00512 CGS	0 m	25 m
2	101 m	151 m	60°	0.00516 CGS	0 m	50 m
3	101 m	151 m	60°	0.00518 CGS	0 m	75 m

Table 4.3 shows parameter estimates from the component and gradient data for a dyke with infinite depth extent, in which the test model is the same as shown in Figure 4.1. All the determinations from the gradient data for different sample intervals (25m, 50m and 75m) are in good agreement with the parameters of the test body. However the precision of determinations from the component data are slightly reduced when the sample interval is increased. The reason for causing this difference is explained as follows.

The anomaly of a vertical dyke with infinite depth extent is characterized by a single peak (maximum) at the centre of the anomaly. The anomaly tends to the background level away from the source. There are no obvious minima on either side of the peak. A similar dyke with limited depth extent produces a similar central peak but also produces a minimum on either side of the central high and these lows are the effect of the limited depth extent. Therefore, by increasing the length of the window, the difference between the two kinds of anomalies increases and the precision of depth estimates is reduced.

However, the gradient anomalies caused by these two types of models are very similar, because the vertical gradient data reflects the effect from the shallow body or the top part of the body. If the depth extent of the body is great, the effect from the bottom part of the body is almost ignored, which leads to less differences between the two kinds of anomalies. Therefore all the depth estimates are very close.

Table 4.3 highlights the fact that the most accurate estimates are calculated from the data with a small sampling interval. In general, if the window length of the calculated theoretical curve is sufficient to cover the target anomaly, in which the length is a product of the sampling interval and the number of the samples, the data from the smallest interval will provide the

Error Analysis of Thin Dyke for Varying Depth Extent

(Using New Designed Dyke Model)

Relative Error of Depth Estimation

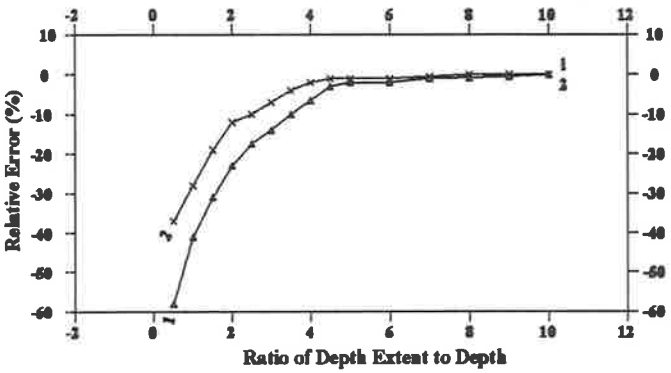

Absolute Error of Width Estimation

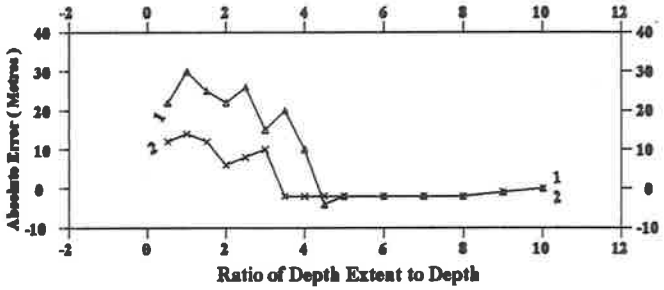

1: Error from Component Data

2: Error from Gradient data

Figure 4.4

Error Analysis of Thick Dyke for Varying Depth Extent

(Using New Designed Dyke Model)

Relative Error of Depth Estimation

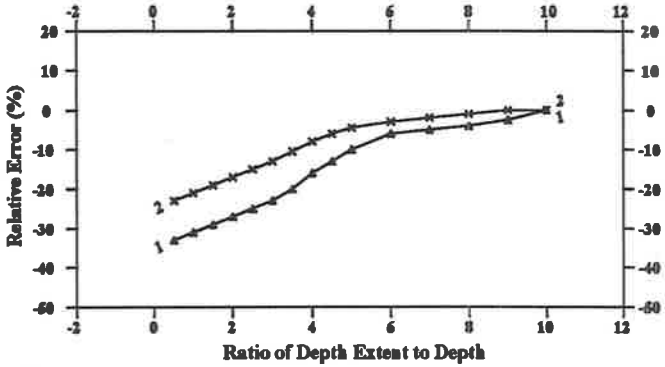

Absolute Error of Width Estimation

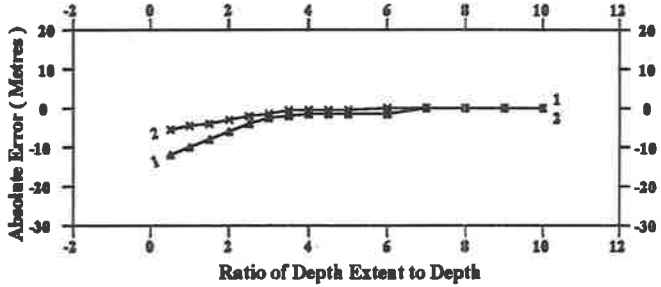

1: Error from Component Data

2: Error from Gradient data

Figure 4.5

Error Analysis of Dyke for Varying Width

(Using New Designed Dyke Model)

Relative Error of Depth Estimation

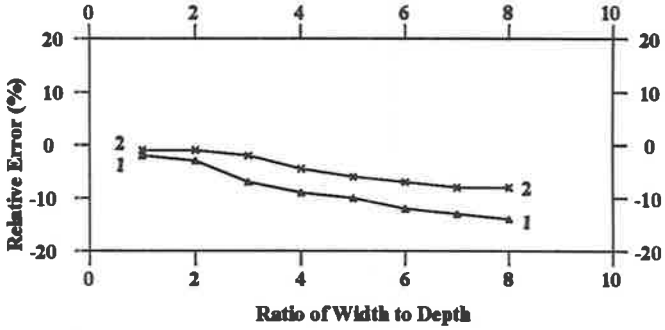

Absolute Error of Width Estimation

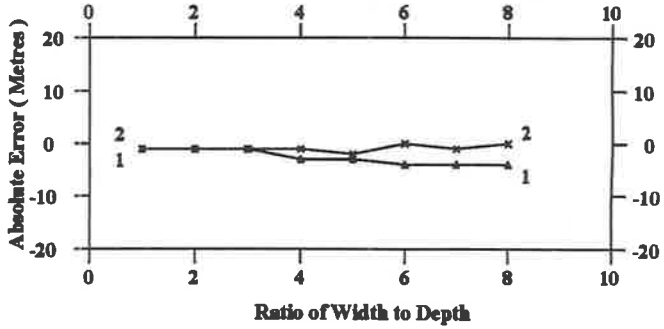

1: Error from Component Data

2: Error from Gradient data

Figure 4.6

Table 4.4: Input information for using AUTOMAG to check two sets of dykes with varying depth extent

Initial Model		No. of Sample Intervals	Sample Interval	Number of Window Points	
Depth	$\frac{Width}{2}$			Thin Dyke	Thick Dyke
60 m	60 m	1	25 m		
120 m	120 m	2	50 m	21	41
180 m	180 m	3	75 m		

best results. After a great amount of model testing, it has been found that ratio of the detected depth and sampling interval of the data should usually be chosen as four or more. For example if the target depth is 100 metres, a sampling interval of 25 metres or less may provide good estimates. If the sampling interval is greater than 25 metres, it may introduce some error.

4.3.2 Error analysis for varying depth extent

So far the error as a result of limited depth extent has been discussed. As mentioned in Section 3.4.2, a body with large width and the dip angle close to the horizontal plane would introduce errors in parameter estimation. In order to check the effect of applying AUTOMAG with the new standard model, a set of error tests for the depth and width estimates by varying the depth extent, width and dip were carried out.

Models used for analysing results here are the same as shown in figures 4.2 and 4.3 (also see Table 3.5, Chapter 3). The profile is along south to north direction where the spacing interval of the profile is 25 metres. The error analysis uses relative or absolute errors and errors present along the vertical axis, in which a positive value indicates an over-estimated error and a negative value represents an under-estimate.

The error effect for varying depth extent (DE) is illustrated. Figures 4.4 and 4.5 show errors of the depth and width estimates from the component data and gradient data both for two sets of thin and thick dykes, in which the ratios between DE and depth to the top of the body (h) vary from 0.5 to 10. Parameters of the initial model used in the calculation are given in Table 4.4. According to all the error curves, ratios of DE to h ranging from four to five seem to be important: if ratios are greater than four to five, errors of estimates for both dykes are less than 10%, otherwise great errors occur. Additionally, the estimates calculated from gradient data provide better solutions than those from component data.

Error Analysis of Thin Dyke Model for Varying Dip of Body

(Using New Designed Dyke Model)

Relative Error of Depth Estimation

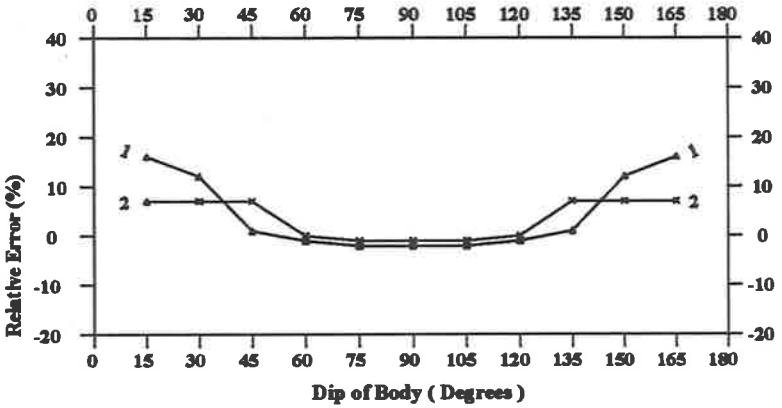

Absolute Error of Width Estimation

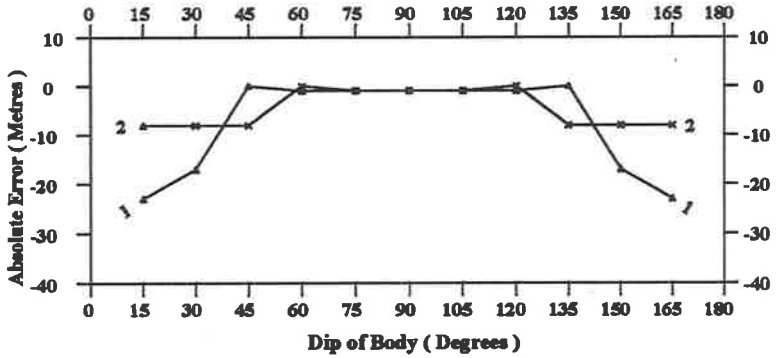

1: Error from Component Data
2: Error from Gradient data

Figure 4.7: Thin Dyke

Error Analysis of Thick Dyke Model for Varying Dip of Body

(Using New Designed Dyke Model)

Relative Error of Depth Estimation

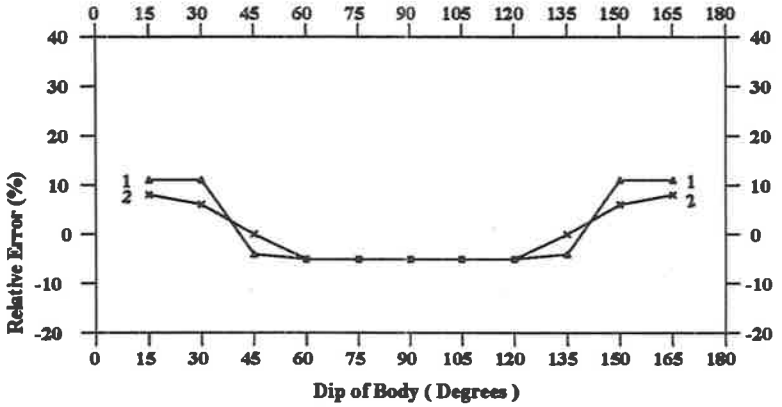

Absolute Error of Width Estimation

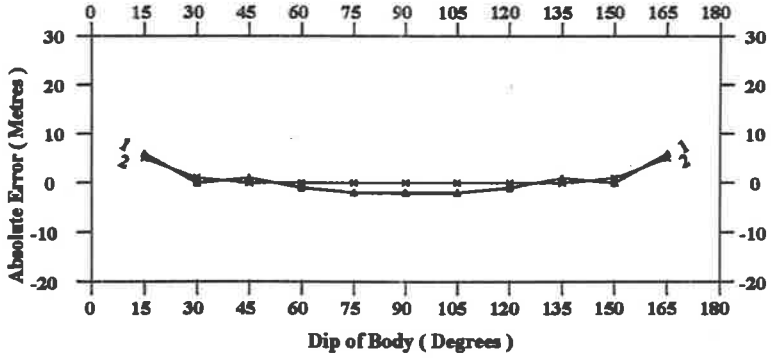

1: Error from Component Data
2: Error from Gradient data

Figure 4.8: Thick Dyke

Table 4.5: Input information for using AUTOMAG to check two sets of dykes with varying width

Initial Model		No. of Sample Intervals	Sample Intervals	Number of Window Points	
Depth	$\frac{Width}{2}$			Thin Dyke	Thick Dyke
60 m	60 m	1	25 m		
120 m	120 m	2	50 m	$21 + 10 \times (R - 1)$	$41 + 10 \times (R - 1)$
180 m	180 m	3	75 m		

Note:
R: The ratio of the width to the depth; in the calculation the number of the window points varies when the width of the body changes.

4.3.3 Error analysis for varying width

This section demonstrates the error effect for estimating depth and width if the width (w) is changed for a set of models in which the parameters of the bodies are the same as shown in Chapter 3 (see Table 3.4). Figure 4.6 illustrates the error distributions. Parameters of the initial model are given in Table 4.5.

According to the error curves, the smaller the ratio of width to depth, the smaller the error. If the ratio is greater than five, the error is gradually increased. It also shows that errors from the gradient data are smaller than the errors from the component data. By comparing the two sets of error analyses (varied depth extent and varied width), it has been found that the size of the error for the case of varying width are obviously smaller than the case of varying depth extent. This indicates that error effect from varied width of the body is less than the error from varied depth extent. Over all possible depth extents and widths, the error is, on average, less for delinquent widths than for delinquent depth extents.

4.3.4 Error analysis for varying dip

It is shown in Chapter 3 (Section 3.4.2) that if the dip of the body is close to the horizontal plane, the error in parameter estimates is greater than the error which occurs in the case of a causative body with a near vertical dip angle. Figures 4.7 and 4.8 show the effect of varied dip of body respect to thin and thick dykes. Parameters of those models are the same as shown in Chapter 3 (see Table 3.6) and the input information for using AUTOMAG is given in Table 4.6.

Relative errors of depth estimates (Figure 4.7) are shown at the top of the graphs and the dip on horizontal axis ranges from 15° to 165° (physically, when a dyke model has a dip less than 15° or greater than 165°, it is considered to be a "thin plate" rather than a dyke). Both error curves from the thin and thick dykes are similar as indicated below.

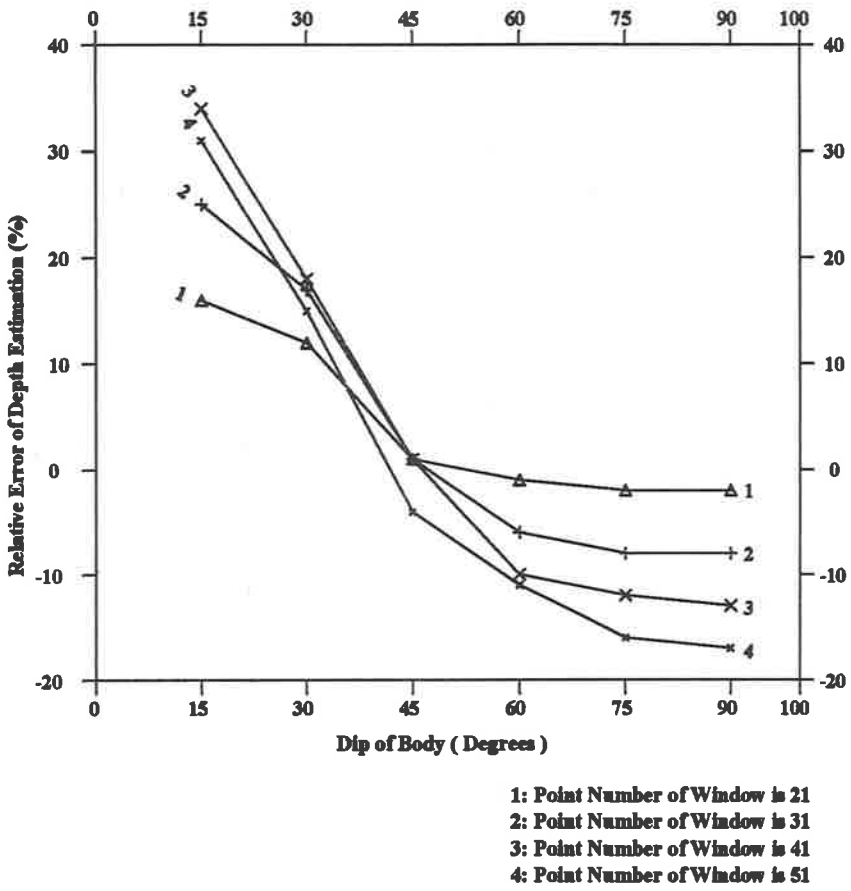

Figure 4.9a: Using Component Data

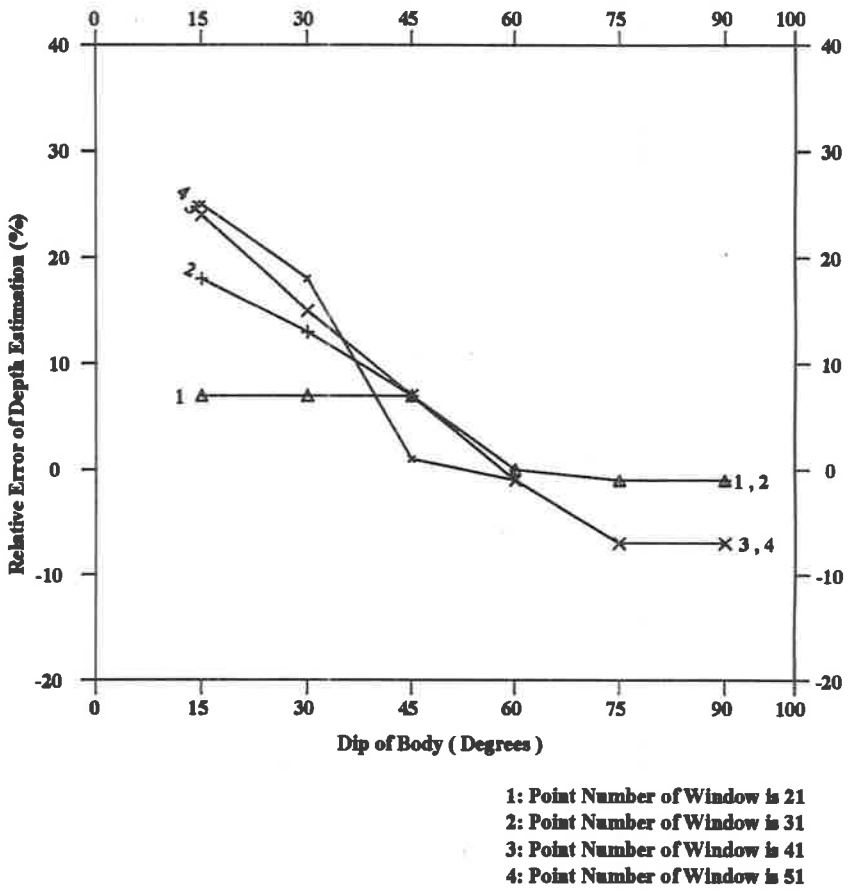

Figure 4.9b: Using Gradient Data

Table 4.6: Input information for use of AUTOMAG to check models with varied dip angles

Model Case	Initial Model		No. of Sample Intervals	Sample Intervals	Number of Window Points
	Depth	$\frac{Width}{2}$			
Thin Dyke	60 m	60 m	1	25 m	21
Thick Dyke	60 m	120 m	1	25 m	31

1. They are symmetrical about the axis through 90°;

2. If the dip is between 45° to 135°, the error is small and the value is about 5%;

3. If the dip is close to the horizontal plane, the error increases rapidly.

Similar results are produced in the case of width estimates (curves shown at the bottom of figures 4.7 and 4.8). If the dip is close to vertical, the relative error is small; on the other hand if the dip is close to horizontal, the error increases, especially in the case of thin dykes.

Reasons for this error for a near-horizontal dyke are explained as follows. If a dyke is nearly horizontal, the magnetic effects from the bottom and top are separated and the effect from the bottom part is more significant than in the case of a near vertical dyke. In applying the Naudy technique, an important step is to transform an arbitrary shaped anomaly into a symmetrical one. Obviously the transformed anomaly arising from a near horizontal dipping body will be more difficult to match to a theoretical curve than the anomaly caused by a near vertical body.

The choice of window length (or point number of window) also affects the curve matching. By choosing a suitable window length, the symmetrical curve from the original anomaly will be close to the theoretical curve. If the length is great, the transformed symmetrical anomaly will be too complex to match to the theoretical curve. Therefore the error is significant. Figure 4.9 gives an example to demonstrate the error effect of changing point number of window.

As the errors are symmetrically distributed about the vertical axis through 90°, only a half set of error curves are displayed in the figure, in which the dip and the relative error of depth are respectively along the horizontal and vertical axes and the number of the window points is marked at the ends of each curve. The parameters of the tested models are the same as shown in Figure 4.7. Part A in Figure 4.9 demonstrates error distributions from the component data and Part B in Figure 4.9 illustrates errors from the gradient data. According to the distributions of the error from the gradient data, the anomaly caused by a near vertical dipping body (dip angle between 60° to 120°) is not overly affected by changing the window length. However in the case of near-horizontal dips (the angle less than 30 or greater than 150°), the error is sensitive to small changes in the window length. If the number is fixed, the errors from the model with dip near vertical are stable, but in the other case (dip near zero) the errors are unstable (except for the case of N=21). This emphasizes the effect of changing the dip angle.

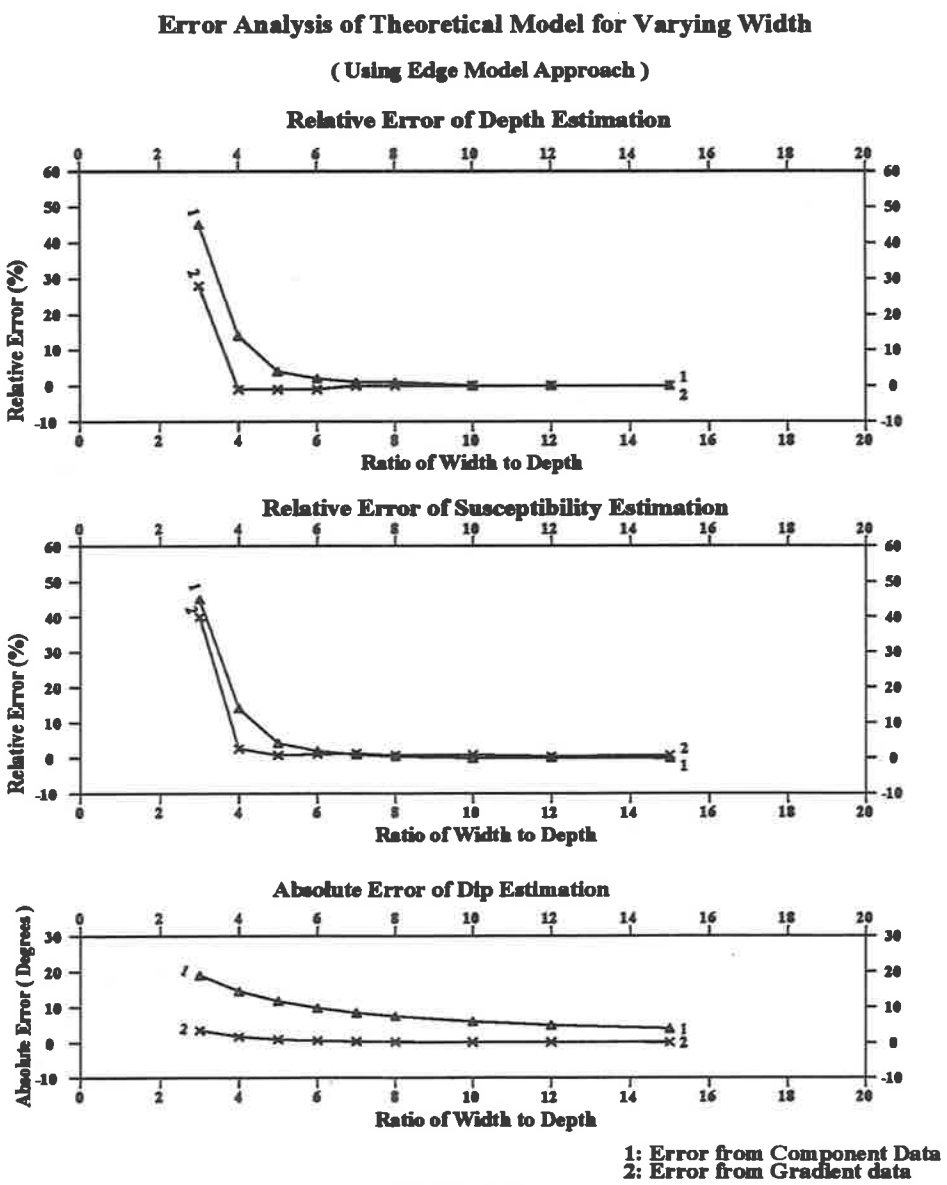

Figure 4.10

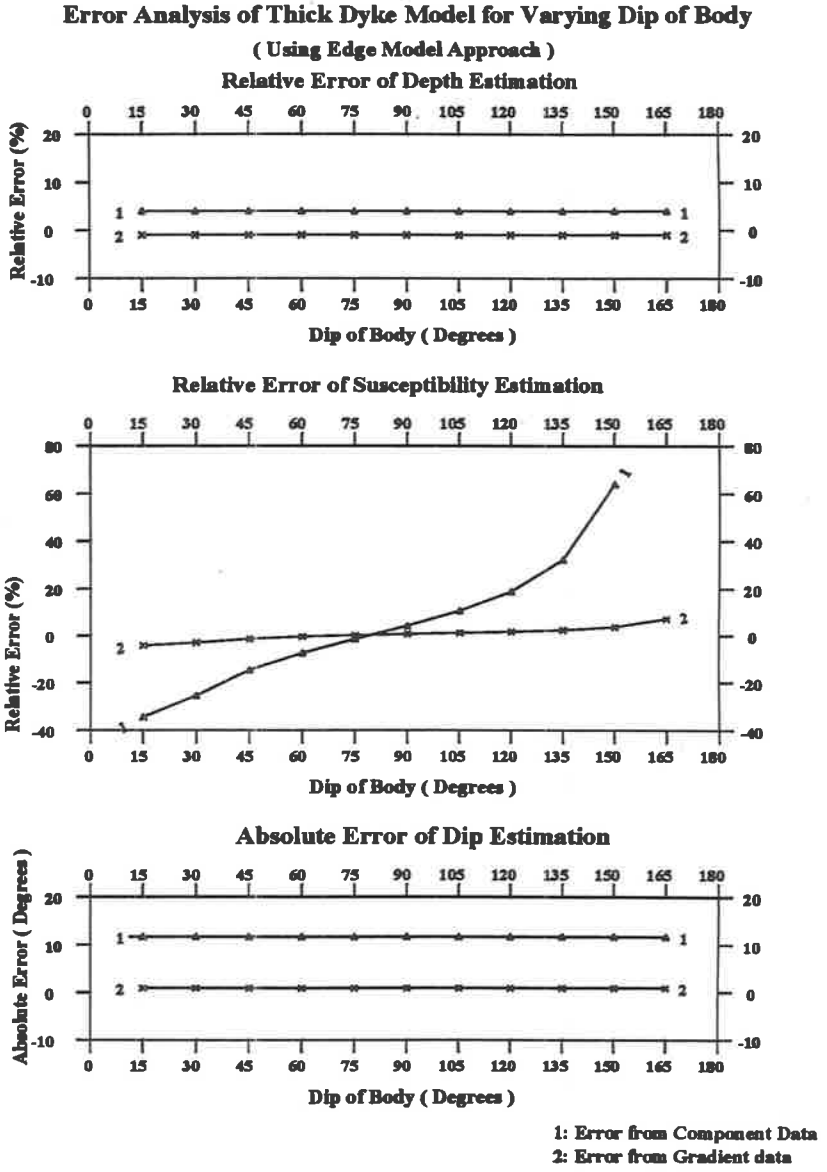

Figure 4.11

In the case of component data (Part A in Figure 4.9), characteristics of error are similar to the gradient data. However, the error from component data is more sensitive to the change of point number. Irrespective of the size of the angle, the greater the number, the large the error.

4.3.5 Summary of dyke model

1. Depth extent, width and dip of the body are important factors affecting the accuracy of the parameter estimates; the smaller the depth extent, or the greater the width, or the smaller the dip angle, the greater the error of the estimate.
2. If depth extent is greater than five times the depth to the top of body (h), width is less than four or five times h, and dip of body is between 45° and 135°, the errors for estimating depth and width are less than 10% if using field data and less than 5% for gradient data.
3. Among these three factors, the depth extent is the most important.
4. If the dip is close to zero and the depth extent is very limited, using the dyke model to process data would not provide satisfactory results. Such a body should be considered as a plate model.
5. The sample interval and point number of calculated window also influence the precision of the estimates. Especially, when the ratio of detected depth to the sample interval is less than four and the length of the window is smaller or much greater than the width of the detected anomaly, both situations would introduce certain error for estimating depth and other parameters.

In practice, locating the centre of an extremely wide anomaly by using a dyke model would prove problematic. Therefore it is necessary to find a way to solve this problem and the solution is to use an edge model, which is discussed in the next section.

4.4 Edge model of infinite depth extent

This section focuses on error analyses for determining depth and width for a very wide magnetic body, which may either have an infinite depth extent or a finite depth extent. Based on the discussion in Section 3.4.3: if the width of the body is greater than five times the depth to the top of body, the edge model is a suitable model to apply.

The major factor which introduces errors in this edge model approach is the width of the body. Figure 4.10 illustrates the error analyses for estimating depth, dip and susceptibility of a set of dyke bodies with variable widths and the depth extent of the body being infinity. The parameters of this set of models and the input information of the program are given in Table 4.7. From the figure, if the ratio of w to h is small (less than four), the error tends to be a great value; as soon as the ratio increases (greater than four), the errors are not significant. The bottom

Table 4.7: Parameters of dyke model and input information using AUTOMAG for checking error effect of varied width

Parameters of Dyke Model					
Depth	**Depth Extent**	**Dip**	**Susceptibility**	**Center of Body**	**Sample Interval**
100 m	∞	90°	0.005 CGS	0 m	25 m

Input Information Using AUTOMAG Program				
Initial Model		**No. of Sample Intervals**	**Sample Intervals**	**Number of Window Points**
Depth	$\frac{Width}{2}$			
60 m	30 m	1	25 m	21

graph shows absolute errors of the dip estimates, in which the gradient data provide excellent estimates. If the ratio is greater than four, the absolute error is less than 2°. The estimate from component data has a large error, but as the ratio of width to depth increases, the error gradually decrease. The middle graph shows the relative error from estimated susceptibility; when the ratio is greater than five, the errors from both the component and gradient data are less than 5%. Combining all the information above indicates that the ratio of the width to the depth to the top of the body equal to five is a critical number.

Figure 4.11 illustrates the effect on the error of changing the dip angle on a set of wide dyke bodies. The other parameters are the same as given in Table 4.7, except that the width of the body is fixed at five times h (500 m) and the dip angles varies from 15° to 165°. The input parameters for the calculation are also the same as shown in Table 4.7. From the top and bottom graphs, it can be readily seen that changing dip does not interfere with the estimates of the depth and dip. Both the cases show straight lines (corresponding to the component and gradient data respectively) against the dip axis and errors remain constant. In this example, the constant errors in the dip estimates are 11.7° (curve 1 in Figure 4.11) for component data and 0.9° for gradient data (curve 2 in Figure 4.11). These constant errors are introduced as a result of the limited width of the body.

The error in the susceptibility estimate from the gradient data is smaller and approximately a constant. If the dip varies from 15° to 150°, the error is less than 5%. However the error from component data is significant. If the dip is outside the range from 45° to 120°, the error is greater than 20%. The reason behind such significant errors is that the estimate of susceptibility depends mainly on the accuracy of the estimated dip and some other factors (see Section 3.4.1). Because of great errors in the dip estimate from the component data, erroneous susceptibility estimates are produced. This is especially so when the the body is close to horizontal.

Summary of the test from the edge model with infinite depth extent is as follows:

1. The most important factor for estimating parameters for a wide dyke model with an infinite

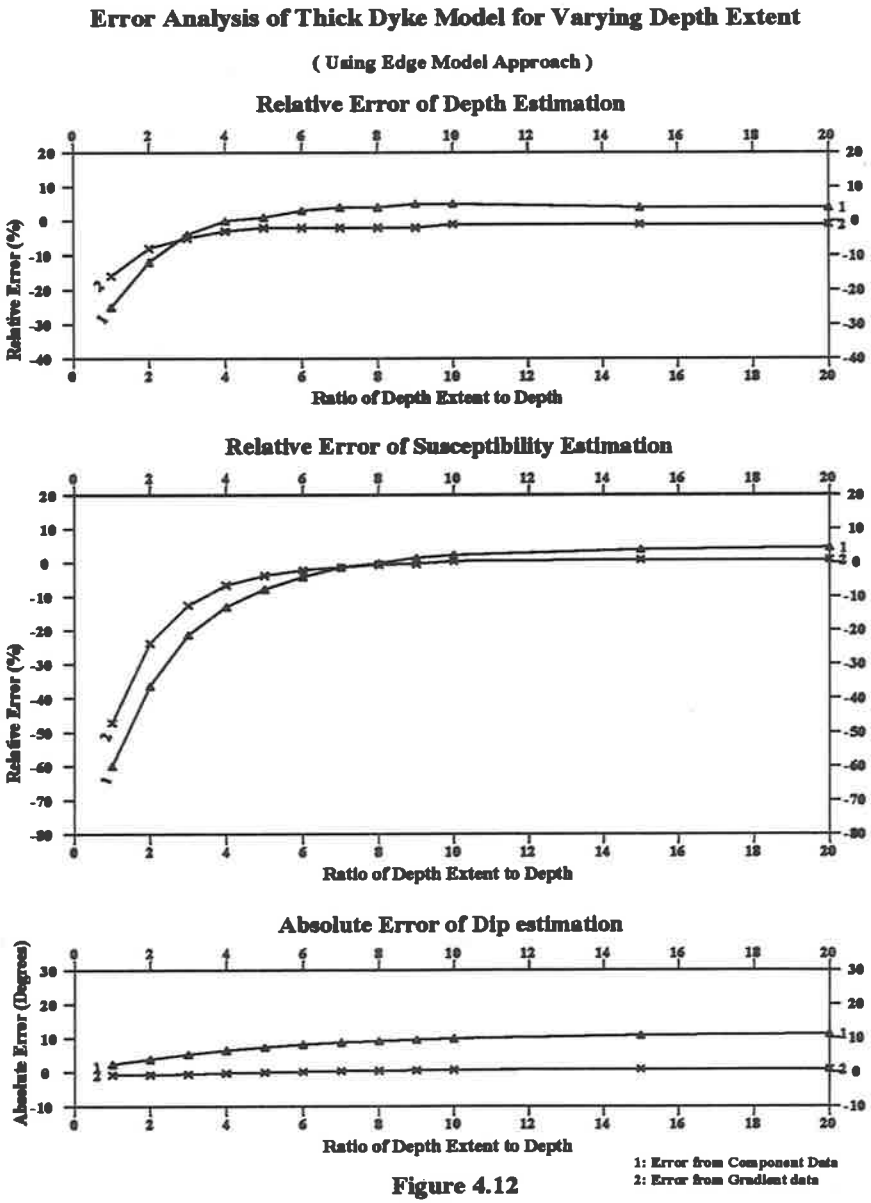

Figure 4.12

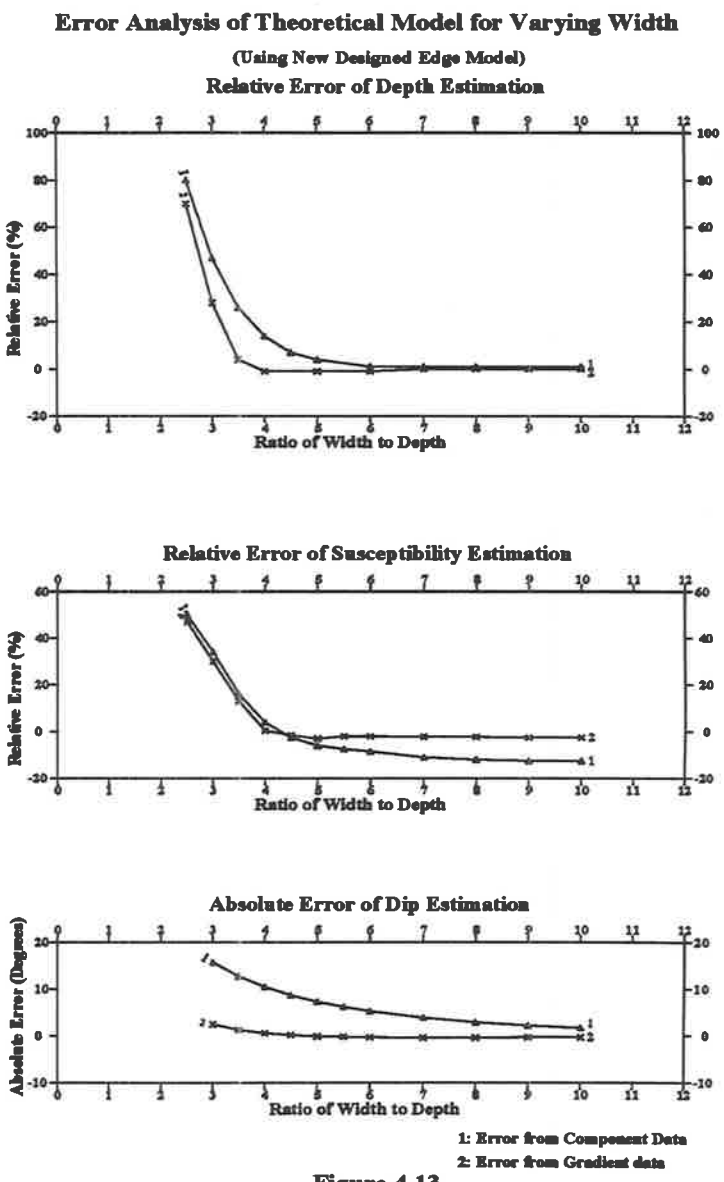

Figure 4.13

depth extent is the width of the body.

2. The ratio of the width to the depth to the top of the body equal to five is a critical number. Beyond this value most estimates both from the component data and gradient data have very small errors (less than 5%).

3. The dip angles mainly affect the estimates of susceptibility when component data is analysed.

4. The results from the gradient data have much higher precision than those calculated from the component data.

4.5 Edge model with finite depth extent

When dealing with dyke type anomalies, AUTOMAG provides a new standard dyke model in which the depth extent of the body is ten times the depth to the top of the body. In real geological situations, the depth extent of the body with a large lateral extent often has limited extent along the vertical direction. In order to satisfy this situation, a new standard model is required for the edge type of anomalies. This section provides a determination of the new model and also analyses the errors if this model is used.

4.5.1 New standard edge model

In using an edge model to process observed data, a thin sheet model is introduced to match the horizontal gradient of the original data. If processing vertical gradient data, a horizontal cylinder is introduced to match the anomaly. Therefore, if dealing with a considerably wide anomaly, a theoretical curve with a narrow width model is considered. In the section on the error analyses for the dyke anomaly, it was shown that for a thin dyke model if the ratio of DE to h is greater than four, AUTOMAG provides better estimates than the thick dyke case (see figures 4.4 and 4.5). Therefore the new model can be designed with a smaller depth extent than the dyke. Further discussion is made from a serial error tests for determining appropriate parameter using the edge model approach.

Figure 4.12 shows the error curves of a set of wide anomalies arising from thick dykes with variable depth extent ranging from 100 metres to infinity. The depth to the top of the body is fixed at 100 metres, the width of the basic body at 500 metres and the dip of the body is 90°. The theoretical models used in AUTOMAG are an infinite thin sheet for processing the component data and a horizontal cylinder for processing the gradient data.

The top graph illustrates the error curve of the depth estimates for changing depth extent. If ratios of the depth extent (DE) to the depth (h) are less than three, errors are significant. If the ratio is about five, the errors from component data and gradient data tend to be a constant values (less 5%) relative to a body with infinite depth extent. The bottom graph shows the error in the dip estimate. Considering the ratio of DE to h equal to five, the absolute error

Error Analysis of Thick Dyke Model for Varying Depth Extent

(Using New Designed Edge Model)

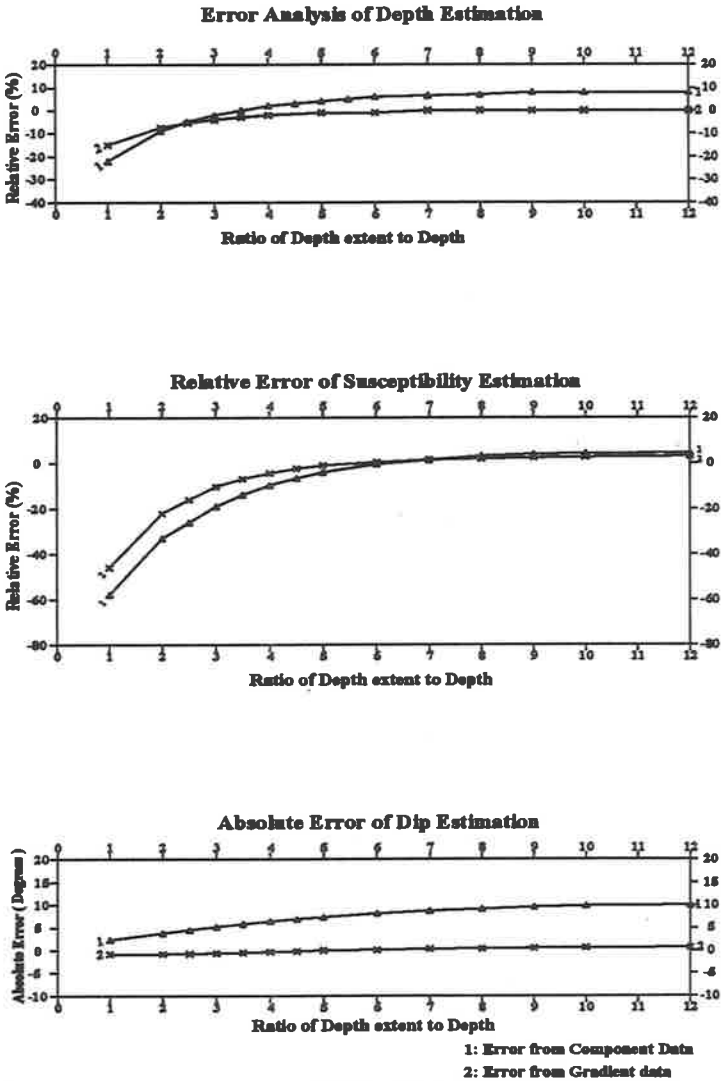

Figure 4.14

Error Analysis of Thick Dyke Model for Varying Dip of Body

(Using New Designed Edge Model)

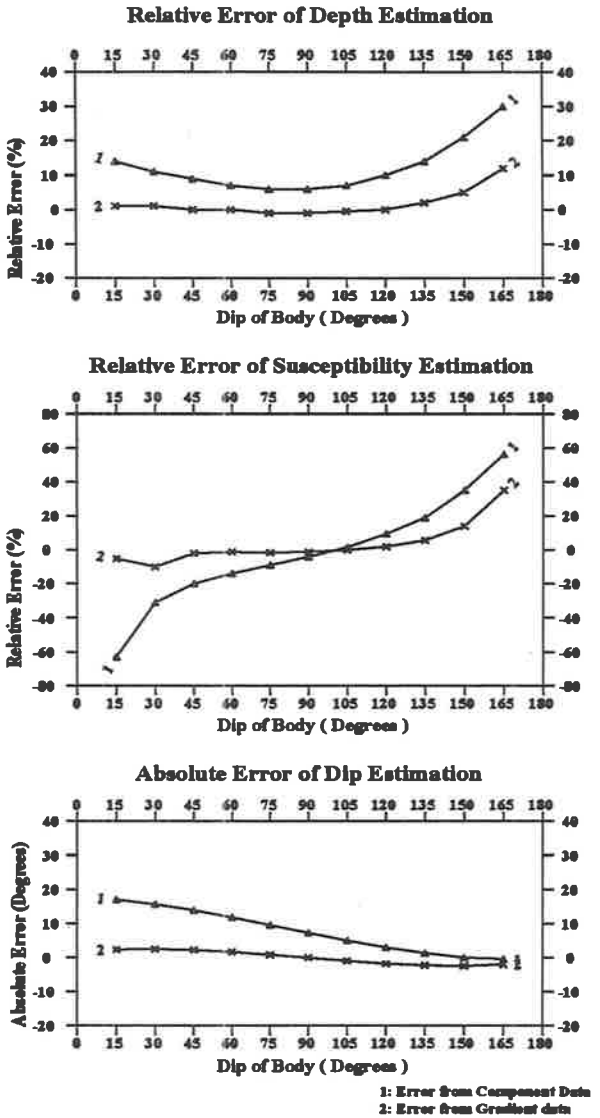

Figure 4.15

Table 4.8: Parameters of edge model for different tests

Parameters for Varying Width				
Depth metres	**Depth Extent** metres	**Dip** degrees	**Susceptibility** $10^{-6} \times SI$	**Width** metres
100	500	90°	5000	250,300,400,...,1000
Parameters for Varying Width				
Depth metres	**Width** metres	**Dip** degrees	**Susceptibility** $10^{-6} \times SI$	**Depth Extent** metres
100	500	90°	5000	100,200,300,...,1000
Parameters for Varying Dip				
Depth metres	**Width** metres	**Depth Extent** metres	**Susceptibility** $10^{-6} \times SI$	**Dip** degrees
100	500	500	5000	15,30,45,...,150

from the component data is only 4° relative to the error from the ratio tending to infinity. The corresponding error from the gradient data is only 1°. The results from the susceptibility estimate also provide reliable determinations for the ratio of DE to h equal to 5. Combining these conclusions and producing a model which is suitable for most geological structures, the new model is designed with the depth extent to be five times the depth to the top of the body.

4.5.2 Error analysis for using new edge model

The error analyses of the depth and width estimates for varying width, depth extent and dip of body using a new designed edge model in AUTOMAG are demonstrated. The parameters of the test model are presented in Table 4.8. The input parameters of the initial model using in AUTOMAG are the same as shown in Table 4.7.

Figure 4.13 shows all the error curves of parameter estimates when changing the width of the body. From the curves, it can be readily seen that if the width is greater than four, relative errors of estimates are less than 15% for the determinations of depth and susceptibility and the absolute error of the dip estimates are equal to or less than 10°. However if the ratio of w to h is less than four, the errors are significant.

Figure 4.14 illustrates the errors which result from changing the depth extent of the body. In the error curves of the depth and susceptibility estimates, if the ratio of DE to h is less than three, errors become significant. If the ratio of DE to h is greater than five, the errors become small and stable and tend to constant values. These constant errors are combined error effects from limited width and limited depth extent. The error values of the depth and susceptibility are less than 10% for the component data and less than 5% for the gradient data. The estimates from gradient data are obviously better than the estimates from component data.

Figure 4.15 shows the effect on the error by varying the dip angle of the body. The errors for parameter estimates are the combined effects of variable dip, limited width and finite depth extent of the body (each model has independent depth extent but all the lengths of the bodies are fixed at five times the depth to the top of the body). The error curve from gradient data are regularly distributed, in which all the curves are nearly symmetrical or antisymmetrical about the axis of the error at 90°. In general, the value of the error is small, most of them are less than 5%, except for the errors of susceptibility estimates for angles greater than 140° and less than 40°.

Visually, the error curves from the component data are complicated. However if a background value in each error curve, which is defined by the error at 90°, is removed from them, a similar error distribution as shown in the case of the gradient is presented. However the values of errors are much greater than the errors from the gradient data.

So far the error analyses for the edge model has been discussed and the summary is given below.

1. The width of the body is the most important factor which affects the precision of the estimates.
2. Small depth extent and low dip angles also reduce the precision of the estimates.
3. If both the width and depth extent are greater than five times the depth, and the dip angle is between 60° and 120°, the errors of the parameter determinations from the component data are less than 15% and the errors from the gradient data are less than 5%.
4. It is worth noting that the edge model approach may work well for very wide low noise anomalies, which could not be dealt with by the dyke model approach. Therefore combining these two model type approaches to deal with the real data can provide a better solution.

4.6 Thin plate model

The last model to be used in AUTOMAG is a thin plate. In natural geological situations, a lava flow or sill may be represented by the thin plate. In geophysical terms, the thin plate is a body with limited depth extent, usually less than one tenth of the depth to the top of the body and the dip of the body is defined as 90°. Based on the formulae shown in Appendix B.8, the vertical and horizontal components and their vertical gradients are composed of an even and an odd function. The symmetrical anomalies can be easily decomposed from either the component anomalies or the gradient anomalies. After applying AUTOMAG, the parameter estimates can be obtained.

Note that there are limited ideal thin plate bodies in the real geological situations. In general, magnetic layers often have finite depth extent. If the depth extent of the layer is great, this

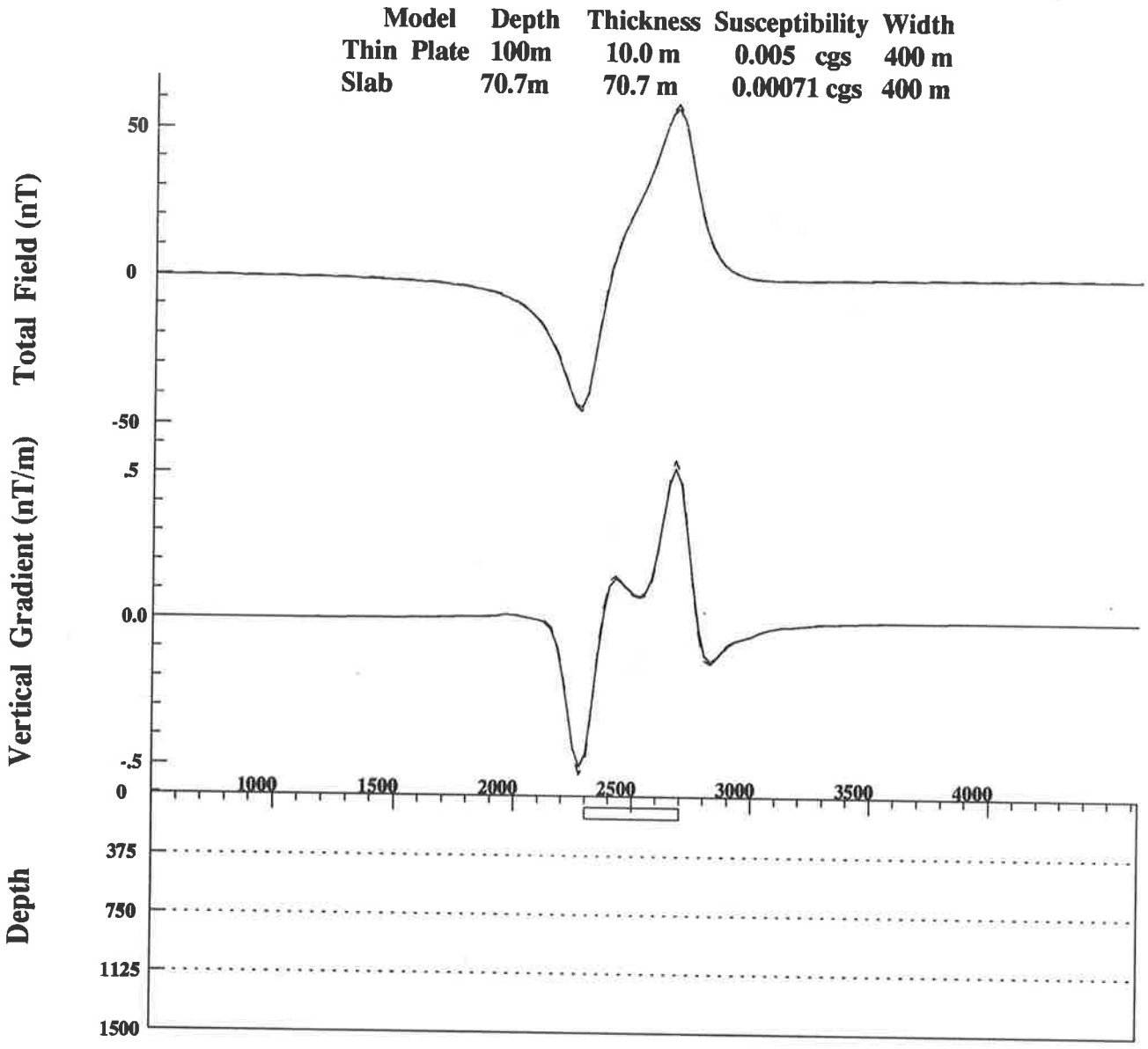

Figure 4.16: Comparison of Total Field Between Thin Plate and Slab
Solid line: Thin plate; Dashed line: Slab

layer can be considered as a wide dyke or an edge body. Only if the depth extent is less than the depth or three times the depth (in this case, the dyke or edge model could not provide better estimates), an expanded thin plate is considered. In this section, the relationship between a theoretical thin plate and a slab (or thick plate) in which the depth extent is equal to the depth to the top of the body is revealed. This slab is designated as the expanded plate model used in AUTOMAG. The error analyses are also presented.

4.6.1 Expanded thin plate

Figure 4.16 shows a pair of total magnetic fields and their vertical gradients, the solid lines represent anomalies caused by a thin plate model and the dashed lines display anomalies produced by a slab model. The parameters of the two models are given in the figure. With the curves in Figure 4.16, it can be readily seen that the two sets of curves from two models are almost identical. It demonstrates a relationship between the two models, which is that the total field caused by a thin plate closely approximates the total field produced by a slab model in which the depth to the top of the body is equal to 70.7% of the depth of the thin plate. The susceptibility of the slab is proportional to the susceptibility of the thin plate. The detailed derivations of the relationship are presented in Appendix D. Here only the results are presented.

In applying the Improved Naudy Technique, only symmetrical components of the anomalies are required. The formulae, i.e. the vertical components in the vertical magnetisation direction, for the thin plate and the slab are expressed as follows.

The vertical component of the thin plate in the vertical magnetisation condition can be expressed as :

$$\Delta Z = 2K_v Tb[\frac{x + w/2}{(x + \frac{w}{2})^2 + h^2} - \frac{x - w/2}{(x - \frac{w}{2})^2 + h^2}] \tag{4.1}$$

and the vertical component of the slab with the depth extent (or thickness) equal to the depth to the top of the body is approximated as:

$$\Delta Z \approx 2KDTb[\frac{x + w/2}{(x + \frac{w}{2})^2 + H^2} - \frac{x - w/2}{(x - \frac{w}{2})^2 + H^2}]. \tag{4.2}$$

The explanation of the factors in the two expressions are shown in Table 4.9.

By comparing each term in the expressions (4.1) and (4.2), the relationship between the two depths (h and H) and the susceptibilities (K_s and K) can be given as follows.

From the slab to the thin plate:

$$h = 1.4H,$$

$$K_v = K \cdot D,$$

Table 4.9: Factors in (4.1) and (4.2)

Factor	Explanation
K_v	the volume susceptibility of the thin plate body, it is equal to the area susceptibility K_s times the thickness of the body (t)
T	the total intensity of the geomagnetic field
b	the component in the plane crossed the observed profile of unit vector in the magnetisation direction (see Appendix B)
x	the horizontal distance between the observed point and the center of the body
w	the width of the body
h	the vertical distance between the observed plane and the top of the thin plate
K	the susceptibility of the slab
H	the depth to the top of the slab body
D	the thickness of the slab body

or

$$K_s = \frac{K \cdot D}{t}; \tag{4.3}$$

from the thin plate to the slab:

$$H = 0.707h,$$

$$K = \frac{K_v}{D} = \frac{K_s \cdot t}{D}. \tag{4.4}$$

Note that widths of the two bodies are the same and both dips are defined as 90°. Now the standard model in the thin plate approach can be defined as this slab. The advantages of using this model are explained below.

1. Parameters of the thin plate can be easily transformed from the results of the slab model.
2. An anomaly caused by a slab type body, in which the depth extent of the body is less than three times the depth to the top of the body, can be processed by using this slab model.
3. There are many magnetic anomalies arising from slab type bodies in the real geological situation, therefore this model should be useful for processing magnetic data.

In order to emphasise the function of the thin plate model, the approach is still called the thin plate approach.

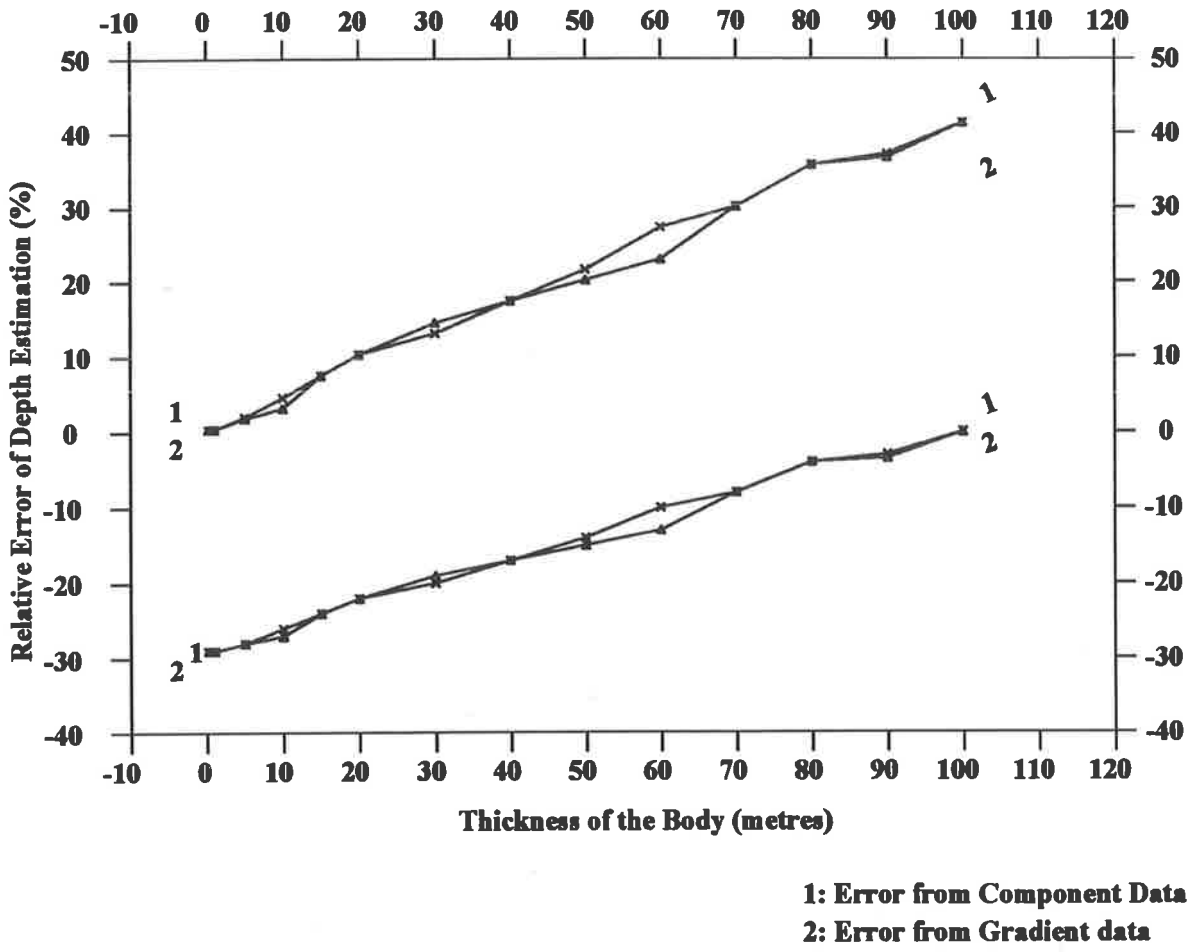

Figure 4.17: Error analysis of depth estimation using a plate model.

4.6.2 Error analysis for thin plate and slab models

The same procedure as shown in the other models has been carried out for the thin plate and slab models. This section shows error analyses of parameter determinations of the thin plate and slab model respectively. Briefly speaking, the depth extent (or thickness of the body), width and dip of the body are important factors which affect the precision of the estimates; among them the depth extent is the most important. If the depth extent is greater than three times the depth to the top of the body, the error of the depth estimate is up to 30%; if the width is greater than five times the depth to the top of the body and the dip angle is near the horizontal plane, the errors are also increased. The results from the gradient data are not significantly better than the estimates from the component data.

Thin plate model

Figure 4.17 illustrates error curves of the parameter estimates for a set of models, in which the shape of the body gradually changes from a thin plate to a slab (the thickness is equal to the depth of the slab). The horizontal axis presents the thickness of the body changed from 0.2 metres to 100 metres. The line marked 1 with the triangle symbol represents the error curves from the component data and the line marked 2 with the cross symbol corresponds to the gradient data. Two sets of curves are shown in the graphs, graphs at the top show an increasing error along the horizontal axis and the values of errors range from 0% to 41%. These curves correspond to the errors from the model calculated based on the formulae of the thin plate. The errors of the second set of curves decrease along the horizontal axis and the values range from -29% to 0%, and these curves represent errors of depth estimates using the new designed slab model.

Table 4.10 lists the basic parameters of the test models shown in Figure 4.17 and input information for use of AUTOMAG. The estimated results from AUTOMAG and the conversion of depth and susceptibility using expressions in (4.3) and (4.4) for component and gradient data are presented in Table 4.11 and Table 4.12 respectively.

The procedure of conversion can be described as follows: the depth h of the thin plate is equal to 1.4 times the obtained depth estimate H. The susceptibility K_s of the thin plate is equal to the product of the estimated susceptibility K and the ratio of the two thicknesses, which are the obtained thickness estimate D which is equal to the estimated depth H and the thickness of the thin plate body t. Because the thickness of the thin plate t is difficult to know, the accurate area susceptibility K_s may not be obtained. Only the volume susceptibility K_v can be determined from the product of the estimated thickness D and the estimated susceptibility K.

According to Table 4.11 and Table 4.12, no matter how the depth extent is changed, the estimates of the width and dip for both component and gradient data are close to the true values. For the case of thin plate models, If the thickness of the body is less than 10% of the depth, errors of depth estimates are less than 0.4%. If the thickness of the body is increased,

Error Analysis of Theoretical Model for Varying Depth Extent

(Using Plate Model Approach)

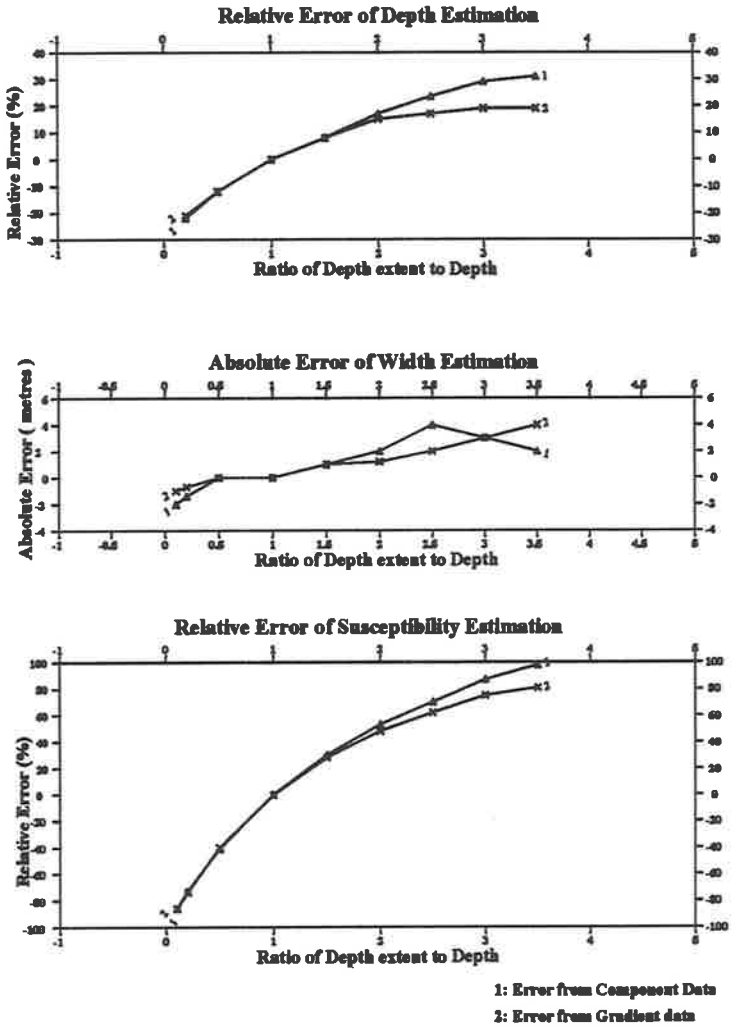

Figure 4.18

Error Analysis of Theoretical Model for Varying Width

(Using Plate Model Approach)

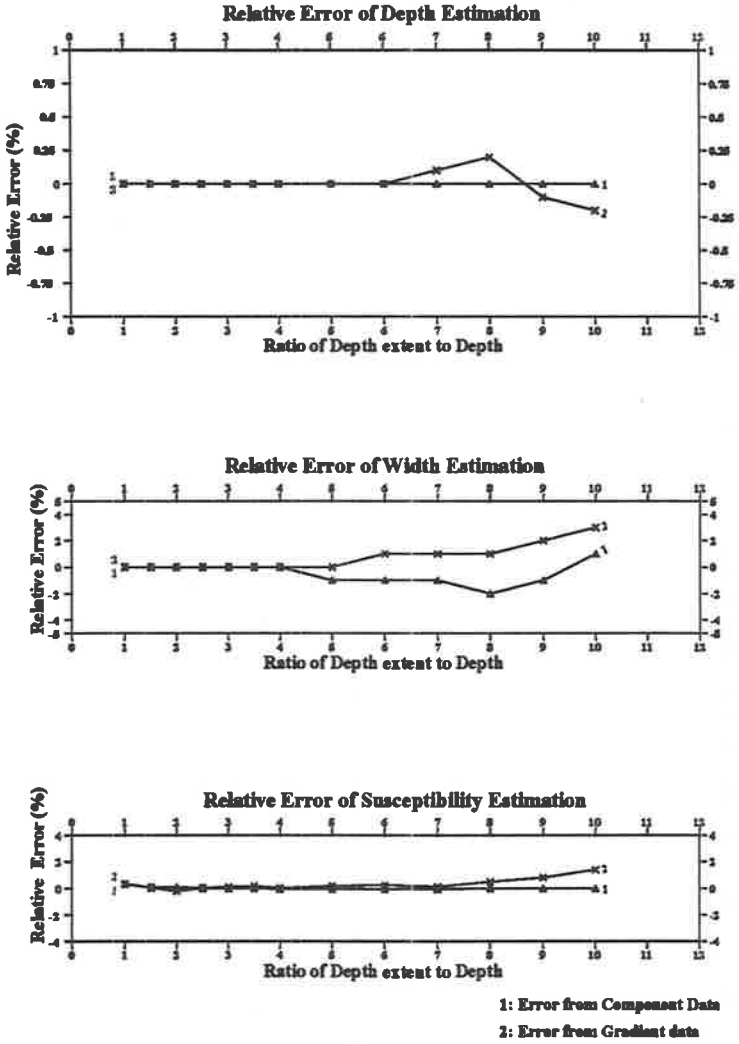

Figure 4.19

Table 4.10: Parameters of thin plate and input information using AUTOMAG for checking error effect of varied thickness

Parameters of Thin Plate				
Depth metres	$\frac{Width}{2}$ metres	Dip degrees	Susceptibility $10^{-6} \times SI$	Sample Interval metres
100	250	90°	5000	25
Input Information Using AUTOMAG Program				
Initial Model		No. of Sample	Sample Interval	Number of
Depth	$\frac{Width}{2}$	Intervals		Window Points
60 m	60 m	1	25 m	41
120 m	120 m	2	50 m	41
180 m	180 m	3	75 m	41
240 m	240 m	4	100 m	41

the error is also increased. The test shows that the new thin plate approach provides reliable parameter estimates from the anomalies of the thin plate type. It also works for the slab with depth extent less than three times the depth to the top.

Slab model

Figure 4.18 illustrates the error analysis for the slab model for varying depth extent. Parameters of a basic model and the input information using AUTOMAG are the same as shown in Table 4.10.

1. The top graph shows the error curves of the depth estimates from component and gradient data and the two curves are very similar. If the ratio of the depth extent to the depth is close to unity, the error of the estimate is minimum, but if the ratio is greater than unity, the error increases. Particularly if the ratio is greater than three, the error is greater than 30% for component data and 20% for gradient data.

2. Errors of the width estimates are considerably smaller and in this range of depth extent, both errors from component and gradient data are less than 5%.

3. The estimated susceptibilities contain significant errors and the estimates cannot be accepted. The reason behind these unacceptable estimates is that the formula based on the thin plate model is not suitable to determine the susceptibility of the slab body.

In conclusion, using the thin plate approach to estimate the parameters of a slab body, only the depth and width estimates can be accepted. The thin plate approach is not suitable for susceptibility and dip determinations.

Table 4.11: Estimates and conversion parameters using thin plate from component data

T	h		κ		$\frac{W}{2}$	Dip
metres	H_E	H_C	κ_E	κ_C	m	
0.2 m	71 m	100.4 m	13.3	4910	249 m	90°
1 m	71 m	100.4 m	69.5	4910	249 m	90°
5 m	72 m	101.8 m	351	5050	249 m	90°
10 m	73 m	103.2 m	684	5060	250 m	90°
15 m	76 m	107.5 m	1000	5050	251 m	90°
20 m	78 m	110.3 m	1280	4996	250 m	90°
30 m	81 m	114.5 m	1868	4981	249 m	90°
40 m	83 m	117.4 m	2418	5020	249 m	90°
50 m	85 m	120.2 m	2920	5020	249 m	90°
60 m	87 m	123.0 m	3350	5030	250 m	90°
70 m	92 m	130.1 m	3807	5003	250 m	90°
80 m	96 m	135.7 m	4187	5020	250 m	90°
90 m	97 m	136.5 m	4695	5060	250 m	90°
100 m	100 m	141.4 m	4990	4990	250 m	90°

Note:

T: thickness of body,

H: the depth to the top of the body,

H_E: depth estimated using AUTOMAG of slab model (the depth extent equal to the depth),

H_C: depth converted using formula (4.3),

κ: susceptibility of the body,

κ_E: susceptibility estimated using AUTOMAG of slab model,

κ_C: susceptibility converted using (4.4), the thickness of two bodies are know,

$\frac{W}{2}$: half width of the body.

Table 4.12: Estimates and conversion parameters using thin plate from component data

T	h		κ		$\frac{W}{2}$	Dip
metres	H_E	H_C	κ_E	κ_C	m	
0.2 m	71 m	100.4 m	14.3	5080	250 m	90°
1 m	71 m	100.4 m	71.5	5070	249 m	90°
5 m	72 m	101.8 m	355	5120	250 m	90°
10 m	74 m	104.6 m	692	5050	249 m	90°
15 m	76 m	107.5 m	1010	5120	249 m	90°
20 m	78 m	110.3 m	1310	5110	249 m	90°
30 m	80 m	113.1 m	1897	5120	250 m	90°
40 m	83 m	117.4 m	2440	5060	250 m	90°
50 m	80 m	121.6 m	3000	5100	250 m	90°
60 m	90 m	127.3 m	3448	5000	251 m	90°
70 m	92 m	130.1 m	3851	5060	250 m	90°
80 m	96 m	135.7 m	4218	5060	249 m	90°
90 m	97 m	137.2 m	4666	5002	251 m	90°
100 m	100 m	141.4 m	5000	5000	250 m	90°

Note:

T: the thickness of body,

H: the depth to the top of the body,

H_E: depth estimated using AUTOMAG of slab model (the depth extent equal to the depth),

H_C: depth converted using formula (4.3),

κ: susceptibility of the body,

κ_E: susceptibility estimated using AUTOMAG of slab model,

κ_C: susceptibility converted using (4.4), assuming the thickness of the two bodies are known,

$\frac{W}{2}$: the half width of the body.

Error Analysis of Theoretical Model for Varying Dip

(Using Plate Model Approach)

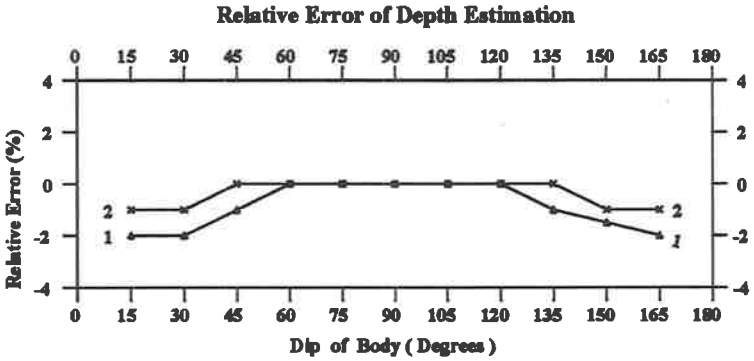

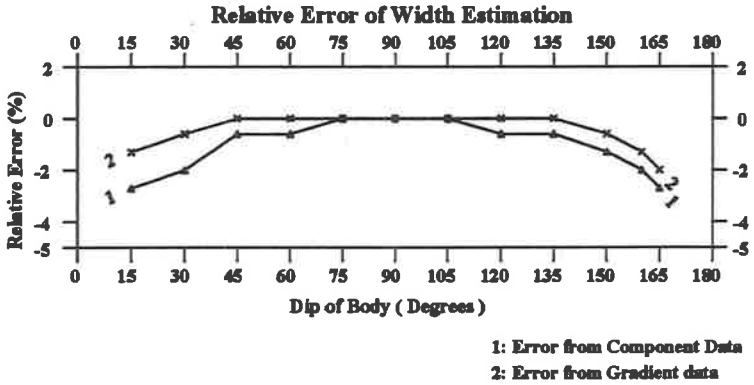

Figure 4.20a

Error Analysis of Theoretical Model for Varying Dip

(Using Plate Mode Approach)

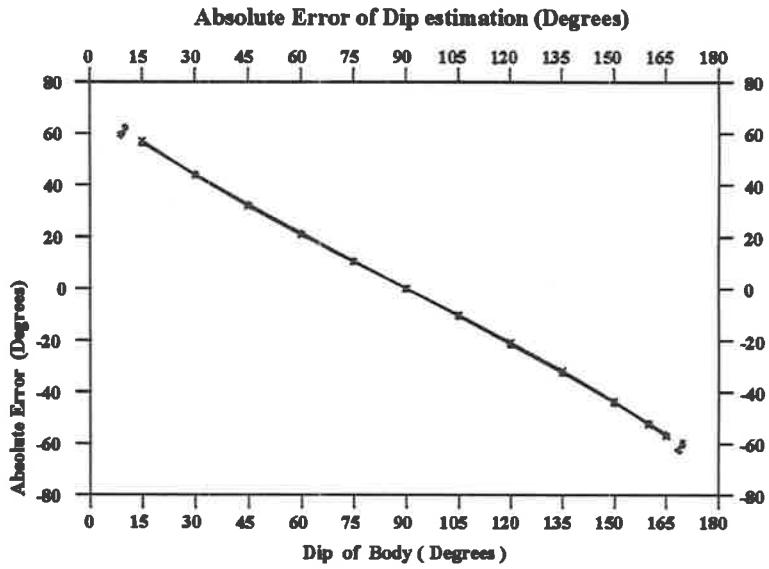

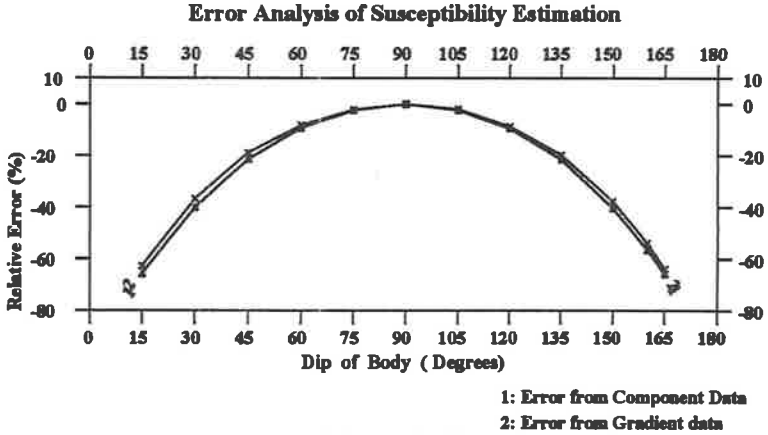

Figure 4.20b

Figures 4.19 and 4.20 shows the error effect from changing width and dip of the body respectively. The parameters of the basic model are chosen as for a standard slab, i.e. the thickness is equal to the depth. The width and dip of the model are varied, such that the dip is fixed at 90° for varying the width and the width is fixed at three times the depth for varying the dip. From Figure 4.19, it is readily seen that the error effect from the varied width is small, therefore the effect can be ignored. The error effect from changing the dip angle is limited for the depth and width estimates. However the estimated dip and susceptibility can have large errors.

In conclusion, in the error analyses for the thin plate and slab models, the depth extent is the most important factor in introducing errors. If the depth extent is greater than three times this depth, the error for depth estimate is significant and the estimate is not accepted. The error effects from the width and dip are limited for estimating depth and width. The results from the gradient data are not much better than from the component data. The estimates from the anomaly caused by a thin plate model have appreciable precision. The results are converted by using formulae (4.3) and (4.4), in which the maximum error of the depth estimate is 4%.

4.7 Summary of simple model test

Three standard models are designed in AUTOMAG, which will be suitable to apply to a variety of geological situations. From the error analyses of above tests, AUTOMAG provides reliable estimates of the depth, width, dip or susceptibility of the magnetic causative body, e.g. a dyke, an edge, a thin plate and a slab. In general, the results from the gradient data are better than the estimates from the component data. Note that the Improved Naudy Technique can be used to interpret a single anomaly. What is the result for processing a complex anomaly? The following sections will give the answer.

4.8 Complex model tests

Real airborne or ground magnetic anomalies are much more complex than synthetic single source anomalies. Real anomalies are the combined effect of many individual anomalies arising from some simple geometrical bodies, e.g. dyke, edge and thin plate. In order to simulate the real situation, some more complicated model data are tested and some suggestions for effectively using the approach are provided.

4.8.1 Multiple dykes with varying dip

The following test was carried out to check the estimated error from a set of infinite depth extent dykes with different dip angles. The test also compares the true parameters with the estimates calculated from the three types of model approaches.

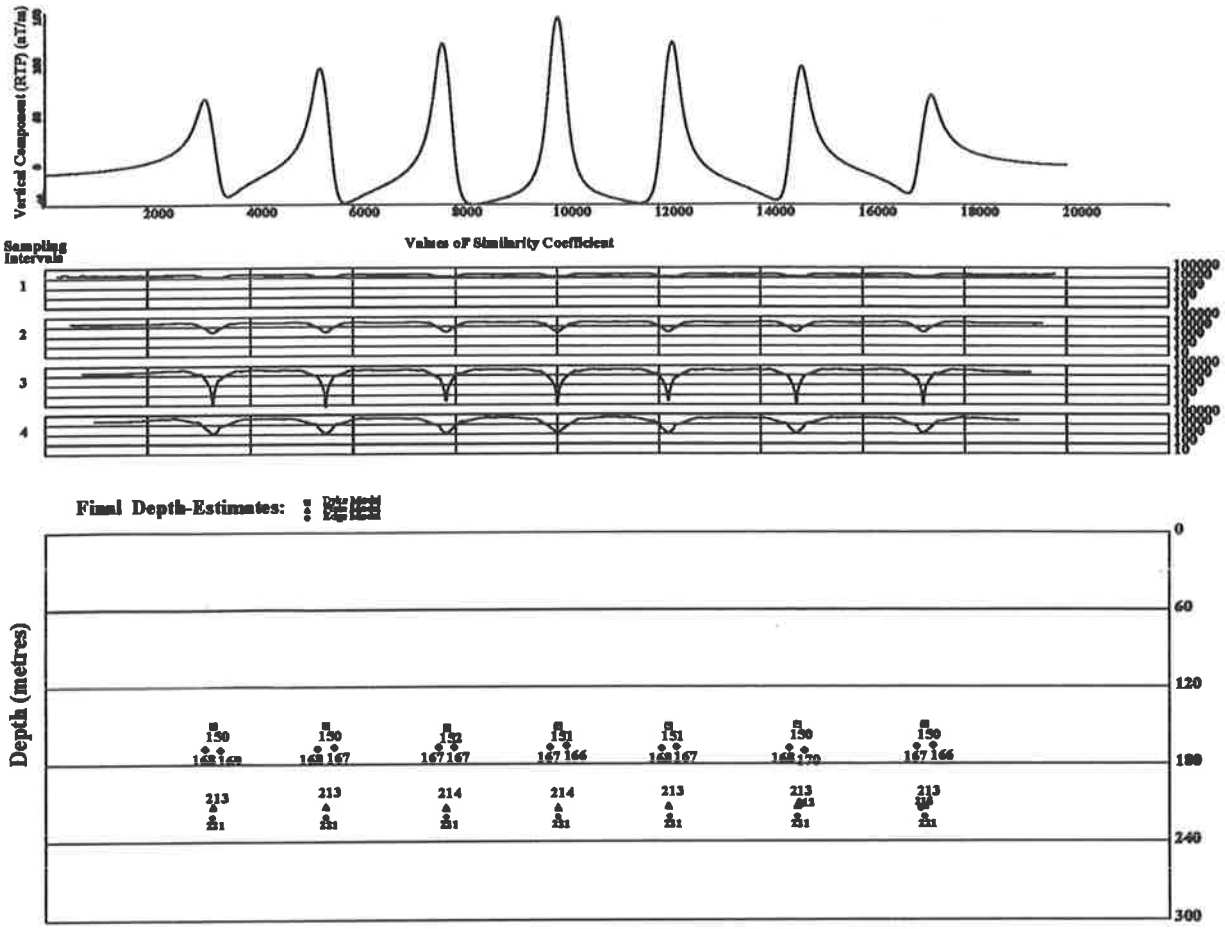

Figure 4.21a: Combination of Depth Estimates using Dyke, Edge & Thin Plate Models from Component Data

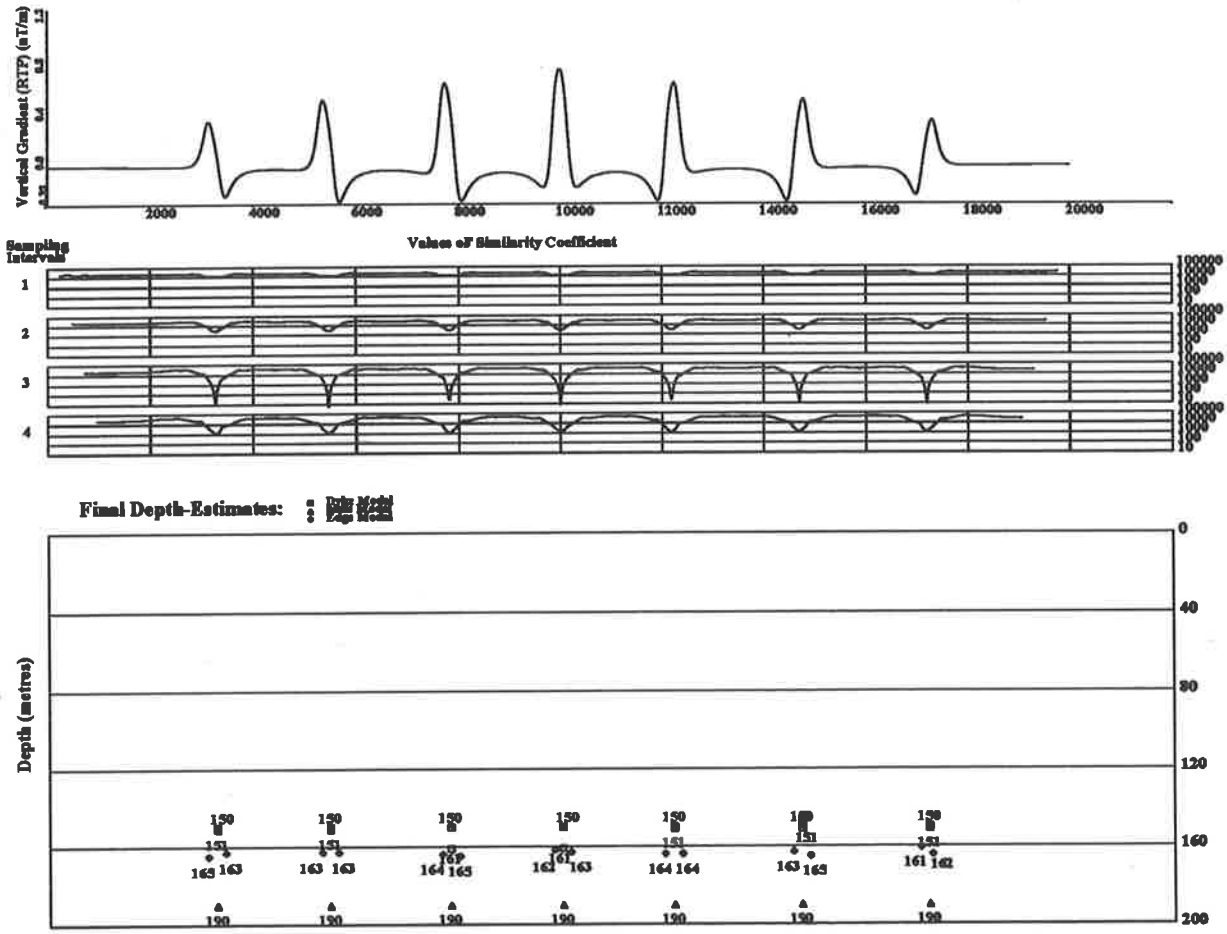

Figure 4.21b: Combination of Depth Estimates Using Dyke, Edge & Thin Plate Models from Gradient Data

Figure 4.21 illustrates the results from seven dyke bodies with the same depth, width, susceptibility but different dips. The parameters of bodies are given in Table 4.13. Three types of models, i.e. dyke, edge and thin plate, are applied to the component and gradient data and the estimated depths are presented in Figure 4.21 respectively. The input information of the three intial models are slightly different and this is also given in Table 4.13. In the figure the square symbol represents the estimates from dyke model, the diamond from applying the edge model and the triangle from applying the thin plate model. It can be readily seen from estimated depths corresponding to any specific body that the shallowest depth is obtained using the dyke model approach, the greatest depth using the thin plate and the intermediate depth using the edge model. Table 4.14 lists the comparison between the parameters of the theoretical models and the estimates from component data using dyke and thin plate model approaches. The results from gradient data are given in Table 4.15.

By comparing the results, if each individual anomaly is well isolated, the varied dip angle (in the range of 30° to 150°) does not much affect the accuracy of the estimates. Among the three approaches, the estimates from the dyke model provides the most satisfactory estimate, but the other two models have some errors, which indicates the choice of the initial model is important. The reasons why the edge and thin plate models do not provide good solutions can be explained as follows.

1. The edge model only suits an anomaly caused by a wide body in which the ratio of the width and the depth is greater than three times.
2. The thin plate model should be applied to an anomaly with a limited depth extent which requires the depth extent to be less than three times the depth to the top.
3. The results from applying the dyke model also produces some errors because the depth extent of the basic dyke model in AUTOMAG is ten times the depth but not infinity.

Additionally by comparison of results from component and vertical gradient data, it indicates the solution from gradient data is better than the information from component data.

4.8.2 Multiple bodies with varied width

In this section, a set of data with 9 theoretical bodies having the same depth, dip, depth extent and susceptibility but varying width is tested using dyke and edge models in AUTOMAG. The parameters of the tested theoretical bodies and the input information of the initial model used in AUTOMAG are given in Table 4.16.

Part A in Figure 4.22 illustrates the depth estimates using dyke model from component data. From the first four anomalies, in which the ratio of the width to depth is less than three, a single depth related to each centre of an anomaly is determined. When the width of body is increased, a pair of depths corresponds to two edges of a single anomaly are provided where the localities for the two edges can be readily seen from the similarity coefficient curves at some

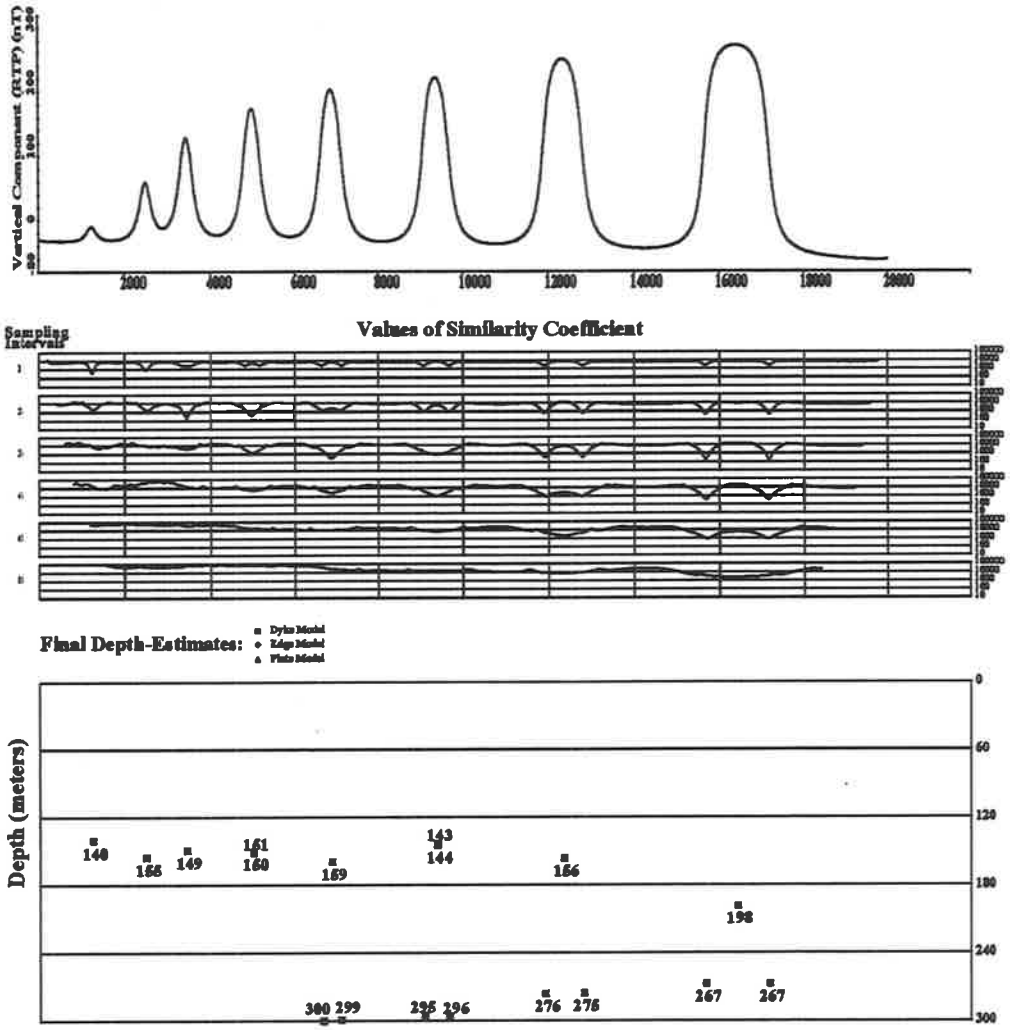

Figure 4.22a: N-S Profile in Northern Hemisphere (i=60°)
Initial Dyke: h=100m b=50m dx=20m N=21
The depth of all Theoretical Bodies at 148 m

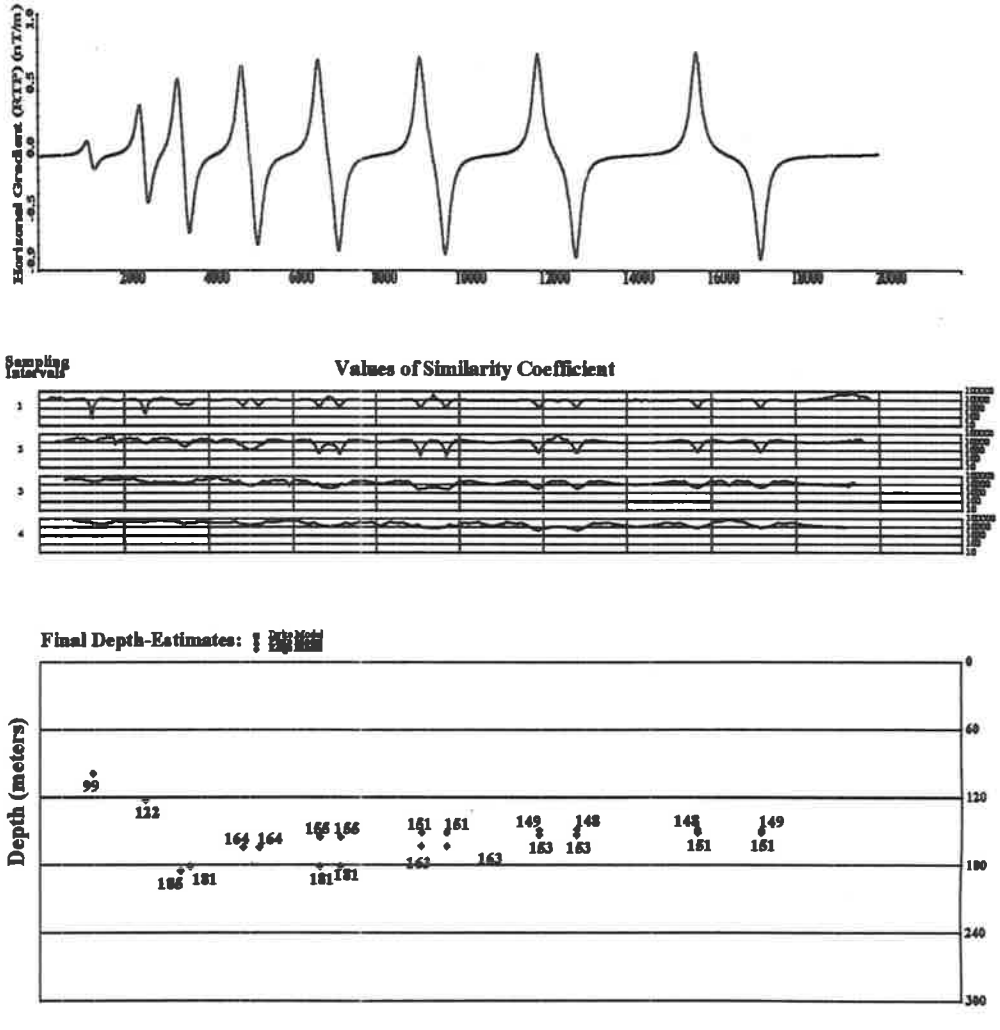

Figure 4.22b: N-S Profile in Northern Hemisphere (i=60°)
Initial Edge: h=100m b=50m dx=20m N=21
The depth of all Theoretical Bodies at 148 m

Table 4.13: Parameters of test dykes with varied dips and input information using AUTOMAG

Parameters of Dyke				
Depth (metres)	$\frac{Width}{2}$ (metres)	Depth Extent (metres)	Susceptibility ($10^{-6} \times SI$)	Sample Interval (metres)
148	150	∞	1000	20
Varied dips of 7 dykes are from S-N as 150°, 135°, 120°, 90°, 60°, 45°, 30°				

Input Information of Initial Model Using AUTOMAG				
Initial Dyke		No. of Sample Intervals	Sample Interval	Number of Window Points
Depth	$\frac{Width}{2}$			
50 m	50 m	1	20 m	25
100 m	100 m	2	40 m	25
150 m	150 m	3	60 m	25
200 m	200 m	4	80 m	25
Initial Edge		No. of Sample Intervals	Sample Interval	Number of Window Points
Depth	$\frac{Width}{2}$			
100 m	50 m	1	20 m	17
200 m	100 m	2	40 m	17
300 m	150 m	3	60 m	17
400 m	200 m	4	80 m	17
Initial Plate		No. of Sample Intervals	Sample Interval	Number of Window Points
Depth	$\frac{Width}{2}$			
100 m	100 m	1	20 m	25
200 m	200 m	2	40 m	25
300 m	300 m	3	60 m	25
400 m	400 m	4	80 m	25

Note:

Profile direction is from south to north,

Dip is measured from north,

Inclination of the earth's magnetic field is $-60°$,

Intensity of total magnetic field is 60,000 nT.

Table 4.14: Comparisons between true parameters and estimates from component data for a set of dykes with varied dips

Results from Dyke Model								
No. of Dyke	H (m)		$\frac{W}{2}$ (m)		Dip		κ ($10^{-6}CGS$)	
	H_T	H_E	$\frac{W}{2}_T$	$\frac{W}{2}_E$	dip_T	dip_E	κ_T	κ_E
1	**148**	150	**150**	150	150°	146.3°	**1000**	771
2	**148**	150	**150**	150	135°	132.3°	**1000**	870
3	**148**	152	**150**	151	120°	122.7°	**1000**	938
4	**148**	151	**150**	150	90°	89.4°	**1000**	933
5	**148**	151	**150**	150	60°	56.7°	**1000**	967
6	**148**	150	**150**	150	45°	48.2°	**1000**	904
7	**148**	150	**150**	150	30°	36.4°	**1000**	793
Results from Thin Plate Model								
No. of Dyke	H (m)		$\frac{W}{2}$ (m)		Dip		κ ($10^{-6}CGS$)	
	H_T	H_E	$\frac{W}{2}_T$	$\frac{W}{2}_E$	dip_T	dip_E	κ_T	κ_E
1	**148**	213	**150**	140	150°	146.3°	**1000**	2025
2	**148**	213	**150**	140	135°	132.3°	**1000**	2284
3	**148**	214	**150**	140	120°	116.8°	**1000**	2325
4	**148**	214	**150**	141	90°	89.4°	**1000**	2450
5	**148**	213	**150**	140	60°	56.7°	**1000**	2541
6	**148**	213	**150**	140	45°	48.2°	**1000**	2375
7	**148**	213	**150**	140	30°	36.4°	**1000**	2084

Note:

H: the depth to the top of the body,

H_T: the true depth from theoretical model,

H_E: depth estimated using AUTOMAG

$\frac{W}{2}$: the half width of the body,

$\frac{W}{2}_T$: the true half width of the body,

$\frac{W}{2}_E$: the estimated half width of body,

dip: the dip of body measured from north,

dip_T: the true dip of theoretical body,

dip_E: the estimated dip,

κ: susceptibility of the body,

κ_T: true susceptibility of model,

κ_E: estimated susceptibility.

Table 4.15: Comparison between true parameters and estimates from gradient data for a set of dykes with varied dips

Results from Dyke Model								
No. of Dyke	H (m)		$\frac{W}{2}$ (m)		Dip		κ ($10^{-6}CGS$)	
	H_T	H_E	$\frac{W}{2}_T$	$\frac{W}{2}_E$	dip_T	dip_E	κ_T	κ_E
1	**148**	150	**150**	150	150°	154.0°	**1000**	1152
2	**148**	150	**150**	150	135°	134.6°	**1000**	1000
3	**148**	150	**150**	150	120°	116.8°	**1000**	977
4	**148**	150	**150**	150	90°	90.1°	**1000**	1009
5	**148**	150	**150**	150	60°	63.3°	**1000**	977
6	**148**	150	**150**	150	45°	46.8°	**1000**	980
7	**148**	150	**150**	150	30°	30.2°	**1000**	1010
Results from Thin Plate Model								
No. of Dyke	H (m)		$\frac{W}{2}$ (m)		Dip		κ ($10^{-6}CGS$)	
	H_T	H_E	$\frac{W}{2}_T$	$\frac{W}{2}_E$	dip_T	dip_E	κ_T	κ_E
1	**148**	190	**150**	151	150°	154.0°	**1000**	2267
2	**148**	190	**150**	151	135°	134.6°	**1000**	1968
3	**148**	190	**150**	151	120°	116.8°	**1000**	1922
4	**148**	190	**150**	151	90°	90.1°	**1000**	1984
5	**148**	190	**150**	151	60°	63.3°	**1000**	1923
6	**148**	190	**150**	151	45°	46.8°	**1000**	1929
7	**148**	190	**150**	151	30°	30.2°	**1000**	1987

Note:

H: the depth to the top of the body,

H_T: the true depth from theoretical model,

H_E: depth estimated using AUTOMAG

$\frac{W}{2}$: the half width of the body,

$\frac{W}{2}_T$: the true half width of the body,

$\frac{W}{2}_E$: the estimated half width of body,

dip: the dip of body measured from north,

dip_T: the true dip of theoretical body,

dip_E: the estimated dip,

κ: susceptibility of the body,

κ_T: true susceptibility of model,

κ_E: estimated susceptibility.

Table 4.16: Parameters of test bodies with varied width and input information using AUTOMAG

Parameters of Dyke				
Depth (metres)	Dip (degrees)	Depth Extent (metres)	Susceptibility ($10^{-6} \times SI$)	Sample Interval (metres)
148	90°	∞	**1000**	20
Varied $\frac{Width}{2}$ of 8 bodies are from S-N as 15 m, 60 m, 120 m, 180 m, 240 m, 300 m, 450 m, 750 m				

Input Information of Initial Model Using AUTOMAG				
Initial Dyke		No. of Sample Intervals	Sample Interval	Number of Window Points
Depth	$\frac{Width}{2}$			
100 m	50 m	1	20 m	21
200 m	100 m	2	40 m	21
300 m	150 m	3	60 m	21
400 m	200 m	4	80 m	21
600 m	300 m	6	120 m	21
800 m	400 m	8	160 m	21
Initial Edge		No. of Sample Intervals	Sample Interval	Number of Window Points
Depth	$\frac{Width}{2}$			
100 m	50 m	1	20 m	21
200 m	100 m	2	40 m	21
300 m	150 m	3	60 m	21
400 m	200 m	4	80 m	21

Note:
Profile direction is from south to north,
Inclination of Earth's magnetic field is 60°,
Intensity of total magnetic field is 60,000 nT.

Table 4.17: Comparisons between true and estimated parameters using dyke model approach for varied width bodies

No. of Dyke	H (m)		$\frac{W}{2}$ (m)		Dip		κ ($10^{-6}CGS$)	
	H_T	H_E	$\frac{W}{2}_T$	$\frac{W}{2}_E$	dip_T	dip_E	κ_T	κ_E
1	**148**	140	**15**	64	90°	165.2°	**1000**	3203
2	**148**	155	**60**	88	90°	43.8°	**1000**	2029
3	**148**	149	**120**	118	90°	73.9°	**1000**	962
4	**148**	151	**180**	180	90°	85.5°	**1000**	948
5	**148**	159	**240**	238	90°	87.8°	**1000**	998
6	**148**	144	**300**	303	90°	92.9°	**1000**	997
7	**148**	156	**450**	453	90°	95.6°	**1000**	1074
8	**148**	150	**750**	751	90°	104.2°	**1000**	1227

Note:

H: the depth to the top of the body,

H_T: the true depth from theoretical model,

H_E: depth estimated using AUTOMAG

$\frac{W}{2}$: the half width of the body,

$\frac{W}{2}_T$: the true half width of the body,

$\frac{W}{2}_E$: the estimated half width of body,

dip: the dip of body measured from north,

dip_T: the true dip of theoretical body,

dip_E: the estimated dip,

κ: susceptibility of the body,

κ_T: true susceptibility of model,

κ_E: estimated susceptibility.

Table 4.18: Comparisons between true and estimated parameters using edge model for varied width bodies

No. of Dyke	H (m)			$\frac{W}{2}$ (m)		Dip			κ ($10^{-6}CGS$)		
	H_T	H_l	H_r	$\frac{W}{2}_T$	$\frac{W}{2}_E$	dip_T	dip_l	dip_r	κ_T	κ_l	κ_r
1	**148**	99		**15**	44	90°	2.9°		**1000**	2286	
2	**148**	122		**60**	53	90°	173.0°		**1000**	4389	
3	**148**	185	181	**120**	120	90°	125.5°	57.4°	**1000**	1295	1222
4	**148**	164	164	**180**	190	90°	104.3°	73.7°	**1000**	1003	1027
5	**148**	155	155	**240**	250	90°	100.5°	79.1°	**1000**	979	988
6	**148**	151	151	**300**	300	90°	104.3°	80.5°	**1000**	1013	988
7	**148**	149	148	**450**	450	90°	98.6°	83.1°	**1000**	1000	991
8	**148**	148	148	**750**	750	90°	92.2°	82.2°	**1000**	987	1013

Note:

H_l: the estimated depth at left side of body,

H_r: the estimated depth at right side of body,

$\frac{W}{2}_E$: the estimated half width of body, calculated from the distance between two centers of a pair edge bodies,

dip_l: the estimated dip at left side of body,

dip_r: the estimated dip at right side of body,

κ_l:the estimated susceptibility at left side of body,

κ_r:the estimated susceptibility at right side of body.

Table 4.19: Parameters of test bodies with varied depth extent and input information using AUTOMAG

Parameters of Dyke				
Depth (metres)	$\frac{Width}{2}$ (metres)	Dip (degrees)	Susceptibility ($10^{-6} \times SI$)	Sample Interval (metres)
146	150	90°	1000	10
Varied depth extent of five dykes are from S-N as 20 m, 50 m, 100 m, 300 m, 500 m				

Input Information of Initial Model Using AUTOMAG				
Initial Dyke		No. of Sample Intervals	Sample Interval	Number of Window Points
Depth	$\frac{Width}{2}$			
50 m	50 m	1	10 m	41
100 m	100 m	2	20 m	41
150 m	150 m	3	30 m	41
200 m	200 m	4	40 m	41
Initial Edge		No. of Sample Intervals	Sample Interval	Number of Window Points
Depth	$\frac{Width}{2}$			
100 m	50 m	1	10 m	21
200 m	100 m	2	20 m	21
300 m	150 m	3	30 m	21
400 m	200 m	4	40 m	21
Initial Plate		No. of Sample Intervals	Sample Interval	Number of Window Points
Depth	$\frac{Width}{2}$			
50 m	50 m	1	10 m	31
100 m	100 m	2	20 m	31
150 m	150 m	3	30 m	31
200 m	200 m	4	40 m	31

Note:
Profile direction is from south to north,
Inclination of Earth's magnetic field is $-60°$,
Intensity of total magnetic field is 60,000 nT.

Table 4.20: Comparison between true parameters and estimates from component data for varied depth extent, bodies with varied depth extent

Results from Dyke Model								
No. of Dyke	H (m)		$\frac{W}{2}$ (m)		Dip		κ ($10^{-6}CGS$)	
	H_T	H_E	$\frac{W}{2}_T$	$\frac{W}{2}_E$	dip_T	dip_E	κ_T	κ_E
1	**146**	88	**150**	142	90°	83.6°	**1000**	60
2	**146**	90	**150**	144	90°	85.8°	**1000**	153
3	**146**	103	**150**	143	90°	88.3°	**1000**	279
4	**146**	133	**145**	147	90°	91.4°	**1000**	614
5	**146**	136	**150**	149	90°	92.3°	**1000**	748
Results from Thin Plate Model								
No. of Dyke	H (m)		$\frac{W}{2}$ (m)		Dip		κ ($10^{-6}CGS$)	
	H_T	H_E	$\frac{W}{2}_T$	$\frac{W}{2}_E$	dip_T	dip_E	κ_T	κ_E
1	**146**	115	**150**	149	90°	83.6°	**1000**	156
2	**146**	125	**150**	149	90°	90.0°	**1000**	392
3	**146**	137	**150**	150	90°	88.3°	**1000**	697
4	**146**	168	**150**	150	90°	91.4°	**1000**	1453
5	**146**	186	**150**	149	90°	92.3°	**1000**	1865

Table 4.21: Comparisons between true and estimated parameters using edge model from component data, bodies with varied depth extent

No. of Dyke	H (m)			$\frac{W}{2}$ (m)		Dip			κ ($10^{-6}CGS$)		
	H_T	H_l	H_r	$\frac{W}{2}_T$	$\frac{W}{2}_E$	dip_T	dip_l	dip_r	κ_T	κ_l	κ_r
1	**146**	114	117	**150**	155	90°	92.8°	82.7°	**1000**	107	113
2	**146**	126	125	**150**	155	90°	98.1°	84.7°	**1000**	251	251
3	**146**	136	136	**150**	160	90°	96.4°	84.1°	**1000**	425	435
4	**146**	150	152	**150**	155	90°	105.2°	73.7°	**1000**	779	814
5	**146**	155	156	**150**	155	90°	110.7°	72.7°	**1000**	943	907

Note:

H_l: the estimated depth at left side of body,

H_r: the estimated depth at right side of body,

$\frac{W}{2}_E$: the estimated half width of body, calculated from the distance between two centers of a pair edge bodies,

dip_l: the estimated dip at left side of body,

dip_r: the estimated dip at right side of body,

κ_l:the estimated susceptibility at left side of body,

κ_r:the estimated susceptibility at right side of body.

Table 4.22: Comparison between true parameters and estimates from gradient data, bodies with varied depth extent

Results from Dyke Model								
No. of Dyke	H (m)		$\frac{W}{2}$ (m)		Dip		κ ($10^{-6}CGS$)	
	H_T	H_E	$\frac{W}{2}_T$	$\frac{W}{2}_E$	dip_T	dip_E	κ_T	κ_E
1	**146**	91	**150**	145	90°	91°	1000	89
2	**146**	97	**150**	145	90°	89.1°	1000	207
3	**146**	112	**150**	145	90°	90.7°	1000	380
4	**146**	135	**150**	147	90°	91.9°	1000	753
5	**146**	137	**150**	151	90°	89.3°	1000	864
Results from Thin Plate Model								
No. of Dyke	H (m)		$\frac{W}{2}$ (m)		Dip		κ ($10^{-6}CGS$)	
	H_T	H_E	$\frac{W}{2}_T$	$\frac{W}{2}_E$	dip_T	dip_E	κ_T	κ_E
1	**146**	115	**150**	149	90°	91°	1000	192
2	**146**	137	**150**	150	90°	89.1°	1000	457
3	**146**	137	**150**	150	90°	90.7°	1000	766
4	**146**	170	**150**	152	90°	91.9°	1000	1494
5	**146**	171	**150**	153	90°	89.3°	1000	1694

Table 4.23: Comparisons between true and estimated parameters using edge model from gradient data, bodies with varied depth extent

No. of Dyke	H (m)			$\frac{W}{2}$ (m)		Dip			κ ($10^{-6}CGS$)		
	H_T	H_l	H_r	$\frac{W}{2}_T$	$\frac{W}{2}_E$	dip_T	dip_l	dip_r	κ_T	κ_l	κ_r
1	**146**	126	113	**150**	155	90°	81.0°	92.2°	**1000**	182	151
2	**146**	140	131	**150**	140	90°	96.1°	77.5°	**1000**	457	410
3	**146**	138	135	**150**	145	90°	91.3°	80.6°	**1000**	660	641
4	**146**	143	139	**150**	145	90°	89.6°	72.8°	**1000**	984	1012
5	**146**	150	155	**150**	150	90°	95.2°	82.5°	**1000**	1165	1252

Note:

H_l: the estimated depth at left side of body,

H_r: the estimated depth at right side of body,

$\frac{W}{2}_E$: the estimated half width of body, calculated from the distance between two centers of a pair edge bodies,

dip_l: the estimated dip at left side of body,

dip_r: the estimated dip at right side of body,

κ_l:the estimated susceptibility at left side of body,

κ_r:the estimated susceptibility at right side of body.

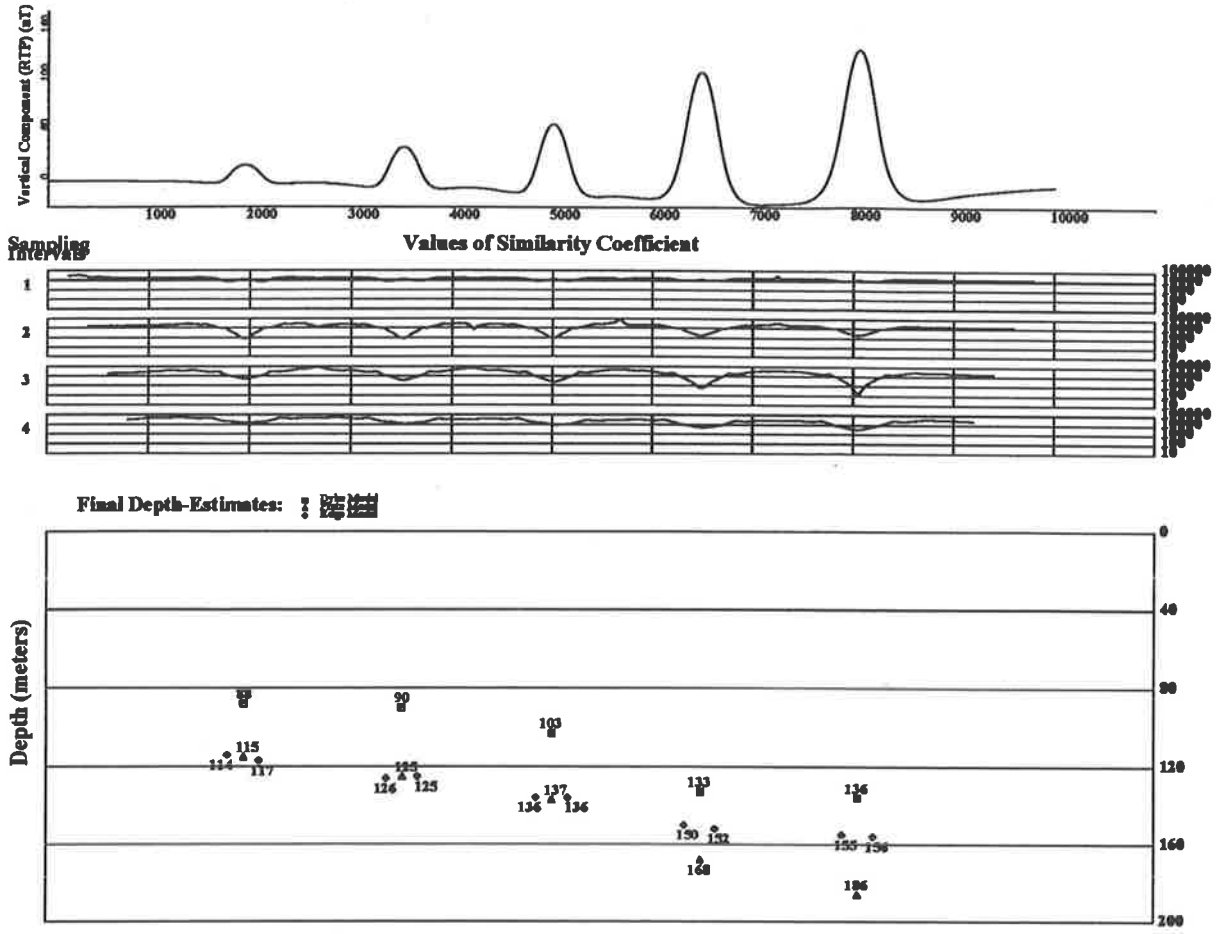

Figure 4.23a: Combination of Depth Estimates Using Dyke, Edge & Thin Plate Models from Component Data

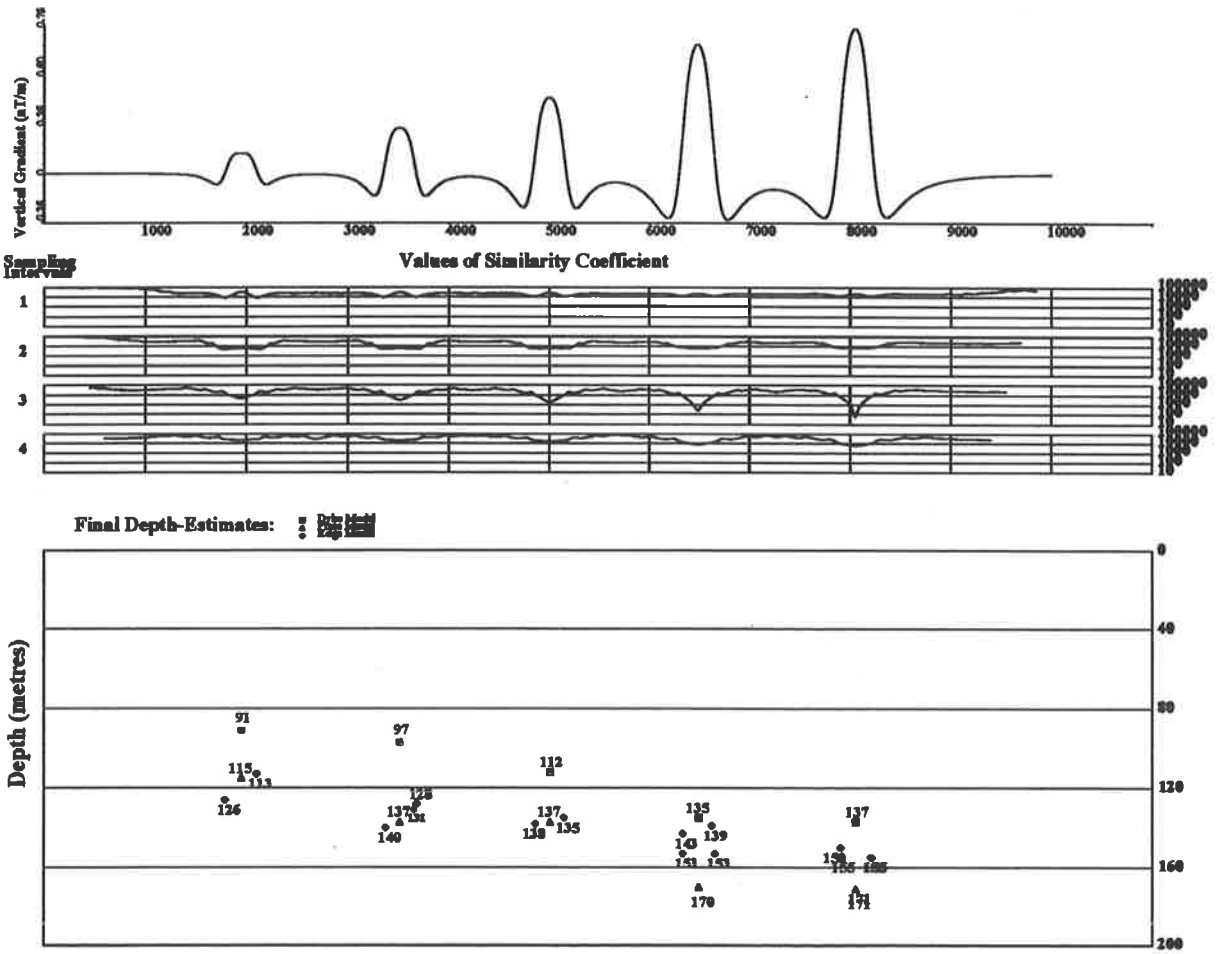

Figure 4.23b: Combination of Depth Estimates Using Dyke, Edge & Thin Plate Models from Vertical Gradient Data

level with a small number of sample interval. When the sample interval increases, the window length becomes proportionately large. A single centre will be located and a set of parameters (with better solution) of this body can be calculated. However if the anomaly is too wide, the estimates will be in error. In this case it is better to use the edge model approach. Table 4.17 demonstrates the comparison between the true parameters and the estimated parameters using the dyke model approach.

Part B in Figure 4.22 presents the depths using the edge model approach. Most depths exist in pairs: each pair of depths are related to the edges of an anomaly and the accuracy of the estimates is increased as the width of the body increases. The first two anomalies of narrow dykes only provide two single depths with certain errors. The results of the comparison between the theoretical and experiments are shown in Table 4.18.

4.8.3 Bodies with different depth extent

A set of theoretical bodies with the same depth, width, dip and susceptibility but with different depth extent is examined using the three model approaches. The parameters of each body and the input information in AUTOMAG are listed in Table 4.19. Figure 4.23 demonstrates the combined results using the dyke, edge and thin plate models from component and gradient data. None of the three models can provide a good solution for all five anomalies.

As all five theoretical models have limited depth extents, in which the ratio of the depth extent to the depth is less than three, the dyke model would not provide a better solution. In this case, the estimated depths using a dyke are shallower than the true depth. The reason for this can be explained as follows.

An anomaly caused by a limited depth extent body is characterised by a central high of which amplitude is high but flat and the slopes of the two flanks of the anomaly are steep. However an anomaly arising from a body of great depth extent is characterised by a high amplitude and sharp central anomaly, and two flanks with a more gentle slope. Note that a thin plate produces two anomalies which appear to be approximately the same as a broad dyke at a shallower depth. Therefore, if using a dyke model curve to match an anomaly arising from a body with limited depth extent, the only way to arrive at a better fit is to make the body shallower. As a result, using the dyke approach a shallow depth is produced.

The comparisons (see Figure 4.23) between the theoretical parameters and the estimates using three model approaches from component and gradient data are presented in Tables 4.20 to 4.23. Tables 4.20 and 4.22 show the results using dyke and thin plate approaches for the component and gradient data respectively. Tables 4.21 and 4.23 shows the results using edge model from component and gradient data respectively.

The summary of the results using three model approaches for this set of data is given as follows.

1. Using dyke approach:

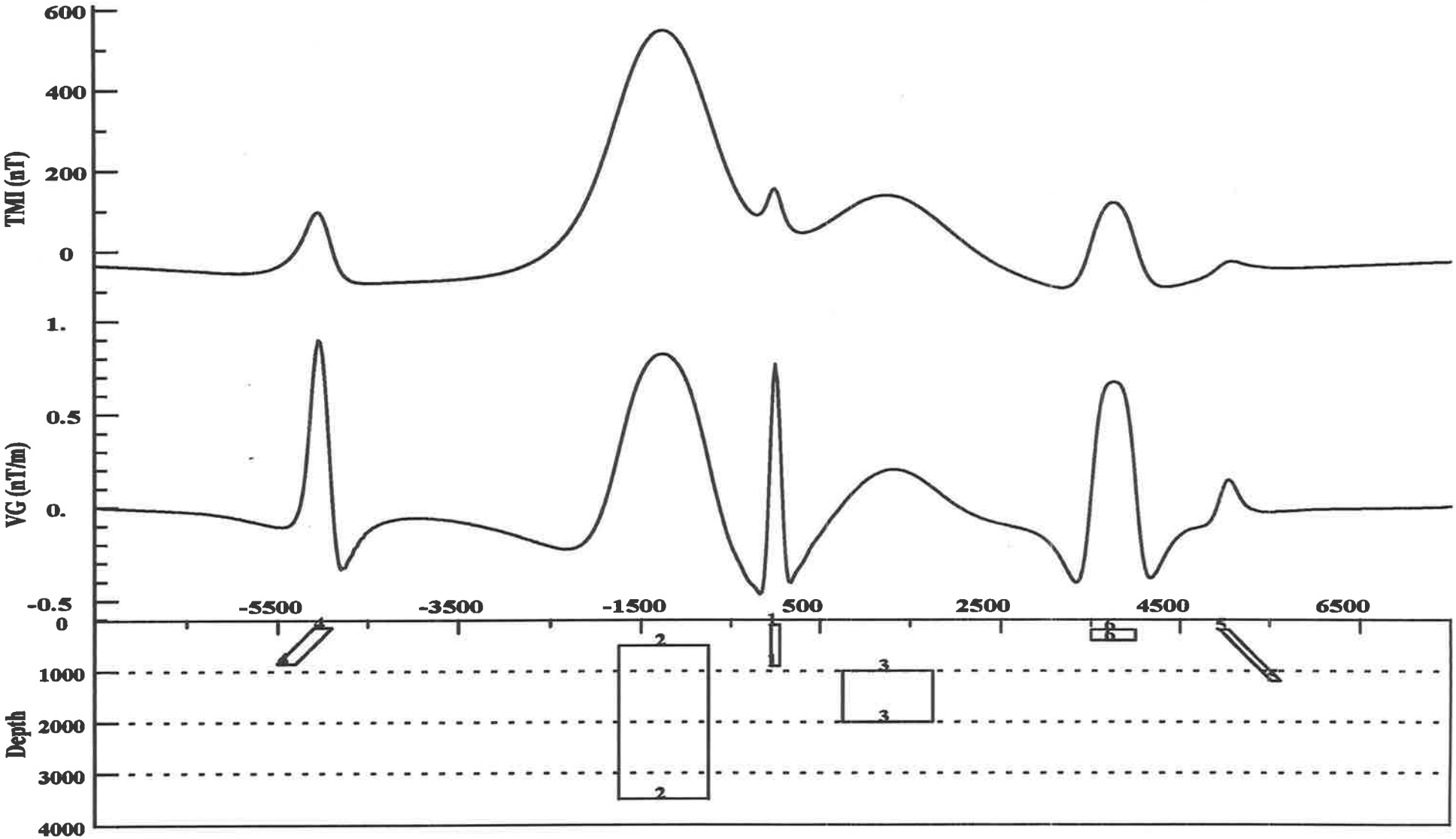

Figure 4.24: Total Magnetic Intensity Anomalies of six Models

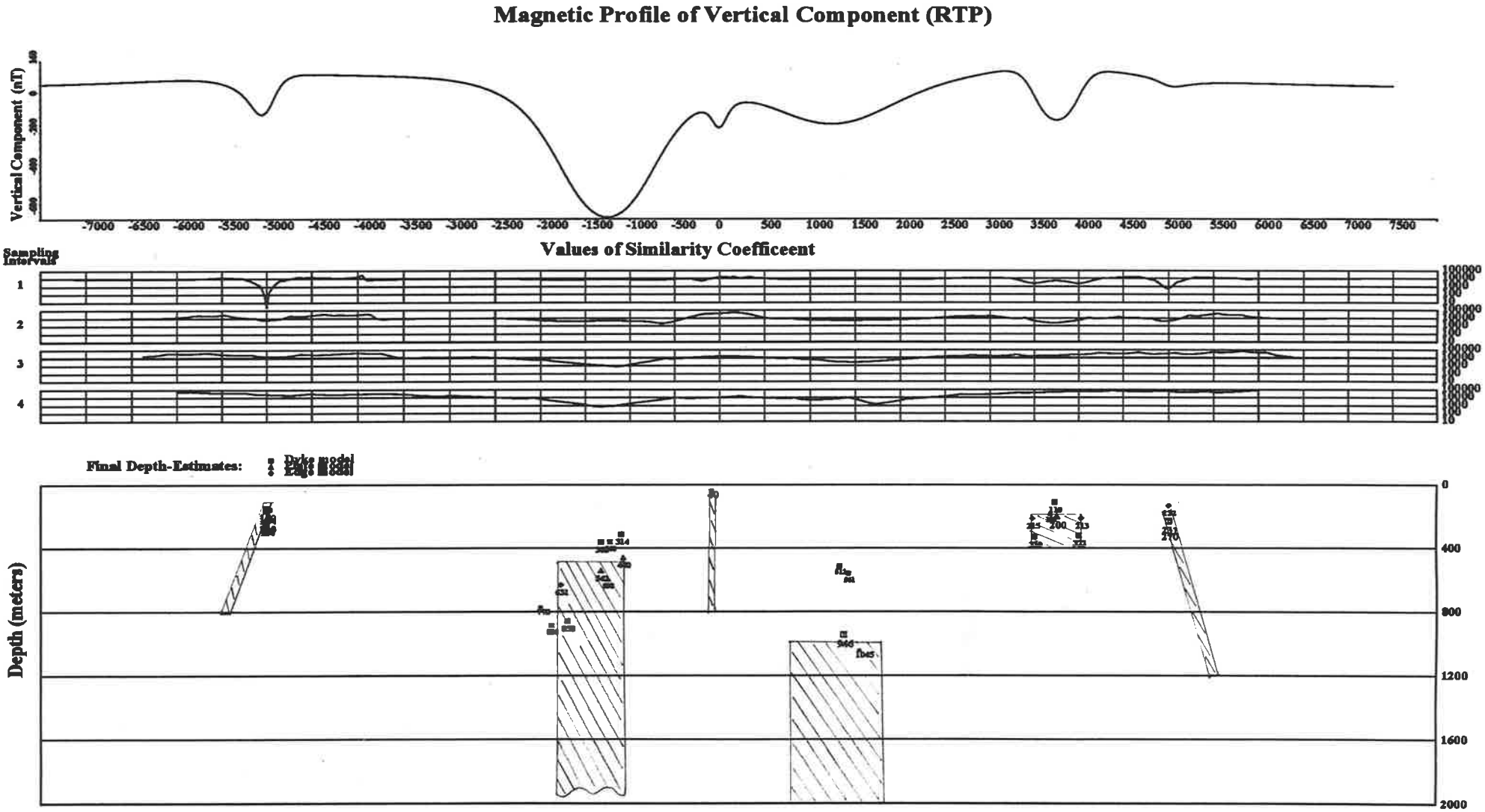

Figure 4.25: Depth Estimates of 6 Theoretical Bodies Using AUTOMAG
E-W Profile in Southern Hemisphere, inclination: -60°
Initial Model: h=150m b=100m dx=25m N=31)

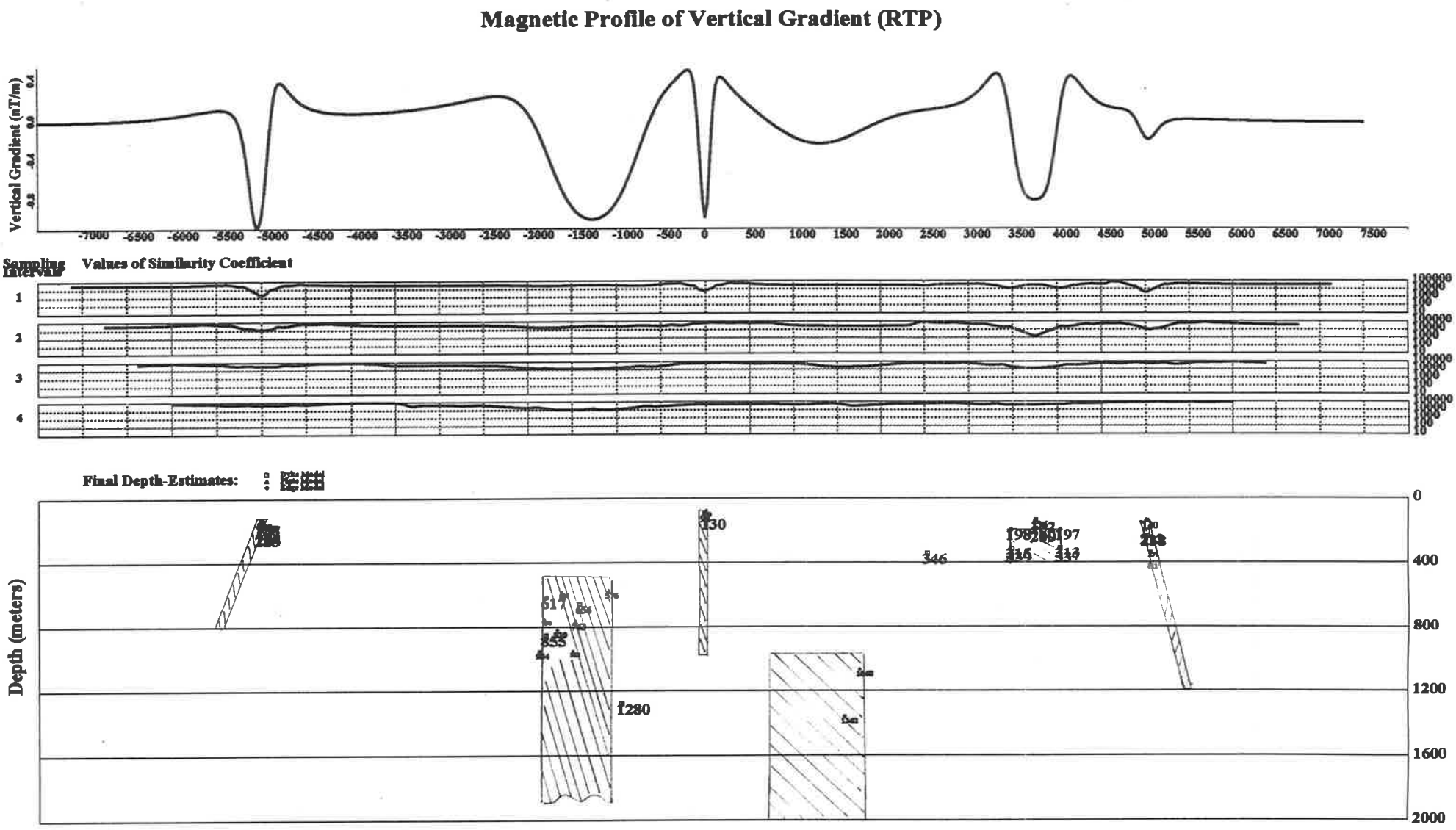

Figure 4.26: Depth Estimates of 6 Theoretical Bodies Using AUTOMAG
E-W Profile in Southern Hemisphere, inclination: -60°
Initial Model: h=100m b=100m dx=25m N=31)

The depth estimates are smaller than the true depth: the smaller the depth extent, the greater the error of the estimate.

The estimates of the width and dip for all five bodies are made with high precision compared with the parameters of theoretical bodies. The relative errors are less than 3.3%. However if the depth extent of the body is small, the estimated susceptibility is erroneous; if the depth extent becomes greater, the error is reduced.

2. Using thin plate approach:

   The errors of the depth estimates for five bodies are varied: if the depth extent of the body is less than 146 metres, which is the depth of the five theoretical bodies, the estimates are less than the true depth and vice versa. Note that the basic model in the thin plate approach is a slab, whose depth extent is equal to the depth, and is therefore not a true thin plate. In the case of a real thin plate anomaly, the estimated depth should be corrected using the formulae shown in (4.3). The corrected depth for the first body is 162 m; although there is still an error of 11% but the result is better than the original determination (21%). As the causative body for the third anomaly is close to the basic slab in the approach, the estimated depth has smallest error among the five bodies.

   The estimates of width and dip are precise; e.g. the error in the width is less than 2%, for both component and gradient data. There is a substantial error in estimated susceptibilities.

3. Using edge model approach:

   The edge approach seems to provide a better solution than the other two for the depth estimates, e.g. for the last three anomalies the errors of depth estimates are less than 7%. The estimates of susceptibility for the last two anomalies are acceptable, but the dip is significantly incorrect. As the width of the body is determined by the distance between localities of the two edges related to an anomaly, the error could be affected by the sampling interval. Note that the sample interval for this set of data is 10 metres (the other two are 20 metres); adequate sampling of data is an important factor for providing a better solution from the edge model approach.

4.8.4 Combination models

This set of synthetic model data is a combination of different types of bodies. The geometries of 6 theoretical models and their anomalies of the total magnetic intensity and vertical gradient are presented in Figure 4.24. The combination results of depth estimates using three model approaches for component and gradient data are demonstrated in Figures 4.25 and 4.26 respectively.

With the figures, it is readily seen that most depths calculated from AUTOMAG are around those of model bodies but with some errors. The reasons for the errors are listed below.

- The data are complex as they are produced from different types of bodies.

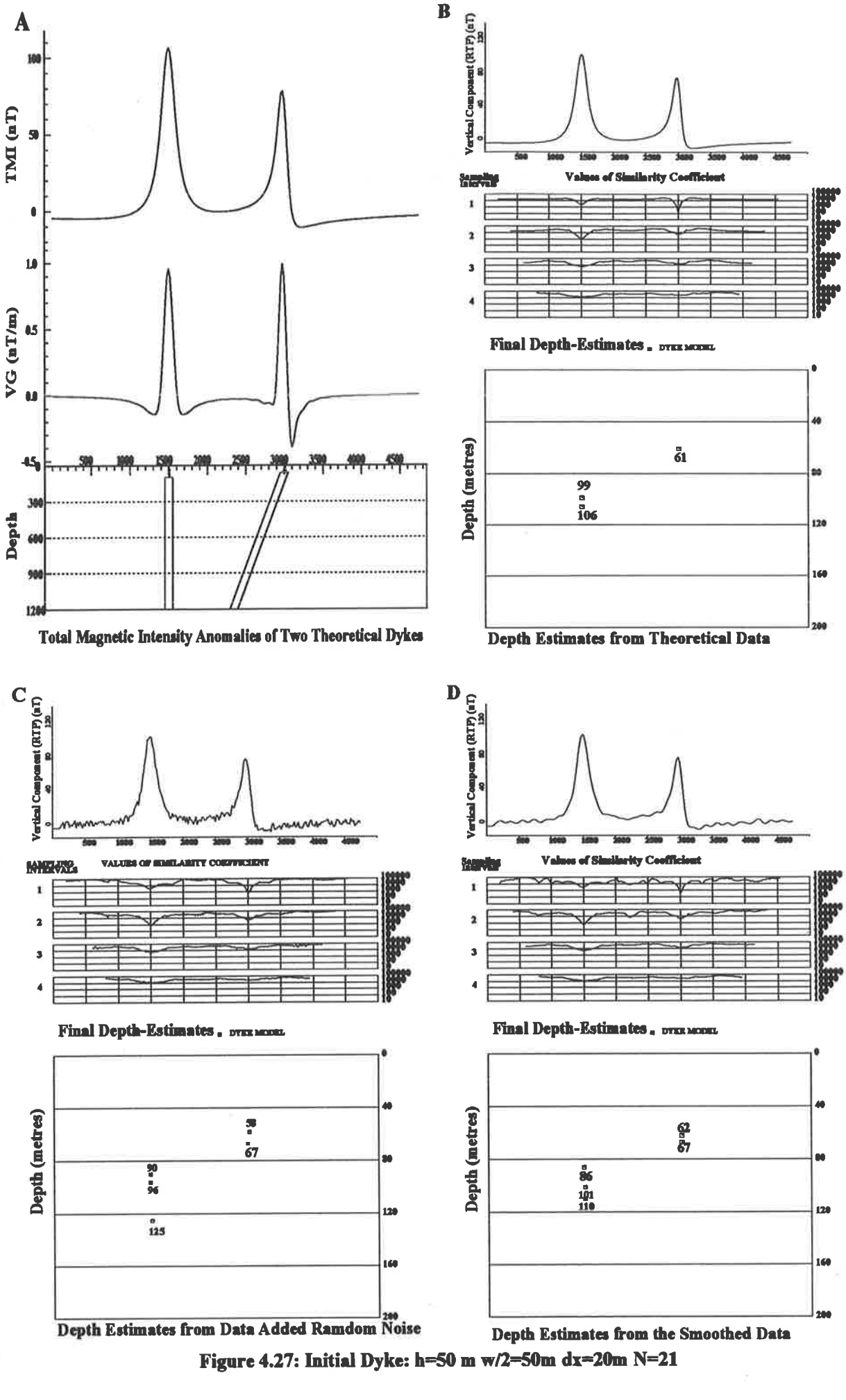

Figure 4.27: Initial Dyke: h=50 m w/2=50m dx=20m N=21

Table 4.24: Parameters of two dykes and input information for using AUTOMAG

Parameters of Dyke Model						
Dyke No.	**Depth** (m)	$\frac{Width}{2}$ (m)	**Dip**	**Susceptibility** ($10^{-6} \times CGS$)	**Depth Extent** (m)	**Sample Interval** (m)
1	100	50	90°	1000	2000	20
2	60	50	120°	600	2000	20

Input Information of Initial Model Using AUTOMAG				
Initial Dyke		No. of Sample Intervals	Sample Interval	Number of Window Points
Depth	$\frac{Width}{2}$			
50 m	50 m	1	20 m	21
100 m	100 m	2	40 m	21
150 m	150 m	3	60 m	21
200 m	200 m	4	80 m	21

Note:
Profile direction is from west to east,
Inclination of Earth's magnetic field is $-60°$,
Intensity of total magnetic field is 60,000 nT,
Dip angle is measured from E-W.

Table 4.25: Comparison between true parameters and estimates from three sets of data for testing error from random noise

Dyke Number	H (m)		$\frac{W}{2}$ (m)		Dip		κ ($10^{-6}CGS$)		No. of Sample Interval
	H_T	H_E	$\frac{W}{2}_T$	$\frac{W}{2}_E$	dip_T	dip_E	κ_T	κ_E	
Results from Theoretical Data									
1	**100**	99	**50**	48	90°	87°	**1000**	1078	1
1	**100**	106	**50**	35	90°	87°	**1000**	1500	1
2	**60**	61	**50**	49	120°	122.4°	**600**	685	1
Results from Data Added Random Noise									
1	**100**	90	**50**	71	90°	76.4°	**1000**	750	1
1	**100**	125	**50**	10	90°	84.7°	**1000**	588	2
1	**100**	96	**50**	86	90°	76.4°	**1000**	693	3
2	**60**	58	**50**	57	120°	119.8°	**600**	568	1
2	**60**	67	**50**	60	120°	107.9°	**600**	551	2
Results from Smoothed Data									
1	**100**	86	**50**	71	90°	78.5°	**1000**	738	1
1	**100**	110	**50**	54	90°	87.4°	**1000**	1079	2
1	**100**	101	**50**	80	90°	87.4°	**1000**	738	3
2	**60**	62	**50**	56	120°	122.5°	**600**	652	1
2	**60**	67	**50**	53	120°	122.5°	**600**	705	2

Note:

H: the depth to the top of the body,

H_T: the true depth from theoretical model,

H_E: depth estimated using AUTOMAG

$\frac{W}{2}$: the half width of the body,

$\frac{W}{2}_T$: the true half width of the body,

$\frac{W}{2}_E$: the estimated half width of body,

dip: the dip of body measured from east,

dip_T: the true dip of theoretical body,

dip_E: the estimated dip,

κ: susceptibility of the body,

κ_T: true susceptibility of model,

κ_E: estimated susceptibility.

Several sets of estimates are determined using different sample intervals.

- The estimates are calculated using three model approaches which also produce slightly different solutions under their own assumptions.
- Some anomalies are superimposed on the others. This affects the precision in estimating the parameters of these bodies, especially affecting the wider anomalies more seriously.

Although the results are in error, they still show that the method is effective and reliable. Once again, the gradient data provides more accurate estimates than the component data.

4.9 Error effect from random noise

In reality, the observed airborne or ground magnetic data often contains noise including observation, measurement or geological noise e.g. from near-surface maghaemite. Therefore the effect of random noise on the results needs to be tested.

A test of error effect from random noise is demonstrated in Figure 4.27. In the figure, Part A illustrates the geometries of two dyke models and their anomalies of total magnetic intensity and vertical gradient. The parameters of the two bodies are given in Table 4.24. Part B presents the depth estimates using AUTOMAG on original model data in which the results are very precise. Part C illustrates the results from the original data after adding 10% random noises. Obviously some errors are introduced. The estimates from the data (in Part C) after smoothing using a low pass filter (Hou, 1981) are shown in Part D. It can be readily seem that the some of the added noise has been filtered out and the resolution of the estimates is improved. The comparisons between the parameters of the theoretical bodies and the estimates from the three sets of data shown in (Part B, Part C and Part D) are present in Table 4.25.

According to the figures and the table, the smoothed data provides a better solution than the data to which noise has been added. For example, the estimates of depth calculated from the data after adding 10% random noise are in error with the error ranging from 10% to 25%. The errors for the same estimates from smoothed data range from 1% to 14%. For the all three sets of data, different sample intervals (20 m, 40 m or 60 m) provide different solutions (see Table 4.25). It is worth noting that after smoothing the data the width of anomaly becomes wider and the amplitude is slightly reduced. Therefore the interpreted body is often deeper and/or wider than the undisturbed body.

These error tests show that AUTOMAG works well both with complex model anomalies and with model anomalies to which noise has been added. A summary and some suggestions for effectively using the technique on observed data is given as follows.

4.10 Summary

In the first part of this chapter, a great number of simple models were tested and the error effects as a result of varying depth, width, depth extent and dip of the body were analysed. As

a result, three new basic models were designed for AUTOMAG in order to satisfy most common geometries in real geological situations. The second part focussed on the analyses of the error effect from more complicated models. The final part presented an error test synthetic data to which random noise had been added. Summarising all the tests, some suggestions are given for using this technique most effectively.

1. Choices of model type and initial parameters of model

   In order to successfully interpret real magnetic anomalies, at least two types of models (dyke and edge) should be chosen to analyse each profile. The dyke model is suitable for narrow shaped anomalies and the edge model is used to process wider anomalies.

   Although the program has a function to establish a set of different shapes of geometrical bodies which are based on the given initial model (see Section 2.7.4, this set of models is used to match the observed data to provide better solution for estimating parameters. The parameters of the initial model and their extensions (multiply the initial parameters of model and the number of sample interval) are used to search for the centres of the anomalies. Therefore a single type of initial model is often not satisfactory for finding all kinds of bodies. Using two different types of initial model (one narrow, the other wide) is an easy way to locate as many anomalies as possible.

2. Choice of sample interval

   The choice of sample interval is very important. If the sampling is too dense, more computer time costs are incurred and high frequency noises are emphasised which can obscure or distort the main target. If the sampling is too coarse, useful information will be lost. The choice of the sample interval is also linked to the detectable depth of the main targets (see Section 4.3.1. Therefore care is required in choosing the sample interval. In processing airborne magnetic data, the minimum detected depth is greater than the average altitude of aircraft. A simple way to determine the sample interval is $\frac{1}{4}$ or $\frac{1}{5}$ of this height. For example, if the average altitude is 100 metres, the sample interval is chosen as 20 meters. When dealing with data from major sedimentary basins where the anomalies are much flatter and amplitudes are very low, the sample interval should be chosen after selecting and analysing a few typical anomalies from the region.

3. Choice of window length

   Another important factor for using AUTOMAG is the choice of the window length (see Section 4.3.4) which is determined by a product of the sample interval, frequency of sampling (number of sampling) and the number of window points. The window length cannot be chosen too large, because then the neighbouring anomalies will influence the curve matching between the theoretical anomaly and the target anomaly. The window length also cannot be too small; if so only a part of anomaly is matched, and errors will be introduced. In real data processing, so many anomalies are dealt with, it is difficult to find a perfect choice of the window length. The length or the number of window points can only be selected from the average width of most anomalies in the profile. Therefore some erroneous depths will be produced by the incorrect window length. For example, in Part

A of Figure 4.22 the greater depths are the result of the small window size for matching a part of the anomaly.

4. Non-uniqueness

   The non-uniqueness solution is a common problem in interpreting geophysical data, and it also affects the application AUTOMAG. Powell (1967), Hutchison (1958), Reford (1978) and Minty (1981) presented a family of dyke model curves in which the curves are matched very well. These curves are controlled by a critical distance (r) which is determined by $r = \sqrt{h^2 + (\frac{w}{2})^2}$. Under the condition of the same critical distance, the curves arising from a family of dykes have very similar shapes. Therefore a set of parameters can be estimated to represent the same anomaly. In Part A of Figure 4.24, two pairs of estimated parameters ($h = 99m$ and $\frac{w}{2} = 48m$, resulting $r_1 = 110m$ and $h = 106m$ and $\frac{w}{2} = 35m$, resulting $r_2 = 111.6m$) present this relationship.

5. Error effect from shape of causative body

   Note that using thin plate and edge model provides greater depths than using the dyke model (see figures 4.21 and 4.23). This is important in judging the estimated results. When the body has a great depth extent, the solution from the dyke model should be reliable. However when the body has limited depth extent, the estimated depth from applying the dyke model will be too shallow. If some geological information can be provided to indicate the depth extent of the geological bodies in the study area, this would help the interpretor make the choice of the best model type.

6. Smoothing function

   Random noise in the data will cause errors in the parameter estimates. Therefore a smoothing function is required to apply to seriously affected data. It is worth noting that the smoothing function will itself introduce some error into the parameter estimates. The estimated depth may be greater than the true depth and the width may be wider than the true width.

AUTOMAG is a useful and convenient tool for interpreting magnetic profile data. However it is essential to understand the principles of the technique. Choosing the input parameters of the program carefully can help the interpretor to use the method most effectively.

Chapter 5

Spectral analysis & frequency filtering for grid data

The Improved Naudy Technique developed and described in the previous chapters processes local anomalies. The regional anomalies, however are analysed by using the spectral technique to provide a systematic quantitative interpretation of the major geological bodies.

In Chapter 2, it was pointed out that spectral analysis is an appropriate approach and can provide regional information on geology. However it needs to be refined in order to be applied to real potential field data. The spectral analysis extended to the gravity data by the author (Shi and Li, 1987) provides a starting point for the current research in application to the gravity field. This Chapter focuses on the development of techniques for quantitative interpretation including anomaly separation and average depth estimates of gravitational field data. In order to illustrate and test these techniques, a complicated theoretical model is constructed and the effectiveness of the methods is tested on a synthetic data set from the model. Instructions are also provided to help people apply these techniques.

As a result, contour maps of anomalies of different depths are obtained and a map of the average depths in the same area is also constructed, both provide information used for a preliminary interpretation of geology in the area. All the techniques mentioned above can with some modification be applied to the magnetic field data.

This Chapter is composed of three parts:

1. A description of separation filtering and model tests
2. Average depth estimate of synthetic Bouguer gravity data by using the spectral analysis
3. Quantitative interpretation combined with anomaly separation and average depth estimate applied to the synthetic data

5.1 Separation filtering techniques

In procedures of analysis on potential field data, a useful step is to separate anomalies from superimposed sources where the bodies are in different horizontal levels. Many geophysicists have contributed to this knowledge (Spector, 1968; Spector and Grant, 1970; Kane, Hildenbrand and Hendricks, 1981; Kane and Godson, 1985; Jacobsen, 1987). Three kinds of techniques, which are widely applied in this field with the aid of computer techniques, are:

1. upward continuation,
2. optimum filtering including matched filtering,
3. wavelength filtering.

In this section, the principle of each separation filtering is described briefly below

1. Upward continuation

   The characteristics of the anomalies from the different sources are: as observation levels are increased the amplitude of the high frequency anomalies caused by near-surface sources are attenuated rapidly. On the other hand, the amplitudes of anomalies due to deep and broad bodies do not decay obviously with an increase in the height of observation. Based on this fact the upward continuation can be used to calculate the regional field and the residual anomalies can be obtained by subtracting the regional field from the original field. Furthermore Jacobsen (1987) revealed a relationship between the height of upward continuation (z_0) and the depth of the sources (h_0) from a study of "sandwich source distribution" (Jacobsen, 1987). He concluded that the regional field can be extracted from the total field by using upward continuation, in which the depth of the regional source h_0 is equal to $\frac{z_0}{2}$, i.e. the upward continuation field at height z_0 represents the field caused by the sources at the depth of half z_0. The filter for the extraction of a regional field is $e^{(-2rz_0)}$, where r is the wave-number. The filter of the residual field is $1 - e^{(-2rz_0)}$. The filter for the sources at depths between h_1 and h_2 ($h_2 > h_1$) is $e^{(-2rh_1)} - e^{(-2rh_2)}$. Part A of Figure 5.1 shows a set of responses of the upward continuation filters, demonstrating that the filter suppresses the spectra not only in the high frequency section but also affects the low frequency portion.

2. Optimum filtering

   The matched filtering method developed by Spector (1968) is one approach of the Wiener optimum filtering techniques, which was generalised by Jacobsen (1987), covering several previous filters (Strakhov, 1964a and 1964b; Spector, 1968; Clarke, 1969; and Gupta and Ramani, 1980 and 1982). The matched filtering technique is briefly introduced to demonstrate the principle of optimum filtering method.

   As is well known potential field anomalies are comprised of different sources from differing depths with varied sizes in horizontal dimensions and in physical properties. In general,

deep seated sources representing regional geological structures have great widths and depth extents, but the near surface bodies often are thin and have small sizes and extents. The spectra of the anomalies caused by these masses are obviously distinctive. In terms of the Spector's approach, if the spectrum of the deep sources ($A_1(r)$) is concentrated at the low frequency end, the spectrum can be simplified as Be^{-Hr}, where B is a factor which refers to the source strength and its dimensions; H indicates the depth of deep sources and r is the radial wave-number. The spectrum from shallow bodies ($A_2(r)$) is distributed in the high frequency part which can be approximated to a similar expression as the deep sources, i.e. be^{-hr}, where b corresponds to B as a factor of the shallow sources and h represents an average depth of the shallow bodies. The energy spectrum of the total field consisting of these two different sources can be approximated as

$$\begin{aligned} E(r) &\approx |A_1(r) + A_2(r)|^2 \\ &= |Be^{-Hr}(1 + \frac{b}{B}e^{(H-h)r})|^2 \\ &= |A_1(r) \cdot \frac{1}{W_1}|^2 \end{aligned}$$

where $W_1 = (1 + \frac{b}{B}e^{(H-h)r})^{-1}$, which is an optimum filter for the extraction of deep masses; the filter operator of the remaining shallow sources is given as $W_2 = (1 + \frac{B}{b}e^{(h-H)r})^{-1}$.

Part B of Figure 5.1 shows a pair of filters representing matched filtering. According to the characteristics of the filters, it seems that they are better than the upward continuation filter. The low and high frequency components of spectrum can be separated by this filter. Another advantage gained by using the matched filter is that the filtered anomalies can be related to the sources at certain depths, which presents some quantitative meanings. In practice, it is difficult to determine the parameters of the filter, which affects the practical application of this technique.

3. Wavelength filtering

   The wavelength filtering is based on the same principle of spectral characteristics in different source anomalies. The filtering operator's design is based on the cut-off length of the wavelength in the selected anomalies. Since the ideal filter requires to be very sharp in the section of the cut-off frequency and the Gibbs phenomena often occurs to introduce some side ripples on the filtered anomalies. Therefore the filter is difficult to design. In addition, the resultant anomalies are only interpreted in the qualitative sense.

Several separation filters have been introduced, but so far no satisfactory filter has been found. In order to separate the superimposed anomalies and also to indicate the quantitative meaning of the field, an application of a "compensation smoothing filter" so named by Hou (1981) combining the information of radial energy spectrum is introduced here.

The procedures of applying this combination technique are given as follows:

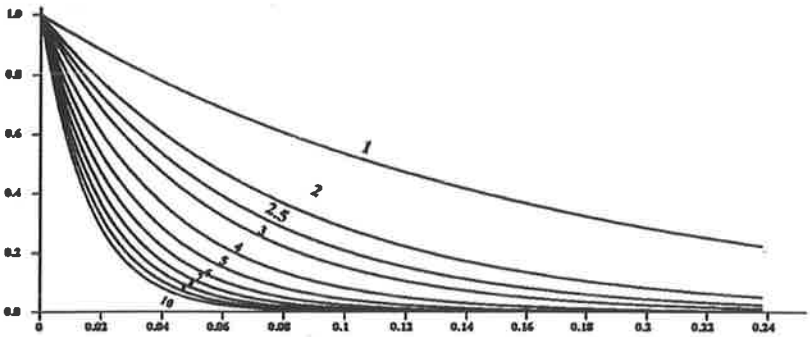

H = 1, 2, 3, 4, 5, 6, 7, 8, 9, 10

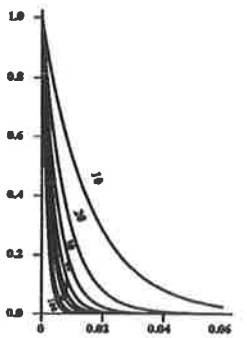

H = 10, 20, 30, 40, 50, 60, 80, 100

H: height of upward continuation (unit: in sample interval)

A: Responces of upward continuation filter.

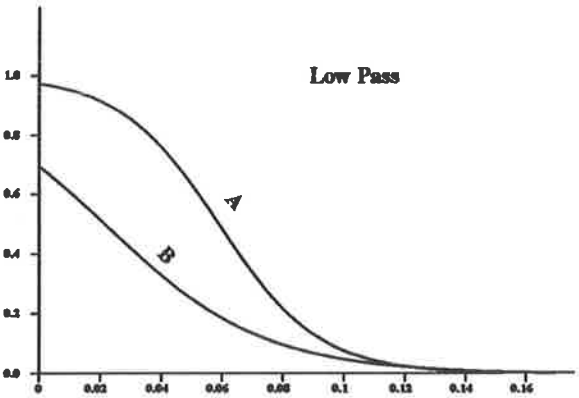

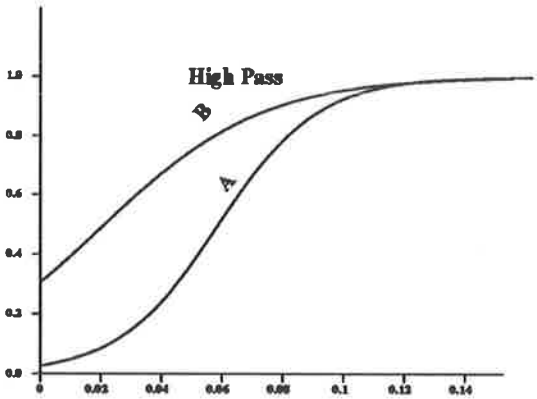

Set A: H1=10 H2=0.284 B=0.02748, Set B: H1=10 H2=3.88 B=0.44

H1: deep depth, H2: shallow depth (unit: in sample interval); B: source factor

B: Responces of matched filtering filter.

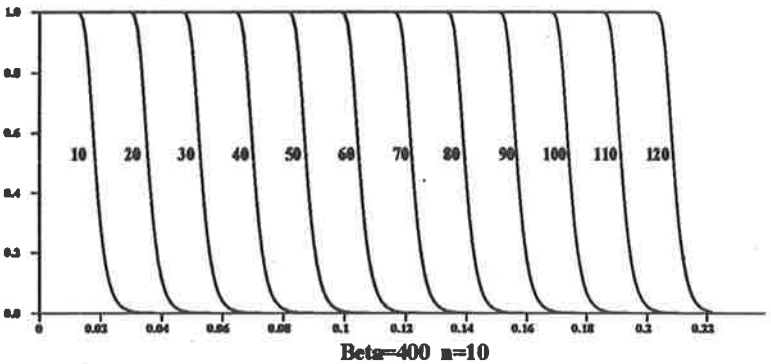

Beta=400 n=10

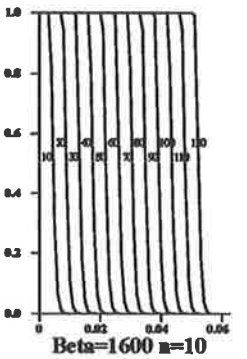

Beta=1600 n=10

C: Responces of compensation smoothing filter.

Figure 5.1: Responces of three frequency filters

- The average depths of the regional and local anomalies in the whole area are computed by using the energy spectral analysis.
- The cut-off frequencies are determined from the logarithmic radial energy spectrum.
- Applying the "compensation smoothing filter", several different wavelength anomalies are produced, which correspond to sources from certain depths.

In order to compare with the different separation filters above, an experiment with a set of comprehensive model data is carried out and results are given in the later sections. The next part introduces the "compensation smoothing filter" (Hou, 1981).

5.2 The "compensation smoothing filter"

The "compensation smoothing filter" (Hou, 1981) is introduced briefly as follows. The filter ($\phi(u)$) for one dimensional data is given as

$$\phi_n(u) = [2 - \phi_{n-1}(u)]\phi_{n-1}(u) \tag{5.1}$$

$$\phi_0(u) = \exp(-\beta u) \tag{5.2}$$

where u is the wave-number, unit in cycles per sample interval;

$\phi_0(u)$ is the initial filter of the smoothing factor, and β is a exponential factor.

$\phi_n(u)$ is the n orders factor, which can be obtained from the previous factor $\phi_{n-1}(u)$;

Part C of Figure 5.1 gives two examples of this filter, it shows two sets of curve families, in which all the filters are paralleled one to another and the amplitude of the filters is unity. The number (n) marked on each curve is the order of the compensation smoothing which can be related to a certain cut-off frequency. The major difference between the two sets of the filter family is the sharpness of the curve which is controlled by the factor of the exponential (β). The greater the value of β, the sharper the curve of the filter. Another difference between the two filter families is the frequency span between the filter from a same order number (n). For example, the filter from a small β shows a great span, but the filter from a great β shows that there is a small interval.

Obviously the above filters are low pass filters but it is easy to obtain a high or a band pass filter according to the expressions 5.1 and 5.2. The high pass filter can be obtained by $1 - \phi_n(u)$ and the band pass filter can be obtained from $\phi_m(u) - \phi_n(u)$, where m and n are chosen according to two cut-off frequencies. Based on the characteristics of the above examples shown in Part C of Figure 5.1, the filter with a small β is suitable to design a high or band pass filters and the filter with a great β is more likely as a low pass filter. So far the one dimensional filters are given and it is easy to extend them to two dimensional cases as well as more complicated cases.

After preparing sets of family curves from the "compensation smoothing filter", the usage of this filter is very flexible and easy. The next section uses a set of synthetic data as an example to show the procedure of the application of this filter.

5.3 Model experiment for comparisons of different separation filters

The regional gravity data can be considered as constructed from three kinds of anomalies:

1. regional anomalies from deep seated masses,
2. local anomalies from shallow to intermediate bodies
3. and random noise composed of the geological noise of near surface under or over sampled individual anomalies and noise from observation, instrument and correction of data.

Based on these assumptions synthetic data sets are constructed from:

1. deep seated bodies having a range of depth from 10 km to 22 km, the depth extents of these bodies range from 5 km to 10 km.
2. shallow to medium bodies, which have depths between 1 km to 6 km and the thicknesses of these bodies ranges from 0.5 km to 2 km,
3. random noise that range from -0.5 to 0.5 mgal.

Table 5.3 lists all the parameters of this set of model bodies and Figure 5.11 shows the distributions of the bodies.

Notation of the symbols in Table 5.3

σ: Density contrast,

W: Width of body,

L: Length of body,

T: Thickness of body,

X_0: Central coordinate of body along easting direction,

Y_0: Central coordinate of body along northing direction,

H: Depth to the top of the body,

A

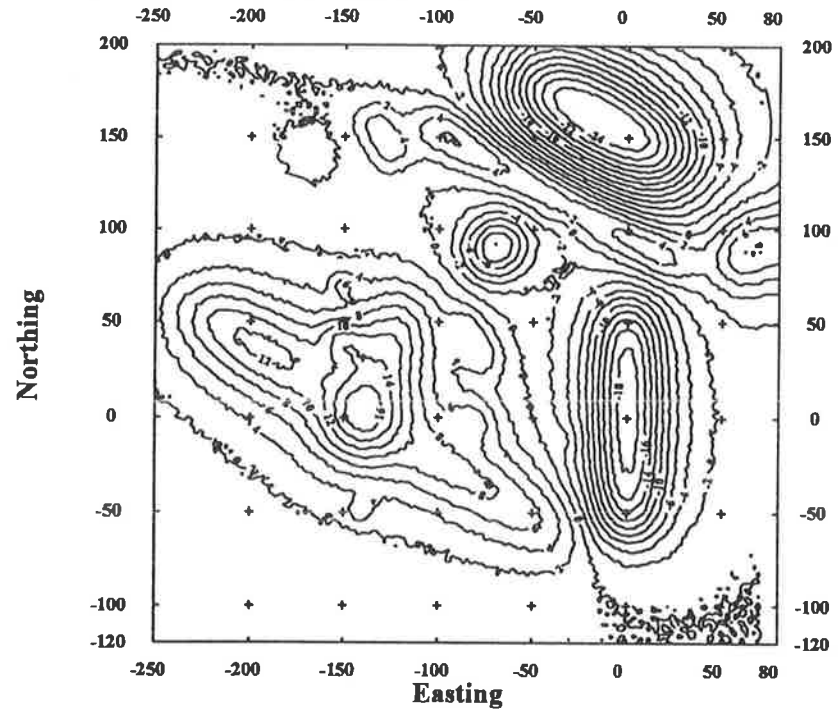

Figure 5.2a

B

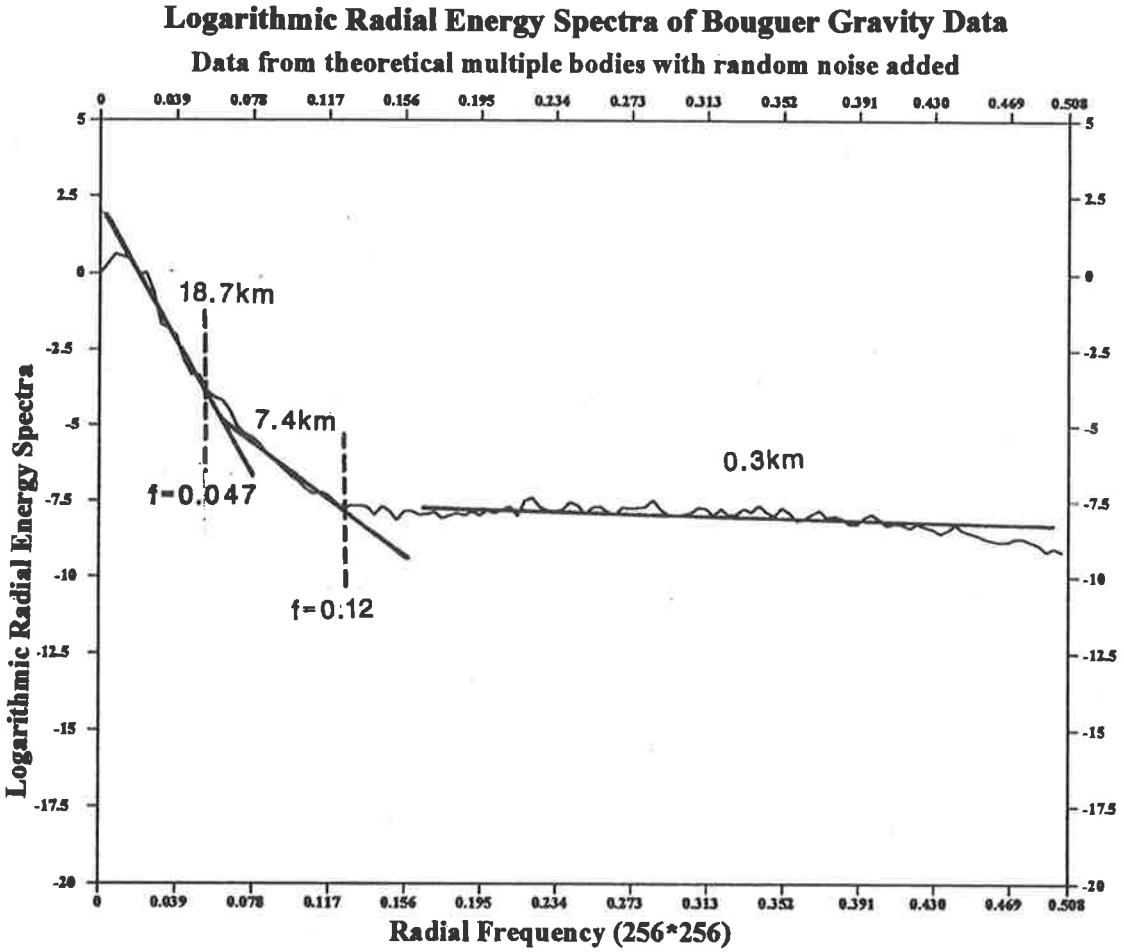

Figure 5.2b

α: Strike direction counted from geographic north to the body,

dip: dip of body.

The theoretical Bouguer gravity field for the models is calculated by using the **Potent** program written by Richard Almond. In order to simulate the virtual observed regional gravity data and due to the restrictions of the size of model calculations in this program the sample intervals of calculated data are chosen at 10 km for deep masses and 5 km for shallow to intermediate bodies. Based on these two sets of model data a set of grid data is generated in which the mesh size has a 2 km spacing. The random noise, which is generated by using a standard subroutine in the Vax Fortran, are added to the gridded data set. The size of the whole data set is 330 km and 320 km respectively on the west to east and south to north directions.

Spectral analysis of gravity data has been developed to determine average depths and deep crustal structures in recent years (Mishra and Tiwari, 1981; Negi and Agrawal, 1986; Dimitriadis *et al.*, 1987; Shi and Li, 1987; Tselentis *et al.*, 1988). Application of spectral analysis to the gravity data in this thesis was extended by the author (Shi and Li, 1987), which follows in Spector's technique applied to the magnetic data. The application principle in gravity data is very simple and is based on Poisson's equation. It establishes a relationship between magnetic and gravitational potentials; e.g. the vertical gradient of the gravitational potential is equivalent to the magnetic potential in the vertical magnetisation direction. The relation of the magnitude of the gravity and magnetic effect is a function of the assumed density and susceptibility. However, in practice some problems occur in the calculation of the energy spectra of the gravity data. The author has solved them (Shi and Li, 1987) and has written a set of programs to calculate the logarithmic radial energy spectra of the gravity data. It is worth noting that the above spectra are not directly calculated from **original gravity field** but the spectra are computed from the **vertical gradient** of the gravity anomalies. The spectra of the vertical gradient of gravity will simply be called the spectra of the gravity anomalies through out the rest of the thesis.

Figure 5.2 shows a contour map calculated from the synthetic data as well as its logarithmic averaged radial energy spectrum of the field. According to the energy spectrum curve from the model data, it can be readily seen that the spectrum can be divided into three sections corresponding to three different source bodies. In the high frequency section, which occupies two thirds of the whole frequency axis, the slope of the spectrum is close to zero; showing characteristics typical for white noise spectrum. At the low frequency end the slope of a regression line through the spectrum indicates the average depth as 19 km. In the same section an obvious peak occurs in the spectrum, this shows the thicknesses of the deep bodies is limited which is consistent with the designed deep bodies. The medium part of the energy spectrum presents another slope which corresponds to the average depth of the medium bodies. The value of this average depth is approximately 7.4 km which is an over-estimate of the depth for the medium masses. The reasons that the calculated depth is greater than the true depth probably are:

1. effect from the horizontal size factor (details see Section 2.6.2);

2. under-sampling of the small dimensional bodies.

Theoretical Bouguer Gravity Anomalies

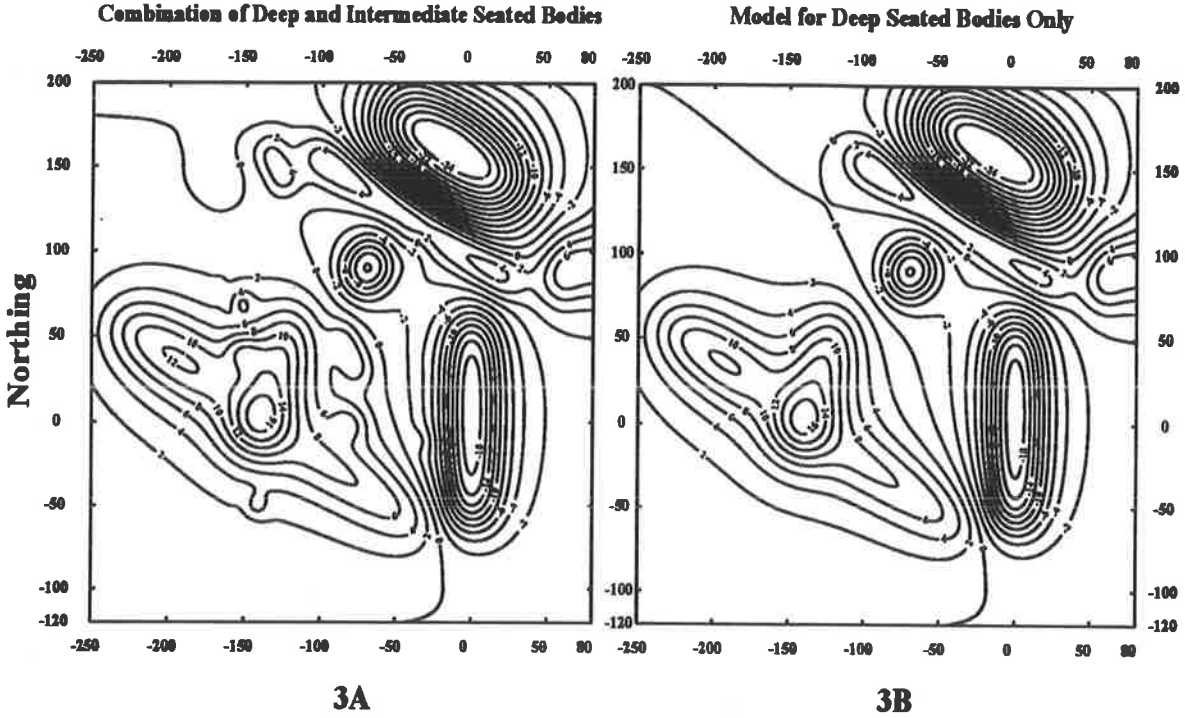

3A 3B

Long Wavelength Anomalies of Bouguer Gravity

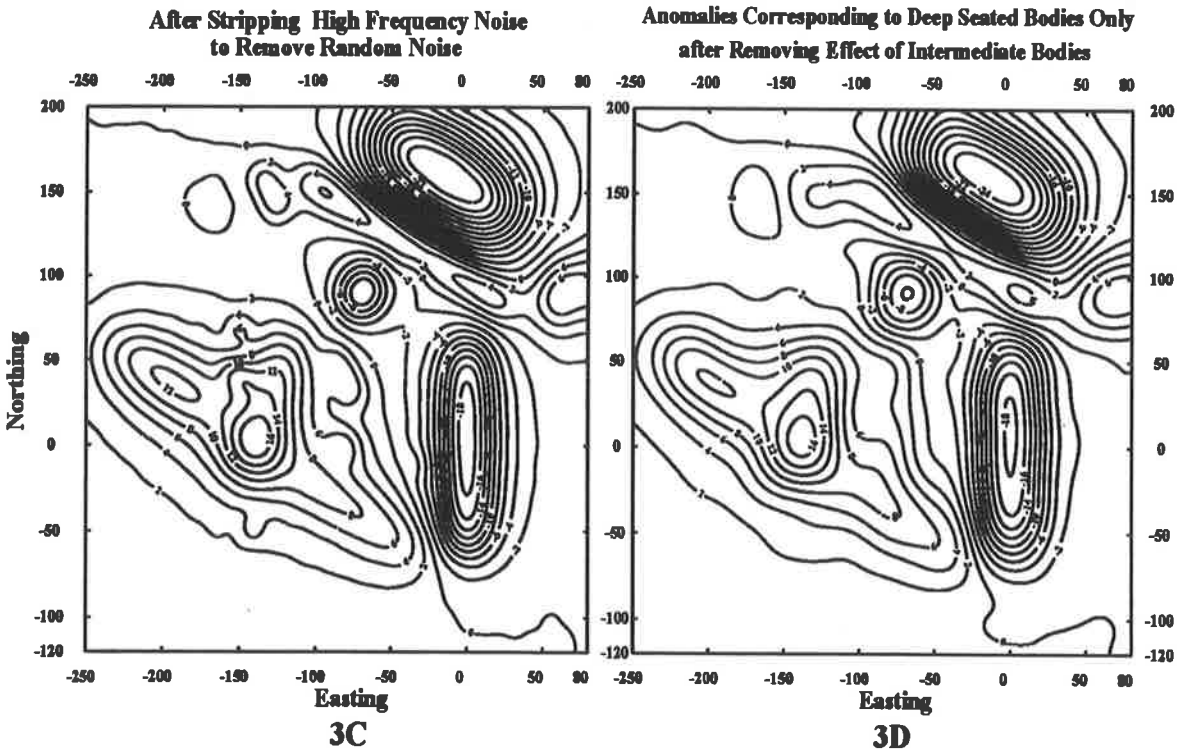

3C 3D

Figure 5.3

According to these three frequency sections of the radial energy spectrum, two cut-off frequencies are defined as shown in the graph of the spectrum. The unit of the radial frequency is in cycles per sample interval, which can be calculated by the reciprocal of the total points from the calculated numbers. In order to strip the random noise or near surface geological interferences and then to emphasise the deep bodies, two sets of wavelength filters are applied to the data to which has been added random noise. The first filter strips the high frequency noise, in which the cut-off frequency is set at 0.12 cycles per sample interval. The factors of the related filter are chosen as $\beta = 400$ and $n = 60$ (see Part C of Figure 5.1). The second filter is designed to strip both the high and medium distributions of the frequency contents. The factors of this filter are chosen as $\beta = 1600$ and $n = 105$, which is correlated to the cut-off frequency of 0.047 cycles per sample interval (see Part C of Figure 5.1). Two contour maps representing the theoretical Bouguer gravity for the combination of the deep and medium multiple bodies and the deep bodies only are shown at the top of Figure 5.3 respectively. The result after the two low pass filters is given at the bottom of Figure 5.3. By comparing the theoretical anomalies with the filtered anomalies, better correlations can be found not only in their shapes but also in their magnitude of their extreme values.

Alternative methods of anomaly separation are: upward continuation and matched filtering technique. Figure 5.4 shows the results obtained by using these two methods when applied to the same data with the addition of random noise data. The computer programs used were developed by the author and her colleagues in China. Based on Jacobsen's assumption (Jacobsen, 1987), the upward continuation field at a height of 2 km represents the field caused by the sources below a depth of $h = 1km$. The upward continuation map (see Part A in Figure 5.4) shows that this method removes the very high frequency random noise, but the amplitudes of the extreme values are slightly reduced. The shallowest depth (upper limit depth) for the deep sources of this set model is 10 km; according to the Jacobsen's theory, upward continuation should be up to 20 km. It has been found that the upward continuation field down to 20 km produces a result too weak to represent the deep sources (greater than 10 km). The field of upward continuation to 5 km (see Part B in Figure 5.4) shows that even so it still lost a lot of low frequency information. The responses of these two filters at the heights of 2 km and 5 km, which correspond to the curves of $H = 1$ and $H = 2.5$ respectively, can be found in Part A of Figure 5.1.

The results obtained by applying the matched filtering technique are shown in Part C and Part D in Figures 5.4. The field, after stripping the high frequency noise (Part C in Figure 5.4), gives an excellent relation to the theoretical field but the extracted fields of the deep seated bodies (Part D in Figure 5.4) have been distorted seriously, greatly reducing the amplitudes of the anomalies. The filtering operators (A and B) corresponding to these two filters are given in the left part of Figure 5.1 in Part B.

After comparing these three filters (see Part A to Part C in figures 5.1), the obvious differences between the "compensation smoothing filter" with the upward continuation and the matched filtering technique are the shape of filter and the sharpness at the cut-off frequency. The former has a better shape and contains more low frequency components and the sharpness is much steeper than the other two. Therefore it is better suited to separate different frequency contents. Another advantage of this filter is that the design of the cut-off frequency depends on

Bouguer Gravity Anomalies of Upward Continuations

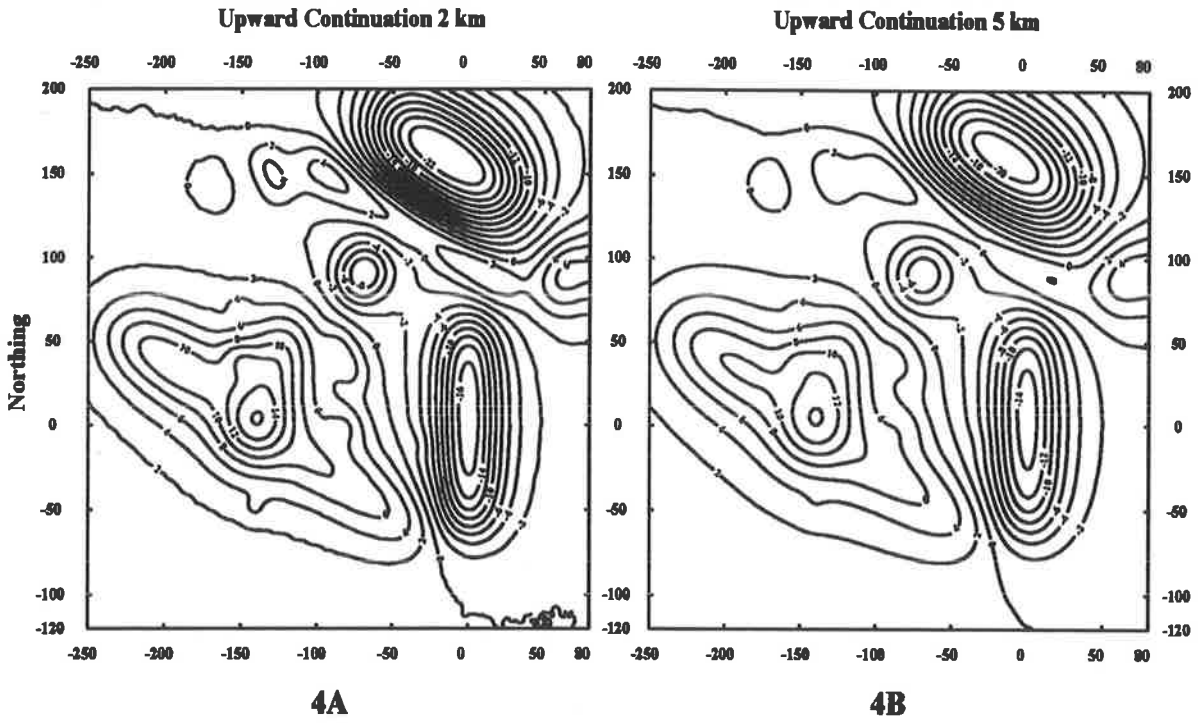

4A 4B

Bouguer Gravity Anomalies after Matched Filtering

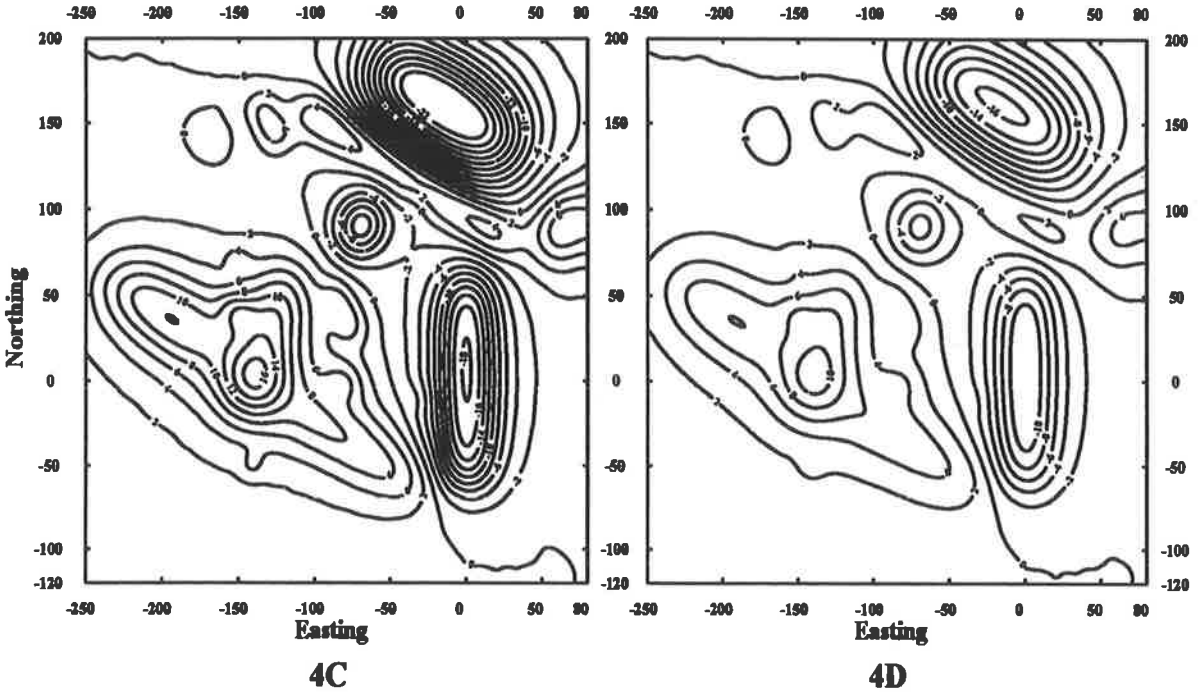

4C 4D

Figure 5.4

property of distributions for radial energy spectrum. To some extent the resultant wavelength anomalies can be related to different level sources which can provide some quantitative interpretation. However it should be mentioned that in reality, the geological sources are more complex than the theoretical models. The components of the spectrum may be mixed up and it is often difficult to break the radial spectrum into different sections. In this case, none of filters will be successful in separating the anomalies into different depth slices.

All the calculation done in using the programs are written as part of this research work.

The next section gives some examples of the calculations of average depths which are done by using the energy spectral analysis on the synthetic data.

5.4 Estimation of average depth from synthetic data

In Section 2.6.2, the principle of average depth determination in an area by using energy spectral analysis was introduced. Applying this approach to the gravity data is one of the aims of this research. From a practical point of view, the approach still has some problems for application. For example, how should frequency sections be chosen to determine the average depth? How does the sample interval influence depth estimations? How does the shape of anomaly effect the determination of depth estimation? How does the extrapolation of anomalies (e.g. edge anomalies derived from the application of the FFT technique) influence the estimation? .... To answer those practical questions it is necessary to investigate them through sets of synthetic data derived from models of known shape, position and depth and in this way understand the problems this assisting in the interpretation of real data.

The aim of this section is:

1. to investigate the characteristics of the logarithmic radial energy spectra for several different types of model data;
2. to study the influences from different sample intervals and from the extrapolation of anomalies;
3. to apply the technique in block data sets in which a set of grid data is separated into different blocks, for each block of data the technique is applied so as to calculate the average depth of the block data.

5.4.1 The characteristics of energy spectra of Bouguer gravity data

Using a program developed by the author, three sets of theoretical Bouguer gravity model data were tested using this technique. The sample intervals of each set of data were 2 km. The radial spectra were computed, while the original data were extrapolated from 161 (row numbers) by 166 (column numbers) into 256 by 256 data points in order to be suitable for use in the FFT

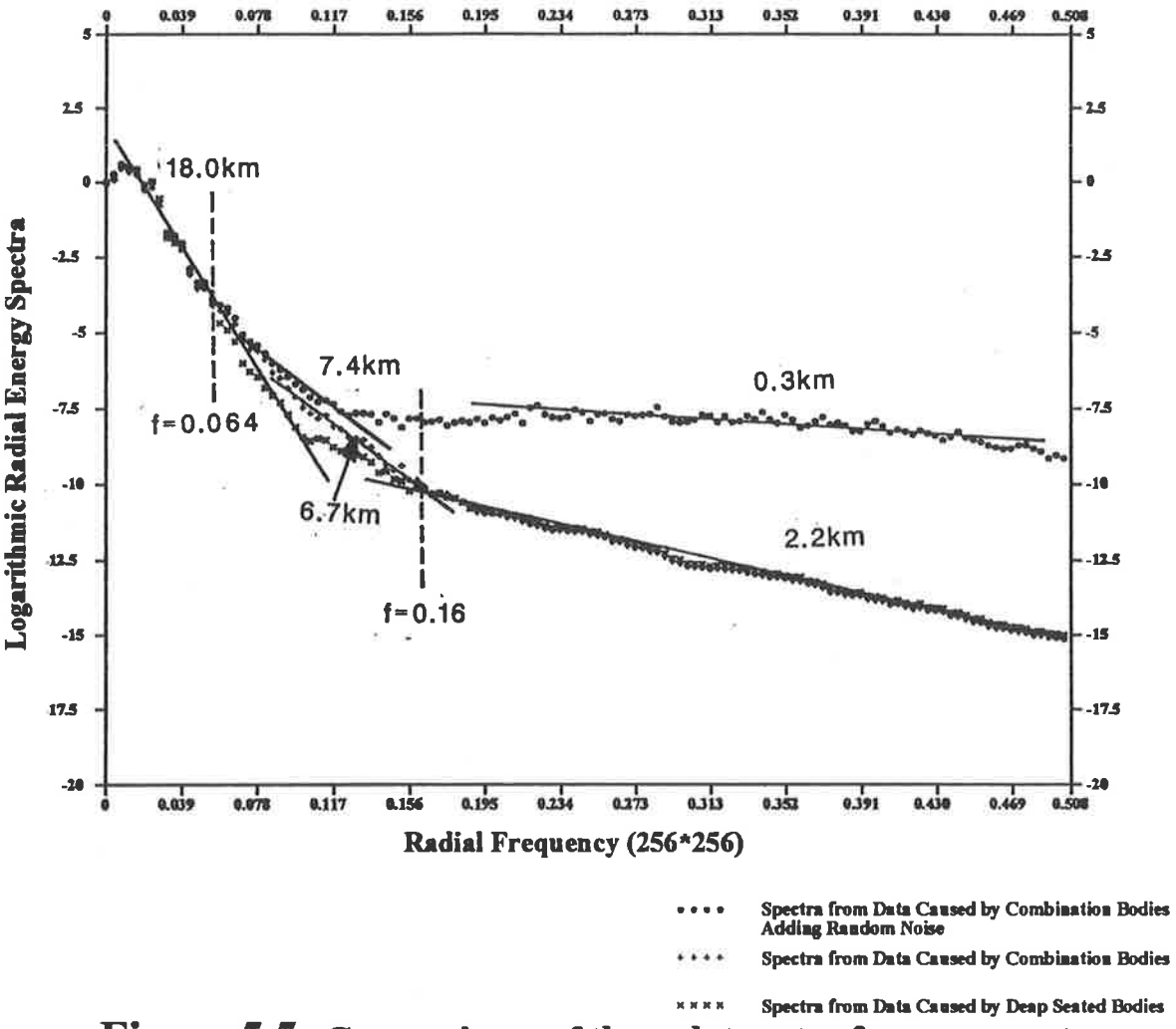

Figure 5.5: Comparisons of three data sets of energy spectra.

technique. The contour maps from the three sets of model data are shown in Figures 5.2 and 5.3. The detailed model compositions are listed below.

1. Models only including nine deep seated bodies have a range of depth from 10 km to 22 km, the average depth is 17 km (details see Table 5.3). The contour map is shown in Part A of Figure 5.3.
2. Combination models including nine deep and eleven shallow bodies have a range depth from 1km to 6km where an average depth is 4km (see Table 5.3). The Bouguer gravity anomalies are shown in Part B (Figure 5.3).
3. Adding random noise level at ± 0.5 mgal to the combination model data (see Figure 5.2).

Figure 5.5 shows the logarithmic radial energy spectra for these three sets. Each set of spectrum uses a different symbol on the figure. After comparing one spectrum to another, several features can be found:

- All three different symbols fall nearly on a same track at the low frequency end (frequency less than 0.064 cycles/sample interval), the average depth of them is about 18 km, which is very close to the average depth of the theoretical deep bodies (17 km).
- The spectra of the data with pure deep masses and with the combination bodies in the high frequency parts (frequency greater than 0.16 cycles/sample interval) are identical. The interesting thing is that the estimated depth based on the slope at this section is equal to 2.2 km, which is related to the sample interval of the data sets (2 km).

  The difference between the two spectra is in the medium parts of the spectra.

  The spectrum from the combination model gives an obvious break-up between low frequency and medium frequency and arrives at an average depth of 6.7 km which is greater than true depth of the models.
- The spectrum with random noise data shows clear white noise characteristics, in which the slope of the curve is near zero.

  The spectra on the medium frequency section shrink towards the low frequency part; this is probably caused by the "intrusion" of the random noise.

  The estimated average depth (7.4 km) of shallow to medium bodies is similar to the average depth of the combination model.

This model experiment demonstrates that the approach and program were both successful when applied to the theoretical model data. The demonstration of the relationship between the slope and the sample interval in the high frequency section is very useful. It shows that depth derived from the high frequency section of the spectrum must be interpreted with caution. More examples are given below.

Figure 5.6 shows three sets of spectra, in which the data sets are produced only by the deep seated bodies but also have different sample intervals (2km, 3km and 4km). According to the graphs, several features can be seen readily and are described as follows.

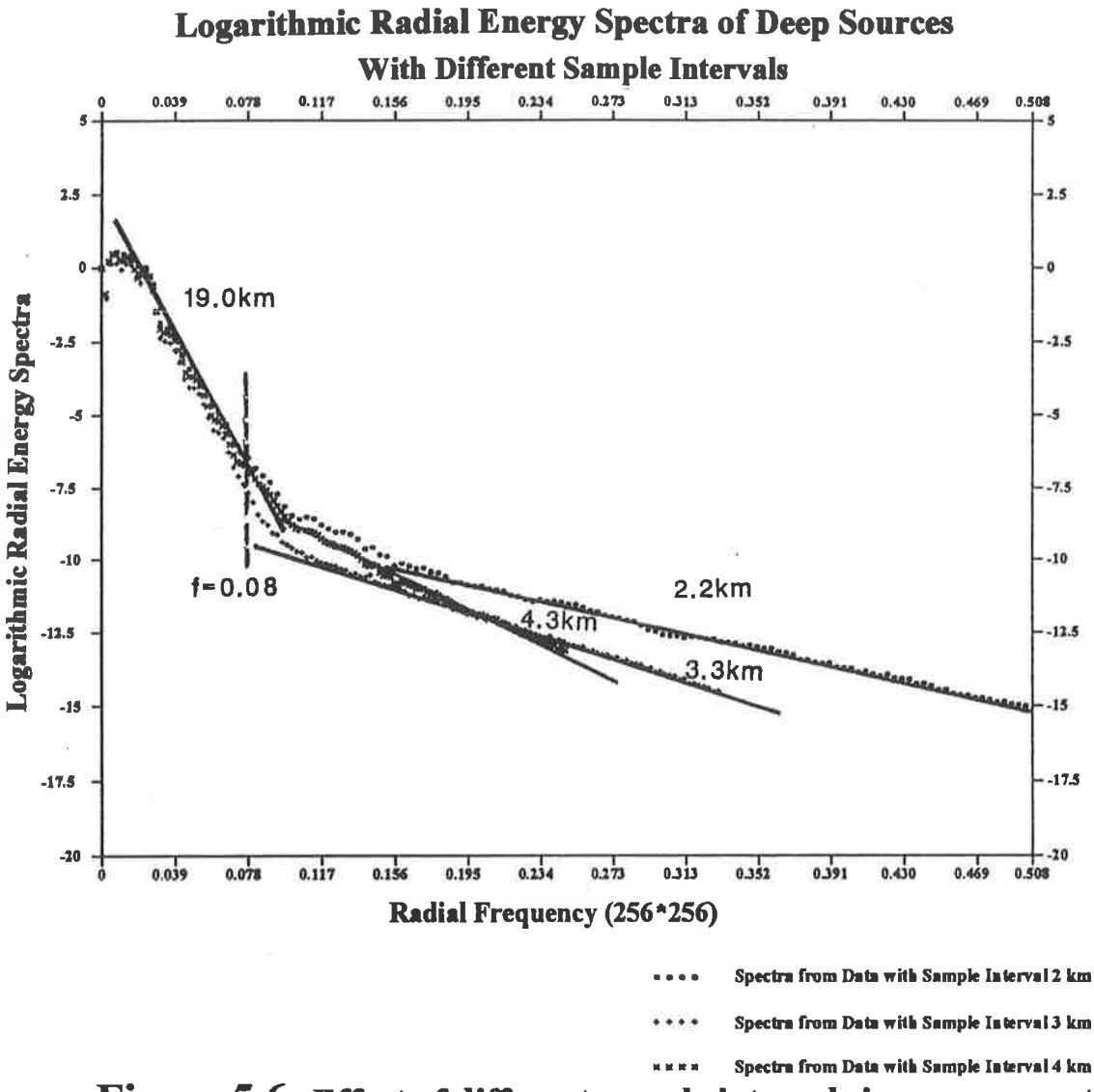

Figure 5.6: Effect of different sample intervals in energy spectra.

Table 5.1: Comparisons of depth estimations for two sets of model data

Model Type	Average depth estimation		
	from high frequency	from medium frequency	from low frequency
Body with great depth extent	2.6 km	6.2 km	16.5 km
Body with small depth extent	2.2 km	6.7 km	18.4 km

1. These three sets of spectra in the low frequency section (less than 0.08 cycles/sample interval) are identical, in which the average depth is around 19 km, but their spectra in the medium and high frequency range are obviously different.

2. The high frequency information is lost with increasing sample intervals; the effect depends on the size of the sample interval, i.e. the greater the sample intervals are, the more of the higher frequency information is lost, as would be expected.

3. The average depths calculated by the slopes in the high frequency parts are 2.2 km, 3.25 km and 4.2 km respectively related to the sample intervals as 2 km, 3 km and 4 km. It is further evident that if the data were not disturbed by serious random noise, the detected depth from the high frequency section would be very close to the value of the sample interval. In other words, the estimated depth from the high frequency section is not reliable and should be ignored.

The above examples show that if the majority of the anomalies are caused by deep seated bodies, the average depth calculated from the spectra in the high frequency part indicates the effect from the sample interval. In order to check out the relationship of the spectra between the shallow to medium depth sources and sample interval, another set of models is calculated. This model set is similar to the combination model set, in which all the deep bodies and the depth, location and size of the shallow to medium bodies are the same as the previous one; the only difference is the depth extents of non-deep seated bodies are much greater than the one derived from the data set of the combination model.

Table 5.2 lists the parameters of this set of shallow to medium bodies. Figure 5.7 shows a comparison between these two sets of spectra and Table 5.1 gives the average depths from the different frequency sections of their spectra. It is worth noting that because of the strong influence from the shallow to medium sources, the spectra in the intermediate parts are consistent and occupy almost half of the frequency range. The average depth from this section is 6.2 km which is slightly shallower than the 6.7 km from the combination model. Another important point is that the high frequency section becomes short and the depth estimation (2.6 km) is greater than the previous one (2.2 km). On the other hand, the value of the depth of the deeper set reduces. All these changes are easy to understand because naturally the distributions of the energy spectra reflect the effects from the causative bodies.

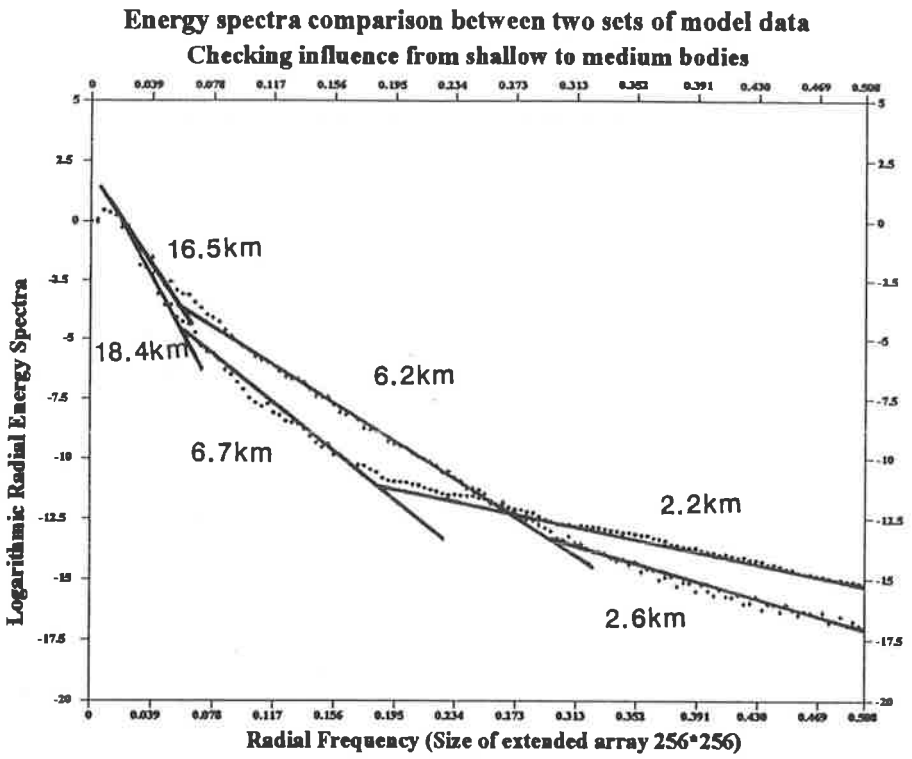

Figure 5.7

.... Shallow to medium bodies with small depth extent

.... Shallow to medium bodies with great depth extent

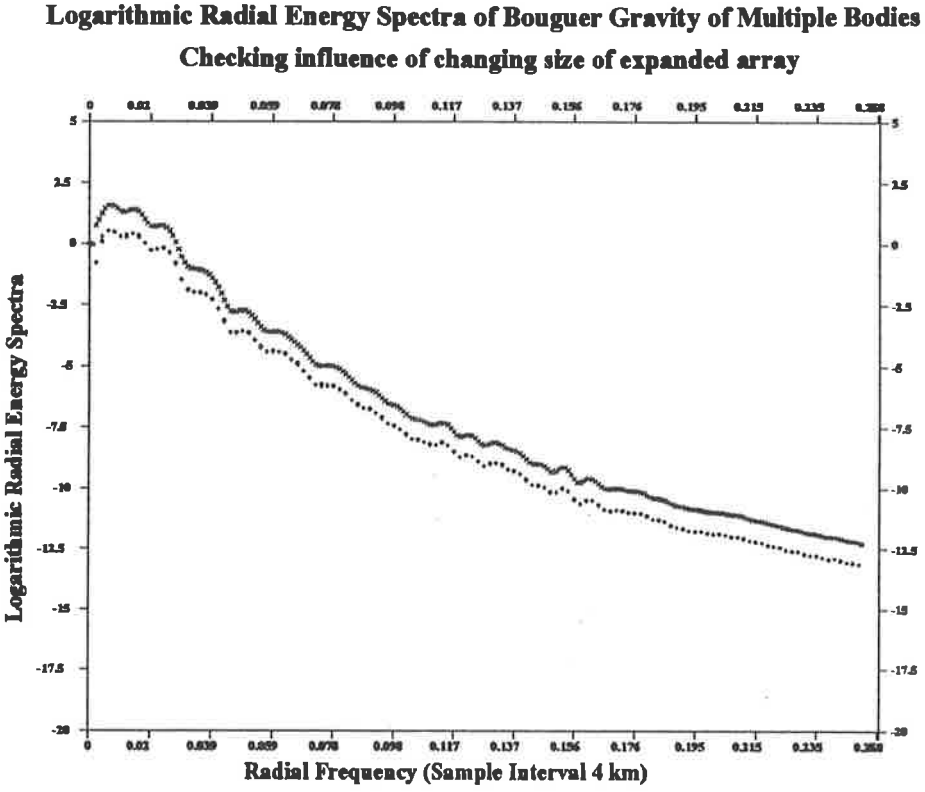

Figure 5.8

.... Spectra from Data Expanded to 128*128

.... Spectra from Data Expand to 256 *256

.... Spectra from Data Expand to 512*512

Table 5.2: Parameters of shallow to medium models in new model set

Model No	σ (g/cm^3)	W (km)	L (km)	T (km)	X_0 (km)	Y_0 (km)	H (km)	α (degree)	dip (degree)
1	0.2	5.0	9.0	**6.0**	-140	-50	1.0	60°	90°
2	0.2	7.0	4.0	**6.0**	-150	70	1.0	90°	90°
3	0.3	10.0	2.0	**5.0**	-30	-10	2.0	30°	90°
4	0.1	10.0	3.0	**5.0**	-125	40	3.0	−70°	90°
5	0.2	35.0	18.0	**6.0**	-130	150	5.0	0°	90°
6	-0.1	3.0	5.0	**5.0**	-30	40	3.0	0°	90°
7	-0.05	20.0	13.0	**6.0**	-170	140	6.0	45°	90°
8	-0.05	26.0	6.0	**8.0**	-35	100	4.0	−60°	90°
9	0.1	20.0	12.0	**5.0**	-150	40	5.0	30°	90°
10	0.1	35.0	14.0	**7.0**	-80	40	5.0	60°	90°
11	0.1	20.0	14.0	**6.0**	-80	0	5.0	30°	90°

In summary the relationship between the sample interval and average depth calculated from the spectra in the high frequency section is as follows:

1. If the anomalies are caused mainly by deep seated bodies, the average depth in the high frequency section is close to the value of the sample interval.
2. If the anomalies include much random noise, the estimated depth is close to zero or much smaller than the sample interval; the spectrum in this section is often oscillatory.
3. If the anomalies have a strong influence from the shallow to medium depth bodies; e.g. bodies with great depth extents, the value of the average depth from the high frequency section is greater than the sample interval and the length of this frequency section becomes shorter.

The following test is done to check the effect of changing the size of an extrapolated array, which is the result obtained from expanding the original data into a new data set (in order to perform the FFT technique). The row and column numbers of the new data are constructed by two individual exponents in which the base is 2. An example will make the procedure clear. There is an original data set with 81 rows and 88 columns, the extrapolated array for calculating the energy spectra can be 128 by 128, or 256 by 256, or 512 by 512. What happens when using these different sizes of expanding arrays? Figure 5.8 shows the result. The original synthetic data set is taken from the combination model (see Table 5.3); the sample interval is 4 km. Three groups of expanding arrays are applied to calculate the energy spectra. Two characters are found as follows.

1. In general, the three sets of spectra are parallel to one another, especially the spectra from the two small data sets which are a coincidence, this indicates that when applying

Table 5.3: Parameters of theoretical combination models

Model	σ (g/cm^3)	W (km)	L (km)	T (km)	X_0 (km)	Y_0 (km)	H (km)	α (degree)	dip (degree)
No	Parameters of shallow to medium bodies of Bouguer gravity								
1	0.2	5.0	9.0	1.0	-140	-50	1.0	60°	90°
2	0.2	7.0	4.0	2.0	-150	70	1.0	90°	90°
3	0.3	10.0	2.0	1.0	-30	-10	2.0	30°	90°
4	0.1	10.0	3.0	0.5	-125	40	3.0	−70°	90°
5	0.2	35.0	18.0	1.0	-130	150	5.0	0°	90°
6	-0.1	3.0	5.0	0.6	-30	40	3.0	0°	90°
7	-0.05	20.0	13.0	3.0	-170	140	6.0	45°	90°
8	-0.05	26.0	6.0	2.0	-35	100	4.0	−60°	90°
9	0.1	20.0	12.0	3.0	-150	40	5.0	30°	90°
10	0.1	35.0	14.0	2.0	-80	40	5.0	60°	90°
11	0.1	20.0	14.0	2.0	-80	0	5.0	30°	90°
No	Parameters of deep seated bodies of Bouguer gravity								
12	0.3	25.0	25.0	8.0	-140	0	20.0	−60°	90°
13	0.2	20.0	35.0	5.0	65	90	15.0	45°	90°
14	0.3	100.0	10.0	5.0	-70	-40	20.0	30°	90°
15	0.3	45.0	15.0	5.0	-125	40	20.0	−70°	90°
16	-0.3	20.0	120.0	5.0	0	0	15.0	0°	90°
17	-0.2	20.0	25.0	5.0	-70	90	10.0	45°	90°
18	-0.2	25.0	100.0	15.0	-15	160	22.0	−60°	90°
19	0.3	75.0	7.0	13.0	-200	40	20.0	30°	90°
20	0.2	160.0	10.0	5.0	-40	120	10.0	30°	90°

A

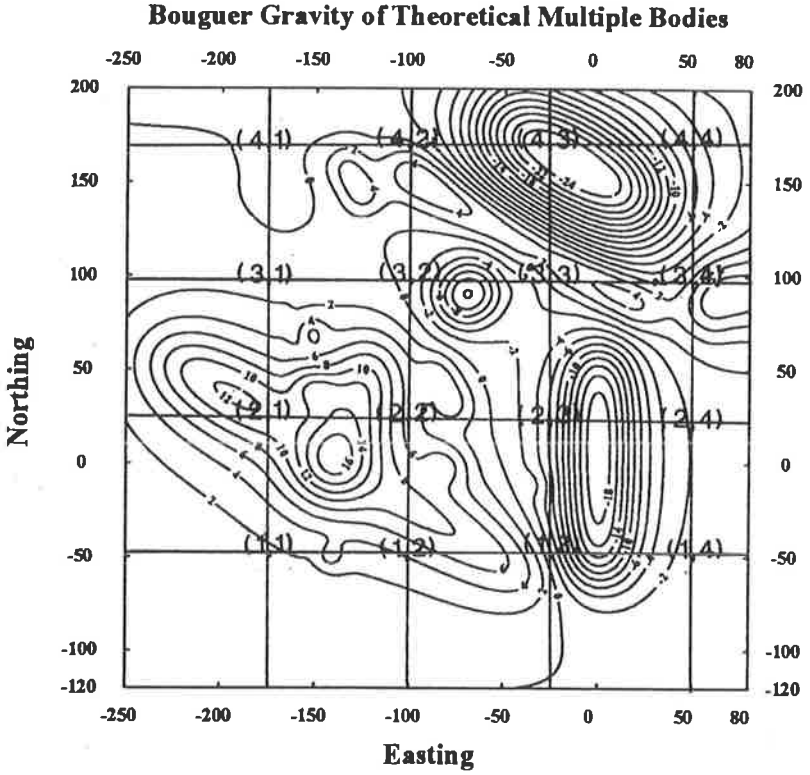

B

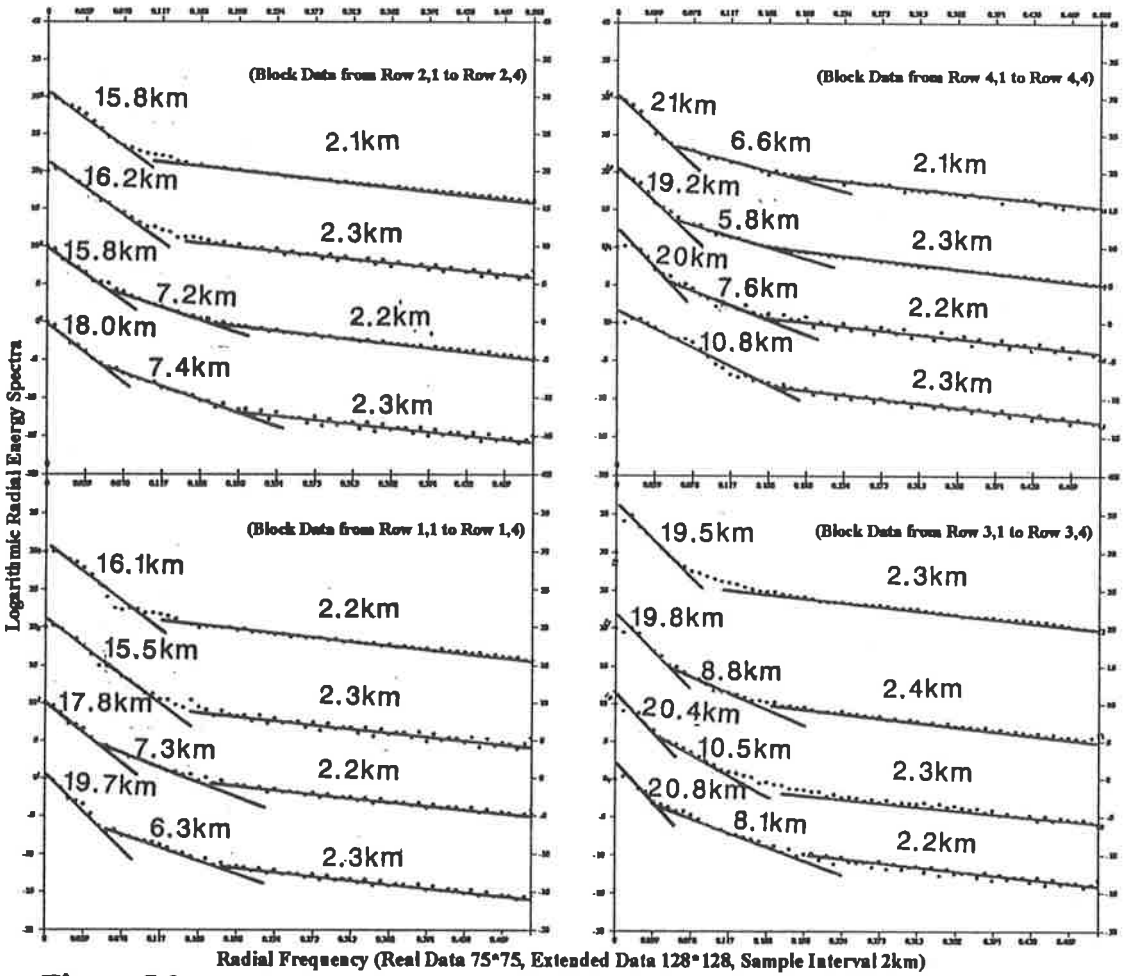

Figure 5.9: Distributions of block data with their spectra and average depths.

an appropriate extrapolation function, the size of the expanding array does not affect the shape of the spectrum.

2. The greater the size of the data set, the denser the frequency interval. In a way the greater size of the extension could provide more spectral information, but this really depends on the shape of the edge anomalies and the edge function for the extrapolation. More details are discussed in later sections.

5.4.2 Average depth from block size of data

For the purpose of the regional tectonic interpretation, the depth distributions from the deep sources or medium bodies are very useful. The above experiment has shown that average depths of the Bouguer gravity statistical models can be determined by using energy spectral analysis. Therefore applying this technique by using a moving window to compose a set of consecutive blocks of data and computing the average depths of the deep or medium seated masses at each block, a regional contour map of the depth can be constructed. The aim, by using the sequential block data sets, is to make computation easy and to develop a procedure which can be used as a semi-automatic depth estimation method. To use this approach effectively several questions must be answered. What is the optimum scheme to divide the block size? What effects are produced if the edge of the block does not include the whole of the anomaly? What is the effect of the extrapolated data? What is the maximum depth that can be detected in a block of data?

In order to answer all these questions, another set of tests is carried out. The original data set is from the theoretical combination models, in which the sample interval of the data is 2 km and the data is taken from a block which is 330 km along the easting and 320 km along the northing direction. The greatest depth in the models is 22 km and the shallowest depth is 1 km.

The division of the block is described as follows. The first block starts at the left bottom corner of the data, and the size of the block or the moving window is designed by the user; a square block is recommended. Moving the window along easting and northing directions respectively and shifting them by half the size of the block length at each time, the central coordinates of each block records the average depth of this block. These following two sets of tests demonstrate the details of the procedure.

- First test

  The first test chooses the size of block as 150 km by 150 km i.e. 75 by 75 data points and the size of the extrapolated data to compute spectra is 128 by 128 points. A total of 16 block depths are computed. The contour map of the data with the block divisions marked is shown in Part A of Figure 5.9. Part B of Figure 5.9 gives the logarithmic radial energy spectra for all block of data and the slopes of the spectra, as well as their corresponding average depths.

  Generally speaking, the average depth of the deep seated bodies coincides with the true depth very well. The calculated shallow depth is about 2.25 km which indicates the effect

A

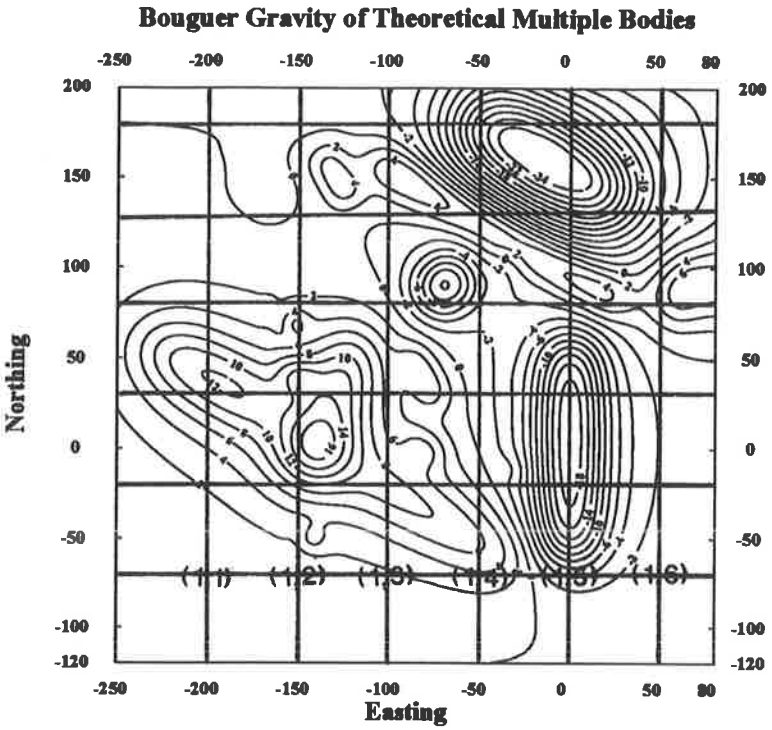

B

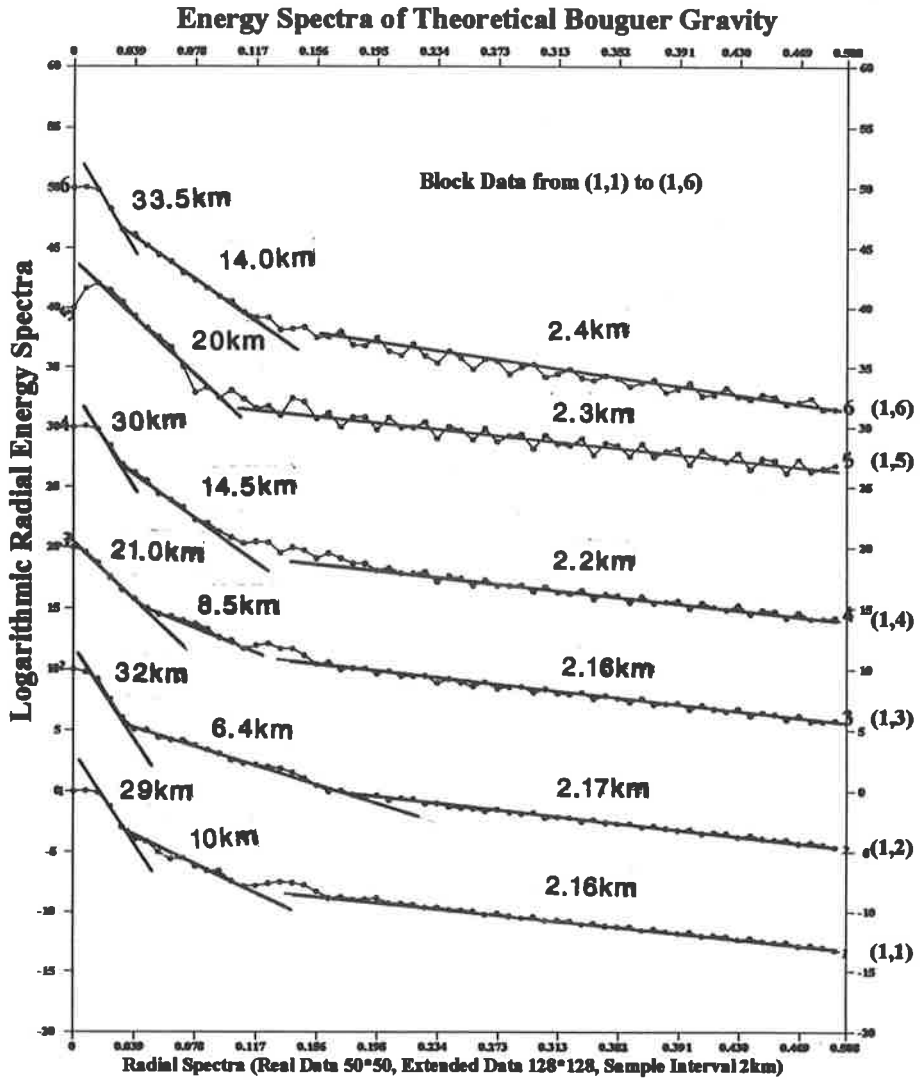

Figure 5.10: Distributions of block data with examples of spectra and average depths

of the sample interval. The estimated depths of the medium bodies are often about 50% greater than the true values. It is worth noting that nearly every block cuts off the edge of an anomaly, but good results can still be produced. This means that when a block covers enough of an anomaly, the spectrum can recover the depth of the geological bodies. Based on model experiments, the size of an anomaly to compute the average depth should cover at least one third of the anomaly. Using the same block of data, another group of spectra are calculated using the extrapolated array as 256 by 256 points. The results are very similar to the previous ones but seem to display more detailed information on these spectra.

- Second test

  The second set of block data has a chosen size of the blocks as 100 km by 100 km, i.e. 50 by 50 number points. The size of the extrapolated array for calculating spectra at each block data is 128 by 128 points. Most average depths of deep bodies relate well to the real depth values, but some blocks derive spurious depths which result because not enough of the anomaly is covered by the block. Part A of Figure 5.10 shows the contour map with the distributions of all blocks. Some examples of the energy spectra and their estimated depths (see in Part B of Figure 5.10), which are calculated from the blocks at the bottom of the map, display the problem of inadequate cover of an anomaly which produce excessive depth. The average depths from the low frequency end at the blocks (1,1), (1,2), (1,4) and (1,6) (in the brackets the first number indicates the row number and the second one shows the column number), show great depths of 30 km. These values are obviously incorrect and come from the effect of the extrapolations from the truncated anomalies. The other two blocks (1,3) and (1,5) give good correlations to the great depths, in which two blocks cover half and one third of the anomalies individually. Except for the average depth from the low frequency end, the spectra at a lower medium frequency for the blocks (1,4) and (1,6) clearly show another set of average depths about at 14 km which corresponds to the true depths of the deep bodies.

The spurious depths are produced from data with seriously truncated anomalies, which also indicates the effect from the size of extrapolated array. In general, when dealing with a truncated anomaly, the large extension will introduce a spurious great depth because the extended part of an anomaly beyond the body is composed from a very low frequency component. Therefore, some researchers (Lehmann, 1970; Cassano and Rocca, 1975) concluded that the approach of energy spectrum is not suitable for automatic depth estimation. However, by carefully applying this technique, useful information can be extracted. A few points should be noted.

- In order to satisfy the FFT approach, the mean value of the calculated areal data must be subtracted. If the subtraction of the regional background is properly done, the error effect from the extrapolation is limited.

- The best choice for the size of extrapolation array is an intermediate number. If the extension number is too big, a spurious depth may be produced; but if the number is small, it could not bring enough information about spectrum. For example, the original

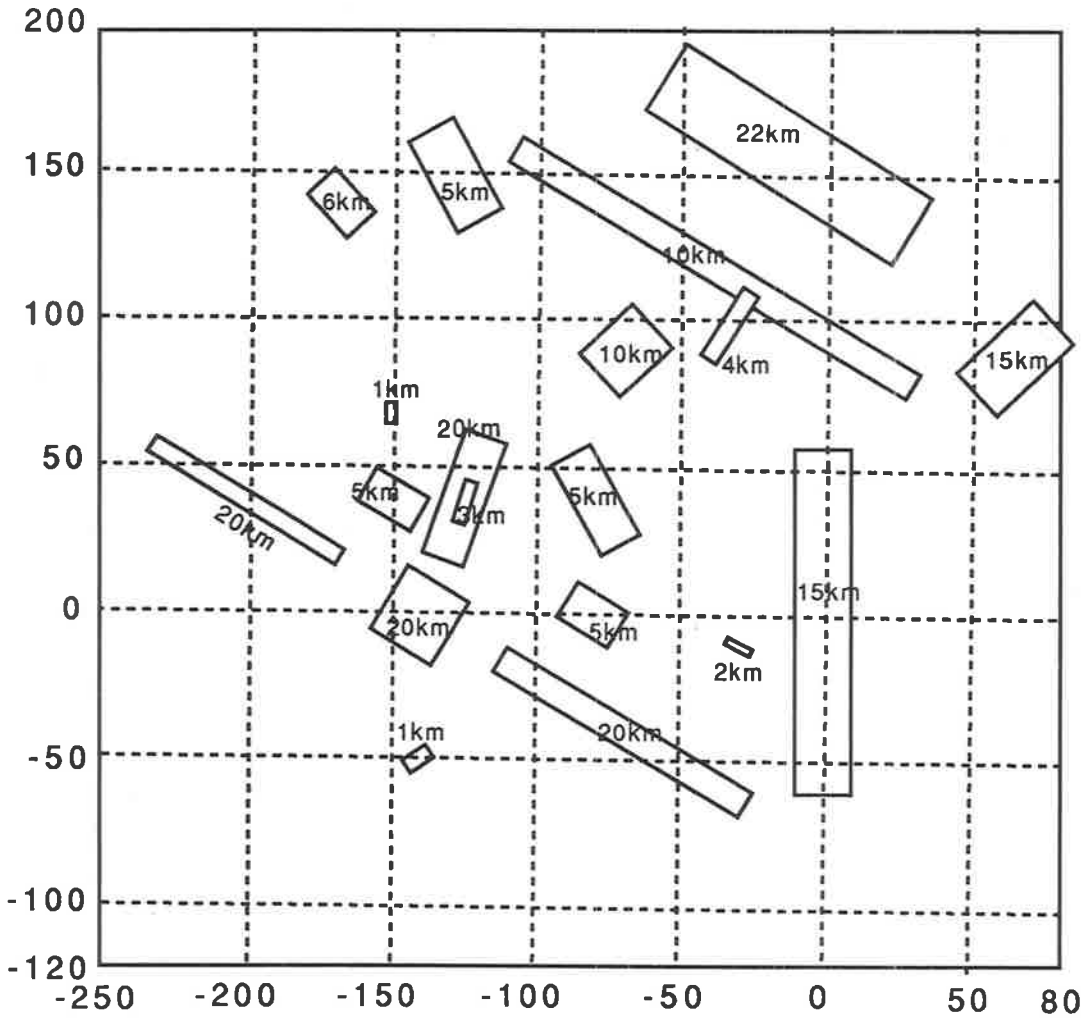

Figure 5.11: Plan view of distributinons of combination models and their depth.

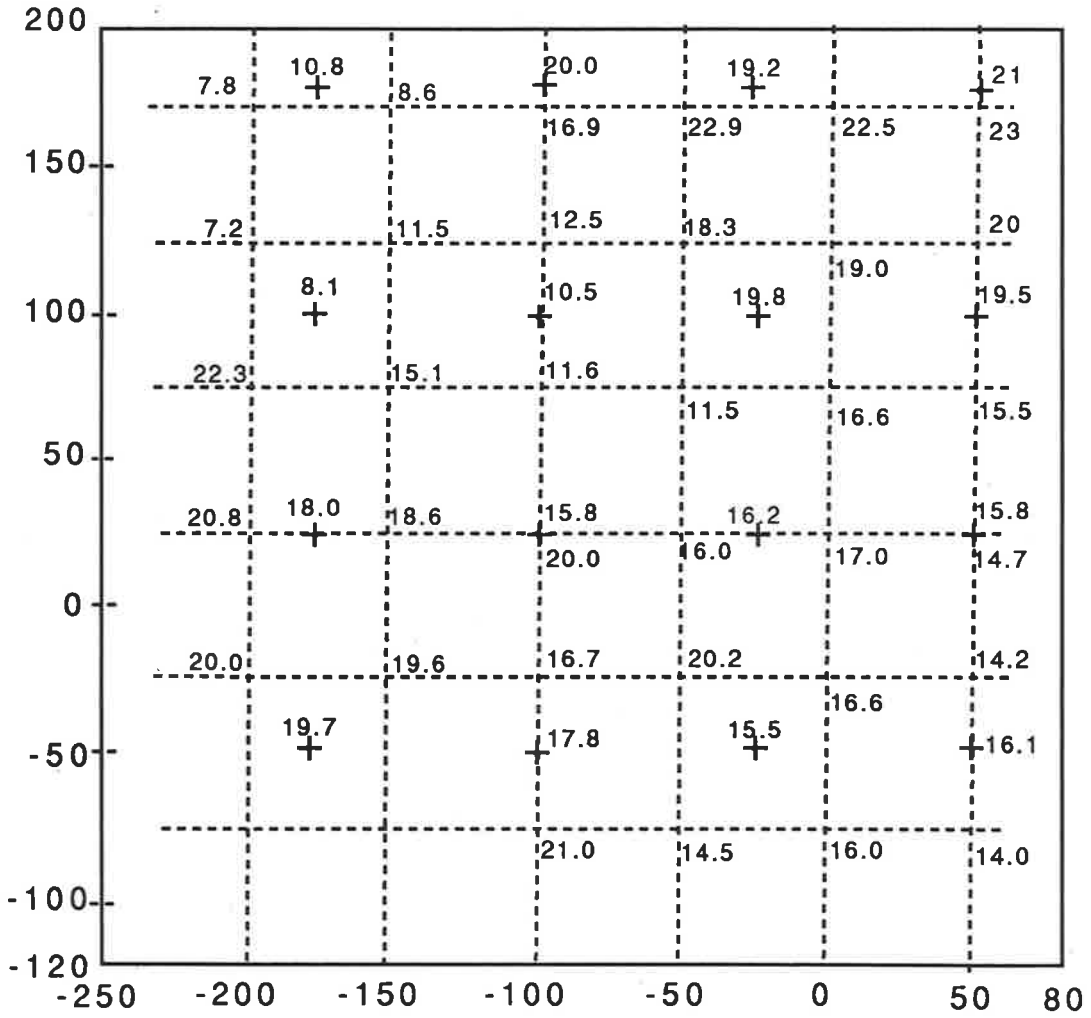

Figure 5.12: Combination results from two sets of block data .

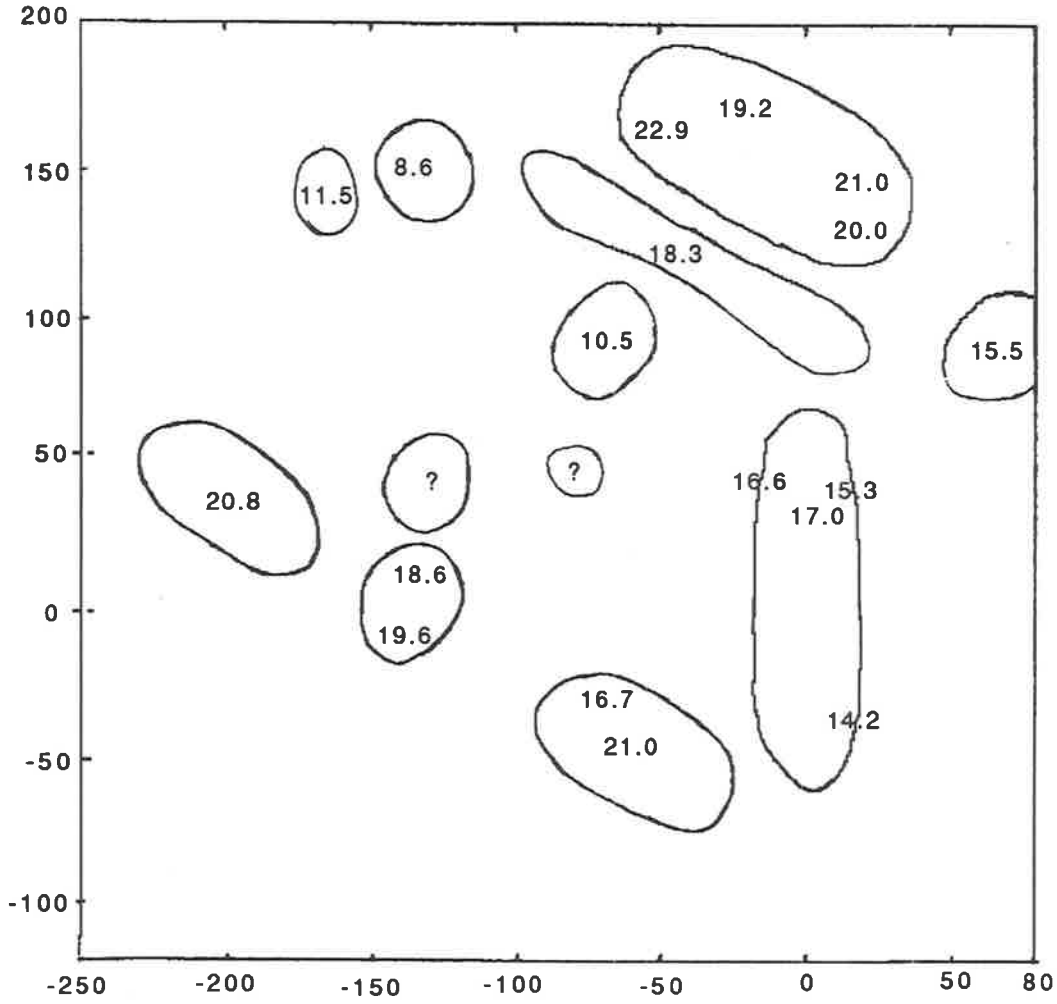

Figure 5.13: Preliminary interpretation map of deep seated bodies.

data size is 50 by 50 points, the size of the extension array can be 64 by 64, 128 by 128 or 256 by 256. The best choice is 128 by 128.

- If a set of block data covers complete anomalies, it can provide reliable results. Therefore, a procedure is recommended, in which the whole areal data is divided into several individual large size blocks named control blocks. The average depths of these blocks are computed, they are used to adjusts the results from the moving window blocks.

From the model experiment, the maximum detected depth in an area obtained by using the spectral analysis is about 10% of the length of the extended window size. For example, to get information about the Moho at a depth of 35 km, the window size of extension array should be greater than 256 km (in the case of sample interval 2 km). Experience using real data suggests that a larger window is required; for details see next chapter about the application of the real data by using the energy spectral analysis.

So far the model experiment of average depth estimation and a new approach of the anomaly separation has been given. The next section discusses how to represent these interpretation results.

5.5 Quantitative interpretation

Figure 5.11 shows a plan view of the distributions of combination models and the depth values are marked within the bodies. The average depths caused by deep seated bodies from the two sets of block data are shown in Figure 5.12 in which the values are marked at their block centres. By comparison of two maps, a problem of presenting the depth estimates occurs where the values of the estimates are close to the real depths, but some of them are not in the correct positions corresponding to the model bodies. Therefore searching for a good way to display them would improve the results of interpretation.

In the earlier sections, the long wavelength anomalies (see Figure 5.3) were computed and are related to the deep sources. Because the average great depths are coincident with these anomalies, an interpretation map connecting these two sets of information can be produced. As is well known, the extreme values (maxima and minima) of the horizontal gradient of a magnetic (or gravity) anomaly can roughly locate the boundaries of broad causative bodies along the direction of the calculated horizontal gradient; the maximum values (minimum for negative anomaly) of the vertical gradient of this anomaly can indicate the centre of the body and the zero lines of the vertical gradients around broad anomalies also indicate the boundary of the causative bodies (Hou and Shi, 1982; Cordell and Grauch, 1985). Therefore, with the help of the directional horizontal gradient (four directions, e.g. 0°, 45°, 90° and 135° are often applied) and vertical gradient data, a distribution map of the magnetic or gravity causative bodies can be produced. Generally in the case of magnetic field, this procedure requires that the data is reduced to the pole.

Figure 5.13 shows the outlines of the deep bodies, it can be seen that the outlines correspond to most model bodies, but obvious errors occur in the narrow parts of the bodies. The reason is probably caused by a great sample interval in the data. After producing this outline map of the deep bodies, a new interpretation map can be constructed by comparing the block depth data with the outline map and shifting the positions of the corresponding depth values so as to align them with the obvious anomalies. Figure 5.13 shows these results with the outlines of the deep bodies.

In the next chapters, the theory will be put into practise using real gravity (see Chapter 6) and magnetic data (see Chapter 7) in the Eyre Peninsula, South Australia.

Part III

Applications and interpretation of real data

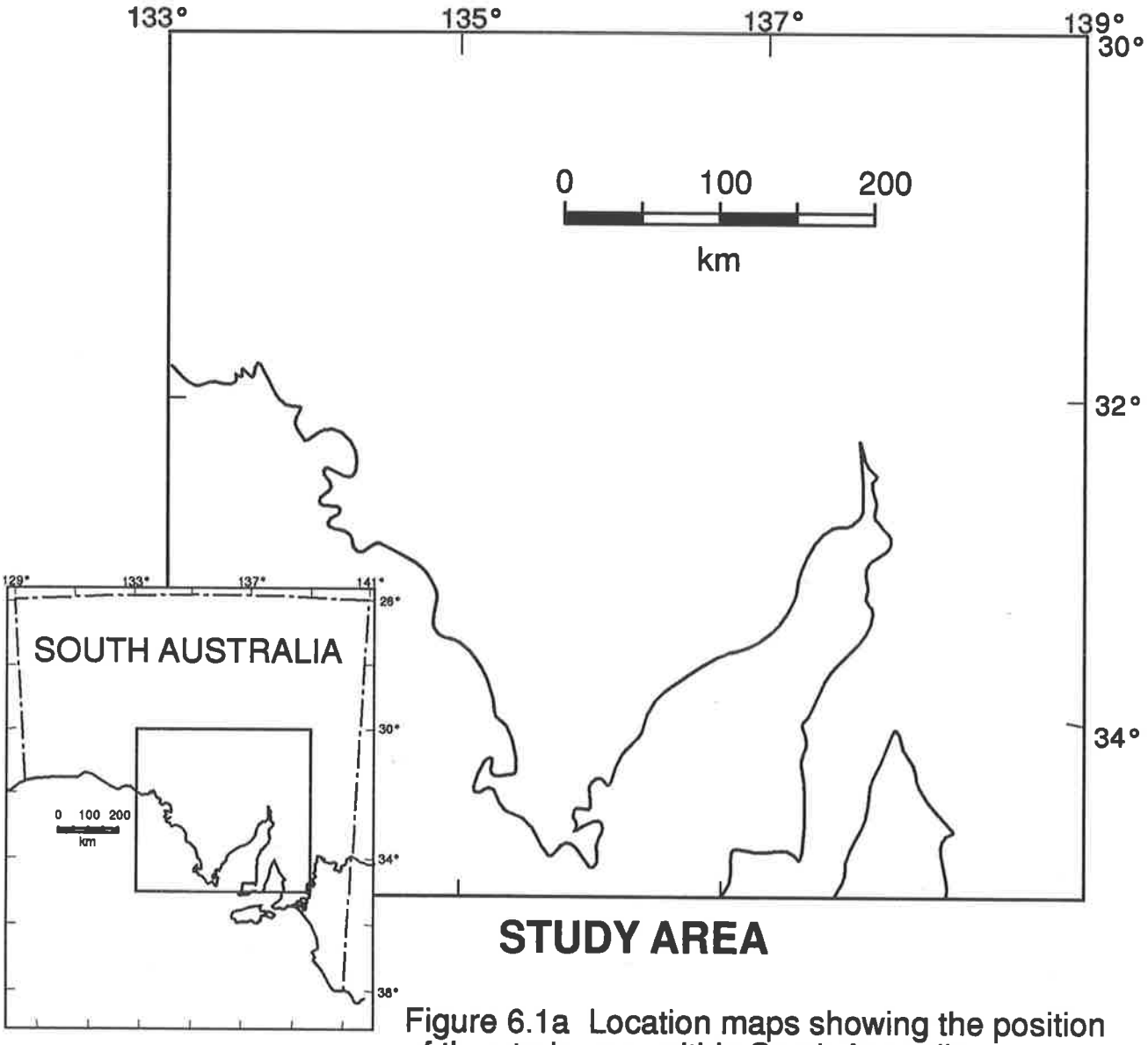

Figure 6.1a Location maps showing the position of the study area within South Australia

Chapter 6

Eyre Peninsula: Regional gravity interpretation

The last chapter shows how the spectral analysis and anomaly separation techniques were used to interpret a series of gravity model data sets and demonstrates that the methods provide reliable information about the depth and extent of the sources of anomalies.

The aim of this Chapter is to apply these techniques shown in Chapter 5 to the real gravity data in the Eyre Peninsula and the surrounding areas (see Figure 6.1a) and to demonstrate some examples for solving real geological problems. The gravity data are also applied to other conventional methods of data interpretation, e.g. vertical and horizontal gradients, image processing of shaded relief. As a result Bouguer gravity anomalies can be related to sources at different depths; some anomalies reflect shallow sources and high frequency noise levels, while others delineate the intermediate structures of this region and some represent the effect produced by the lower crustal masses.

It is important to be able to get geological information from the shallow, intermediate and lower parts of the crust, in order to understand better the procedures which control the structure of the surface rock and the distribution of the mineral deposits. In many places the shallow information is obtained by geological mapping but in some places in Australia much of the information about the near surface rock must come from aeromagnetic surveys, because there is no outcrop over large areas. In all parts of Australia most of the information about the geology at great depths comes from geophysical surveys.

The Eyre Peninsula is typical of many areas in Australia; there are only a few outcrops and very limited geological drilling information is available, so little is known about the detailed geology of the area. For this reason the geophysical data and their interpretation in this area are especially significant. The regional gravity data provide important structural information, while spectral analysis is used together with anomaly separation technique to interpret geophysical data in order to provide not only the outlines of the structural geology but also a quantitative analysis of the data. In this way, information is obtained about the lower crust and upper mantle which is otherwise only available from a few expensive seismic sections.

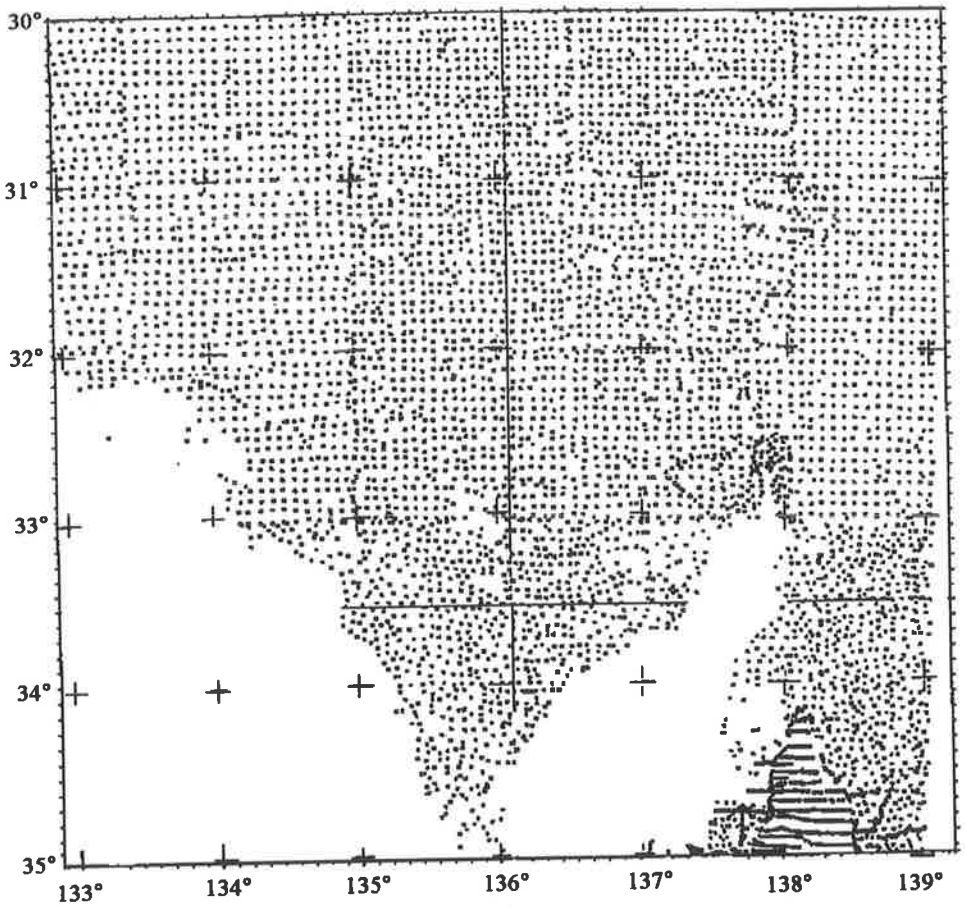

Figure 6.1b: Gravity station location map
Eyre Peninsula,South Australia.

The results of this work, which is the first exercise in applying these techniques to a real regional gravity data set in South Australia, are presented in a series of maps, and show the distribution of regional trends and lineaments, outlines of major gravity features, Bouguer gravity anomalies correlated to sources at different depths, lower crustal structure map, and the depth distribution of the intermediate bodies. All the maps provide the information which is used for a preliminary geological interpretation.

6.1 Original gravity data

The original land gravity data were obtained from the South Australian Department of Mines and Energy (SADME). The gravity surveys were carried out by BMR (now the Australian Geological Survey Organisation) and SADME between 1956 and 1976. The gravity data in the study area provide coverage with a spacing of about 7 km for the most part; an exception to the interval spacing occurs in the Adelaide area in which the stations are closely spaced along several traverse lines. The station location map is given in Figure 6.1b.

The original gravity data mainly cover a land area of approximately 238,000 km^2 between $30°S$ and $35°S$ latitude and between $133°E$ and $139°E$ longitude. These data consist of more than 6200 observed stations.

The theoretical gravity (standard gravity field on ellipsoid) is computed using the Geodetic Reference System formula by:

$$G = 978049(1 + 0.0052884 \sin^2 \phi - 0.0000059 \sin^2 2\phi)$$

where ϕ is the latitude of the station and the gravity field units are in milligal (mgal) or 10 $\mu m/sec^2$.

Bouguer gravity anomalies Δg were computed at mean sea level and with the assumption of an average crustal density of $2.67 g/cm^3$. The topography in this area is relatively smooth and terrain corrections were negligible and not applied.

The original gravity data listing contains four components: observed gravity, latitude, longitude and elevation. In preparation for gridding data, the geodetic coordinates were converted into X-Y coordinates, by using an Albers equal-area projection with a central meridian of longitude 135° E. The data were transformed into an equally spaced grid with 2 km spacing intervals by using a gridding and contouring program named MASTER written by Paine (see Appendix C). The size of the resultant grid is about 282 rows by 289 columns of approximately 81,500 data points.

Part A in Figure 6.2 shows a contour map of the original Bouguer gravity data with a contour interval of 2 mgal. The station data cover mainly the land area and also include more than 15 gravity traverses on the sea floor of the St. Vincent Gulf between the York Peninsula and the Adelaide area. Broad offshore anomalies around Eyre Peninsula are artificial ones generated by

Original Bouguer Gravity Anomalies - Eyre Peninsula, South Australia

A

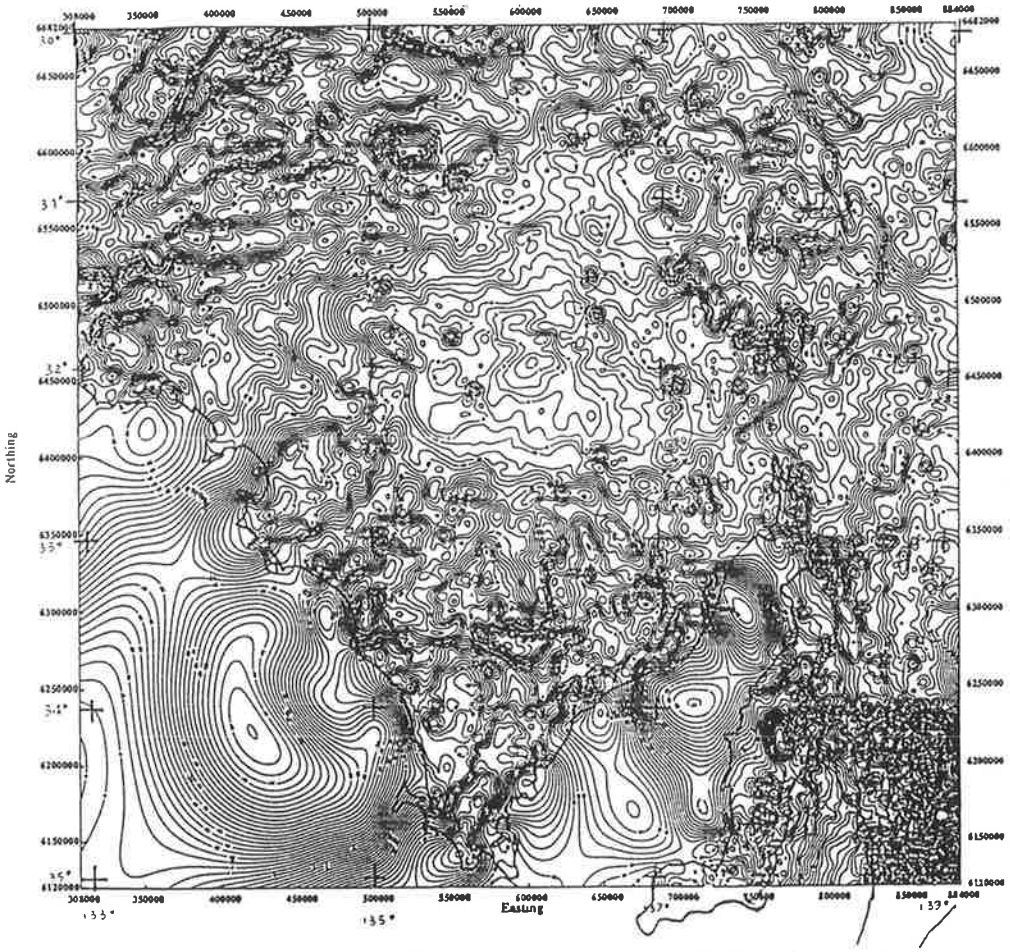

Note: Contours in offshore area are generated by computer extrapolating onshore data see Figure 6.1b

Logarithmic Radial Energy Spectra of Bouguer Gravity in Eyre Peninsula

B

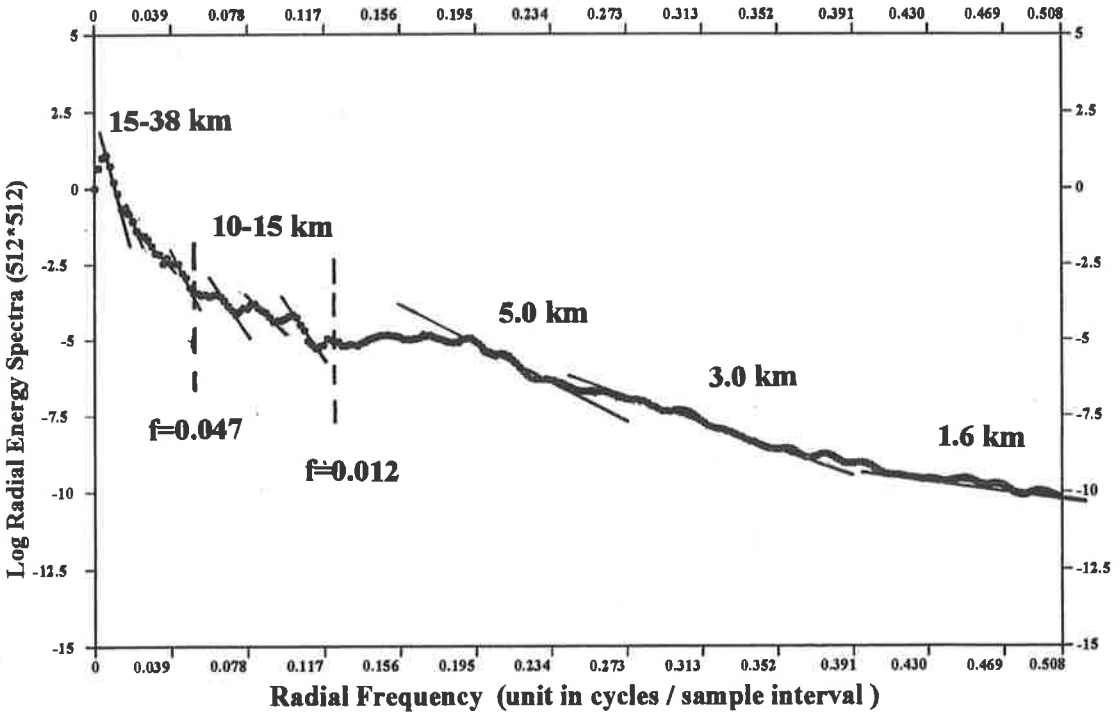

Figure 6.2

the computer from extrapolation of the onshore data, and thus have no meaning at all. After checking the original gravity contour and location maps, it appears that many isolated anomalies are produced from individual observations. It can also be seen that some anomalies seem to be distributed along the longitude lines 135° and 137°, and latitude line 33°. These are due to matching errors in the margins of different gravity surveys. In the corner of the SE part of the map of the Adelaide area, the data are incorrect introducing serious errors into the contour map. In order to remove these errors and noise from the observation and near surface geological bodies the spectral analysis is applied.

6.2 Application of anomaly separation and spectral analysis

6.2.1 Anomaly separation

Part B in Figure 6.2 gives the logarithmic radial energy spectrum from the Bouguer gravity data of the whole area. According to the distribution of the spectrum, it can be readily divided into three sections:

- In the high frequency ($f > 0.12$ cycles/sample) part of the radial spectrum, the characteristics of white noise are present where the slopes of three sections of the spectrum are not consistent. Some sections show a depth of 1.6 km, which is less than the sample interval (gridded data) of 2 km, as well as two depths of 3 km and 5 km which correspond to two obvious slopes. As the original spacing of the gravity survey is 7 km, the shallow depths which are less than the spacing of the survey must be used with caution.
- The medium part of the spectrum ($0.047 < f < 0.12$) shows several section slopes which give the average depth range from 10 to 15 km as the significant layer of density change.
- The radial spectrum in the low end of the frequency shows the average depths range from 15 km to 38 km. It can be further divided into two parts: average depths of bodies which are greater than 20 km ($0.0 < f < 0.022$) and average depths between 15 to 20 km ($0.022 < f < 0.047$). The estimated depth of 38 km probably indicates an average depth of the Moho discontinuity in the whole region.

According to the characteristics of the energy spectral distributions, the original Bouguer gravity field is separated into four slices of anomaly groups at different depths by using the "compensation smoothing filter" (Hou, 1981).

1. The short wavelength anomalies correlate to the shallow bodies and noise level with the average depth of the causative bodies being less than 5 km (see Part A in Figure 6.3). These anomalies were calculated by choosing the factors of the filter as $\beta = 400$ and $n = 60$ (the filter response is shown in Part C of Figure 5.1). The short wavelength anomalies can be calculated by using the high pass filter to keep the high frequency component with

Bouguer Gravity Anomalies of Shallow Sources (h<5km) - Eyre Peninsula

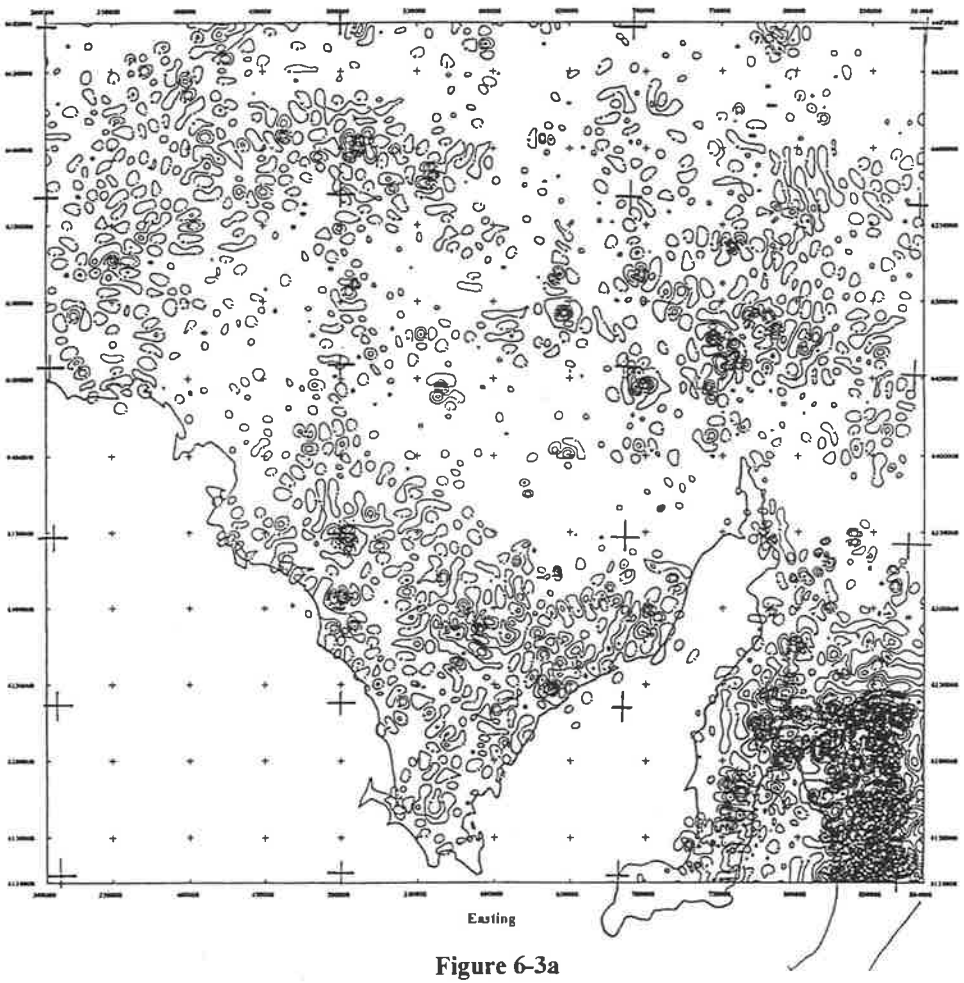

Figure 6-3a

Bouguer Gravity Anomalies-Removed Shallow Sources (h>5km), Eyre Peninsula

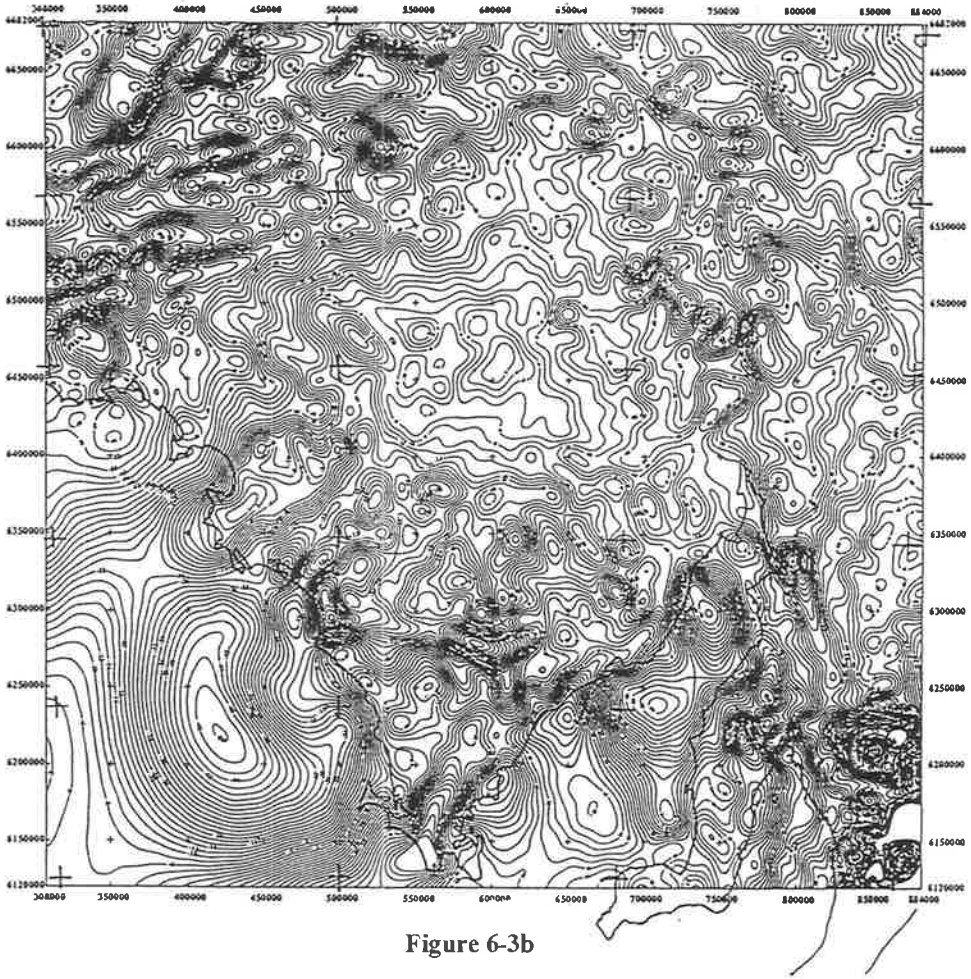

Figure 6-3b

Note: Contours in offshore area are generated by computer extrapolating onshore data see Figure 6.1b

Bouguer Gravity Anomalies of Deep Sources (h>10km) - Eyre Peninsula

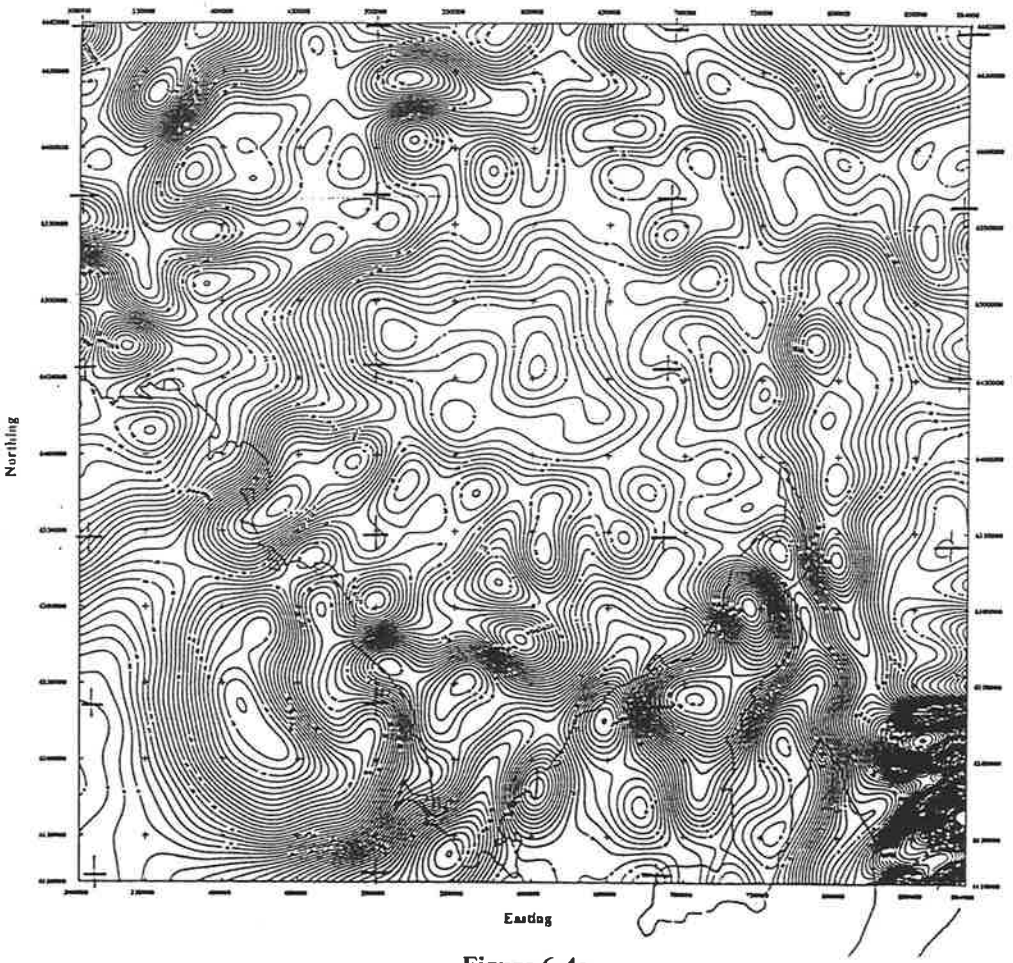

Figure 6-4a

Bouguer Gravity Anomalies of Deep Sources (h>20km) - Eyre Peninsula

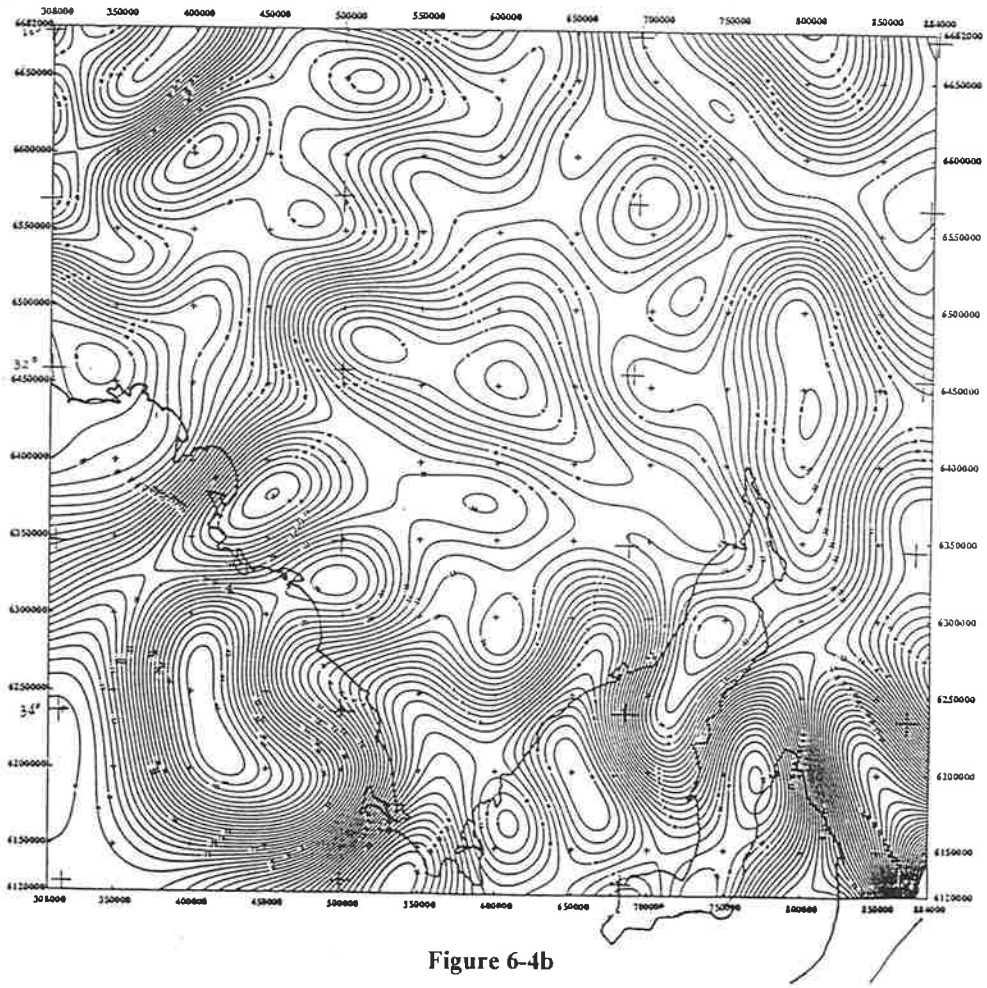

Figure 6-4b

Note: Contours in offshore area are generated by computer extrapolating onshore data see Figure 6.1b

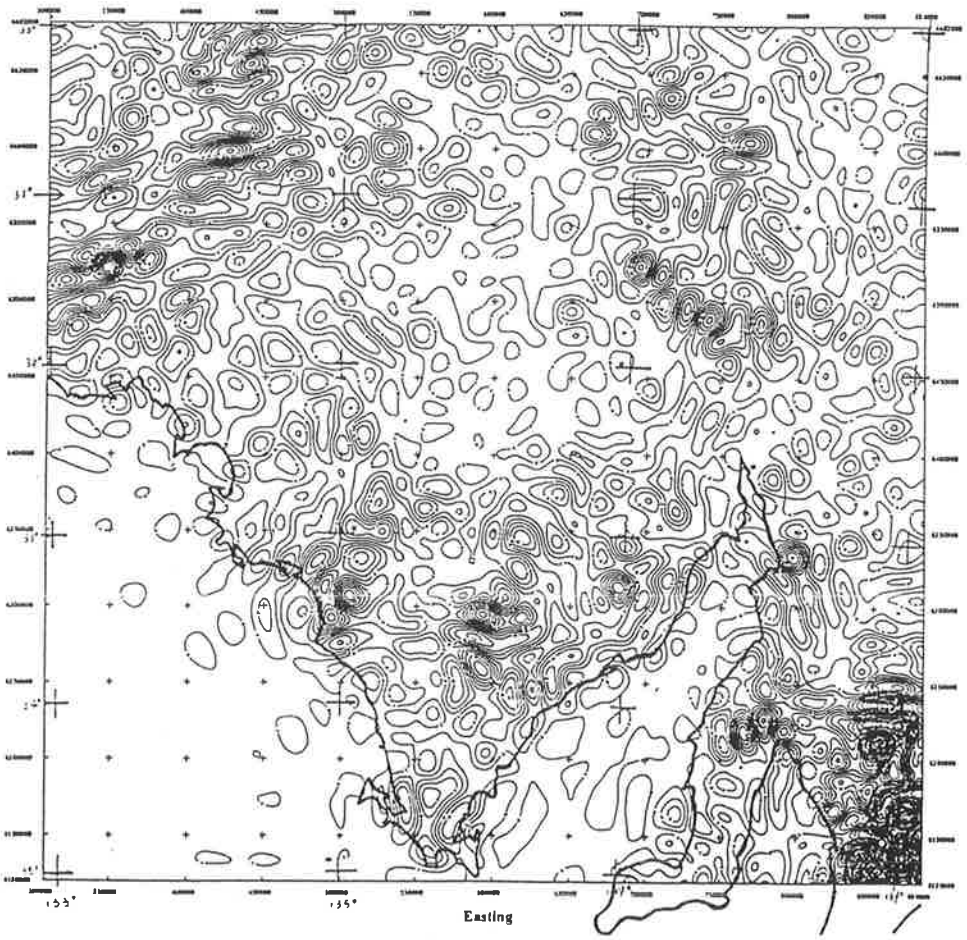

Figure 6.5: Bouguer gravity of middle layer (10 km>h>5km) -- Eyre Peninsula.

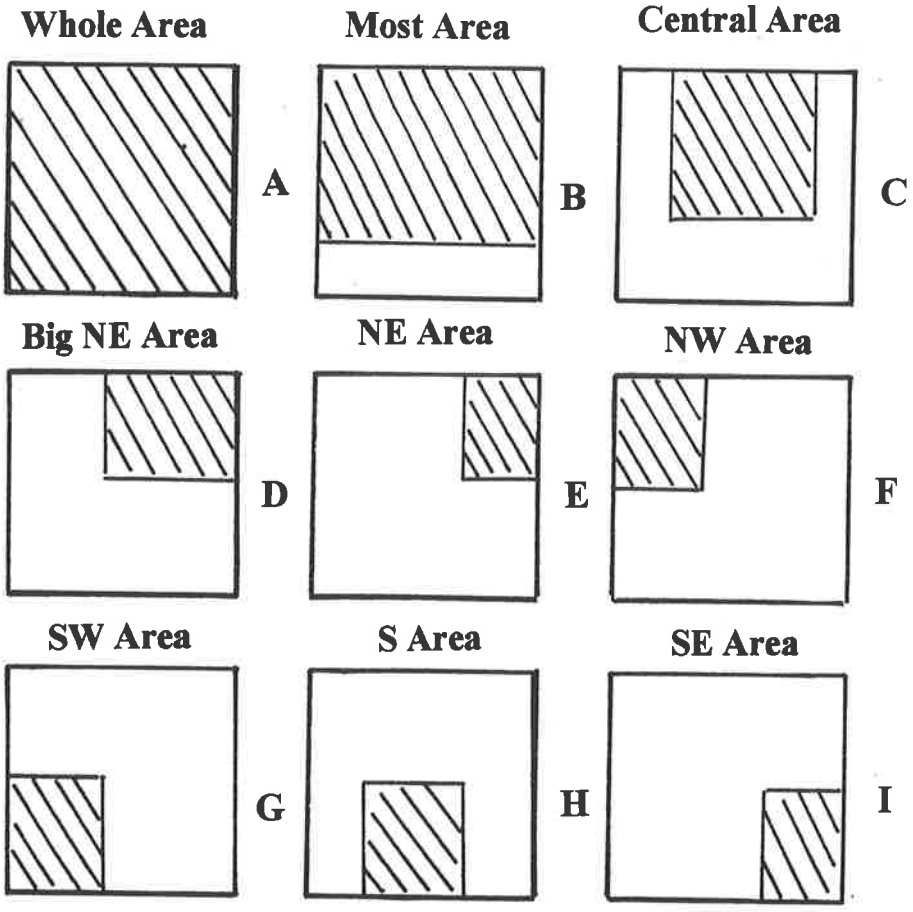

Figure 6.6: Distribution map of sub-areas for calculating energy spectra.

$f > 0.12$. However in order to avoid unnecessary high frequency interference introduced by procedures of calculation corresponding low pass filtering was applied. The result was derived by subtracting the long-wavelength anomalies from the observed Bouguer gravity. This map with the short wavelength anomalies emphasises the isolated anomalies and noise. With the help of this map, it is easy to check these individual anomalies. Some anomalies may be due to errors made during observations and corrections. Some isolated anomalies are probably due to small but very dense or light bodies, for example gabbro intrusion or salt diapir.

2. After removing the effect from these short wavelength anomalies shown in Part A of Figure 6.3, Part B (Figure 6.3) gives a much clearer picture of the regional geological influence. The map of the Bouguer gravity anomalies corresponds to the effects from bodies which occur below a depth which is probably greater than 5 km. As mentioned above (in the last paragraph) the long wavelength anomalies were calculated by using the same factors in "compensation smoothing filter" as used for the short wavelength anomalies, except that low pass filtering was chosen.

3. Part A in Figure 6.4 shows the Bouguer gravity anomalies of deep seated bodies in this region, in which the average depths of the bodies are greater than 10 to 15 km. Low pass filtering was applied by choosing the filter factor of $\beta = 1600$ and $n = 105$, which cuts off the high frequency components of $f > 0.047$. Part B in Figure 6.4 presents anomalies due to even deeper seated bodies in which the average depths are greater than 15 to 20 km. This map probably delineates features in the lower crust or upper mantle.

4. The anomalies of the intermediate layers with average depths of the bodies roughly between 5 km to 10 or 20 km are shown Figure 6.5. This calculation can be done by using a band pass filter. However, Figure 6.5 was produced by subtracting the data in Part A of Figure 6.4 from the data in Part B of Figure 6.3. These anomalies in Figure 6.5 are therefore related to the bodies lying from 5 to 10 kilometres deep.

6.2.2 Average depths for sub-division areas

In order to better control the information about the depth distributions of the deep seated bodies in the whole area (the standard regional gravity data with the interval between the observed station being 7 km can not provide detailed information on shallow bodies), the average depths covering several big blocks were calculated. The area is divided into several sub-areas and the distribution of each division and their energy spectra are shown in Figure 6.6 and Figure 6.7. Table 6.1 lists the coordinates of each division.

The spectral characteristics for each block are quite different. Table 6.2 summarises the average depth correlation to the low, medium and high frequency sections for each sub-area. A summary is given below.

- The estimated depth corresponding to the high frequency section indicates the influences from the sample interval, noise level and depth extent of the shallow sources. Most es-

Figure 6.7: Logarithmic radial energy spectra of Bouguer gravity -- Eyre Peninsula.

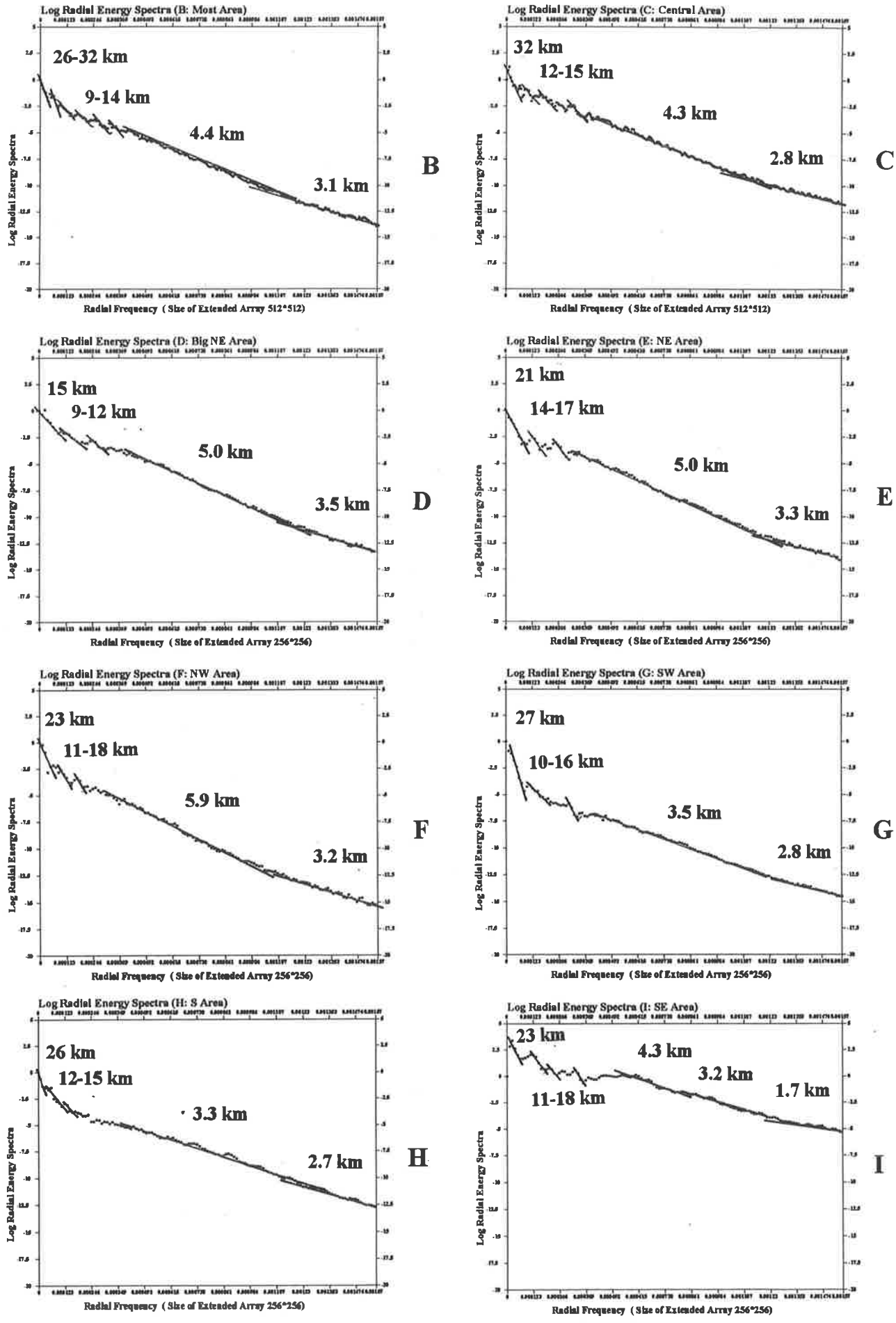

Table 6.1: Coordinates of sub-divisions

No.	Area Code	Location of Area	Easting		Northing	
1	A	Whole Area	308,000	884,000	6,120,000	6,682,000
2	B	Most Area	308,000	884,000	6,240,000	6,682,000
3	C	Central Area	420,000	800,000	6,320,000	6,682,000
4	D	Big NE Area	550,000	884,000	6,400,000	6,682,000
5	E	NE Area	700,000	884,000	6,400,000	6,682,000
6	F	NW Area	308,000	550,000	6,400,000	6,682,000
7	G	SW Area	308,000	550,000	6,120,000	6,400,000
8	H	S Area	420,000	800,000	6,120,000	6,400,000
9	I	SE Area	700,000	884,000	6,120,000	6,400,000

Table 6.2: Average depth of sub-division area

No.	Name of Area	Low Frequency	Medium Frequency	High Frequency	
		$0.047 > f > 0$	$0.12 > f > 0.047$	$0.35 > f > 0.12$	$f > 0.35$
1	Whole Area	15-38 km	10-15 km	3.0-5.0 km	1.6 km
2	Most Area	26-32 km	9-14 km	4.4 km	3.1 km
3	Central Area	32 km	12-15 km	4.3 km	2.8 km
4	Big NE Area	15 km	9-12 km	5.0 km	3.5 km
5	NE Area	21 km	14-17 km	5.0 km	3.3 km
6	NW Area	23 km	11-18 km	5.9 km	3.2 km
7	SW Area	$27km^*$	10-16 km	3.5 km	2.8 km
8	S Area	$26km^*$	12-15 km	3.3 km	2.7 km
9	SE Area	23 km	11-18 km	3.2-4.3 km	1.7 km

Notation:

*: the estimated depth is unreliable.

timated depths are greater than the sample interval (2 km), except the Whole Area and SE Area. The spectrum of the Whole Area (Part B in Figure 6.2) in the high frequency section is very similar to the one from the SE Area data (Part I in Figure 6.7) which includes a large block of unsatisfactory data. This is evidence that the noise data obscure the real shape of the spectrum. The average estimated depths from the rest are about 3 kilometres; this indicates the depth extent of the shallow masses is substantial.

- The spectrum (Part B in Figure 6.7) from the data in Most Area (Part B in Figure 6.6), which omits the incorrect data, give a very clear pattern of the spectral distributions of the shallow bodies. The average depth derived from the high frequency section is 3.1 kilometres.

- It seems that the average depths from the high frequency sections in the southern part of the whole area ($h \approx 3.3km$) are shallower than the ones from the northern part ($h \approx 5.5km$). In addition the average depth of the whole area is approximated to 4.4 kilometres.

- The depths derived from the medium frequency part in the whole area are varied and range from 11 to 20 kilometres; the average depths derived from the low frequency parts in most sub-areas range from 15 to 23 kilometres. Does this perhaps indicate that a Conrad discontinuity exists in the studied area?

- The spectrum from SW Area (Part G in Figure 6.6), which includes a large computer generated artificial anomaly in the sea area, where there is no data, give a depth of 27 kilometres (see Part G in Figure 6.7). The spectrum of the S Area (Part H in Figure 6.6) also show a depth of 26 kilometres (Part H in Figure 6.7). Both cases indicate that the extent of the depths represents the effects of artificial anomalies. If the effects were removed from the artificial anomalies, the average depths (10-16 km) in the southern part of Eyre Peninsula would be obviously shallower than the depths (21-23 km) in the northern part. In fact some Archaean rocks crop out in the southern part of Eyre Peninsula, which may be evidence that there is a shallower discontinuity in the middle crust and the average depth is 13 km.

- The NE Area (Part E in Figure 6.6) covering part of the Adelaide Fold Belt is within the Big NE Area (Part D in Figure 6.6) which covers most of the Gawler Range volcanic province (GRV). After comparing these two radial spectra (parts D and E in Figure 6.7), it appears that the two sets of spectra in the high frequency sections are identical, but the spectra in the rest of the sections are significantly different. The Big NE Area (Part D in Figure 6.7) shows a much shallower depth estimate (9 to 15 km) than the depth (14 to 21 km) in the NE Area. It is suggested that the depth (12-15 km) of the bodies produced the gravity high in the Gawler Range volcanic province is shallower than the layer (17-21 km) in the Adelaide Fold Belt. The estimated depth of body in the Gawler Range volcanic province is in accord with the average depth (12-15 km) in the Central Area (Part C in Figure 6.7), which covers the whole area of Gawler Range volcanic province. The interpretation of the Gawler Range gravity high is given in the Section 6.5.2.

- The deepest bodies derived from data of the Whole Area (Figure 6.2), Most Area (parts B in Figures 6.6 and 6.7) and Central Area (parts C in Figures 6.6 and 6.7) range from 32 to

38 km, which is consistent with the Moho depth (range from 33 to 44 km) determined from both explosion and earthquake seismic investigations in the South Australia and specifically in the Adelaide Fold Belt region (Bolt, Doyle & Sutton, 1956; Doyle & Everingham, 1964; White, 1969; Stewart, 1971 & 1972; Shackleford, 1978; Shackleford and Sutton, 1979 and 1981; Finlayson, et. al., 1974 and 1979; and Finlayson, 1982; Wellman and Greenhalgh, 1988; Greenhalgh, Tapley and Singh, 1989).

In conclusion, the average depths from the sub-area data provide useful information about the upper crust and the upper mantle. The depth estimates are consistent with the information derived from the deep seismic work. Based on the seismic work in the area of the Adelaide Fold Belt there exists a discontinuity or some transition which occurs in the mode of strain release in the middle crust at a depth of $18 \pm 5km$ (Shackleford, 1978 and Shackleford and Sutton, 1979) or up to 20 -25 km (Stewart, 1972). This is consistent with the result from current study (depths from NE and SE areas). The seismic work combining with inferred surface geology and magnetic interpretation (Stewart, 1972; Shackleford, 1978; Shackleford and Sutton, 1979; Finlayson, 1982; and Preiss, 1987) shows that the sediment thickness of the Adelaide Fold Belt increases from south to north and the values change from 1 to 6 km in the south and up to 10 km in the north area. These values are also in accord with estimates obtained using spectral analysis from the gravity data.

6.2.3 Average depth from block size of data

In order to construct a relief map of deep structures, average depths from two sets of block size data were calculated. These two block sizes are chosen as 150 km by 150 km and 100 km by 100 km both with a sample interval of 2 km. Both data sets (75 rows by 75 columns for first set and 50 rows by 50 columns for second set) were extended into 128 by 128 data points. Most of the spectra are easily divided into three sections from which arise different average depths from differing sources. Because the shallowest depth is derived from the high frequency section, this part of spectrum indicates an effect from the sample interval and noise level, thus these depths are ignored. The data set with the large area (150 km by 150 km) will give a better solution for deep sources than the small data set. The small data set will present more information about the intermediate masses. Therefore two sets of maps with depths at different level are constructed: great depth from the large data set and intermediate depth from the small data set.

It was mentioned in Chapter 5 that the depth contour map is not an appropriate way to present the results. Because a location of average depth from a block of data may not correspond with the position of the actual bodies thus the map of average depths will be distorted. By combining the information from the vertical gradient and four directional (0°, 45°, 90° and 135°) horizontal gradients of the long wavelength anomalies (body depth greater than 10 km), outlines of deep seated bodies are constructed. A brief description of constructing outlines of major bodies was given in Section 5.5.

An average depth for each of the bodies is given based on the calculations from the block size data. The combination of the outline of body and the value of average depth is given in Part

Outline and Average Depth (km) of Deep Sources - Eyre Peninsula

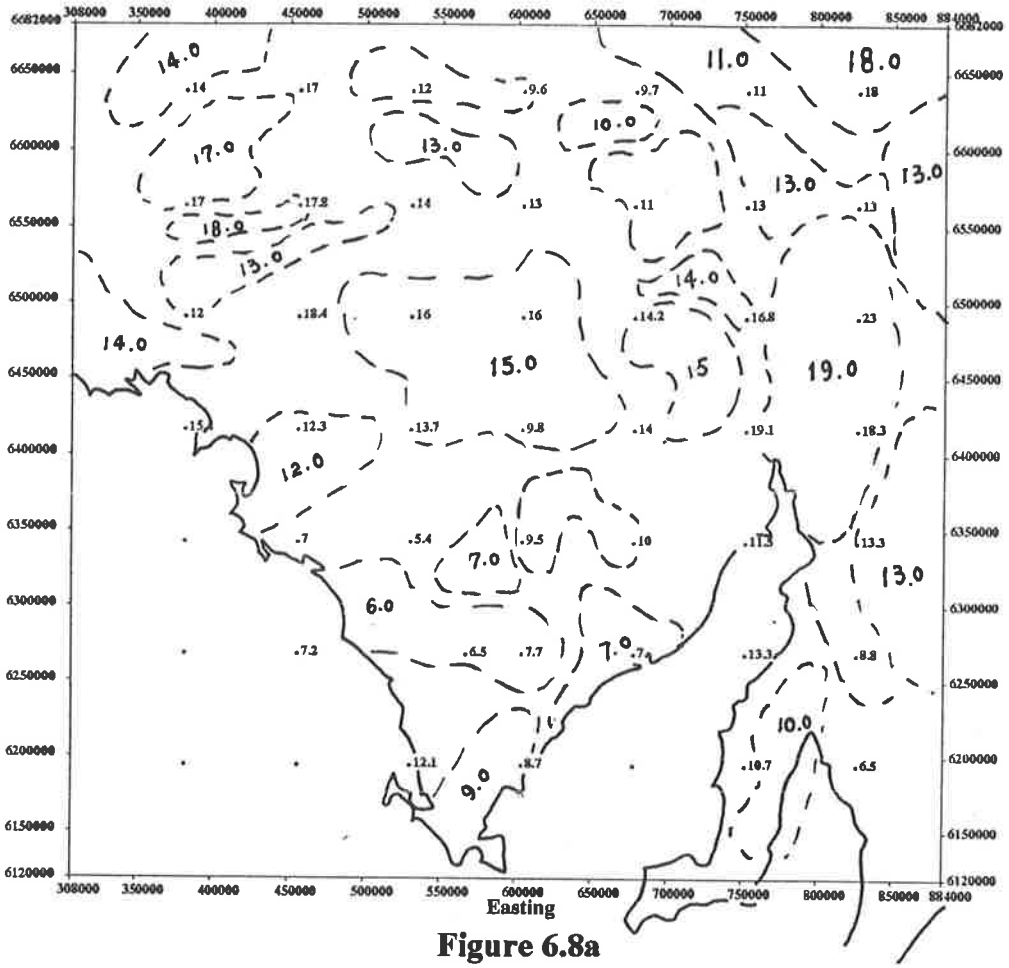

Figure 6.8a

Average Depth (km) of Intermediate Layers - Eyre Peninsula

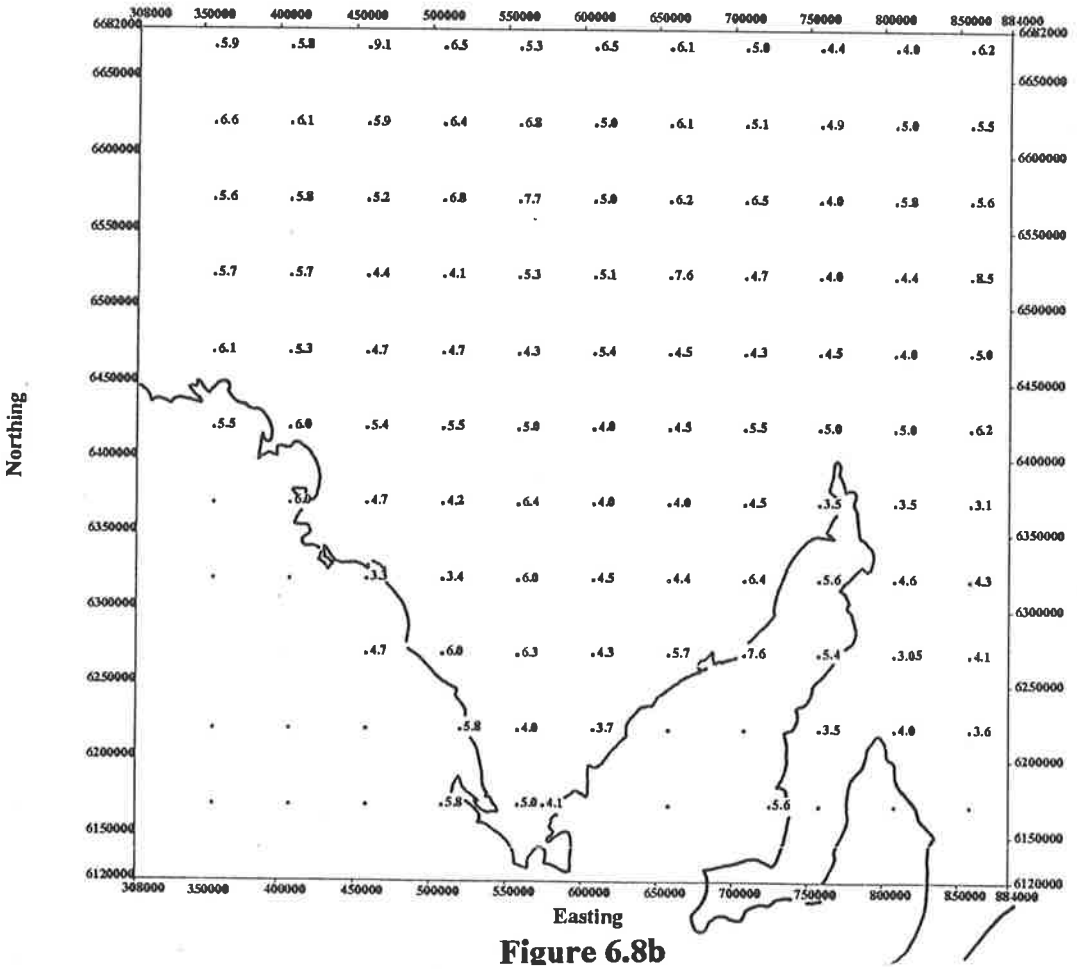

Figure 6.8b

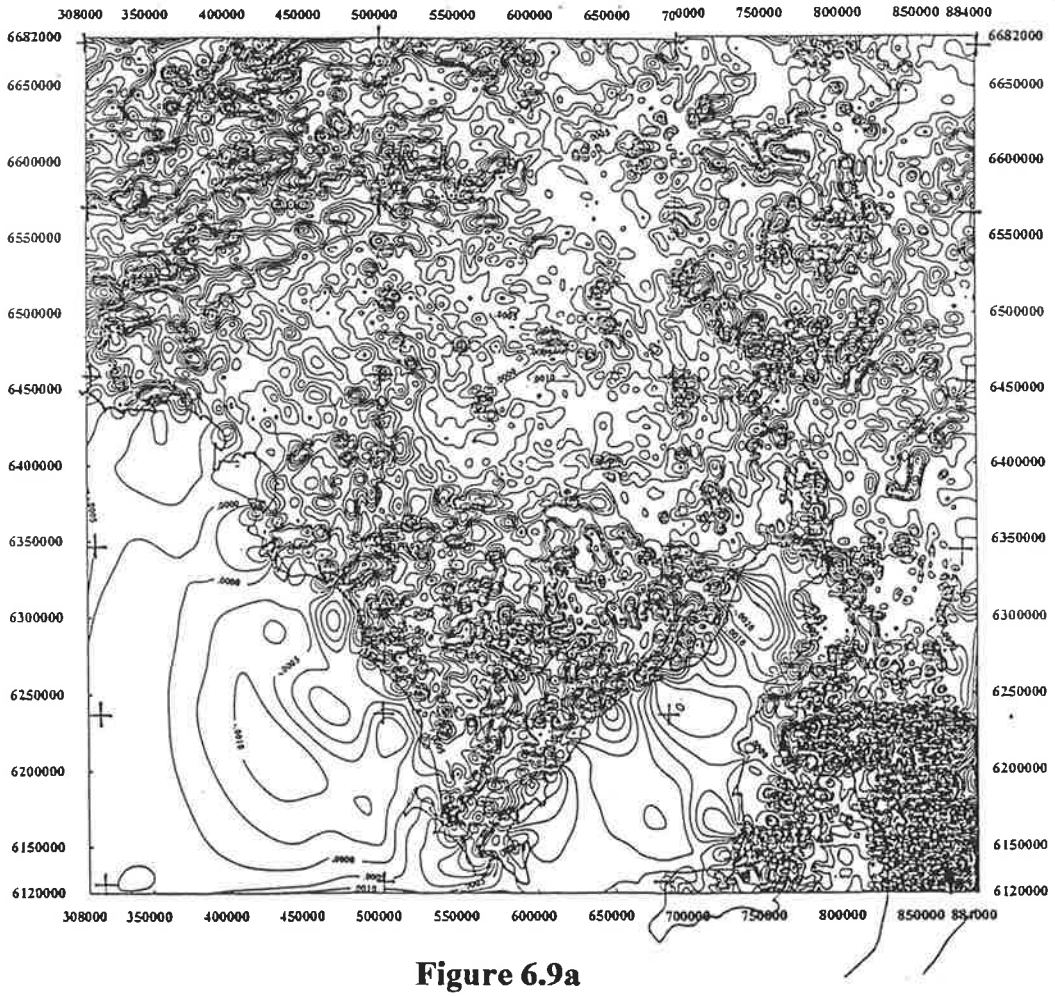

Figure 6.9a

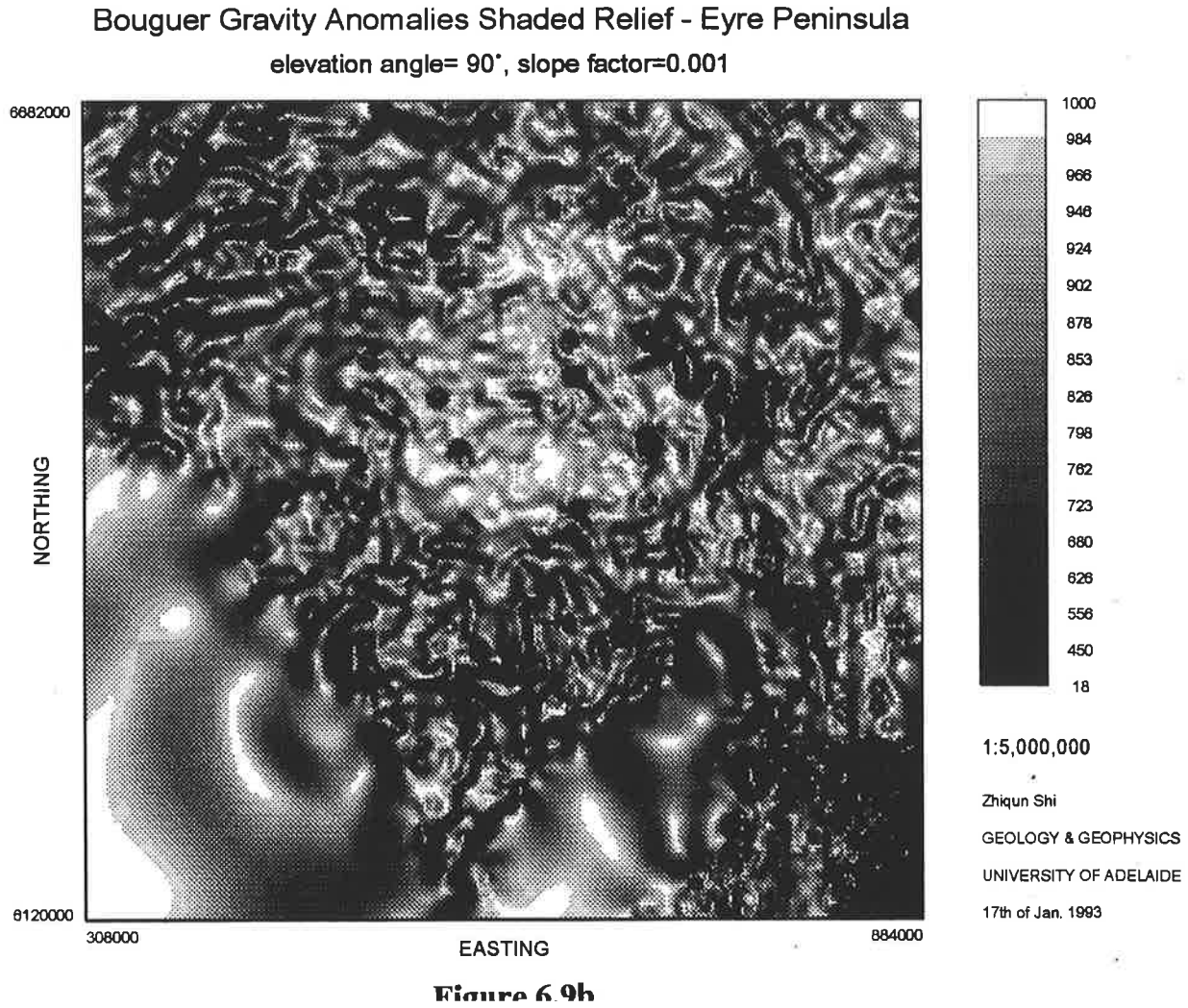

Figure 6.9b

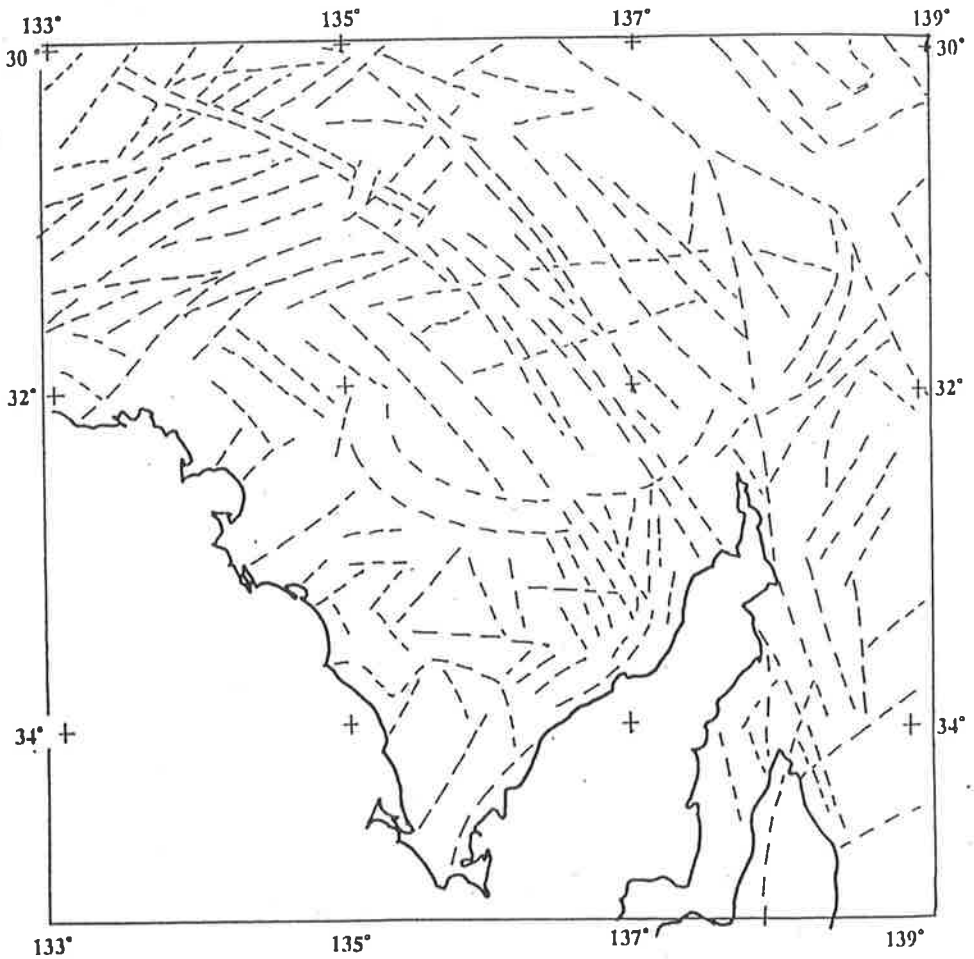

Figure 6.10: Interpretation of Regional Linearments – Eyre Peninsula

A of Figure 6.8. The values of the depths for the intermediate bodies are shown in Part B of Figure 6.8. It is quite difficult to relate the bodies occurring in the medium layers to their depths because the size of calculated block is greater than these anomalies. In reality the intermediate layer for different location may not link to one another. However these values are given a range from 3 to 8 km and the average value is 4 to 5 km, the depths indicate there is probably a layer change in the upper crust of the studied area.

These two sets of depths from the deep sources and intermediate bodies coincide well with the results from the calculations of the sub-area data, which are shown in Table 6.2.

6.3 Application of other methods

As well as processing the data by using spectral analysis techniques, several other conventional methods were applied to the original or long wavelength Bouguer gravity anomalies. The vertical gradient of a Bouguer gravity anomaly is computed to enhance features such as trends, lineament and shallow sources; the contour map is shown in Part A of Figure 6.9. In order to outline the shapes of the deep structures better, the vertical gradient and horizontal gradients along four directions (0°, 45°, 90° and 135°) are applied. The shaded relief method is applied to the original data and is calculated along six azimuth angles (0°, 30°, 60°, 90° and 120°, 150°), in order to enhance lineaments in the different directions of the regional features. Part B of Figure 6.9 shows an example of the shaded relief grey-image with an elevation angle 90° and the slope factor 0.001.

Based on above gravity maps and the regional magnetic map published by SADME, an interpretation map of the regional lineaments and curvilinear structures in the study area is given in Figure 6.10. The patterns present major trends from anomalies due to contacts between different physical properties of rock formations and boundaries of large bodies and may be caused by faults, steeply dipping metasediments, metavolcanics or mafic dykes. The predominant trends are along ENE and WNW directions which are associated with right-lateral differential movements along multiple basement shear zones which occur through cental and south-eastern Australia (Hills, 1956; Rudd, 1961; O'Driscoll, 1968).

The delineation of the lower crustal geological structure map is given in Figure 6.11, which is derived from the long wavelength anomalies at depths greater than 10 to 20 kilometres (see Figure 6.4) and their vertical and directional horizontal gradients. In the figure the marked symbol of H and L represent gravity high and gravity low respectively.

6.4 Measurements of rock density and susceptibility

As is well known a proper analysis and interpretation of gravity data relies on reliable information of rock densities in the study area (Gibb, 1968; Smithson, 1971; Subrahmanyam and Verma, 1981 and 1982). Density values for 178 samples mainly covering the Gawler Range

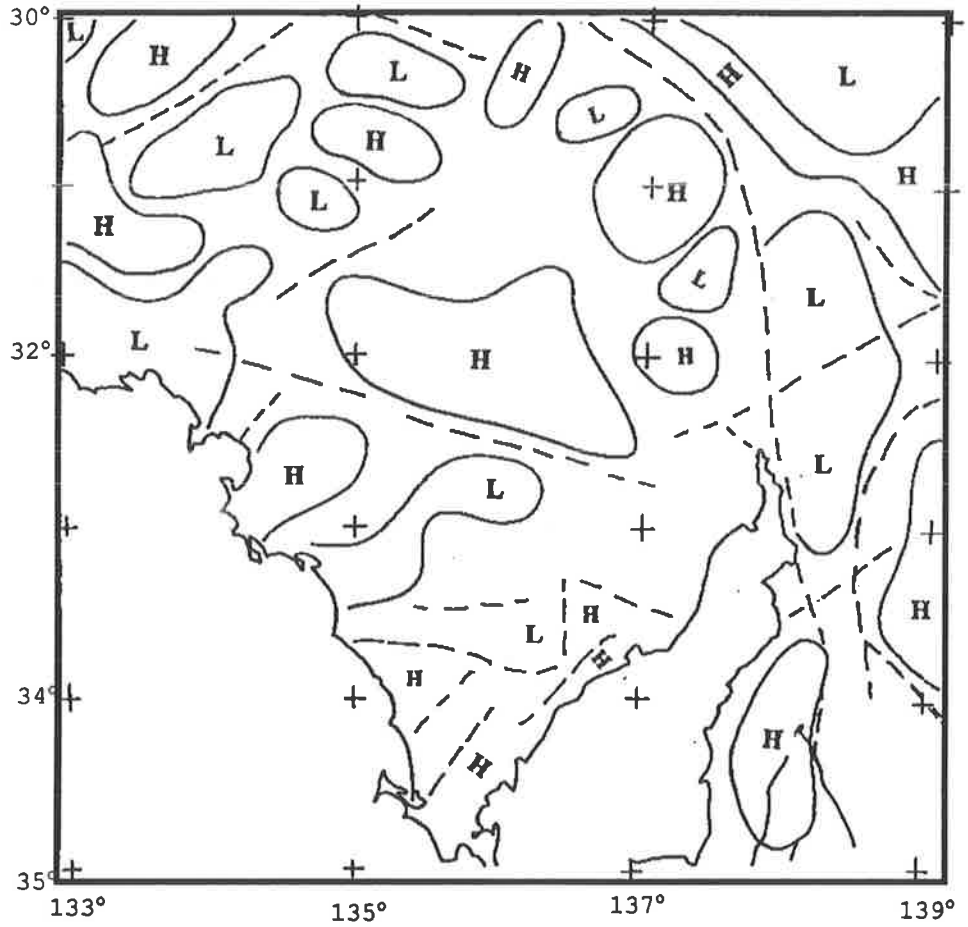

Figure 6.11: Interpretation of lower crustal structure--Eyre Peninsula.

volcanic province and Streaky Bay of Eyre Peninsula have been used in the present research. The samples were collected by SADME, Stewart and the author; most of the measurements were made by the author. The summaries of the rock properties including density and susceptibility are listed in the Appendix F. Histogram of the measurements for each different type of rock is shown in Figure 6.12. The vertical axis represents the distribution of the frequency of the sample and the horizontal axis is the value of density or susceptibility. Tables 6.3 and 6.4 summaries the rock properties in the study area.

Based on above density measurements of the rocks in the study area the order of the formations with increasing density is shown to be: the Adelaide Fold Belt sediments, Hiltaba Granite equivalents, Gawler Range volcanic province, Archaean rocks and Hutchinson Group metasediments and metavolcanics. The information of the rock properties plays an important role to control and analyse gravity anomalies, e.g. the application of this knowledge in Gawler Range volcanic province to a significant gravity positive anomaly.

6.5 Examples of application of spectral analysis

So far the applications of new developed and conventional methods to the regional gravity data have been presented. In order to further demonstrate how the techniques solve real geological problems, two examples for using energy spectral analysis are given below.

6.5.1 The crustal depth and structure

The current gravity study indicates that the estimated crustal thickness and depth of the Moho discontinuity are consistent with the results from the seismic velocity/depth determination (both results shown in Table 6.5). The fact is that by using the spectral analysis technique the regional gravity data provide reliable, adequate information in the deeper crust and upper mantle, which is a key to understanding tectonic processes.

Although the same information can be acquired from the seismic method, the high cost limits the application. Particularly, the deep seismic profiles will be several-ten even several-hundred kilometers apart, thus the detailed tectonic information would not be obtained from them.

The regional gravity survey has carried out in the whole Australia by the AGSO. Therefore the application of spectral analysis to these available regional data including gravity and magnetics is probably the most effective and economical way of extending the information derived from seismic surveys to the rest of the Australia continent. Equally important this work can be done now whereas many of the deep seismic profile will not be made for many years yet.

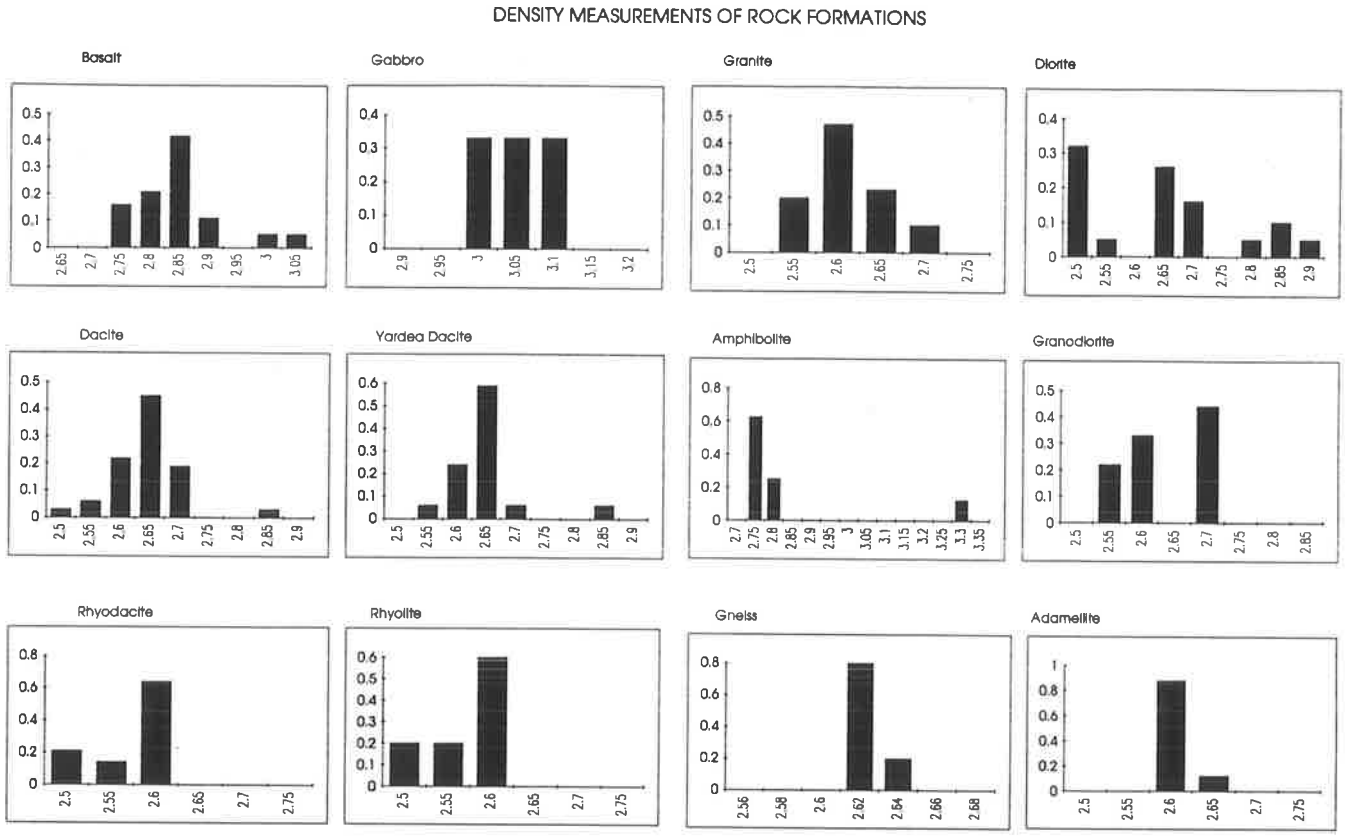

Histogram of density measurements of rock formations in the study area. The vertical axis is the frequency and the horizontal axis is the value of density, in g/cm .

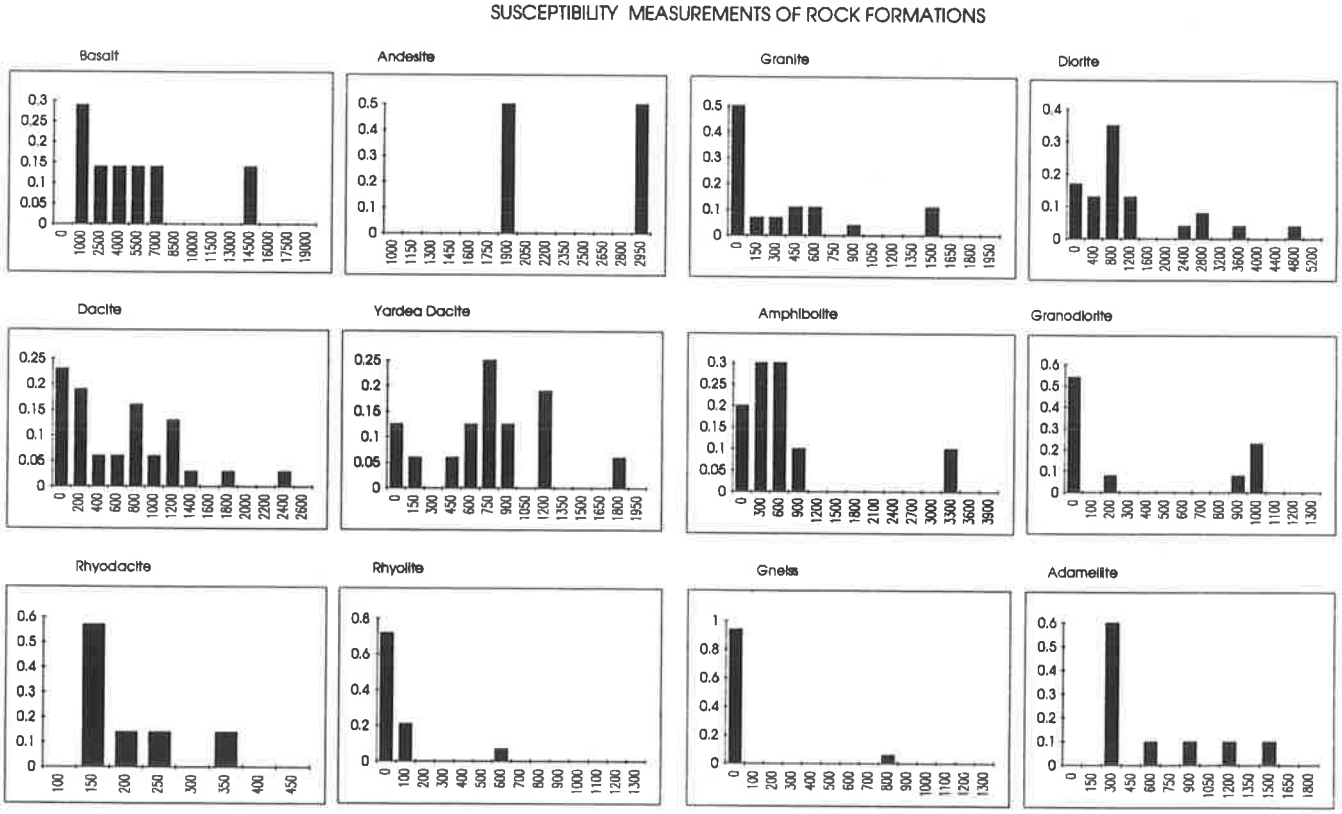

Histogram of density measurements of rock formations in the study area. The vertical axis is the frequency and the horizontal axis is the value of susceptibility, in Six10 .

Figure 6.12: Histograms of density and susceptibility of rock samples in Eyre Peninsula.

Table 6.3: Densities of major rock types in the study area

Sample Number	Rock Type	Locality	No. of Samples	Mean g/cm^3	S.D. g/cm^3	Range g/cm^3
1	Basalt	GRV	19	2.86	0.05	2.76 – 3.09
2	Gabbro	GRV	3	3.02*		2.97 – 3.08
3	Dacite	GRV	31	2.66	0.05	2.51 – 2.88
4	Yardea Dacite	GRV	17	2.66	0.05	2.57 – 2.88
5	Black Dacite	GRV	2	2.68*		2.67 – 2.69
6	Rhyodacite	GRV & SB	11	2.61	0.05	2.52 – 2.63
7	Rhyolite	GRV & SB	15	2.61	0.05	2.52 – 2.64
8	Granite	GRV & SB	30	2.63	0.05	2.56 – 2.72
9	Diorite	SB	19	2.50, 2.68, 2.83	0.05	2.47 – 2.97
10	Amphibolite	SB	8	2.78 3.30	0.05	2.75 – 3.30*
11	Granodiorite	SB	9	2.70	0.05	2.57 – 2.72
12	Gneiss	SB	11	2.62	0.02	2.62 – 2.64
13	Adamellite	SB	8	2.63	0.05	2.61 – 2.68
14	Aplite	SB	3	2.55*		2.52 – 2.58
15	Monzonite	SB	4	2.83*		2.83
16	Adesite	GRV	2	2.71*		2.68 – 2.74
17	Conglomerate	GRV	1	2.82*		2.82

Notation:
Mean: Mean density
S.D.: Standard deviation
2.71* : * single value in measurements represents a mode of frequency distribution.
2.78, 3.30* : multiple values represent multi-modal in distribution.
GRV : Gawler Range volcanic province
SB : Streaky Bay, Eyre Peninsula

Table 6.4: Susceptibility of major rock types in the study area

Sample Number	Rock Type	Locality Samples	No. of $SI \times 10^{-5}$	Mean $SI \times 10^{-5}$	S.D. $SI \times 10^{-5}$	Range
1	Basalt	GRV	7	1200	1500	1200 – 15000
2	Andesite	GRV	2	2450*		2000 – 2900
3	Dacite	GRV	31	100	200	20 – 2300
4	Yardea Dacite	GRV	16	750, 1200*	150	50 – 1800
5	Rhyodacite	GRV & SB	7	160	50	160 – 360
6	Rhyolite	GRV & SB	14	50	100	4 – 660
7	Granite	GRV & SB	28	100, 500	40	10 – 1500
8	Diorite	SB	24	800	400	50 – 5000
9	Amphibolite	SB	10	600, 3300	300	50 – 3500
10	Granodiorite	SB	13	20, 1200	100	20 – 1000
11	Gneiss	SB	12	0, 800	100	0 – 800
12	Adamellite	SB	10	300	150	300 – 1500
14	Aplite	SB	3	3		0 – 5

Notation:

Mean: Mean susceptibility

S.D.: Standard deviation

2450*: * for single value in measurements represents a mode of frequency distribution.

750, 1200*: * in multiple values represent multi-modal in distribution.

GRV: Gawler Range volcanic province

SB: Streaky Bay, Eyre Peninsula

Table 6.5: Estimates of depths of crust and upper mantle in South Australia

Source	Area	Upper Crust (km)	Middle Crust (km)	Lower Crust & Upper Mantle (km)
Bolt, Doyle & Sutton (1958)	SA			36
Doyle &Everingham (1964)	SA			39 ± 4
Hawkins *et al.* (1965)				$11 - 18$ (offshore)
White (1969)	SA			38 ± 6
Thomas (1969)	SA			35
White (1971)	SA			39
Stewart (1971a)	SA			35 ± 2
Stewart (1972)	SA(AGS)	6	20-25	37 ± 1
Denhem *et al.* (1972)	SA			40
Shackleford (1978)				
Shackleford and Sutton (1979)	AGS	1-5	18 ± 5	38.5 ± 5
Shackleford and Sutton (1981)	AGS		16-19	39 ± 5
Shackleford and Sutton (1981)	EEP		8	39 ± 5
Finlayson *et al.* (1974)	AGS		20	$34 - 40$
Singh, R. (1985)	AGS			26-30
Greenhalgh *et al.* (1989)	AGS & EEP		20	26-48 or 36 ± 10
Shi	study area		12-23	32-38

Note:

SA: South Australia

AGS: Adelaide Fold Belt

SEP: Southern part of Eyre Peninsula

EEP: Eastern part of Eyre Peninsula

study area: $30°S$ to $35°S$ and $133°E$ to and $139°E$

6.5.2 The Gawler Range volcanics

Geological problem

The area of Gawler Range volcanic province in South Australia was subjected to a Ph.D study (Stewart, 1993). The rocks composing the Gawler Range volcanics are predominantly dacite to rhyolite with minor basalt and andesite (less than 1% of total outcrop). Unlike most other large volume felsic volcanic provinces in the world, which are associated with negative gravity anomalies, e.g. Yellowstone (Smith and Christinasen, 1980; Smith and Braile, 1984), the Gawler Range volcanics are characterized by a distinct positive anomaly. This phenomenon is uncommon but there are similar examples including the western central Snake River Plain (Lum *et al.*, 1989) and the Caddilac Mountain Granite (Wiebe, 1992).

Why should the area covered by less density felsic volcanics have a significant positive gravity anomaly (see Part B of Figure 6.4)? The answer is that under the Gawler Range volcanics there exists a layer with denser material. This is consistent with the conclusion of Stewart's research (1993).

Geological situation

The Gawler Range volcanics, which formed in the middle Proterozoic age about 1600 to 1590 Ma, consists of acid volcanics (Blissett, 1975; Giles, 1977; Branch, 1978; and Fanning *et al.*, 1988). To the south of the volcanics the nearest outcropping basement rocks are metasediments of the Hutchison Group (mainly Warrow Quartzite) with small areas of granite gneiss and migmatites. Also the southern and western edges of the Gawler Range area have numerous outcrops of the Hiltaba Granite Suite. These granites which intruded after 1590-1580 Ma (Parker, 1990) are slightly younger than the volcanics and are assumed to be associated with them. To the north-east and east of the volcanic outcrop (NE of Lake Gairdner) no basement is exposed and the area is covered by a younger thick quartzose sandstone of the Pandurra Formation and Quaternary sediments. West of the volcanic province the only outcrops showing through the Quaternary cover are outcrops of the Hiltaba Granite, but the aeromagnetic map indicates that there are gneisses (dominantly granite gneisses) also in the area.

Characteristics of geophysics

The signature of a positive gravity anomaly over the Gawler Range volcanic province is 'quiet and flat' with an amplitude about $+20\,mgals$. The province coincides with a large, WNW-trending, gravity high (see Part B of Figure 6.4). To the south, a SE-trending boundary cuts through the volcanics (see Figure 6.11). To the north-east, the block has a gentle dip to the north below the Stuart Shelf.

The Hiltaba Granites associated with the acid volcanics (Parker, Fanning and Flint; 1985) are typically indicated by gravity lows. The western, southwestern and northwestern limits of

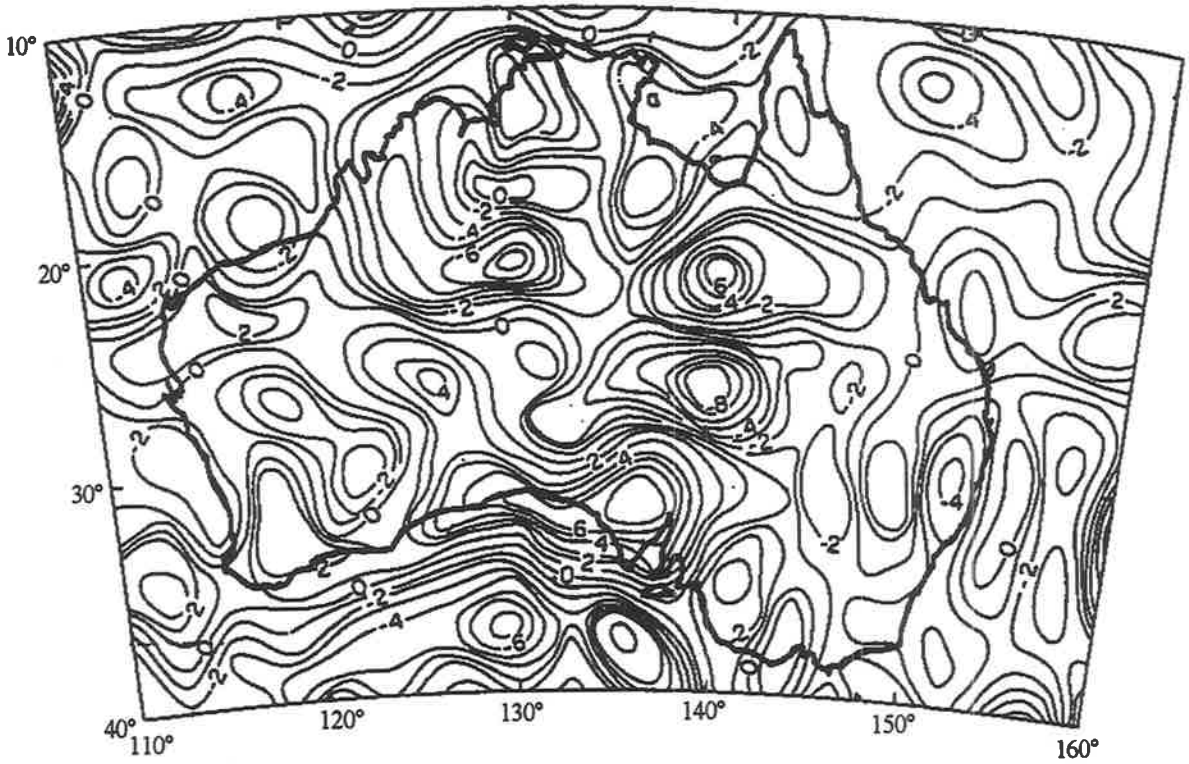

Figure 6.13: Computed magnetization anomalies from MAGSAT data
Australian Continent, after Mayhew et al., 1980

the Gawler Range volcanic province are bounded by granite intrusion. The eastern contact is with the Stuart Shelf.

Depth of the gravity anomaly source from spectral analysis

Based on the density measurements in the area (see Section 6.3) none of the volcanic rocks (mean density range of $2.61-2.66 g/cm^3$), the Hiltaba Granite (mean density 2.63), the Pandurra Formation sediment or the older gneisses (mean density 2.62) can produce such a high gravity anomaly with an amplitude greater than 20 mgal. Therefore there must exist a dense body underneath the felsic volcanics. In addition, this large positive anomaly does not appear in part A of figures 6.3 and 6.5 where the sources of the anomalies are located within the depth less than 5 to 10 kilometres. By the contrast, the maps of the anomalies at depths greater than 10 km (see Figure 6.4), show a significant positive anomaly. By using the spectral technique and simple characteristic point method, the average depth of this body is about 12 to 15 km within the upper and middle part of the crust but not at the bottom of the crust. The estimated depth of the body under the Gawler Range volcanic province from gravity data is influenced by the choice of the petrological model.

This dense body is likely to be a gabbroic body and it may be either caused by crystallization of basic magma from the mantle or it may be the mafic lower part of a large zoned magma chamber (Stewart, 1993). Evidence has been found at the Lake Inkster in the south-west of the Gawler Range volcanic province that an apophysis of undeformed gabbro, which is associated with a positive gravity anomaly similar to the anomaly of Gawler Range volcanic province, was intersected in a number of shallow holes drilled by SADME in the early 1960s. Based on analyses of Sm-Nd, Rb-Sr mineral isochron and also isotopic determination for the gabbro by Stewart, she concluded the crystallization age of the Inkster gabbro to be approximately 1590 Ma: Stewart suggests this is the age of the large mid-crustal body and the intrusion of this large volume of mafic magma was contemporaneous with the period of dominantly silicic volcanism in the Gawler Range province. Stewart further pointed out that the mafic magma derived from the mantle played an important role in the generation of the Gawler Range volcanics, it not only provides a heat flux into the crust but also was itself an important source component for the resultant magmatism, both mafic and felsic. She proposed that the dense body beneath the Gawler Range volcanics is the lower part of a large zoned mafic magma chamber.

The concept is consistent with some other regional geophysical investigations. Recently work of regional aeromagnetic data in South Australia done by the group of geophysicists in the Adelaide University (Kivior, Shi and Boyd, in press) shows that there is a depth discontinuity of 10 to 15 kilometers above the area of Gawler Range volcanics. Another example is from the MAGSAT data. Long-wavelength satellite-altitude (400-700 km) magnetic anomalies over Australia were modelled by an equivalent source technique (Mayhew, Johnson and Langel, 1980). The map of the apparent magnetization contrast model (See Figure 6.13) indicates a body with high magnetization immediately below the Gawler Range volcanic province which coincides with the gravity high. The gravity and magnetic data provide quantitative information about body which appears to be the same as the large and thick zoned mafic magna chamber proposed by

Stewart (1993).

6.6 Summary

The spectral analysis and anomaly separation techniques coupled with other methods are successfully applied to real gravity data in Eyre Peninsula. A series of maps of Bouguer gravity anomalies which are correlated to the sources at different depths are produced. They provide new information of shallow sources, intermediate bodies and deep crustal structure. Average depth of deep-seated bodies in the whole area or average depths from a set of block size data provide depth information from crust. Particularly, the deep crustal information is provided and it is consistent with the results from seismic and other geophysical data.

The interpretation of gravity anomaly in the area of Gawler Range Volcanics is coincident with the postulation of geologist (Stewart, 1993) and it demonstrates an application for using spectral analysis.

While seismic surveys play a central role in understanding the structures of the crust, the high cost for acquisition of the data restricts its application to widely separated lines. This research shows that by applying spectral analysis to the available gravity data it is possible to extend the information about crustal layers beyond the immediate area of the seismic lines. As regional gravity and aeromagnetic data are available for the whole Australian continent and part of offshore areas, the application of spectral analysis to already available gravity and magnetic data provides the opportunity to construct a map of the deep crustal structure in the whole of Australia.

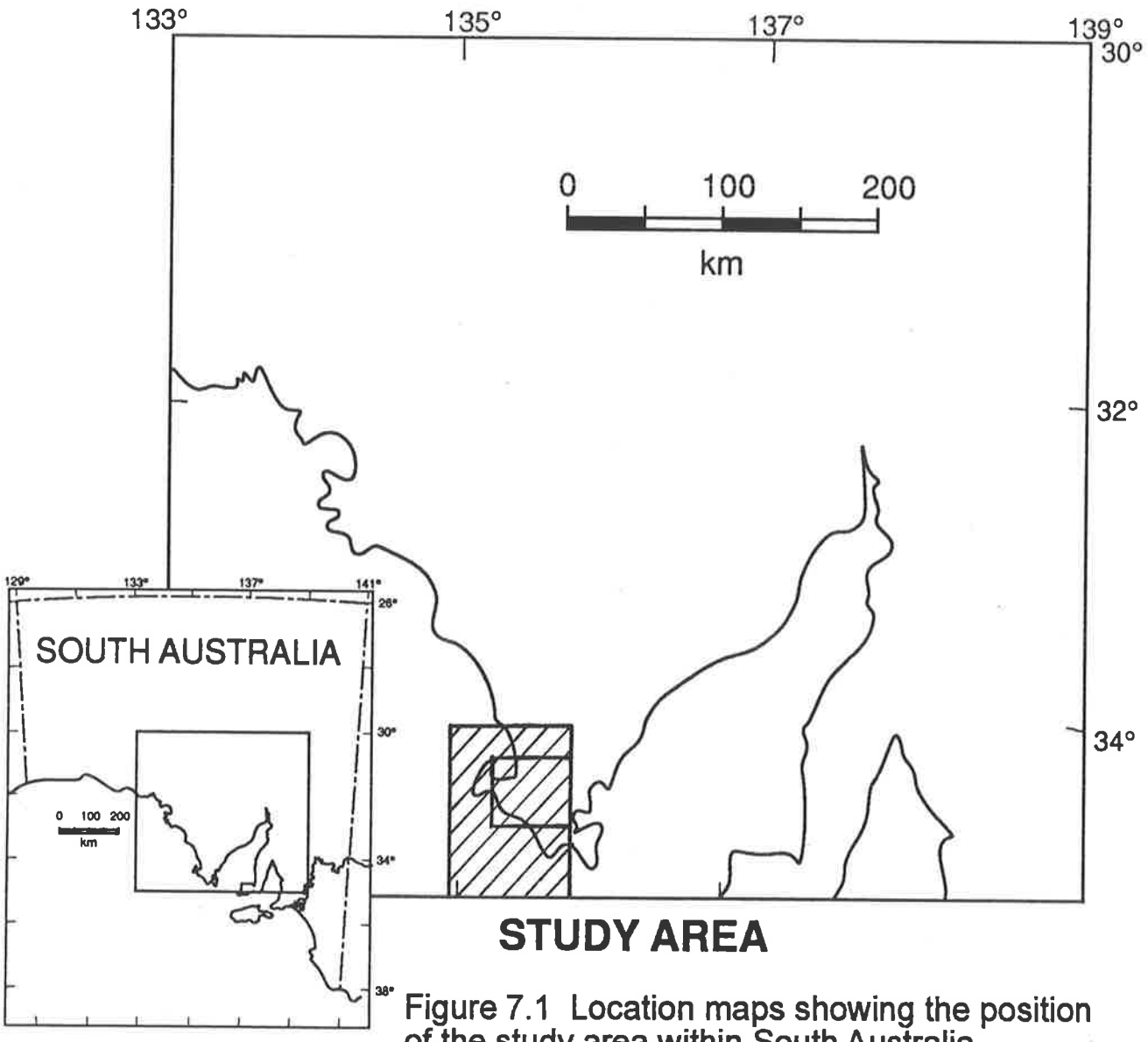

Figure 7.1 Location maps showing the position of the study area within South Australia

Chapter 7

Eyre Peninsula: Application of AUTOMAG

The use of regional gravity data is effective on a large scale in providing information about the large and the deep structures but the wide spacing of the stations, 7 kilometres, makes it unsuitable for extracting information about the smaller near surface structures. For this type of problem aeromagnetic surveys with line spacings of one and a half kilometres or less and with observations made at less than twenty metres along the lines yield much superior information.

High resolution aeromagnetic surveys have the potential to provide a great deal of information; the practical problem is the great amount of data which must be processed to provide results.

A qualitative interpretation of the data can be made by displaying the data in the form of a contour map or an image and treating the shapes of the features in much the same way as aerial photographs are interpreted. This is a powerful approach, see Boyd (1967, 1983) and Isles and Valenta (1993), and has made an enormous contribution to geological mapping and mineral exploration. For some problems this approach does not provide the necessary precision and in this case which includes the central problem of this research project, it is necessary to provide a quantitative interpretation.

In the past quantitative interpretation has been carried out after specific problems have been identified and selected as a consequence of the qualitative interpretation. This is frequently done by forward modelling. This is a logical approach to the problem but it tends to be slow and costly. For extensive quantitative interpretation an automatic interpretation method is required if it is to be practical and AUTOMAG based on the Naudy method does this. The method has been tested on artificial data as explained in Chapter 4. In this chapter it is used with real data to solve real problems.

Before getting on to the demonstration of how the method is used it must be pointed out that the actual problems of magnetic interpretation to which the automatic method can be applied are of great variety and complexity and to apply it to any extent to even one is well beyond the

scope of this Ph.D research project. The research started with problem of providing estimates of the depth of soil cover over large areas using the available regional aeromagnetic data collected by SADME and this is still the central part of the research.

7.1 Original aeromagnetic survey data

The regional aeromagnetic survey used in this study was flown along east-west lines spaced 1000 metres apart, at a mean elevation of 105 metres above ground surface, the tie lines which were flown along north-south were spaced at 10 km and the average interval between observation along the flight line is 13 meters (0.2 seconds recording), resulting is the high quality data required for the application of the method developed here.

The data for the whole area were studied for this research, but as it was not possible to include all of them in a standard thesis, one small part of the data has been selected to demonstrate how the methods work. This selected area is part of the Lincoln 1:250,000 scale map and lies between latitudes 34°03′ and 35°07′, and longitudes 134°54′ and 135°47′ (see Figure 7.1). The data in this region were used to demonstrate the applications of the methods for the study of the regional geology (see Section7.2). Within the region a specific area was chosen (Figure 7.1) for studying the improved Naudy technique (AUTOMAG).

The original locality data were levelled and the regional gradient removed using the 1985 IGRF by Pitt Research Pty Ltd. The data were transformed to a Lambert Conformal Projection using a central meridian of 135 degrees. All further work was done in the Department of Geology and Geophysics, the University of Adelaide. The data were gridded (cell size: 200 m by 200 m) using a gridding software written by Paine.

The survey was carried out and funded by the SADME and BMR in 1988 as part of an initiative to encourage lead-zinc exploration in Eyre Peninsula.

7.2 Regional data processing and interpretation

The main aim of the research was to develop a method to estimate thickness of soil cover and depth of weathering. This central problem can rarely be isolated from the rest of an interpretation and for various reasons the most reliable results will be obtained when the data are studied in a wider context. Therefore a number of conventional methods were used to process the new surveyed aeromagnetic data in the areas including Lincoln, Yardea, Streaky Bay and part of Kimba in the Eyre Peninsula, South Australia. Only the results from Lincoln area (Figure 7.1) are presented in the section. The methods used include linear transformation, energy spectral analysis for calculating average depth of magnetic bodies, automatic gain control technique developed by Rajagopalan, and grey scale image processing incorporating shaded relief, vertical gradient as well as the normal total magnetic intensity.

Figure 7.2: Contour map of pseudo gravity in Lincoln Area.

Parameters chosen: susceptibility=0.001 cgs, Density=2.7 g/cm

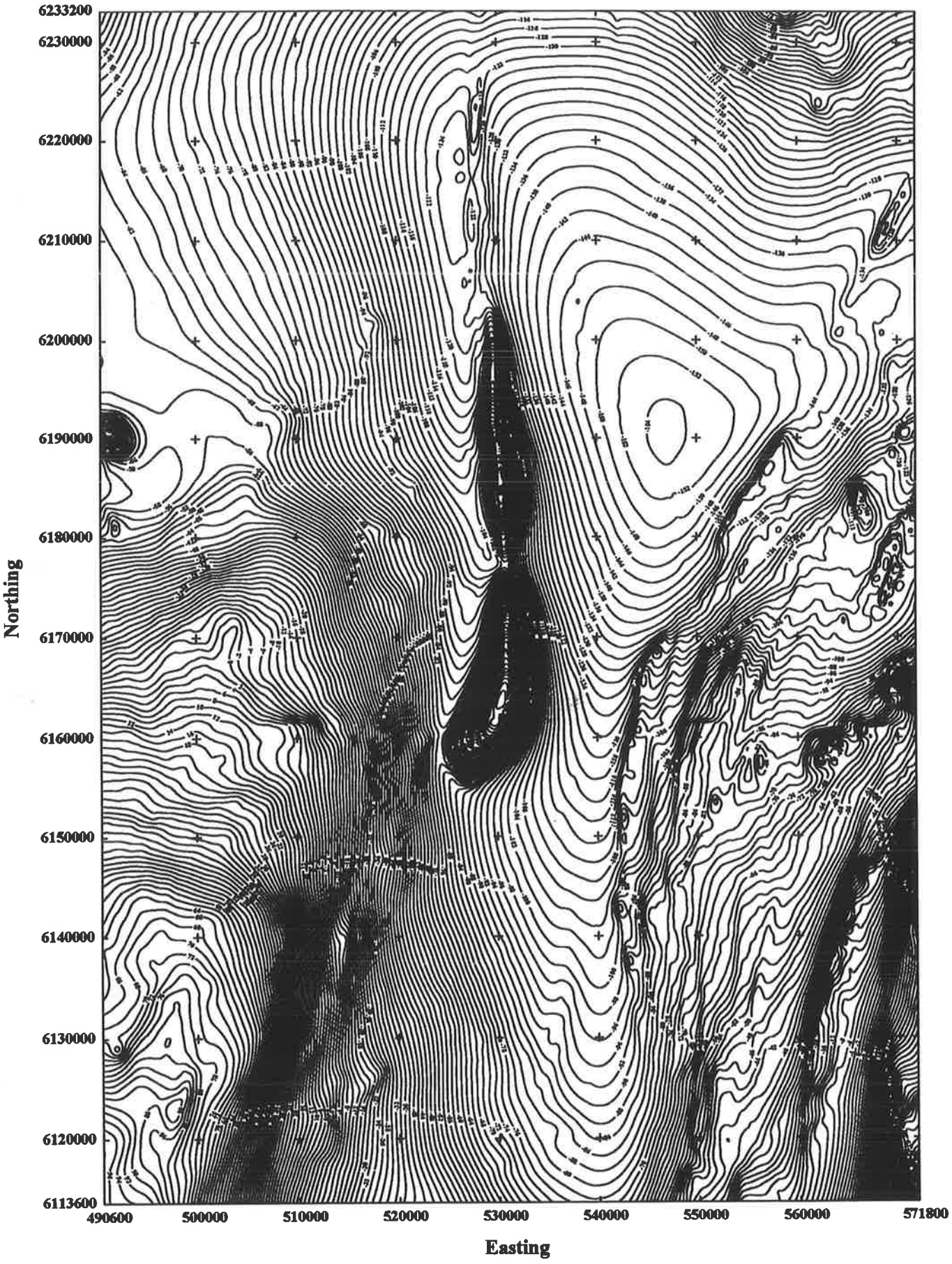

Figure 7.3: Contour map of total magnetic intensity in Lincoln Area.

The amplitudes have subtracted mean value of the area data (1895 nT)

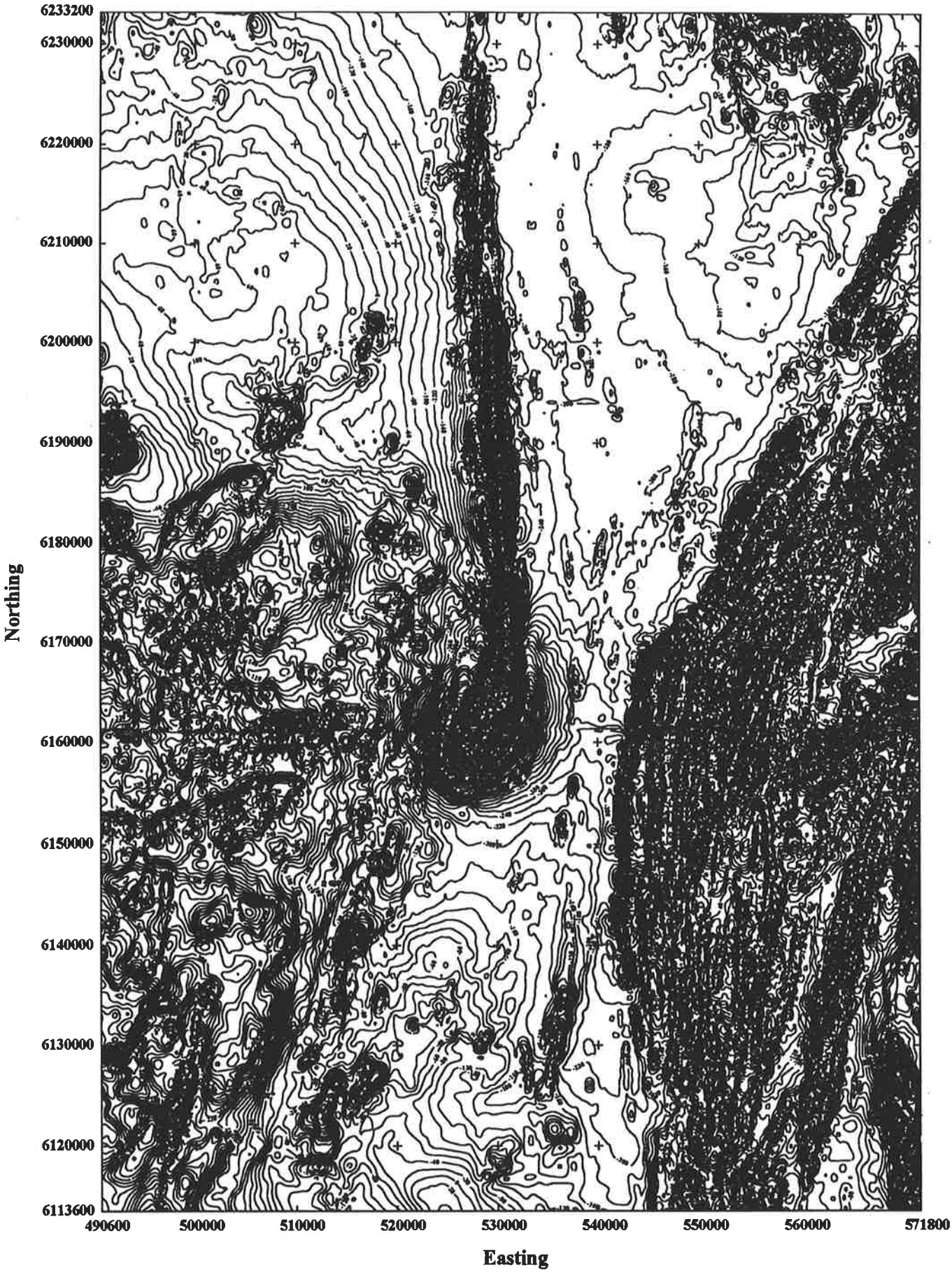

Figure 7.4: Contour map of magnetic anomalies reduction to the pole in Lincoln Area.

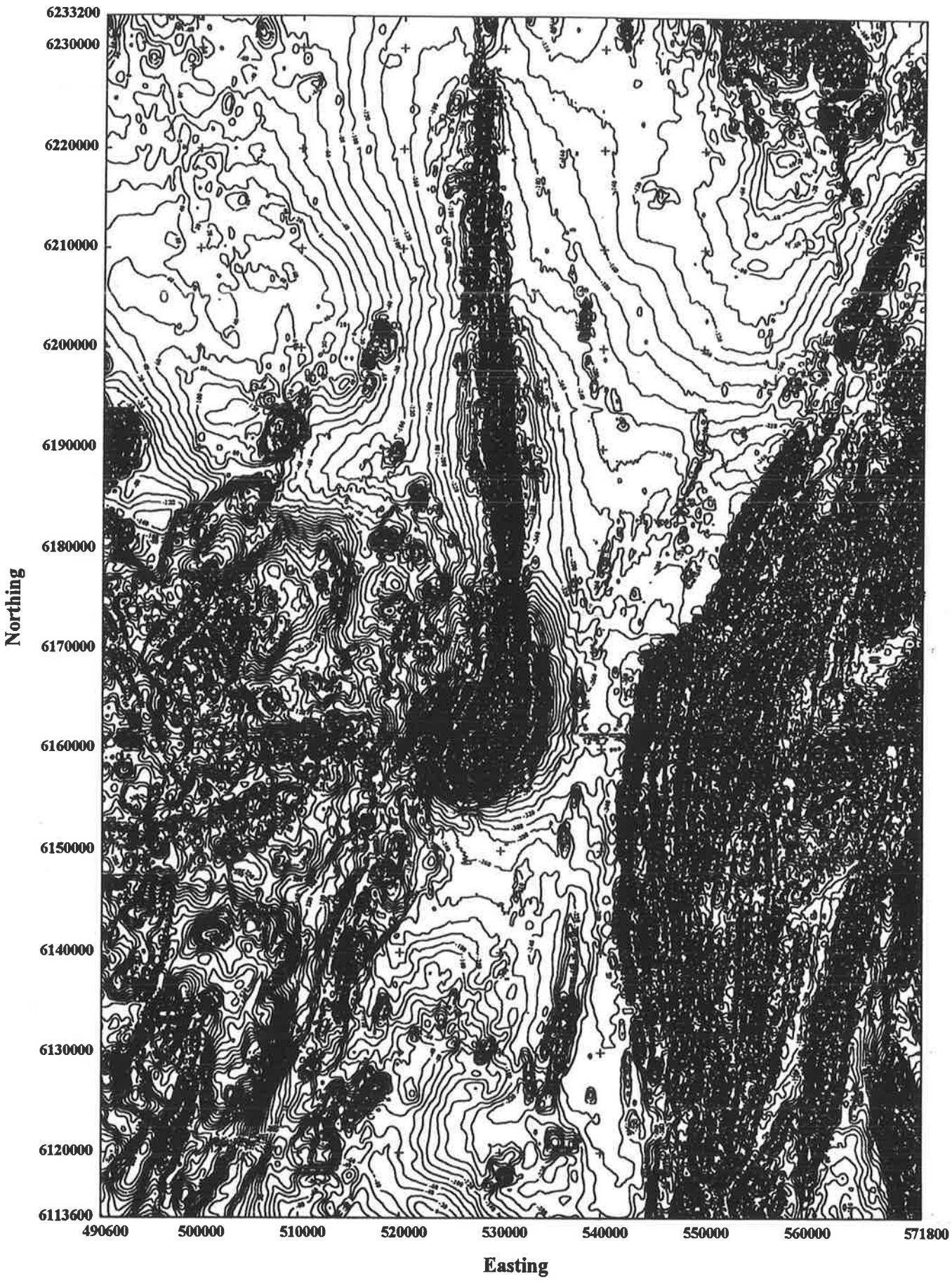

Figure 7.5: Contour map of total magnetic intensity of upward continuation 100m.

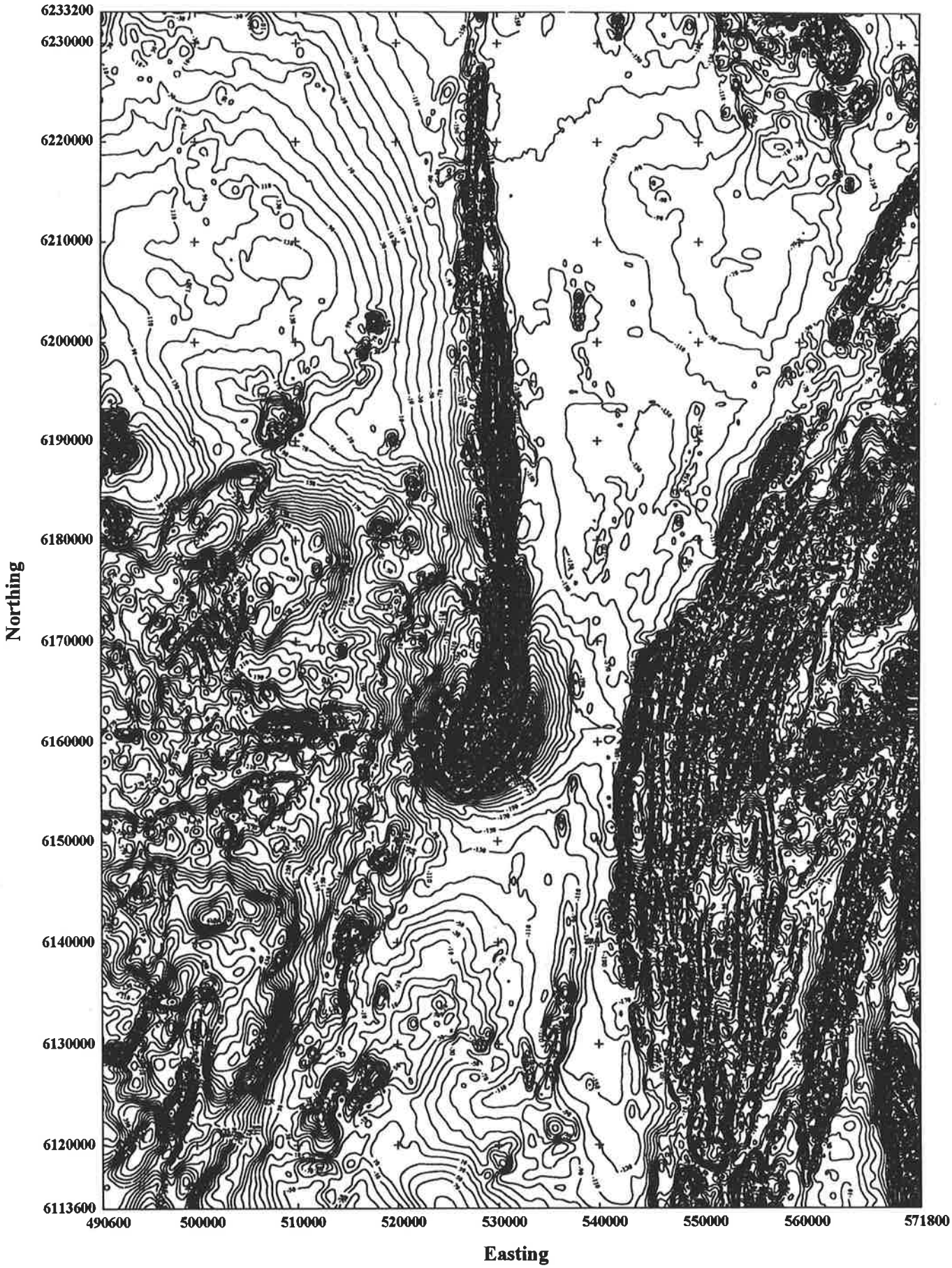

Application of these methods provides a lot of basic information for helping execution of the AUTOMAG as well as the basis for a full geological interpretation. Examples of the kinds of results obtained are as follows: using the first derivatives (vertical gradient or horizontal gradient) and shaded relief, different zones are distinguished and the shallow features are enhanced in which the strike of the anomaly is clearly given and this used to provide the strike correction in AUTOMAG. The details of the processing and application are given below.

7.2.1 Linear transformations technique

The total magnetic intensity data are processed by using the conventional linear transformation method, which converts potential field data in the space domain into the frequency domain using FFT technique; linear filters are then used to transforms the original data into the modified field. TRANSF program written by the author and her Chinese colleagues achieved the aims of above functions. The transformed fields in this data set which are described more fully below include pseudo gravity, reduction to the pole, vertical gradient and upward-continuations with the height of 100 m, 500 m, 1000 m, 1500 m and 2000 m. In order to make the data suitable for the program to allow the application of FFT, a mean value of the whole data in this area (1895 nT) is subtracted from the original field, so that the data are suitable for processing of use FFT technique.

Pseudo gravity and reduction to the pole

Pseudo gravity maps are used to compare the pseudo gravity with the real gravity anomaly to find if there is a relationship between the magnetic causative bodies and sources of the gravity anomalies. A brief comparison between the real gravity data and the pseudo gravity map was made in Lincoln area which indicates some relationships between dense rocks and magnetic basement. The pseudo gravity map can also provide a regional picture of the study area, because the pseudo gravity corresponds to the potential of the magnetic field (based on the Poisson's equation). The pseudo gravity contour map is shown in Figure 7.2.

The original total magnetic intensity anomalies and their reduction to the pole are presented in Figures 7.3 and 7.4 (the inclination used is $-65°$ and declination 7.5°). Comparison of shapes of anomalies between the fields after reduction to the pole and total magnetic intensity shows that there is little difference, because the geomagnetic inclination in the area is high; the amplitudes of the transformed data are increased and the centres of the anomalies move slightly to south.

Note that from the contours along west to east at the position of 6161400 N, there is obvious gap in the map, due to data missing between two sets of gridded data; another gap between different gridded data occurs at position of 6194000 N (see Figures 7.3 and 7.4).

Figure 7.6: Contour map of total magnetic intensity of upward continuation 2000m.

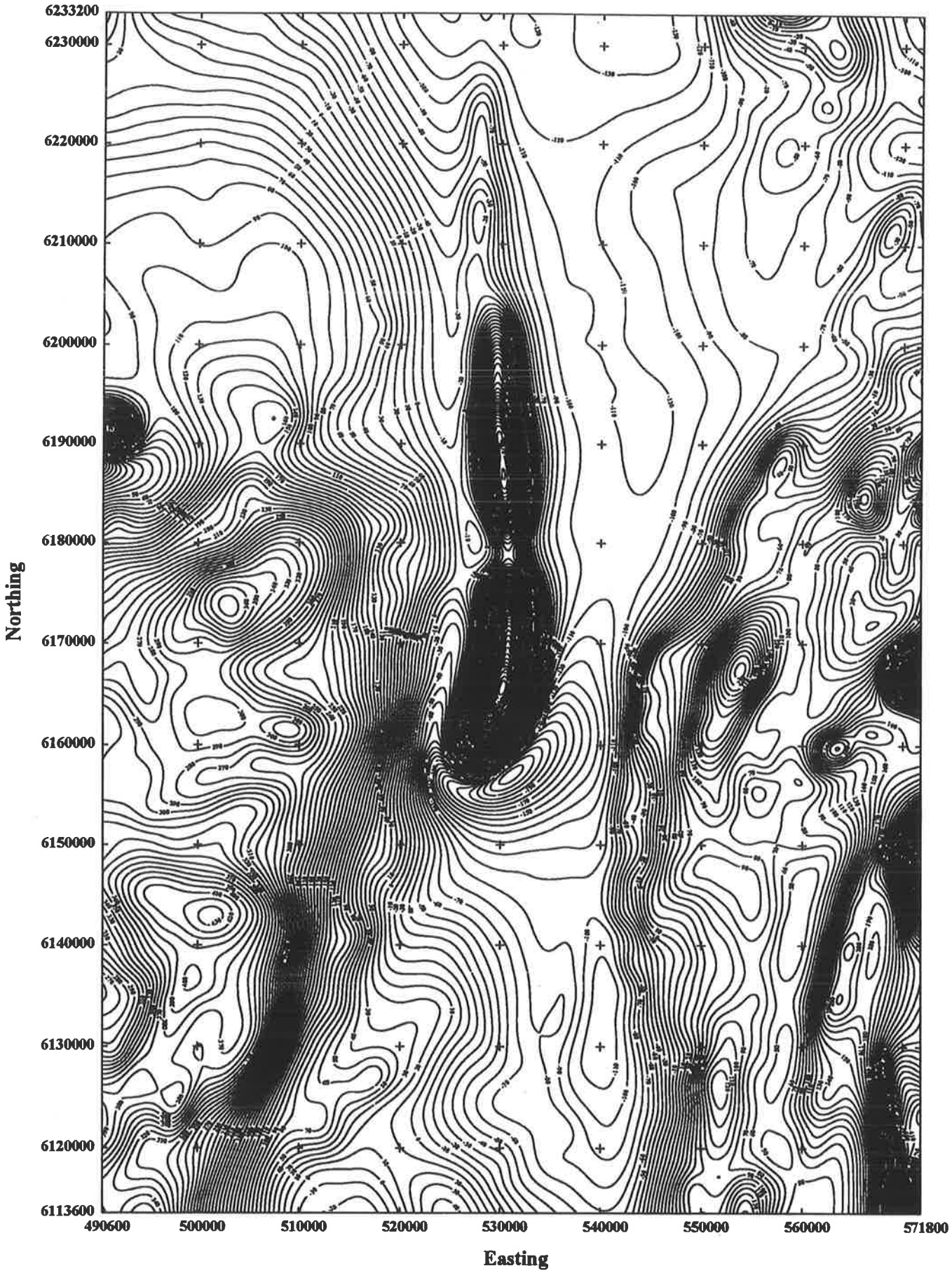

Figure 7.7: Contour map of total magnetic intensity of upward continuation 1500m.

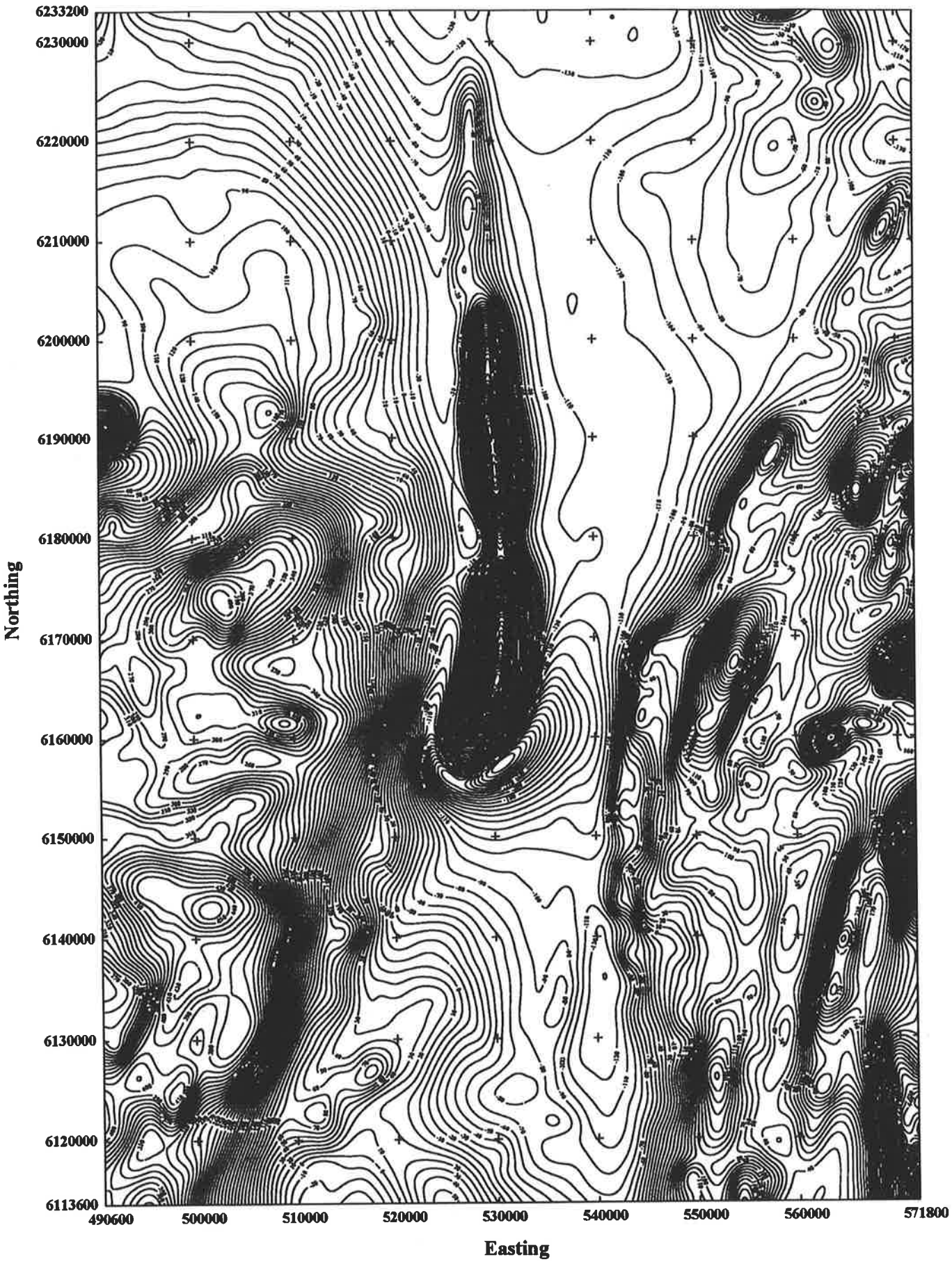

Figure 7.8: Contour map of total magnetic intensity of upward continuation 1000m.

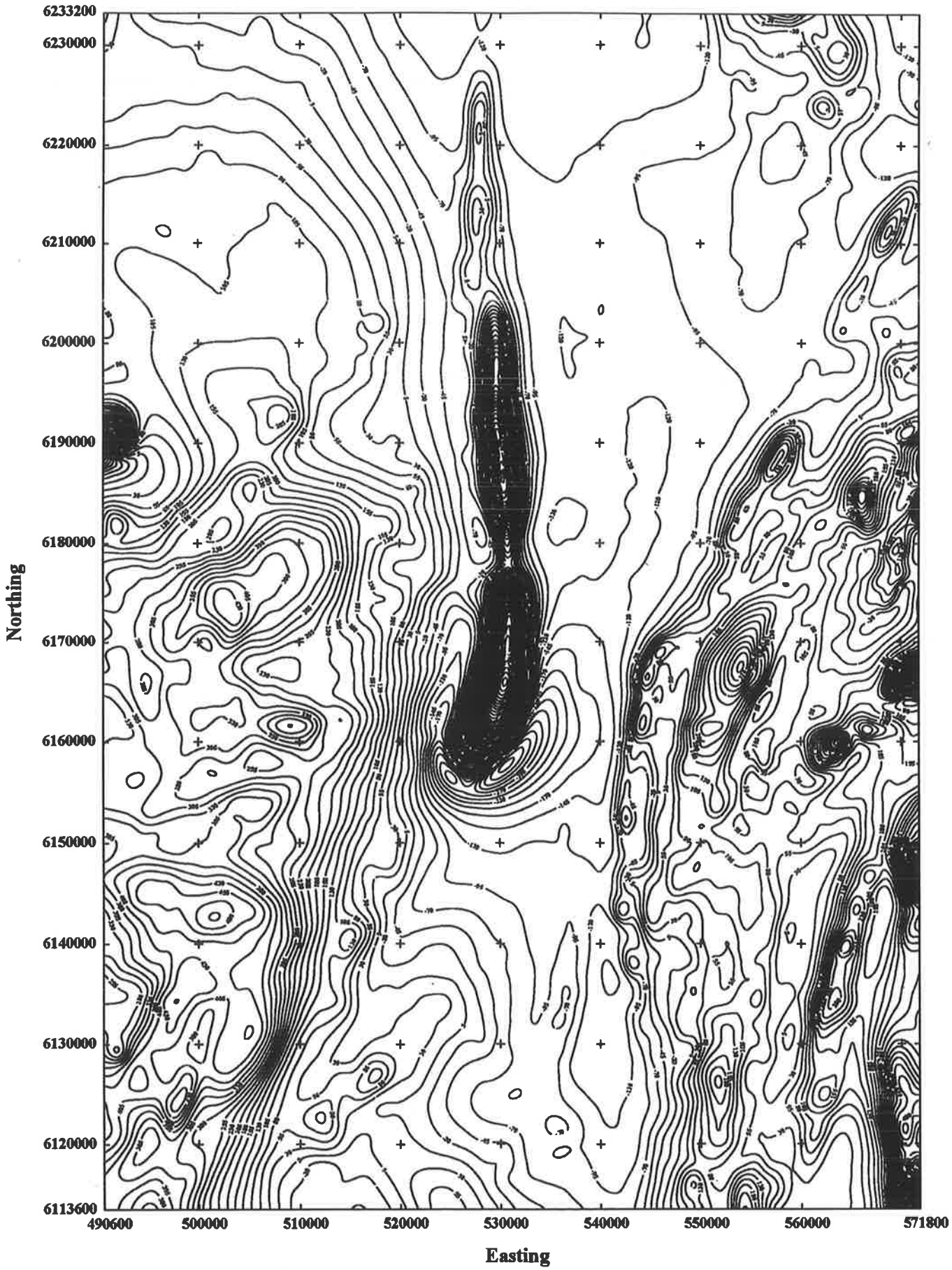

Figure 7.9: Contour map of total magnetic intensity of upward continuation 500m.

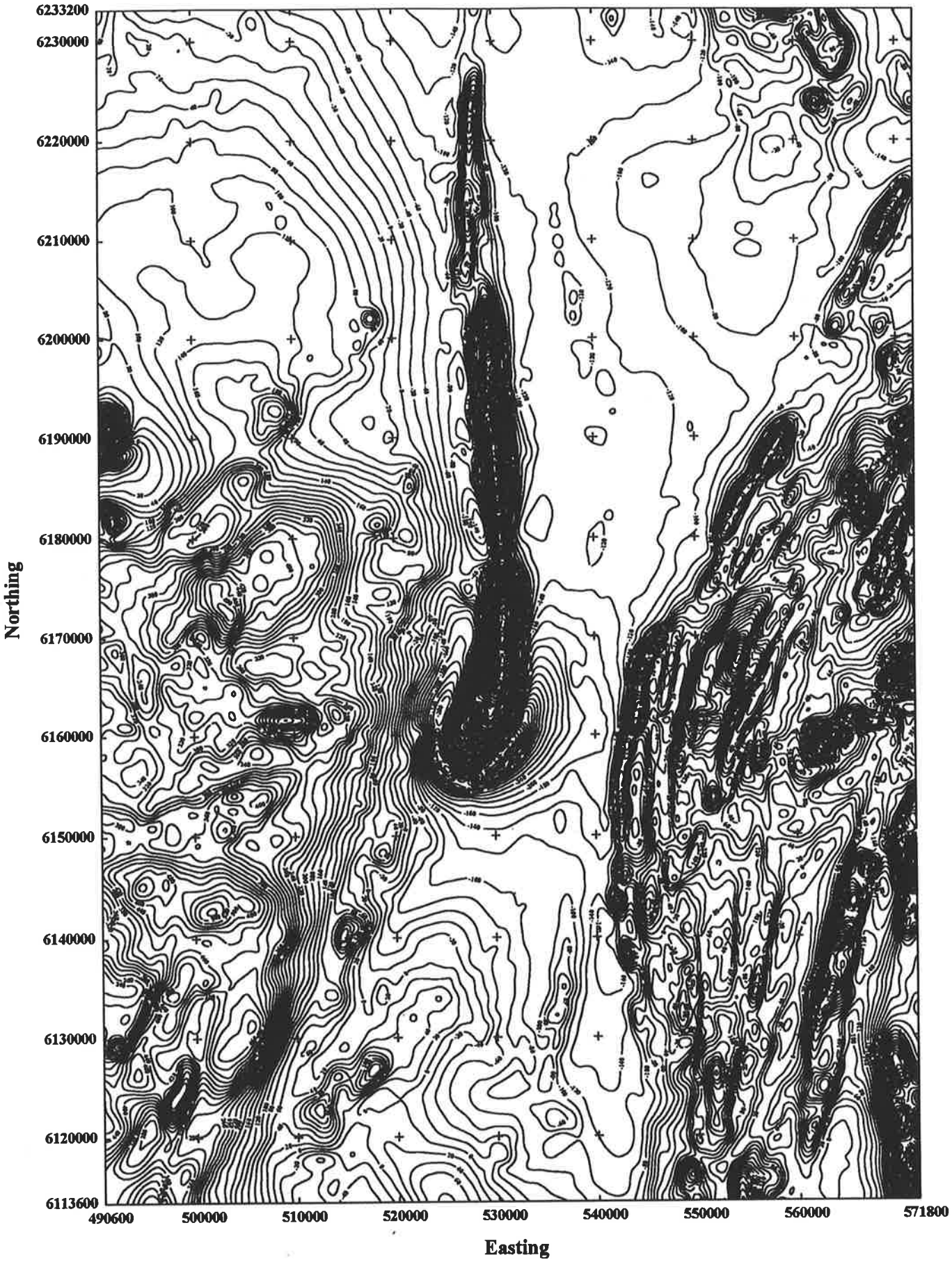

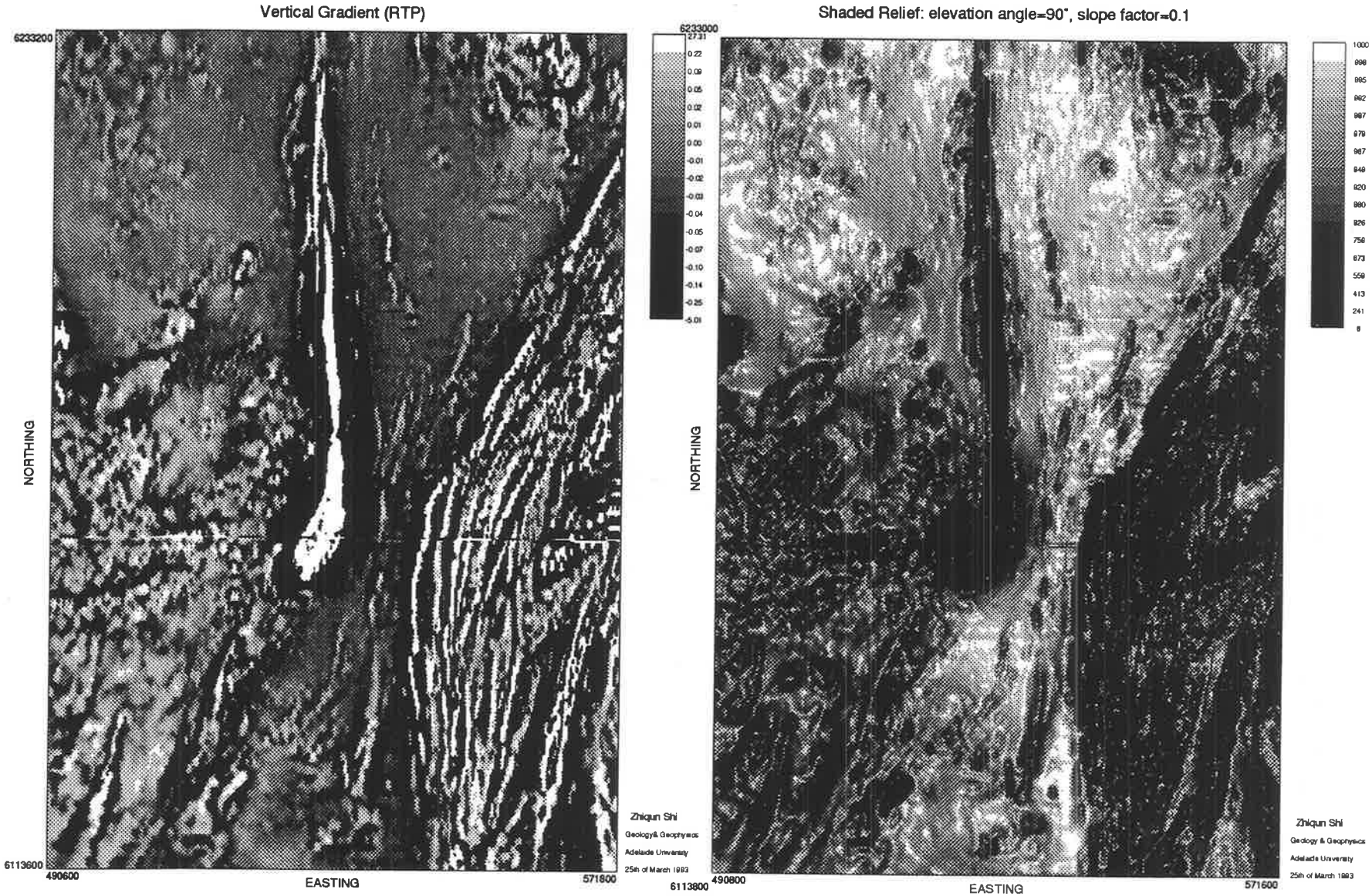

A: Lincoln Area Magnetic Vertical Gradient Anomalies

B: Lincoln Area Magnetic Anomaly Reduced to the Pole

Figure 7.11: Comparison of vertical gradient (RTP) with shaded relief (RTP)

Upward continuation

Upward continuation is a routine technique to suppress the anomalies with high frequency content and highlight the effect from the deep sources. The upward continuation 100 metres map with the contour interval 20 nT is given in Figure 7.5. The map shows a clearer patterns of the strong linear magnetic anomalies (on the eastern part of the area) than the original total magnetic intensity map (Figure 7.3) and this simplification of the anomaly map is one of the uses of upward continuation.

A sequence of upward continuation fields to heights of 2000 m, 1500 m, 1000 m and 500 m are computed and shown in Figures 7.6 to 7.9. Choice of the interval (500 m) of the upward continuation is based on the results from average depths of the magnetic basement calculated by means of energy spectral analysis (for details see Section 7.2.3). In the south-western part of the map showing average depth of magnetic basement, the maximum values of the depth are approximated to 1100 metres, by contrast, in the south-eastern part the maxima of the depths range from 500 to 700 meters (see Figure 7.13). There appears to be a difference in depth of 500 metres between the south-eastern and south-western part of the study area.

A set of upward continuation maps seems to support this postulate. By comparison of a sequence of upward continuation maps (2000 m, 1500 m, 1000 m, 500 m and 100 m), the patterns of the anomalies in the south-western (SW) part are similar to the shapes of anomalies in the south-eastern (SE) part which were additionally upward continued to 500 metres. In both SW and SE areas, there are clear boundaries between weak magnetic background and high magnitude anomalies which show obvious lineaments and similar fold structures. The major difference between SW and SE areas is in intensity of the background, the SW part has a higher regional field than the other.

Vertical gradient

Vertical gradient has a higher resolution of anomalies and enhances effects from shallow sources. As it also enlarges the noise in the data, it is often difficult to plot the vertical gradient using contours; the grey scale image is usually a better way to display the results. The detailed geological structures such as dykes, folds, faults and linear trends can be easily found from the image. The intensity of the anomalies can also be represented by a range of colour. So that the high or low amplitude of anomalies is clearly displayed.

The true amplitude of anomalies cannot be quantitatively characterised by using some other techniques such as shaded relief or directional filtering. The image map of the vertical gradient after reduction to the pole is give in Part A of Figure 7.11.

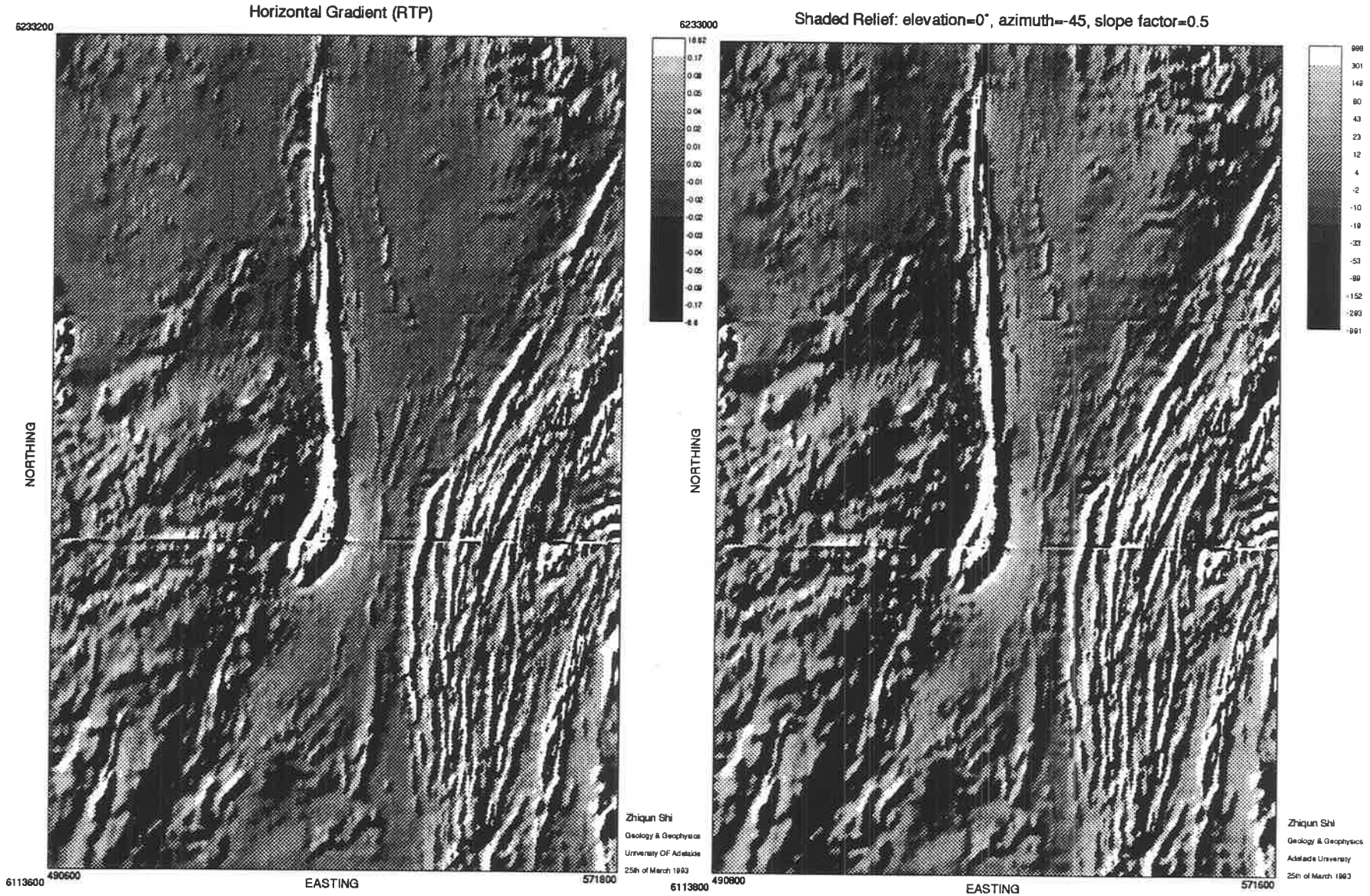

A: Lincoln Area Magnetic Horizontal Gradient (135°)

B: Lincoln Area Magnetic Anomomaly Reduced to the Pole

Figure 7.10: Comparison of horizontal gradient (RTP) with shaded relief (RTP)

7.2.2 Shaded relief method

Application of the method

Shaded relief method is a most effective approach to enhance and reveal various structures with specific strike directions. Kowalik and Glenn (1987) explain the principle and applications of the method. The technique creates the appearance of a topographic surface illuminated from a given direction. For each element of illuminated image, brightness is proportional to the cosine of the angle between the surface normal and the vector that points to the specified source of illumination. The method has been successfully applying to potential field data making the change of field strength appear similar to topographic relief.

Application of this method is controlled by three factors (elevation angle, azimuth angle and scalar slope factor), a study of the functions of the factors and how to choose them is given in Appendix G. A program named ILLUM to compute the shaded relief written by the author is used in the Department of Geology & Geophysics, the University of Adelaide and is also applied to the data in this project. The program for creating grey-images and printing them using a laser printer was developed by S. Rajagopalan and is used to produce all the image maps.

Based on the study, the best presentation of the image is obtained from this method by choosing the elevation angles (θ) of 90° and 0°. If the elevation angle is non-zero degrees, the azimuth angle (ϕ) plays a role of enhancing or subduing certain directional structures, in which the structures paralleled the azimuth are enhanced and the structures perpendicular to the azimuth are subdued.

The scalar slope factor (f_{ss}) controls the enhanced anomaly shape. If the anomalies to be studied are regional, the factor chosen is a large value with range from 0.01 to 1; if the object is local anomaly, the factor is a small value with the range from 0.001 to 0.01. Table G.1 (Appendix G) refers to the values for choosing slope factor both for magnetic and gravity cases.

The effect of the shaded relief method is similar to first derivative. If the elevation angle is less than 60 degrees, the technique has a similar function to the horizontal gradient; otherwise it is similar to vertical gradient. Figure 7.10 shows a comparison between horizontal gradient (directional angle = 135°) and the shaded relief ($\theta = 0°$, $\phi = -45°$ and $f_{ss} = 0.5$) in the Lincoln area. The two results are so similar that the patterns of the strong magnetic anomalies are identical. However the differences occur in the low amplitude anomaly area where the shaded relief method highlights the weaker anomalies. It appears that the shaded relief method has more advantages than the horizontal gradient method; since the calculation is much simpler and faster than the other and it also greatly enhances the weak anomalies.

The comparison between vertical gradient and shaded relief with elevation angle 90° is shown in Figure 7.11. Both of them enhance anomalies of shallow sources. The patterns of the shaded relief are characterised by follows:

1. they are similar to a contour map;

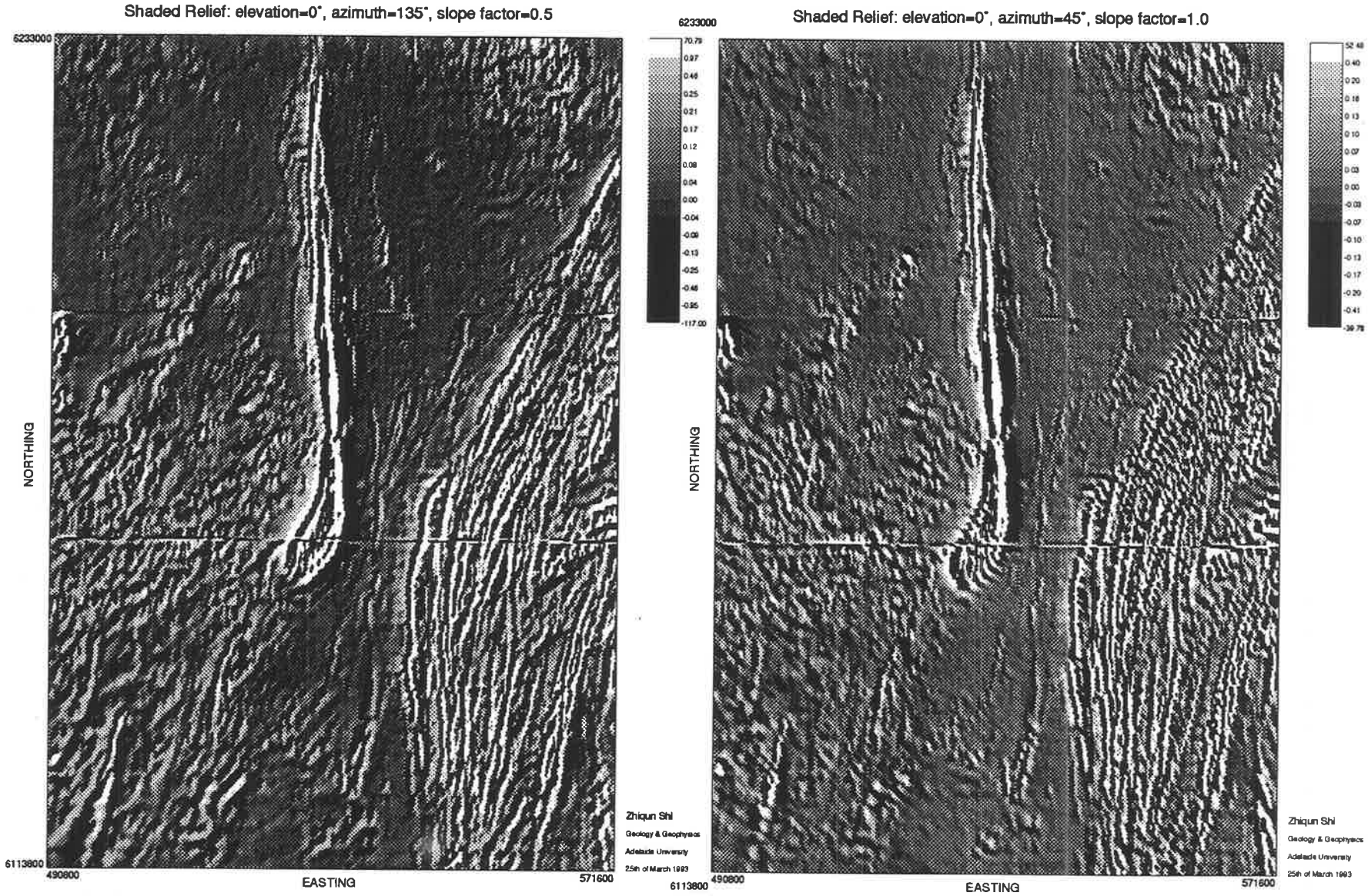

A: Lincoln Area Magnetic Vertical Gradient Anomomaly (RTP)

B: Lincoln Area Magnetic Vertical Gradient Anomomaly (RTP)

Figure 7.12: Two examples of shaded relief of vertical gradient (RTP)

2. linear brightness high inside an anomaly indicates the peak of the anomaly;
3. brightness high enclosed the anomaly outlines the boundary of the anomaly;
4. brightness low represents the steep gradient of the anomaly;
5. wide range of brightness high represents a flat and low amplitude anomaly zone.

These characteristics are discussed for more details in Appendix G. It is important to note that the brightness high or low in the shaded relief has no meaning to compare with high and low of amplitudes, but the vertical gradient does.

In order to enhance certain directional structures, the shaded relief of the vertical gradient gives clearer patterns (see Figure 7.12). In the previous sections, it was noted that there may exist lineaments with greater depths in the western part of the Lincoln area. Figure 7.12 appears to prove this point.

The elevation angles of 90°, and 0° associated with 4 different azimuth angles (0°, 45°, 90° and 135°) are used to produce the grey-image maps of the recently surveyed (1989) aeromagnetic data in the Lincoln, Yardea and Streaky Bay areas. The other grey-image presentation in the same areas of aeromagnetic anomalies and of radiometric data including total count, potassium, uranium, and thorium images. Because of limited space in the thesis, these results are not presented.

Conclusion of shaded relief method

The shaded relief method is effective in displaying linear structures, and in enhancing weak anomaly information. It can also dramatically outline the boundaries of causative bodies and locate centres of geological structures. The method has similar functions to the first derivative methods. If the elevation angle is 90°, the result can be compared with the vertical derivative. Both of them enhance near surface features. However the shaded relief method enhances effects of the weaker anomalies. The patterns of the shaded relief is more like a contour map, but the high or low brightness does not respond to the true amplitude of the field.

If the elevation angle is less than 60°, particularly 0°, the results match the horizontal derivatives. The advantages of the shaded relief method are as follows: the calculation is simple and much faster than the horizontal derivatives. By choosing the right slope factor and 0° elevation angle, the patterns in the strong amplitude parts from two methods are identical; in the part of weaker anomalies the image from the shaded relief is more effective.

The shaded relief method has many advantages, but care should be taken in choosing the parameters.

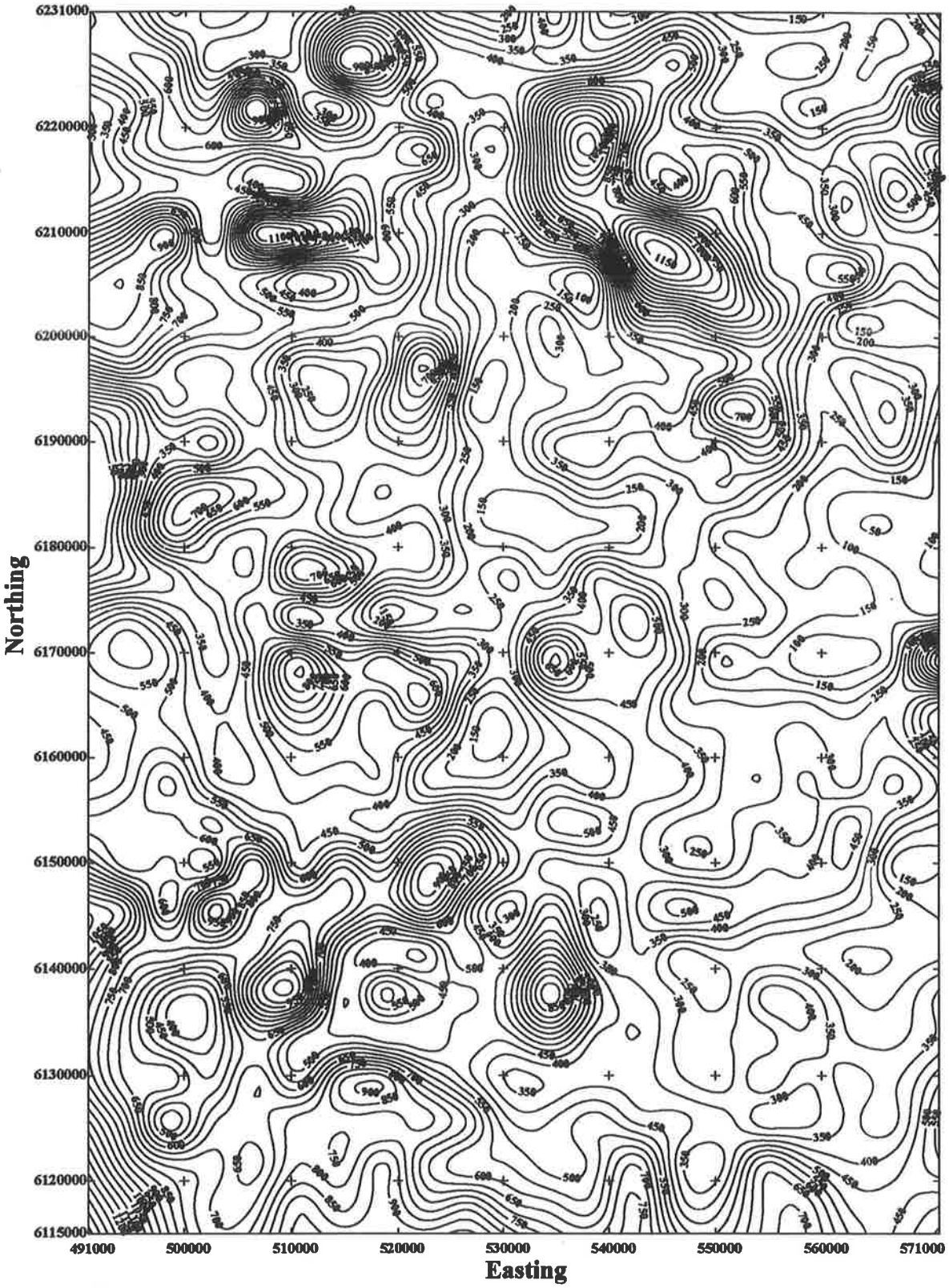

Figure 7.13: Shallow magnetic sources determined from spectral analysis Contour interval in 50m, Lincoln Area, South Australia

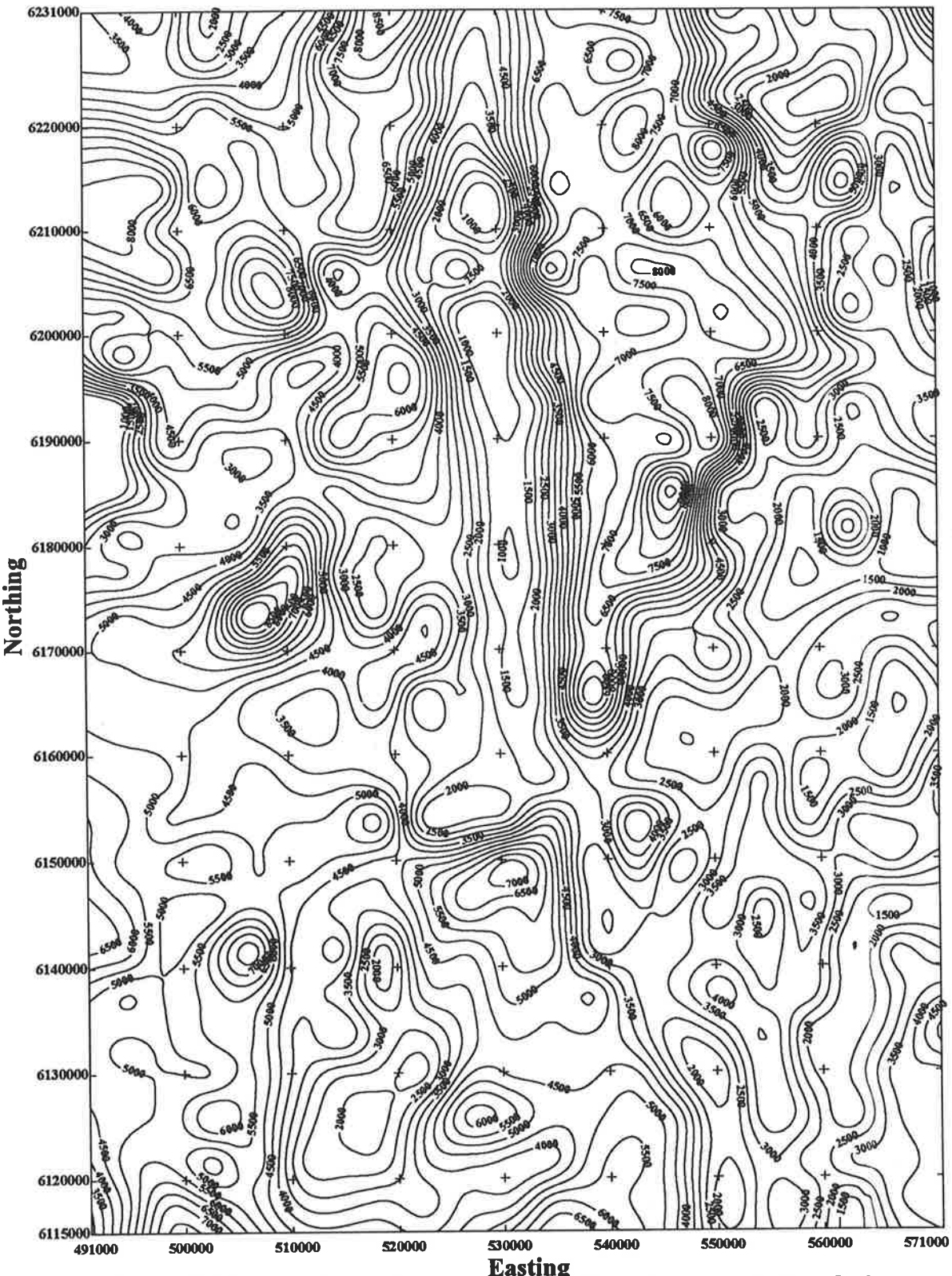

Figure 7.14: Deep Magnetic sources determined from spectral analysis Contour interval in 500m, Lincoln Area, South Australia

7.2.3 Application of energy spectral analysis

The energy spectral analysis is applied to the grid data in the Lincoln area. The principle of the technique was introduced in Section 2.6.2, and the model experiment and applications of the regional gravity data in Eyre Peninsula were given in chapters 5 and 6 respectively. For the application of magnetic field in this area, the size of a block of data is chosen as 8 km by 8 km (40 by 40 data points) and the size of the extended array ($25 \times 25km^2$) was chosen as 128 by 128 data points.

Two sets of average depths were calculated. The shallow depths range from 50 to 1400 metres and the great depths range from 750 to 10,000 metres. A mean altitude value of aircraft, 105 metres, was subtracted from the calculated average depths for both the shallow and deep magnetic sources. Contour maps of both level average depths are shown in figures 7.13 and 7.14 respectively. In general, distributions of the depth are coincident with the geological features. For instance, on the shallow depth map, the small values of the average depths occur on the top of the stronger intensity of magnetic anomalies and the deeper sources correspond to the area with low amplitude and weak anomalies. Most areas with outcrops and drill-holes reaching to the shallow basement correspond to the place with shallow values in the depth map. It is worth noting that the magnetic data can only provide the information of magnetic basement. Therefore shallow non-magnetic basement cannot be detected by magnetic techniques.

The spectral analysis is applied to the gridded data to construct the distributions of average depths for deep and shallow magnetic sources. This regional view of the magnetic basement in the depth provides a starting point to discover the more detailed information in the area. As the sample interval of the grid data is 200 m, it is impossible to obtain detailed depth information of less than 100 m (below ground level). The depth of soil cover and weathering in a large area can easily be obtained by using an automatic interpretation method such as AUTOMAG.

7.3 Application of AUTOMAG

AUTOMAG was originally used to process total magnetic intensity data. In order to reduce the effect of the interference from the adjacent anomalies and to remove the influence from the background field, the first vertical derivative of the field was also interpreted using AUTOMAG. Three types of initial bodies: dyke, edge and thin plate, which cover most cases of geological situations, can be used as the model for the source of the real magnetic anomalies.

Before examining the results of the new technique to the Eyre Peninsula data, a general explanation of the procedures involved is provided here. This involves describing clearly the geological problem which is to be solved and the sequence of steps to produce the information required using AUTOMAG.

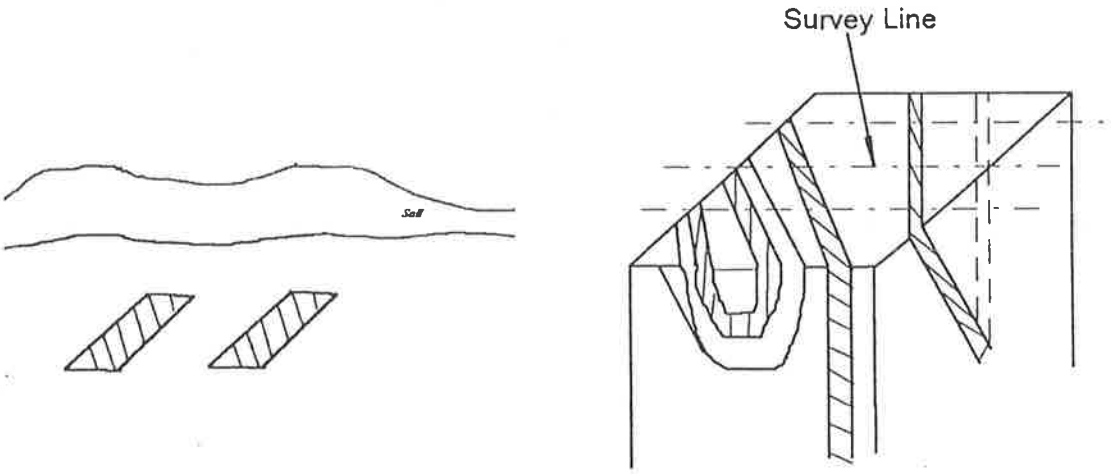

(A) (B)

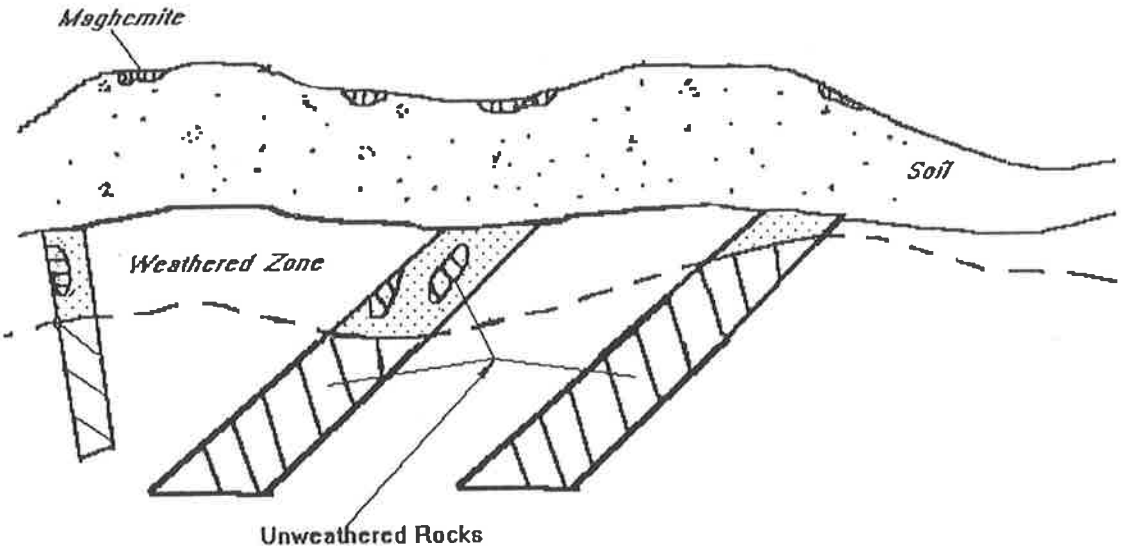

(C)

Figure 7.15: Simplified geological situations.
A: Unweathered rocks and the overburden.
B: Bodies with complicated shapes and the strikes of bodies non-perpendicular to the flight lines.
C: Overburden pocked of maghaemites, weathered zone and fresh magnetic rocks.

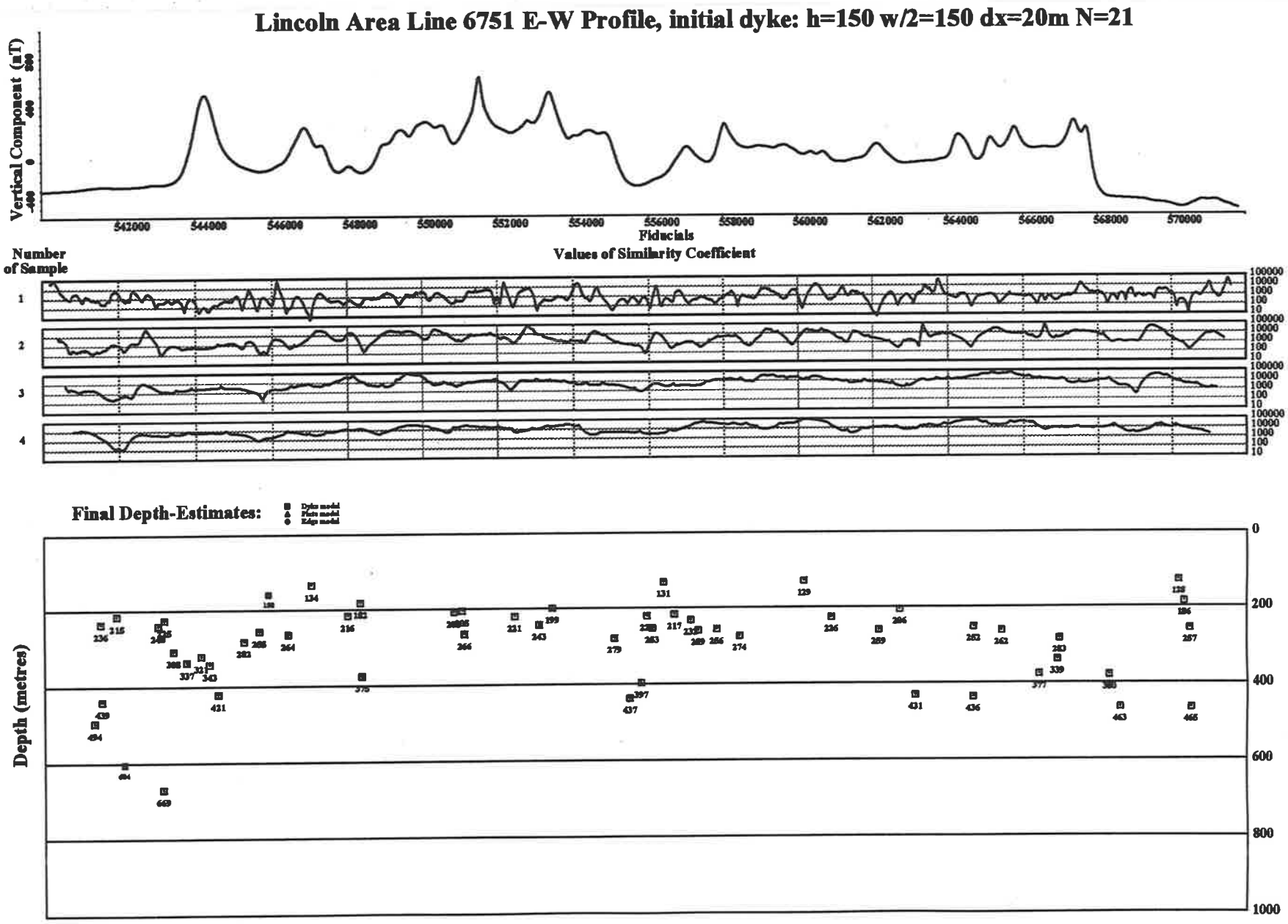

Figure 7.16: Example of depth estimation using AUTOMAG

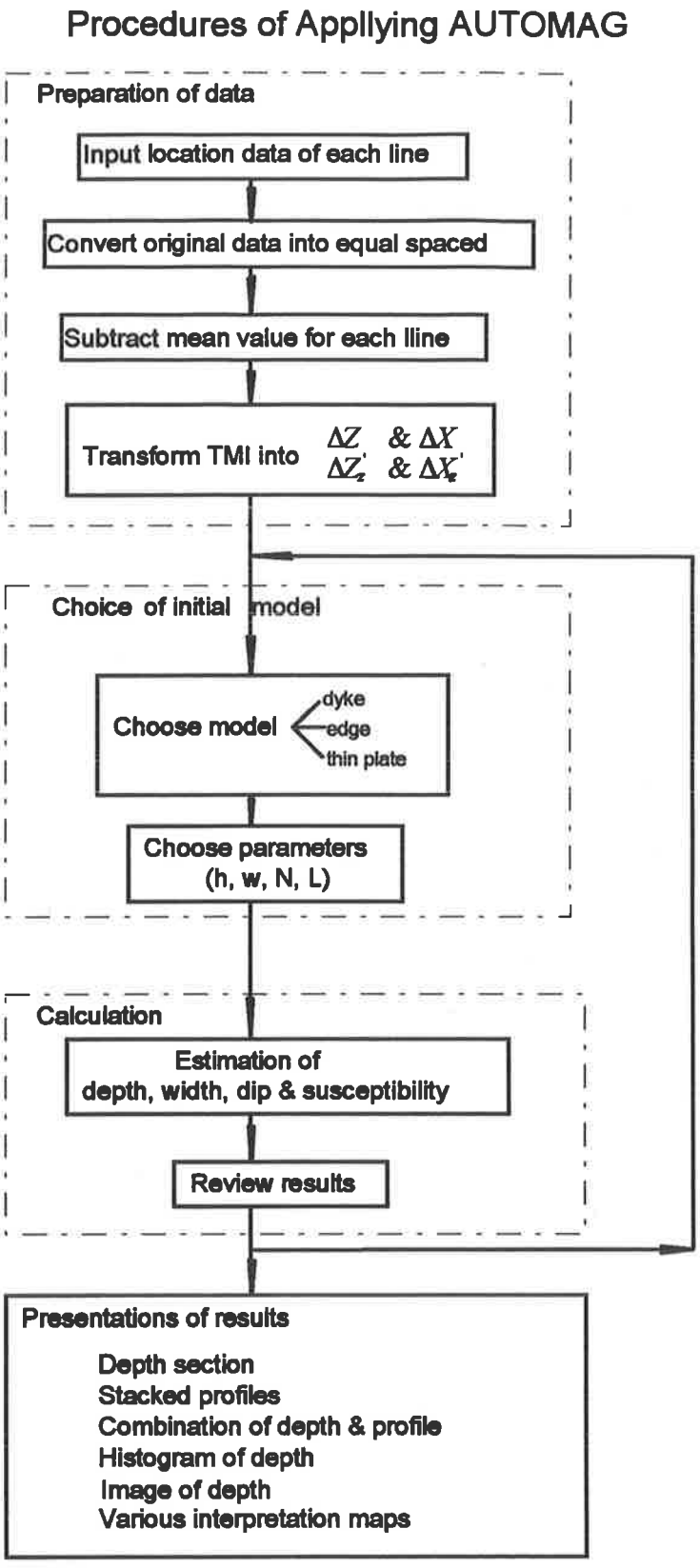

Figure7.17: Flow chart showing procedures of applying AUTOMAG

7.3.1 Geology and physical properties of overburden

1. The aim is to estimate the top of magnetic basement; there are a number of problems:
   (a) bodies may be deeper than the bottom of the soil cover (see Part A in Figure 7.15),
   (b) bodies may appear deeper because the strike is not at right angles to the flight line or because the shape of the body is complex (see Part B in Figure 7.15),
   (c) bodies may appear shallower because the assumptions about body shape are wrong (see depth limited body in Part B, Figure 7.15) or because of the effect of noise on the record.
2. If the basement rocks have been weathered then the magnetic basement may be the depth of weathering which is deeper than the bottom of the soil cover (see Part C in Figure 7.15).
   There may be three separate magnetic levels which are detected from the magnetic profile:
   (a) the land surface where there may be pockets of maghaemite in the soil and stream channels,
   (b) unweathered rocks occurring above the base of weathering,
   (c) the base of the weathered zone.

The complexity of the problem may be compared with some of the procedures encountered in the interpretation of reflection seismic data which also includes problems due to the variable thickness of the weathered zone, multiple reflections, velocity changes and sideswipe.

7.3.2 Procedures of applying AUTOMAG program

AUTOMAG is not a method which will give instant answers but is a method of processing magnetic data which will reveal more information than is seen in the untreated data. A profile of processed data in Figure 7.16 makes this point clear.

The sequence of steps (Figure 7.17) involved in the application of the program using a SUN SPARC 2 workstation and a Vax-780 computer is:

- Step 1: Preparation of magnetic profile data to convert them into a form which can be processed by the algorithms.
  1. Located data from the flight record are read into the memory with the necessary annotations of line number, coordinates of the easting and northing, total magnetic field and aircraft altitude.
  2. In order to satisfy the requirements of the technique, all sets of line data are transformed or interpolated into equal-spaced data using Lagrange or linear interpolation algorithms.

3. The mean value of the profile is subtracted from each data point; this is required for the use of FFT technique.
4. The new data set, total magnetic intensity (TMI), is then transformed into vertical and horizontal components (ΔZ & ΔX) or vertical gradients of the vertical and horizontal components ($\Delta Z'_z$ & $\Delta X'_z$) by means of FFT algorithm (the reasons for using these components are explained in Chapter 3). Note that in the profiles it is ΔZ or $\Delta Z'_z$, and not the TMI, which are plotted in the output graphs (Figure 7.16).

- Step 2: Choice of initial model

  The parameters used must be selected so that they are appropriate for the problem to be solved.

  1. The type of model must be selected, a dyke or edge (and very occasionally a thin plate).
  2. The initial depth h, width w, number of data points to cover the window N, number of sample intervals S_n and window length L which is defined as $L = dx \times N \times S_n$ (dx: the original sample interval) must be chosen to sample a single anomaly adequately.

  It may take a few test runs to set up the initial parameters of models for the entire data set, after which the calculations for the whole data set are simple and fast.

- Step 3: Calculation of depth and other parameters of magnetic bodies

  According to the characteristics of the magnetic anomalies on a profile, the calculations are chosen from a set of transformed components (ΔZ & ΔX) and/or gradients ($\Delta Z'_z$ & $\Delta X'_z$) of magnetic data. As a result, a set of estimations of parameters for magnetic bodies which include depth, width, dip and susceptibility, are determined.

  Note that the four estimated parameters are only applicable to the dyke model, the width is not applicable to the edge model and dip is not applicable to the thin plate model. Additionally, the estimated dip and susceptibility are obtained by assuming induced magnetisation.

- Step 4: Presentation of results

  The processed results must be presented in a fashion which allows the interpreter, i.e. geologist or mineral explorer, to appreciate easily the significance of the results; this is done by presenting the results

  1. in a series of separate sections,
  2. in a series of stacked sections, and
  3. other types of maps.

  The details are discussed later.

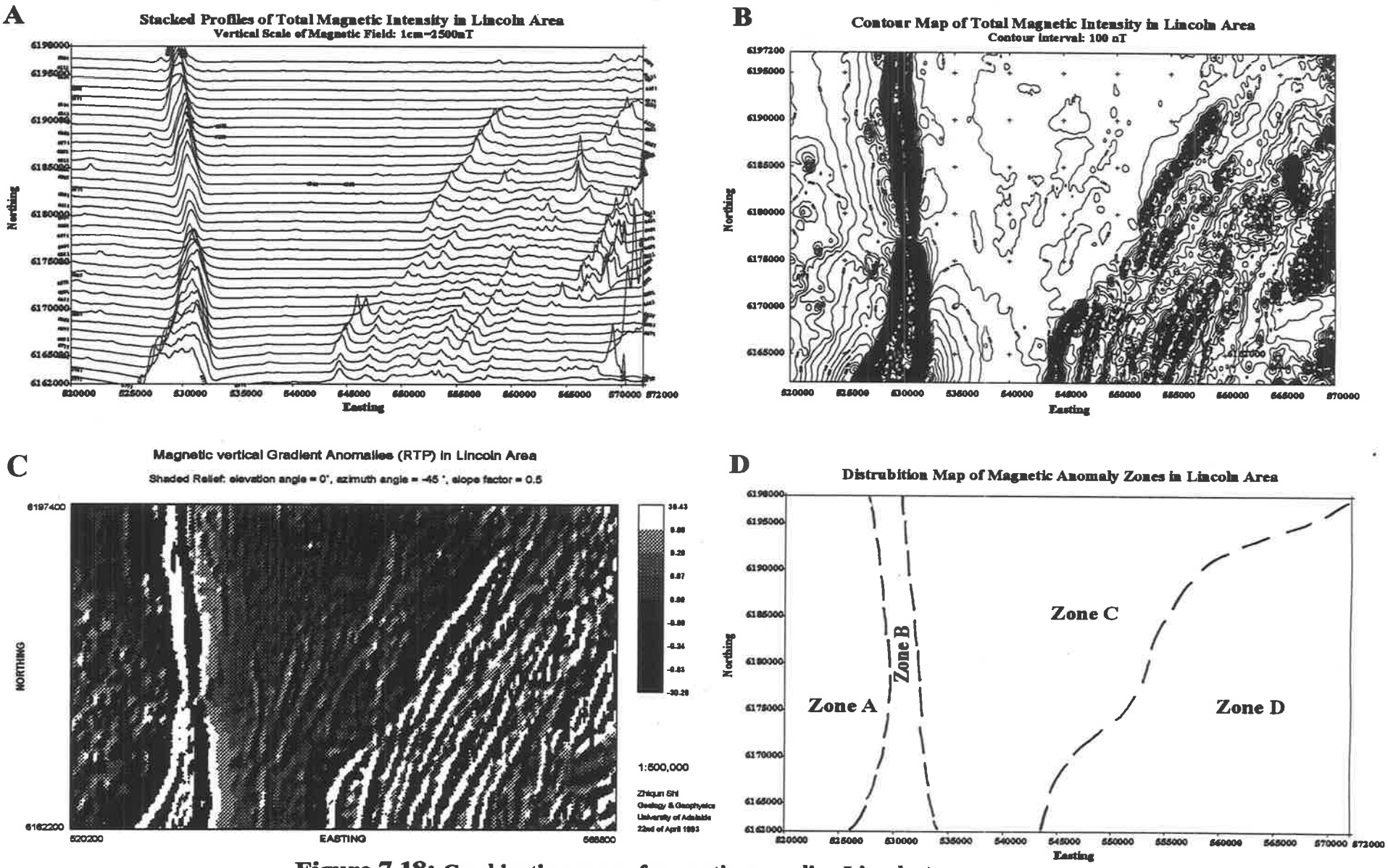

Figure 7.18: Combination maps of magnetic anomalies, Lincoln Area

Table 7.1: Initial parameters of chosen models for AUTOMAG

Type of Model	Type of Fields	h (m)	$\frac{w}{2}$ (m)	dx (m)	N	S_n
Dyke	ΔZ & ΔX	150	50-150	20	21-31	1, 2, 3, 4
	$\Delta Z'_z$ & $\Delta X'_z$	150	50-150	20	17-21	1, 2, 3, 4
Edge	ΔZ & ΔX	150	50-100	20	19-21	1, 2, 3, 4
	$\Delta Z'_z$ & $\Delta X'_z$	150	50-100	20	17-19	1, 2, 3, 4

7.3.3 Practical matters in the method

The study area (see Figure 7.18) includes several different magnetic zones (Part D in Figure 7.18) in which the data needed to be processed differently in each area. They are shown in the stacked profiles (Part A in the figure), contour map (Part B) and shaded relief of vertical gradient (Part C), which are described as follows.

- End of eastern part: the zone with quiet magnetic background anomalies and some isolated anomalies arise from 3-D bodies (Zone A shown in Part D);
- Eastern part: cucumber shaped broad and high magnetic amplitude anomaly in which at the end of the southern part the width of anomaly is greater than 5 km and at the north the width is about 1 km (Zone B shown in Part D);
- Central part: a low amplitude anomaly area with a few weak linear anomalies (Zone C shown in Part D);
- Western part: very strong magnetic lineament zone with the width of the anomalies ranging from 200 to 700 metres (Zone D shown in Part D).

Most of the anomalies in the area are suitable for interpretation by the use of AUTOMAG in which the dyke model was applied to all the linear anomalies and the edge model was used to calculate the broad cucumber shaped anomalies. A total of 35 lines of 50 km length profiles were processed for both the data of components (ΔZ & ΔX) and vertical gradients ($\Delta Z'_z$ & $\Delta X'_z$) by using dyke and edge models. The initial parameters of chosen models in the whole area are shown in Table 7.1.

The initial depth of 150 metres was chosen; it is the sum of the average altitude level (100m) and the normal depth of weathering (50m). The chosen half width of the body was based on the shape of the anomaly: the broad body was used for searching wide anomalies and the narrow body then for the narrow anomalies. The window lengths (the product of the sample interval (dx), number of points (N) and the number of samples (S_n)) were defined for locating varied length anomalies ranging from 400m to 2000m.

Lincoln Area Line 6111 Depth estimation from different types of dykes

A

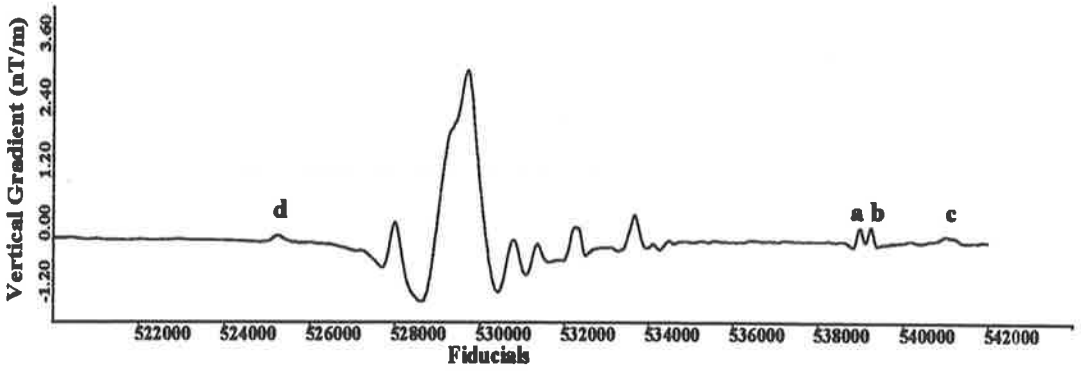

B

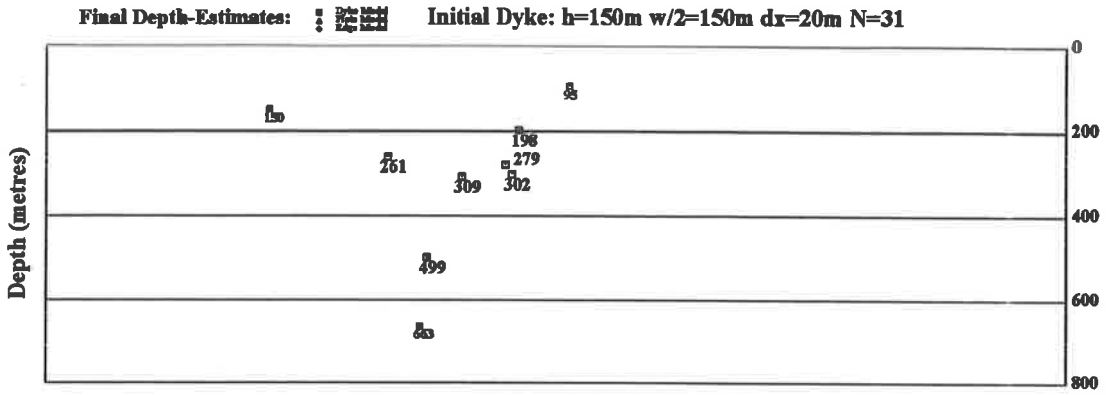

C

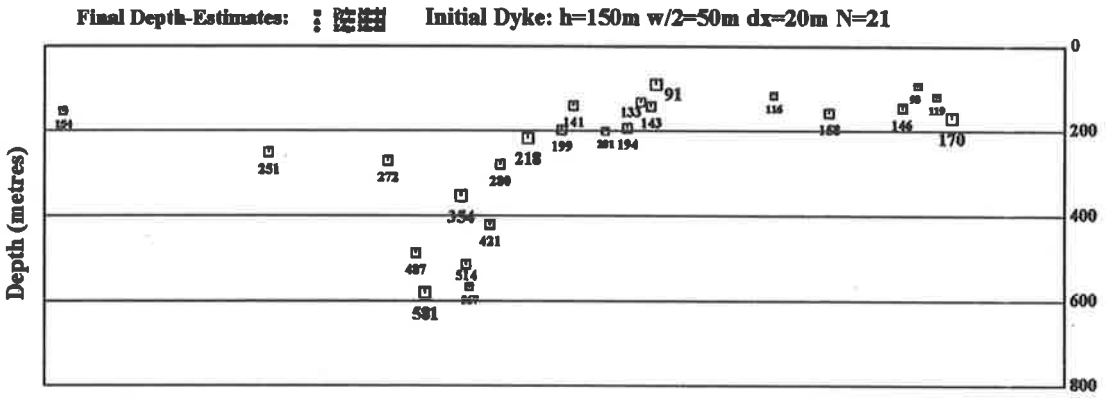

D

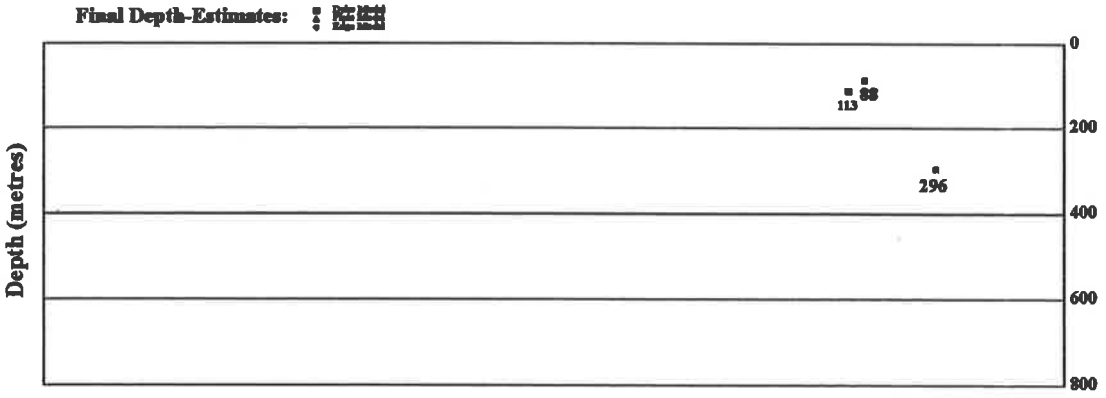

Figure 7.19: A: Vertical gradient profile. B: Using thick dyke. C: Using thin dyke. D: Depth calculated by directly reading coordinates

The first step for the data processing was to run AUTOMAG through the entire profile data, ΔZ & ΔX and/or $\Delta Z'_z$ & $\Delta X'_z$, using different types of initial models and a series of maps was produced, which are shown in Section 7.3.5. The next step was to check the results, to find small anomalies which have been missed, to fill the gap where needed to do more detailed work. Figure 7.19 illustrates this procedure.

- The vertical gradient of the magnetic field in the flight line 6111 in the Lincoln area is shown at the top of the graphs.
- In order to detect the depth of the main body in the profile, a wide dyke, in which both the depth (h) and the half width ($\frac{w}{2}$) are 150 metres, was applied to search centres of anomalies. The results from the first step are displayed in Part B. Obviously some small and low intensity magnetic anomalies were missed.
- Another set of parameters of a narrow dyke ($h = 150m$ and $\frac{w}{2} = 50m$) was chosen to repeat the calculation of the profile. The estimates of the depths are displayed in Part C. Most small and narrow anomalies were detected but a few of them (a, b, c shown in Part A) were still missed.
- AUTOMAG provides a semi-automatic function in which the centre of the anomaly is specified by the operator. This is easily done as the coordinates of the magnetic anomalies to be checked can be read directly from the profiles, and the depths of these causative bodies can be determined. This semi-automatic procedure is very flexible and useful for computing depths from specific anomalies. Two very small anomalies (a & b shown in Part A) between easting 538000 and 540000 and another low intensity anomaly (c shown in Part A), which were missed on the automatic processing, have been calculated; the results are shown in Part D.
- By combining the information shown in Parts B, C and D, a preliminary estimate of depths is obtained. Note that the depths are not measured from the ground but from the sensor height in the aircraft.

After these procedures some further work was required:

1. corrections were made for the effect of strike direction of the anomalies if necessary (for details see Appendix E) and the altitude of aircraft along the flight lines and other geological factors;
2. the mean depth of surfaces was identified on each flight lines from the AUTOMAG plots;
3. errors and discrepancies in depths were checked using forward modelling (details are given in Section 7.3.4);
4. the results were compared and reconciled with depths known from drilling (see Section 7.4) or seismic studies.

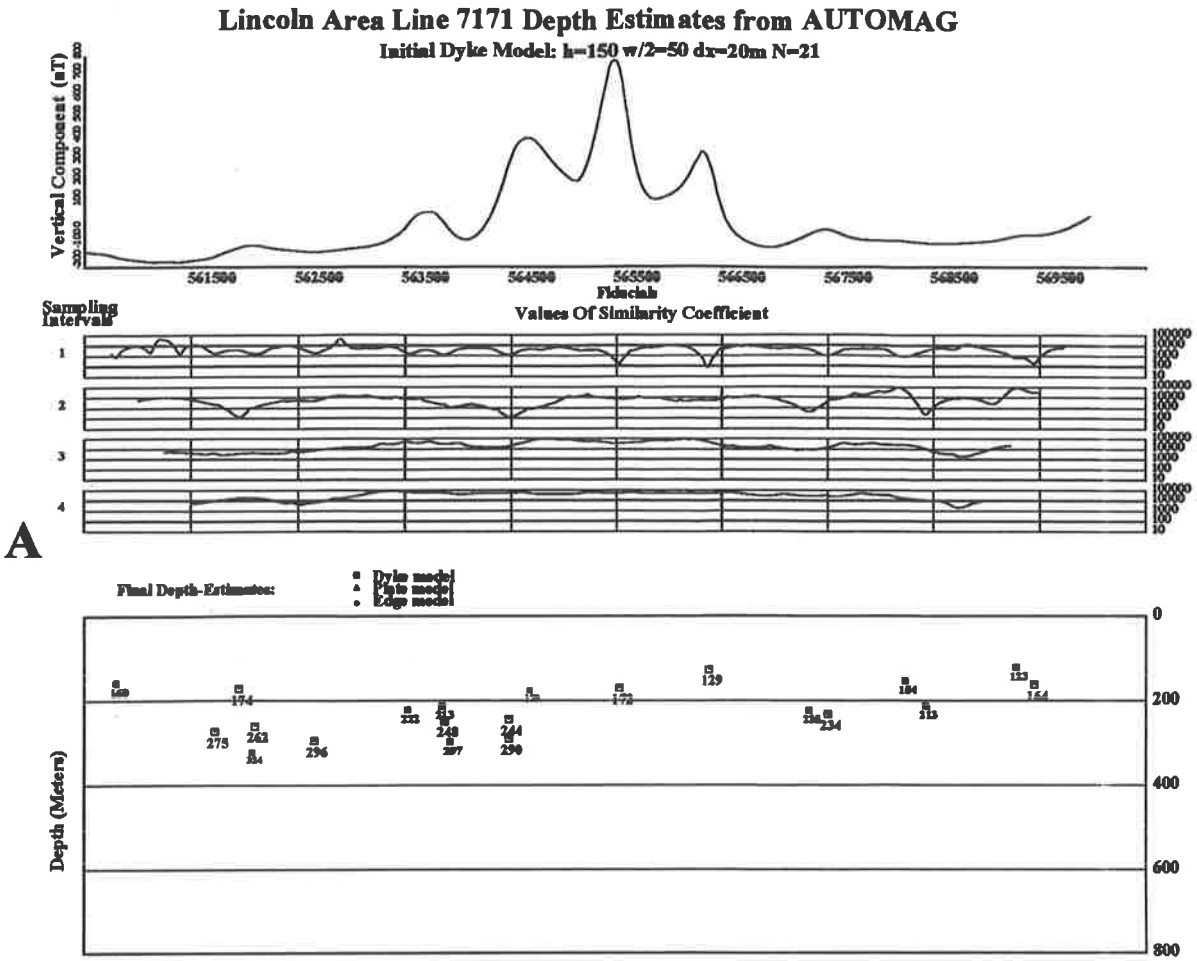

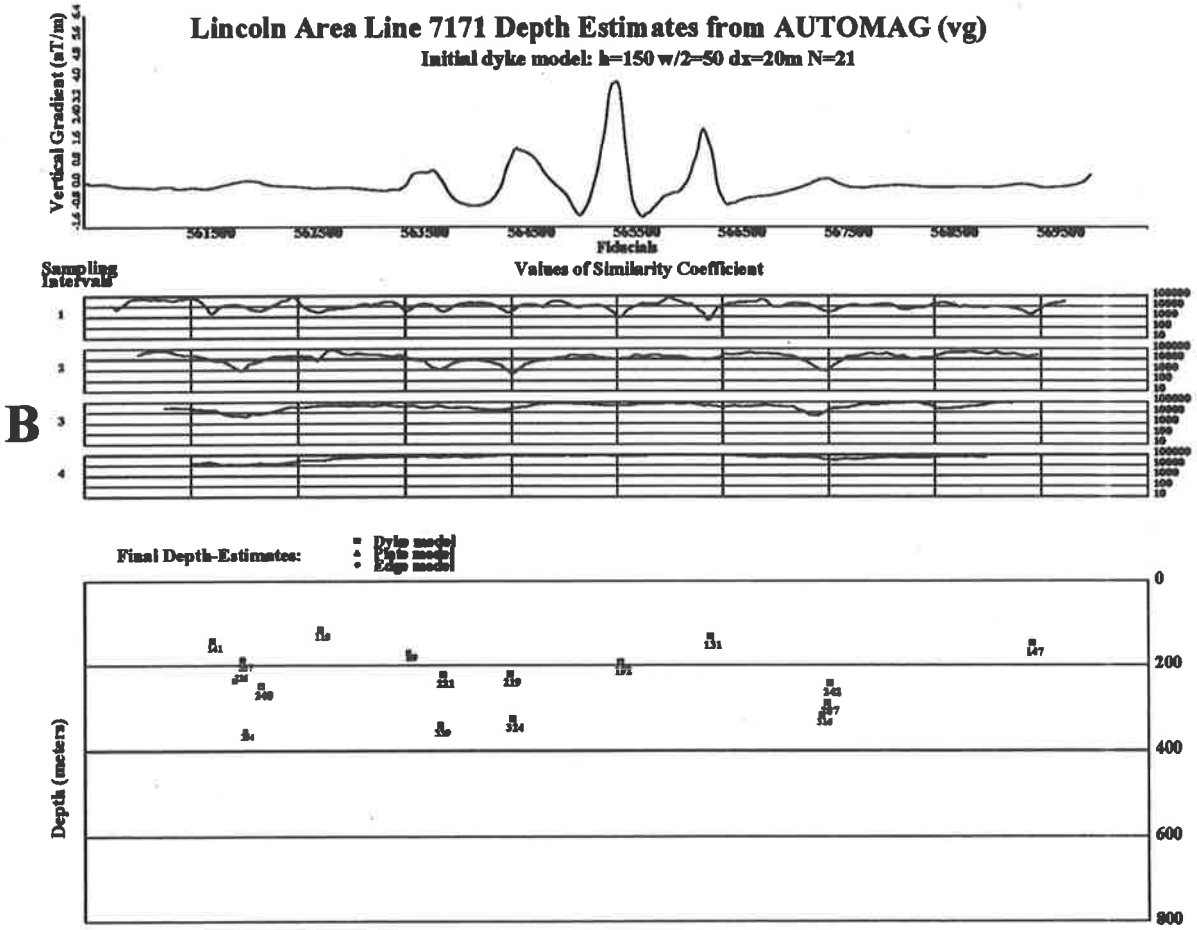

Figure 7.20: A: Depth from component data
B: Depth from vertical gradient data

7.3.4 Further use of the method

The purpose of using AUTOMAG is actually to deal with the large amount of data and to provide preliminary interpretation results. In order to correctly adjust the differences or errors from the varied results (see parts B and C in Figure 7.19: to investigate discrepancies in the depths of anomaly **d**) and to provide a better estimate, it may be necessary to use a forward modelling program.

Because AUTOMAG can provide all the parameters of simple bodies very quickly, it makes it possible to establish a set of initial parameters which are an excellent starting point to run forward modelling or inversion programs. An example of combining AUTOMAG and GAMMA, a forward modelling program of magnetic field written by Paine, is shown in Figures 7.20 and 7.21.

The section of the magnetic profile is taken from Lincoln area line 7171. The results calculated from TMI data by using AUTOMAG are given in Part A (Figure 7.20) and the results from the vertical gradient data is shown in Part B (Figure 7.20). Figure 7.21 shows the results by using GAMMA, the calculated models are selected from the results shown in Figure 7.20. In Part A and Part B (see Figures 7.21), the parameters of forward models are directly taken from the estimates provided by AUTOMAG. In general, the theoretical curves match the observed profiles reasonably well. However the results still need to be improved; after slight modification of the parameters, a better match for both TMI and vertical gradient anomalies was achieved (Part C and Part D in Figure 7.21). An initial estimate of parameters obtained from AUTOMAG makes the interpretation using forward modelling very much faster, and more efficient, accurate and reliable.

7.3.5 Presentation of depth information

While the large amount of depth information provided by using AUTOMAG, there was a problem in relation to presentation of large amounts of data. After trying a number of alternative approaches the present system was developed in two parts; one showing the results in a series of individual profiles and the other presenting the whole data set as a map or stacked profiles.

1. Profile section presentation

   The profile section (see Figure 7.16 and Figure 7.19) is the most informative presentation. It shows:

   1) the profile of the transformed vertical magnetic field or vertical gradient along the flight line,

   2) selection criteria curves (similarity coefficient) and

   3) a depth section showing the estimated depth are plotted. From this presentation, it is possible to see both the basic data and the results.

Figure 7.21: Forward Modelling using results from AUTOMAG line 7171, Lincoln Area

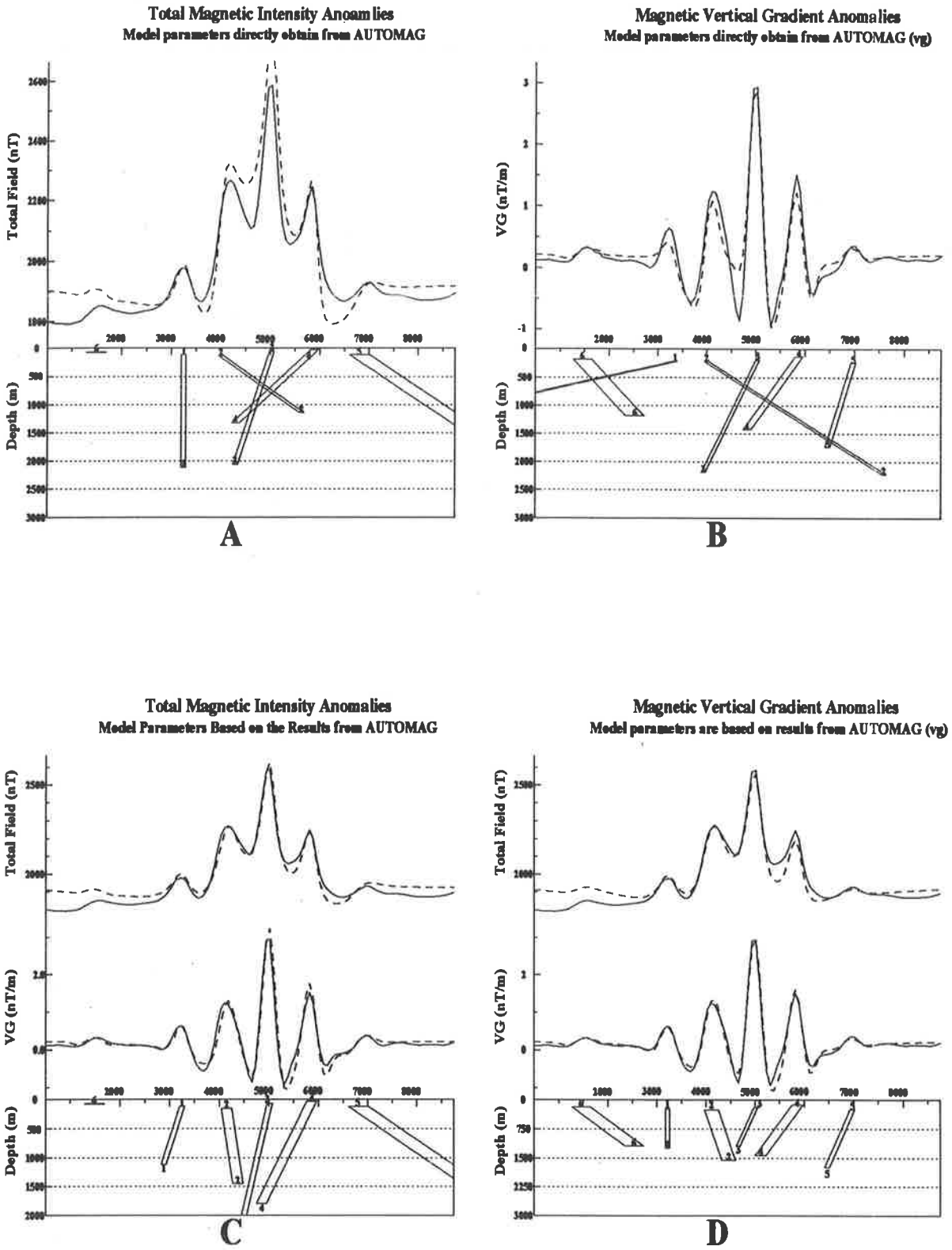

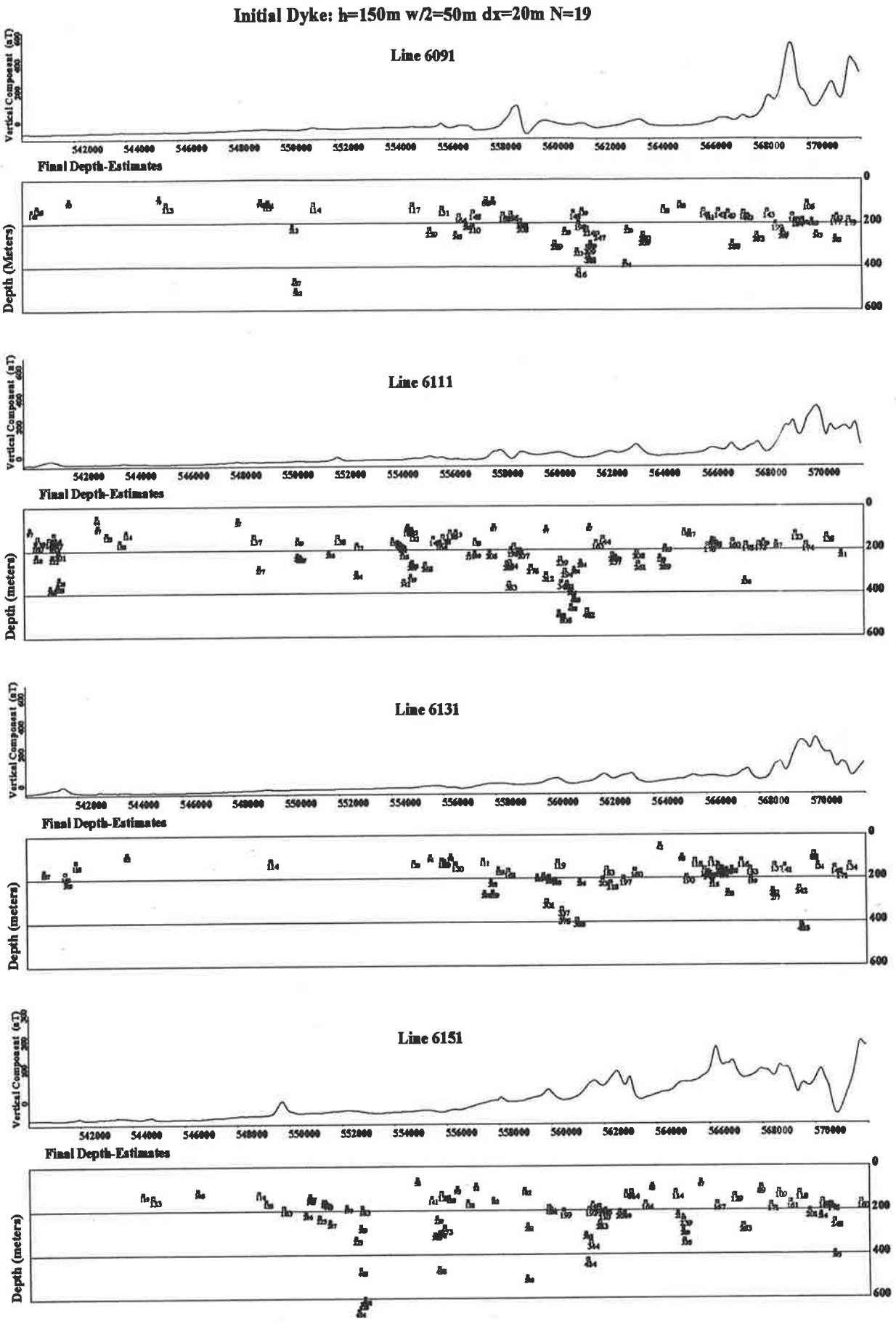

Figure7.22: Combination Map of Depth Estimates and profiles, Lincoln Area

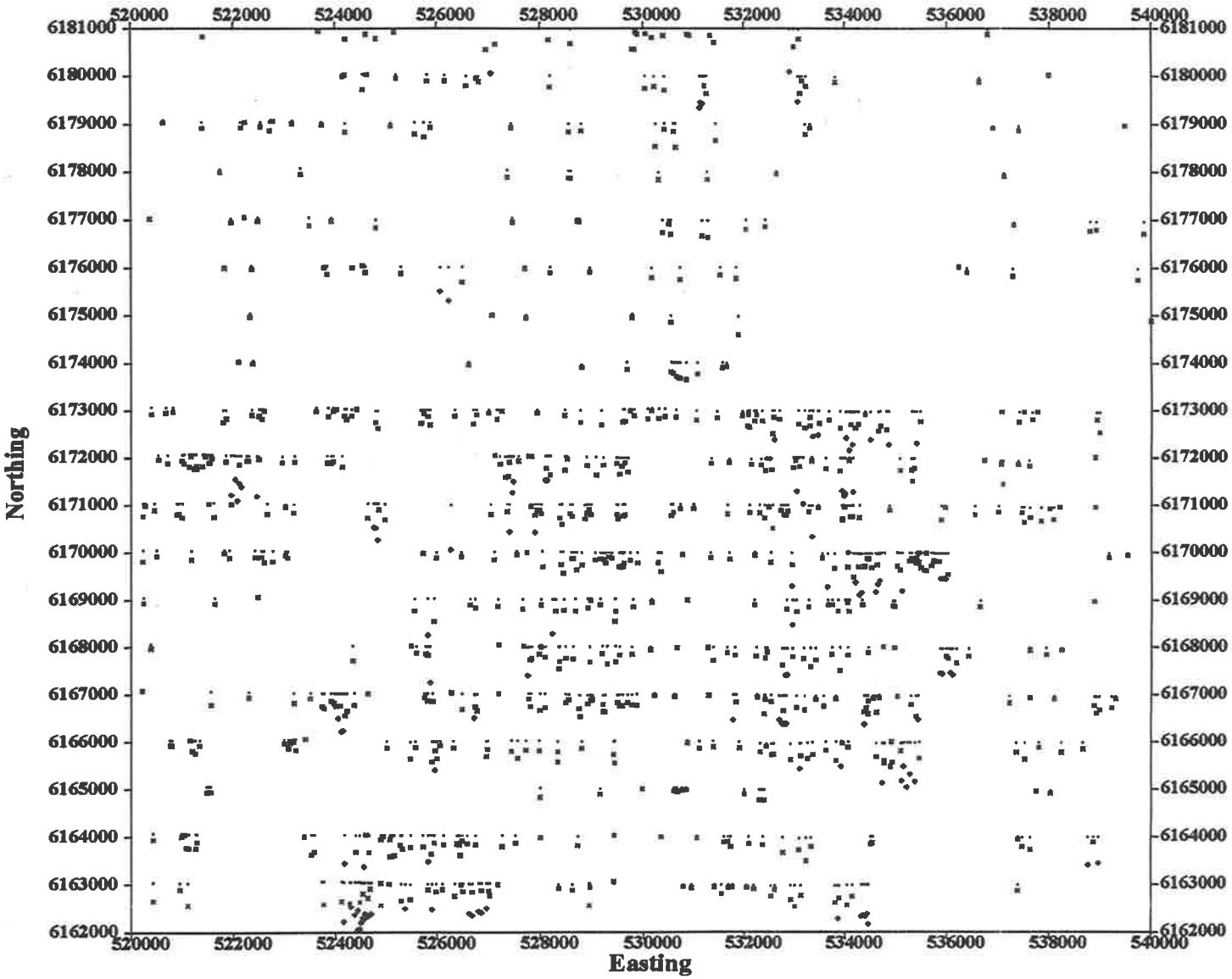

Figure 7.23: Stacked Profiles of Depth Estimation, Lincoln Area.

(a) The depth estimated from different models can be presented by different symbols (square for dyke, diamond for edge and triangle for thin plate); the two examples only show the dyke model.

(b) The size of the symbol in the plot varies is based on the values of similarity coefficients; the bigger the size, the smaller the value of the coefficient and vice versa, i.e. the larger symbols indicate a better match between the model and observed curves.

(c) The plot also shows details of the sample interval (dx), the number of data points (N) and the number of samples (S_n).

The section created by AUTOMAG is then used by interpreter like to a seismic section to select one, two or three depth levels and to decide if, and where, forward modelling or other interpretation methods should be applied.

2. Map presentation

Several types of maps are used to present the depth information from a number of lines or the whole data set at one time.

(a) Combination map

It can be presented as a depth combination map (Figure 7.22) which is composed of magnetic anomalies and their corresponding depth information along a set of profiles. This type of map displays the relationships of the depths of profiles to one another. Note that the difference in the horizontal and vertical scales.

(b) Stacked profiles

The results can also present as a form of stacked profiles (Figure 7.23) which show the depths as well as their locations on each line related to other lines in the area. The depth value and position are presented by a number of symbols; in the example the dot represents the location, the cross represents the depth with the value less than 500 metres and the diamond indicates the depths greater than 500 metres. In order to distinguish each profile, the survey lines are shown by linking to these locations. The scales of x-axis (Easting) and z-axis (both Northing and depth) are identical. Stacked profiles can be plotted at 1:50,000 or 1:100,000 scale to match standard maps. Figure 7.23 shows the results only in part of the area, because the total area is too large to be displayed on a single page at a suitable scale.

3. Depth interpretation map

Marking the depth values, which are selected by the interpreter on an interpretation map, is another form of displaying results. The author created such a map for the cucumber shaped anomaly in Lincoln area, the map provides information of depth along each flight lines.

7.3.6 Information of dip and other parameters

It is worth noting that the additional information about dip, width and susceptibility of magnetic bodies may produce very important information for other research in the area but they are of secondary concern in this work and are dealt with only briefly.

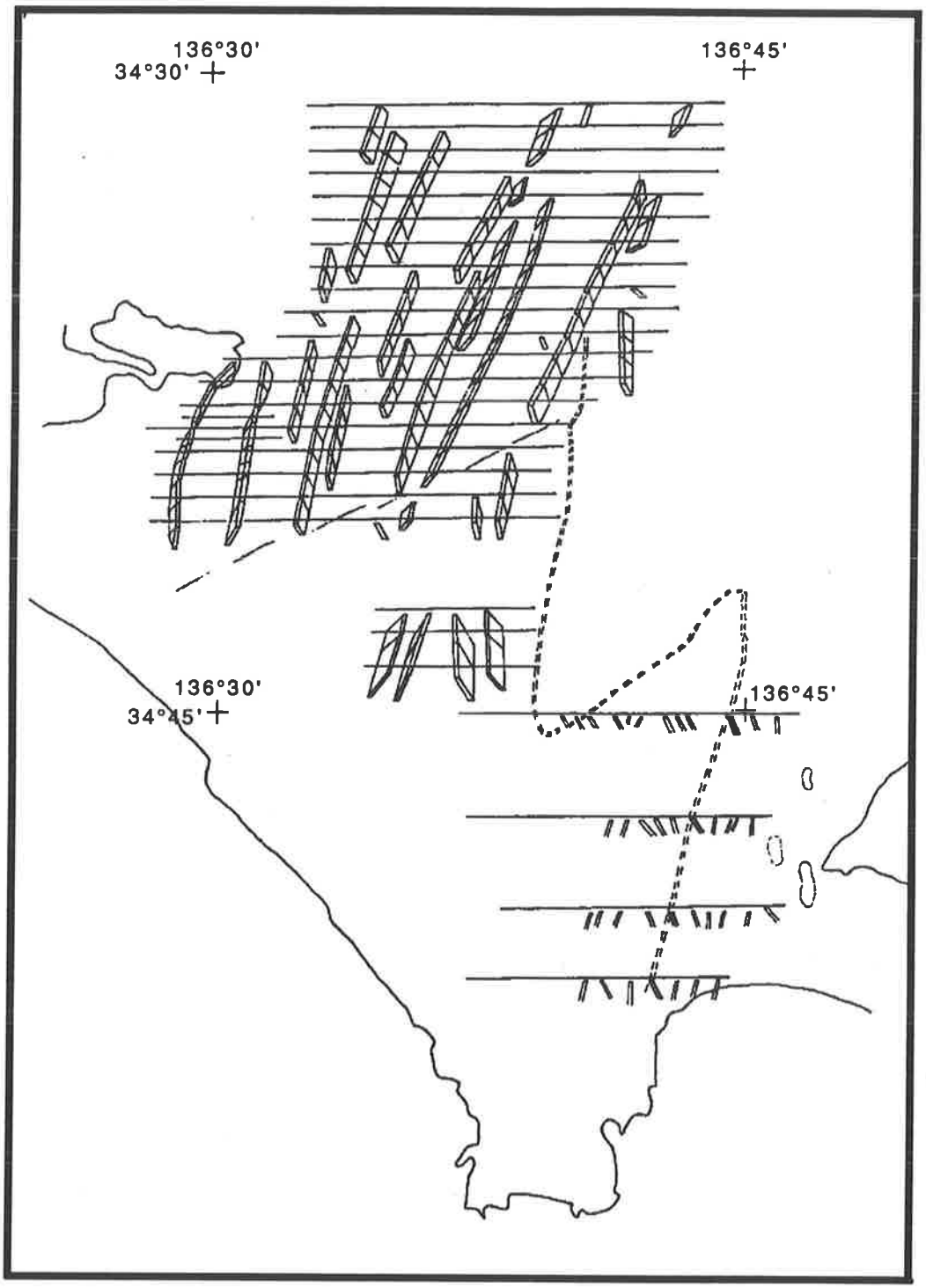

Figure 7.24 Simple structure map in sketching dips of magnetic lineaments in Lincoln area.

It was pointed out earlier in this chapter that this method provides information about dips of magnetic bodies as well as their depths and this will assist in geological studies of the area. The estimated dips of two-dimensional bodies after strike correction can be used to construct a structure map. Figure 7.24 presents a result displaying dip information of the linear structure in the Lincoln area.

The information of depth, dip or width can be combined in an interpretation map with the values marked at the location of each anomaly. AUTOMAG was used by McCoy (1992) to analyse the Gairdner Dyke Swarm; the interpretation which combined with the results from the forward modelling were presented in this way (McCoy, 1992).

The calculated susceptibility can also be plotted as a magnetisation map. However as this estimated parameter contains greater uncertainty than the other estimates, the results should be used very carefully.

7.4 Testing AUTOMAG using drilling information

AUTOMAG was tested by using artificial data as described in Chapter 4. The test against real data is often difficult, because there rarely exists a place in which the information of the depths of soil cover and weathering zone are provided and the magnetic survey was also carried out. In 1989 and 1990, the author participated in the project of "Eyre Peninsula Pb-Zn Preliminary Drill Target" conducted by SADME (Shi, 1991b); this provided a good opportunity to obtain the information required. The example shown below indicates that the estimated depths using AUTOMAG are close to the results from drilling.

The ground magnetic traverse EP19 in Bunora, Kimba combined with the drilling information and an interpreted geology section (Cowley, 1991) is shown in Figure 7.25 and the corresponding drilling information, lithology and magnetic susceptibility measurements of the cores are given in Table 7.2. Figure 7.26 shows the stacked profiles and contour map of the aeromagnetic data which covers about 100 km^2 area relevant to the ground magnetic survey (see Figure 7.26: the ground traverse is between flight lines 3672 and 3693, the marked numbers along it indicate the drill hole positions; the section of the path of flight line 3693 is also shown in the figure).

AUTOMAG was applied to the aeromagnetic data in the surrounding area of the line EP19; both components (ΔZ and ΔX) and vertical gradients ($\Delta Z'_z$ & $\Delta X'_z$) were used to estimate the depths. The combination maps of magnetic profile and depth estimates (below aircraft) for the two types of data are given in Figures 7.27 and 7.28.

1. Comparison of AUTOMAG results from aeromagnetic data and drilling

   Analysing the depth estimates from the airborne magnetic data, several facts stand out as follows:

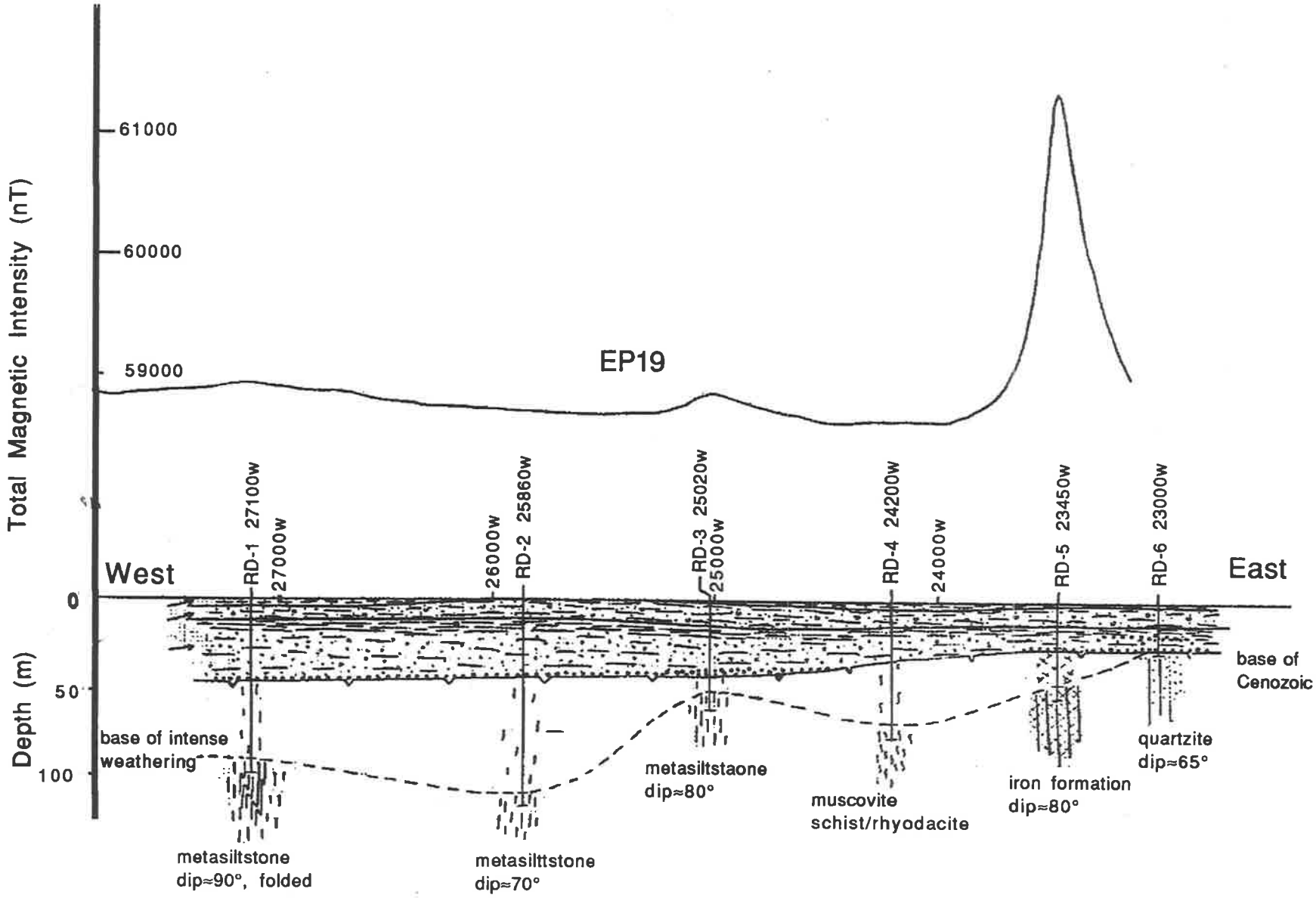

Figure 7.25 Ground magnetic profile combined with drilling information and geology section in Bunora, Kimba. After Cowley (1991).

Table 7.2: Drilling information and magnetic susceptibility measurements of cores in Bunora Kimba, South Australia

Hole	**RS**	**Depth**	**Lithology**	**Magnetic Susceptibility (κ)**			
				RDG[1]	size[2] &	factor	corrected
Bunora	6131RS	(metre)		$SI \times 10^{-5}$	C.L.[3]		$SI \times 10^{-5}$
RD-1	148	95.5	biotite metasiltstone, marble	15	$\frac{1}{2}$core 4.0cm	3.75	60
	149	97.0	biotite metasiltstone				
RD-2	150	70.0-76.0	nodular siderite	150	cuttings 2 mb[4]	3	450
	151	117.3	biotite metasiltstone	25	$\frac{1}{2}$core 5.0cm	3.75	90
RD-3	152	55.0	metasiltstone graphitic quartzite	15-22	$\frac{3}{4}$core 10.5cm	2	30-40
RD-4	153	74.0-78.0	muscovite+quartz schist	10-16	cuttings 1mb	4	40-64
RD-5		48.9-49.85	BIF	not available for sampling			
	154	51.9-52	BIF	20000-35000	$\frac{1}{1}$core 7cm	2.25	45000-79000
	155	54.5-54.6	ferruginous altered garnet-bearing schist	600-2000	$\frac{1}{1}$ 12cm	1.5	900-3000
RD-6	156	29.35-29.45	metaquartzite	± 1	$\frac{1}{2}$core 11.5cm	2.5	± 2

Notion:

[1] RDG: readings from susceptibility meter, the values are mean or typical range.

[2] size: core size

[3] C.L.: core length (cm)

[4] 1mb: approximately 1 match box size.

Lithology identification by W. Cowley SADME

The correction work was under guided by D. Tucker.

Stacked Profiles of Total Magnetic Intensity in Bunora, Kimba

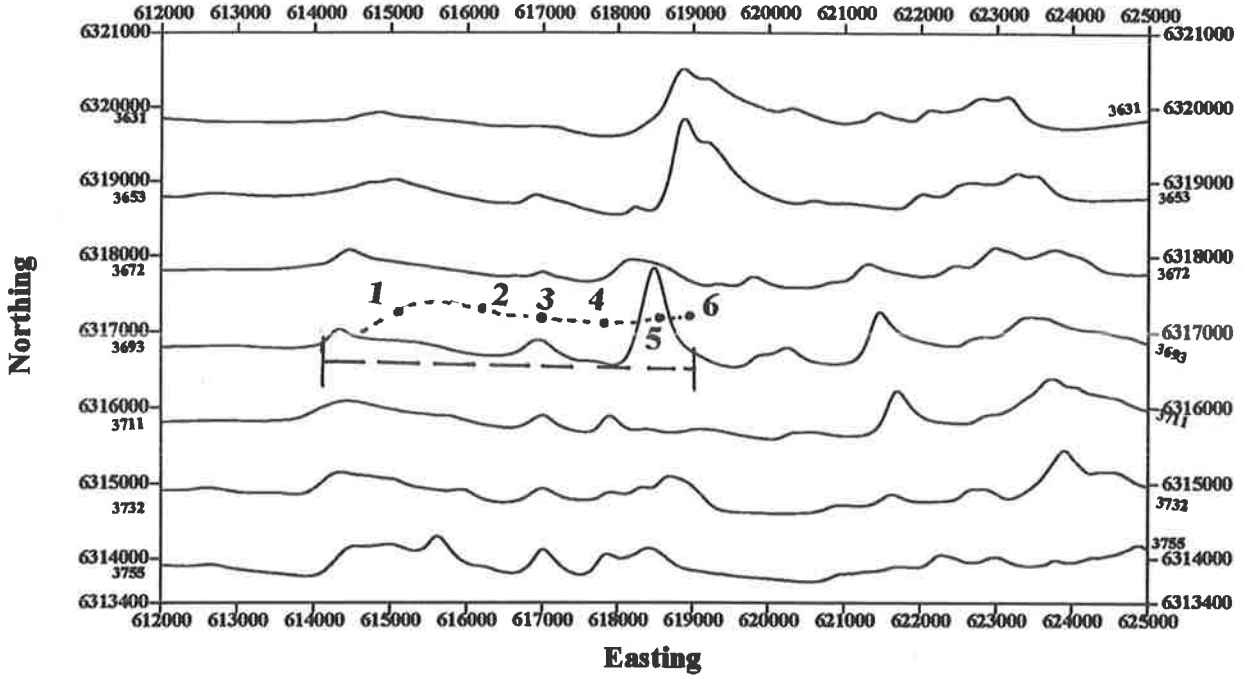

Contour Map of Total Magnetic Intensity in Bunora, Kimba

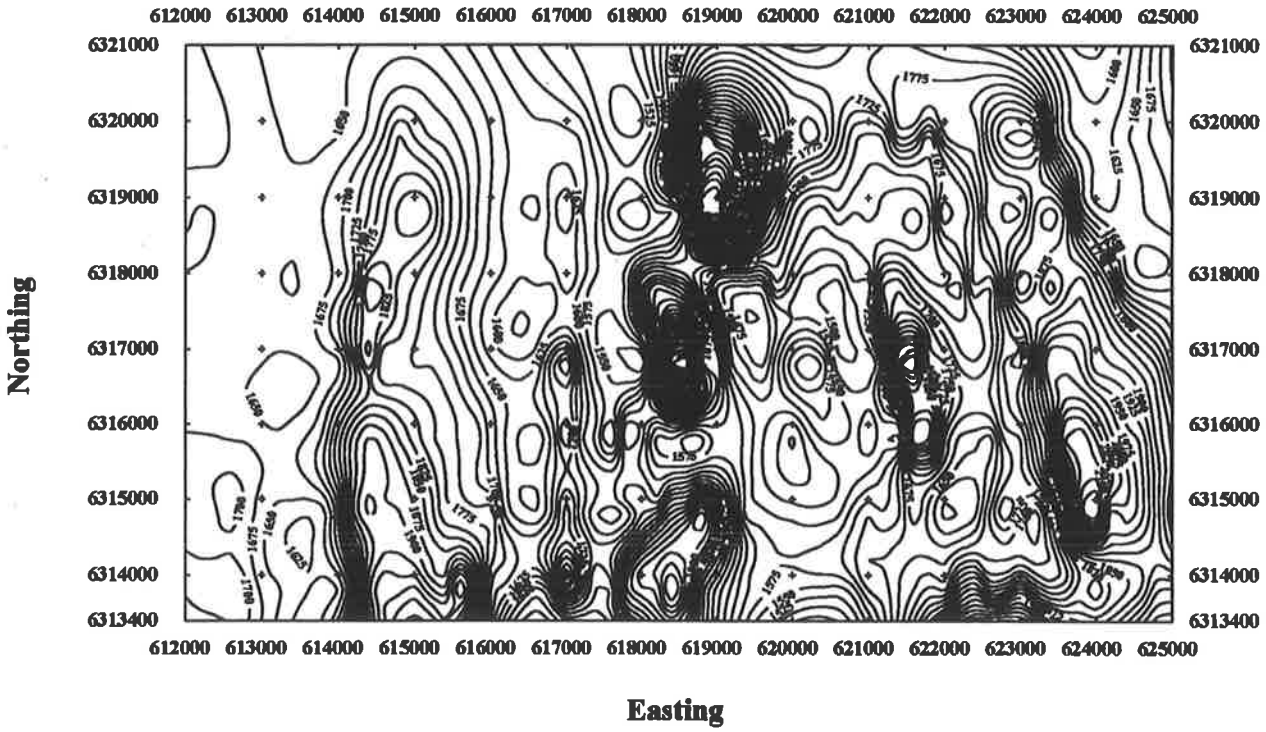

Figure7.26: Stacked profile and contour maps of TMI in area adjacent to ground profile EP 19

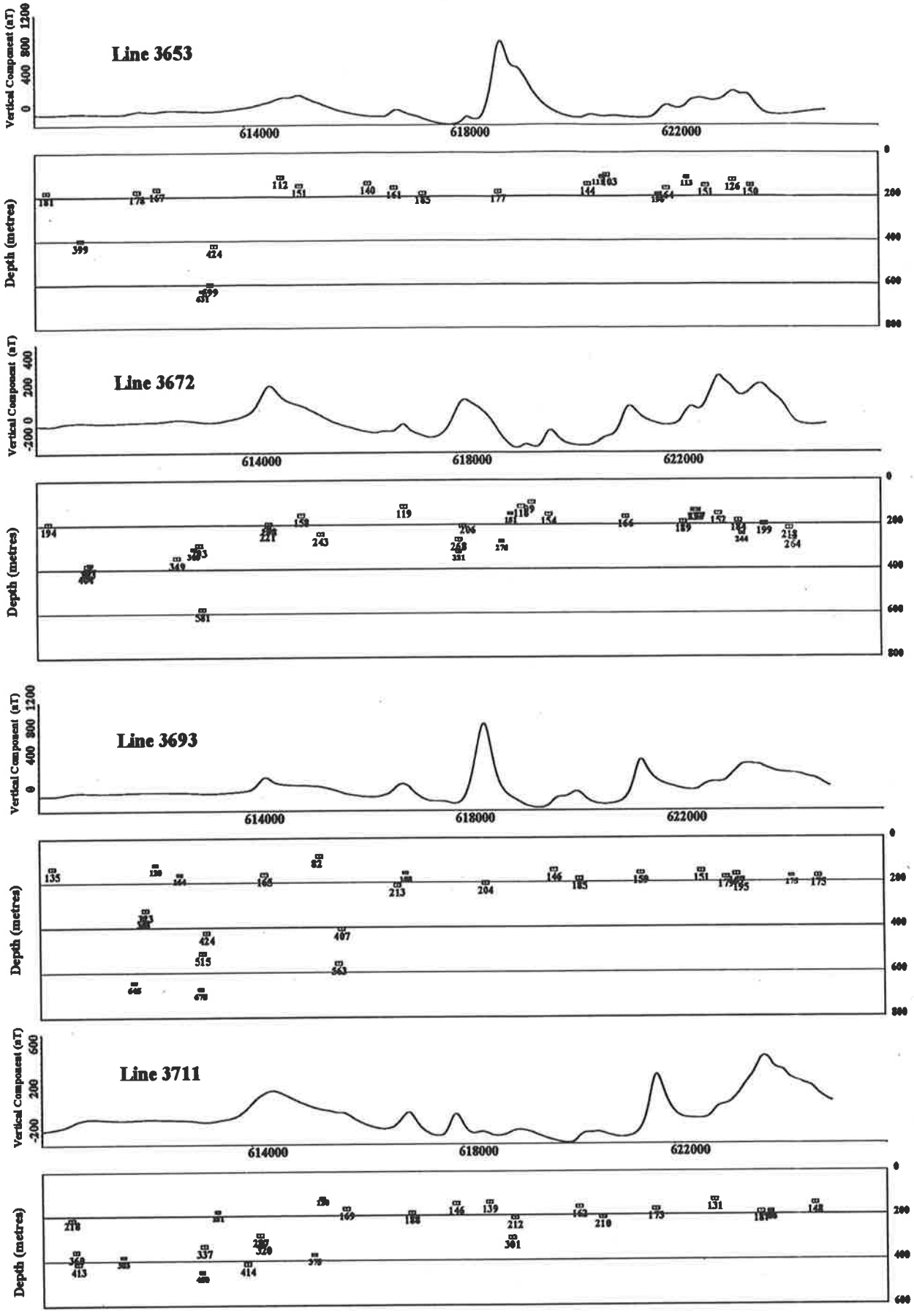

Figure 7.27: Combination Map of Profile & Depth (Component Version)

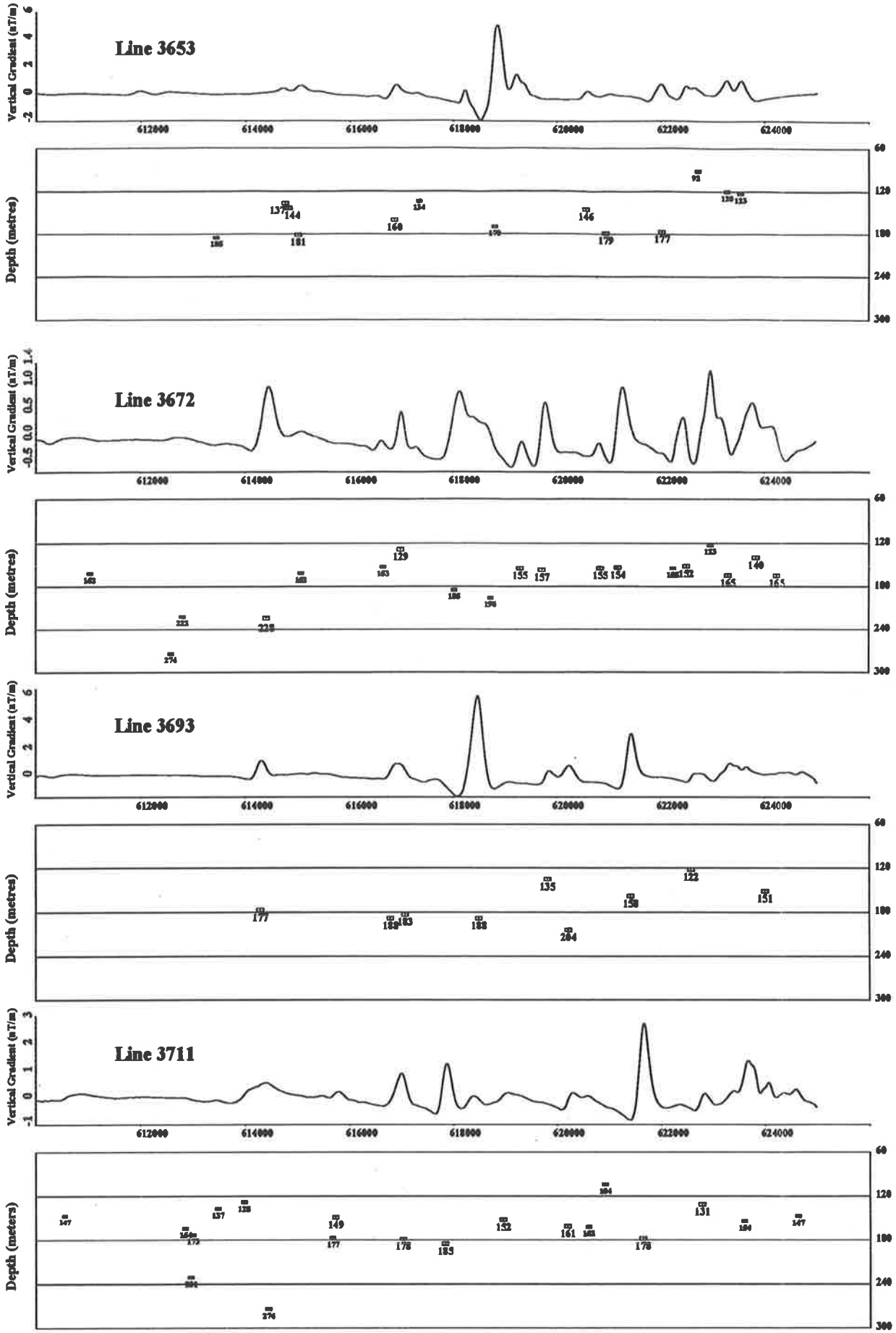

Figure 7.28: Combination Map of Profile & Depth (Gradient Version)

(a) The area can be divided into two parts (western and eastern), based on drilling information, from the easting 617000 which corresponds to the position of drill hole RD-3 (see figures 7.25 and 7.26); the western part (about 100 m) seems to be deeper than the eastern part (about 50 m).

(b) In the eastern part, AUTOMAG indicates two layers: one is about 40 m (140 m below aircraft) and the other is about 70 m (170 m below aircraft) (see figures 7.27 and 7.28).

(c) In the western part, at least two depth levels are noted; the shallow depth ranges from near surface to 70 m (170 m below aircraft) and the great depths are greater than 150 m (250 m below aircraft) and some values are up to 300 m and 500 m (400 m and 600 m below aircraft).

2. Comparisons of results from airborne, ground and drilling data

(a) Comparison of AUTOMAG results from aeromagnetic and ground data
In order to compare the depth estimates from the ground and airborne magnetic surveys, Figure 7.29 represents the results using both component and gradient versions. The profile of ground survey is EP19 and the flight line of aeromagnetic survey is 3693; the locations of the two profiles are shown in Figure 7.26. As the depths estimated from aeromagnetic data have been corrected using the radar altimeter, all the depths from two surveys are directly below the surface. It can be readily seen that the depth estimates of the major body A (in the eastern end of the profile) from both surveys are consistent with each other with values ranging from 80 m to 110 m.

(b) Comparison of results from AUTOMAG and forward modelling
A comparison of results from AUTOMAG with the depth from drill holes for the major anomaly A, indicates that the depth estimate (80m to 110 m) of this BIF body with a strong magnetic anomaly is deeper than the depth reached from the drill hole RD-5 (50 m). Forward modelling work was used to further test AUTOMAG results and to understand the drilling information (as shown in Figure 7.30).

Parts A and C in the figure show comparison of forward model curves and the ground magnetic and aeromagnetic profiles respectively, based on the parameters directly obtained from AUTOMAG. The estimated parameters from AUTOMAG are shown in Table 7.3 in which the dip and susceptibility ($dip = 83°$ and $\kappa = 57550SI \times 10^{-5}$) of the body in the EP19 are consistent very well with the results from the hole ($dip = 80°$ and $\kappa = 45000$ to $79000\ SI \times 10^{-5}$) (see Table 7.2).

Part B shows an unlikely solution using forward modelling in which the depth and susceptibility are based on the values from the drill hole (RD-5). This is calculated using an optimized inversion in the GAMMA program. In the calculation, it seems to be impossible to fit only one body which is consistent with the three parameters (depth, dip and susceptibility) which are obtained from drilling. The model presented in the Part B of Figure 7.30 is an unsatisfactory result and this occurs because the information obtained from the drill hole is not a good sample of the geology.

Part D gives a possible solution for interpreting this anomaly which is consistent with the drilling result. Body 1 is determined by AUTOMAG and body 4 is determined

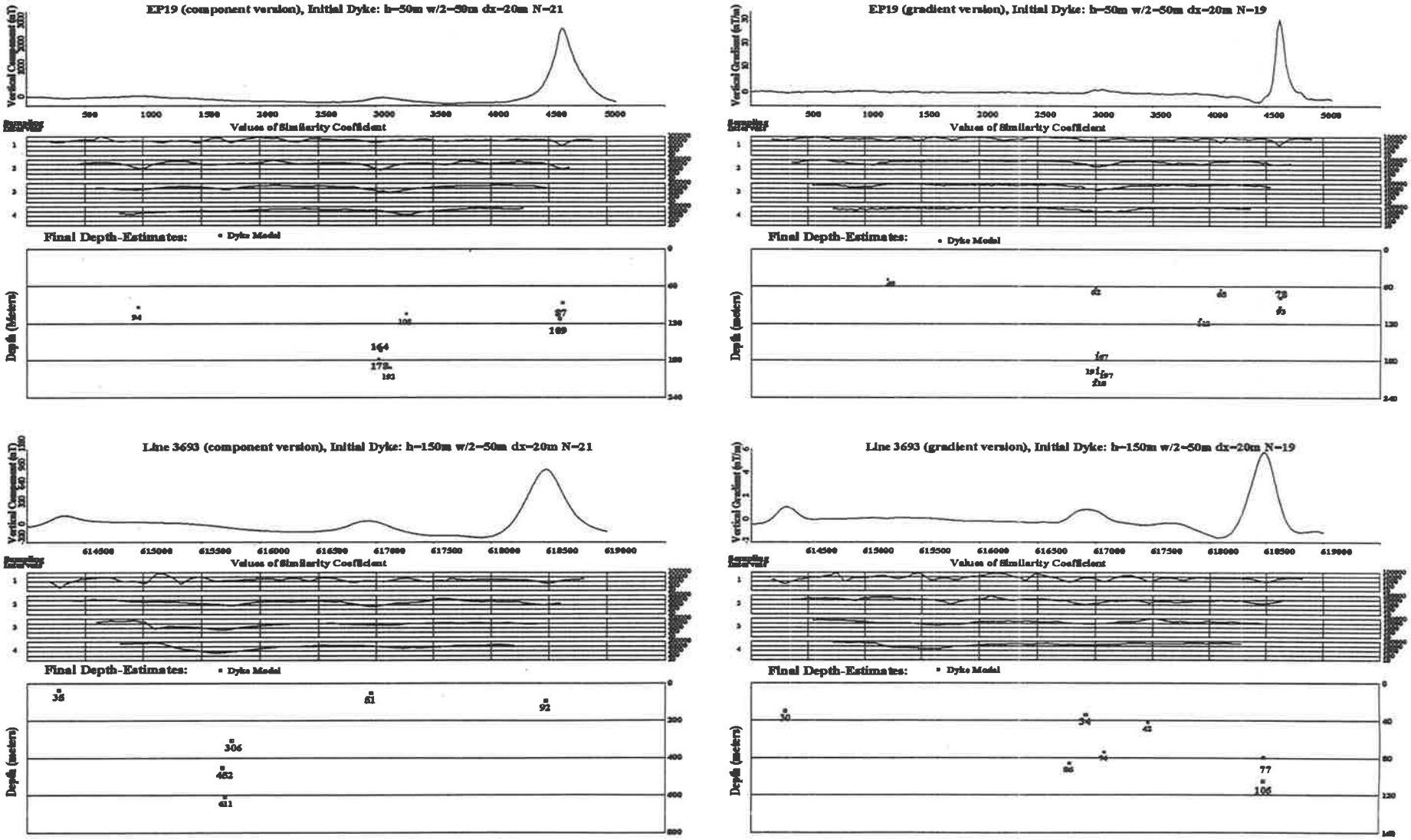

Figure 7.29: Comparisons of results from AUTOMAG between ground magnetic anomaly and airborne magnetics.

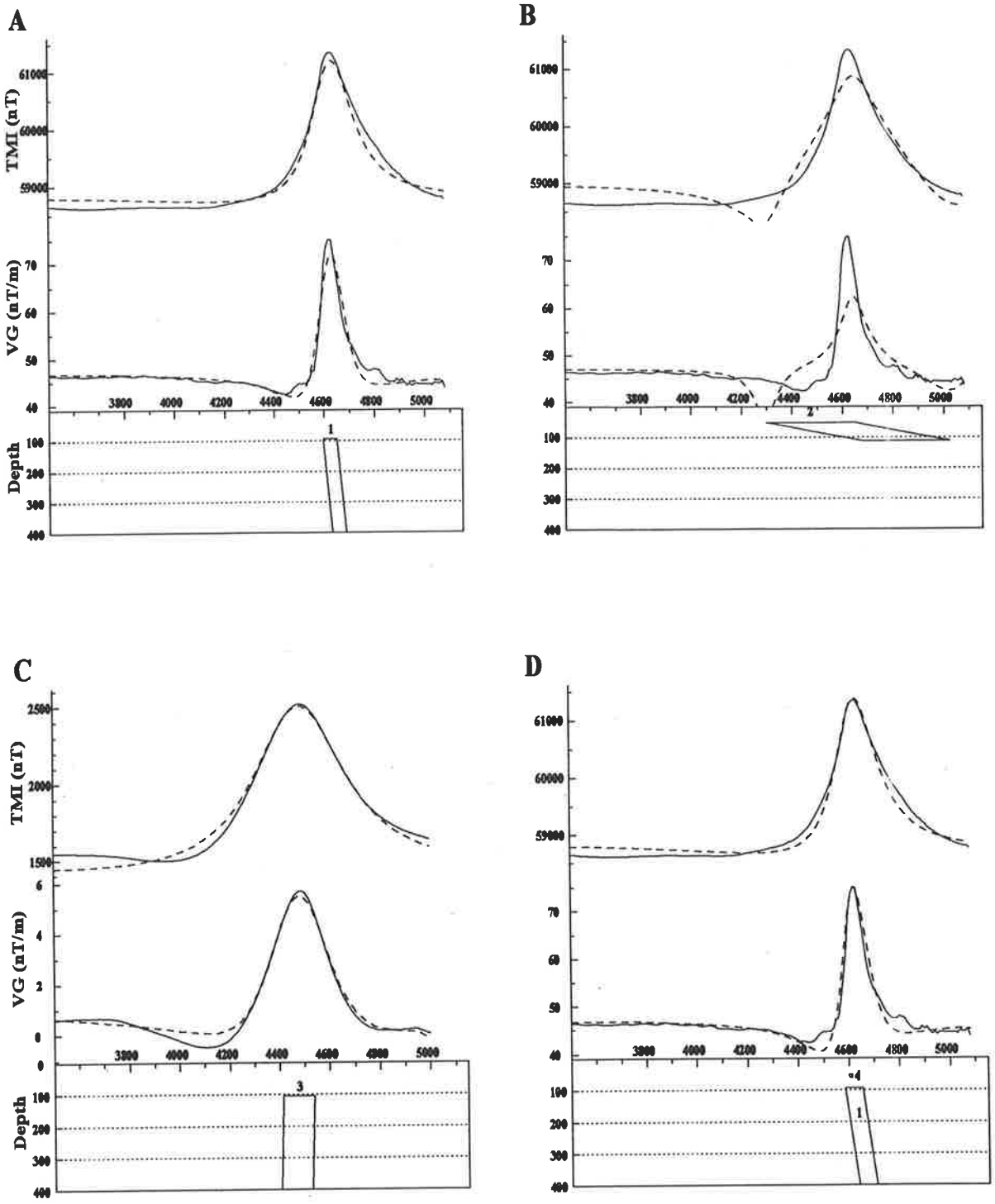

Figure 7.30: Comparisons of forward modelling among ground, airborne surveys and drilling information, Burena.

A: Forward modelling of ground magnetic profile EP19 using parameters directly from AUTOMAG.

B: Forward modelling of the profile EP19, depth & susceptibility are based on drilling information.

C: Forward modelling of aeromagnetic profile using parameters directly from AUTOMAG.

D: Forward Modelling combined AUTOMAG results and drill hole information.

Figure 7.31: Depth of bedrock based on drilling and estimated depths using AUTOMAG

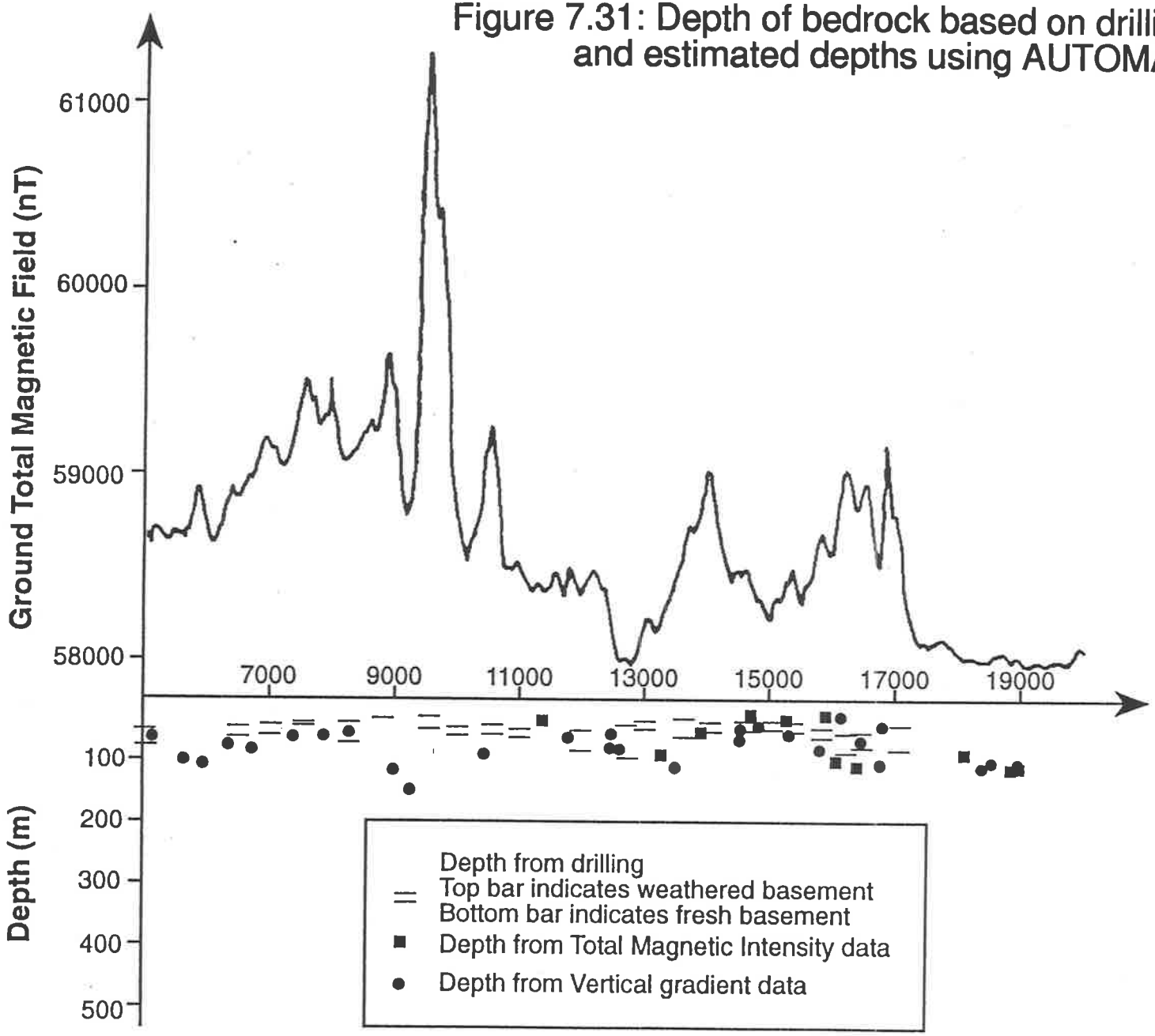

Table 7.3: Parameters of forward models obtained from AUTOMAG & drilling

Model in Figure	Source of parameters	Line	h (m)	w (m)	dip	κ $SI \times 10^{-5}$	t (m)
Part A	AUTOMAG	EP19	93	54	83°	56550	1000
Part B	AUTOMAG	3693	105	123	92°	25133	2000
Part C	Drilling	EP19	50	346	9°	47750	59
Part D	AUTOMAG	EP19	93	54	83°	56550	1000
	& Drilling		50	12	80°	47750	5

Note:
h: depth below surface,
w: width of the dyke model,
dip: dip of the body measured from east,
κ: susceptibility of the body,
t: thickness of the body.

using three parameters (h = 50 m, dip = 80° and $\kappa = 47750SI \times 10^{-5}$) from the drilling but only has a very limited depth extent (12 m) and width (10 m) of the body. The combination of the two anomalies gives a better result. From this solution, it implies that the depth of 50 metres from drill hole may indicate the depth of weathering zone and the depth of the fresh basement is probable up to 90 metres.

The parameters used in the four sets of forward modelling (Figure 7.30) are shown in Table 7.3.

Another test recently carried out in western South Australia where more than twenty holes which reach bedrock can be compared with the depth estimates using AUTOMAG from a recent high quality low level aeromagnetic survey (see Figure 7.31). The results from AUTOMAG are close to the depths from drilling which is a further evidence that AUTOMAG is a useful tool for detecting basement depths.

7.5 Discussion

7.5.1 Speed of AUTOMAG and comparison with a manual processing

AUTOMAG has the advantage of providing a fast interpretation of thousands line kilometres of data covering a very large area. An example of the time spent for the complete operation and for each step in processing the data, which have been explained in the previous sections, is given as follows.

The study area is 1872 km^2 (52 km along easting and 36 km along northing) (see Figure 7.18).

There are 35 aeromagnetic profiles 50 kilometres long in the area and the sample interval for the calculation is 20 metres: each profile contains 2600 data points. it may be assumed that each line has 30 individual anomalies and the total anomalies in the area is more than 1000.

Assuming 20 minutes is spent interpreting each anomaly, the time spent for a geophysicist to interpret these anomalies using standard (non-automatic) methods is at least 350 hours or about 7 weeks. The total time spent using AUTOMAG was about 40 hours or about a week and will be greatly reduced with experience; this time includes printing the depth estimation maps (an example shown in Figure 7.13) for whole processed profiles and each profile using at least two kinds of models (dyke and edge) both for TMI and vertical gradient data. As each calculation of a profile was however, in fact, performed 4 times, this demonstrates the high speed of the AUTOMAG processing.

A summary of time spent on each procedure of the data processing is shown below. This count does not include the time spent in preparing the original data and their contour maps and images, which would be required for both manual and automatic interpretation. In some cases reading original location data from a tape or other media takes more time than the data processing. For example, for a recent aeromagnetic survey carried out in South Australia, it took five weeks for flying and a further five weeks for the initial corrections and map preparations. This data would have been taken straight from the aircraft and depth information produced within hours.

- A half day was spent choosing a suitable area to be processed from the contour, stacked profile and image maps, and extracting each line data from the whole data set and planning for data processing.
- A half day was spent in testing and setting up the initial models to be used in the area.
- Three days were required to process profile data by using AUTOMAG and produce depth output on the profiles (more than 100 sheets of A4 paper). The calculations use a SUN SPARC 2 workstation. Due to shortage of graphic soft package in the Unix computer of this Department, the results needed to be transferred to the Vax-780 computer for generating postscript files; this was inconvenient and added to the time required to process the data.
- A half day was spent in reviewing results and repeating specific profiles. A semi-automatic interpretation method was used for this. An example is shown in Section 7.3.3.
- A half days were required for correcting strike effect, subtracting the altitude values and producing other maps, e.g. stacked profiles (Figure 7.23).

This was the first step in the development of a preliminary interpretation in the study area. After combining the geophysical interpretation with the geological information, a further study was required but a further work towards a complete interpretation still needs to be done by using forward modelling and other methods. This work will normally take longer time than using AUTOMAG but will provide more detailed and accurate information. However it would not be practical to apply to a large area without the results produced by AUTOMAG. Note

that with a bigger printer it would have been possible to process profile lines as two or three times as long as using a A4 printer but the time spent is almost the same as before.

7.5.2 Limitation and restriction of AUTOMAG

While AUTOMAG is a useful tool for interpreting magnetic profile data, some limitations exist in the program.

1. The program is efficient in the interpretation of isolated anomalies; but with superimposed and/or interfering anomalies it may not provide accurate results, because of the magnetic effects from underlying magnetic bodies and the interference from adjacent magnetic bodies. Applying the program to the vertical gradient data helps to reduce the effect from overlapping bodies. However the side-effect of this is to enhance some noises from the original anomalies, e.g. areas with lot of maghaemite in the soil, which may make the results less reliable.

2. The program assumes that anomalies arise from 2-D bodies; in the case of $2\frac{1}{2}$-D or 3-D bodies, an error will be introduced.

3. The calculation of dip and susceptibility is based on the assumption of induced magnetisation. If the causative bodies have very strong remanent magnetisation, the estimates would become unreliable.

4. With AUTOMAG, the similarity coefficients are used to judge the quality of the estimations. This method is based on the assumption that the smaller the coefficient, the better the solution. This is, however, not always true. In some cases if the window length is not long enough to cover whole anomaly, it may also produce apparently good correlation coefficient between the theoretical curve and that part of the anomaly.

Therefore the user must understand the principle of the method in order to obtain reliable results. In spite of these limitation, however, AUTOMAG provides a fast analysis technique to interpret magnetic profile data and is useful for preliminary interpretation.

Chapter 8

Conclusion

The general aim of this research was to develop better practical methods to estimate the depth of physical discontinuities using potential field data. The specific aim of the research was to obtain estimates of the depth of the metamorphic and igneous rocks which lie beneath the overburden in the Gawler Craton using aeromagnetic data.

The research project dealt with and developed two related but very different interpretation methods:

- AUTOMAG which can be used for providing estimation of the thickness of overburden and the depth of sedimentary basin from aeromagnetic profile data, and
- Spectral analysis which can be used to obtain the depth of sedimentary basin and the depth of layers in the crust from both gravity and magnetic grid data.

AUTOMAG produces immediately practical information for mineral exploration. Spectral analysis is important for basic science, because it provides information about the deep crust about which virtually nothing was previous known.

8.1 AUTOMAG

8.1.1 Summary

- AUTOMAG provides information about the thickness of cover and structure of the underlying rocks which will help geologists and mineral exploration companies to understand better the scientific and economic potential of the areas covered by the high quality aeromagnetic surveys flown in South Australia in 1992/93 by the South Australian Department of Mines and Energy.

- The mathematical and computing aspects of the work have been firmly established by modification of the original Naudy technique which make it more universally applicable; the tests carried out on shape problems in chapter 4 have led to models which reduce the errors due to the approximations made in assumptions about the shape of the real magnetic bodies; further refinements for shape variation can be made as the total system is now demonstrated to be functioning; the tests reported in chapter 4 also allow a better understanding of the effect of the window length on the depth estimates: the correlation curves printed in the sections relate depth estimates to window length.

- AUTOMAG has been tested using synthetic data arising from a variety of simple and complex models and real data. The test shows that the method provides reliable results.

  1. The biggest source of error is the effect of depth extent – this error is reduced by using the vertical gradient in preference to TMI.
  2. With simple steeply dipping bodies with a depth extent greater than 4 times the distance from aircraft to the source the error for TMI data was less than 10% and for gradient data less than 5% (see Section 4.3.5).
  3. Many automatic interpretation methods do not work well with noisy data. With a set of synthetic data arising from two dyke models and in addition of 10% random noise, using TMI data the error is up to 25%; but if the data is smoothed the error drops to 14% (shown in Section 4.9).
  4. As vertical gradient enhances the high frequency surface noise, the data with noise is less satisfactory.

- AUTOMAG has been applied to real data which allows a comparison between a ground magnetic survey and the airborne survey (see Section 7.4). The estimated depths from the two surveys correspond closely; the difference between the depth estimates are less than 7% in which the calculation is based on: a ratio between the difference of the depths estimated from the two surveys and the total depth below the aircraft.

- A comparison between AUTOMAG estimates and drilling results appears good (see section 7.4), but it is not possible to express the quality of fit in terms of percentage error.

- AUTOMAG can be used for all depths, e.g. the thickness of overburden (depth < 100 or $200m$) and basement underneath sedimentary basin (depth > 1000 or more).

- AUTOMAG can be used to provide input parameters of the models computed in forward or inversion modelling; this step makes the modelling work more efficient.

- The information of dip and susceptibility of causative bodies can be used to construct geological structure map and magnetisation distribution map.

8.1.2 Discussion

Further work is required in the following problems.

- Magnetic properties of the overburden

  Soil is complex, it is a very difficult to obtain an adequate and representative sample from depths of tens of metres to study; the distribution of the magnetic minerals within the soils is not well understood; there is much more work to be done here by geologists; the interpreted sections generated by AUTOMAG may contribute to the solution of some of the soil researches.

- Data quality

  The accuracy obtainable by the methods used in this research depends on the quality of the data, both the accuracy of the measurement of the magnetic field and the accuracy with which the position of the sensor is established; in principle this kind of research could have been done any time within the last thirty years since digital recording of the magnetic field has been made on magnetic tape; the method has only been practical for this problem in the last decade when the accuracies and frequency of measurements of the total magnetic intensity and positioning have increased dramatically. This is no reason to think that the ultimate in data quality has been reached.

- Data noise

  In parts of Australia surface noise for low level surveys can be a severe test of any method; AUTOMAG will work with model data incorporating 10% noise and still give satisfactory results; it may also be desirable to run noisy data through a low pass filter to improve the final estimates; appropriate filters have been designed to do this but have not been tested adequately on real data.

- Presentation of results

  The presentation of very large quantities of results may also present a hurdle because of the great volume of paper (output) produced and the difficulties of handling and filing the sections efficiently. This is a production problem and not a research problem. However, it becomes more important as the method is applied. The problem needs to be solved in the further application.

  The graphics need go through a VAX which is awkward for the user. A new graphical system needs to be established in the SUN SPARC workstation.

- Application of AUTOMAG to $2\frac{1}{2}$-D and 3-D bodies

  AUTOMAG is a tool for interpreting profile data arising from 2-D bodies. When applying AUTOMAG to $2\frac{1}{2}$-D and 3-D bodies, some errors are introduced. Further research is required to find ways of correcting such errors which include a test of bodies with limited strike using AUTOMAG.

- Non-uniqueness solution

  One problem for AUTOMAG is non-uniqueness or spurious solutions; examples were shown in Section 4.8 where a few estimated depths occur related to an anomaly or some estimated depths have no corresponding bodies. Two reasons, i.e. window length and critical distance, for this were discussed in Section 4.10. Another reason is the type of judgement

(e.g. similarity coefficient) used for determining the best depth estimates. As it is impossible to find a perfect criterion (R_m, see Section 2.7.4) which is suitable for a variety of anomalies, this phenomenon is unavoidable. It is important that the interpreter can recognise and understand these situations. An improvement can be carried out by using a semi-automatic approach (see Section 7.3.3). However, by doing this the speed of the procedure is reduced. Ambiguity is still a problem in the application of AUTOMAG.

AUTOMAG has been used to interpret real aeromagnetic data. However, it is still a prototype and problems exist in the application; the refinement of program, improvements of facilities and extensive testing are required for the next stage.

8.2 Spectral analysis

8.2.1 Summary

Spectral analysis provides new information about the existence and depth of density discontinuities in the middle and lower crust using the regional gravity data which were collected by SADME and AGSO during the last thirty years. This part of the research was developed initially as a side line from the main project. Nothing similar has been published in South Australia. This research has become the basis of a new research project which is independent of the present Ph.D. program and combines both gravity and magnetic data.

Spectral analysis has tested a sets of synthetic data simulating real geological situations in Chapter 5. It shows that the technique combined with other traditional methods can provide a preliminary quantitative interpretation including depth, location and outline of the body. The technique has been used to analyse Bouguer gravity data covering the Eyre Peninsula area (30°S to 35°S, 133°E to 139°E) in chapter 6 and it shows the distribution of anomalously dense bodies in the middle and lower crust.

The technique was combined with the "compensation smoothing filter" (Hou, 1981) to achieve anomaly separations and to provide depth slice maps in the Eyre Peninsula area, South Australia (see Chapter 6). The greatest depth of 32 to 38 km probably indicates the Moho discontinuity. This is the same as the depth of the Moho based on seismic data. Another application is to determine the depth at 15 km of a dense body underlain Gawler Range Volcanics.

The spectral analysis technique used in this thesis has been the subject of research of a number of geophysicists. The author during many years of research working with a team of Chinese scientists contributed in a great degree to final development of this method (Hou, Liu and Shi, 1980; Hou and Shi, 1985).

The spectral analysis has been also applied to magnetic data (see Section 7.2). A research project using the grid of aeromagnetic field intensities prepared by John Pitt for the recently completed the South Australian Magnetic map is already in progress; the project uses both

the gravity and magnetic data to define features in the lower and middle crust (Boyd, Shi and Kivior, 1993).

A similar approach could be made to applying spectral analysis to the whole of Australia using the grids prepared for making the images of the gravity and magnetic field; such a study should be integrated with the results of the deep seismic profile already made.

8.2.2 Problems and further work

Spectral analysis has been widely used to provide depth information in a regional scale both from magnetic and gravity data. The technique is very useful but it still contains some problems and need to be solved.

- Choice of thin plate or prism model

  The method of spectral analysis was extended by the author (Shi and Li, 1987) based on the method developed by Spector and Grant for magnetic data (Spector and Grant, 1970). It is worth noting that in recent years several other authors also presented their applications of spectral analysis to gravity data (Mishra and Tiwari, 1981; Negi and Agrawal, 1986; Dimitriadis *et al.*, 1987; Tselentis *et al.*, 1988). They analysed energy spectral of gravity data directly using the Fourier transform of **original data**. However the method used here calculates the Fourier transform of the **vertical gradient** of the gravity data. The basic model in the other methods is a horizontal thin layer (or thin sheet) with random polarization (Naidu, 1968); the model in this author's method is a thick rectangular prism. Therefore a problem arises from the assumption of the basic model applied in spectral analysis to gravity data.

  Considering the assumption of the model, e.g. **thin layer** from the other methods and the procedure of data processing using the **vertical gradient** from this method, a clear correlation is found between the two approaches. The spectra of thin layer can be directly used to estimate its depth (Mishra and Tiwari, 1981). The vertical gradient (VG) of a thick body can identify effects from two layers which are from the top and bottom of the body. In the case when thickness of the body is great, VG mainly represents an effect from a thin layer (which corresponds to the top of the body and the effect arising from the bottom part is ignored). Therefore both approaches are based on the same principle, but using a different assumption to deal with the real problem.

  However the solutions are very different, the estimated depth used the other methods are much greater than the solution from that developed by the author. Judging the two approaches is not simple; more theoretical model tests need to be examined and detailed knowledge of the crust distribution hypothesis of this kind that may be obtained from deep seismic section are required. This is one of the author's unsolved problems and it will be solved in the future.

- Sideswipe

  Another problem in use of spectral analysis for estimating depth is to identify a true depth from deepest sources and spurious depths obtained from extended data at the lower frequency end (Chapters 2 and 5). This is not a trivial problem, for it directly affects the reliability of the solutions. One way to solve this problem is to select an area satisfied under a condition where high amplitude anomalies are at the central area and low magnitude anomalies surround them. Under this restrictive condition, the depth estimates from the block size of data (see chapters 5 and 6) would not work at all. A realizable solution for this problem is to find a reasonable edge correction function which is specially satisfactory to characteristics of gravity or magnetic fields. The author did some effective work: established such a function for profile data and tested it in different situations of truncated data. Satisfactory results were obtained from spectral analysis in profile data. However, the work needs to be continued and expanded to gridded data.

8.3 The next stage for geophysical interpretation

Australia has been become a world leader in the mineral exploration. A large number of high quality low level aeromagnetic surveys have been carried out over all states in Australia in recent years. An important target for the geophysicists is to develop and improve quantitative interpretation methods and to establish various effective and economic interpretation systems. AUTOMAG and spectral analysis has provided a starting point to achieve this aim.

Part IV

Appendices

Appendix A

Magnetic fields arising from various simple models

A.1 Introduction

In this appendix, the formulae for the magnetic fields, including total field (ΔT), vertical and horizontal components (ΔZ and ΔH), and their first vertical derivatives (T'_z, Z'_z and H'_z) arising from edge, step, dyke (with infinite and limited depth extent), thin sheet, horizontal thin sheet, thin plate and horizontal cylinder models are presented. These derivations are based on Reford's work (Reford, 1978). In this study, it is assumed that the intensity of the magnetic field is measured in a constant direction, and the magnetisation of the body is homogeneous. Furthermore, demagnetisation effects are ignored and the direction of the profile is perpendicular to the strike of the body. To compute the magnetic fields arising from these two-dimensional models, the effective magnetic field is taken into account to simplify the calculation (see Appendix B).

Each field gives two different magnetisation cases: the arbitrary magnetisation and the induced magnetisation. Each formula of the model is analysed, and the basic even and odd functions in these formulae are indicated (if they exist), which will be useful for analysing the characteristics of the fields. Based on the formulae for these simple models and the expression in the paper of Nabighian (1972), a common representation can be found (see expression A.1) which reveals the relationships between the different fields and gradients. The details are as follows.

Each field or gradient is composed of a product of two triangle functions (cosine and sine) and two common functions (F_1 and F_2) which may be either even or odd. A combined amplitude factor ($2sc \sin d$), which involves a magnetisation (or polarization) factor s and a unit vector component c of magnetic field, also plays a part in the field or gradient. A general field or gradient (ΔF or F'_z) can be expressed as

$$\Delta F \ (F'_z) = 2sc(F_1 \cos\Theta + F_2 \sin\Theta) \sin d, \tag{A.1}$$

where d is the dip of the body.

The amplitude factor $2s \sin d$ is fixed and the two functions (F_1 and F_2) are identical for the same model case. However, the value of Θ in the triangle functions ($\cos\Theta$ or $\sin\Theta$) and the factor c are different in the various fields or gradients. Table A.1 shows values of Θ and c for each field or gradient.

It is well known that when the effective inclination is 90°, the total magnetic field in both the arbitrary magnetisation and the induced magnetisation is equal to the vertical component of the vertical magnetisation; i.e. the total field reduced to the pole, except for a constant b. Therefore in these cases, the anomalies of the total magnetic intensity and its reduction to the pole have same shapes.

Another interesting relationship between the two fields is as follows: for the induced magnetisation case, if the effective inclination i is equal to 45 degrees, the value of Θ in the total magnetic field (or the gradient of the total field) is $90° - d$. This value is equal to the value of Θ in the horizontal field (or the gradient of the horizontal field), in which the effective inclination i is equal to 90 degrees. Based on the formula (A.1), the expressions of the two fields have similar form; i.e. the shapes of anomalies for these two fields are the same, except for a constant factor in the amplitudes. In conclusion, the pair of fields considered as a total field of i equal to 45° ($\Delta T_{i=45°}$) and its reduction to the pole ($\Delta Z_{i=90°}$) are equivalent to the pair of horizontal and vertical fields ($\Delta H_{i=90°}$ and $\Delta Z_{i=90°}$), both in the vertical magnetisation direction.

Based on Table A.1, it is obvious that the values of Θ in the vertical and horizontal components are always shifted by 90°. This means these two components in any magnetisation case are always different.

In the next sections, geometries of eight simple models are presented with their six or eight field and gradient formulae.

- **Explanations of the parameters used in the formulae and diagrams:**

X: direction of the profile,

A: position of the arbitrary observation point along the profile,

x: distance from the observation point to the origin (O),

h: depth to the top of the body,

D: depth to the bottom of the body,

w: width of the body,

d: dipping angle of the body measured clockwise from the positive x-axis,

R: distance from the observed point to the corner of the edge model,

Table A.1: Θ and c for total, vertical, and horizontal fields or vertical gradients

	Total Field (ΔT) and **Vertical Gradient** of ΔT	**Vertical Field** (ΔZ) and **Vertical Gradient** of ΔZ	**Horizontal Field** (ΔH) and **Vertical Gradient** of ΔH
Θ			
arbitrary magnetisation	$i + j - d$	$90° + j - d$	$j - d$
induced magnetisation	$2i - d$	$90° + i - d$	$i - d$
c			
arbitrary magnetisation	Bb	B	B
induced magnetisation	b^2	b	b

Note:

j: effective inclination of magnetisation,

$b = \sqrt{(1 - \cos^2 I \cdot \sin^2 D')}$

$B = \sqrt{(1 - \cos^2 J \cdot \sin^2 A')}$

I: inclination of the earth's magnetic field,

D': angle between magnetic north and the positive direction of the profile,

J: inclination of the magnetisation,

A': angle between magnetisation and positive profile direction.

R_1, R_2: distances from the observed point to the upper corners of the causative body,

R_3, R_4: distances from the observed point to the bottom corners of the causative body,

θ: angle between the observed point to two upper or bottom corners of the causative body,

ϕ: angle between the line joining the observed point to the corner of the step body and the vertical axis.

i: effective inclination of the earth's magnetic field,

j: effective inclination of magnetisation,

k: susceptibility contrast of the body,

T: intensity of the earth's magnetic field,

P: polarization,

b: component of the total field unit vector in the xz-plane (see Figure B.2),

B: component of the magnetisation unit vector in the xz-plane (see Figure B.3),

ΔT: total magnetic field,

ΔZ: vertical magnetic field,

ΔH: horizontal magnetic field,

T'_z: vertical gradient of the total field,

Z'_z: vertical gradient of the vertical field,

H'_z: vertical gradient of the horizontal field, this is equal to the horizontal gradient of the vertical field (Z'_x),

Z'_x: horizontal gradient of the vertical field,

H'_x: horizontal gradient of the horizontal field.

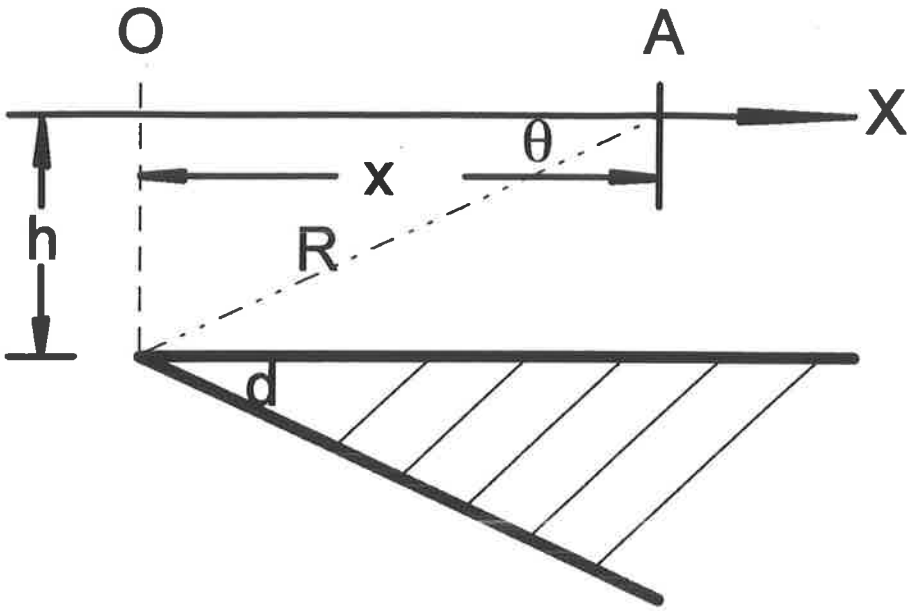

Figure A-1. Geometry of the edge model in the xz-plane.

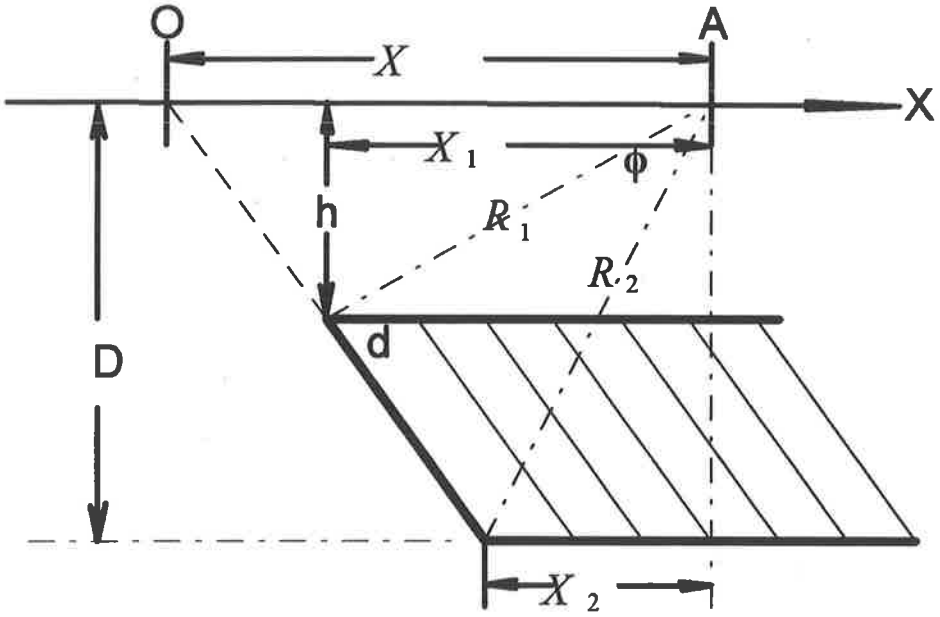

Figure A-2. Geometry of the step model in the xz-plane.

A.2 Edge model

Geometry of edge model is shown in Figure A.1.

- **Arbitrary magnetisation case:**

$$\Delta H = 2PB\sin d\Big[-\cos(j-d)\ln R+\sin(j-d)\tan^{-1}\frac{x}{h}\Big] \tag{A.2}$$

$$\Delta Z = 2PB\sin d\Big[\sin(j-d)\ln R+\cos(j-d)\tan^{-1}\frac{x}{h}\Big] \tag{A.3}$$

$$\Delta T = 2PBb\sin d\Big[-\cos(i+j-d)\ln R+\sin(i+j-d)\tan^{-1}\frac{x}{h}\Big] \tag{A.4}$$

$$H'_z = 2PB\sin d\Big[\cos(j-d)(\frac{h}{R^2})+\sin(j-d)(\frac{x}{R^2})\Big] \tag{A.5}$$

$$Z'_z = 2PB\sin d\Big[-\sin(j-d)(\frac{h}{R^2})+\cos(j-d)(\frac{x}{R^2})\Big] \tag{A.6}$$

$$T'_z = 2PBb\sin d\Big[\cos(i+j-d)(\frac{h}{R^2})+\sin(i+j-d)(\frac{x}{R^2})\Big] \tag{A.7}$$

$$Z'_x = 2PB\sin d\Big[\cos(j-d)(\frac{h}{R^2})+\sin(j-d)(\frac{x}{R^2})\Big] \tag{A.8}$$

$$H'_x = 2PB\sin d\Big[\sin(j-d)(\frac{h}{R^2})-\cos(j-d)(\frac{x}{R^2})\Big] \tag{A.9}$$

- **Induced magnetisation case:**

$$\Delta H = 2kTb\sin d\Big[-\cos(i-d)\ln R+\sin(i-d)\tan^{-1}\frac{x}{h}\Big] \tag{A.10}$$

$$\Delta Z = 2kTb\sin d\Big[\sin(i-d)\ln R+\cos(i-d)\tan^{-1}\frac{x}{h}\Big] \tag{A.11}$$

$$\Delta T = 2kTb^2\sin d\Big[-\cos(2i-d)\ln R+\sin(2i-d)\tan^{-1}\frac{x}{h}\Big] \tag{A.12}$$

$$H'_z = 2kTb\sin d\Big[\cos(i-d)(\frac{h}{R^2})+\sin(i-d)(\frac{x}{R^2})\Big] \tag{A.13}$$

$$Z'_z = 2kTb\sin d\Big[-\sin(i-d)(\frac{h}{R^2})+\cos(i-d)(\frac{x}{R^2})\Big] \tag{A.14}$$

$$T'_z = 2kTb^2\sin d\Big[\cos(2i-d)(\frac{h}{R^2})+\sin(2i-d)(\frac{x}{R^2})\Big] \tag{A.15}$$

$$Z'_x = 2kTb\sin d\Big[\cos(i-d)(\frac{h}{R^2})+\sin(i-d)(\frac{x}{R^2})\Big] \tag{A.16}$$

$$H'_x = 2kTb\sin d\Big[\sin(i-d)(\frac{h}{R^2})-\cos(i-d)(\frac{x}{R^2})\Big] \tag{A.17}$$

where $R=(x^2+h^2)^{\frac{1}{2}}$.

From the above field formulae, it can be readily seen that the common function $\ln R$ is the even function which comprises the symmetric part, while $\tan^{-1}(\frac{x}{h})$ is the odd function which is the anti-symmetric part. For the first vertical-derivatives, the common function $\frac{h}{R^2}$ is the even function, while $\frac{x}{R^2}$ is the odd function.

A.3 Step model

Geometry of step model is given in Figure A.2.

- **Arbitrary magnetisation case:**

$$\Delta H = 2PB\sin d\Big[\cos(j-d)\ln\frac{R_2}{R_1}+\sin(j-d)\cdot\phi\Big] \tag{A.18}$$

$$\Delta Z = 2PB\sin d\Big[-\sin(j-d)\ln\frac{R_2}{R_1}+\cos(j-d)\cdot\phi\Big] \tag{A.19}$$

$$\Delta T = 2PBb\sin d\Big[\cos(i+j-d)\ln\frac{R_2}{R_1}+\sin(i+j-d)\cdot\phi\Big] \tag{A.20}$$

$$H'_z = 2PB\sin d\Big[\cos(j-d)(\frac{h}{{R_1}^2}-\frac{D}{{R_2}^2})+\sin(j-d)(\frac{x_1}{{R_1}^2}-\frac{x_2}{{R_2}^2})\Big] \tag{A.21}$$

$$Z'_z = 2PB\sin d\Big[-\sin(j-d)(\frac{h}{{R_1}^2}-\frac{D}{{R_2}^2})+\cos(j-d)(\frac{x_1}{{R_1}^2}-\frac{x_2}{{R_2}^2})\Big] \tag{A.22}$$

$$T'_z = 2PBb\sin d\Big[\cos(i+j-d)(\frac{h}{{R_1}^2}-\frac{D}{{R_2}^2})+\sin(i+j-d)(\frac{x_1}{{R_1}^2}-\frac{x_2}{{R_2}^2})\Big] \tag{A.23}$$

- **Induced magnetisation case:**

$$\Delta H = 2kTb\sin d\Big[\cos(i-d)\ln\frac{R_2}{R_1}+\sin(i-d)\cdot\phi\Big] \tag{A.24}$$

$$\Delta Z = 2kTb\sin d\Big[-\sin(i-d)\ln\frac{R_2}{R_1}+\cos(i-d)\cdot\phi\Big] \tag{A.25}$$

$$\Delta T = 2kTb^2\sin d\Big[\cos(2i-d)\ln\frac{R_2}{R_1}+\sin(2i-d)\cdot\phi\Big] \tag{A.26}$$

$$H'_z = 2kTb\sin d\Big[\cos(i-d)(\frac{h}{{R_1}^2}-\frac{D}{{R_2}^2})+\sin(i-d)(\frac{x_1}{{R_1}^2}-\frac{x_2}{{R_2}^2})\Big] \tag{A.27}$$

$$Z'_z = 2kTb\sin d\Big[-\sin(i-d)(\frac{h}{{R_1}^2}-\frac{D}{{R_2}^2})+\cos(i-d)(\frac{x_1}{{R_1}^2}-\frac{x_2}{{R_2}^2})\Big] \tag{A.28}$$

$$T'_z = 2kTb^2\sin d\Big[\cos(2i-d)(\frac{h}{{R_1}^2}-\frac{D}{{R_2}^2})+\sin(2i-d)(\frac{x_1}{{R_1}^2}-\frac{x_2}{{R_2}^2})\Big] \tag{A.29}$$

where

$x_1 = x - h\cot d,$

$x_2 = x - D\cot d,$

${R_1}^2 = {x_1}^2 + h^2,$

${R_2}^2 = {x_2}^2 + D^2,$

$\phi = \tan^{-1}(\frac{x_1}{h}) - \tan^{-1}(\frac{x_2}{D}).$

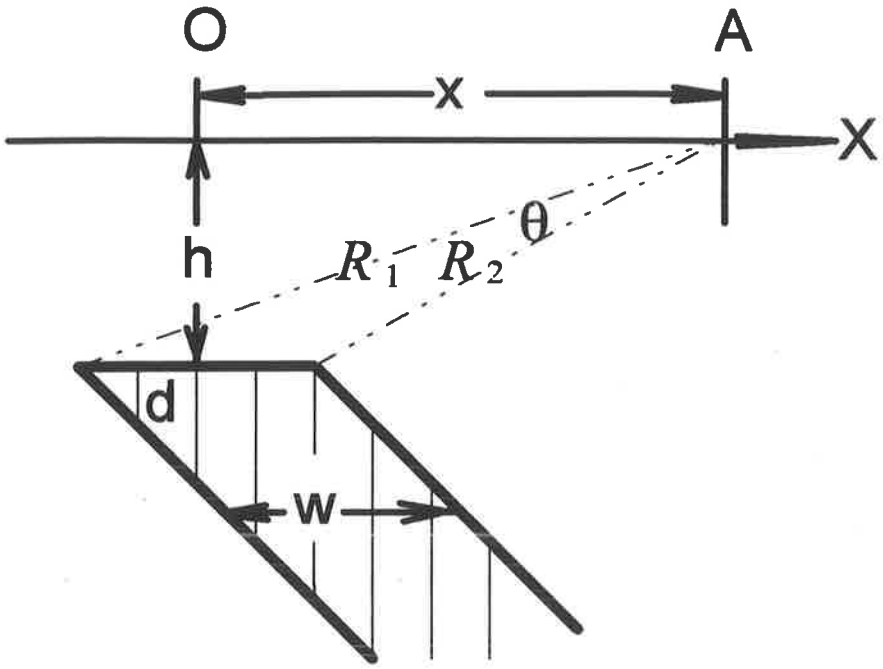

Figure A-3. Geometry of the dyke model with infinite depth extent.

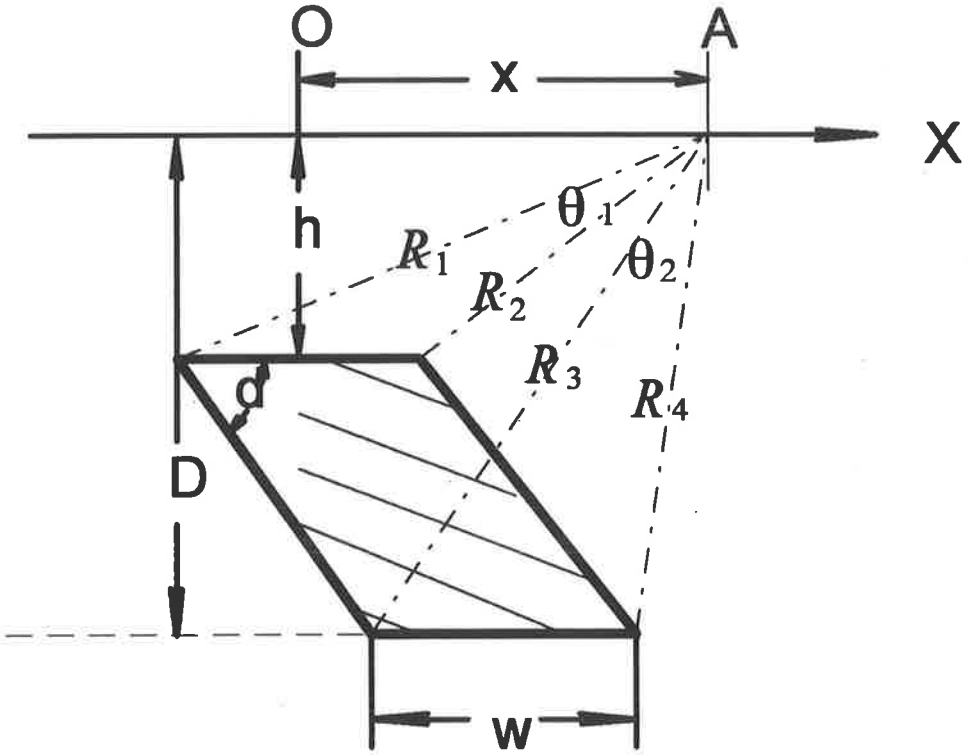

Figure A-4. Geometry of the dyke model with finite depth extent.

When the step is vertical, it is readily seen that the common function $\ln(\frac{R_2}{R_1})$ is the even function which comprises the basic symmetric part, while the common function ϕ is the odd function which is the anti-symmetric part. For the first vertical derivative (gradient) formulae, the common function $(\frac{h}{{R_1}^2} - \frac{D}{{R_2}^2})$ is even, while $(\frac{x_1}{{R_1}^2} - \frac{x_2}{{R_2}^2})$ is the odd function. When the step is non-vertical, the expressions can not be divided into two simple even and odd functions.

A.4 Dyke model with infinite depth extent

Geometry of dyke model with infinite depth extent is shown in Figure A.3.

- **Arbitrary magnetisation case:**

$$\Delta H = 2PB\sin d\Big[\cos(j-d)\ln\frac{R_2}{R_1} + \sin(j-d)\cdot\theta\Big] \quad \text{(A.30)}$$

$$\Delta Z = 2PB\sin d\Big[-\sin(j-d)\ln\frac{R_2}{R_1} + \cos(j-d)\cdot\theta\Big] \quad \text{(A.31)}$$

$$\Delta T = 2PBb\sin d\Big[\cos(i+j-d)\ln\frac{R_2}{R_1} + \sin(i+j-d)\cdot\theta\Big] \quad \text{(A.32)}$$

$$H'_z = 2PB\sin d\Big[\cos(j-d)(\frac{h}{{R_1}^2} - \frac{h}{{R_2}^2}) + \sin(j-d)(\frac{x_1}{{R_1}^2} - \frac{x_2}{{R_2}^2})\Big] \quad \text{(A.33)}$$

$$Z'_z = 2PB\sin d\Big[-\sin(j-d)(\frac{h}{{R_1}^2} - \frac{h}{{R_2}^2}) + \cos(j-d)(\frac{x_1}{{R_1}^2} - \frac{x_2}{{R_2}^2})\Big] \quad \text{(A.34)}$$

$$T'_z = 2PBb\sin d\Big[\cos(i+j-d)(\frac{h}{{R_1}^2} - \frac{h}{{R_2}^2}) + \sin(i+j-d)(\frac{x_1}{{R_1}^2} - \frac{x_2}{{R_2}^2})\Big] \quad \text{(A.35)}$$

- **Induced magnetisation case:**

$$\Delta H = 2kTb\sin d\Big[\cos(i-d)\ln\frac{R_2}{R_1} + \sin(i-d)\cdot\theta\Big] \quad \text{(A.36)}$$

$$\Delta Z = 2kTb\sin d\Big[-\sin(i-d)\ln\frac{R_2}{R_1} + \cos(i-d)\cdot\theta\Big] \quad \text{(A.37)}$$

$$\Delta T = 2kTb^2\sin d\Big[\cos(2i-d)\ln\frac{R_2}{R_1} + \sin(2i-d)\cdot\theta\Big] \quad \text{(A.38)}$$

$$H'_z = 2kTb\sin d\Big[\cos(i-d)(\frac{h}{{R_1}^2} - \frac{h}{{R_2}^2}) + \sin(i-d)(\frac{x_1}{{R_1}^2} - \frac{x_2}{{R_2}^2})\Big] \quad \text{(A.39)}$$

$$Z'_z = 2kTb\sin d\Big[-\sin(i-d)(\frac{h}{{R_1}^2} - \frac{h}{{R_2}^2}) + \cos(i-d)(\frac{x_1}{{R_1}^2} - \frac{x_2}{{R_2}^2})\Big] \quad \text{(A.40)}$$

$$T'_z = 2kTb^2\sin d\Big[\cos(2i-d)(\frac{h}{{R_1}^2} - \frac{h}{{R_2}^2}) + \sin(2i-d)(\frac{x_1}{{R_1}^2} - \frac{x_2}{{R_2}^2})\Big] \quad \text{(A.41)}$$

where

$x_1 = x + \frac{w}{2}$,

$x_2 = x - \frac{w}{2}$,

$R_1{}^2 = x_1{}^2 + h^2$

$R_2{}^2 = x_2{}^2 + h^2$

$\theta = \tan^{-1}\frac{x_1}{h} - \tan^{-1}\frac{x_2}{h}$

The common field functions are $\ln\frac{R_2}{R_1}$ (even, symmetric) and θ (odd, anti-symmetric). For the first derivatives, $\frac{h}{R_1{}^2} - \frac{h}{R_2{}^2}$ is the even function and $\frac{x_1}{R_1{}^2} - \frac{x_2}{R_2{}^2}$ is the odd function.

A.5 Dyke model with finite depth extent

Geometry of dyke model with finite depth extent is given in Figure A.4.

- **Arbitrary magnetisation case:**

$$\Delta H = 2PB\sin d\Big[\cos(j-d)(\ln\frac{R_2}{R_1} - \ln\frac{R_4}{R_3}) + \sin(j-d)\cdot(\theta_1-\theta_2)\Big] \quad \text{(A.42)}$$

$$\Delta Z = 2PB\sin d\Big[-\sin(j-d)(\ln\frac{R_2}{R_1} - \ln\frac{R_4}{R_3}) + \cos(j-d)\cdot(\theta_1-\theta_2)\Big] \quad \text{(A.43)}$$

$$\Delta T = 2PBb\sin d\Big[\cos(i+j-d)(\ln\frac{R_2}{R_1} - \ln\frac{R_4}{R_3}) + \sin(i+j-d)\cdot(\theta_1-\theta_2)\Big] \quad \text{(A.44)}$$

$$H'_z = 2PB\sin d\Big[\cos(j-d)((\ln\frac{R_2}{R_1})'_z - (\ln\frac{R_4}{R_3})'_z) + \sin(j-d)\cdot((\theta_1)'_z - (\theta_2)'z)\Big] \quad \text{(A.45)}$$

$$Z'_z = 2PB\sin d\Big[-\sin(j-d)((\ln\frac{R_2}{R_1})'_z - (\ln\frac{R_4}{R_3})'_z) + \cos(j-d)\cdot((\theta_1)'_z - (\theta_2)'_z)\Big] \quad \text{(A.46)}$$

$$T'_z = 2PBb\sin d\Big[\cos(i+j-d)((\ln\frac{R_2}{R_1})'_z - (\ln\frac{R_4}{R_3})'_z) + \sin(i+j-d)\cdot((\theta_1)'_z - (\theta_2)'_z)\Big] \quad \text{(A.47)}$$

- **Induced magnetisation case:**

$$\Delta H = 2kTb\sin d\Big[\cos(j-d)(\ln\frac{R_2}{R_1}-\ln\frac{R_4}{R_3})+\sin(j-d)\cdot(\theta_1-\theta_2)\Big] \quad \text{(A.48)}$$

$$\Delta Z = 2kTb\sin d\Big[-\sin(j-d)(\ln\frac{R_2}{R_1}-\ln\frac{R_4}{R_3})+\cos(i-d)\cdot(\theta_1-\theta_2)\Big] \quad \text{(A.49)}$$

$$\Delta T = 2kTb^2\sin d\Big[\cos(2i-d)(\ln\frac{R_2}{R_1}-\ln\frac{R_4}{R_3})+\sin(2i-d)\cdot(\theta_1-\theta_2)\Big] \quad \text{(A.50)}$$

$$H'_z = 2kTb\sin d\Big[\cos(i-d)((\ln\frac{R_2}{R_1})'_z-(\ln\frac{R_4}{R_3})'_z)+\sin(i-d)\cdot((\theta_1)'_z-(\theta_2)'z)\Big] \quad \text{(A.51)}$$

$$Z'_z = 2kTb\sin d\Big[-\sin(i-d)((\ln\frac{R_2}{R_1})'_z-(\ln\frac{R_4}{R_3})'_z) + \cos(i-d)\cdot((\theta_1)'_z-(\theta_2)'_z)\Big] \quad \text{(A.52)}$$

$$T'_z = 2kTb^2\sin d\Big[\cos(2i-d)((\ln\frac{R_2}{R_1})'_z-(\ln\frac{R_4}{R_3})'_z) + \sin(2i-d)\cdot((\theta_1)'_z-(\theta_2)'_z)\Big] \quad \text{(A.53)}$$

where

$x_1 = x+\frac{w}{2}$, $x_2 = x-\frac{w}{2}$,

$x_3 = x_1-(D-h)\cot d$, $x_4 = x_2-(D-h)\cot d$,

${R_1}^2 = {x_1}^2+h^2$, ${R_2}^2 = {x_2}^2+h^2$,

${R_3}^2 = {x_3}^2+D^2$, ${R_4}^2 = {x_4}^2+D^2$,

$\theta_1 = \cos^{-1}\frac{{R_1}^2+{R_2}^2-w^2}{2R_1R_2}$, or, $\theta_1 = \tan^{-1}\frac{x_1}{h}-\tan^{-1}\frac{x_2}{h}$

$\theta_2 = \cos^{-1}\frac{{R_3}^2+{R_4}^2-w^2}{2R_3R_4}$, or, $\theta_2 = \tan^{-1}\frac{x_1}{D}-\tan^{-1}\frac{x_2}{D}$

$(\ln\frac{R_2}{R_1})'_z = -\frac{2hxw}{{R_1}^2{R_2}^2}$,

$(\ln\frac{R_4}{R_3})'_z = -\frac{2D[x-(D-h)\cot d]w}{{R_3}^2{R_4}^2}$,

$(\ln\frac{R_2}{R_1})'_z-(\ln\frac{R_4}{R_3})'_z = \frac{h}{{R_1}^2}-\frac{h}{{R_2}^2}-\frac{D}{{R_3}^2}+\frac{D}{{R_4}^2}$,

$(\theta_1)'_z-(\theta_2)'_z = \frac{x_1}{{R_1}^2}-\frac{x_2}{{R_2}^2}-\frac{x_3}{{R_3}^2}+\frac{x_4}{{R_4}^2}$.

In this case, neither the fields nor the first derivatives can be expressed as the sum of two simple even or odd functions.

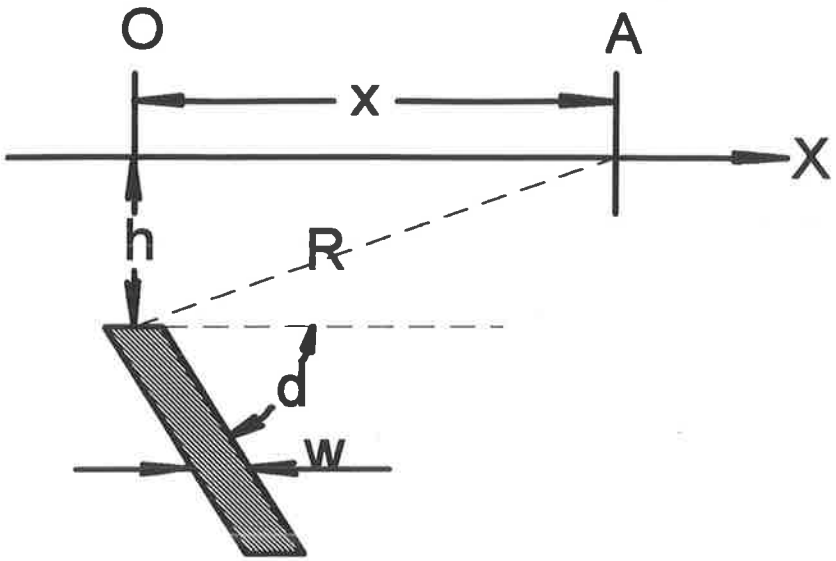

Figure A-5. Geometry of the thin sheet model.

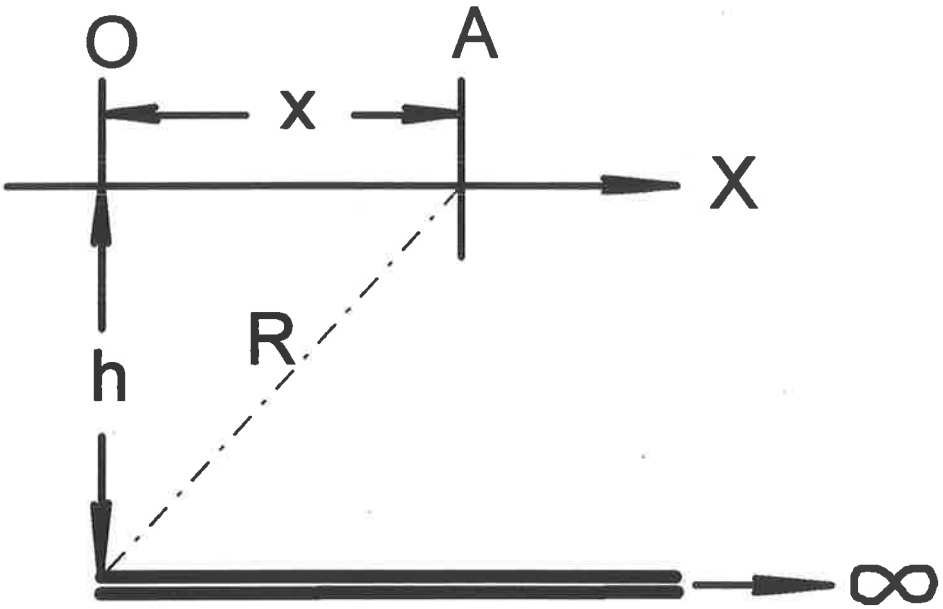

Figure A-6. Geometry of the horizontal thin sheet model.

A.6 Thin sheet model

Geometry of thin sheet model is shown in Figure A.5.

- **Arbitrary magnetisation case:**

$$\Delta H = 2PBw\sin d\Big[-\cos(j-d)\cdot(\frac{x}{R^2})+\sin(j-d)\cdot(\frac{h}{R^2})\Big] \quad (A.54)$$

$$\Delta Z = 2PBw\sin d\Big[\sin(j-d)\cdot(\frac{x}{R^2})+\cos(j-d)\cdot(\frac{h}{R^2})\Big] \quad (A.55)$$

$$\Delta T = 2PBbw\sin d\Big[-\cos(i+j-d)\cdot(\frac{x}{R^2})+\sin(i+j-d)\cdot(\frac{h}{R^2})\Big] \quad (A.56)$$

$$H'_z = 2PBw\sin d\Big[-\cos(j-d)(\frac{2hx}{R^4})+\sin(j-d)(\frac{h^2-x^2}{R^4})\Big] \quad (A.57)$$

$$Z'_z = 2PBw\sin d\Big[\sin(j-d)(\frac{2hx}{R^4})+\cos(j-d)(\frac{h^2-x^2}{R^4})\Big] \quad (A.58)$$

$$T'_z = 2PBbw\sin d\Big[-\cos(i+j-d)(\frac{2hx}{R^4})+\sin(i+j-d)(\frac{h^2-x^2}{R^4})\Big] \quad (A.59)$$

- **Induced magnetisation case:**

$$\Delta H = 2kTbw\sin d\Big[-\cos(i-d)\cdot(\frac{x}{R^2})+\sin(i-d)\cdot(\frac{h}{R^2})\Big] \quad (A.60)$$

$$\Delta Z = 2kTbw\sin d\Big[\sin(i-d)\cdot(\frac{x}{R^2})+\cos(i-d)\cdot(\frac{h}{R^2})\Big] \quad (A.61)$$

$$\Delta T = 2kTb^2w\sin d\Big[-\cos(2i-d)\cdot(\frac{x}{R^2})+\sin(2i-d)\cdot(\frac{h}{R^2})\Big] \quad (A.62)$$

$$H'_z = 2kTbw\sin d\Big[-\cos(i-d)(\frac{2hx}{R^4})+\sin(i-d)(\frac{h^2-x^2}{R^4})\Big] \quad (A.63)$$

$$Z'_z = 2kTbw\sin d\Big[\sin(i-d)(\frac{2hx}{R^4})+\cos(i-d)(\frac{h^2-x^2}{R^4})\Big] \quad (A.64)$$

$$T'_z = 2kTb^2w\sin d\Big[-\cos(2i-d)(\frac{2hx}{R^4})+\sin(2i-d)(\frac{h^2-x^2}{R^4})\Big] \quad (A.65)$$

where $R^2 = x^2 + h^2$.

The common field functions are $\frac{h}{R^2}$ (even, symmetric) and $\frac{x}{R^2}$ (odd, anti-symmetric). For the first derivatives, $\frac{h^2-x^2}{R^4}$ is the even function and $\frac{2hx}{R^4}$ is the odd function.

A.7 Horizontal thin sheet model

Geometry of horizontal thin sheet model is shown in Figure A.6.

- **Arbitrary magnetisation case:**

$$\Delta H = 2PB\Big[\sin j \cdot (\frac{h}{R^2}) - \cos j \cdot (\frac{x}{R^2})\Big] \tag{A.66}$$

$$\Delta Z = 2PB\Big[\cos j \cdot (\frac{h}{R^2}) + \sin j \cdot (\frac{x}{R^2})\Big] \tag{A.67}$$

$$\Delta T = 2PBb\Big[\sin (i+j) \cdot (\frac{h}{R^2}) - \cos (i+j) \cdot (\frac{x}{R^2})\Big] \tag{A.68}$$

$$H'_z = 2PB\Big[\sin j \cdot (\frac{h^2-x^2}{R^4}) - \cos j \cdot (\frac{2hx}{R^4})\Big] \tag{A.69}$$

$$Z'_z = 2PB\Big[\cos j \cdot (\frac{h^2-x^2}{R^4}) + \sin j \cdot (\frac{2hx}{R^4})\Big] \tag{A.70}$$

$$T'_z = 2PBb\Big[\sin (i+j) \cdot (\frac{h^2-x^2}{R^4}) - \cos (i+j) \cdot (\frac{2hx}{R^4})\Big] \tag{A.71}$$

- **Induced magnetisation case:**

$$\Delta H = 2kTb\Big[\sin i \cdot (\frac{h}{R^2}) - \cos i \cdot (\frac{x}{R^2})\Big] \tag{A.72}$$

$$\Delta Z = 2kTb\Big[\cos i \cdot (\frac{h}{R^2}) + \sin i \cdot (\frac{x}{R^2})\Big] \tag{A.73}$$

$$\Delta T = 2kTb^2\Big[\sin (2i) \cdot (\frac{h}{R^2}) - \cos (2i) \cdot (\frac{x}{R^2})\Big] \tag{A.74}$$

$$H'_z = 2kTb\Big[\sin i \cdot (\frac{h^2-x^2}{R^4}) - \cos i \cdot (\frac{2hx}{R^4})\Big] \tag{A.75}$$

$$Z'_z = 2kTb\Big[\cos i \cdot (\frac{h^2-x^2}{R^4}) + \sin i \cdot (\frac{2hx}{R^4})\Big] \tag{A.76}$$

$$T'_z = 2kTb^2\Big[\sin (2i) \cdot (\frac{h^2-x^2}{R^4}) - \cos (2i) \cdot (\frac{2hx}{R^4})\Big] \tag{A.77}$$

where $R^2 = x^2 + h^2$.

The common field functions are $\frac{h}{R^2}$ (even, symmetric) and $\frac{x}{R^2}$ (odd, anti-symmetric). For the first derivatives, $\frac{h^2-x^2}{R^4}$ is the even function and $\frac{2hx}{R^4}$ is the odd function.

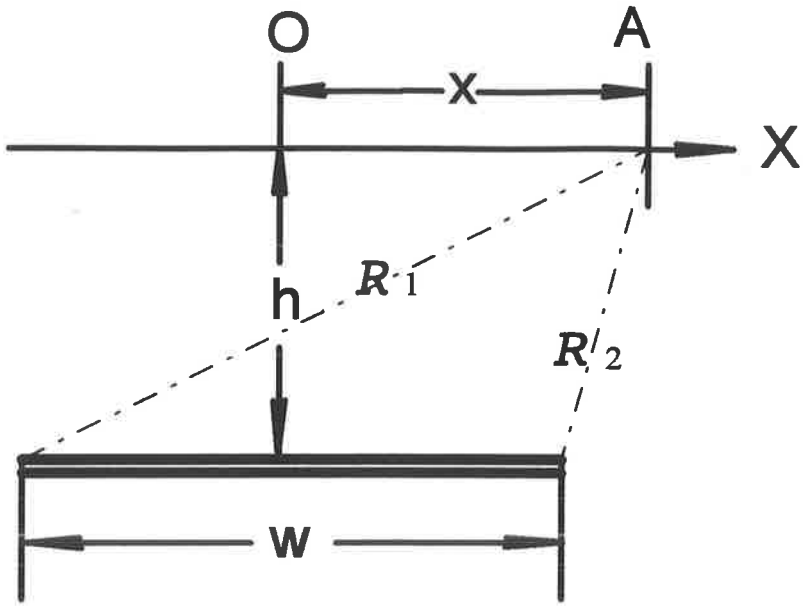

Figure A-7. Geometry of the thin plate model.

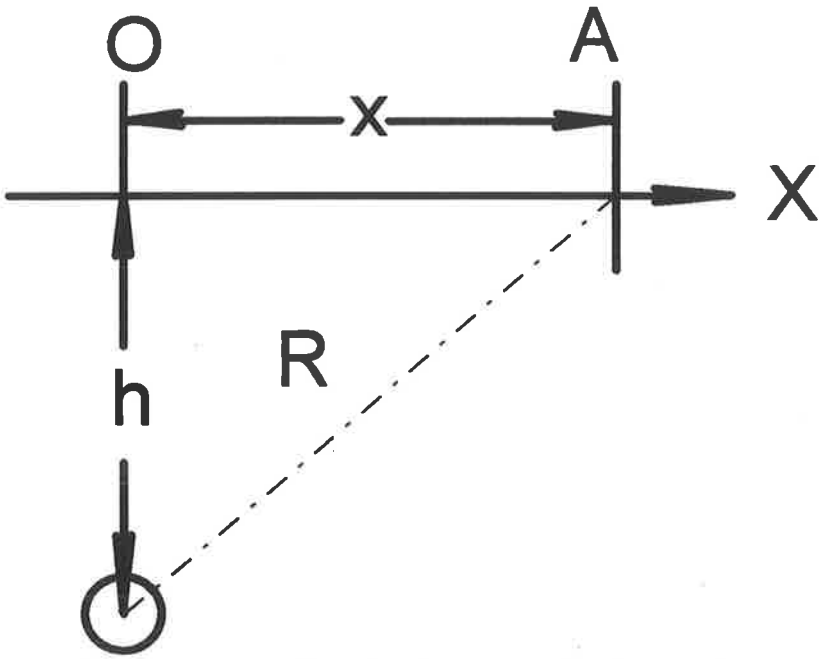

Figure A-8. Geometry of the horizontal cylinder model.

A.8 Thin plate model

Geometry of thin plate model is given in Figure A.7.

- **Arbitrary magnetisation case:**

$$\Delta H = 2PB\Big[\sin j\cdot(\frac{h}{{R_1}^2}-\frac{h}{{R_2}^2})-\cos j\cdot(\frac{x_1}{{R_1}^2}-\frac{x_2}{{R_2}^2})\Big] \quad (A.78)$$

$$\Delta Z = 2PB\Big[\cos j\cdot(\frac{h}{{R_1}^2}-\frac{h}{{R_2}^2})+\sin j\cdot(\frac{x_1}{{R_1}^2}-\frac{x_2}{{R_2}^2})\Big] \quad (A.79)$$

$$\Delta T = 2PBb\Big[\sin(i+j)\cdot(\frac{h}{{R_1}^2}-\frac{h}{{R_2}^2})-\cos(i+j)\cdot(\frac{x_1}{{R_1}^2}-\frac{x_2}{{R_2}^2})\Big] \quad (A.80)$$

$$H'_z = 2PB\Big[\sin j\cdot(\frac{h^2-{x_1}^2}{{R_1}^4}-\frac{h^2-{x_2}^2}{{R_2}^4})-\cos j\cdot(\frac{2hx_1}{{R_1}^4}-\frac{2hx_2}{{R_2}^4})\Big] \quad (A.81)$$

$$Z'_z = 2PB\Big[\cos j\cdot(\frac{h^2-{x_1}^2}{{R_1}^4}-\frac{h^2-{x_2}^2}{{R_2}^4})+\sin j\cdot(\frac{2hx_1}{{R_1}^4}-\frac{2hx_2}{{R_2}^4})\Big] \quad (A.82)$$

$$T'_z = 2PBb\Big[\sin(i+j)\cdot(\frac{h^2-{x_1}^2}{{R_1}^4}-\frac{h^2-{x_2}^2}{{R_2}^4})-\cos(i+j)(\frac{2hx_1}{{R_1}^4}-\frac{2hx_2}{{R_2}^4})\Big] \quad (A.83)$$

- **Induced magnetisation case:**

$$\Delta H = 2kTb\Big[\sin i\cdot(\frac{h}{{R_1}^2}-\frac{h}{{R_2}^2})-\cos i\cdot(\frac{x_1}{{R_1}^2}-\frac{x_2}{{R_2}^2})\Big] \quad (A.84)$$

$$\Delta Z = 2kTb\Big[\cos i\cdot(\frac{h}{{R_1}^2}-\frac{h}{{R_2}^2})+\sin i\cdot(\frac{x_1}{{R_1}^2}-\frac{x_2}{{R_2}^2})\Big] \quad (A.85)$$

$$\Delta T = 2kTb^2\Big[\sin(2i)\cdot(\frac{h}{{R_1}^2}-\frac{h}{{R_2}^2})-\cos(2i)\cdot(\frac{x_1}{{R_1}^2}-\frac{x_2}{{R_2}^2})\Big] \quad (A.86)$$

$$H'_z = 2kTb\Big[\sin i\cdot(\frac{h^2-{x_1}^2}{{R_1}^4}-\frac{h^2-{x_2}^2}{{R_2}^4})-\cos i\cdot(\frac{2hx_1}{{R_1}^4}-\frac{2hx_2}{{R_2}^4})\Big] \quad (A.87)$$

$$Z'_z = 2kTb\Big[\cos i\cdot(\frac{h^2-{x_1}^2}{{R_1}^4}-\frac{h^2-{x_2}^2}{{R_2}^4})+\sin i\cdot(\frac{2hx_1}{{R_1}^4}-\frac{2hx_2}{{R_2}^4})\Big] \quad (A.88)$$

$$T'_z = 2kTb^2\Big[\sin(2i)\cdot(\frac{h^2-{x_1}^2}{{R_1}^4}-\frac{h^2-{x_2}^2}{{R_2}^4})-\cos(2i)\cdot(\frac{2hx_1}{{R_1}^4}-\frac{2hx_2}{{R_2}^4})\Big] \quad (A.89)$$

where

$x_1 = x+\frac{w}{2}$,

$x_2 = x-\frac{w}{2}$,

${R_1}^2 = {x_1}^2+h^2$,

${R_2}^2 = {x_2}^2+h^2$.

The common field functions are $\frac{x_1}{{R_1}^2}-\frac{x_2}{{R_2}^2}$ (even, symmetric) and $\frac{h}{{R_1}^2}-\frac{h}{{R_2}^2}$ (odd, anti-symmetric). For the first derivatives, $\frac{2hx_1}{{R_1}^4}-\frac{2hx_2}{{R_2}^4}$ is the even function and $\frac{h^2-{x_1}^2}{{R_1}^4}-\frac{h^2-{x_2}^2}{{R_2}^4}$ is the odd function.

A.9 Horizontal cylinder model

Geometry of horizontal cylinder model is shown in Figure A.8.

- **Arbitrary magnetisation case:**

$$\Delta H = -2PB\Big[\sin j\cdot(\frac{2hx}{R^4})+\cos j\cdot(\frac{h^2-x^2}{R^4})\Big] \tag{A.90}$$

$$\Delta Z = 2PB\Big[-\cos j\cdot(\frac{2hx}{R^4})+\sin j\cdot(\frac{h^2-x^2}{R^4})\Big] \tag{A.91}$$

$$\Delta T = -2PBb\Big[\sin(i+j)\cdot(\frac{2hx}{R^4})+\cos(i+j)\cdot(\frac{h^2-x^2}{R^4})\Big] \tag{A.92}$$

$$H'_z = -4PB\Big[\cos j\cdot\frac{(h^2-3x^2)h}{R^6}-\sin j\cdot\frac{(x^2-3h^2)x}{R^6}\Big] \tag{A.93}$$

$$Z'_z = 4PB\Big[\sin j\cdot\frac{(h^2-3x^2)h}{R^6}+\cos j\cdot\frac{(x^2-3h^2)x}{R^6}\Big] \tag{A.94}$$

$$T'_z = -4PBb^2\Big[\cos(i+j)\cdot\frac{(h^2-3x^2)h}{R^6}-\sin(i+j)\cdot\frac{(x^2-3h^2)x}{R^6}\Big] \tag{A.95}$$

- **Induced magnetisation case:**

$$\Delta H = -2kTb\Big[\sin i\cdot(\frac{2hx}{R^4})+\cos i\cdot(\frac{h^2-x^2}{R^4})\Big] \tag{A.96}$$

$$\Delta Z = 2kTb\Big[-\cos i\cdot(\frac{2hx}{R^4})+\sin i\cdot(\frac{h^2-x^2}{R^4})\Big] \tag{A.97}$$

$$\Delta T = -2kTb^2\Big[\sin(2i)\cdot(\frac{2hx}{R^4})+\cos(2i)\cdot(\frac{h^2-x^2}{R^4})\Big] \tag{A.98}$$

$$H'_z = -4kTb\Big[\cos i\cdot\frac{(h^2-3x^2)h}{R^6}-\sin i\cdot\frac{(x^2-3h^2)x}{R^6}\Big] \tag{A.99}$$

$$Z'_z = 4kTb\Big[\sin i\cdot\frac{(h^2-3x^2)h}{R^6}+\cos i\cdot\frac{(x^2-3h^2)x}{R^6}\Big] \tag{A.100}$$

$$T'_z = -4kTb^2\Big[\cos(2i)\cdot\frac{(h^2-3x^2)h}{R^6}-\sin(2i)\cdot\frac{(x^2-3h^2)x}{R^6}\Big] \tag{A.101}$$

The common field functions are $\frac{h^2-x^2}{R^4}$ (even, symmetric) and $\frac{2hx}{R^4}$ (odd, anti-symmetric). For the first derivatives, $\frac{(h^2-3x^2)h}{R^6}$ is the even function and $\frac{(x^2-3h^2)x}{R^6}$ is the odd function.

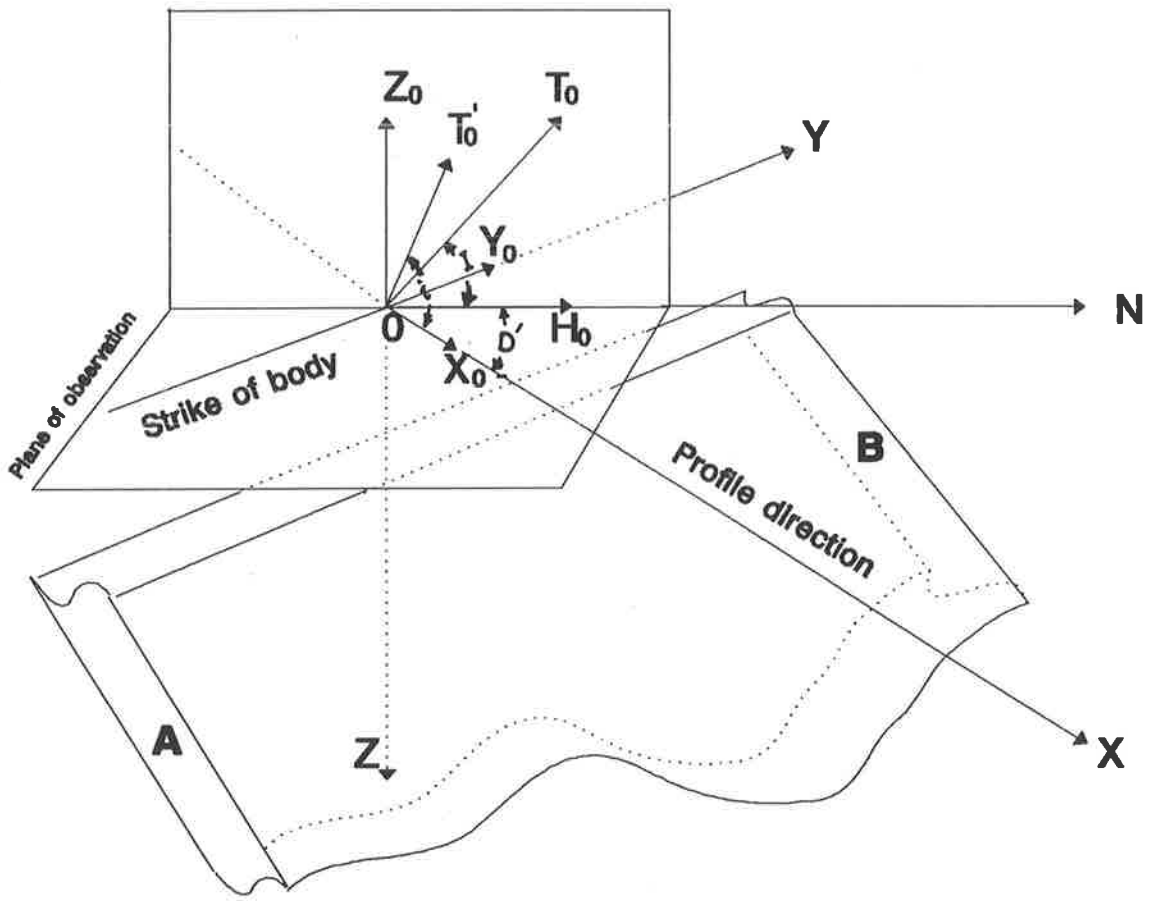

Figure B.1 Geometric and spatial relationship between a 2-D body and the elements of the magnetic field.

Appendix B

Derivation of the effective magnetic field

The following figures illustrates the geometry and spatial relationships (see Figure B.1) between a two-dimensional body and the elements of the magnetic field in which both the induced and remanent magnetisation exist (Figures B.2 & B.3). The diagram also demonstrates the derivation of the effective magnetic field (Gay, S.P., 1963).

The following terminology is used in the Appendix:

X: the axis along the observed profile (perpendicular to the source strike),

Y: the axis along the direction of the body's strike,

Z: the axis pointing vertically downward,

N: the axis pointing towards magnetic north,

T_0: intensity of the induced magnetic field,

Z_0: the vertical component of T_0,

H_0: the horizontal component of T_0 towards the magnetic north,

X_0:the horizontal component of T_0 along the x-axis,

Y_0:the horizontal component of T_0 along the$y$-axis,

i: effective inclination of the induced magnetic field from horizontal,

I: inclination of the earth's magnetic field from horizontal (negative in the southern hemisphere),

T_0': effective induced magnetic field intensity,

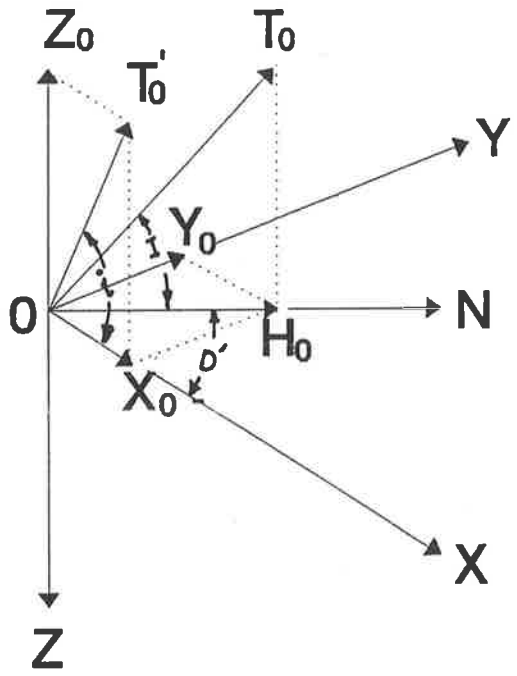

Figure B.2 **Elements of the magnetic field with induded magnetisation**

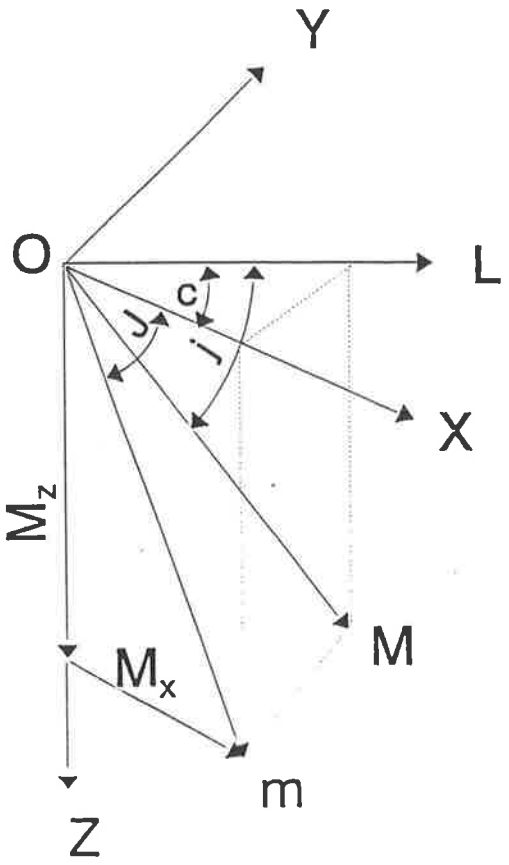

Figure B.3 **Elements of the magnetic field with remanent magnetisation.**

D': the angle between magnetic north and profile direction,

b: component of the total field unit vector in xz-plane.

J: inclination of the magnetisation from horizontal,

c: azimuth between the remanent magnetisation direction and profile direction,

j: effective inclination of the magnetisation,

M: remanent magnetisation,

M_x: the horizontal component of the remanent magnetisation along the x-axis,

M_z: the vertical component of the remanent magnetisation,

m: the effective remanent magnetisation,

P: the effective resultant magnetisation,

n: the effective inclination of resultant magnetisation.

The total magnetic field T_0' in the xz-plane depends on Z_0 and X_0, and is called the effective magnetic field on the profile (see Figure B.2); the effective inclination can be obtained from

$$\tan i = \frac{Z_0}{X_0} = \frac{T_0 \sin I}{T_0 \cos I \cos D'},$$

whence,

$$\tan i = \frac{\tan I}{\cos D'}, \tag{B.1}$$

or

$$i = \tan^{-1}\left(\frac{\sin I}{\cos I \cos D'}\right) = \tan^{-1}(\tan I \sec D'). \tag{B.2}$$

The effective magnetic field T_0' can be obtained from the relationship

$$Z_0 = T_0' \sin i = T_0 \sin I,$$

from which it follows

$$T_0' = T_0 \frac{\sin I}{\sin i}, \tag{B.3}$$

or

$$T_0' = T_0 b, \tag{B.4}$$

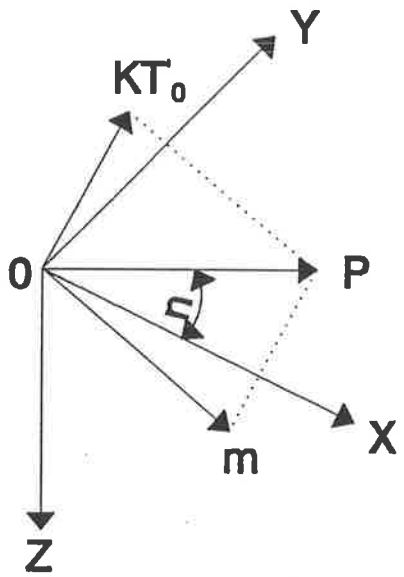

Figure B.4 **Effective resultant magnetisation (P) and its effective inclination (n).**

where $b = \frac{\sin I}{\sin i}$ or $b^2 = 1 - \cos^2 I \cdot \sin^2 D'$. b is the component in the xz-plane of a unit vector in the direction of the induced magnetic field.

When the remanent magnetisation exists, the effective resultant magnetisation (P) is the vector sum of the effects of the induced magnetisation and the remanent magnetisation. The effective remanent magnetisation can be obtained by using the same procedure as for the induced magnetisation case. The remanent magnetised effect (M) can be resolved into two parts: one component is along the strike direction (in the case of the two-dimensional body, this effect is negligible) and the other is the effective magnetised field (m) in the xz-plane (see Figure B.3). Combining the two effective magnetised components, the resultant effective magnetised field can also be obtained (see Figure B.4). Note that the effective induced magnetisation of a body is the product of the effective intensity (T_0') and its susceptibility (κ).

When interpreting the anomalies of regional aeromagnetic fields, it is difficult to obtain information about the inclination and intensity of the resultant magnetised field because of the lack of information about the remanent magnetisation. In general, this is only concerned with the effect of the earth's magnetic field; i.e. the induced magnetic field.

Appendix C

Summary of programs used in this thesis

C.1 Introduction

Efficient tools in the form of computer software are required to interpret magnetic and gravity data. Most of the computer programs which were used in this project were written by the author during the period of this research; some were written when she worked at the Beijing Computer Centre, Ministry of Geology and Mineral Resources, China (BCCMC). The major programs used are listed below, together with a brief description of their function. Programs written by other people are indicated as such.

C.2 Software and hardware requirements

Most of these programs are written in FORTRAN 77 and were developed and tested on the University of Adelaide Department of Geology and Geophysics' SPARC 2, and the computer Centre's VAX 780. Most applications have been run on a Sun workstation, or a VISUAL 550 terminal which is a relatively low resolution VT100 emulator. Output has commonly been an A4 paper via a laser printer and has also been produced on a Zeta plotter.

Programs may easily modified to run on most computers with a FORTRAN 77 compiler. Software modification may however be necessary to obtain graphical output for various plotting devices.

C.3 List of major programs

The programs listed below (see Table C.1) are cataloged into three groups,

Table C.1: List of the programs used in the project

Name of Program	Author
MASTER	J. Paine & A. Mitchell
POLYGON & IMAGE	S. Rajagopalan
STATS & GRIDVIEW	A. Lewis
AUTOMATIC_GAIN_CONTROL	S. Rajagopalan
GAMMA	J. Paine
POTENT	R. Almond
DYKE	Z. Shi
ILLUM	Z. Shi
TRANSF	Z. Shi[1]
MATCHED_FILTER	Z. Shi
BLOCK_DEPTH	Z. Shi
LONG	Z. Shi
AUTOMAG	Z. Shi
EQUAL	Z. Shi
ONED2	Z. Shi
DEPTH & DEPTHVG	Z. Shi[2]
ALTITUDE_COR	Z. Shi
PLOT_H & PLOT_VG	Z. Shi[3]

Note:

[1] The original program TRANS was written by the group in BCCMC including the author, the program was revised by the author in order to be compatible for the computers in VAX-VMS or UNIX systems.

[2] The original program DEPTH was written by B. Minty in 1981 for application of the original Naudy technique. The new program was significantly modified by this author to achieve the aim of the Improved Naudy Technique.

[3] The programs were revised based on the original program PLOT written by B. Minty in 1981.

1. common tools for producing grid data, contour map, stacked profiles and images;
2. conventional methods in potential field calculation;
3. specific data processing or interpretation of potential field data.

C.4 Summaries of program functionality

The functions of the programs are presented briefly as follows. The first section lists programs frequently used in the project; the second section emphasises the AUTOMAG program system.

C.4.1 Functions of commonly used programs

1. MASTER:

   Authors: J. Paine and A. Mitchell

   A series of programs which are basic routine tools for processing magnetic or gravity data; the functions of the programs are generating grid data, producing contour map, and displaying profile graph and stacked profiles. The output can be produced either on a Zeter Plotter or on a laser printer.

2. POLYGON & IMAGE:

   Author: S. Rajagopalan

   The two programs generate colour or grey images which can be output either on a screen or a laser printer.

3. STATS & GRIDVIEW

   Author: A. Lewis

   These programs are used to provide a statistical analysis of a set of data and to split or combine different data sets.

4. AUTOMATIC_GAIN_CONTROL

   Author: S. Rajagopalan

   The method developed by S. Rajagopalan is used to enhance the trend of weak anomalies on a set of profile data (Rajagopalan, 1987).

5. GAMMA

   Author: J. Paine

   GAMMA is a forward and inverse modelling program for VAX computers for 2-D magnetic bodies including dyke, sheet, edge, slab and polygonal models.

6. POTENT

   Author: R. Almond

   This is a powerful forward modelling program designed for an IBM PC, for applying either gravity or magnetic data of various 2-D and 3-D models.

7. DYKE

   Author: Z. Shi

   This program is used to calculate total magnetic intensity, vertical & horizontal components, and their first derivatives of magnetic fields of a 2-D dyke model with arbitrary strike angle. The program was used to test AUTOMAG.

8. ILLUM

   Author: Z. Shi

   The program, which is based on Kowalik and Glenn's work (Kowalik and Glenn, 1987), plays a role in calculation of shaded relief of potential data.

9. TRANSF

   Author: Beijing Computer Centre, revised by Z. Shi

   The program, which deals with potential field data in the form of a grid, makes various linear transformations in the frequency domain by using the Fast Fourier Transformation (FFT) algorithm. The functions of the program include component transformations, upward & downward continuations, the first and second derivatives of various components along arbitrary directions and transformations of magnetisation direction (e.g. reduction to the pole).

10. MATCHED_FILTER

    Author: Z. Shi

    The program is based on Spector and Grant's theory of energy spectral analysis (Spector and Grant, 1971) to determine average depths of ensemble shallow and deep magnetic bodies and to obtain factors related to the two level sources in an area. The information obtained above is used to design a filter and two different level of fields are separated. The method was extended by the author to process gravity data and to provide the depth information in an area.

11. BLOCK_DEPTH

    Author: Z. Shi

    The program is an extension of MATCHED_FILTER to provide a series of depth information (of at least two levels) at the centre of each block, in which the data in a large area are divided into many blocks and the method is applied to each block of data.

12. LONG

    Author: Z. Shi

    The program plays a role of anomaly separations by using different types of filters (high pass, band pass and low pass) which designed by Hou (Hou, 1980). After combining

information of radial energy spectra in a gridded data set, the anomalies at different depth levels are resolved. As a result, a set of depth-slice maps are produced for some area.

C.4.2 Instruction of AUTOMAG

AUTOMAG is a computer program system to interpret profile magnetic data, either from aeromagnetic or from ground magnetic survey. The depth, width, dip, susceptibility and location of the magnetic causative body can be determined, after running the following set of programs:

- EQUAL
- ONED2
- DEPTH & DEPTHVG
- ALTITUDE_COR
- PLOT_H & PLOT_VG

1. EQUAL

   author: Z. Shi

   The program is used to interpolate and thus convert irregularly spaced data to equally spaced data, by using a linear or Lagrange interpolation algorithm. The trace of the profile is based on the regression line of the original profile. The original data can be filtered and smoothed by chosen smoothing functions. The average value of the original field has been subtracted from the resultant interpolation data, in order to suit the FFT technique.

   Entire data are translated in order that observation sets are placed in a west to east or south to north sequence. Data variables must include at least line number, easting, northing, field and/or altitude. The input and output data can be formatted or unformatted.

2. ONED2

   author: Z. Shi

   The program has the same functions as program TRANSF does, which calculates various potential field transformations using FFT technique, however it is applied to profile data. The functions of the transformation are available as follows.

   (a) The total magnetic field can be converted into vertical component, horizontal component and total field, in which the magnetisation can be set to an arbitrary direction (reduction to the pole is a particular case).

   (b) The original field can be converted into the first and second derivatives along vertical and the horizontal directions.

   (c) All these transformed components can be continued upward and downward.

(d) The program also provides some other functions, such as pseudo gravity, magnetic potential, the module of the total field ($\sqrt{(\Delta Z)^2 + (\Delta H)^2}$), the module of the total gradient ($\sqrt{(\Delta Z'_z)^2 + (\Delta H'_z)^2}$), different wavelength anomalies and so on.

(e) The program can process gravity and airborne magnetic data as well as ground magnetic data.

3. DEPTH and DEPTHVG

The original DEPTH program was written by Brian Minty; the present one makes very significant modifications to the Naudy depth estimation technique (see Chapter 3). The program provides depth, width, dip and susceptibility values of the magnetic causative body on profile data. DEPTH uses components data (transformed horizontal component ΔH and vertical component ΔZ) and DEPTHVG uses first derivative data (horizontal gradient $\Delta H'_x$ and vertical gradient $\Delta Z'_z$).

The program can be used to interpret the total magnetic field data from either airborne or ground surveys.

4. PLOT_H & PLOT_VG

The original PLOT program was written by Brian Minty; it was revised by the author to suit to the VAX computer environment of the University of Adelaide.

According to the results obtained from DEPTH or DEPTHVG programs, the function of the program is to create a plot file on a Zeta plotter. The magnetic profile, the similarity coefficients between theoretical curve and magnetic anomalies and the depth estimates are shown in the plot file.

5. PSVIEW, which is included in MASTER

author: J. Paine

The program is used to convert a Zeta plot file into a postscript file.

Figure D.1: Comparison of the fields between thin plate and slab models

Model	Depth	Thickness	Susceptibility	Half Width
Thin Plate	100 m	10.0 m	0.005 cgs	200 m
Slab	70.7m	70.7 m	0.00071 cgs	200 m

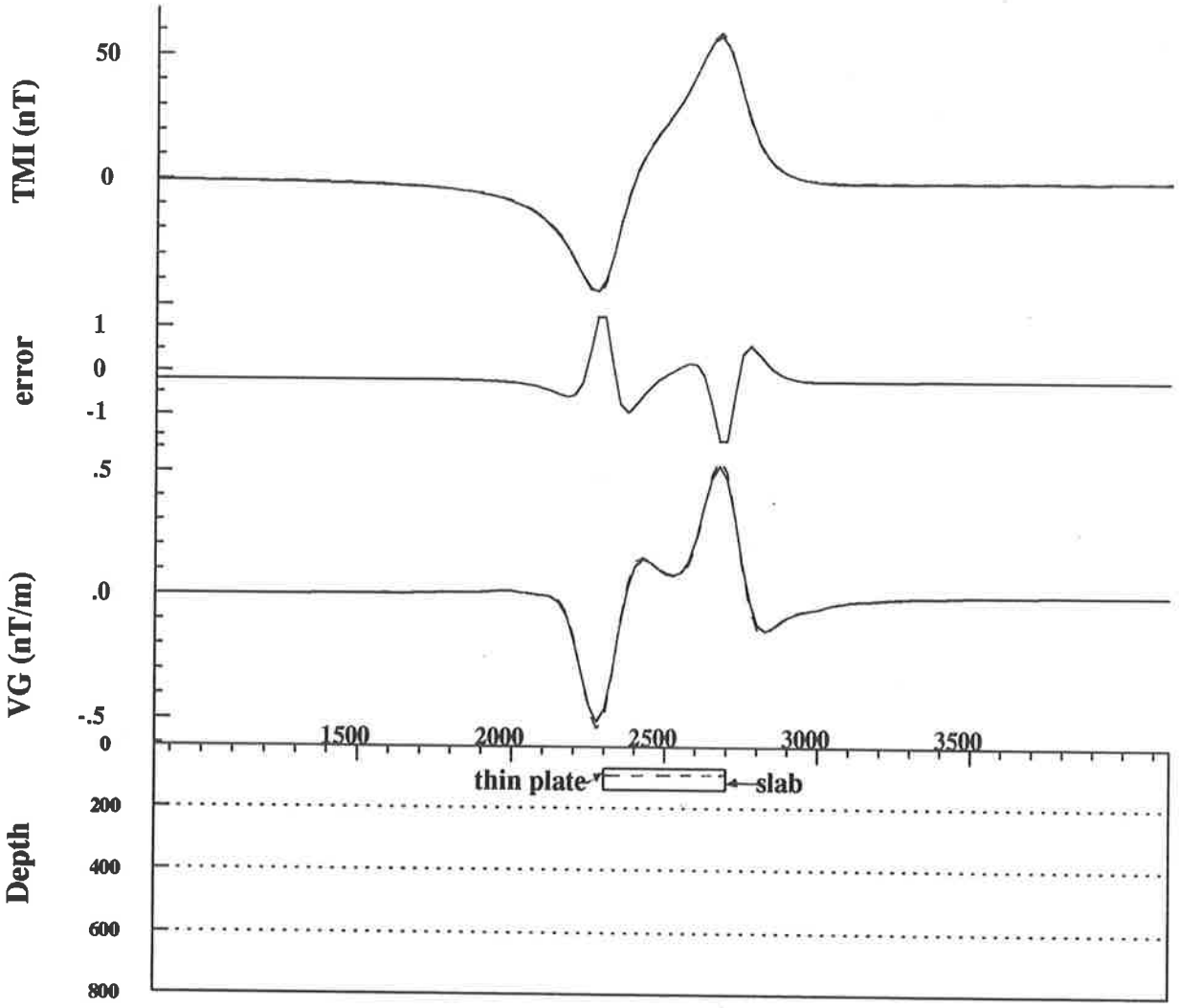

Solid Line : Thin Plate
Dashed Line: Slab

Appendix D

Relationship of magnetic fields of thin plate & slab

In this appendix, relationships are derived in the total magnetic field and the vertical gradient between a thin plate and a slab model in which the thickness (or depth extent) of the slab is equal to the depth to the top of the body.

Figure D.1 shows that the profiles of the total magnetic field and the vertical gradient for a thin plate model are coincident with those arising from a vertical slab. The parameters of two models are given in Table D.1. Note that the thickness of the slab is equal to its depth to the top of the body and the slab has the same width and dip as the thin plate. From Table D.1, it is readily seen that the ratio of the depths for the thin plate and the slab is 1.414 (i.e. $\sqrt{2}$) and that the products of the thickness and susceptibility are the same. The relationships between these two sets of models are illustrated by the formulae below.

Based on formulae (A.50) and (A.53) in Appendix A, the total magnetic field and its vertical gradient for this particular vertical slab, where the thickness is equal to the depth to the top of the body, can be easily obtained and is expressed as:

$$\Delta T(thick) = 2kTb^2 \left\{ \sin(2i) \left[\frac{1}{2} \cdot \ln \frac{(x-\frac{w}{2})^2 + h^2}{(x+\frac{w}{2})^2 + h^2} - \frac{1}{2} \cdot \ln \frac{(x-\frac{w}{2})^2 + 4h^2}{(x+\frac{w}{2})^2 + 4h^2} \right] \right\}.$$

Table D.1: Parameters of the thin plate and slab models

	Depth (m)	Width (m)	Thickness (m)	Susceptibility (10^{-6} cgs)	Susceptibility (10^{-5} SI)	Dip (Degrees)
Thin Plate	100	400	10	5000	6283	90
slab	70.7	400	70.7	707	888	90

$$- \cos(2i)\left[\tan^{-1}\frac{x+\frac{w}{2}}{h} - \tan^{-1}\frac{x-\frac{w}{2}}{h} - \tan^{-1}\frac{x+\frac{w}{2}}{2h} + \tan^{-1}\frac{x-\frac{w}{2}}{2h}\right]\Bigg\} \qquad (D.1)$$

and

$$T'_z(thick) = 2kTb^2\left\{\sin(2i)\left[\frac{h}{(x+\frac{w}{2})^2+h^2} - \frac{h}{(x-\frac{w}{2})^2+h^2} - \frac{2h}{(x+\frac{w}{2})^2+4h^2} + \frac{2h}{(x-\frac{w}{2})^2+4h^2}\right]\right.$$
$$\left. - \cos(2i)\left[\frac{x+\frac{w}{2}}{(x+\frac{w}{2})^2+h^2} - \frac{x-\frac{w}{2}}{(x-\frac{w}{2})^2+h^2} - \frac{x+\frac{w}{2}}{(x+\frac{w}{2})^2+4h^2} + \frac{x-\frac{w}{2}}{(x-\frac{w}{2})^2+4h^2}\right]\right\} \qquad (D.2)$$

The total field and its vertical gradient of a thin plate body can be directly obtained from formulae (A.86) and (A.89) in Appendix A:

$$\Delta T(plate) = 2k_vTb^2\left\{\sin(2i)\cdot\left[\frac{H}{(x+\frac{w}{2})^2+H^2} - \frac{H}{(x-\frac{w}{2})^2+H^2}\right]\right.$$
$$\left. - \cos(2i)\cdot\left[\frac{x+\frac{w}{2}}{(x+\frac{w}{2})^2+H^2} - \frac{x-\frac{w}{2}}{(x-\frac{w}{2})^2+H^2}\right]\right\} \qquad (D.3)$$

and

$$T'_z(plate) = 2k_vTb^2\left\{\sin(2i)\cdot\left[\frac{H^2-(x+\frac{w}{2})^2}{[(x+\frac{w}{2})^2+H^2]^2} - \frac{H^2-(x-\frac{w}{2})^2}{[(x-\frac{w}{2})^2+H^2]^2}\right]\right.$$
$$\left. - \cos(2i)\cdot\left[\frac{2H\cdot(x+\frac{w}{2})}{[(x+\frac{w}{2})^2+H^2]^2} - \frac{2H\cdot(x-\frac{w}{2})}{[(x-\frac{w}{2})^2+H^2]^2}\right]\right\} \qquad (D.4)$$

where

k_v is the volume susceptibility of the thin plate body, which is equal to the areal susceptibility k_s times the thickness of the body d which is less than one tenth of the depth,

T is the total intensity of the geomagnetic field,

b is the ratio of $\sin I$ to $\sin i$ (for details see Appendix B),

x is the horizontal distance between the observed point and the centre of the body,

w is the width of the body,

H is the depth to the top of the thin plate,

k is the susceptibility of the slab,

h is the depth to the top of the slab,

D is the thickness of the slab.

Based on the formulae shown above, it can be readily seen that the structures of all the formulae are similar. They consist of the sum of the product of $\sin(2i)$ and an odd function, and the product of $\cos(2i)$ and an even function. Their amplitudes $(2kTb^2)$ have the same value. By looking at each pair of formulae, the comparisons can be divided into four parts as follows:

1. the even function parts of the total field between two models,
2. the odd function parts of the total field between two models,
3. the even function parts of the vertical gradient between two models,
4. the odd function parts of the vertical gradient between two models.

The next step is to compare these functions and to analyse the errors from them. The assumption is made that the forms of the even and odd functions for the thin plate are the standard functions, therefore the corresponding functions from the slab can be approximated by those forms. The approximating expressions and the error analyses are provided in the following sections.

D.1 Comparison of even functions of TMI

The even function of the total field for the thin plate ($EVEN_{plate}$) given by (D.3) is

$$EVEN_{plate} = \frac{x + \frac{w}{2}}{(x + \frac{w}{2})^2 + H^2} - \frac{x - \frac{w}{2}}{(x - \frac{w}{2})^2 + H^2} \tag{D.5}$$

The even part of the total field of the slab ($EVEN_{slab}$) given by (D.1) can be expressed as

$$EVEN_{slab} = \tan^{-1}\frac{x + \frac{w}{2}}{h} - \tan^{-1}\frac{x - \frac{w}{2}}{h} - \tan^{-1}\frac{x + \frac{w}{2}}{2h} + \tan^{-1}\frac{x - \frac{w}{2}}{2h} \tag{D.6}$$

Rearranging and simplifying leads to

$$EVEN_{slab} = \tan^{-1}\frac{h \cdot (x + \frac{w}{2})}{(x + \frac{w}{2})^2 + 2h^2} - \tan^{-1}\frac{h \cdot (x - \frac{w}{2})}{(x - \frac{w}{2})^2 + 2h^2} \tag{D.7}$$

The Taylor series expansion for arctangent is

$$\tan^{-1} y = y - \frac{y^3}{3} + \frac{y^5}{5} + \cdots + (-1)^{n+1}\frac{y^{2n-1}}{2n-1} + \cdots \tag{D.8}$$

where $|y| < 1$.

Hence, if the absolute values of the functions inside the arctangent in (D.7) are less than unity, (D.7) can be further simplified. The proof of this fact is as follows:

For any two positive numbers, their algorithmic average is not less than their algebraic average; i.e. $\frac{A+B}{2} \geq (A \cdot B)^{\frac{1}{2}}$, or $(A \cdot B)^{\frac{1}{2}} \leq \frac{A+B}{2}$.

Let $A = 2h^2$ and $B = (x + \frac{w}{2})^2$ then it follows that

$$\left[2h^2 \cdot (x + \frac{w}{2})^2\right]^{\frac{1}{2}} \leq \frac{2h^2 + (x + \frac{w}{2})^2}{2}$$

which leads to

$$\frac{2^{\frac{3}{2}} \cdot |h \cdot (x + \frac{w}{2})|}{2h^2 + (x + \frac{w}{2})^2} \leq 1$$

that is

$$\begin{aligned} \frac{|h \cdot (x + \frac{w}{2})|}{2h^2 + (x + \frac{w}{2})^2} &\leq \frac{1}{2^{\frac{3}{2}}} \\ &\leq 0.3561 \end{aligned}$$

Using the same procedure as shown above, it also can be proved that

$$\begin{aligned} \frac{|h \cdot (x - \frac{w}{2})|}{2h^2 + (x - \frac{w}{2})^2} &\leq \frac{1}{2^{\frac{3}{2}}} \\ &\leq 0.3561 \end{aligned}$$

Therefore the absolute values for both the functions inside the arctangent in (D.7) are less than one. As a result, the expression (D.6) can be approximated by:

$$\begin{aligned} EVEN_{slab} &\approx h \cdot \left[\frac{x + \frac{w}{2}}{(x + \frac{w}{2})^2 + 2h^2} - \frac{x - \frac{w}{2}}{(x - \frac{w}{2})^2 + 2h^2}\right] \\ &= EVEN_{slab}{}^{approx} \end{aligned} \tag{D.9}$$

The error of the approximation (D.9) and the even part of the slab (D.6) can be obtained as follows:

Based on the expanded series of the tangent function shown in (D.8), the error of the approximation for the first term is $\frac{y^3}{3}$ and the maximum error for each term in (D.9) is $\frac{(0.3561)^3}{3}$;

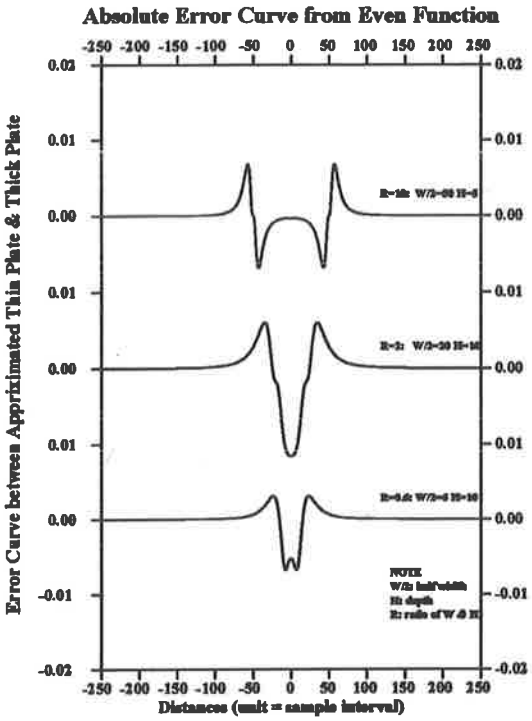

Figure D.2a

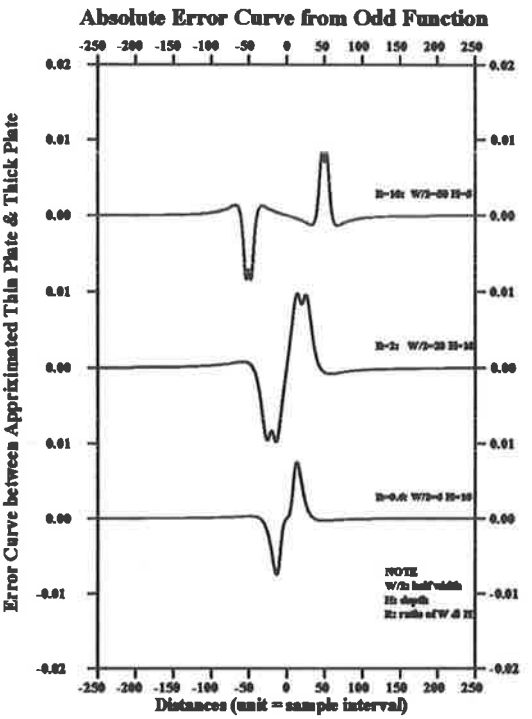

Figure D.2c

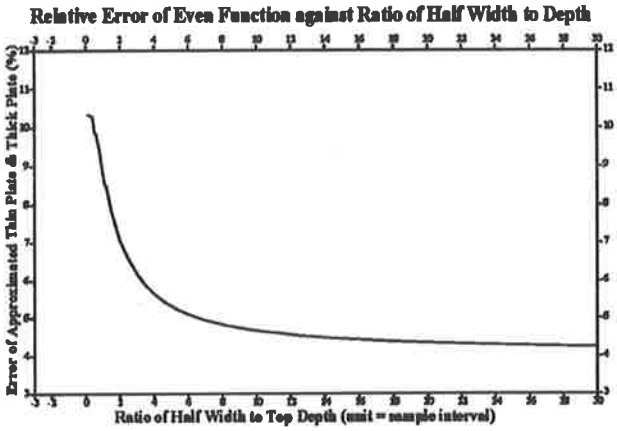

Figure D.2b

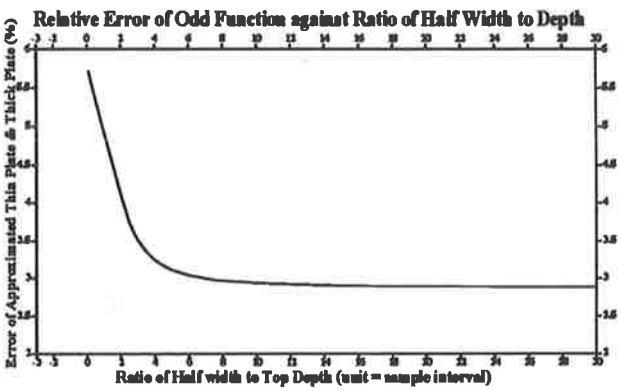

Figure D.2d

Figure D.2: Error analysis between thin plate and slab model curves for even and odd functions of component data.

i.e. 0.015. Thus, the maximum error of the approximation for the even function is less than 3%. Part A in Figure D.2 gives an example of the error distributions in which three typical models are presented and their key parameters ($W/2$: half width and H: depth to the top of the body) are given. From their distributions, it can be seen readily that large errors occur at centres of anomalies, especially in the area adjacent to two corners corresponding to the critical distance of the body; i.e. the distance from centre of the body to the located point at $+\left[(W/2)^2+H^2\right]^{\frac{1}{2}}$ or at $-\left[(W/2)^2+H^2\right]^{\frac{1}{2}}$ (Reford, 1978).

In order to quantify the error of the even function between the slab and its approximated thin plate, the relative errors against the ratios of the half width and the depth of the body are calculated, in which the relative errors are related to the maxima of the approximated errors. The formula for the relative error (R_{error}) is given by

$$R_{error} = \left| \frac{EVEN_{slab} - EVEN_{slab}{}^{approx}}{EVEN_{slab}} \right|$$

The Part B in Figure D.2 shows the changes of the relative errors against the ratio of the half width to the depth ($\frac{W/2}{H}$). From the curve, it can be seen that when the ratio is very small (less than 2), the relative error is appreciable but still less than 11%; when the ratio is large, the relative error tends towards a limiting value which is less than 5. Since these relative errors correspond to the maximum approximated errors, and the amplitudes of the errors are limited, the approximation using the slab formula instead of the formula of the thin plate is acceptable.

Comparing (D.9) with (D.5), two differences can be found. One is from the depth and the other is from the amplitude. It is clear that the relationship between these two depths is $H^2 = 2h^2$; i.e. $H = 1.414h$; the amplitude of the thin plate is 1 and the value for the slab is h. Since the thickness of this slab is equal to the depth, the factor of the amplitude h can be represented as the thickness of the slab (D). From the original formulae (D.1) and (D.3), another relationship between the susceptibilities can be determined: $k_v = k \cdot D$ or $k_s \cdot d = k \cdot D$, which leads to $\frac{k_s}{k} = \frac{D}{d}$; i.e. the ratio of the two susceptibilities is equal to the reciprocal ratio of these two thicknesses.

As a result of these two even function parts, the ratio of the depths between the thin plate and the slab is 1.414, the ratio of the susceptibilities between thin plate and the slab is $\frac{D}{d}$ and the error of the approximated expression is less than 3%.

D.2 Comparison of odd functions of TMI

The odd function of the total field for the thin plate given by (D.3) is

$$ODD_{plate} = \frac{H}{(x+\frac{w}{2})^2+H^2} - \frac{H}{(x-\frac{w}{2})^2+H^2} \tag{D.10}$$

The odd part of the total field of the slab given by (D.1) can be expressed as

$$ODD_{slab} = \frac{1}{2} \cdot \left[\ln \frac{(x-\frac{w}{2})^2 + h^2}{(x+\frac{w}{2})^2 + h^2} - \ln \frac{(x-\frac{w}{2})^2 + 4h^2}{(x+\frac{w}{2})^2 + 4h^2} \right] \tag{D.11}$$

Rearranging the logarithm terms,

$$ODD_{slab} = \frac{1}{2} \cdot \left[\ln \frac{(x-\frac{w}{2})^2 + h^2}{(x-\frac{w}{2})^2 + 4h^2} - \ln \frac{(x+\frac{w}{2})^2 + h^2}{(x+\frac{w}{2})^2 + 4h^2} \right] \tag{D.12}$$

The Taylor series expansion for the logarithm is

$$\ln y = 2 \left\{ \frac{y-1}{y+1} + \frac{1}{3} \cdot \left[\frac{y-1}{y+1} \right]^3 + \cdots + \frac{1}{2n-1} \cdot \left[\frac{y-1}{y+1} \right]^{2n-1} + \cdots \right\} \tag{D.13}$$

where $y > 0$.

Obviously, the functions inside the logarithm in (D.12) are greater than zero. Therefore (D.12) can be simplified as follows.

$$\begin{aligned} ODD_{slab} &= \frac{\frac{(x-\frac{w}{2})^2+h^2}{(x-\frac{w}{2})^2+4h^2} - 1}{\frac{(x-\frac{w}{2})^2+h^2}{(x-\frac{w}{2})^2+4h^2} + 1} + r_1 - \frac{\frac{(x+\frac{w}{2})^2+h^2}{(x+\frac{w}{2})^2+4h^2} - 1}{\frac{(x+\frac{w}{2})^2+h^2}{(x+\frac{w}{2})^2+4h^2} + 1} - r_2 \\ &= \frac{-3h^2}{2(x-\frac{w}{2})^2 + 5h^2} - \frac{-3h^2}{2(x+\frac{w}{2})^2 + 5h^2} + r_1 - r_2 \end{aligned}$$

where r_1, r_2 are the errors of the approximation for the first term by using the logarithm expansion.

r_1 corresponds to the term $\ln \frac{(x-\frac{w}{2})^2+h^2}{(x-\frac{w}{2})^2+4h^2}$ and r_2 corresponds to the term $\ln \frac{(x+\frac{w}{2})^2+h^2}{(x+\frac{w}{2})^2+4h^2}$. The size of these errors will be discussed later.

Rearranging the first and the second terms, ODD_{slab} can be written as

$$\begin{aligned} ODD_{slab} &= \frac{3h^2}{2(x+\frac{w}{2})^2 + 5h^2} - \frac{3h^2}{2(x-\frac{w}{2})^2 + 5h^2} + r_1 - r_2 \\ &= \frac{1.5h^2}{[(x+\frac{w}{2})^2 + 2h^2] + \frac{1}{2}h^2} - \frac{1.5h^2}{[(x-\frac{w}{2})^2 + 2h^2] + \frac{1}{2}h^2} + r_1 - r_2 \\ &= \frac{2\frac{1}{2}h^2(1+0.0608)}{[(x+\frac{w}{2})^2 + 2h^2] + \frac{1}{2}h^2} - \frac{2\frac{1}{2}h^2(1+0.0608)}{[(x-\frac{w}{2})^2 + 2h^2] + \frac{1}{2}h^2} + r_1 - r_2 \end{aligned} \tag{D.14}$$

In order to approximate the expression (D.14) with respect to the odd function of the total field for the thin plate model, the approximation of each term in (D.14) is considered. The first term can be rewritten as

$$\frac{2\frac{1}{2}h^2(1+0.0608)}{[(x+\frac{w}{2})^2 + 2h^2] + \frac{1}{2}h^2} = \frac{2\frac{1}{2}h^2(1+0.0608)}{[(x+\frac{w}{2})^2 + 2h^2]\,1.25} + r_3$$

where r_3 is given by

$$
\begin{aligned}
r_3 &= \frac{2\frac{1}{2}h^2(1+0.0608)}{[(x+\frac{w}{2})^2+2h^2]+\frac{1}{2}h^2} - \frac{2\frac{1}{2}h^2(1+0.0608)}{[(x+\frac{w}{2})^2+2h^2]\,1.25} \\
&= \frac{2\frac{1}{2}h^2\cdot 1.0608\cdot(x+\frac{w}{2})^2\cdot 0.25}{\{[(x+\frac{w}{2})^2+2h^2]+\frac{1}{2}h^2\}\{[(x+\frac{w}{2})^2+2h^2]\,1.25\}} \\
&= \frac{h^2\cdot(x+\frac{w}{2})^2\cdot 0.3}{\{[(x+\frac{w}{2})^2+2h^2]+\frac{1}{2}h^2\}\,[(x+\frac{w}{2})^2+2h^2]}
\end{aligned}
$$

The second term in (D.14) can be rewritten as

$$
\frac{2\frac{1}{2}h^2(1+0.0608)}{[(x-\frac{w}{2})^2+2h^2]+\frac{1}{2}h^2} = \frac{2\frac{1}{2}h^2(1+0.0608)}{[(x-\frac{w}{2})^2+2h^2]\,1.25} + r_4
$$

where similarly to r_3, r_4 can be expressed as

$$
r_4 = \frac{h^2\cdot(x-\frac{w}{2})^2\cdot 0.3}{\{[(x-\frac{w}{2})^2+2h^2]+\frac{1}{2}h^2\}\,[(x-\frac{w}{2})^2+2h^2]}
$$

Now the odd function of the total field for the slab model can be rewritten as

$$
\begin{aligned}
ODD_{slab} &= \frac{2\frac{1}{2}h^2(1+0.0608)}{[(x+\frac{w}{2})^2+2h^2]\,1.25} - \frac{2\frac{1}{2}h^2(1+0.0608)}{[(x-\frac{w}{2})^2+2h^2]\,1.25} + r_1 - r_2 + r_3 - r_4 \\
&= \left[\frac{2\frac{1}{2}h^2}{[(x+\frac{w}{2})^2+2h^2]} - \frac{2\frac{1}{2}h^2}{[(x-\frac{w}{2})^2+2h^2]}\right]\cdot(1-0.15) + r_1 - r_2 + r_3 - r_4 \\
&= \left[\frac{2\frac{1}{2}h^2}{[(x+\frac{w}{2})^2+2h^2]} - \frac{2\frac{1}{2}h^2}{[(x-\frac{w}{2})^2+2h^2]}\right] + R_1 + R_2 + R_3 \qquad \text{(D.15)}
\end{aligned}
$$

where R_1, R_2 and R_3 are given as follows:

$$
R_1 = -\left[\frac{2\frac{1}{2}h^2}{[(x+\frac{w}{2})^2+2h^2]} - \frac{2\frac{1}{2}h^2}{[(x-\frac{w}{2})^2+2h^2]}\right]\cdot 0.15
$$

$$
\begin{aligned}
R_2 &= r_1 - r_2 \\
&= \frac{1}{3}\cdot\left\{\left[\frac{-3h^2}{2(x-\frac{w}{2})^2+5h^2}\right]^3 - \left[\frac{-3h^2}{2(x+\frac{w}{2})^2+5h^2}\right]^3\right\}
\end{aligned}
$$

$$
\begin{aligned}
R_3 &= r_3 - r_4 \\
&= \frac{0.3h^2\cdot(x+\frac{w}{2})^2}{[(x+\frac{w}{2})^2+2.5h^2]\,[(x+\frac{w}{2})^2+2h^2]} - \frac{0.3h^2\cdot(x-\frac{w}{2})^2}{[(x-\frac{w}{2})^2+2.5h^2]\,[(x-\frac{w}{2})^2+2h^2]}
\end{aligned}
$$

Since the error of the approximation from the odd function of the total field between the slab and the approximated thin plate is very complicated, the error probably can not be expressed

by a simple analytic formula. The qualitative and quantitative analyses of the errors can be made by using the functions R_1, R_2 and R_3, and from a test model which uses the same model set as shown in the last section. The effect of the absolute errors of the odd function are then revealed, the details are as follows.

1. Qualitative error analysis:

   It can be seen from the above error formulae that as x becomes very large, each of the errors R_1, R_2 and R_3 become negligible, regardless of the width and depth of the body. The most significant errors occur near the centre of the anomaly, and particularly at the corner corresponding to the critical distance of the body. The error test is shown in Part C in Figure D.2 for the same three models as those shown in Part A of Figure D.2. The error distributions show the same characteristics as described for the error functions (R_1, R_2 and R_3).

2. Quantitative error analysis:

   A similar procedure as for the even function (see Section D.1) is used to deal with the odd function, in which the relative errors for the ratio of half width to top depth are calculated and shown in Part D of Figure D.2. A similar trend as for the even function has been found in the odd function: if the ratios are increased from a value close to zero, the relative errors rapidly drop off; when the ratios are greater than 4, the errors tend towards a constant whose value is less than 3.

   The result of the error analysis of the odd function for the approximated thin plate and the slab models is that the maximum amplitude of the relative error is less than 6%.

By comparing the expression (D.12) for the thin plate model and the expression (D.15) for the slab model, the same relationships between the depths and the amplitudes can be found; i.e. the depth (H) of the thin plate is 1.414 times the depth (h) of the slab and the ratio of the two amplitudes between slab and thin plate is h.

According to the results of the error analyses for the even and odd functions of the total fields which arise from the thin plate and the slab model in which the depth extent is equal to the top depth, the thin plate model can be approximated by its corresponding slab, with acceptable accuracy.

D.3 Comparison of even functions of vertical gradient

The even part of the vertical gradient of the thin plate is given by

$$EVEN_{plate}{}^{vg} = \left[\frac{2H(x+\frac{w}{2})}{[(x+\frac{w}{2})^2+H^2]^2} - \frac{2H(x-\frac{w}{2})}{[(x-\frac{w}{2})^2+H^2]^2}\right] \tag{D.16}$$

The even part of the vertical gradient of the slab can be expressed as

$$EVEN_{slab}{}^{vg} = \left[\frac{x+\frac{w}{2}}{(x+\frac{w}{2})^2+h^2} - \frac{x-\frac{w}{2}}{(x-\frac{w}{2})^2+h^2} - \frac{x+\frac{w}{2}}{(x+\frac{w}{2})^2+4h^2} + \frac{x-\frac{w}{2}}{(x-\frac{w}{2})^2+4h^2}\right]$$

This expression can be decomposed into

$$EVEN_{slab}{}^{vg} = part1 + part2$$

where

$$\begin{aligned} part1 &= \frac{x+\frac{w}{2}}{(x+\frac{w}{2})^2+h^2} - \frac{x+\frac{w}{2}}{(x+\frac{w}{2})^2+4h^2} \\ &= \frac{3(x+\frac{w}{2})h^2}{\left[(x+\frac{w}{2})^2+h^2\right]\left[(x+\frac{w}{2})^2+4h^2\right]} \\ part2 &= \frac{x-\frac{w}{2}}{(x-\frac{w}{2})^2+h^2} - \frac{x-\frac{w}{2}}{(x-\frac{w}{2})^2+4h^2} \\ &= \frac{3(x-\frac{w}{2})h^2}{\left[(x-\frac{w}{2})^2+h^2\right]\left[(x-\frac{w}{2})^2+4h^2\right]} \end{aligned}$$

$part1$ can be rewritten in the following way:

$$\begin{aligned} part1 &= \frac{1.5h\cdot 2h(x+\frac{w}{2})}{(x+\frac{w}{2})^4+5h^2(x+\frac{w}{2})^2+4h^4} \\ &= \frac{\left[2\cdot 2^{\frac{1}{2}}\cdot h^2(x+\frac{w}{2})\right]+0.173h^2(x+\frac{w}{2})}{\left[(x+\frac{w}{2})^2+2h^2\right]^2+h^2(x+\frac{w}{2})^2} \\ &= \frac{\left[2\cdot 2^{\frac{1}{2}}\cdot h^2(x+\frac{w}{2})\right](1+0.06)}{\left[(x+\frac{w}{2})^2+2h^2\right]^2(1+t)} \end{aligned}$$

where t is a number varying from 0 to 0.125.

The proof of this fact is given below: as previously mentioned, the algorithmic average of two positive numbers is greater than or equal to their algebraic average; i.e. $\frac{(A+B)}{2} \geq (A\cdot B)^{\frac{1}{2}}$, hence $(A+B)^2 \geq 4A\cdot B$ or $\frac{A\cdot B}{2} \leq \frac{(A+B)^2}{8}$. Put $A=(x+\frac{w}{2})^2$ and $B=2h^2$, then

$$h^2(x+\frac{w}{2})^2 \leq 0.125\left[(x+\frac{w}{2})^2+2h^2\right]^2 \tag{D.17}$$

so that,

$$h^2(x+\frac{w}{2})^2 = t\cdot\left[(x+\frac{w}{2})^2+2h^2\right]^2$$

where t is a positive number which is not greater than 0.125.

Therefore $part1$ can be further rewritten as:

$$part1 = \frac{2\cdot\sqrt{2}\cdot h^2(x+\frac{w}{2})}{\left[(x+\frac{w}{2})^2+2h^2\right]^2}\cdot\frac{1.06}{(1+t)}$$

Using this same procedure, $part2$ can be expressed as:

$$part2 = \frac{2 \cdot \sqrt{2} \cdot h^2 (x - \frac{w}{2})}{\left[(x - \frac{w}{2})^2 + 2h^2\right]^2} \cdot \frac{1.06}{(1+t)}$$

$EVEN_{slab}{}^{vg}$ is the combination of these parts:

$$\begin{aligned} EVEN_{slab}{}^{vg} &= \left\{ \frac{2 \cdot \sqrt{2} \cdot h^2 (x + \frac{w}{2})}{\left[(x + \frac{w}{2})^2 + 2h^2\right]^2} - \frac{2 \cdot \sqrt{2} \cdot h^2 (x - \frac{w}{2})}{\left[(x - \frac{w}{2})^2 + 2h^2\right]^2} \right\} \cdot \frac{1.06}{(1+t)} \\ &= \left\{ \frac{2 \cdot \sqrt{2} \cdot h^2 (x + \frac{w}{2})}{\left[(x + \frac{w}{2})^2 + 2h^2\right]^2} - \frac{2 \cdot \sqrt{2} \cdot h^2 (x - \frac{w}{2})}{\left[(x - \frac{w}{2})^2 + 2h^2\right]^2} \right\} \cdot (1+r) \end{aligned} \tag{D.18}$$

Where the relationship between r and t is

$$r = \frac{0.06 - t}{1+t}$$

It is easy to prove that r is an absolute error of this even function; $r = -6\%$ if $t = 0.125$, and $r = 6\%$ if $t = 0$.

Comparing expression (D.16) for $EVEN_{plate}{}^{vg}$ with expression (D.18) for $EVEN_{slab}{}^{vg}$, the same relationships as shown in the above sections about two depths and amplitudes can be found. The absolute error (r) between the approximation of the thin plate model and the slab model is less than 6%.

D.4 Comparison of odd functions of vertical gradient

The odd part of the vertical gradient of the thin plate can be expressed as

$$ODD_{plate}{}^{vg} = \frac{H^2 - (x + \frac{w}{2})^2}{\left[(x + \frac{w}{2})^2 + H^2\right]^2} - \frac{H^2 - (x - \frac{w}{2})^2}{\left[(x - \frac{w}{2})^2 + H^2\right]^2} \tag{D.19}$$

The odd part of the vertical gradient of the slab can be expressed as

$$ODD_{slab}{}^{vg} = \left[\frac{h}{(x + \frac{w}{2})^2 + h^2} - \frac{h}{(x - \frac{w}{2})^2 + h^2} - \frac{2h}{(x + \frac{w}{2})^2 + 4h^2} + \frac{2h}{(x - \frac{w}{2})^2 + 4h^2} \right] \tag{D.20}$$

After rearranging expression (D.20), it can be written as

$$ODD_{slab}{}^{vg} = part1 + part2$$

where

$$part1 = \frac{h}{(x + \frac{w}{2})^2 + h^2} - \frac{2h}{(x + \frac{w}{2})^2 + 4h^2}$$

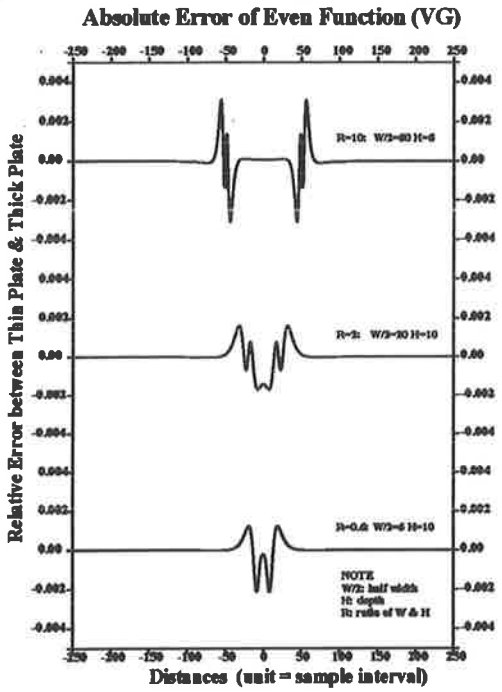

Figure D.3a

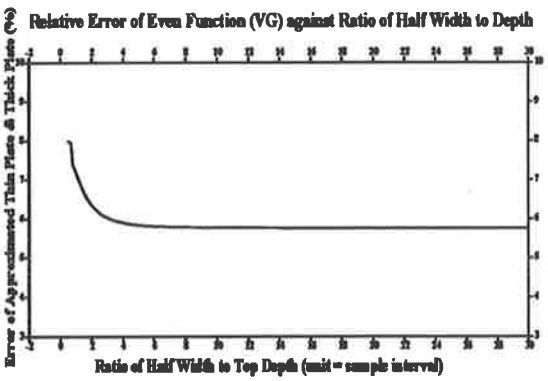

Figure D.3b

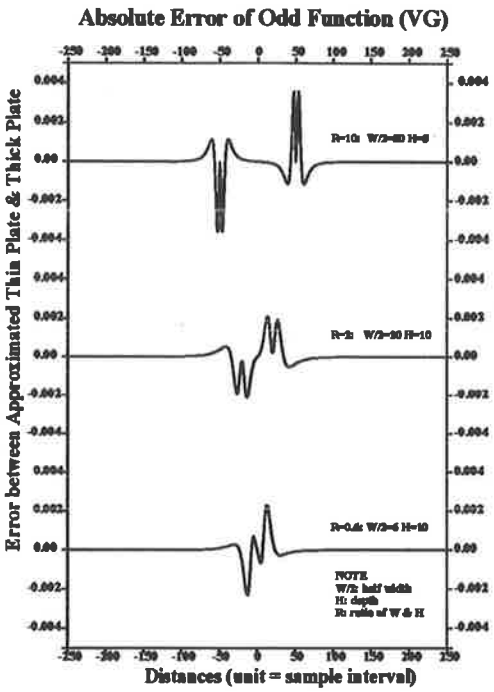

Figure D.3c

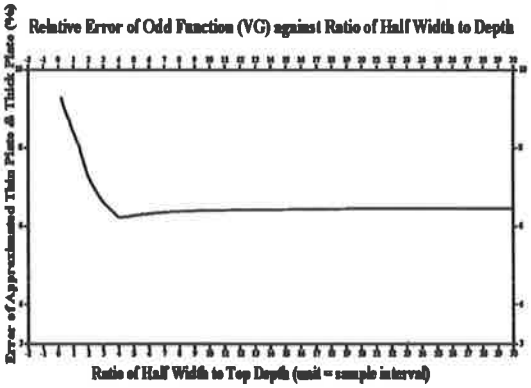

Figure D.3d

Figure D.3: Error analysis between thin plate and slab model curves for even and odd functions of vertical gradient data.

$$= \frac{h\left[2h^2-(x+\frac{w}{2})^2\right]}{\left[(x+\frac{w}{2})^2+2h^2\right]^2+h^2(x+\frac{w}{2})^2}$$

$$part2 = \frac{h}{(x-\frac{w}{2})^2+h^2}-\frac{2h}{(x-\frac{w}{2})^2+4h^2}$$

$$= \frac{h\left[2h^2-(x-\frac{w}{2})^2\right]}{\left[(x-\frac{w}{2})^2+2h^2\right]^2+h^2(x-\frac{w}{2})^2}$$

According to (D.17); i.e. $h^2(x+\frac{w}{2})^2 \leq 0.125\left[(x+\frac{w}{2})^2+2h^2\right]^2$, these can be simplified to

$$part1 = \frac{h\left[2h^2-(x+\frac{w}{2})^2\right]}{\left[(x+\frac{w}{2})^2+2h^2\right]^2(1+t)}$$

$$part2 = \frac{h\left[2h^2-(x-\frac{w}{2})^2\right]}{\left[(x-\frac{w}{2})^2+2h^2\right]^2(1+t)}$$

where t varies from 0 to 0.125. Combining these parts, it leads to

$$ODD_{slab}{}^{vg} = \left\{\frac{h\left[2h^2-(x+\frac{w}{2})^2\right]}{\left[(x+\frac{w}{2})^2+2h^2\right]^2}-\frac{h\left[2h^2-(x-\frac{w}{2})^2\right]}{\left[(x-\frac{w}{2})^2+2h^2\right]^2}\right\}\cdot(1+r) \qquad (D.21)$$

where

$$r = \frac{-t}{1+t}$$

If $t = 0.125$, $r = -11\%$ and if $t = 0$, $r = 0\%$.

Comparing expression (D.19) for $ODD_{plate}{}^{vg}$ and (D.21) for $ODD_{slab}{}^{vg}$, relationships about the two depths and amplitudes can be found. The absolute error of the approximation for slab model is less than 11%.

The error analyses for both the even and odd functions of the vertical gradient are shown in parts A, B, C and D in Figure D.3 respectively, in which the same procedure and model type are chosen as were given in the case of the total magnetic field. Based on the distributions of the graphs, similar conclusions are made:

1. The major errors occur at the centre of the anomalies or at the corner corresponding to the critical distance.
2. The values of the relative errors are less than 10%.
3. When the ratio of the half width to the top depth moves away from the origin, the relative error rapidly decreases and tends to some constant.

The four parts of the total field and gradient data for the thin plate and slab models have been compared. Under the error analyses, all the results show the same relationships between two depths and two amplitudes; i.e. the depth (H) of the thin plate is 1.414 times the depth

(h) of the slab and the ratio of the amplitudes of thin plate and slab is h (depth or thickness of the slab). This shows that the total field or its vertical gradient caused by the thin plate model can be modelled by the field or gradient created by the vertical slab model in which the depth extent of the body is equal to the depth of the body.

Appendix E

Correction of 2-D body with oblique strike

E.1 Introduction

The error in depth estimation introduced by the strike of a 2-D body being non-perpendicular to the profile is one of the problems in using an automatic interpretation technique which processes data along a line (e.g. Werner deconvolution, Euler depth estimation and the Naudy technique), as well as for other methods (e.g. graphical and characteristic point methods). Methods dealing with the profile data assume that the direction of the observed profile is perpendicular to the strike direction of a causative body, and this introduces errors into the estimations. The relative errors between the true parameters (e.g. depth and width) and their corresponding estimated values can be greater than 150%, these depend on the size of the angle (γ) between the directions of the strike and observed profile. The smaller the angles, the greater the errors are. The errors for estimating depth and width can be determined by

$$error = 1 - \frac{1}{|\sin\gamma|} \tag{E.1}$$

The derivation is given in Section E.2. Since errors occur in the application of the automatic interpretation and other techniques, it is necessary to search for a solution to remove the effect on the estimation, for situations where the observed profile is non-perpendicular to the strike.

McGrath and Hood (1970) and Shuey (1972) considered a strike correction between the observed data and a line perpendicular to the strike of the body, which is fundamental to the correction of parameters. Some authors (Naudy, 1971 and Hartman *et al.*, 1971) have mentioned a correction of the depth estimation by an angle between the directions of the strike and the observed profile, but they have not given the detailed derivation and also left some questions for other parameter corrections. This author provides two methods to solve this problem; both solutions are suitable to the case of magnetic or gravity field.

E.2 Parameter correction between true and interpreted body

E.2.1 Presentation of the method

This method can be applied to any 2-D bodies provided the strike direction, which can be obtained from their magnetic or gravity contour maps, are known. If the parameters of a 2-D dyke body in which the strike is in an arbitrary direction, can be estimated by using an automatic interpretation or some other methods, the true or corrected parameters can be obtained by using the following formulae (E.2) to (E.5):

$$h = h'|\sin\gamma|, \tag{E.2}$$

$$w = w'|\sin\gamma|, \tag{E.3}$$

$$d = 2i - 2i' + d', \tag{E.4}$$

$$k = k'\frac{b'^2 \cdot \sin d'}{b^2 \cdot \sin d}, \tag{E.5}$$

where

h: depth to the top of the true body,

w: width of the true body,

d: dip of the true body measured clockwise from the positive of the principle profile which is perpendicular to the strike direction,

k: susceptibility of the true body,

h': apparent depth calculated from interpretation programs,

w': apparent width calculated from interpretation programs,

d': apparent dip calculated from interpretation programs,

k': apparent susceptibility calculated from interpretation programs,

γ: angle between the directions of the observed profile and strike of body.

i: effective inclination angle related to the observed profile (for details see Appendix B),

i': effective inclination angle related to the principle profile,

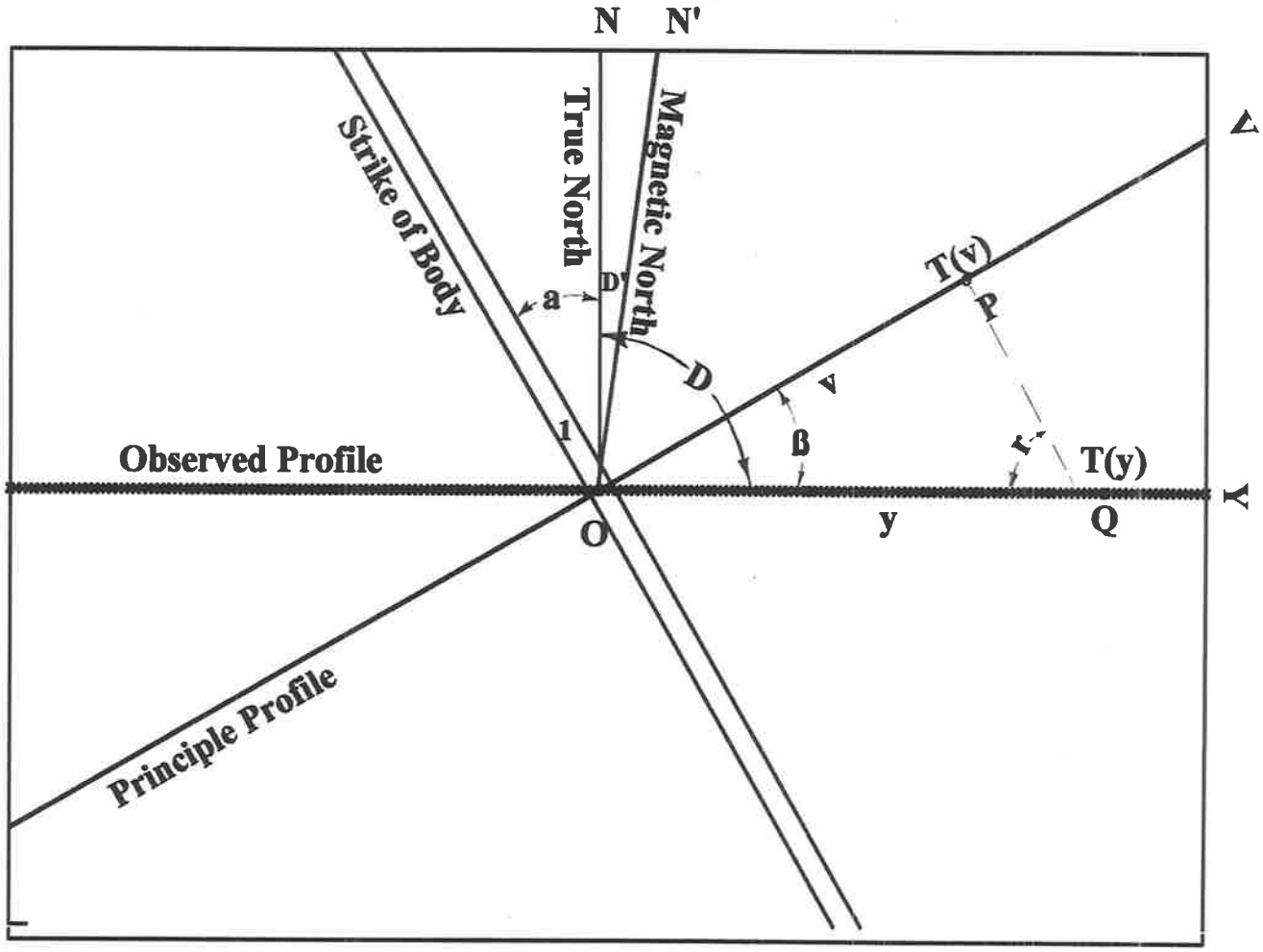

Figure E.1: **Plan view of 2-D body related to its principle profile and observed profile.**

I: inclination of the earth's magnetic field,

b: ratio of $\sin I$ to $\sin i$ (for details see Appendix B),

b': ratio of $\sin I$ to $\sin i'$.

Note that in the case of gravity data, the corrections are only available to depth and width, the dip is unaffected and the susceptibility is not applicable.

Details of the derivation are given in following sections.

E.2.2 Derivation

Several steps are needed to find the relationship between the true and interpreted bodies in which the estimates of parameters are obtained under an assumption of the principle profile:

1. The first step is to establish the magnetic field formula on a profile in which the two-dimensional causative body is at an arbitrary strike direction.
2. Assume that the observed profile is a principle profile, from the field of this profile the parameters of body are determined, which are called apparent parameters.
3. The final step is to compare the two sets of parameters and find the relationships between them.

It is well known that magnetic effects caused by a two-dimensional body at those positions, which are parallel to the direction of the body strike, are the same. Figure E.1 illustrates the relationship among magnetic fields along two different profiles in which the Y-axis represents a measured profile and the V-axis represents a profile perpendicular to the direction of the strike of the body. It can be readily seen that the two total magnetic fields $\Delta T(Q)$ and $\Delta T(P)$ are equal in the segment where PQ is parallel to the strike. Based on this fact, a further relationship between the total magnetic fields of these two profiles is revealed. The case of a thin sheet body with infinite depth extent is given as an example. Before discussing this case, general explanations for the parameters used in the formulae and diagrams are provided:

N: direction of the true north,

N': direction of the magnetic north,

Y: the axis along the observed profile,

V: the axis perpendicular to the strike of the true body,

α: strike angle measured clockwise from the true north direction,

D: azimuth angle between the observed profile and true north, measured clockwise from the true north,

D': declination of the earth's magnetic field (negative in the west),

I: inclination of the earth's magnetic field,

i: effective inclination of the induced magnetic field measured from horizontal,

b: ratio of $\sin I$ to $\sin i$ (for details see Appendix B),

T: intensity of the earth's magnetic field,

h: depth to the top of the body,

w: width of the body,

d: dip of the body measured clockwise from the positive V-axis,

k: susceptibility of the body,

DE: depth extent of the body,

h': apparent depth calculated from interpretation programs,

w': apparent width calculated from interpretation programs,

d': apparent dip calculated from interpretation programs,

k': apparent susceptibility calculated from interpretation programs,

v: vertical distance between the observed point P and the 2-D body,

O: intersection point of the axis of the 2-D body, the V-axis and Y-axis,

y: distance between points O and Q,

ds: sample interval of the profile,

A: azimuth angle between magnetic north and the calculated profile direction.

The total magnetic field $\Delta T(v)$ caused by a thin sheet body at location P on the principle profile (V-axis) can be expressed as

$$\Delta T(v) = 2kTb^2 w \sin d \left[-\cos(2i-d) \cdot \left(\frac{v}{v^2+h^2}\right) + \sin(2i-d) \cdot \left(\frac{h}{v^2+h^2}\right) \right] \qquad \text{(E.6)}$$

Note that the effective inclination i is calculated from the profile V.

From Figure E.1, the distance v can be expressed as a function of y; i.e.

$$v = y \cos \beta,$$

where β is the angle between the observed profile and the principle profile,

or

$$v = y\sin\gamma = y\sin(180^\circ - \gamma).$$

This leads to

$$v = y\sin(D-\alpha),$$

where $D-\alpha$ is the angle between the strike and the observed profile direction. Equation E.6 can be rewritten as a function of y

$$\Delta T(y) = 2kTb^2 w\sin d\left[-\cos(2i-d)\frac{y\sin(D-\alpha)}{(y\sin(D-\alpha))^2+h^2} + \sin(2i-d)\frac{h}{(y\sin(D-\alpha))^2+h^2}\right] \tag{E.7}$$

Because the total magnetic field $\Delta T(y)$ at location Q on profile Y is equivalent to $\Delta T(v)$ at location P on profile V, $\Delta T(y)$ can be represented by (E.7). After rearranging equation E.7, $\Delta T(y)$ is given by:

$$\Delta T(y) = 2kTb^2\frac{w}{\sin(D-\alpha)}\sin d\left[-\cos(2i-d)\frac{y}{y^2+(\frac{h}{\sin(D-\alpha)})^2} + \sin(2i-d)\frac{\frac{h}{\sin(D-\alpha)}}{y^2+(\frac{h}{\sin(D-\alpha)})^2}\right] \tag{E.8}$$

This equation gives the total magnetic field of an observed profile in which the strike of the body is not perpendicular to the profile direction. It is worth mentioning that the effective inclination i is calculated from the V-axis and not from the Y-axis.

Considering the observed profile as a principle profile; i.e. imaging a two-dimensional body which is perpendicular to the Y-axis, and assuming that the total magnetic field caused by this imaginary body is the same as the field of the observed profile. Therefore $\Delta T(y)$ can be expressed by another form related to a new body in which the parameters of the body are denoted by symbol ($'$) after each parameter,

$$\Delta T(y) = 2k'Tb'^2 w'\sin d'\left[-\cos(2i'-d')\cdot(\frac{y}{y^2+h'^2}) + \sin(2i'-d')\cdot(\frac{h'}{y^2+h'^2})\right] \tag{E.9}$$

The parameters of the new body can be obtained from some interpretation methods, for example, Werner deconvolution, the improved Naudy technique or graphical methods. Note that these parameters are not real values of the true body. By comparing each term in (E.8) and (E.9), relationships between the two sets of parameters can be easily found; the results are listed below. Since distances (h or w) are involved, absolute values of triangle functions are adopted.

$$h = h'|\sin(D-\alpha)| = h'|\sin\gamma|,$$

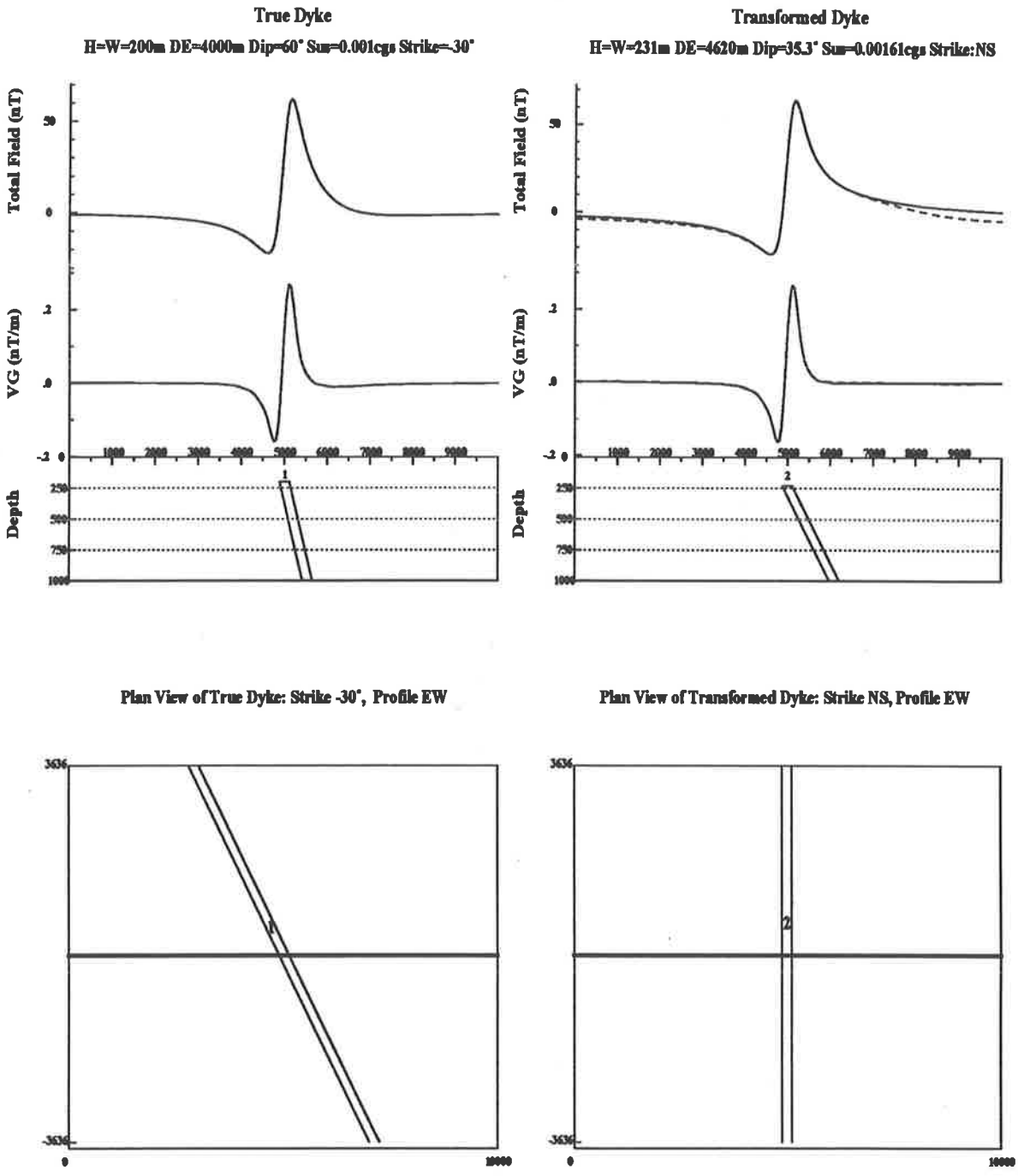

Figure E.2 Comparison of true dyke with its transformed dyke using Method One

or

$$h = h'|\cos\beta|, \tag{E.10}$$

$$w = w'|\sin(D-\alpha)| = w'|\sin\gamma|,$$

or

$$w = w'|\cos\beta|, \tag{E.11}$$

$$d = 2i - 2i' + d', \tag{E.12}$$

$$k = k'\frac{b'^2 \cdot \sin d'}{b^2 \cdot \sin d}, \tag{E.13}$$

where the effective inclination i corresponds to profile V, which is given by

$$i = \tan^{-1}\frac{\tan I}{\cos(D - D' - \beta)}$$

or

$$i = \tan^{-1}\frac{\tan I}{\cos[90^\circ - (D' - \alpha)]}$$

and the effective inclination i' is related to profile Y and given by

$$i' = \tan^{-1}\frac{\tan I}{\cos(D - D')},$$

$$b = \frac{\sin I}{\sin i},$$

$$b' = \frac{\sin I}{\sin i'}.$$

The error from the estimated depth or width can be calculated by

$$error = \frac{h - h'}{h}$$

or

$$error = \frac{w - w'}{w}.$$

According to (E.10) and (E.11), the error can be determined by (E.1).

The relationships between the parameters of the true body and the apparent parameters of the imaginary body are revealed. In order to test the result, an example from the theoretical model is shown in Figure E.2, and the two sets of body parameters are listed in Table E.1. The upper graphs show the total magnetic field and its vertical gradient as well as the geometry

Table E.1: Parameters of the true dyke and transformed dyke

Parameters of True Dyke										
Strike	**Profile**	**Depth**	**Width**	**Dip**	**Depth Extent**	k	I	D'	i	b
$-30°$	EW	200 m	200 m	60°	4 km	0.001 cgs	$-65°$	7.5°	$-74.15°$	0.942
Parameter of Imaginary Dyke										
Strike	**Profile**	**Depth**	**Width**	**Dip**	**Depth Extent**	k'	I	D'	i'	b'
0°	EW	231 m	231 m	35.3°	4620 m	0.0016 cgs	$-65°$	7.5°	$-86.52°$	0.908

of the body; the lower graphs show plan views of the profile and the strike of the body. The left side of the figure shows the case of the true body and right side shows the imaginary body. With the graphs on the top right it is readily seen that two sets of total magnetic field match very well. The dashed lines show the results of the imaginary body and the solid lines show the fields caused by the true body.

This correction of the parameters for an infinite thin sheet can be extended into an infinite dyke, edge, thin plate and other two-dimensional bodies. It has been found that the body with limited depth extent will give rise to some error in the corrections, but the gradient data produces a better solution than the total field data. If the magnetic data are reduced to the pole or the gravity data are applied, the correction is simplified. It need only be applied to the estimations of the depth and width, since the values of the dip and susceptibility are unaffected.

If the strikes of bodies in the study area vary considerably then this method is time consuming, since the correction must be done for each anomaly individually. The following method provides the other approach for correcting parameters.

E.3 Entire profile correction

The second method is only applicable in areas where a dominant strike direction exists for the majority of 2-D bodies.

This method considers a conversion between magnetic field data on two different profiles arising from the same two-dimensional body, in which one is the observed profile (Y-axis) and another is the profile perpendicular to the strike direction (V-axis) (see Figure E.1). The first method showed that the relationships between these two field data and their coordinates is

$$\Delta T_P(v) = \Delta T_Q(y)$$

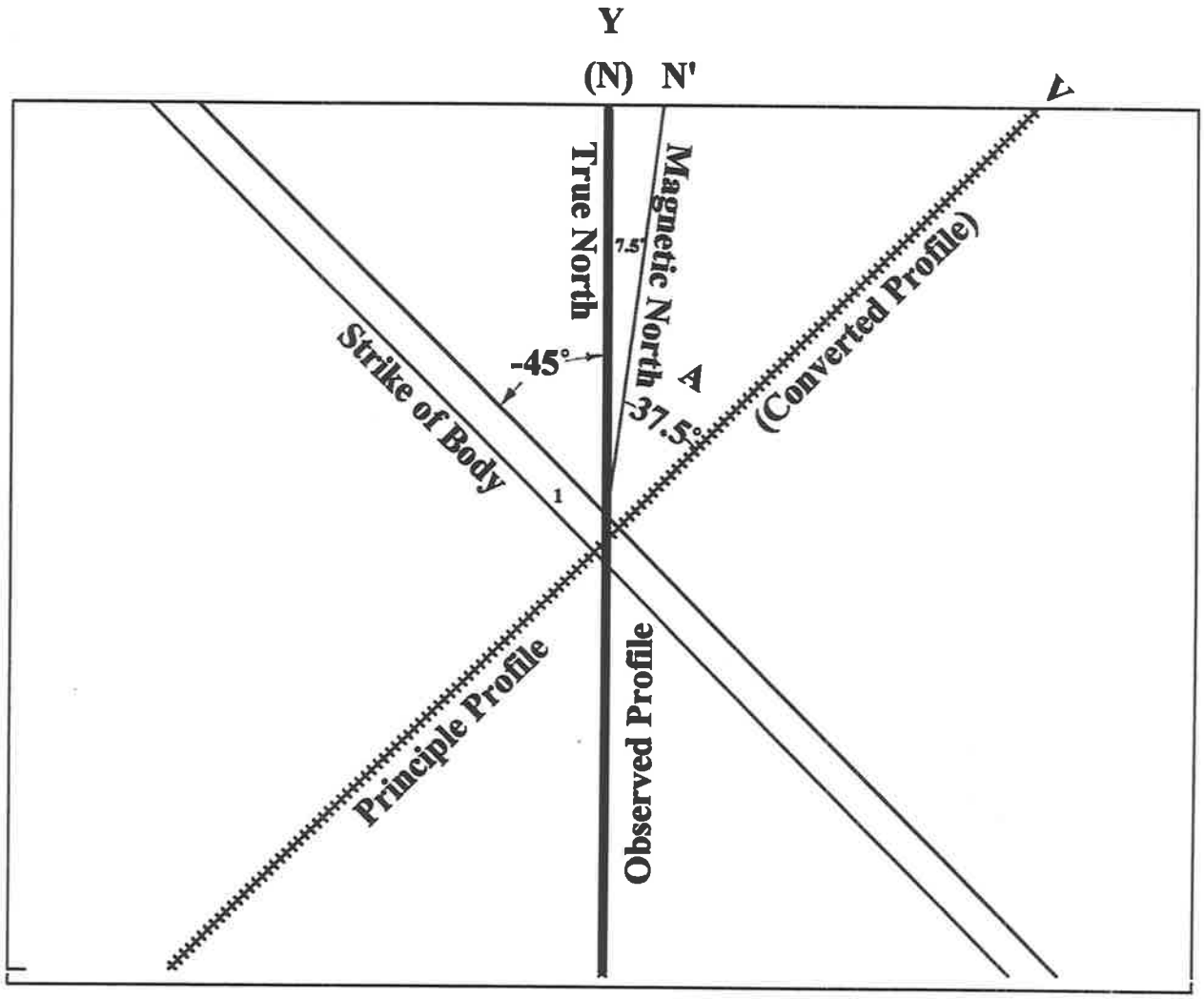

Figure E.3: **Plan view of the example (shown in Fig. E.4) of 2-D body related to its principle profile and observed profile.**

and

$$v = y\sin(D - \alpha). \tag{E.14}$$

The first step for the second method is to convert the observed field data on the Y-axis into appropriate data on the V-axis. After analysing the converted data by using an interpretation program, the estimated parameters of the causative body are obtained. These determinations directly show the parameters of the causative body. Details of the application and limitation of this method are shown below.

In practice, the magnetic field on the observed profile can be converted into the field on a principle profile. The actual procedure for this conversion is very simple: the converted data have the same values as the observed data, the only requirement is to change the sample interval based on equation (E.14). When applying an interpretation program, the azimuth angle between the calculated profile and magnetic north is required to calculate the effective inclination. Therefore one should carefully determine the azimuth angle, which is the angle (A) between N'-axis and V-axis (see Figure E.3).

A theoretical model has been tested using this method. Figure E.3 illustrates distributions of the observed and converted profiles and the strike of the true thick dyke body, in which the observed profile (Y-axis) is in the same direction as true north (N-axis) and the converted profile is the V-axis. In Figure E.4 the magnetic field and its vertical gradient and their causative bodies are shown. The graph on the left illustrates the magnetic field and geometry from the true body, while the right side shows the case of an interpreted body. It is seen that the shapes of the two sets of anomalies are exactly the same, as are the parameters of the two dykes. The only differences are the coordinate of the profile, which indicates the difference between the two sample intervals, and the azimuth angle between magnetic north and the profile direction.

Table E.2 shows the comparison of the parameters for the same dyke model as in Figure E.4, with estimations of the interpreted dyke using the improved Naudy technique (vertical gradient version). It is readily seen that the estimations coincide perfectly with the true parameters (depth, width, dip, susceptibility and depth extent). Differences between these two sets of bodies occur for the sampling interval, azimuth angle and effective inclination parameters. The position of the centre of the body is also different, the calculated position needs to be corrected by (E.14).

E.4 Conclusions

In conclusion, both methods are convenient to use and can obtain high quality estimations.

1. The first method works directly on the original profile, the estimated parameters of the causative body need to be corrected by equations (E.2) to (E.5).
2. If the data have been reduced to the pole, the first method becomes simpler to use; the corrections are only applied for the depth and width, and not for the dip and susceptibility.

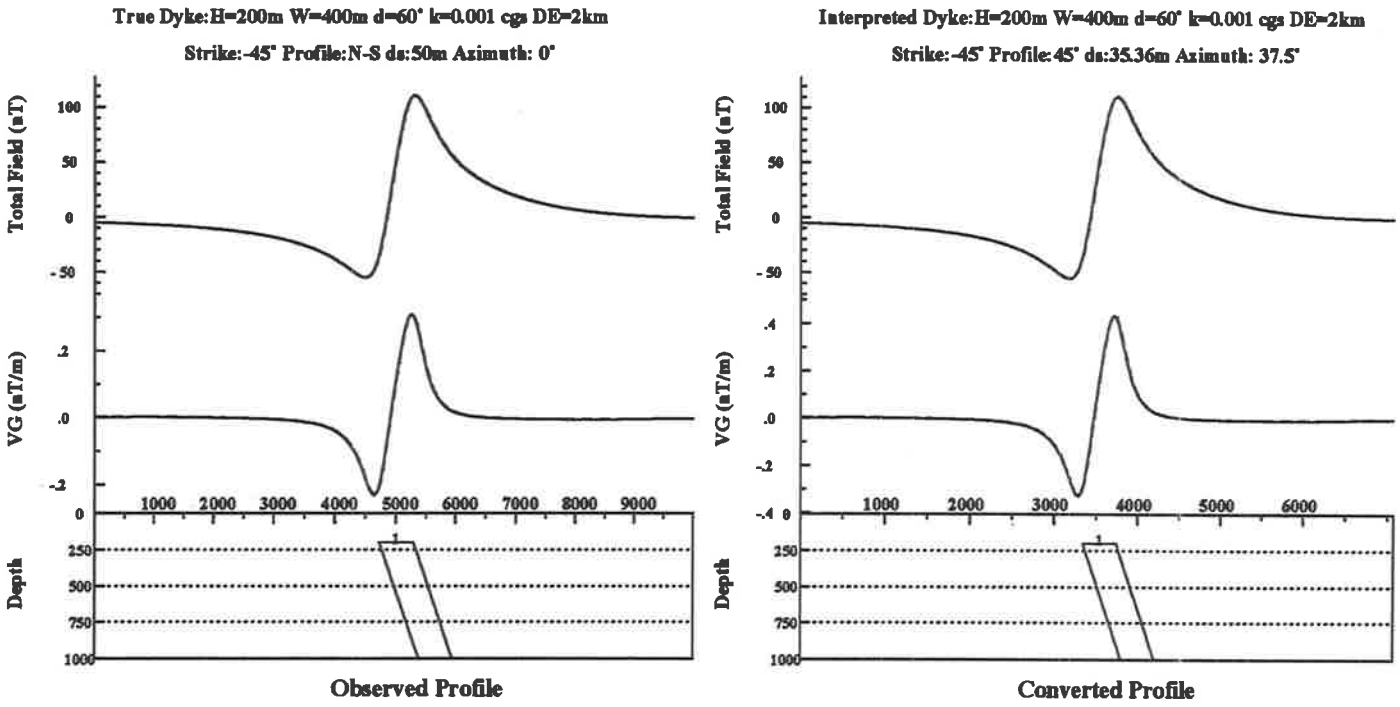

Figure E.4: Comparison of true dyke with its interpreted dyke using Method Two.

Table E.2: Parameters of the true dyke and transformed dyke

Parameters of True Dyke									
Strike	**Profile**	**Depth**	**Width**	**Dip**	**Depth Extent**	k	i	A	ds
$-45°$	N-S	200 m	400 m	60°	2000 m	0.001 cgs	$-74.15°$	7.5°	50 m
Parameter of Transformed Dyke									
Strike	**Profile**	**Depth**	**Width**	**Dip**	**Depth Extent**	k'	i'	A	ds'
$-45°$	45°	200 m	400 m	60.6°	2000 m	0.001004 cgs	$-65.2°$	37.5°	35.36 m

3. The second method works on the converted profile, in which the sampling interval and azimuth angle are different to the observed profile, and the determinations from the converted profile are directly related to the estimated parameters of the body.

4. The second method is far more time efficient than the first method if it is applied to a suitable area.

5. If the strikes of the major geological bodies are not identical in a study area, the second method is not applicable.

Appendix F

Tables of rock properties in Eyre Peninsula

In this appendix, the rock properties including densities and susceptibilities of major rock formations in the study area, Eyre Peninsula are presented. The rocks were collected by SADEME, K. Stewart and the author. Part of measurements were made by K. Stewart but majority of measurements were made by the author. She participated in the project of "Eyre Peninsula Pb-Zn Preliminary Drill Target" conducted by SADME, more susceptibility measurements of the core samples were made and the results were included in a SADME report (Cowley, 1991).

Table F.1: Rock properties (density and susceptibility) in Gawler Range area (1)

Site No. of Rock Sample	Rock Type	Location	Numbers of Sample	Densities g/cm^3	Susceptibility $SI \times 10^{-5}$
884 GH1	Basalt	Lake Everard	1	2.86	5500
884 GH2	Basalt	Lake Everard	1	2.87	4500
884 GH4	Dacite	Lake Everard	1	2.63	no reading
884 GH5	Andesite	Lake Everard	1	2.74	2900
884 GH6	Dacite	Lake Everard	1	2.71	1000
884 GH7	Dacite	Lake Everard	1	2.73	250
884 GH8	Dacite	Lake Everard	1	2.70	100
884 GH9	Rhyolite Dyke	Lake Everard	1	2.50	4
884 GH10	Dacite	Lake Everard	1	2.66	1500
884 GH11	Dacite	Lake Everard	1	2.70	200
884 GH12	Yantea R/Dacite	Lake Everard	1	2.62	360
884 GH13	Dacite	Lake Everard	1	2.51	120
884 GH14	Yantea R/Dacite	Lake Everard	1	2.60	250
884 GH15	Rhyolite	Lake Everard	1	2.54	33
884 GH18	Bunburn Dacite	Lake Everard	1	2.61	170
884 GH19	Rhyolite	Lake Everard	1	2.53	180
884 GH20	Dacite	Lake Everard	1	2.57	230
884 K1	Hiltaba Granite	Kokatha Area	1	2.62	320
884 K3	Basalt	Kokatha Area	1	2.90	1200
884 K5	Basalt	Kokatha Area	1	2.87	15,000
884 K6	Dacite	Kokatha Area	1	2.67	22-74
884 K7	Dacite	Kokatha Area	1	2.63	59
884 K8	Basalt	Kokatha Area	1	2.91	7500

Note:

The measurement was carried out (made) by K. Stewart.

Locations of the samples are shown in that thesis (Stewart, 1992).

Table F.2: Rock properties (density and susceptibility) in Gawler Range area (2)

Site No. of Rock Sample	Rock Type	Location	Numbers of Sample	Densities g/cm^3	Susceptibility $SI \times 10^{-5}$
884 K11	Rhyolite	Kokatha Area	1	2.64	660
884 K12	Basalt	Kokatha Area	1	2.78	2800
884 K16	Basalt	Kokatha Area	1	2.76	2000
884 K17	Andesite	Kokatha Area	1	2.68	2000
884 K19	Dacite	Kokatha Area	1	2.70	2400
884 K22	Dacite	Kokatha Area	1	2.66	530
884 K25	Rhyolite	Kokatha Area	1	2.63	42
884 Y1A	Yardea Dacite	Southern Gawler Range	1	2.70	1800
884 Y1B	Yardea Dacite	Southern Gawler Range	1	2.88	60
884 Y2	Yardea Dacite	Southern Gawler Range	1	2.64	52
884 Y4	Yardea Dacite	Southern Gawler Range	1	2.67	900
884 Y5	Yardea Dacite	Southern Gawler Range	1	2.65	640
884 Y10	Yardea Dacite	Southern Gawler Range	1	2.66	1200
884 Y11	Yardea Dacite	Southern Gawler Range	1	2.65	840
884 Y12	Yardea Dacite	Southern Gawler Range	1	2.65	1000
884 Y14	Yardea Dacite	Southern Gawler Range	1	2.65	1300
884 Y15	Yardea Dacite	Southern Gawler Range	1	2.65	560
884 Y16	Yardea Dacite	Southern Gawler Range	1	2.65	240
884 Y17	Yardea Dacite	Southern Gawler Range	1	2.64	810
884 Y18	Yardea Dacite	Southern Gawler Range	1	2.65	1200
884 Y19	Yardea Dacite	Southern Gawler Range	1	2.64	830
884 Y21	Yardea Dacite	Southern Gawler Range	1	2.64	800
884 Y20	Yardea Dacite	Southern Gawler Range	1	2.61	690

Note:

The measurements were carried out (made) by K. Stewart.

Locations of the samples are shown in that thesis (Stewart, 1992).

Table F.3: Density measurement of rock in Gawler Range area (3)

Site No. of Rock Sample	Rock Type	Location	Numbers of Sample	Densities g/cm^3
884 H1	Granite	Everard Lake?	1	2.58
884 H2	Granite	Everard Lake?	1	2.59
884 H3	Granite	Everard Lake?	1	2.67
884 H4	Granite	Everard Lake?	1	2.65
884 H5	Granite	Everard Lake?	1	2.61
275	Basalt	Gawler Range Area	1	3.03
IR2 213′2″ – 217′2″	Gabbro	Inkster	1	2.97
IR2 215′6″ – 217′2″	Gabbro	Inkster	1	3.02
IR2 251′ – 252′	Gabbro	Inkster	1	3.08
IR2 252′4″ – 253′	?	Inkster	1	2.77
IR3 287′ – 288′	?	Inkster	1	2.66
908 21	Basalt	Kokatha	1	2.84
908 22	Basalt	Kokatha	1	2.80
908 71	Basalt	Kokatha	1	2.89
908 72	Basalt	Kokatha	1	2.88
908 118	Basalt	Kokatha	1	2.88
908 120	Basalt	Kokatha	1	2.83
908 123	Basalt	Kokatha	1	2.85
908 150	Basalt	Kokatha	1	2.89

Note:

The samples were collected from K. Stewart.

The density of the rock was measured by O. Tual a high school student on work experience.

Table F.4: Density measurement of rock in Gawler Range area (4)

Site No. of Rock Sample	Rock Type	Location	Numbers of Sample	Densities g/cm^3
0/1	Rhyolite	Quarry	1	2.63
0/1	Rhyolite	Quarry	1	2.56
0/1	Rhyodacite	Quarry	1	2.58
1/1	Basalt	Kokatha	1	2.84
1/2	Basalt	Kokatha	1	3.09
1/4	Rhyodacite	Kokatha	1	2.63
1/5	Rhyodacite	Kokatha	1	2.62
1/7	Basalt	Kokatha	1	2.78
1/11	Rhyodacite	Everard Lake	1	2.52
2/1	Wheepool Rhyolite	Everard Lake	1	2.57
2/4	Hiltaba Granite	Yarna	1	2.63
2/5	Hiltaba Granite	Yarna	1	2.56
2/7	Yardea Dacite	Yarna	1	2.57
2/10	Black Dacite	Yardea	1	2.69
2/10	Black Dacite	Yardea	1	2.67
2/10	Rhyodacite	Yardea	1	2.53
3/1	Conglomerate	Mount Allalone	1	2.82

Note:
The sample collected by Z. Shi during the Gawler Range Excursion (October, 1989) organised by Geological Society of Australia.

Table F.5: Density of rock samples in Streaky Bay, Eyre Peninsula (5)

Site No. of Rock Sample	Rock Type	Location	Numbers of Sample	Densities g/cm^3
Nunyait R.H.	Granite ϱ_{γ_h}	Nunyait R.H.	1	2.61
5632 RS 2 P1123/74	Hornblende Diorite	Point Brown	1	2.83
5632 RS 3 9SP B	Granite	Point Brown	1	2.59
5632 RS 3 P1097/74	Granite	Point Brown	1	2.57
5632 RS 4 9SP C	Hornblende Adamellite	Point Brown	1	2.68
5632 RS 13	Red Microgranite	Olives Is	1	2.60
5632 RS 14 1038 1 SP B P1218/74	Granite	NE Olives Is	3	2.72
5632 RS 15 1038 1 SP B	Aplite	NE Olives Is	2	2.58
5632 RS 16 P821 /71	Granite	?	3	2.69
5632 RS 17 P1414/73	Amphibolite	?	2	2.78
5632 RS 18 P1415/73	Monzonite	Point Brown 2	4	2.83
5632 RS 19 P1416/73	Granite Gneiss	Point Brown 3 ws1	4	2.63

Table F.6: Density of rock samples in Streaky Bay, Eyre Peninsula (6)

Site No. of Rock Sample	Rock Type	Location	Numbers of Sample	Densities (g/cm^3)
5633 RS 145	Diorite ϱ_{β_3}	St. Peters 1	4	2.51
5633 RS 146	Rhyodacite ϱ_{ν}	St. Peters 2	4	2.60
5633 RS 147	Diorite ϱ_{β_3}	St. Peters 3	2	2.65
5633 RS 148	Diorite ϱ_{β_3}	St. Peters 4	2	2.45
5633 RS 149	Diorite ϱ_{β_3}	St. Peters 5A	3	2.47 – 2.57
5633 RS 150	Rhyolite ϱ_{ν}	St. Peters 5b/1	2	2.61
5633 RS 151	Rhyolite ϱ_{ν}	St. Peters 5b/2	2	2.60
5633 RS 152	Rhyolite ϱ_{ν}	St. Peters 5b/3	2	2.60
5633 RS 153	Rhyolite ϱ_{ν}	St. Peters 5b	1	2.59
5633 RS 155	Quarts-feldspar Gneiss ϱ_{γ_2}	St. Peters 9	2	2.64
5633 RS 156	Fine Grained Granite Gneiss ϱ_{γ_2}	St. Peters 10a	3	2.63
5633 RS 157	Medium-grained Granite ϱ_{γ_3}	St. Peters 10b	2	2.68
5633 RS 158	Granodiorite	St. Peters 13a	1	2.64

Table F.7: Density of rock samples in Streaky Bay, Eyre Peninsula (7)

Site No. of Rock Sample	Rock Type	Location	Numbers of Sample	Densities g/cm^3
5633 RS 159	Hornblende Granodiorite	St. Peters 13b	1	2.72
5633 RS 160	Diorite ϱ_{β_1}	St. Peters 13c	1	2.77
5633 RS 161	Amphibolite ϱ_{β_1}	St. Peters ?	3	2.75
5633 RS 162	Granodiorite ϱ_{γ_3}	St. Peters 15b	3	2.70
5633 RS 163	Aplite ϱ_{γ_6}	St. Peters 20a	1	2.52
5633 RS 164	Diorite ϱ_{β_1}	St. Peters 20B	3	2.70
5633 RS 165	Diorite ϱ_{β_1}	St. Peters Is 21	2	2.89
5633 RS 166	Diorite ϱ_{β_1}	St. Peters Is 29a	1	2.69
5633 RS 167	Adamellite ϱ_{γ_4}	St. Peters Is 29b	1	2.61
5633 RS 168	Granodiorite ϱ_{γ_2}	St. Peters Is 29c	1	2.60
5633 RS 169	Amphibolite ϱ_{β_1}	St. Peters Is 30a	1	2.82
5633 RS 170	Porphyritic Adamellite ϱ_{γ_4}	St. Peters Is 30b	1	2.63

Table F.8: Density of rock samples in Streaky Bay, Eyre Peninsula (8)

Site No. of Rock Sample	Rock Type	Location	Numbers of Sample	Densities g/cm^3
5633 RS 171	Diorite ϱ_{β_3}	St. Peters Is 37.1	1	2.97
5633 RS 172	Foliated Granite ϱ_{γ_2}	St. Peters Is 38a	3	2.64
5633 RS 173	Amphibolite ϱ_{β_1}	St. Peters Is 38b	1	2.83
5633 RS 174	Granite ϱ_{γ_2}	?	1	2.60
5633 RS 175	Granite $\varrho_{\gamma_{h_2}}$	Goat Is 1	1	2.59
5633 RS 176	Granodiorite $\varrho_{\gamma_{h_1}}$	Goat Is 5	2	2.57
5633 RS 177	Porphyritic Granodiorite $\varrho_{\gamma_{h_1}}$	Taop 4	1	2.60
5633 RS 178	Porphyritic Adamellite $\varrho_{\gamma_{h_1}}$	Taop 11	5	2.63
5633 RS 179	Granite $\varrho_{\gamma_{h_2}}$	Goat Is 13	2	2.61
5633 RS 180	Granite Gneiss ϱ_{γ_2}	Murat Bay Bird Rock	1	2.62
5633 RS 181	Granite ϱ_{γ_2}	Cape Beaufort	1	2.60
5633 RS 182	Leucocratic Porphyritic Granite $\varrho_{\gamma_{h_3}}$	Cape Beaufort	3	2.61
5633 RS 183	Amphibolite ϱ_{β_1}	St. Peters Is	1	3.30

Table F.9: Susceptibility of rock samples in Streaky Bay (9)

Site No. of Rock Sample	Rock Type	Location	Numbers of Sample	Susceptibility ($SI \times 10^{-5}$)
Nunyait R.H.	Granite ϱ_{γ_h}	Nunyait R.H.	1	1000
5632 RS 1	? Soil Soil(8 S)	Point Brown Streaky Bay	Powder	100
5632 RS 2 P1123/74	Hornblende Diorite	Point Brown	1	50
5632 RS 3 9SP B	Granite	Point Brown	1	30
5632 RS 3 P1097/74	Granite	Point Brown	1	30
5632 RS 4 9SP C	Hornblende Adamellite	Point Brown	1	1300
5632 RS 13	Red Microgranite	Olives Is	1	25
5632 RS 14 1038 1 SP B P1218/74	Granite	NE Olives Is	3	30
5632 RS 15 1038 1 SP B	Aplite	NE Olives Is	2	5
5632 RS 16 P821 /71	Granite	?	3	600
5632 RS 17 P1414/73	Amphibolite	?	2	50
5632 RS 18 P1415/73	Monzonite	Point Brown 2	4	40
5632 RS 19 P1416/73	Granite Gneiss	Point Brown 3 ws1	4	50

Table F.10: Susceptibility of rock samples in Streaky Bay, Eyre Peninsula (10)

Site No. of Rock Sample	Rock Type	Location	Numbers of Sample	Susceptibility ($SI \times 10^{-5}$)
5633 RS 145	Diorite ϱ_{β_3}	St. Peters 1	4	1100
5633 RS 146	Rhyodacite ϱ_{ν}	St. Peters 2	4 Crushed Rocks	160 200
5633 RS 147	Diorite ϱ_{β_3}	St. Peters 3	2	1200
5633 RS 148	Diorite ϱ_{β_3}	St. Peters 4	2	800
5633 RS 149	Diorite ϱ_{β_3}	St. Peters 5A	3 Crushed Rocks	50 50
5633 RS 150	Rhyolite ϱ_{ν}	St. Peters 5b/1	2	100
5633 RS 151	Rhyolite ϱ_{ν}	St. Peters 5b/2	2 Crushed Rocks	10 10
5633 RS 152	Rhyolite ϱ_{ν}	St. Peters 5b/3	2 Crushed Rocks	15 10
5633 RS 153	Rhyolite ϱ_{ν}	St. Peters 5b	1	45
5633 RS 154	Sands Recent Sands	St. Peters		2500
5633 RS 155	Quarts-feldspar Gneiss ϱ_{γ_2}	St. Peters 9	2 Crushed Rocks	0 0
5633 RS 156	Fine Grained Granite Gneiss ϱ_{γ_2}	St. Peters 10a	3 Crushed Rocks	0 0
5633 RS 157	Medium-grained Granite ϱ_{γ_3}	St. Peters 10b	2 Crushed Rocks	5 10
5633 RS 158	Granodiorite	St. Peters 13a	1 Crushed Rocks	20 20

Table F.11: Susceptibility of rock samples in Streaky Bay (11)

Site No. of Rock Sample	Rock Type	Location	Numbers of Sample	Susceptibility ($SI \times 10^{-5}$)
5633 RS 159	Hornblende Granodiorite	St. Peters 13b	1 Crushed Rocks	1000 900
5633 RS 160	Diorite ϱ_{β_1}	St. Peters 13c	1 Crushed Rocks	800 900
5633 RS 161	Amphibolite ϱ_{β_1}	St. Peters ?	3 Crushed Rocks	600 400
5633 RS 162	Granodiorite ϱ_{γ_3}	St. Peters 15b	3	1200
5633 RS 163	Diorite Aplite ϱ_{γ_6}	St. Peters 20a	1	0
5633 RS 164	Diorite ϱ_{β_1}	St. Peters 20B	3	400
5633 RS 165	Diorite ϱ_{β_1}	St. Peters 21	2	3000 – 5000
5633 RS 165	Diorite ϱ_{β_1}	St. Peters 21	Crushed Rocks	3000
5633 RS 166	Diorite ϱ_{β_1}	St. Peters 29a	1	1200
5633 RS 167	Adamellite ϱ_{γ_4}	St. Peters 29b	1 Crushed Rocks	1500 950
5633 RS 168	Granodiorite ϱ_{γ_2}	St. Peters 29c	1 Crushed Rocks	250 250
5633 RS 169	Amphibolite ϱ_{β_1}	St. Peters 30a	1	1000
5633 RS 170	Porphyritic Adamellite ϱ_{β_1}	St. Peters 30b	1	700
5633 RS 171	Diorite ϱ_{β_3}	St. Peters 37.1	1 Crushed Rocks	3700 2500

Table F.12: Susceptibility of rock samples in Streaky Bay (12)

Site No. of Rock Sample	Rock Type	Location	Numbers of Sample	Susceptibility ($SI \times 10^{-5}$)
5633 RS 172	Foliated Granite ϱ_{γ_2}	St. Peters 38a	3 Crushed Rocks	1500 1000
5633 RS 173	Amphibolite ϱ_{β_1}	St. Peters 38b	1 Crushed Rocks	500 500
5633 RS 174	Granite ϱ_{γ_2}	?	1 Crushed Rocks	150 100
5633 RS 175	Granite $\varrho_{\gamma_{h_2}}$	Goat Is 1	1 Crushed Rocks	10 20
5633 RS 176	Granodiorite $\varrho_{\gamma_{h_1}}$	Goat Is 5	2 Crushed Rocks	0 20
5633 RS 177	Porphyritic Granodiorite $\varrho_{\gamma_{h_1}}$	Taop 4	1 Crushed Rocks	10 20
5633 RS 178	Porphyritic Adamellite $\varrho_{\gamma_{h_1}}$	Taop 11	5 Crushed Rocks	300 300
5633 RS 179	Granite $\varrho_{\gamma_{h_2}}$	Goat Is 13	2 Crushed Rocks	100 160
5633 RS 180	Granite Gneiss ϱ_{γ_2}	Murat Bay Bird Rock	1	800
5633 RS 181	Granite ϱ_{γ_2}	Cape Beaufort	1	100
5633 RS 182	Leucocratic Porphyritic Granite $\varrho_{\gamma_{h_3}}$	Cape Beaufort	3 Crushed Rocks	500 400
5633 RS 183	Amphibolite ϱ_{β_1}	St. Peters Is	1	3500

Appendix G

A study of the shaded relief method

G.1 Principle of the method

The shaded relief is a simple but effective enhancement technique (Kowalik and Glenn, 1987). The method calculates the intensity of light for a shaded area which is from a certain directional light source on a cell in a set of gridded data. The magnitude of the shaded area is defined by a cosine angle (γ) between the direction of the light source ($\vec{S}$) and the normal direction ($\vec{N}$) of the surface on the cell, which is composed of 3×3 data points and the result is recorded at the central point. Figure G.1 illustrates the relationship between vector $\vec{S}$ and vector $\vec{N}$. Based on the scalar product rule, the cosine γ is given by:

$$\cos\gamma = \frac{\vec{N} \cdot \vec{S}}{|\vec{N}| \cdot |\vec{S}|} \tag{G.1}$$

where the surface normal $\vec{N}$ can be presented by $\{-p, -q, 1\}$ and the light source vector $\vec{S}$ is determined by $\{-p_0, -q_0, 1\}$. The factor p or p_0 is the east-west component along x-axis and q or q_0 is the north-south component along y-axis, the vertical component is 1.

Calculating the dot product, (G.1) can be expressed as following form (Horn, 1981 and Kowalik and Glenn, 1987),

$$\cos\gamma = \frac{1 + p_0 p + q_0 q}{\sqrt{1 + p^2 + q^2}\sqrt{1 + {p_0}^2 + {q_0}^2}} \tag{G.2}$$

The components p_0 and q_0 of the vectors ($\vec{S}$) are determined as

$$\begin{aligned} p_0 &= -\sin\phi \cdot \tan(90° - \theta) \\ q_0 &= -\cos\phi \cdot \tan(90° - \theta) \end{aligned}$$

where ϕ is the azimuth angle measured clockwise from the north, and θ is the elevation angle.

The components p and q are the x and y directional cosine of the vector $\vec{S}$, they can be obtained by differencing as

$$p = \frac{\Delta Z}{\Delta x}$$

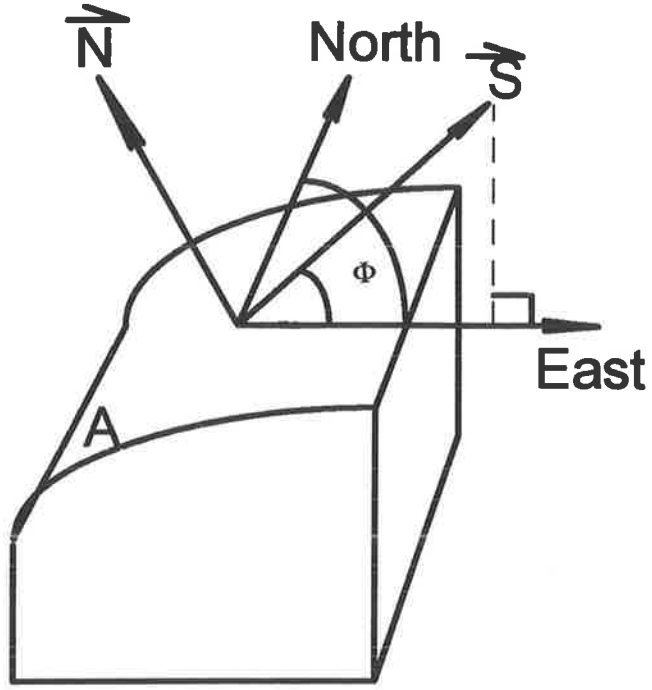

Figure G.1: Illustration of shaded relief method

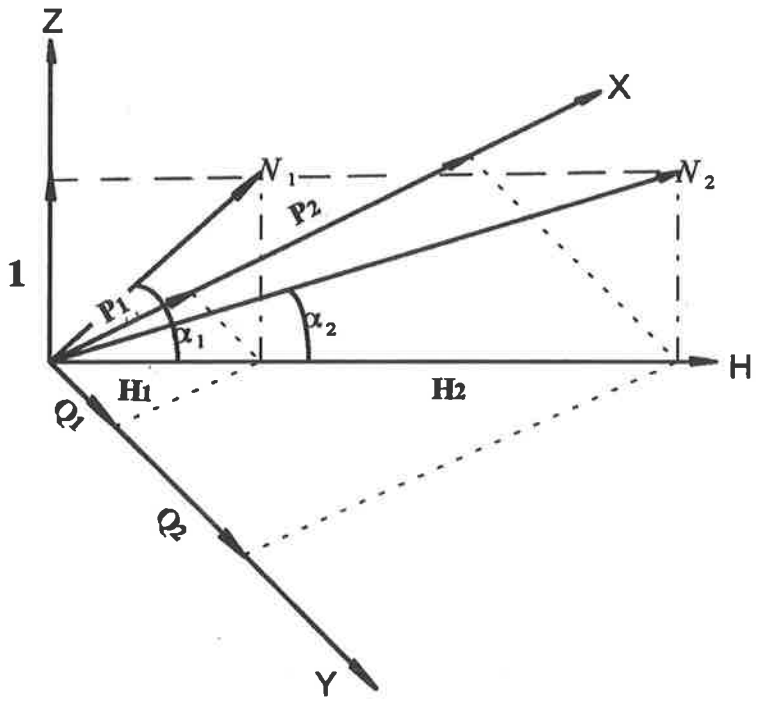

Figure G.2: Effect of slope factor

$$q = \frac{\Delta Z}{\Delta y}$$

where Z represents the surface relief of the field.

The parameters p and q are calculated approximately by applying a pair of simple filters (F_x and F_y) which are composed of a 3×3 boxcar window. The calculations are obtained by moving window to each cell of the original data then weighting them. The details are given as follows.

The filter (F_x) for p is

$$F_x = \begin{bmatrix} -1 & 0 & 1 \\ -2 & 0 & 2 \\ -1 & 0 & 1 \end{bmatrix}$$

and filter (F_y) for q is

$$F_y = \begin{bmatrix} 1 & 2 & 1 \\ 0 & 0 & 0 \\ -1 & -2 & -1 \end{bmatrix}$$

Note that symbol [...] in F_x and F_y is not a form of matrix; it presents the boxcar filter.

A cell of original data are distributed as

$$\begin{matrix} Z_{1,-1} & Z_{1,0} & Z_{1,1} \\ Z_{0,-1} & Z_{0,0} & Z_{0,1} \\ Z_{-1,-1} & Z_{-1,0} & Z_{-1,1} \end{matrix}$$

Applying the filters F_x and F_y to each cell of original data, it leads to

$$p = \frac{Z_{1,1}+2Z_{0,1}+Z_{-1,1}-Z_{1,-1}-2Z_{0,-1}-Z_{-1,-1}}{M} \quad \text{(G.3)}$$

$$q = \frac{Z_{1,-1}+2Z_{1,0}+Z_{1,1}-Z_{-1,-1}-2Z_{-1,0}-Z_{-1,1}}{M} \quad \text{(G.4)}$$

where M is a scalar slope factor which controls the effective slope of the field surface (Kowalik and Glenn, 1987).

M can be expressed

$$M = 8 \cdot \Delta s \cdot f_{ss}, \quad \text{(G.5)}$$

where 8 is the number of weighting data, Δs is the distance of sample interval and f_{ss} is the effective scalar slope factor simply called slope factor.

It can be seen that the most important factor in using this method is the choice of the elevation angle, azimuth angle and scalar slope factor. A brief discussion follows.

G.2 Function of elevation angle

The elevation angle indicates the direction of an illumination source in the vertical section. The angle ranges from 0 to 90 degrees. Note that if the elevation angle is 0°, $\cos\gamma$ cannot be

calculated directly from (G.2). The approximate expression is

$$\cos\gamma = \frac{-p\sin\phi - q\cos\phi}{\sqrt{1+p^2+q^2}} \tag{G.6}$$

After testing functions of the different elevation angles by the author, a suggestion is made as the most suitable angles to be chosen in the method are 90° and 0°.

For the case of elevation angle equal to 90 degrees, the value ranges from 0 to 1, in which the entire data are the positive values, because (G.2) is converted into

$$\cos\gamma = \frac{1}{\sqrt{1+p^2+q^2}}.$$

The position of the maximum value of output indicates the trace of a peak or a valley or a wide flat surface of the field. The output is also called brightness. The bright high inside of an anomaly indicates the position of the center of the causative body. The lower value of brightness indicates a belt of the maximum gradient in an anomaly, which is usually associated with a linear brightness high enclosed the belt. Thus the belt and the linear brightness high outline the boundary of the anomaly, from which can also be estimated the width of a structure. The high value over a wide area indicates a flat magnetic field.

If the elevation angle is 0 degree, which indicates a light source coming from a horizontal direction, the brightness only depends on the cosine of an angle between the surface normal and the vector of horizontal direction. This filter is more like a horizontal gradient filter where the direction of the filtering depends on the azimuth angle. The difference between the two filters is discussed in later section. The characteristics of the horizontal elevation angle are listed below:

1. The intensities of the brightness high and low are nearly equal and range from -1 to 1.
2. The brightness high indicates the gradient variations of the anomaly which strikes in the direction of the illumination, and the brightness low shows the gradient belt of the anomaly to be opposite the light direction.
3. The boundary between a pair of black and white bands locates the center of the linear structure.

If the elevation angle lies between 0° and 90°, the characteristics of the output is similar to the typical case (i.e. $\theta = 0°$ or $\theta = 90°$) but it depends on the angle close to which case: if $60° > \theta > 0°$, results are similar to $\theta = 0°$; if $\theta > 60°$, the results are similar to $\theta = 90°$. The amplitude of the output ranges approximately from $-\cos\theta$ to 1.

In processing the data of the Lincoln sheet, the elevation angles are chosen as 90° and 0°.

G.3 Functions of azimuth

The aim of changing the azimuth angle is to enhance or subdue certain directional structures. For example, in choosing the azimuth angle of 45 degrees, the structures along NE-SW direction

Table G.1: Reference value of scalar slope factor

Type of Field	Elevation angle(θ)	Characteristics of structure	Reference value (f_{ss})
Magnetics	90°	Regional structure	0.01 - 1
Magnetics	$0° < \theta < 90°$	Regional structure	0.1 - 1
Magnetics	90°	Local structure	0.001 - 0.01
Magnetics	$0° < \theta < 90°$	Local structure	0.01 - 0.1
Gravity	90°	Regional structure	0.001 - 0.01
Gravity	$0° < \theta < 90°$	Regional structure	0.01
Gravity	90°	Local structure	0.0001 - 0.001
Gravity	$0° < \theta < 90°$	Local structure	0.001

are subdued and those in NW-SE are enhanced. For the purpose of searching for structures along all difference directions, four directional angles (0°, 45°, 90°, 135°) are chosen. If the elevation angle is 90 degrees, the azimuth angles is not relevant.

G.4 Functions of scalar slope factor

The scalar slope factor is used to change the slope of the surface normal. This can be found from the expressions (G.4), (G.4) and (G.5). If the slope factor f_{ss} is small for example 0.01, both p and q, horizontal components of the surface normal $\vec{N}$, are increased both in a same ratio ($\frac{1}{f_{ss}} = 100$) which compare with the value of f_{ss} as 1. Figure G.2 illustrates the slope variation of the surface normal, when f_{ss} changing. The smaller the slope factor ($\frac{1}{f_{ss}}$ is large), the flatter the slope angle (see α_2 in Figure G.2) and vice versa (see α_1 in Figure G.2). Therefore the slope factor controls the slope of the surface normal. If the factor f_{ss} is bigger, the regional anomalies are emphasised; otherwise the local anomalies are emphasised. However if f_{ss} is chosen as a very small value, the patterns of local anomalies in the image map become very flattened. As a result, the anomalies become distorted. Therefore the choice of a suitable value of the scalar slope factor is very important. According to the author's experiences, the preferred parameters are given as shown in Table G.1.

References

Ackerman, H. A. and Reford, M. S., 1962, *A method of magnetic interpretation*, S. E. G. meeting, Sep 20, Calgary, Alberta.

Al-Chalbi, M., 1971, *Some studies relating to non-uniqueness in gravity and magnetic inverse problems*, Geophysics, 36: 835-855.

Al-Chalbi, M., 1972, *Interpretation of gravity anomalies by non-linear optimisation*, Geophysical Prospecting, 20: 1-16.

Atchuta Rao, D., Ram Babu, H. V. and Sanker Narayan, P. V., 1980, *Relationship of magnetic anomalies due to subsurface features and the interpretation of sloping contacts*, Geophysics, 45: 32-36.

Atchuta Rao, D., Ram Babu, H. V. and Sanker Narayan, P. V., 1981, *Interpretation of magnetic anomalies due to dikes: The complex gradient method*, Geophysics, 46: 1572-1578.

Backus, G. E. and Gilbert, J. F., 1967, *Numerial application of a a formalism for geophysical inversion problems*, Geophys. J. R. Astr. Soc. 13: 247-276.

Backus, G. E. and Gilbert, J. F., 1968, *The resolving power of gross earth data*, Geophys. J. R. Astr. Soc. 16: 169-205.

Backus, G. E. and Gilbert, J. F., 1970, *Uniqueness in the inversion of inaccurate gross earth data*, Phil. Trans. Roy. Soc. London, Ser. A 266: 123-192.

Baranov, V., 1957, *A new method for interpretation of aeromagnetic maps: pseudo-gravimetric anomalies*, Geophysics, 22: 359-383.

Baranov, V. and Naudy, H., 1964, *Numerical calculation of the formula of reduction to the magnetic pole*, Geophysics, 16: 67-79.

Barnett, C.T., 1976, *Theoretical modelling of magnetic and gravitational fields of an arbitrary shaped three-dimensional body*, Geophysics, 41:1353-1364.

Barongo, J. O., 1984, *Euler's differential equation and the identification of the magnetic point-pole and point-dipole sources*, Geophysics, 49: 1549-1553.

Barongo, J. O., 1985, *Method for depth estimation on aeromagnetic vertical gradient anomalies*, Geophysics, 50: 963-968.

Behrendt J. C. and Grim M. S., 1985, *Strucure of the U.S. Atlantic continental margin from derivative and filtered maps of the magnetic filed*, The Utility of Regional Gravity and Magnetic Anomaly Maps (Society of Exploration Geophysicists): 325-338.

Bhattacharyya, B. K., 1965, *Two-dimensional harmonic analysis as a tool for magnetic interpretation*, Geophysics, 30: 829-857.

Bhattacharyya, B. K., 1966a, *A method for computing the total magnetization vector and dimensions of a rectangular block-shaped body from magnetic anomalies*, Geophysics, 31: 74-96.

Bhattacharyya, B. K., 1966b, *Continuous spectrum of the total magnetic field anomaly due to a rectangular prismatic body*, Geophysics, 31: 97-121.

Bhattacharyya, B. K. and Leu, Lei-Kuang, 1966c, *Analysis of magnetic anomalies over Yellowstone National Park: mapping of Curie point isothermal surface for geothermal reconnaissance*, Journal Geophysical Research, 80: 4461-4465.

Bhattacharyya, B. K. and Navolio, M. E., 1976, *A Fast Fourier Transform method for rapid computation of gravity and magnetic anomalies due to arbitrary bodies*, Geophys. Prosp., 24: 633-649.

Bhattacharyya, B. K. and Leu, L., K., 1977, *Spectral analysis of gravity and magnetic anomalies due to rectangular prismatic bodies*, Geophysics, 42: 41-50.

Bhimasankaram, V. L. S., Nagendra, R., and Seshagiri Rao, S. V., 1977, *Interpretation of gravity anomalies due to finite inclined dikes using Fourier Transformation*, Geophysics, 42: 51-59.

Blissett, A.H., 1975, *Rock units in the Gawler Range Volcanics, South Australia*, Quart. Geol. Notes, Geol. Surv. S. Aus., 55: 2-14.

Bolt, B. A., Doyle, H. A. and Sutton, D. J., 1958, *Seismic observations from the 1956 atomic explosions in Australia*, Geophysical Journal of the Royal Astronomical Society, 1: 135-135.

Bose, P. K. and Sengupta, B. J., 1984, *Spectral analysis of offshore magnetic data for computing depths to the basement rocks*, Marine Geophysical Research, 6: 245-256.

Bott, M. H. P., 1963, *Two methods applicable to computers for evaluating magnetic anomalies due to finite three-dimensional bodies*, Geophysical Prospecting, 11: 292-299.

Boyd, D. M., 1967, *The contribution of airborne magnetic surveys to geological mapping*, In : Morley, L.W.(ed.),Mining and Groundwater Geophysics, Geological Survey of Canada, Economic Geology Report, 26: 213-227.

Boyd, D. M. and Richards, D., 1983, *Interpretation of airborne magnetic surveys*, Australian Mineral Foundation Incorporated.

Boyd, D. M., Shi, Z. and Kivior, I., 1993, *Analysis of regional gravity and magnetic data as a guide for mineral exploration in the next century*, SEG Conference, Moscow, Abstract (in press).

Branch, C. D., 1978, *Evolution of the middle Proterozoic Chandabooka caldera. Gawler Range acid volcano-plutonic province. South Australia.*, Journal of the Geological Society of Australia, 25: 199-216.

Cassano, E. and Rocca, F., 1975, *Interpretation of magnetic anomalies using spectral estimation techniques*, Geophysical Prospecting, 23: 663-681.

Chai, Y. and Hinze, W. J., 1988, *Gravity inversion of an interface above which density contrast varies exponentially with depth*, Geophysics, 53: 837-845.

Chenot, D. and Debeglia, N., 1990, *Three-dimensional gravity or magnetic constrained depth inversion with lateral and vertical variation of crust*, Geophysics, 55: 327-335.

Cianciara, B. and Marcak, H., 1976, *Interpretation of gravity anomalies by means of local power spectra*, Geophysical Prospecting, 24: 273-286.

Clement, W. G., 1973, *Basic principles of two-dimensional digital filtering*, Geophysical Prospecting, 21: 125-145.

Clarke, G. K. C., 1969, *Optimum second-derivative and downward-continuation filters*, Geophysics, 34: 424-437.

Cooley, J. W. and Tukey, J. W., 1965, *An algorithm for the machine calculation of complex Fourier series*, Math. Comput., 19: 297-301.

Cook, K. L., 1950, *Quantitative interpretation of magnetic anomalies over veins*, Geophysics 15: 667-686.

Corbato, C. E., 1965, *A least-squares procedure for gravity interpretation*, Geophysics, 29: 517-531.

Cordell, L., and Henderson, R. G., 1968, *Iterative three-dimensional solution of gravity anomaly data using a digit computer*, Geophysics, 33: 596-601.

Cordell, L. and Grauch, V. J. S., 1982, *Reconciliation of the Discrete and Integral Fourier Transforms*, Geophysics, 47: 237-243.

Cordell, L. and Grauch, V. J. S., 1985, *Mapping basement magnetization zones from aeromagnetic data in the San Juan Basin, New Mexico*, In Hinze, W. J.(Ed.), The utility of regional gravity and magnetic anomaly map, Society of Exploration Geophysics, 181-197.

Cowley, W., 1991, *South Australian Department of Mines and Energy*, Report Book, 91/37.

Cribb, J., 1976, *Application of the generalized linear inversion to the inversion of static potential data*, Geophysics 41: 1365-1369.

Cull, J. P. and Denham, D., 1979, *Regional variations in Australian heat flow*, BMR Journal of Australian Geology and Geophysics, 4: 1-13.

Dean W. C., 1958, *Frequency analysis for gravity and magnetic interpretation*, Geophysics, 23: 97-127.

Fedi, M., 1990, *Estimation of depth and magnetization of magnetic sources from magnetic data: The linearized continuous inverse problem for $2\frac{1}{2}D$ structures*, PAGEOPH, 134: 451–471.

Dimitriadis, K., Tselentis, G. A. and Thanassoulas, K., 1987, *A basic program for 2-D spectral analysis of gravity data and source-depth estimation*, Computers and Geosciences, 13: S49-S60.

Doyle, H. A. and Everingham, I. B., 1964, *Seismic velocities and crustal structure in southern Australia*, Geophysical Journal of the Royal Astronomical Society, 11: 141-141.

Enmark T., 1982, *Development of optimization procedures for gravity and magnetic interpretation and their application to some geological structures in Northern Sweden*, PhD thesis of University of Lulea, (unpubl).

Fanning, C. M., Flint, R. B., Parker, A. J, Ludwig, K. R. and Blissett, A. H., 1988, *Refined Proterozoic evolution of the Gawler Craton. South Australia, through U-Pb zircon geochronology*, Precambrian Res., 40/41: 363-386.

Fedi, M., 1990, *Estimation of depth and magnetization of magnetic sources from magnetic data: The linearized continuous inverse problem for $2\frac{1}{2}D$ structures*, PAGEOPH., 134: 451-471.

Finlayson D. M., 1982, *Geophysical differences in the lithosphere between Phanerozoic and Precambrian Australia*, Tectonophysics, 84: 287-312.

Finlayson, D. M., Cull, J. P. and Drummond, B. J., 1974, *Upper mantle structure from the Trans-Australia Seismic Survey (TASS) and other seismic refraction data*, Journal of the Geological Society of Australia, 21: 447-458.

Finlayson, D. M., Prodehl C. and Collins, C. D. N., 1979, *Explosion seismic profiles, and implications for crustal evolution, in southeastern Australia*, BMR Journal of Australian Geology and Geophysics, 4: 243-252.

Fisher, N. J. and Howard, L. E., 1980, *Gravity interpretation with the aid of quadratic programming*, Geophysics, 45: 403-419.

Gay S. P., 1963, *Standard curves for interpretation of magnetic anomalies over long tabular bodies*, Geophysics, 28: 161-200.

Gerard, A. and Deberglia, N., 1975, *Automatic three-dimensional modeling for the interpretation of gravity or magnetic anomalies*, Geophysics, 40: 1014-1034.

Giles, C. W., 1977, *Rock units in the Gawler Range Volcanics, Lake Everand area*, Quart. Geol. Notes, Geol. Surv. S. Aus., 61: 7-16.

Giles, C. W., 1988, *Petrogenesis of the Proterozoic Gawler Range Volcanics, South Australia*, Precambrian Res., 40/41: 407-427.

Gibb, R. A., 1968, *The densities of Precambrian rocks from northern Manitoba*, Can. J. Earth Sci., 5: 433-438.

Grant, F. S., 1972, *Review of data processing and interpretation methods in gravity and magnetics, 1964-71*, Geophysics, 37: 647-661.

Grant, F. S. and Martin, L., 1966, *Interpretation of aeromagnetic anomalies by the use of characteristic curves*, Geophysics, 31: 135-148.

Green, A. G., 1972, *Magnetic profile analysis*, Geophysical Journal of the Royal Astronomical Society, 30: 393-403.

Green, R. and Stanley, J. M., 1975, *Application of a Hilbert transform method to the interpretation of surface-vehicle magnetic data*, Geophysical Prospecting, 23: 18-27.

Green, W. R., 1975, *Inversion of gravity profiles by use of a Backus-Gilbert approach*, Geophysics, 40: 763-772.

Greenhalgh, S.A., Singh, R. and Parham, R. T., 1986a, *Earthquake in South Australia*, Trans. R. Soc. Aust., 110 (4): 145-154.

Greenhalgh, S.A., Tapley, D. and Singh, R., 1986b, *Crustal structure of South Australia from earthquake and explosion data*, Geol. Soc. Aust., Abstracts, 15: 87-88.

Greenhalgh, S.A., Tapley, D. and Singh, R., 1989, *Crustal heterogeneity in South Australia, earthquake evidence*, Geophysical Journal, 96: 85-99.

Gudmundsson, G., 1966, *Interpretation of one-dimensional magnetic anomalies by use of the Fourier-transform*, Geophys. J. R. Astr.Soc., 12: 87-97.

Gunn, P. J., 1975, *Linear transformations of gravity and magnetic fields*, Geophysical Prospecting, 23: 300-312.

Gunn, P. J., 1976, *Direct mapping of interfaces and thicknesses of layers using gravity and magnetic data*, Geoexploration, 14: 75-80.

Gupta, V. K. and Ramani, N., 1980, *Some aspects of regional-residual separation of gravity anomalies in a Precambrian terrain*, Geophysics, 45: 1412-1426.

Gupta, V. K., and Ramani, N., 1982, *Optimum second vertical derivatives in geological mapping and mineral exploration*, Geophysics, 47: 1706-1715.

Guspi, F., 1992, *Three-dimensional Fourier gravity inversion with arbitrary density contrast*, Geophysics, 47: 131-135.

Hahn, A., 1965, *Two applications of Fourier's analysis for the interpretation of geomagnetic anomalies*, J. Geomag. Geol., 17: 195-225.

Hahn, A., Kind, E. G. and Mishra, D. C., 1976, *Depth estimation of magnetic sources by means of Fourier amplitude spectra*, Geophysical Prospecting, 24: 287-308.

Hall, D. H., 1959, *Direction of polarization determined from magnetic anomalies*, Jour. Geoph. Res., 64: 1945-1959.

Hammer, P. T. C., Hildebrand, J. A. and Parker, R., L., 1991, *Gravity inversion using seminorm minimization: Density modelling of Jasper Seamount*, Geophysics, 56: 68-79.

Hartman, R. R., Teskey, D. J. and Friedberg, J., 1971, *A system for rapid digital aeromagnetic interpretation*, Geophysics, 36: 891-918.

Hessing, R. C., Lee, H. K., Pierce A. and Powers, E. N., 1972, *Automatic contouring using bicubic functions*, Geophysics, 37: 669-674.

Hills E. S., 1956, *The tectonic style of Australia*, Geotekt, Sympos. zu Ehren von A. Stille, Deutsch. Geol. Gesellsch., 336-346.

Hood, P. J., 1975, *The GSC aeromagnetic gradiometer, a new mapping tool for mineral exploration*, The Northern Miner, 61: 20-21.

Hood, P. J., Holroyd, M. T. and McGrath, P. H., 1979, *Magnetic methods applied to base metal exploration*, In Hood, P. J., Ed., Geophysics and geochemistry in the search for metallic ores, Geol. Surv. Can. Econ. Geol. Rep., 31: 527-544.

Hood, P. J., Sawatzky, P., Kornik, L. J. and McGrath, P. H., 1976, *Aeromagnetic gradiometer survey, White Lake, Ontario (NTS31F/7SE)*, Geol. Surv. Canada, open file rep.

Horton, C. W., Hempkins, W. B. and Hoffman, A. A. J., 1964, *A statistical analysis of some aeromagnetic maps for the northwestern Canadian Shield*, Geophysics, 29: 582-601.

Hou, C., 1981, *Compensation smoothing filter*, Geophysical Prospecting of Petroleum 2: 22-29 (in Chinese).

Hou, C., 1989, *Method for calculating and compiling the map of Curie-point surface*, Computation Techniques for Geophysical and Geological Exploration, 4: 306-311 (in Chinese).

Hou, C., Liu, X and Shi, Z., 1980, *Introduce the matched filtering method*, Dizhi Jisuan Jishu (Geological Computing Technique), 1: 1-25 (in chinese).

Hou, C. and Shi, Z., 1982, *Interpretation system of potential field transform. Wuhuatan Jisuan Jishu*, Computing Techniques for Geophysical and Geochemical Exploration, No.4, Vol. 13: 1-10 (in Chinese).

Hou, C. and Shi, Z., 1985, *Experimental analysis for calculating depth of magnetic source via energy spectrum*, Dizhi Xinxi Jishu (Geological Information Technique), No.1, Vol. 1: 22-36 (in Chinese).

Hutchison, R. D., 1958, *Magnatic analyis by logarithmic curves, 1958*, Geophysics, 23: 749-769.

Isles, D. J. and Valenta, R., 1993, *Interpretation and structural analysis of aeromagnetic data*, Australian Mineral Foundation.

Jachens, R. C. and Griscom, A., 1985, *An isostatic residual gravity map of California-A residual map for interpretation of anomalies from intracrustal sources*, In: Hinze, W. J., (ed.), The Utility of regional gravity and magnetic anomaly maps. Soc. Explor. Geophys.: 347-360.

Jacobsen, B. H., 1987, *A case for upward continuation as a standard separation filter for potential-field maps*, Geophysics, 52: 1138-1148.

Jain, S., 1976, *An automatic method of direct interpretation of magnetic profiles*, Geophysics, 41: 531-541.

Johnson, W. W., 1969, *A least-squares method of interpreting magnetic anomalies caused by two-dimensional structures*, Geophysics, 34: 65-74.

Kane. M. F., Hildenbrand, T. G., Simpson, R. W., Jr, Godson, R. H., and Brachen, R. E,, 1982, *Crust and mantle structure of the conterminous U.S. from wavelength-filtered gravity data*, Tech. Program Abstr. Biograph., SEG 52nd Annu. Meet., Dallas, Tex.: 232.

Kane, M. F. and Godson, R. H., 1985, *Features of a pair of long-wavelength ($> 250km$) and short-wavelength ($< 250km$) Bouguer gravity maps of the United States*, The Utility of Regional Gravity and Magnetic Anomaly Maps (Society of Exploration Geophysicists): 46-61.

Keating, P. B. and Pilkington, M., 1990, *An automated method for the interpretation of magnetic vertical-gradient anomalies*, Geophysics, 55: 336-343.

Kilty, K. T., 1983, *Werner deconvolution of profile potential field data*, Geophysics, 48: 234-237.

Kivior, I., Shi, Z. and Boyd, D., 1994, *Crustal studies of South Australia based on energy spectral analysis of regional magnetic data*, ASEG Conference, Perth (in press).

Koulomzine, Th. and Massé, L., 1947, *Magnetic anomaly of inclined vein of infinite length*, American Institute of Mining Engineers Technical Publication No. 2260.

Koulomzine, Th., Lamontagne, Y. and Nadeau, A., 1970, *New method for the direct interpretation of magnetic anomalies caused by inclined dikes of infinite length*, Geophysics, 35: 812-830.

Kowalik, W. S. and Glenn, W. E., 1987, *Image processing of aeromagnetic data and integration with Landsat image for improved structural interpretation*, Geophysics, 52: 875-884.

Ku, C. C. and Sharp, J. A., 1983, *Werner deconvolution for automated magnetic interpretation and its refinement using Marquardt's inverse modeling*, Geophysics, 48: 754-774.

Lehmann, H. J., 1970, *Examples for the separation of fields of magnetic sources in different depth by the harmonic analysis method*, Boll. Geofis. Teor. Appl., 12: 97-117.

Levin, F. K., Bayhi, J. F., Dunkin, J. W., Lea, J. D., Moore, D. B., Warren, R. K. and Webster, G. M., 1976, *Developments in exploration geophysics, 1969-74*, Geophysics, 41: 209-218.

Lum, C. C. L., Leeman, W. P., Foland, K. A., Kargel, J. A. and Fitton, J. G., 1989, *Isotopic variations in continental basaltic lavas as indicators of mantle heterogeneity: Examples from the Western U.S. Cordillera, J.*, Geophys. Res., 94: 7871-7884.

Mayhew, M. A., Johnson, B. D. and Langel, R. A., 1980, *An equivalent source model of the satellite-altitude magnetic anomaly field over Australia*, Earth and Planetary Science

Letters, 51: 189-198.

Mayhew, M. A., Wasilewski, P. J. and Johnson, B. D., 1991, *Crustal magnetization and temperature at depth beneath the Yilgarn block, Western Australia inferred from Magsat data*, Earth and Planetary Science Letters, 107: 515-522.

McCoy, A., 1992, *Analysis of the Gairdner Dyke Swarm using automatic magnetic modelling*, Honours thesis, University of Adelaide.

McGrath, P. H., and Hood, P. J., 1970, *The dipping dike case: A computer curve-matching method of magnetic interpretation*, Geophysics, 35: 831-848.

McGrath, P. H., and Hood, P. J., 1973, *An automatic least-squares multimodel method for magnetic interpretation*, Geophysics: 38: 349-358.

Marquardt, D. W., 1963, *An algorithm fast least-squares estimation of non-linear parameters: J. Soc*, Indust. Appl. Mat., v. 11,p: 431-441.

Marquardt, D. W., 1970, *Generalized inverses, ridge regression, biased linear estimation and nonlinear estimation*, Technometrics, 12: 591-612.

Minty, B. R. S., 1981, *Automatic depth estimates on aeromagnetic profile*, Unpublished M. Sci. Thesis, Geophysical Survey of South Africa.

Mishra, D. C. and Naidu P., 1974, *Two-dimensional power spectral analysis of aeromagnetic fields*, Geophysical Prospecting, 22: 345-353.

Mishra, D. C. and Tiwari, R. K., 1981, *Spectral study of the Bouguer anomaly map of a rift valley and adjacent areas in Central India*, Pure and Applied Geophysics, 119: 1051-1062.

Mishra, D. C. and Pedersen, L. B., 1982, *Stattical analysis of potential field from subsurface reliefs*, Geoexploration, 19: 247-265.

Mufti, I. R., 1972, *Design of small operators for the continuation of potential field data*, Geophysics, 37: 488-506.

Nabighian, M. N., 1972, *The analytic signal of two-dimensional magnetic bodies with polygonal cross-section: its properties and use for automated anomaly interpretation*, Geophysics, 37: 507-517.

Nabighian, M. N., 1974, *Additional comments on the analytic signal of two-dimensional magnetic bodies with polygonal cross-section*, Geophysics, 39: 85-92.

Nabighian, M. N., 1984, *Toward a three-dimensional automatic interpretation of potential field data via generalized Hilbert transforms: Fundamental relations*, Geophysics, 49: 780-786.

Nagata, T., 1938a, *Magnetic anomalies and the corresponding subterranean structure*, Bulletin of the Earthquake Research Institute. Tokyo Imperial University, 14: 176-181.

Nagata, T., 1938b, *Magnetic anomalies and the corresponding subterranean mass distribution*, Bulletin of the Earthquake Research Institute. Tokyo Imperial University, 16: 550-577.

Naidu, P., 1968, *Spectrum of the potential field due to randomly distributed sources*, Geophysics, 33: 337-345.

Naidu, P., 1969, *Estimation of spectrum and cross-spectrum of aeromagnetic field using Fast Digital Fourier Transform (FDFT) Techniques*, Geophysical Prospecting, 17: 345-361.

Naidu, P., 1970, *Statistical structure of aeromagnetic field*, Geophysics, 35: 279-292.

Naudy, H., 1971, *Automatic determination of depth on aeromagnetic profile*, geophysics, 36: 717-722.

Negi, J. G. and Garde, S. C., 1969, *Symmetric matrix method for gravity interpretation*, J. Geophys. Res., 74: 3804-3807.

Negi, J. G., Agrawal, P. K. and Rao, K. N. N., 1983, *Three dimensional model of the Koyna area of Maharashtra State (India) based on the spectral analysis of aeromagnetic data*, Geophysics, 48: 964-974.

Negi, J. G. and Agrawal, P. K., 1986, *Delineation of crustal layers by the spectral analysis of Bouguer gravity data: A case history for the Deccan Traps(India)*, Tectonophysics, 122: 135-147.

Nelson J. B., 1988, *Comparison of gradient analysis techniques for linear two-dimensional magnetic sources*, Geophysics, 53: 1088-1095.

Nettleton, L. L., 1942, *Gravity and magnetic calculations*, Geophysics, 7: 293-310.

Nielsen, J. O. and Pedersen, L. B., 1979, *Interpretation of potential fields from inclined dikes in the wavenumber domain*, Pure and Applied Geophysics, 117: 761-771.

O'Brien, D. P., 1971, *An automated method for magnetic anomaly resolution and depth-to-source computation. Proc. Sym.*, Treatment and Interpretation of Aeromagnetic Data, Berkley, California.

O'Brien, D., 1972, *CompuDepth: A New Method for Depth to Basement Computation*, 42 Meeting SEG Anaheim, Calif.

O'Driscoll, E. S. T., 1968, *Notes on the structure of the Broken Hill Lode, and its tectonic setting*, Broken Hill Mines.

O'Driscoll, E. S. T., 1977, *A structure syndrome for ore emplacement at Broken Hill, Australia*, Geol. Ges., 124: 257-266.

O'Driscoll, E. S. T., 1983, *Deep tectonic foundations of the Eromanga Basin. Aus*, Petrol. Explor. Aus. J., 23: 5-17.

Odegard, M. E. and Berg, J. W. Jr., 1965, *Gravity interpretation using the Fourier integral*, Geophysics, 30: 424-438.

Okubo, Y., Graf, R. J., Hansen, R. O., Ogawa, K. and Tsu, H., 1985, *Curie Point depths of the Island of Kyushu and Surrounding Areas, Japan*, Geophysics, 53: 481-494.

Oldenburg, D. W., 1974, *The inversion and interpretation of gravity anomalies*, Geophysics, 39: 526-536.

Pal, P. C., Khurana, K. K. and Unnikrishnan, P., 1979, *Two examples of spectral approach to source depth estimation in gravity and magnetics*, Pure and Applied Geophysics, 117: 772-783.

Parker, A. J., Fanning, C. M. and Flint, R. B., 1981, *Archaean to Middle Proterozoic geology of the southern Gawler Craton, South Australia. Excursion guide*, South Australian Department of Mines and Energy report 81/91 (unpublished).

Compiled by A. J. Parker, 1986, *Geological excursions of the Adelaide Geosyncline, Gawler Craton and Broken Hill Regions*, Eighth Australian Geological Convention (February).

Parker, A. J., 1990, *Gawler Craton and Stuart Shelf - regional geology and mineralisation*, In Geology of the Mineral Deposits of Australia and Papua New Guinea, 999-1008.

Parker, R. L., 1973, *The rapid calculation of potential anomalies*, Geophys. J. Roy. Astr. Soc., 31: 447-455.

Parker, R. L. and Huestis, S., 1972, *Inversion of magnetic anomalies in the presence of topography*, J. Geophys. Res., 79: 1587-1593.

Paterson, N. R. and Faessler, C. W., 1957, *Determination of body parameters of a magnetic inclined dyke*, SEG meeting, November, Dallas, Texas.

Pedersen, L. B., 1977, *Interpretation of potential field data-A generalized inverse approach*, Geophysics Prospecting, 25: 199-230.

Peters, L. J., 1949, *The Direct approach to magnetic interpretation and its practical application*, Geophysics, 14: 290-320.

Pilkington, M. and Crossley, D. J., 1986, *Determination of crustal interface topography from potential fields*, Geophysics, 51: 1277-1284.

Powell, D. W., 1967, *Fitting observed profiles to a magnetized dyke or fault-step model*, Geophysical Prospecting, 15: 208-220.

Compiled by Preiss, W. V., 1987, *The Adelaide Geosyncline*, Bulletin 53 Geological Survey of South Australia.

Rajagopalan, S., 1989, *Aeromagnetic interpretation of the Kanmantoo Group, South Australia*, Ph.D. thesis of Adelaide University.

Rao, B. S. R. and Prakasa Rao, T. K. S., 1970, *Easy method of interpreting dike anomalies*, Pure and Applied Geophysics, 78: 32-36.

Rao, B. S. R., Prakasa Rao, T. K. S., Gopala Rao, D. and Kesavamani, M., 1972, *Derivatives and dike anomaly interpretation*, Pure and Applied Geophysics, 113: 625-633.

Rao, K. G. C. and Avasthi, D. N., 1973, *Analysis of the Fourier spectrum of the gravity effect due to two-dimensional triangular prism*, Geophysical Prospecting, 21: 526-542.

Rao, B. S. R., Radhakrishna Murthy and Bhaskara Rao,, 1978, *Interpretation of magnetic anomalies with Fourier transforms employing end corrections*, Journal of Geophysics, 44: 257-272.

Rasmussen, R. and Pedersen, L. B., 1979, *End corrections in potential field modeling*, Geophysical Prospecting, 27: 749-760.

Rayner, J. N., 1971, *An introduction to spectral analysis*, Pion Limited, 174 pages.

Reford, M. S. and Sumner, J. S., 1964, *Review Article: Aeromagnetics*, Geophysics, 29: 482-516.

Reford, M. S., 1978, *Magnnetic anomalies from the edge, dyke, and thin sheet, S.A.G.A.*, Aeromagnetic Course Manual.

Regan, R. D. and Hinze, W. J., 1976, *The effect of finite data length in the spectral analysis of ideal gravity anomalies*, Geophysics, 41: 44-55.

Reid, A. B., Allsop, J. M., Granser, H., Millett, A. J. and Somerton, I. W., 1990, *Magnetic interpretation in three dimensions using Euler deconvolution*, Geophysics, 55: 80-91.

Roy, A. A., 1962, *Ambiguity in geophysical interpretation*, Geophysics, 27: 1-90.

Rudd, E.A., 1961, *Surat basin, Queensland*, Australians J. Sci., 24: 85-87.

Ruotoistenmäki, T., 1983, *Depth estimation from potential field data using the Fourier amplitude spectrum*, Geoexploration, 21: 191-201.

Ruotoistenmäki, T., 1987, *Estimation of depth to potential field sources using the Fourier amplitude spectrum*, Geological Survey of Finland, Bulletin, 340: 1-84.

Seguin, M. K. and Sénéchal, J. N., 1979, *One-dimensional spectral analysis of aeromagnetic data from Temiscouata area and the western sector of the Gulf of St. Lawrence*, Geoploration, 17: 269-283.

Shackleford, P. R. J., 1978, *The determination of crust structure in the Adelaide Geosyncline using quarry blasts as seismic sources*, M.Sc. thesis, Department of Physics, University of Adelaide.

Shackleford, P. R. J. and Sutton, D. J., 1979, *Crustal structure in South Australia using quarry blasts*, D. Denham (Editor), Crust and Upper Mantle of Southwest Australia. Aust. Bur. Miner. Resour., Rec. 1979/2.

Shackleford, P. R. J. and Sutton, D. J., 1981, *A first interpretation of crustal structure in the Adelaide Geosyncline in South Australia using quarry blasts*, Journal of the Geological Society of Australia, 28: 491-500.

Shaw, H. R., 1985, *Links between magma-tectonic rate balances, platonism and volcanism*, J. Geophys. Res., 90: 11275-11288.

Shi, Z., 1991a, *An improved Naudy-based technique for estimating depth from magnetic profile*, Exploration Geophysics, 22: 357-362.

Shi, Z., 1991b, *Eyre Peninsula Pb-Zn preliminary drill target selection*, Report Book of South Australian Department of Mines and Energy, REPT BK No.91/38: 1-128.

Shi, Z. and Li, B., 1987, *Application of matched filtering method for processing gravity data*, Shiyou Wutan (Geophysical Prospecting of Petroleum), No. 3, Vol. 28: 85-97 (in Chinese).

Shuey, R. T., 1972, *Application of Hilbert transforms to magnetic profiles*, Geophysics, 37: 1043-1045.

Shuey, R. T. and Pasquale, A. S., 1973, *End corrections in magnetic profile interpretation*, Geophysics, 38: 507-512.

Shuey, R. T., Schellinger, D. K., Tripp, A. C. and Alley, L. B., 1977, *Curie depth determination from aeromagnetic spectra*, Geophysical Journal of the Royal Astronomical Society, 50: 75-101.

Skeels, D. C., 1947, *Ambiguity in gravity interpretation*, Geophysics, 12: 43-56.

Smellie, D. W., 1956, *Elementary approximations in aeromagnetic interpretation*, Geophysics, 21: 1021-1040.

Smith, R. B. and Christiansen, 1980, *Yellowstone Park as a window on the Earth's interior*, Sci. American, 242: 104-117.

Smith, R. B. and Braile, L. W., 1984, *Crustal structure and evolution of an explosive silicic volcanic system at Yellowstone National Park*, Boyd, F.R.(ed.), Explosive Volcanism: 96-109.

Smithson, S. B., 1971, *Densities of metamorphic rocks*, Geophysics, 36: 690-694.

Sokolov, K. P., 1956, *Geological interpretation of magnetic surveys*, Moscow, Gosgeoltechizdat, 127.

Solovyev, O. A., 1962, *Use of the frequency method for the determination of some parameters of magnetic bodies, Izv. Akad. Nauk*, SSSR, Sibirskoye Otedelniye Geologyai Geofizika, 2: 122-125.

Spector, A., 1968, *Spectral analysis of aeromagnetic data*, Ph.D. thesis, Department of Physics, University of Toronto.

Spector, A. and Bhattacharyya, B. K., 1966, *Energy density spectrum and autocorrelation function of anomalies due to simple magnetic models*, Geophysical Prospecting, 14: 242-272.

Spector, A. and Grant F. S., 1970, *Statistical models for interpreting aeromagnetic data*, Geophysics, 35: 293-302.

Spector, A. and Grant F. S., 1975, *Comments on "Two-dimensional power spectral analysis of aeromagnetic field"*, Geophysical Prospecting, 23: 391.

Sprigg, R. C., 1984, *Arkarroola-Mount Painter in the northern Flinders Ranges, S.A. the last billion years*, Lutheran Publishing House, Adelaide.

Stanley, J. M., 1977, *Simplified magnetic interpretation of the geological contact and thin dike*, Geophysics, 42: 1236-1240.

Stewart, I. C. F., 1971, *Seismic activity in 1969 associated with the eastern margin of the Adelaide Geosyncline*, Ibid., 18: 143-147.

Stewart, I. C. F., 1972, *Seismic interpretation of crustal structure in the Flinders - MT Lofty Ranges and gulf regions, South Australia*, Journal of the Geological Society of Australia, 19: 351-362.

Stewart, I. C. F., Mount, T. J., 1972, *Earthquake mechanisms in South Australia in relation to plate tectonics*, Journal of the Geological Society of Australia, 19: 41-52.

Stewart, I. C. F., Slade., A, and Sutton, D. J., 1972, *South Australia seismicity 1967-1971*, Journal of the Geological Society of Australia, 19: 441-452.

Stewart, K. P., 1992, *High temperature felsic volcanism and the role of mantle magmas in Proterozoic crustal growth: The Gawler Range Volcanic Province unpublished*, Ph.D. thesis of Adelaide University.

Strakhov, V. N., 1964a, *The smoothing of observed strengths of potential fields*, Bull. Acad. Sci. USSR, Geophys. Ser. (English trans.), 10: 897-904.

Strakhov, V. N., 1964b, *The smoothing of observed strengths of potential fields*, Bull. Acad. Sci. USSR, Geophys. Ser. (English trans.), 11: 986-995.

Subrahmanyam, C. and Verma, R. K., 1981, *Densities and magnetic susceptibilities of Precambrian rocks of different metamorphic grade (southern India shield)*, J. Geophys., 49: 101-107.

Sutton, D. J. and Whitte, R. E., 1968, *The seismicity of South Australia*, Journal of the Geological Society of Australia, 15: 25-32.

Syberg, F. J. R., 1972, *A Fourier method for the regional-residual problem of potential field*, Geophysical Prospecting, 20: 47-75.

Talwani, M., 1965, *Computation with the help of a digital computer of magnetic anomalies caused by bodies of arbitrary shape*, Geophysics, 30: 797-817.

Talwani, M., 1973, *Computer usage in the computation of gravity anomalies.*, B. Alder (Editor), Methods in Computational Physics, 13: 343-389.

Talwani, M. and Ewing, M., 1960, *Rapid computation of gravitational attraction of three-dimensional bodies of arbitrary shape*, Geophysics, 25: 203-225.

Talwani, M. and Heirtzler, J., 1964, *Computation of magnetic anomalies caused by two-dimensional structures of arbitrary shape*, In: Computers in Mineral Industries, Part 1, Stanford University. Publ. Geol. Sci., 9: 464-480.

Tanner, J. G., 1967, *An automated method of gravity interpretation*, Geophys. J. R. Astr. Soc., 13: 339-347.

Thompson, D. T., 1982, *Euldph: A new technique for making computer-assisted depth estimations from magnetic data*, Geophysics, 47: 31-37.

Treitel, S., Clément, W. G. and Kaul, R. K., 1971, *The spectral determination of depth to buried magnetic basement rocks*, Geophys. J. R. Astr. Soc. 24: 415-428.

Tsay, L. J., 1975, *The use of Fourier series method in upward continuation with new improvements*, Geophysical Prospecting, 23: 28-41.

Tselentis, G. A., Drakopoulos, J. and Dimitriadis, K., 1988, *A spectral approach Moho depths estimation from gravity measurements in Epirus (NW Greece)*, Journal of Physical Earth, 36: 255-266.

Tsuboi, C., 1937, *The deflections of the vertical, the undulation of the geoid, and gravity anomalies*, Bulletin of the Earthquake Research Institute. Tokyo Imperial University, 15: 650-653.

Tsuboi, C., 1938, *A simple method of approximately determining the thickness of the isostatic earth's crust*, Bulletin of the Earthquake Research Institute. Tokyo Imperial University, 16: 285-287.

Tsuboi, C., 1939, *Relation between the gravity anomalies and the corresponding subterranean mass distribution (III)*, Bulletin of the Earthquake Research Institute. Tokyo Imperial University, 17: 351-384.

Tsuboi, C. and Fuchida, T., 1937, *Relations between gravity values and corresponding subterranean mass distribution*, Bulletin of the Earthquake Research Institute. Tokyo Imperial University, 15: 636-649.

Tsuboi, C. and Fuchida, T., 1938, *Relations between gravity anomalies and the corresponding subterrene mass distribution-II*, Bulletin of the Earthquake Research Institute. Tokyo Imperial University, 16: 273-284.

Turner, A. R., 1975, *The petrology of the Eastern Gawler Ranges Volcanic Complex*, Bulletin 45, Geological Survey of South Australia.

Vacquier, V., Steenland, N. C., Henderson, R. G. and Zietz, I., 1951, *Interpretation of aeromagnetic maps*, Geol. Soc. Amer., Mem. 47: 151.

Watkins, J. S., 1964, *Basement depths from widely spaced aeromagnetic profiles in Kansas and Nebraska*, Geophysics, 26: 80-86.

Wellman, P. and Greenhalgh, S. A., 1988, *Flinders/Mount Lofty Ranges, South Australia; their uplift, erosion and relationship to crystal structure*, Trans. R. Soc. Aust. 112 (1): 11-19.

Werner, S., 1953, *Interpretation of magnetic anomalies at sheet-like bodies*, Stockholm, Sveriges Geologiska undersok, Ser. C.C. Arsbok, 43.

Whitaker, A., Wellman, P., Reith, H. and Cuneen, P., 1987, *The use of gravity and magnetic surveys in mapping greenstone terrane near Kalgoorlie, Western Australia*, Exploration Geophysics, 18: 371-380.

White, R. E., 1969, *Seismic phases recorded in South Australia and their relation to crust structure*, Geophysical Journal of the Royal Astronomical Society, 17: 249-261.

Wiebe, R. A., 1992, *Basaltic replenishments into a floored granitic magma chamber: the Cadillac Mountain Grannite, Coastal Maine (abstract)*, Eos Trans AGU, 73 (14), Spring Meeting Suppl.: 347.

Wiggin, R. A., 1972, *The general linear inverse problem: Implication of surface waves and free oscillations for earth structure*, Rev. Geophys. and Space Phys., 10: 251-285.

Wolff, J. A., Worner, G. and Blank, S., 1990, *Gradients in physical parameters in zoned felsic magna bodies: implications for evolution and eruptive withdrawal*, J. Volcannol. Geotherm. Res., 43: 37-55.

Wuenschel, P. C., Treitel, S., Flinn, E. A., Keller, G. V. and Pickett, G. R., 1969, *Geophysical research and progress in exploration, 1965-1968*, Geophysics, 34: 145-154.

Xia, J. and Sprowl, D. R., 1992, *Inversion of potential-field data by iterative forward modeling in the wavenumber domain*, Geophysics, 57: 126-130.